	⊷∧103 o	A	16H VEL PR 79	J BRAU	IC CO JET NUT ISCH! #	(SE 500	RCE LC: PER≠ C	.ATIOU R GLIE	AND REI	MOIŤDUC D-TOD)~-ETC • TASK S-3003/	6	TC ()
	1 ° 6	1 1 1 1 1	•										
								zλ					
* # 3	údù	2 °			7					À	i		
					-						>		
								1,		1	,		

	
	PHOTOGRAPH THIS SHEET
AD A 1 0 3 6 7 1	LEVEL General Electric Co. Cincinnati OH INVENTORY Asceraft Engine Group High Velocity Jet Noise Source Location and Reduction Task G. Noise Absternant Nozzle Design Guide. Task G. Noise Absternant Nozzle Design Guide. Rept. No. R79AEG 202 Contract DOT-0s-30034 Apr. 79 FAA-RD 76-79-G DISTRIBUTION STATEMENT A Approved for public release; Distribution Unlimited
	DISTRIBUTION STATEMENT
ACCESSION FOR	
NTIS GRAAI DTIC TAB UNANNOUNCED JUSTIFICATION BY DISTRIBUTION / AVAILABILITY COI	
A	AND/OR SPECIAL DATE ACCESSIONED
DISTRIBU	TION STAMP See also Task 6, Supplement, AD H194298.
	DATE RECEIVED IN DTIC PHOTOGRAPH THIS SHEET AND RETURN TO DTIC-DDA-2

DTIC FORM 70A

DOCUMENT PROCESSING SHEET

HIGH VELOCITY JET NOISE SOURCE LOCATION AND REDUCTION TASK 6 - NOISE ABATEMENT NOZZLE DESIGN GUIDE

TECHNICAL CONTRIBUTORS:

J. Brausch W.S. Clapper

W.S. Clapper P.R. Gliebe

R. Lee R. Whittaker

R. Mani

R.E. Motsinger

J. Schloemer

A. Sieckman

E.J. Stringas

J. Wolf

GENERAL ELECTRIC COMPANY AIRCRAFT ENGINE GROUP CINCINNATI, OHIO 45215



APRIL 1979

FINAL REPORT '

Document is available to the U.S. public through the National Technical Information Service, Springfield, Virginia 22161.

Prepared for

U.S. DEPARTMENT OF TRANSPORTATION
FEDERAL AVIATION ADMINISTRATION
Systems Research & Development Service
Washington, D.C. 20590

81 8 25 084

NOTICE

The contents of this report reflect the views of the General Electric Company which is responsible for the facts and the accuracy of the data presented herein. The contents do not necessarily reflect the official views or policy of the Department of Transportation. This report does not constitute a standard, specification or regulation.

1. Report No. PAA-RD-76-79, VI	2. Government Acce	esion No.	3. Recipient's Catalog	No.
4. Title and Subtitle HIGH VELOCITY JET NOISE SOURCE	LOCATION AND RED	UCTION, TASK 6 -	5. Report Date April, 19	179
Noise Abatement Nozzle Design G	outlon, new o	6. Performing Organiz	zation Code	
7. Author(s) J. Brausch, W.S. Clapper, R.E. Motsinger, J. Schloemer, A. R. Whittaker, J. Wolf (E.J. Stri	Sieckman, E.J. S	Stringas,	8. Performing Organiz R79AEG302	
9. Performing Organization Name and Address General Electric Company			10, Work Unit No,	
Group Advanced Engineering Divi	sion		11. Contract or Grant	No.
Aircraft Engine Group Cincinnati, Ohio 45215			DOT-OS-30	034
12. Sponsoring Agency Name and Address			12. Type of Report an Task 6 Fi	d Period Covered
U.S. Department of Transportation	n			- Aug 1978
Federal Aviation Administration			14. Sponsoring Agency	Code
Systems Research and Development Washington, D.C. 20590	Service		ARD-550	
vestigation of Suppression Princip Aeroacoustic Effects; Task 6 - Noi grams: Engineering Correlation (M Model (M*G*B) for Nozzles of Arbit 16. Abstract Quantitative and qualitative guida able to high jet velocity engines The fundamentals of jet noise mech provided. Techniques are presente mechanical design impact on engine mission in the course of maintaini acoustic performance and installat Guidelines to minimize exhaust sys and to combine other functional opincluded. Two independent, acoustic-predicti	se Abatement Noz *\$) Jet Noise Pr rary Shape. R.S nce is provided and/or supersoni anisms are revie d for estimating installation, a ng acceptable si ion penalties ma tem size consist erations with no on methods were	zle Design Guide; Ta ediction Method and . Zuckerman, Program in selecting noise a c cruise vehicles, twed, and basic, quan suppressor acoustic nd how various suppr deline and community be evaluated based ent with flow and suzzle flow area and edeveloped to perform	sk 6 Supplement - Unified Aeroacous Monitor. batement nozzle do meet specific ratitative, design se and aerodynamic essor designs impensive levels. A on empirical corpersonic-expansio xpansion control	computer Pro- tic Prediction esigns, applic- equirements. guide tools are performance, act aircraft erodynamic and relations. n requirements hardware are enctions. An
empirical model, supplemented by g is provided. The model covers a w of the acoustic characteristics of jet-noise-prediction method is mor modeled but provides more details. An aircraft-engine/suppressor inte	ide range of noz a given suppres e restricted in of the aerodynam	zle geometries and p sor nozzle design. terms of nozzle geom ic flow field and th	rovides quantitat A complementary, etries which an b e component acous	ive estimates theoretical, e properly tic mechanisms.
sion level, thrust coefficient, an considered when evaluating a given allows the use of a smaller engine achieve a predetermined noise goal	suppressor desi , relative to it	gn. In general, inc	orporation of a s	uppressor
17. Key Words (Suggested by Author(s))		18. Distribution Statemen	t	
Jet Noise, Suppression, In-Flight Abatement Nozzles, Ejectors, Aerod ance, Suppressor Base Pressure, Su and Size, Acoustic-Scaling and Dis Studies, Aircraft/Engine/Suppresso	ynamic Perform- ppressor Weight tance, Mission	through the M	vailable to the U ational Technical agfield, Virginia	Information
19. Security Classif. (of this report)	20. Security Classif.	(of this page)	21. No. of Pages	22. Price*

*For sale by the National Technical Information Service, Springfield, Virginia 22151

(I)

Unclassified

METRIC CONVERSION FACTORS

	į	• •	: # \$ Ē	3 3 3	8 2	‡ ደ ୫ ፪ ፫ ፮	*	
c Mossures] -	e constant	foot y ands miles	square inches square yads square miles	ounces pounés short tons	fleid ounces piets quents galtons cubic fest cubic yests	Fabrusheit sumperature	8 9 9 9 9 9 9 9 9 9 9 9 9 9 9 9 9 9 9 9
rsions from Matri	Maltiply by LENGTH	9.0	3.3 1.1 0.6 AREA	6.16 1.2 2, 2.5 MASS (weight)	0.036 2.2 1.1 VOLUME	0.03 7.06 9.26 36 1.3	TEMPERATURE (exect) 8/8 (then and 32)	8 0 0 0 0 0 0 0 0 0 0 0 0 0 0 0 0 0 0 0
Approximata Conversions from Matric Mossures	When You Knew	milimatera	meters meters k-iometers	square continues s square meters square titlemeters hectures (10,000 m²)	grame kilograms somes (1000 kg)	militiers liters liters cubic meters cubic meters	TEMI Celsius temperature	0 02- 00- 00- 00- 00- 00- 00- 00- 00- 00-
	Sympo	ē ŧ	i e e 5	î î î î	a 2 -	īī	ي ،	
2 23	E E E	6 ¢ 61				· · / ·		
) • 11 11	 		- 		hilatahaha	2 	1.1.1.1.1.1.1.1.1.1.1.1.1.1.1.1.1.1.1.	1 inches
	State		5 5 e 5	ት ንጉች 2	• Z -	₹ ₹ ₹	. Te Te - \$	9: 286,
Mesures	To Find		Contimeters Contimeters meters kilometers	Square contineters square meders square meders square bidemeders hecteres	grant ki lograns tomes			tebles, see NGS likec. Pu
Appresimente Conversions to Metric	Maniph II	LEBGTN	2.00 de 4.00 de	6.5 6.5 6.2 6.2 6.4	25 0.46 0.5 VOLUME	* * * * * * * * * * * * * * * * * * *	0.03 0.76 TEMPERATURE (02001)	adheracting 32) 32) and more detailed 32) Cassing No. C. 3. 10.296
Appresiment Con	- 1. ·	l	1111		1 1 1 1 1 1 1 1 1 1 1 1 1 1 1 1 1 1 1		cubic feet cubic yards	temperature sedenting temperature 22) 1 n 1 2.54 temachin). For other exert conventions and more detailed tables, see MSS May. Publ. 286, Units of Regime and Research. Price 12.25, 3D Cassing No. C13.10.286.
								! į



PREFACE

This report describes the work performed under Task 6 of the DOT/FAA High Velocity Jet Noise Source Location and Reduction Program (Contract DOT-OS-30034). The objectives of the contract were:

- Investigation of the aerodynamic and acoustic mechanisms, including scaling effects, of various jet noise suppressors.
- Analytical and experimental studies of the acoustic source distribution in such suppressors including identification of source location, nature and strength, and noise reduction potential.
- Investigation of in-flight effects on the aerodynamic and acoustic performance of these suppressors.

The results of these investigations led to the preparation of this design guide report for predicting the overall characteristics of suppressor concepts from models to full-scale and static to in-flight conditions, as well as quantitative and qualitative predictions of the phenomena involved.

The work effort in this program was organized under the following major tasks, each of which is reported in a separate Final Report:

- Task 1 -- Activation of Facilities and Validation of Source Location Techniques
- Task 2 -- Theoretical Developments and Basic Experiments
- Task 3 -- Experimental Investigation of Suppression Principles
- Task 4 -- Development and Evaluation of Techniques for In-flight Investigation
- Task 5 -- Investigation of In-flight Aeroacoustic Effects on Suppressed Exhausts
- Task 6 -- Preparation of Noise Abatement Nozzle Design Guide Report

Task 1 was an investigative and survey effort designed to identify acoustic facilities and test methods best suited to jet noise studies. Task 2 was a theoretical effort complemented by theory verification experiments which extended across the entire contract period of performance. Task 3 represented a substantial contract effort to gather various test data on a wide range of high velocity jet nozzle suppressors. These data, intended to help identify several "optimum" nozzles for in-flight testing under Task 5, provided an extensive high quality data bank useful to preparation of this Task 6 design guide as well as to future studies.



Task 4 was similar to Task 1, except that it dealt with the specific test facility requirements, measurements techniques, and analytical methods necessary to evaluate the in-flight noise characteristics of simple and complex suppressor nozzles. This effort provided the capability to conduct the free-jet, "flight" effects program of Task 5.

Task 6, the subject of the present report (FAA-RD-76-79, VI), embodies the salient results of Tasks 2, 3, 4, and 5, combines them with other contractor results, and arranges them in such a faminion as to permit acoustic and performance prediction of future, high-speed-engine, suppressor installation.

TABLE OF CONTENTS

Section			Page
1.0	SUMA	MARY	1
2.0	INTE	RODUCTION	6
3.0	PREI	LIMINARY NOISE ABATEMENT NOZZLE SELECTION	9
	3.1	Introduction	9
	3.2	Baseline and Suppressor Nozzles	11
	3.3	Preliminary Selection Process	17
		3.3.1 Suppressor Selection 3.3.2 Examples Utilizing the Selection Process	17 45
	3.4	Mechanical and Installation Considerations	45
4.0	ACOU	JSTIC DESIGN OF JET NOISE SUPPRESSORS	54
	4.1	Engineering Correlation Noise Prediction Method	54
		4.1.1 Ranges of Applicability for the Basic	54
		Method and Accuracy 4.1.2 M*S Generated Trend Data	63
		4.1.2.1 Cycle Parameters 4.1.2.2 Geometric Parameters 4.1.2.3 Comments	69 79 100
	4.2	Guides for Good Design Practices	100
		4.2.1 Introduction 4.2.2 Summary - Design Considerations	100 105
	4.3	M*S Computer Program Example Cases	106
5.0	AERO	DOWNAMIC PERFORMANCE OF JET NOISE SUPPRESSORS	107
	5.1	Background	107
	5 2	Acredomenta Dayformana of Multituba Naralas	107

TABLE OF CONTENTS (Continued)

Section			Page
		5.2.1 Introduction	108
		5.2.2 Performance Estimation Methodology	108
		5.2.2.1 Tube Internal Losses	108
		5.2.2.2 Base Pressure Correlation (Static)	111
		5.2.2.3 External Flow (Bare Suppressor)	111
		5.2.2.4 Ejector Performance	116
		5.2.2.5 Example Performance Prediction	116
	5.3	Aerodynamic Performance of Multichute/Spoke Plug Nozzles	116
		5.3.1 Introduction	116
		5.3.2 Performance Estimation Methodology	120
		5.3.2.1 Bare Suppressor	120
		5.3.2.2 Ejectors	130
		5.3.2.3 Example of Performance Prediction	130
6.0	MECH	HANICAL DESIGN CONSIDERATIONS	133
	6.1	Mechanical Suppressor Effects	133
		6.1.1 Exhaust Temperature Limit	133
		6.1.2 Suppressed Performance	133
		6.1.3 Suppressor-Stowed Performance	136
	6.2	Weight, Complexity, and Cost Implications of Jet Noise Suppressors	138
	6.3	Typical Suppressor Installations	146
7.0	CONC	CLUDING REMARKS	151
8.0	RECO	DMMENDATIONS	152
APPENDIX	A -	Fundamentals of Jet Noise Mechanisms	153
APPENDIX	В -	Multielement and Two-Stage-Ejector Nozzle Background I formation	i 188
APPENDIX	c -	Examples of Preliminary Design Selection Methods	200
APPENDIX	D -	Effect of Simulated Flight Upon Noise From High Velocity Jet Nozzles	210

TABLE OF CONTENTS (Concluded)

Section		Page
APPENDIX E -	Predicted Acoustic Design Trands from M*S Method	261
APPENDIX F -	Guide to Good-Acoustic-Design Practices	280
APPENDIX G ~	Engineering Correlation (M*S) Computer Program Example Cases	332
APPENDIX H -	Effect of Exhaust Gas Temperature on Suppressor Aerodynamic Performance	362
APPENDIX I -	Multielement Nozzle Aerodynamic Performance Data	373
APPENDIX J -	Predicted Multielement Nozzle Aerodynamic Performance	433
APPENDIX K -	Aircraft-Engine/Suppressor Integration Assessment by Use of Range as a Merit Factor	443
APPENDIX L -	NOMENCIATURE	453
	REFERENCES	459

LIST OF ILLUSTRATIONS

Figure		Page
1-1.	Roadmap for Utilizing Preliminary Suppressor Selection Section 3.0.	3
2-1.	Task 6 Basic Design Guide Roadmap.	8
3-1.	Determination of Sideline EPNL for a Typical Suppressor.	10
3-2.	Influence of Balanced Field Length on Noise Characteristics of a Typical Baseline and Suppressor Nozzle.	12
3-3.	Typical Baseline Exhaust Nozzles.	14
3-4.	Typical Bare Suppressor Nozzles.	15
3-5.	Typical Suppressor-Plus-Ejector Nozzles.	16
3-6.	Schematics of Typical Single-Flow Suppressor Nozzles for Afterburning Systems.	18
3-7.	Photographs of Typical Single-Flow Suppressor Nozzles for Afterburning Systems.	19
3-8.	Procedure Roadmap.	20
3-9.	Methodology for Baseline and Suppressed Exhaust System Jet Noise Prediction Procedure.	21
3-10.	Nomograph for Obtaining V from P_T/P_0 and T_T .	23
3-11.	Nomograph for Obtaining Mass-Averaged Flow Conditions of Dual-Flow Nozzles.	24
3⊢12.	Variable-Density Index Determination.	25
3-13.	Variation of Density Correction Factor with Jet Velocity, Temperature, and Pressure Ratio.	26
3-14.	Normalized, Static, Peak PNL for Baseline Conical Nozzle.	27
3-15.	Actual Overhead-Distance Correction.	29
3-16.	Peak-Noise-Angle Flight Effects for Baseline Conical Nozzle.	30
3-17.	Flight Peak PNL Conversion to EPNL for Baseline Conical Nozzle.	31

Figure		Page
3-18.	Typical, Static, Peak PNL Suppression Characteristics.	33
3-19.	Generalized Flight Performance and Static Suppression Levels.	34
3-20.	Variation of Flight Gross Thrust Coefficient with Nozzle Pressure Ratio for Multielement Single-Flow and Dual-Flow Nozzles.	35
3-21.	Effect of Ejectors on Multielement Plug, 'Single-Flow Nozzle Flight Aerodynamics Performance.	36
3-22.	Variation of Multitube Flight Gross Thrust Coefficient Due to Nozzle Pressure Ratio and Ejector Installation.	37
3-23.	Suppressor Scale Factor Determination at Constant Installed Thrust.	39
3-24.	Multielement/Plug-Nozzle Static Suppressor Dropoff Characteristics.	41
3-25.	Static Acoustic Effectiveness of Treated Ejectors on Multielement/Plug Nozzles.	42
3-26.	Multitube (Alone) Nozzle Static Suppression Dropoff Characteristics.	43
3- 27 .	Static Acoustic Effectiveness of Treated Ejectors on Multitube Nozzles.	44
3-28.	Peak-Angle Flight Effects Correction for Single-Flow Suppressor Systems Re: Conical Baseline Nozzle.	46
3-29.	Flight Peak PNL - EPNL Sensitivity to Suppressors Re: Conical Baseline Nozzle.	47
3-30.	Typical Single-Flow and Dual-Flow Exhaust System Schematics.	48
3-31.	Relationship Between Nozzle Exit Radius, Throat Area, and Suppressor Area Ratio.	50
3-32.	Typical Single-Flow Suppressor Weight and Geometry Effects.	52
3-33	Tunical Dual-Flow Suppressor Weight and Geometry Effects	53

Figure		Page
4-1.	Typical Turbojet Operating Line Conditions.	55
4-2.	Nozzle Types Included in the Correlation.	56
4-3.	Typical Multitube-Suppressor Configuration.	65
4-4.	Typical Multichute-Suppressor Configuration.	66
4-5.	Typical Dual-Flow, Multichute-Suppressor Configuration.	67
4-6.	Static Predicted PNL Trends with Jet Velocity.	70
4-7.	In-Flight Predicted PNL Trends with Jet Velocity.	71
4-8.	In-Flight Predicted EPNL Trends with Jet Velocity.	72
4-9.	Effect of Cycle Conditions on Conical Nozzle EPNL.	73
4-10.	Effect of Cycle Conditions on Conical Nozzle Peak PNL.	74
4-11.	Effect of Cycle Conditions on Conical Nozzle PNL at $\theta_i = 50^{\circ}$.	75
4-12.	Effect of Cycle Conditions on Suppressor EPNL.	76
4-13.	Effects of Cycle Conditions on Suppressor Peak PNL.	77
4-14.	Effects of Cycle Conditions on Suppressor PNL at $\theta_1 = 50^{\circ}$.	78
4-15.	Conical Nozzle Size and Distance Study, Supersonic.	80
4-16.	Conical Nozzle Size and Distance Study, Subsonic.	81
4-17.	Thirty-Chute Suppressor Nozzle Size and Distance Study, Supersonic, $AR = 1.5$.	82
4-18.	Thirty-Chute Suppressor Nozzle Size and Distance Study, Subsonic, AR ≈ 1.5.	83
4-19.	Thirty-Chute Suppressor Nozzle Size and Distance Study, Supersonic, AR = 3.0.	84
4-20.	Thirty-Chute Suppressor Nozzle Size and Distance Study,	85

Figure		Page
4-21.	Effect of Flight on Conical Nozzle Peak PNL.	86
4-22.	Effect of Flight on Conical Nozzle EPNL.	87
4-23.	Effect of Flight Velocity on Suppression.	88
4-24.	Typical Predicted Static Suppression Trends, Single Flow.	90
4-25.	Typical Predicted Flight Peak PNL Suppression Trends, Single Flow.	91
4-26.	Typical Predicted Flight EPNL Suppression Trends, Single Flow.	92
4-27.	Typical Predicted Static Suppression Trends, Dual Flow.	93
4-28.	Typical Predicted Flight Peak PNL Suppression Trends, Dual Flow.	94
4-29.	Typical Predicted Flight EPNL Suppression Trends, Dual Flow.	95
4-30.	Suppression Trends.	96
4-31.	Typical Predicted Static Hard-Wall-Ejector Suppressor Trends.	97
4-32.	Typical Predicted Flight Hard-Wall-Ejector Peak PNL Suppression Trends.	98
4-33.	Typical Predicted Flight Hard-Wall-Ejector EPNL Suppression Trends.	99
4-34.	Effect of Suppressor Radius Ratio on Suppression.	101
4-35.	Effect of Outer Tube-Row Cant on Suppression.	102
4-36.	Treated Ejector Suppression Trends.	103
5-1.	Multitube Suppressor Nozzle Schematic.	109
5-2.	Multitube Suppressor Internal Performance.	110
5-3.	Correlation of Multitube Nozzle Baseplate Pressures.	112
5-4.	Mean Baseplate Pressure (Static).	113

Figure		Page
5-5.	Conversion Factor (K) for Base Pressure.	114
5-6.	Base Multitube Nozzle Lapse Rate.	115
5-7.	Gross Thrust Coefficient as a Function of Effective Inlet Area, Setback, and EAR/NAR Ratio.	.117
5-8.	Effect of Ejector on Performance.	118
5-9.	Multichute/Spoke Nozzle.	119
5-10	Definition of Geomtric Parameters.	121
5-11 .	Inner-Flow Peak Thrust Coefficient as a Function of External Area Ratio.	128
5-12	Multichute/Ejector Performance.	131
6-1.	Mechanically Suppressed, Single-Stream Exhaust Nozzle Schematic.	134
6-2.	Coannular, Unsuppressed, Dual-Stream Exhaust Nozzle Schematic.	134
6-3.	Mechanically Suppressed-Outer-Stream Exhaust System Schematic.	135
6-4.	Ejector-Shrouded Exhaust System Schematic.	135
6-5.	Typical Mechanical-Suppressor/Plug-Nozzle Elements.	137
6-6.	Multitube/Plug-Nozzle Concept Schematic.	137
6-7.	Multitube/Two-Stage-Ejector Nozzle Schematic.	139
6-8.	Reverser Integration in Single-Stream Plug Nozzle.	139
6 -9 .	Relationship Between Nozzle Exit Radius, Throat Area, and Area Ratio.	141
6-10	. Single-Stream Exhaust Nozzle Weight Increase Versus Radius Ratio and Suppressor Area Ratio.	143
6-11	Dual-Stream Exhaust Nozzle Weight Increase Versus Radius	144

Figure		Page
6-12.	Exhaust System Weight Versus Engine Airflow.	145
6-13.	Exhaust System Complexity Rating.	148
6-14.	Unsuppressed Coannular Exhaust System.	149
6-15.	Dual-Flow Exhaust System with Mechanically Suppressed Outer Flow.	149
6-16.	Mechanically Suppressed Single-Flow Exhaust System.	150
A-1.	Comparison Experimental and Predicted Jet Noise Directivity Patterns for Cold Jets.	157
A-2.	Comparison of Experimental and Predicted Density Exponent for Heated Jets at 90° to the Inlet.	160
A-3.	Comparison of Predicted Shock Noise with Measured Conical Nozzle Spectra.	162
A-4.	Parallel Shear-Flow Model of the Jet.	166
A-5.	Primary Components of a Conical-Nozzle Shock-Cell Noise Spectrum, $D_h = D_{eq}$.	169
A-6 .	Rrimary Components of a Noncircular-Nozzle Shock-Cell Noise Spectrum, $\mathbf{D_h} < \mathbf{D_{eq}}$.	170
A-7.	Shock-Associated Noise Spectrum, 1.5-in. Diameter Conical Nozzle.	171
A-8.	Shock-Associated Noise Spectrum, 6:1 Aspect Ratio Rectangular Jet.	172
A-9.	Generalized Volume Element Model.	174
A-10.	Relative Contributions of Noise Mechanisms to PNL Directivity.	178
A-11.	Relative Contributions of Noise Mechanisms to SPL Spectra at $\theta_1 = 50^{\circ}$.	179
A-12.	Relative Contributions of Noise Mechanisms to SPL. Spectra at $\theta_4 = 90^{\circ}$.	180

Figure		Page
A-13.	Relative Contributions of Noise Mechanisms to SPL Spectra at $\theta_i = 130^{\circ}$.	181
A-14.	PNL Suppression Composition for a 36-Chute, AR = 2.0, Suppressor Nozzle.	183
A-15.	Comparison of Predicted, Basic, Turbulent-Mixing Noise Spectra at $\theta_i = 90^{\circ}$ for a Conical and a 36-Chute Nozzle.	185
A-16.	Modification of Basic Mixing-Noise PNL by Convective Amplification and Fluid Shielding.	186
B-1.	Schematics of Typical Single-Flow Suppressor Nozzles for Afterburning Systems.	189
B-2.	Photographs of Typical Single-Flow Suppressor Nozzles for Afterburning Systems.	190
В-3.	Summary of Characteristics for Typical, Single-Flow, Afterburning Turbojet Suppressors.	191
B-4.	Comparison of Static Performance and Suppression Levels.	192
B-5.	Typical, Static, Peak PNL Suppression Characteristics.	196
B-6.	Generalized Flight Performance and Static Suppression Levels.	198
D-1.	Conical Nozzle Spectra at $\theta_i = 60^{\circ}$.	215
D-2.	Free-Jet Flight Effects on Low-Frequency Jet-Mixing Noise, $\theta_i = 40^{\circ}$.	216
D-3.	Free-Jet Flight Effects on Low-Frequency Jet-Mixing Noise, $\theta_1 = 50^{\circ}$.	217
D-4.	Free-Jet Flight Effects on Low-Frequency Jet-Mixing Noise, $\theta_i = 60^{\circ}$.	218
D-5.	Free-Jet Flight Effects on Low-Frequency Jet-Mixing Noise, $\theta_1 = 70^{\circ}$.	219
D-6.	Free-Jet Flight Effects on Low-Frequency Jet-Mixing Noise, $\theta_1 = 80^{\circ}$.	220
D-7.	Free-Jet Flight Effects on Low-Frequency Jet-Mixing Noise, 9 = 90°.	221

Figure		<u>Page</u>
D-8.	Free-Jet Flight Effects on Low-Frequency Jet-Mixing Noise, $\theta_i = 100^{\circ}$.	222
D-9.	Free-Jet Flight Effects on Low-Frequency Jet-Mixing Noise, $\theta_i = 110^{\circ}$.	223
D-10.	Free-Jet Flight Effects on Low-Frequency Jet-Mixing Noise, $\theta_i = 120^{\circ}$.	224
D-11.	Free-Jet Flight Effects on Low-Frequency Jet-Mixing Noise, $\theta_i = 130^{\circ}$.	225
D-12.	Free-Jet Flight Effects on Low-Frequency Jet-Mixing Noise, $\theta_i = 140^{\circ}$.	226
D-13.	Free-Jet Flight Effects on Low-Frequency Jet-Mixing Noise, $\theta_i = 150^{\circ}$.	227
D-14.	Effect of Jet Velocity on High-Frequency Noise at $\theta_1 = 90^{\circ}$ ($V_0 = 300$ ft/sec).	229
D-15.	Effect of Outer Stream Pressure Ratio on High-Frequency Noise at $\theta_i = 90^{\circ}$ ($V_0 = 300$ ft/sec).	230
D-16.	Effect of Exhaust Total Temperature on High-Frequency Noise at $\theta_i = 90^{\circ}$ (for $V_0 = 300$ ft/sec).	231
D-17.	Free-Jet Flight Effects on High-Frequency Noise Versus Angle ($V_0 = 300 \text{ ft/sec}$, Doppler Shift Removed).	232
D-18.	High-Frequency SPL as a Function of Shock-Noise Parameter (B), Model 51, 2500 Hz.	233
D-19.	High-Frequency SPL as a Function of Shock-Noise Parameter (B), Model 52, 5000 Hz.	234
D-20.	Free-Jet Flight Effects on High-Frequency Noise Versus Angle for Subsonic Exhaust Velocity ($V_0 = 150$ ft/sec, Doppler Shift Removed).	235
D-21.	Free-Jet Flight Effects on High-Frequency Noise Versus Angle for Subsonic Exhaust Velocity ($V_0 = 300 \text{ ft/sec}$, Doppler Shift Removed).	236

Figure		Page
D-22.	Free-Jet Flight Effects on High-Frequency Noise Versus Angle for Subsonic Exhaust Velocity ($V_0 = 400 \text{ ft/sec}$, Doppler Shift Removed).	237
D-23.	Free-Jet Flight Effects on Shock Noise ($V_0 = 150 \text{ ft/sec}$, Doppler Shift Removed).	238
D-24.	Free-Jet Flight Effects on Shock Noise ($V_0 = 275 \text{ ft/sec}$, Doppler Shift Removed).	239
D-25.	Free-Jet Flight Effects on Shock Noise ($V_0 = 300 \text{ ft/sec}$, Doppler Shift Removed).	240
D-26.	Free-Jet Flight Effects on Shock Noise ($V_0 = 400 \text{ ft/sec}$, Doppler Shift Removed).	241
D-27.	Increase in Shock Noise Due to Flight - Conical Nozzles.	242
D-28.	Increase in Shock Noise Due to Flight - Suppressor Nozzles.	243
D-29.	Free-Jet Flight Effects on High-Frequency Noise Versus Angle for Supersonic Exhaust Velocity ($V_0 = 300 \text{ ft/sec}$, Doppler Shift Removed).	245
D-30.	Free-Jet Flight Effects for Various Pressure Ratios from Subsonic to Supersonic Case ($V_0 = 300$ ft/sec, Doppler Shift Removed).	246
D-31.	Comparison of Predicted Premerged and Shock Noise in the Aft Quadrant.	247
D-32.	Correlation Between Measured and Predicted Maximum Perceived Noise Level (PNL), All Nozzles - Static.	251
D-33.	Correlation Between Measured and Predicted Maximum Perceived Noise Level (PNL), All Nozzles - Flight.	252
D-34.	Correlation Between Measured and Predicted Effective Perceived Noise Level (EPNL), All Nozzles - Static.	253
D-35.	Correlation Between Measured and Predicted Effective Perceived Noise Level (EPNL), All Nozzles - Flight.	254
D-36.	Predicted and Measured Static Noise from the Conical Nozzle on the Bertin Aerotrain.	255

Figure		Page
D-37.	Predicted and Measured Moving-Frame Noise from the Conical Nozzle on the Bertin Aerotrain.	256
D-38.	Predicted and Measured Static Noise from the 104-Tube Nozzle on the Bertin Aerotrain.	257
D=39.	Predicted and Measured Moving-Frame Noise from the 104- Tube Nozzle on the Bertin Aerotrain.	258
D-40.	Relative Velocity Index $m(\theta_i)$.	259
E-1.	Effect of Cycle Conditions on Conical Nozzle Noise at High Jet Velocity.	262
E-2.	Effect of Cycle Conditions on Conical Nozzle Noise at Medium Jet Velocity.	263
E-3.	Effect of Cycle Conditions on Conical Nozzle Noise at Low Jet Velocity.	264
E-4.	Effect of Area on Conical Nozzle Noise at High Jet Velocity.	265
E-5.	Effect of Area on Conical Nozzle Noise at Low Jet Velocity.	266
E-6.	Effect of Flight on Conical Nozzle Noise at High Jet Velocity.	267
E-7.	Effect of Flight on Conical Nozzle Noise at Low Jet Velocity.	268
E-8.	Effect of Flight on Suppressor Nozzle Noise at High Jet Velocity.	269
E-9.	Effect of Flight on Suppressor Nozzle Noise at Low Jet Velocity.	270
E-10.	Effect of Area Ratio on Multichute Nozzle Noise at High Jet Velocity.	271
E-11.	Effect of Area Ratio on Multichute Nozzle Noise at Low Jet Velocity.	272
E-12.	Effect of Element Number on Multichute Nozzle Noise at High Jet Velocity.	273
E-13.	Effect of Element Number on Multichute Nozzle Noise at Low Jet Velocity.	274

Figure		Page
E-14 .	Effect of Area Ratio on Multitube Nozzle Noise at High Jet Velocity.	275
E-15.	Effect of Area Ratio on Multitube Nozzle Noise at Low Jet Velocity.	276
E -16.	Effect of Element Number on Multitube Nozzle Noise at High Jet Velocity.	277
E-17.	Effect of Element Number on Multitube Nozzle Noise at Low Jet Velocity.	278
E-18.	Effect of Ejectors on Multitube Nozzle Noise.	279
F-1.	Definition of Multielement Suppressor Geometric Parameters.	281
F-2.	L_{t}/D_{t} Variation Effects on 85-Tube Configuration at Various Jet Velocities.	286
F −3.	Effect of Tube Length Variation on 37- and 61-Tube Configurations.	287
F-4.	Effect of Tube Length Variation on 72-Tube Nozzle Vs. 72-Hole Baseplate.	288
F-5.	Effect of Tube Length Variation on 97-Tube Nozzle Vs. 97-Hole Baseplate.	290
F-6.	Effect of Tube Length Variation on 97-Tube Vs. 97-Hole Nozzles.	291
F-7.	Effect of Tube Length Variation on 104-Tube Vs. 104-Hole Nozzles.	292
F-8.	Effect of Area Ratio on Sideline PNL and Spectra.	294
F-9.	Effect of Tube Spacing Uniformity on 85- and 89-Hole Nozzles.	296
7-10.	Effect of Tube Spacing Uniformity on Boeing 37-Tube Radial and Close-Packed Arrays.	298
F-11.	Effect of Tube-Size Equity and Spacing Uniformity on	299

Figure		Page
F-12.	Effect of Tube-Size Equity on 97-Tube Nozzle with 1.415-and 1.764-in. Diameter Center Holes.	300
F-13.	Effect of Tube-Size Equity on 97-Hole Nozzle with 1.415-in. Round and Greatrex Center Holes.	302
F-14.	Effect of Tube-Size Equity on Full Tube Array Vs. Tubes with Center Hole.	303
F-15.	Effect of Tube-Size Equity on Full Tube Array Vs. Tubes with Varying Center Annulus.	304
F-16.	Effect of 30° and 60° Tube Exit Plane Stagger Relative to Coplanar.	306
F-17.	Effect of Tube Exit Plane Stagger on Peak Noise Angle Spectra Comparisons at Four Jet Velocities.	307
F-18.	Effect of 30° Tube Exit Plane Stagger Relative to Coplanar.	308
F-19.	Effect of 30° and 60° Tube Base Plane Stagger Relative to Flat.	309
F-20.	Effect of Tube Base Plane Stagger on Peak Noise Angle Spectra Comparisons at Four Jet Velocities.	311
F-21.	Effect of Tube Canting on 37-Tube Configuration.	312
F-22.	Effect of Tube Canting: Boeing 61-Tube, Canted-Outer-Row Configuration.	314
F-23.	Effect of Tube End Planform: 37-Tube Greatrex Relative to Plain-Round and Convergent Ends.	316
F-24.	Effect of Tube End Planform on Peak Noise Angle Spectra Changes for Greatrex Relative to Plain Round.	317
F-25.	Effect of Tube End Planform on 85-Tube Greatrex Relative to Plain Round.	319
F-26.	Effect of Tube End Planform on 85-Tube Greatrex Spectra	320

Figure		Page
F-27.	Effect of Trapezoidal and Circular Tube End Planform on $97 ext{-} ext{Hole}$ Baseplates.	321
F-28.	Effect of Element-Type Variation.	323
F-29.	Spectral Comparison of 32-Element Spoke/Chute Configurations.	325
F-30.	Effect of Chute/Spoke Exit Planform Variation.	326
F-31.	Effect of Chute/Spoke Exit Plane Cant Variation.	328
H-1.	Measured Thrust Coefficients for Multitube Suppressor with Ejector.	364
H-2.	Core Plug Pressure Distributions for Tube Suppressor with Ejector, Hot Vs. Cold Flow.	365
н-3.	Fan Plug Pressure Distributions for Tube Suppressor with Ejector, Hot Vs. Cold Flow.	366
H-4.	Ejector Shroud Pressure Distributions for Tube Suppressor with Ejector, Hot Vs. Cold Flow.	367
Н-5.	Integrated Pressure Forces for Tube Suppressor with Ejector, Hot vs. Cold Flow.	368
Н-6.	Base-Pressure and Surface-Temperature Distributions for 32-Chute Suppressor.	369
H-7.	Model and Engine Static Performance Comparisons.	370
н-8.	Conical Nozzle Performance for Exhaust Temperatures of 530° and 1800° R.	371
н-9.	Effect of the Ratio of Specific Heats of the Jet upon the Initial Inclination of the Jet Boundary, $M_{\hat{J}}=1.00$.	372
I-1.	Multitube Suppressor Nozzle Schematic.	375
1-2.	Schematic of Single Tube.	377
1-3.	Tube Entrance Losses.	378
I-4.	Effect of Tube Lergth on Performance.	379
I-5.	Typical Convergent Nozzle Expansion Loss Characteristics.	380

Figure		Page
I-6.	Cfg_{int} as a Function of Tube Length, Tube Number, and Pressure Ratio.	382
I-7.	Multihole Nozzle Hardware used in Parametric Investigations of Area Ratio and Hole Number.	383
I-8.	Effect of Area Ratio on Mean Baseplate Pressure Ratio for 85-Hole Nozzles.	384
I-9.	Trend in Baseplate Drag with Suppressor Area Ratio.	386
I-10.	Multihole Nozzle Hardware used in Parametric Investigation of Hole Number.	387
I-11.	Effect of Hole Number on Mean Baseplate Pressure Ratio.	388
I-12.	Effect of Tube Convergence on Distance Between Tubes.	389
I-13.	Illustration of Elliptical Tubes.	390
I-14.	Effect of Elliptical Convergent Versus Nonconvergent Tubes on Nozzle Performance.	391
I-15.	Multitube Nozzle Arrays.	392
I-16.	Effect of Tube Array on Base Pressure and Drag.	393
I-17.	Effect of Tube Length on Baseplate Pressure.	394
I-18.	Baseplate and Tube Exit Plane Stagger Variations for 72-Tube Nozzle Configurations.	395
I-19.	Effect of Baseplate and Tube Exit Plane Stagger on Mean Baseplate Pressure Ratio.	397
I-20.	Effect of Velocity on the Performance of Suppressors without Ejector.	399
I-21.	Effect of Velocity on Base Drag as a Percentage of Ideal Thrust for NAR 3.3 Suppressor with Various Numbers of Tubes.	400
I-22.	Ejector Inlet Area AA and As,	401
I-23.	Comparison of Performance and Lapse Rate and Crossover Velocity for 37-Tube, NAR 3.3, Close-Packed Array, Bare	404

Figure		Page
I-24.	Thirty-Seven-Tube, NAR = 3.3, Close-Packed, EAR = 3.1 Ejector with Zero Setback.	405
1-25.	Performance Carpets for Different Setbacks of the EAR 3.1 Ejector on a 37-Tube, NAR 3.3, Close-Packed Array with Tube Length Equal 0.5 D $_{\rm eq}$.	407
I-26.	Schematic of Performance Versus Setback.	408
I-27.	Multichute/Spoke Plug Nozzle Schematic.	410
I-28.	Effects of Flow Area Ratio and Inner Nozzle Pressure Ratio on Wind-On, Uninstalled Performance.	416
1-29.	Effects of Plug Suppressor Exit Angle and Chute Depth on Wind-On, Uninstalled Performance.	417
I-30.	Effects of Plug Suppressor Exit Angle and Chute Depth on Wind-On, Uninstalled Performance.	418
I-31.	Effects of Plug Suppressor Exit Angle and Chute Depth on Wind-On, Uninstalled Performance.	419
I-32.	Effects of Chute Depth and Chute Width Ratio (Chute Number) on Wind-On, Uninstalled Performance.	420
I-33.	Effects of Chute Depth and Outer-Duct Radius Ratio on Wind-On, Uninstalled Performance.	421
I-34.	Effects of Chute Depth and Mach Number on Wind-On, Uninstalled Performance.	422
I-35.	Suppressor Nozzles with Two Types of Ejector.	424
I-36.	External Flow Effects on Performance of Chute-Type Suppressor Nozzles.	425
I-37.	Schematic of Annular Plug Nozzle and Multispoke/Plug Nozzles of 32 and 64 Elements.	427
I-38.	Multispoke/Plug Nozzles of 32 and 64 Elements on J85	428

Figure		<u>Page</u>
I-39.	Baseline and Multispoke/Plug Nozzle Static and Flyby Performance (Reference 24).	429
I-40.	Schematic and Photograph of 104-Tube Nozzle or J85 Engine Installed on F-106B Aircraft (Reference 40).	430
I-41.	Schematic and Photograph of 104-Tube Nozzle with Acoustically Treated Shroud on J85 Engine Installed on F-106B Aircraft (Reference 40).	431
I-42.	Nozzle Gross Thrust Coefficient of 104-Tube Suppressor - Static and Flyby (Reference 20).	432
J-1.	Thirty-Seven-Tube, 2.75 Area Ratio, Close-Packed Array with Elliptical, Convergent Tubes.	434
K-1.	Case Study Methodology.	444
K-2,	Suppressor Nozzles Used for Aircraft Integration Case Studies.	446
К-3.	Summary of Aerodynamic Performance Characteristics.	449
K-4.	Summary of Noise and Range Characteristics.	451

LIST OF TABLES

Table		Page
3-1.	Baseline and Suppressor Nozzle Families.	13
3-2.	Nominal Gross Thrust Coefficients for Baseline Type Nozzles.	38
4-1.	Linear Regression Analysis Results for Suppressor Nozzles.	60
4-2.	Predicted Versus Measured Simulated Flight by Free Jet.	61
4-3.	Data Base Used in Flight-Effects Correlation.	62
4-4.	Definition of Multielement Suppressor Geometric Parameters Included in the M*S Model.	64
4-5.	Cycle Conditions Used in Determining Trend Curves.	€8
5-1.	Applicability Range of Parameters in GE Chute/Spoke Data Base.	132
B-1.	Nominal Gross Thrust Coefficients for Baseline Type Nozzles.	197
D-1.	Data Base Used in Flight-Effects Correlation.	212
D-2.	Cycle Conditions.	213
D-3.	Tabulation of Jet-Mixing Noise Relative-Velocity Indices.	214
D-4.	Predictions Versus Measurements, Static.	248
D-5.	Predictions Versus Measurements, Simulated Flight by Free Jet.	249
G-1.	Determination of Conical Nozzle Noise at Takeoff.	333
G-2.	Determination of Conical Nozzle Noise at Cutback.	333
G-3.	Determination of Suppressor Noise at Takeoff.	334
G-4.	Determination of Suppressor Noise at Cutback.	335
1-1.	Comparison of Nozzle Thrust Losses at a Pressure Ratio of 3.0.	412
I-2.	Range of Parameters in GE Chute/Spoke Data Base.	414
1-3.	Summary of Trend Curve Variables.	415
K-1.	Summary of Engine Cycle Conditions.	445
K-2.	Typical Exhaust System Weight Increase Due to	450

1.0 SUMMARY

The High Velocity Jet Noise Source Location and Reduction Program was conceived to bring analytical and experimental knowledge to bear on understanding the fundamentals of jet noise, for simple and complex suppressor nozzles, and to develop design methods. The objective of this noise abatement nozzle design guide is to provide quantitative and qualitative guidance to engineers and designers in selecting the most appropriate suppressor installation, in terms of noise reduction and thrust loss, to meet a specific requirement. The design guide is assembled in a form suitable for rapid retrieval of pertinent design information for static and in-flight, model and full-scale engine, suppressor nozzles.

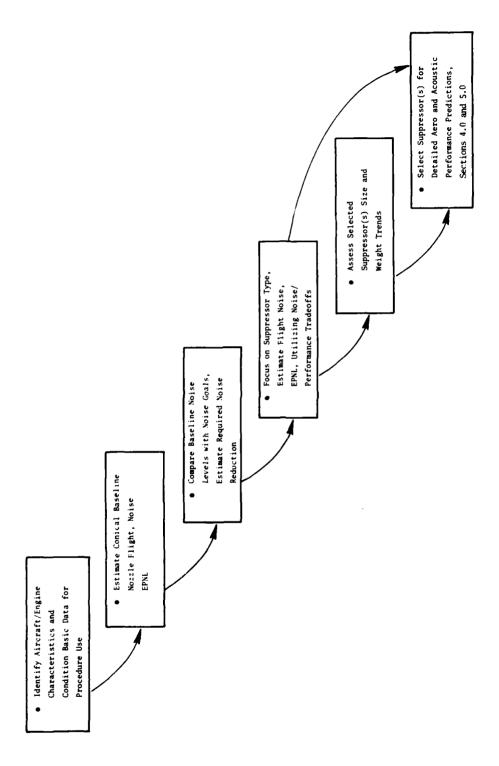
Techniques are presented for estimating jet noise suppressor acoustics and aerodynamic performance, assessing mechanical design impact on engine installation, and evaluating the effect, on a given aircraft mission, of maintaining acceptable sideline and community noise levels.

A central part of any design guide must consist of a performanceprediction method. In this case, both aerodynamic and acoustic performance must be determined, and installation penalties must be evaluated. Methods are presented herein to assess each of these items based on empirical correlations and experience obtained from this and other programs. Two independent acoustic-prediction methods were developed in the current program. Both methods are included in this design guide because they perform complementary functions. The empirical jet noise prediction method (referred to as M*S, designating the last-name initials of the authors, i.e., Motsinger and Sieckman) is developed from engineering correlation of nozzle noise data and is the prime acoustic design technique in this design guide. It covers a wide range of nozzle geometries and provides quantitative estimates of the acoustic characteristics of a given suppressor nozzle design (Section 4.0). The theoretical jet noise prediction (referred to as M*G*B, designating the lastname initials of the authors, i.e., Mani, Gliebe and Balsa) is developed from fundamental analytical methods and is restricted in terms of the nozzle geometries which can be properly modeled. The M*G*B method (as described in Appendix A), however, provides a more detailed picture of the jet plume aerodynamic flow field and the component acoustic mechanisms; therefore, it provides added insight as well as a means of evolving and possible optimizing a given design concept based on theoretical considerations before undertaking a test program.

The first three sections (3.0, 4.0, and 5.0) constitute the basic quantitative design guide tools. Section 3.0, "Preliminary Noise Abatement Nozzle Selection," provides a means of selecting suppressor types which should be subjected to the recommended acoustic and aerodynamic performance prediction techniques of Sections 4.0 and 5.0. (Appendix B presents background information on multielement and two-stage ejector nozzles.) The procedure presented in Section 3.0 represents the gross initial steps of an aircraft-engine/suppressor integration study

(not including mission analysis). Figure 1-1 is a roadmap of the entire preliminary selection procedure presented in Section 3.0. The procedure consists of an empirical correlation method based on peak static perceived noise level (PNL) to effective perceived noise level (EPNL). It adjusts a baseline nozzle (reference conical) to account for the degradation in nozzle thrust due to the installation of a suppressor. The procedure in Section 3.0 requires input on the type of engine cycle, aircraft and flight details (i.e., number of engines, altitude, and aircraft speed), noisemonitoring locations, and the noise goals. The noise goals permit use of static peak-noise suppression (PNL's) versus percent gross thrust coefficient (Cfg) flight loss plots to focus on the magnitude of the noise reduction required in order to suggest a preliminary selection of the type of suppressor. This information is then adjusted as required to facilitate in-flight jet noise estimates. The nozzle selection procedure concludes with several charts and figures which permit an assessment of size and weight based on studies conducted on typical suppressor systems (single and dual flow). Three example cases are presented in Appendix C to demonstrate the selection procedure in step-by-step fashion.

Section 4.0 presents acoustic design guidance, and Section 5.0 presents aerodynamic design guidance. Reasonable estimates of the flight performance characteristics for a given noise abatement nozzle may be obtained from these two sections. The empirical jet noise prediction method (M*S) is presented in Section 4.0. It was developed by correlating static, flight, and simulated flight (free jet) data from this program and other published sources. The data were correlated on the basis of engineering principles and physical parameters. The M*S method is applicable to unsuppressed, single-flow, conical nozzles as well as multitube and multichute, single- or double-flow suppressors with or without ejectors. Conceptually, the M*S method is founded upon round nozzle jet noise characteristics (empirically correlated, conical nozzle data). Multielement nozzles are considered as assemblies of conical nozzle sources from which the air flows in discrete elements. The premerged and postmerged regions are then treated as separate sources with jet noise characteristics defined by conical nozzle plume behavior. A broadband shock-cell-noise treatment is included in the jet noise prediction and is modeled after that proposed by the "SAE/A21 Subcommittee on Jet Noise.' Flight effects (Appendix D) are imposed based on empirical, incremental corrections to the static sound pressure level (SPL) for each of the individual noise sources (premerged, postmerged, and shock). Input required to exercise the M*S prediction method includes: element type, element number, suppressor area and radius ratio, inner and outer area ratio (where applicable), chute/spoke element planform and cant angle, and plug diameter. The prediction accuracy for static conditions is estimated to be + 3.7 PNdB at 95% confidence level; the "flight" prediction accuracy, which is based on a much smaller data base, is estimated to be \pm 3.5 EPNdB at 95% confidence. Appendix E presents predicted acoustic design trends from the M*S method.



Roadmap for Utilizing Preliminary Suppressor Selection Section 3.0. Figure 1-1.

Section 4.0 also introduces the designer to the unified aeroacoustic jet noise prediction model (M*G*B), which is reviewed in Appendix A, and how it can be utilized as a design evaluation tool to study subtle tradeoffs between convective amplification and fluid shielding in the aft quadrant, between convective amplification and shock-noise reduction in the forward quadrant, and between reduced convection effects versus high frequency noise.

The basic M*S jet noise prediction model is supplemented by a discussion of guidelines to good design practice in Appendix F, based on actual experience in designing multielement suppressors, in order to assure that suppression predictions are realistic.

PNL directivity, EPNL, spectral plots, etc. are included to provide insight about how these characteristics are affected by nozzle operating conditions (nozzle pressure ratio, total temperature, and velocity), absolute nozzle size, and distance to the observer. A comprehensive series of trend curves in Section 4.0 and Appendix E includes unsuppressed (conical nozzle) and suppressed, single-and dual-flow configurations derived from exercising the M*S prediction model. Several engineering correlation (M*S) computer program examples are included in Appendix G.

The "Aerodynamic Performance of Jet Noise Suppressors," Section 5.0, addresses two basic multielement exhaust system concepts. These are the multitube suppressor concept and the multichute/spoke plug suppressor concept. This section is supplemented by trends of performance as a function of exhaust gas temperature in Appendix H, and of major geometric and aerodynamic variables in Appendix I, for each suppressor family. The intent is to provide the designer with a quantitative guide for the approaches to take in order to attain good nozzle performance.

Specific performance prediction procedures are outlined. In the case of multitube nozzles, design curves are presented which are based on correlations of scale-model test data with geometric nozzle parameters. The design curves address specific elements of overall performance such as tube internal thrust losses, baseplate drag, flight velocity effects, etc. Performance can be estimated over the full range from a simple bare suppressor at static conditions to the full complexity of a suppressor with ejector in flight.

A different technique is used for the multichute/spoke family of suppressors. Equations, rather than design curves, are used for the direct calculation of major thrust-loss elements. These equations were developed using a linear regression analysis technique. Within specified constraints, these equations can be used to calculate the performance of both single-flow and dual-flow multichute/spoke annular nozzles.



Very limited amounts of multichute/spoke-ejector, scale-model data exist. The available data were generalized to give the nozzle designer an indication of the level of performance to expect. Sample calculations are presented in Appendix J for a multitube nozzle and for a multichute nozzle. These are provided to illustrate each step of the performance estimation procedure.

Section 6.0 discusses mechanical design considerations and provides both a quantitative and qualitative assessment of how the use of a mechanical, retractable suppressor will affect the resultant size and weight of typical baseline engine/exhaust-nozzle systems. Included in the section are installation examples of how exhaust system configuration and size are affected by the jet noise suppression arrangement utilized. Also included are guidelines for designing an exhaust system to minimize the size, consistent with engine/exhaust weight flow and supersonic cruise expansion requirements, and to combine other functional operations with the nozzle discharge flow area and expansion control (e.g., nozzle area ratio) hardware. Increases in size, number of control systems, and number of components generally increase complexity. Sizing relationships for unsuppressed and suppressed, simple and dual-flow nozzles permit the designer to arrive at a representative maximum nozzle radius, given an engine cycle discharge area, for any combination of nozzle radius ratio and suppressor area ratio. Section 6.0 also shows that complexity (which in turn is indicative of system reliability) is related to the number of actuation systems required for a given exhaust system. Although the characteristic plots included in Section 6.0 are derived from specific suppressor/engine installations, they provide a first-order estimate in assessing how engine/exhaust system weight is affected by the suppressor aerodynamic performance and noise reduction characteristics.

To further assist the engineer/designer, this guide includes Appendices which reduce the need to refer to other documents. Appendix K is useful from a commercial supersonic aircraft-engine/suppressor viewpoint. It defines the steps of a generalized procedure for evaluating the impact of suppressor designs using range as a merit factor. Suppression level, thrust coefficient, and weight were identified as three variables (in order of importance) that must be considered when evaluating a given suppressor design. The assessment concludes that the addition of a suppressor to achieve a predetermined noise goal allows the use of a smaller engine than could be accomplished by using a conical nozzle and cutting back the throttle to obtain a lower jet velocity.

The aircraft designer will also find this guide helpful in evaluating configurations and determining the interrelationships among aircraft performance, engine integration, and community noise signatures for his particular application. Where the evaluation of an especially unique airframe/engine configuration is desired, the Task 2 Final Report (FAA-RD-76-79, II) presents an evaluation of several of these unique arrangements which may lend insight to any additional acoustic benefits resulting from aircraft installation variants.

Appendix L is a list of the nomenolature, symbols and abbreviations used in this document.



2.0 INTRODUCTION

Future reduction of the noise levels produced by high jet velocity powered aircraft will be very dependent upon progress made in reducing jet exhaust noise, particularly in the case of supersonic cruise aircraft which utilize advanced turbojet and low-bypass-ratio turbofan engine cycles.

Fundamental jet noise research from this program as well as other contractor effort has considerably expanded and extended aircraft-related jet noise understanding and data. This knowledge and data base will be useful in future suppressor-design efforts as well as in planning further research efforts.

This five-year program has extended the qualitative and quantitative understanding of supersonic jet noise generation and reduction. The noise-generation mechanisms of baseline nozzle (single round and dual-flow types) as well as complex configurations (suppressor nozzles) were subjected to theoretical analyses and to testing. Complex nozzle configurations, such as tubes, chutes in single- or dual-flow installations, etc., were found to exhibit adverse effects on aerodynamic performance by way of added base pressure drag - which is a strong function of base ventilation from entrained or induced flow and flight speed.

The intent of this program was to acquire the fundamental knowledge required to understand the phenomena of acoustic suppression, the effect of flight on suppression, and the thrust performance change attributable to suppressor concepts. The knowledge gained is used in this report to aid in the selection and design of practical noise abatement nozzles.

This report identifies the important design factors and develops quantitative descriptions of their relationship to the resultant flight-noise signature. The report consists of parametric charts, nomographs, formulas, etc. to enable the user to quickly relate important engine exhaust design parameters to noise. During the development of the prediction methods, great emphasis was placed on evolving a format that can be utilized in both the preliminary assessment and the detailed study phases. The extent to which detailed acoustic and aerodynamic prediction methods have been considered has been limited by the state-of-the-art information relating noise and thrust performance to suppressor configuration and by practical considerations of the accuracy requirement of the respective methods.

The report is arranged into four basic sections with eleven supporting appendices and includes:

- Section 3.0 Preliminary Noise Abatement Nozzle Selection
- Section 4.0 Acoustic Design of Jet Noise Suppressors
- Section 5.0 Aerodynamic Performance of Jet Noise Suppressors

- Section 6.0 Mechanical Design Considerations
- Appendix A through Appendix K.

As shown in Figure 2-1, sections 3.0 through 6.0 constitute the prime path to be utilized in predicting acoustic and aerodynamic performance as well as the mechanical design aspects of suppressor installations. The supplemental paths, Appendices A and F, provide added depth and understanding.

Appendix A allows diagnostic assessment of the preliminary suppressor(s), selected in Section 3.0, from the point of view of how the four noise-generation/emission mechanisms, evolved in the course of the Task 2 phase of the program, combine to yield the far-field noise and, more importantly, how the suppressor geometric design can be altered to exhibit a more favorable noise signature. Appendix F supplements the M*S technique and provides design experience which has been assembled either from a first-hand basis or through available literature. It is intended to be used as a guideline, in concert with the M*S model, to assure that basic suppressions are realized.

The basic flow of the design technique presented in Figure 2-1 leads to a particular configuration, on an isolated propulsion system basis, which satisfies the design requirements. It is recognized that unique airframe/engine installation variants may be an additional consideration in meeting requirements. These ancillary benefits should be evaluated, in addition to those determined from the techniques presented, because they enhance the acoustic performance of the configuration. These unique arrangements were studied as part of this overall program and are presented in the Task 2 Final Report (FAA-RD-76-79, II). The reader is urged to refer to this when evaluating installation variants of this type.

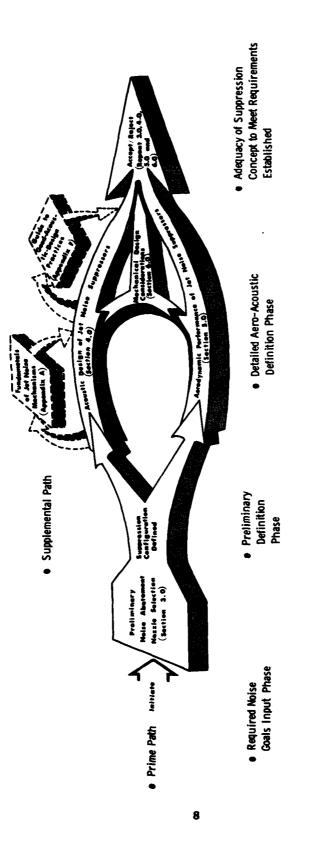


Figure 2-1. Task 6 Basic Design Guide Roadmap,

3.0 PRELIMINARY NOISE ABATEMENT NOZZLE SELECTION

3.1 INTRODUCTION

This Section provides information needed to establish suppression levels which can be achieved by an installed suppressor on turbojet and on over-extracted or inverted-flow turbofan engines applicable for AST aircraft. It is a short-cut noise-prediction technique for the exhaust nozzles of these engines, accounting for the noise-reduction characteristics and the associated aerodynamic performance. The results of this procedure are intended to be used to identify candidate nozzles and to delineate the extent of more detailed design studies to be conducted according to the procedures given in Sections 4.0, 5.0, and 6.0 (acoustic design, aerodynamic performance, and mechanical design, respectively) of this Guide. As a consequence of this procedure, for a given airframe the aircraft mission can be determined in terms of range versus EPNL for the particular nozzles of concern. Case studies conducted as part of this program show that the airport field length is an important variable in such a trade-off study.

As a brief example of such a case study (from Reference 1), the NASA Phase II AST aircraft and mission profiles were used to evaluate several advanced turbojet (ATJ) suppressor configurations over a range of takeoff-thrust conditions. The jet noise prediction procedure given in this Section was used to determine the flight noise levels for a full-span suppressor.

The steps involved in the procedure to account for the effects of performance loss associated with the suppressor, and for the flight-effects on the effective perceived noise level, are illustrated in Figure 3-1. These steps include: an adjustment from the baseline unsuppressed-nozzle curve (A) to the baseline or unsuppressed/suppressed nozzle curve (B) which accounts for the increased thrust required to overcome the degradation of performance introduced by the suppressor; a reduction in the noise level from curve (B) to the "interim" flight EPNL curve (C) to account for the suppressor static noise suppression; then, an adjustment from curve (C) to (D) to account for the flight effects upon the efficacy of the suppressor.

This procedure was augmented by concurrent assessment of the mechanical arrangement of the suppressors and of the associated weight increase of the basic nozzle; the combined effects of the performance decrement and weight increment of the engine then was determined in terms of the aircraft range. Baseline aircraft range, which already reflected the increased airflow size required to meet the required takeoff thrust, was modified to consider the impact of increasing the exhaust system weight due to the incorporation of a mechanical suppressor and the associated increase in exhaust system diameter which manifests itself into an increase in cruise afterbody drag or:

Total Range = RangeBaseline - \(\Delta \text{RangeWeight} \) - \(\Delta \text{RangeDiameter} \)

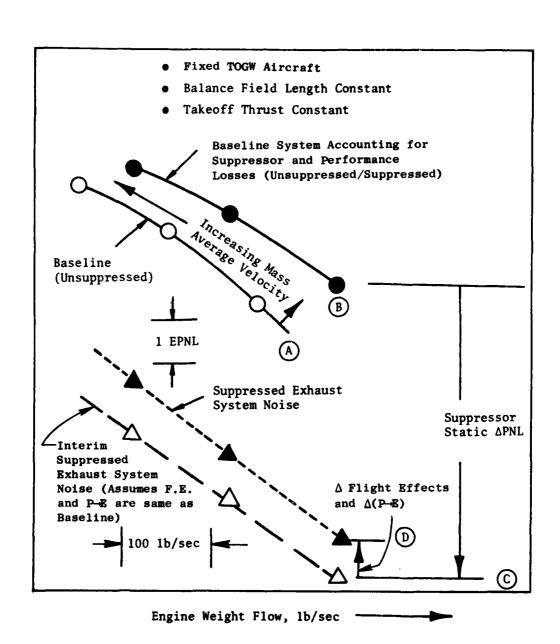


Figure 3-1. Determination of Sideline EPNL for a Typical Suppressor.

The results are summarized in Figure 3-2, for a typical advanced turbojet (single flow) engine, in terms of aircraft range versus "traded" FAR36 EPNL for two field lengths. More details of this example are available in Reference 1, but this summary of results illustrates the intended objective of this Manual.

The remaining portion of the Section includes:

- Definition and discussion of the various nozzle types, both unsuppressed and suppressed, which can be or have been candidates for high velocity jet noise abatement.
- Description of the preliminary suppressor-selection process including detailed charts, figures, and nomographs necessary to encompass the various engine-cycle parameters, thrust degradation of specific nozzles, suppressor potential, and rudimentary suppressor-weight assessments to ultimately arrive at an estimated flyover-noise level (EPNL). Examples of the use of this procedure are included in a stepeby-step fashion in Appendix C.
- Discussion of mechanical design and installation considerations involved in the application of the suppressors evolved in the preceding step.

3.2 BASELINE AND SUPPRESSOR NOZZLES

3.2.1 General Description of Nozzle Types

The types of nozzles useful for high-jet-velocity engines are listed in Table 3-1 and illustrated by schematics and photographs in Figures 3-3 through 3-7 as noted after each nozzle type in the Table.

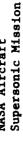
The baseline nozzles (Figure 3-3) include the so-called "conical" (Figure 3-3a) which is actually a converging-area nozzle with the throat at the discharge plane. The "annular plug" (Figure 3-3b) is a variation which, by means of the central plug, allows more control of the area variation and permits a converging/diverging area if desired. The conical and the annular-plug nozzle are both suitable for the single-flow turbojet (ATJ) or mixed-flow, variable-cycle engine (VCE). The "inverted flow, coannular plug" (Figure 3-3c) is an extension of the annular plug to the dual-flow (VCE) engine; in this manual, the dual-flow (VCE) engine cycle always has the higher velocity stream on the outer annular duct.

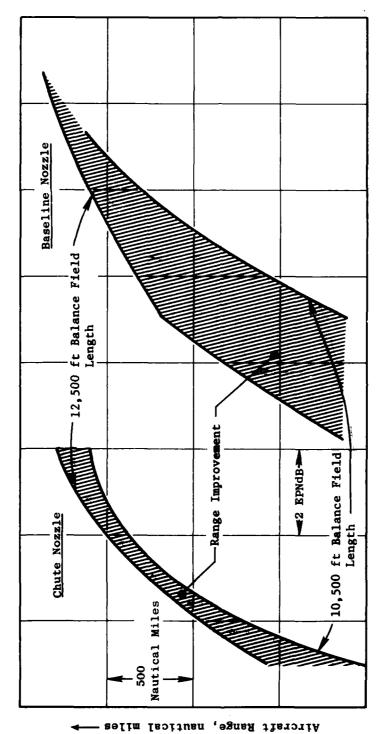
Typical suppressors applied to these baseline nozzles are illustrated in Figure 3-4. A multitube suppressor (Figure 3-4b) is applied to the "conical" nozzle; a multichute suppressor (Figure 3-4a) is applied to the annular-plug baseline nozzle; and a part-span (outer annulus only), multichute suppressor (Figure 3-4c) is applied to the inverted-flow, coannular-plug, baseline nozzle.

The addition of ejectors to these suppressor nozzles is illustrated in Figure 3-5.









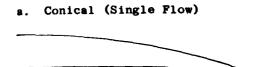
Traded EPNL --

Influence of Balanced Field Length on Noise Characteristics of a Typical Baseline and Suppressor Nozzle. Figure 3-2.

THE PERSON OF TH

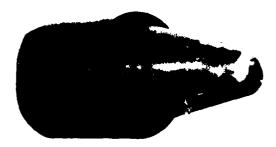
Table 3-1. Baseline and Suppressor Nozzle Families.

Туре	Illustrated in Figure:
Baseline	
 Conical Annular Plug Inverted-Flow, Coannular-Plug 	3-3a 3-3b 3-3c
Bare Suppressors	
 Full-Span, Multichute/Plug Full, Round, Multitube Part-Span, Multichute/Coannular-Plug 	3-4a 3-4b 3-4c
Suppressor Plus Ejector	
 Full-Span, Multichute/Plug Full, Round, Multitube Part-Span, Multichute/Coannular-Plug 	3-5a 3-5b 3-5c
Other	
 Includes SST Afterburning Exhaust Systems; i.e. Primary Tabs, Rods, Compressor Discharge and Secondary Flaps; Staged Ejector 	3-6 (Schematics) and 3-7 (Photographs)

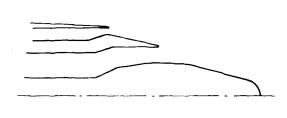




b. Annular Plug (Single Flow)



c. Inverted-Flow, Coannular Plug (Dual Flow)



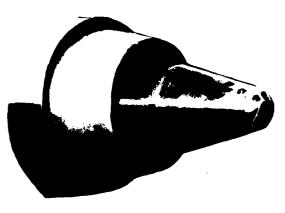
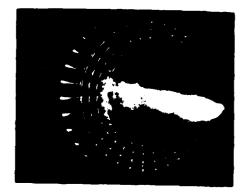


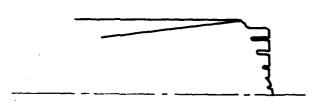
Figure 3-3. Typical Baseline Exhaust Nozzles.

a. Full-Span, Multichute/Plug (Single Flow)





b. Full, Round, Multitube (Single Flow)





c. Part-Span, Multichute/Coannular-Plug (Dual Flow)



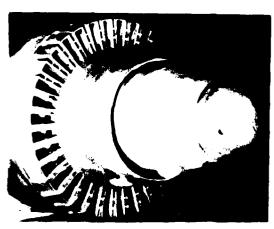
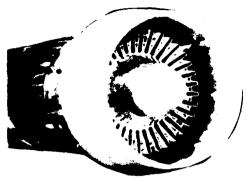


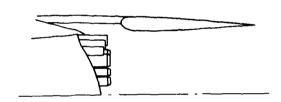
Figure 3-4. Typical Bare Suppressor Nozzles.

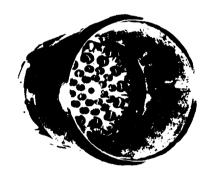
a. Full-Span, Multichute/Plug (Single Flow)



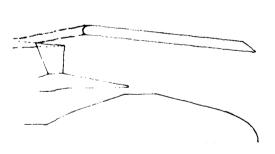


b. Full, Round, Multitube (Single Flow)





c. Part-Span, Multichute/Coannular-Plug (Dual Flow)



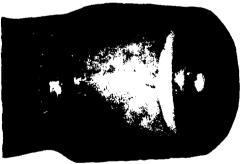


Figure 3-5. Typical Suppressor-Plus-Ejector Nozzles.

year of men and he is

In addition to these "conventional" suppressor nozzles, many concepts were investigated in the prior SST engine program which need to be mentioned for historical purposes (or, perhaps for stimulating innovative engineering in concepts yet to be invented). Examples are shown in Figure 3-6 and Figure 3-7. The original engine for the U.S./SST (Reference 2) was a fully augmented turbojet with a two-stage ejector nozzle. This basic, two-stage ejector nozzle was studied in depth to optimize the geometry for the best pumping characteristics to attain minimum jet noise. Suppressor programs evaluated simple primary-nozzle mechanical suppressors such as primary rods, tabs, and ventilated chutes. These were deployed within the basic, two-stage ejector-nozzle system and, indeed, provided nominal (small) jet-noise reductions. Other systems employing part of the secondary-nozzle reverser mechanism as secondary-flap suppressors were also investigated.

Appendix B reviews some of the noise/performance characteristics of afterburning-turbojet suppressor installations, representative of the U.S. supersonic transport program effort, and then discusses the multitube and multichute suppressors that have been under continuing development subsequently.

3.3 PRELIMINARY SELECTION PROCESS

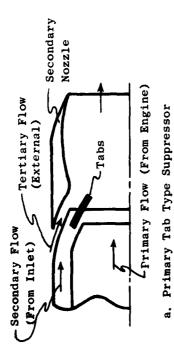
3.3.1 Suppressor Selection

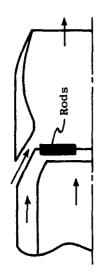
The intent of this section is to aid the user in selecting which suppressor type(s) to evaluate with the detailed acoustic and aerodynamic performanceprediction techniques of Sections 4.0 and 5.0. Although the preliminary selection process included herein is somewhat general, it is oriented to supersonic aircraft applications with attendant high jet-exhaust velocities. Once key engine and aircraft parameters are identified, the user can proceed to utilize the charts, tables, and figures to assess the noise reduction needed to attain a given noise goal. The procedure represents a rudimentary aircraft/engine integration study although it does not extend to the impact of different combinations of engine and suppressor systems on aircraft performance in terms of mission economics and range. Results from some of the aircraft-engine/suppressor integration studies conducted using the simulated flight results obtained in Task 5 of this program (Reference 3) are included in Appendix K to show the impact of various competing influences (noise, performance, suppressor mechanical-design complexity) on the aircraft as a complete system.

Figure 3-8 is a general road map of the entire selection/prediction procedure included herein. Figure 3-9 presents the details of the jet noise prediction methodology that is included for baseline and suppressed exhaust systems. This prediction procedure is derived from that utilized in the aircraft integration study of Task 3 and reported in Reference 1. The procedure can be simply defined as a peak static PNL to EPNL empirical correlation method. Where appropriate, the major element blocks include the pertinent figure and/or table number necessary to carry out the particular calculation step in Figure 3-9. The following paragraphs will summarize the figures and tables to follow using Figures 3-8 and 3-9 as guides.

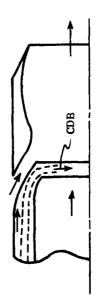
Preliminary identification of an engine cycle, some aircraft information (number of engines, altitude, and aircraft speed), noise-monitoring locations (sideline, community), and noise goals permit the user to estimate the magni-

(41





b. Primary Rod Type Suppressor



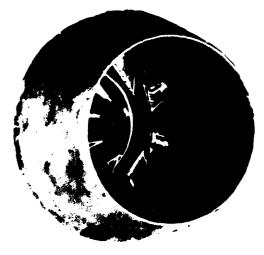
d. Secondary (Flap) Type Suppressor



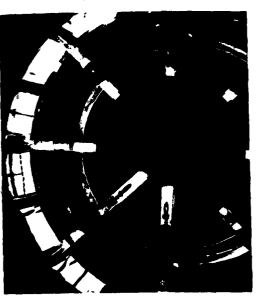
Compressor Discharge Bleed Type Suppressor

ပ

a. Primary Tab Type Suppressor



b. Primary Rod Type Suppressor



c. Compressor Discharge Bleed
Type Suppressor



d. Secondary (Flap) Type Suppressor



Figure 3-7. Photographs of Typical Single-Flow Suppressor Nozzles for Afterburning Systems.

THE STATE OF THE S

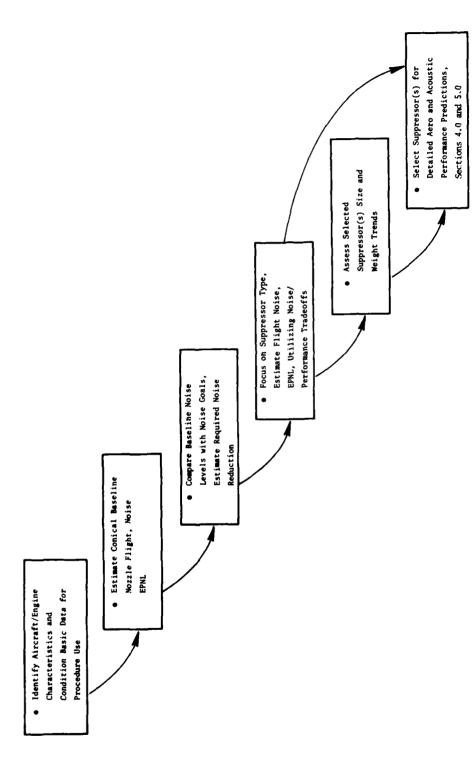


Figure 3-8. Procedure Roadmap.

44)

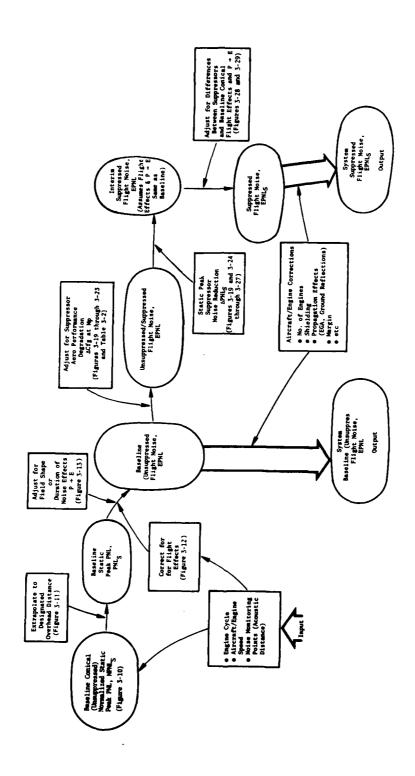


Figure 3-9. Methodology for Baseline and Suppressed Exhaust System Jet Noise Prediction Procedure.

(45)

tude of the noise reduction required as well as to make preliminary selection(s) of the type of suppressor(s) that could conceivably meet the specified noise goals. This information is then conditioned as required to facilitate the flight jet-noise estimates. A step-by-step description of the procedure follows:

Step 1 - The engine cycle parameters including fully expanded isentropic velocity (V), weight flow (W), and total temperature (T_T) are determined (for each stream in the case of a dual-flow cycle). In the event that only nozzle pressure ratio (PT/PO) and total temperature are available, Figure 3-10 can be utilized to obtain the individual jet stream velocities.

Step 2 - The ideal gross thrust, Fg, is obtained from:

•
$$Fg = \frac{W_1}{g} Z_V$$

for dual flow, where

$$z_v = v_i + v_o \beta$$

and

$$\beta = W_0/W_t$$

or Z_v can be obtained from Figure 3-11

•
$$Fg = \frac{WV}{g}$$
 for single flow

Step 3 - Calculate mass-averaged velocity, V_{ma} , and total temperature T_{Tma} , for dual flows from:

$$\bullet \qquad V_{\text{ma}} = \frac{V_{\underline{i}} + V_{\underline{o}}}{1 + \beta} \beta$$

$$\mathbf{T}_{\mathbf{T}_{\mathbf{ma}}} = \mathbf{T}_{\mathbf{T}_{\mathbf{i}}} + \mathbf{T}_{\mathbf{T}_{\mathbf{0}}} \boldsymbol{\beta}$$

Or read V_{ma} and $T_{\begin{subarray}{c} T_{ma} \end{subarray}}$ directly from Figure 3-11.

Step 4 - Use the mass-averaged velocity and total temperature from (3) to estimate the modified, normalized, density parameter 10 $\log (\rho_{\text{ma}}/\rho_0)^{\omega-1}$

• 10 log
$$(\rho_{\text{ma}}/\rho_0)^{\omega+1} = \left[10 \log (\rho_{\text{ma}}/\rho_0)^{\omega}\right] \frac{\omega-1}{m}$$

where wis the Hoch/Cocking (Reference 4) density exponent and is obtained from Figure 3-12, and 10 $\log (\rho_{\rm ma}/\rho_{\rm g})^{(0)}$ is read from Figure 3-13 at $\log V_{\rm ma}/A_{\rm O}$; $V_{\rm ma}$ is from Step 3.

Step 5 - Normalized (i.e. corrected for gross thrust and density ratio) static peak PNL (NPNL_s) at an overhead distance of 2128 ft is obtained from Figure 3-14 for the baseline conical nozzle. This curve was established from data in References 1, 5, 6, and 7.

46

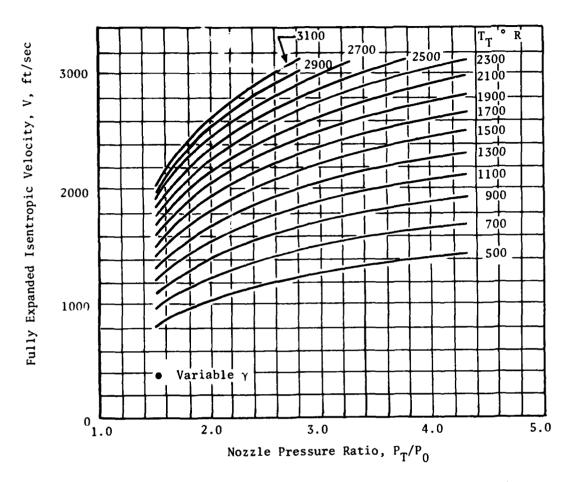


Figure 3-10. Nomograph for Obtaining V from P_T/P_0 and T_T .

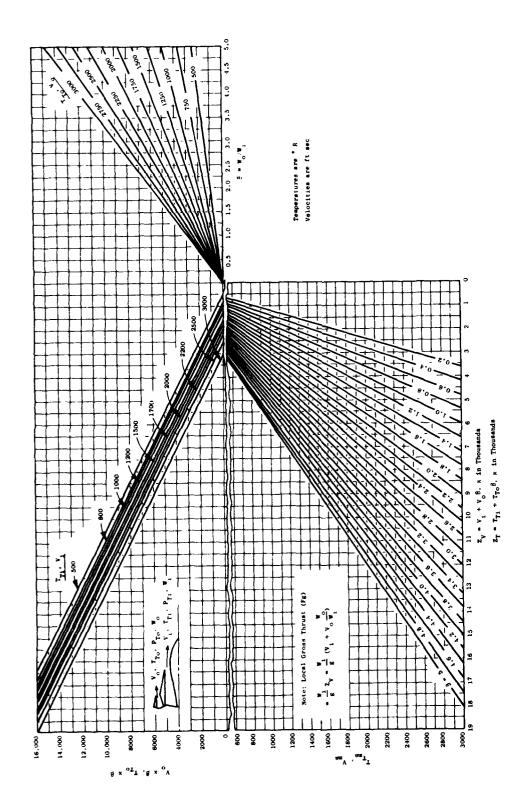


Figure 3-11, Nomograph for Obtaining Mass-Averaged Flow Conditions of Dual-Flow Nozzles.

(48)

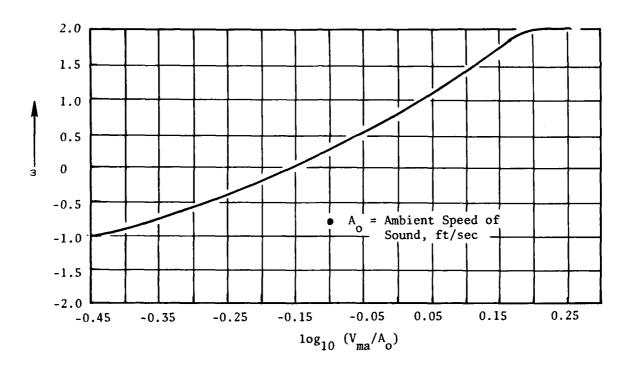
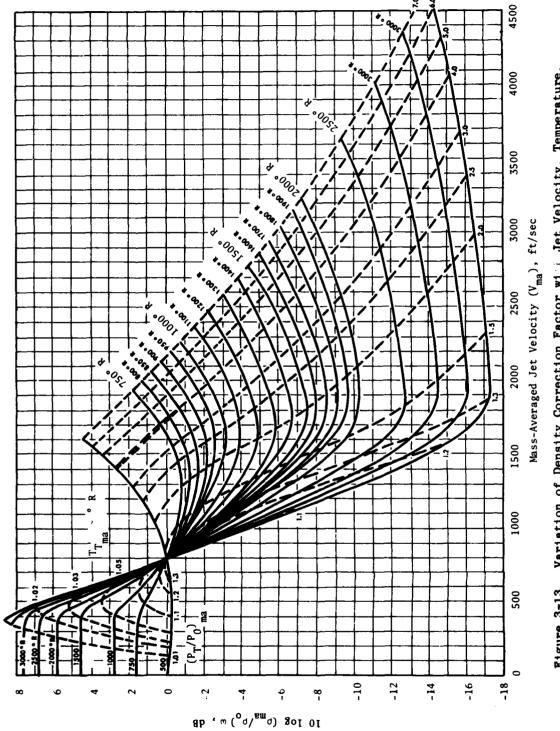


Figure 3-12. Variable-Density Index Determination.



Variation of Density Correction Factor with Jet Velocity, Temperature, and Pressure Ratio. Figure 3-13.

(50)

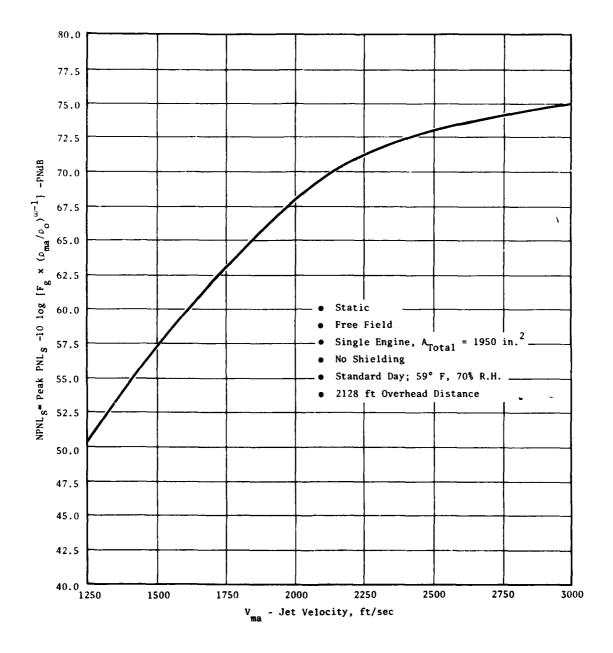


Figure 3-14. Normalized, Static, Peak PNL for Baseline Conical Nozzle.

 $\underline{\text{Step 6}}$ - The static peak PNL (PNLs) for the appropriate single- or dual-flow, mass-averaged conditions and desired overhead distance, R, is then calculated from:

• $PNL_s = NPNL_s + 10 \log F_g + 10 \log (\rho_{ma}/\rho_o)^{(m-1)} + 25 \log R/2128$

where Fg is obtained from (2), 10 log $(\rho_{\rm ma}/\rho_{\rm O})^{\rm w-1}$ from (4), and 25 log R/2128 from Figure 3-15.

Step 7 - The peak-noise-angle flight effects (i.e., static-flight) are then obtained from Figure 3-16 for an inlet angle of 140°. The correction factors of Figure 3-16 are based on the velocity index method of Bushell (Reference 8). The flight peak PNL (PNL_f) is then obtained from:

PNL_f = PNL_s - Flight Effects

where PNL_S is from (6), and flight effects are from Figure 3-16 at proper V_{ma} and V_a .

Step 8 - The effective perceived noise level, EPNL, of the baseline system is then obtained by accounting for the directivity (field shape) or duration of noise effect. The correction factor, designated Net $[P \rightarrow E]$, is obtained from Figure 3-17.

There curves were established by studies in which duration corrections were made using measured noise directivity patterns either corrected for flight or from flight/simulated-flight tests. Figure 3-17 also includes sensitivity curves to account for aircraft velocity and overhead distance. The resultant flight noise or EPNL is estimated as follows:

- EPNL = PNL_f + Net[P + E]
 - = PNL_f + Basic duration correction (i.e., at V_a = 400 ft/sec, R = 2400 ft) + distance correction + aircraft velocity correction
 - = $PNL_f + basic[P \rightarrow E] + 10 log R/2400 + 10 log V_a/400$

where PNLf is obtained from Item (7), Basic [P-E] from Figure 3-17a, 10 log R/2400 from Figure 3-17b, and 10 log $V_a/400$ from Figure 3-17c.

This single-engine EPNL should then be corrected for number of engines, the installation as it affects the total lateral attenuation (i.e. shielding and overground), nonfree-field effects (ground reflections), and appropriate margin. Number of engines can be accounted for by simply adding 10 times the log of the number of engines. Lateral attenuation, often referred to as shielding, is in effect due to ground proximity and shielding by the engine exhaust nozzles. Reference 9 describes studies and measurements made by the British Aircraft Corporation to assess lateral attenuation with respect to elevation angle (from the horizontal to aircraft). The report describes a preliminary technique for estimating shielding effect and overground attenuation factors. The following tabulation (taken from Figure 13 of Reference 9) provides some insight into the magnitude of lateral attenuation factor based on Concordederived PNL and EPNL measurements.



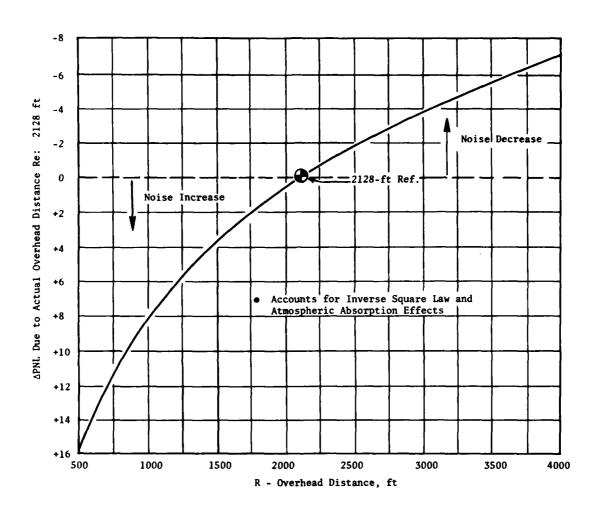


Figure 3-15. Actual Overhead-Distance Correction.

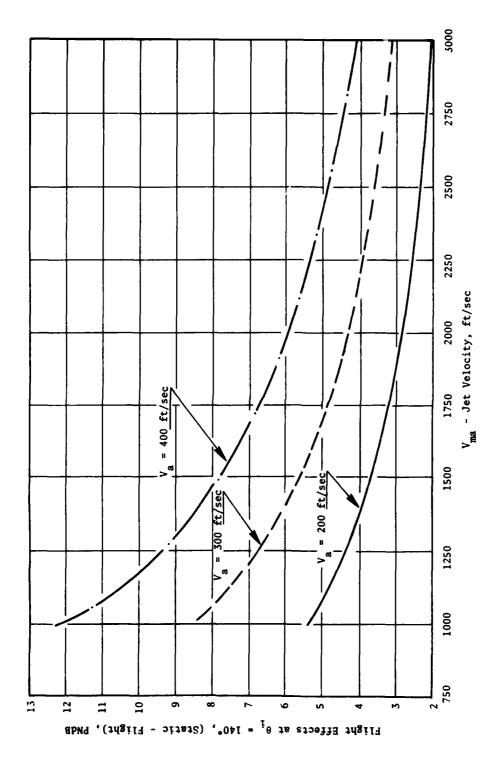


Figure 3-16. Peak-Noise-Angle Flight Effects for Baseline Conical Nozzle.



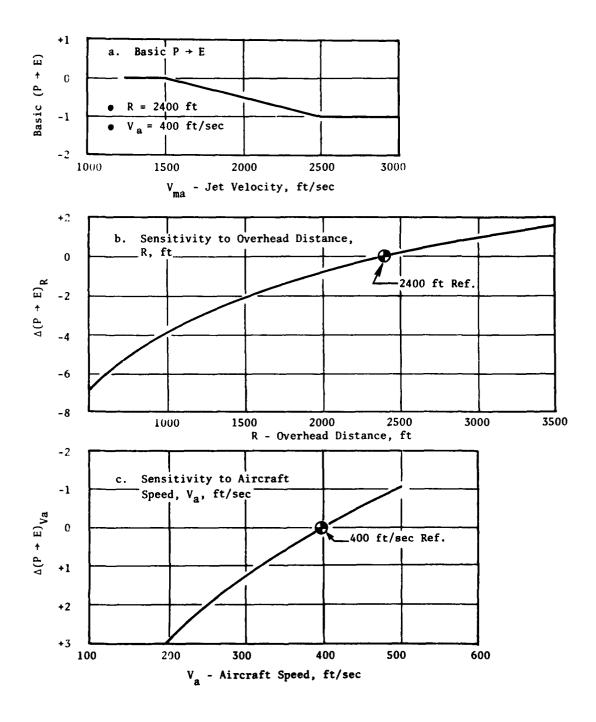


Figure 3-17. Flight Peak PNL Conversion to EPNL for Baseline Conical Nozzle.



Elevation Angle	Lateral Attenuation, (dB)
5°	9.6
10°	7.8
15°	5.4
20°	4.6
25°	3.4
30°	2.5
40	1.3

Previous SCAR studies by General Electric (Under Contract NAS3-19544, Reference 10) suggest that, at aircraft rotation, angle of elevation can be between 20° and 30° which (from the previous table) can result in a reduction of 4.6 to 2.5 dB at this noise-monitoring point. No correction should be applied during the community monitoring point. To account for the fact that noise measurements are taken under nonfree-field conditions (some ground reflection, etc.), it is appropriate to increase the resultant system EPNL by 1-2 dB.

This system baseline noise can be compared to the noise goal previously determined by the user at the initiation of the selection process (see Figures 3-8 and 3-9) to determine the amount of noise reduction that will be required of the suppressor to be selected.

Step 9 - Given a peak noise reduction requirement (i.e., ΔPNL_S), use Table 3-2 to provide the nominal gross thrust coefficient for the baseline conical nozzle (the table also includes several other typical baseline types for reference purposes). Figure 3-18 and Figure 3-19 are then used to determine the static suppression versus mass-averaged velocity and the static-suppression/flight-performance loss, respectively. This information permits the user to obtain a flight performance-degradation estimate for one or more particular suppressor types and for the required ΔPNL_S.

In using Figure 3-19, the data points establish the combinations of static suppression and flight thrust loss which are achievable. The combinations are established by the type of nozzle, which is usually predetermined by engine cycle and installation considerations; therefore, as the type of nozzle is varied in the course of an iterative study, points for that nozzle should be used on Figure 3-19. If the engine cycle conditions are such that they do not conform to the nominal single- and dual-flow conditions of Figure 3-19, then Figure 3-20 can be utilized to accommodate nozzle pressure ratio excursions for single- and dual-flow chute/spoke plug suppressors. In the event the configuration in question includes an ejector, Figure 3-21 may be utilized; however, the Figure 3-21 trend curve is based solely on single-flow configurations. Similarly, Figure 3-22 provides adjustment to account for single-flow nozzle pressure ratio for multitubes alone and multitubes-plusejector suppressor configurations. Having established the basic suppressor thrust loss from Figure 3-19, and any appropriate adjustments, the flight thrust coefficient is obtained from:

Suppressor (Cfg)_f \approx Baseline (Cfg)_f x (1 - Cfg loss) + Δ Cfg_A

(Sb)

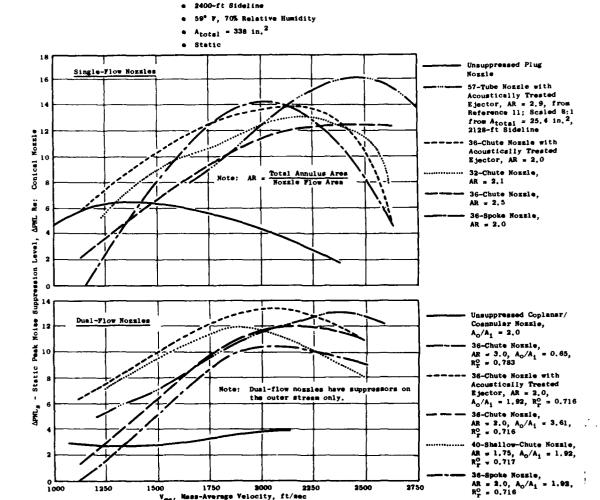


Figure 3-18. Typical, Static, Peak PNL Suppression Characteristics.

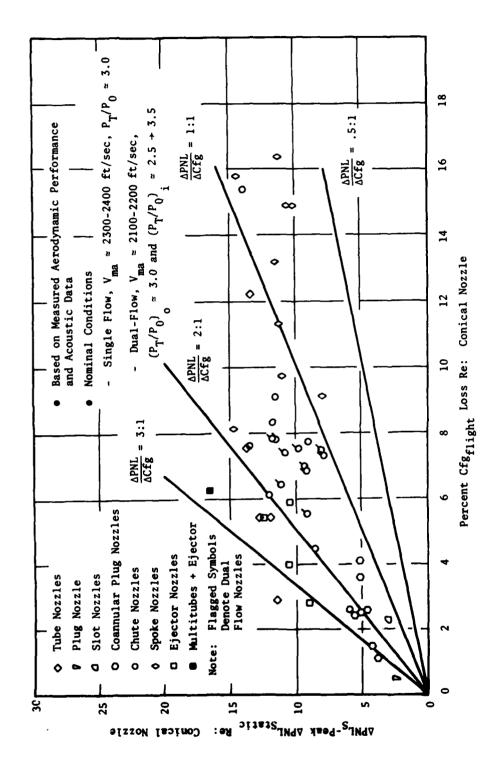


Figure 3-19, Generalized Flight Performance and Static Suppression Levels.



, M

100

Single Flow

Dual Flow

(Applicable for $(P_T/P_0)_i = 2.5-3.5$)

- Valid for all Single- and Dual-Flow Chute/Spoke Plug Systems
- ullet Can be Utilized for ΔC_{fg} Purposes Assuming Conical Nozzle is Essentially Invariant through P_T/P_o Range or Interest 0.03 \bullet M_o \simeq 0.36 0.02 Increase 0.01 0 -0.01 Decrease -0.02 Corresponds to Takeoff/ -0.03 Community Region of Interest for Turbojets and VCE's -0.04 2.5 3.0 2.0 3.5 4.0 4.5 Nozzle Pressure Ratio, P_T/P_O Outer Nozzle Pressure Ratio, $(P_T/P_O)_O$

Figure 3-20. Variation of Flight Gross Thrust Coefficient with Nozzle Pressure Ratio for Multielement Single-Flow and Dual-Flow Nozzles.

- Valid for all Single Flow (1) Chute/Spoke Plug Suppressor Systems
- \bullet Assumes Conical Nozzle $C_{\mbox{fg}}$ is Essentially Invariant through $P_{\mbox{T}}/P_{\mbox{O}}$ Range of Interest

Note: (1) Probably good as a first order approximation for dual-flow systems

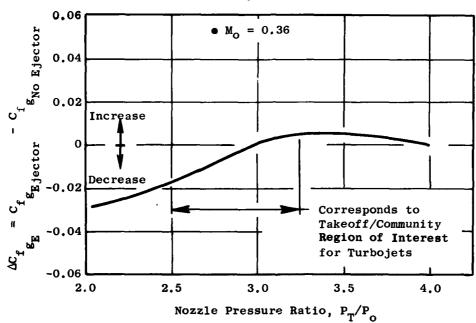
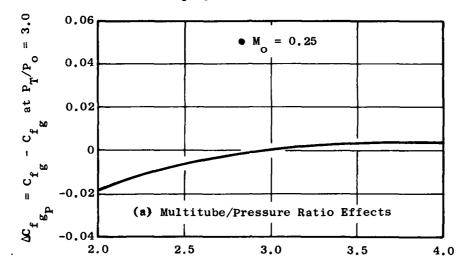


Figure 3-21. Effect of Ejectors on Multielement Plug, Single-Flow Nozzle Flight Aerodynamics Performance.

- Applicable to Full Round Multitube Single-Flow Systems
- \bullet Assumes Conical Nozzle ${\rm C_{f}}_g;$ Essentially Invariant through ${\rm P_T/P_o}$ Range of Interest



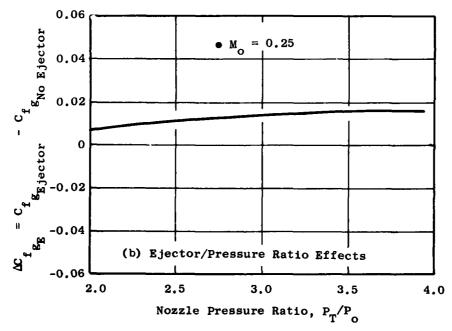


Figure 3-22. Variation of Multitube Flight Gross
Thrust Coefficient Due to Nozzle
Pressure Ratio and Ejector Installation.



where: Baseline (Cfg) $_f \cong 0.985$ (Table 3-2), Cfg loss is from Figure 3-19 for pertinent ΔPNL_s and suppressor type, and $\Delta CfgA$ is additional suppressor performance adjustments from Figures 3-20 through 3-22.

Table 3-2. Nominal Gross Thrust Coefficients for Baseline Type Nozzles.

 M_o ≅ 0.36 Applicable for Takeoff/Community Noise 	
Type Exhaust Nozzle	Nominal Gross Thrust Coefficient (Cfg)
• Conical	≅ 0.985
Annular Plug	≅ 0.981
Inverted Flow Coannular Plug	≅ 0.965

Step 10 - Figure 3-23 is utilized to increase engine size* to compensate for the decrease in suppressor thrust coefficient. If net thrust is held constant, then unsuppressed/suppressed engine size (i.e., weight flow), assuming afterbody and inlet drag = 0, ib obtained from:

• Scale Factor = WSuppressor/WBaseline = YBaseline/YSuppressor

where $Y = (Cfg \ V_{ma} - V_a)$ and Y is obtained from Figure 3-23 at the appropriate V_{ma} , V_a , and Cfg values for both the baseline and suppressor nozzles.

Step 11. - The unsuppressed/suppressed flight-noise level (see Figure 3-9) is obtained as follows:

• EPNL $_{\rm U/S}$ = EPNL of Baseline + 10 log (Scale Factor)

where EPNL of baseline is from Step 8 and scale factor = WSuppressor/WBaseline from Step 10.

^{*}Figure 3-23 can also be utilized if engine weight flow is held constant and the jet velocity is increased to compensate for the thrust loss due to the suppressor performance loss. Once Y of the baseline is established, the user simply assumes that Y of the suppressor is the same and proceeds to use the nomograph to find the new cycle velocity. Assuming the user has sufficient cycle information, the unsuppressed/suppressed noise level has to be computed in its entirety using Figures 3-12 through 3-17 as described in Steps 1 through 8 above.

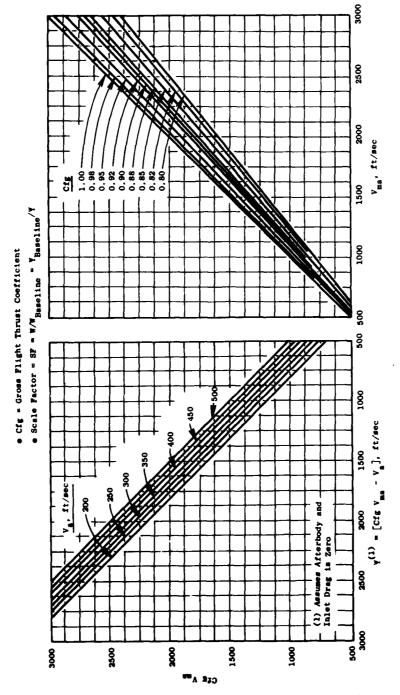


Figure 3-23. Suppressor Scale Factor Determination at Constant Installed Thrust.

(63)

Step 12 - The interim suppressed flight noise, EPNL (assumes flight effects and duration of noise, $P \rightarrow E$, are identical for baseline and suppressor nozzles), is obtained from:

• EPNL_{I/S} = EPNL_{U/S} -
$$\Delta$$
PNL_s + Δ (V_{ma}/V_{ma} at Δ PNL_{peak}) - Δ (Ejector)

where EPNL is from Step 11, Δ PNL is established noise reduction as discussed in Step 9, Δ (V /V at Δ PNL) is obtained from Figure 3-24 or Figure 3-26 to allow for off-nominal cycle conditions noted on Figure 3-19 (always reduces basic, static, peak suppression) and Δ (Ejector) from Figure 3-25 or Figure 3-27 to account for acoustic benefit of treated ejector.

Step 13 - Because the peak noise of single-flow suppressors in flight appears to occur at 120°, rather than 140° as is the case for conical nozzles, Figure 3-28 is included to account for the shift. This shift reduces the single-flow suppressor acoustic effectiveness in flight; i.e., flight effects are greater for a conical nozzle than for a suppressed nozzle. The Task 5 free-jet, dual-flow-suppressor results (Reference 3) show that flight suppression effectiveness is affected by the geometry of the suppressor and the inner and outer streams along with the pressure, temperature, and velocity excursions in the respective streams. The sensitivity of suppressor effectiveness to all these variables is handled by the engineering correlation in Section 4.0. For preliminary design purposes, the following tabulation can be utilized as a first-order correction to account for the dual-flow-suppressor flight effects (relative to a conical nozzle).

V (ft/sec)	Δ (Flight Effects),* dB Conical - Dual Flow Suppressor
1250 -1750	≅ 5.5
1975	≅ 4.6
2000	≅ 3.8
2125	≅ 2. 9
2250	≅ 2. 0
	1250 - 1750 1975 2000 2125

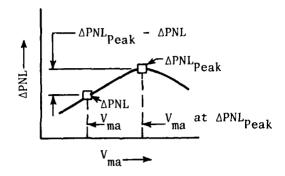
*Applicable for $V_a = 300 - 400$ ft/sec

To account for differences in basic (P-E) between suppressors (single and dual flow) and baseline conical nozzles, the trend curves shown in Figure 3-29, which are generally representative of what was observed in Task 5 free-jet tests (Reference 3), are also included. In general, both Δ (flight effects) and Δ [basic (P-E)| corrections will result in degradation of the static noise-suppression levels of a noise-abatement nozzle. Sensitivity of Δ (P-E) to aircraft velocity and overhead distance is not required since it has been already accounted for in the calculation of the baseline system EPNL (Step 8).

Step 14 - The suppressed flight noise, EPNLs, prior to aircraft and engine adjustments, is estimated from:

• EPNL_s = EPNL_{I/S} + Δ (Flight Effects) + Δ Basic (P->E)





- Applicable to Single- and Dual-Flow Systems with Chutes or Spokes
- Based on FAA SST Phase I and II, and FAA/DOT High Velocity Programs

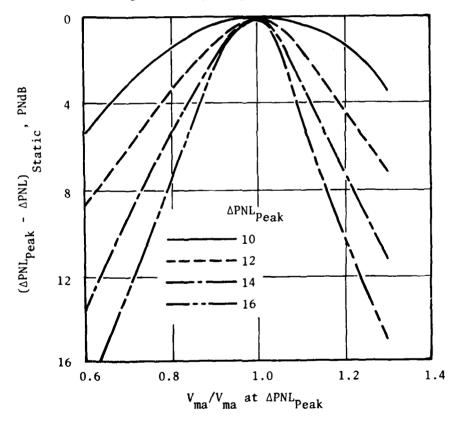


Figure 3-24. Multielement/Plug-Nozzle Static Suppressor Dropoff Characteristics.

- Single- and Dual-Flow Systems with Chutes or Spokes
- Based on FAA/SST Phase II, NASA Lewis/DBTF and FAA/DOT High Velocity Programs

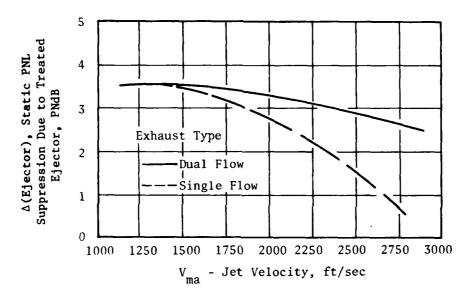
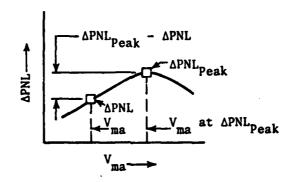


Figure 3-25. Static Acoustic Effectiveness of Treated Ejectors on Multielement/Plug Nozzles.



- Applicable to Full, Round, Multitube Single-Flow Systems
- Based on FAA SST Phase II Programs

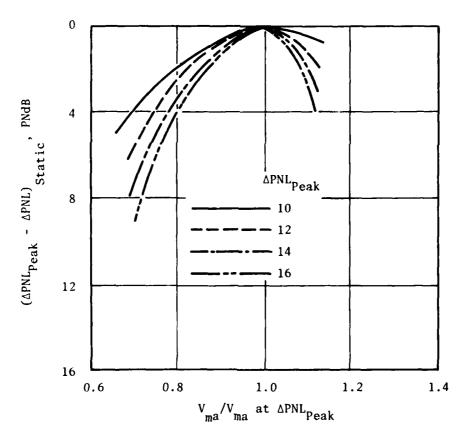


Figure 3-26. Multitube (Alone) Nozzle Static Suppression Dropoff Characteristics.

- Applicable to Full, Round, Multitube Single-Flow Systems
- Based FAA SST Phase I & II Programs

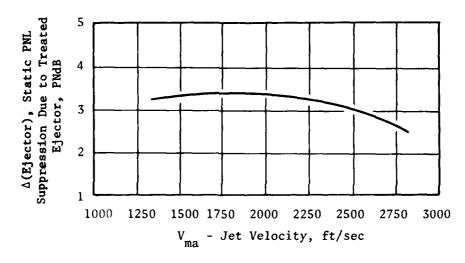


Figure 3-27. Static Acoustic Effectiveness of Treated Ejectors on Multitube Nozzles.

where EPNL_{T/S} is obtained from Step 12, Δ (Flight Effects) is obtained from Figure 3-28 for single-flow suppressors and from the table in Step 13 for dual-flow systems, and Δ [Basic (P·E)] is obtained from Figure 3-29.

The system suppressed flight noise (see Figure 3-9) can be obtained by simply accounting for the pertinent aircraft-engine corrections as described for the system baseline flight noise in Step 8.

The system suppressed flight-noise level, EPNL_S, estimated with Steps 1 through 14 can be compared to the noise goal determined at the initiation of the selection process. If the estimated level is acceptable, the user can proceed with the detailed acoustic prediction (Section 4.0) as well as the aerodynamic performance prediction (Section 5.0) to select the appropriate suppressor geometry for a given engine-cycle/exhaust-system installation (e.g., single or dual flow, partial or full-span suppressor, multichutes or tubes, etc.).

3.3.2 Examples Utilizing The Selection Process

Appendix C presents three sample calculations, utilizing the procedure outlined in Section 3.3.1, at conditions representative of takeoff (sideline) and community flight modes. Single- and dual-flow suppressor configurations are included.

3.4 MECHANICAL AND INSTALLATION CONSIDERATIONS

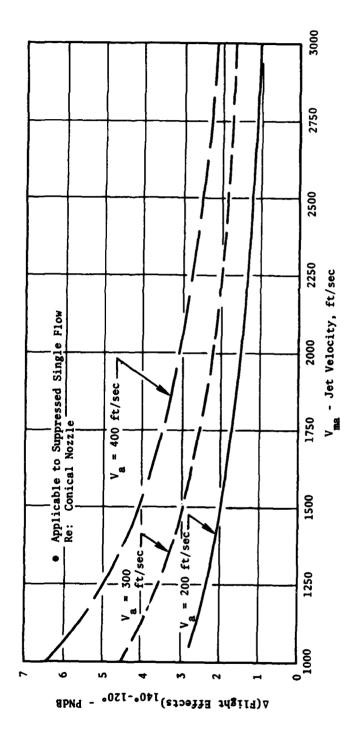
The preliminary selection process must include some qualitative or quantitative assessment of the impact that a mechanical, retractable suppressor would have on the size and weight of the baseline engine/exhaust-nozzle system. The Task 3 Final Report (Reference 1) includes results from a comprehensive aircraft integration study which provide some insight into the mechanical complexities of jet noise abatement nozzles. Figure 3-30 includes schematics of three suppressor configurations along with representative single- and dual-flow baseline nozzles that were studied, from a mechanical design engineer's perspective, to determine weight and maximum-diameter variations.

The suppressor schematics incorporate the respective scaled-up, suppressor model based on the cycle data matched to its configuration. These schematics are typical of the type used to initiate layout drawings and to estimate weights during preliminary design studies. The outline drawings, therefore, permit the designer to define the maximum exhaust system diameter (used to evaluate drag changes) as well as estimate exhaust system weights using standard scaling techniques (which have been derived from past production and from similar current-preliminary-design, exhaust systems). The drawings are discussed in more detail in Section 6.0.

A suppressed exhaust system must be derived by modifications to single-flow or dual-flow baseline nozzles (which for this study were plug nozzles) and should include the following major features:

A plug nozzle to provide a high-radius-ratio exhaust discharge and





Peak-Angle Flight Effects Correction for Single-Flow Suppressor Systems Re: Conical Baseline Nozzle. Figure 3-28.

- V_a = 400 ft/sec
- R = 2400 ft Overhead Distance

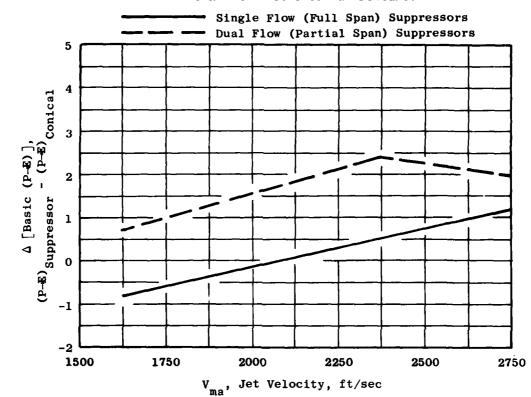
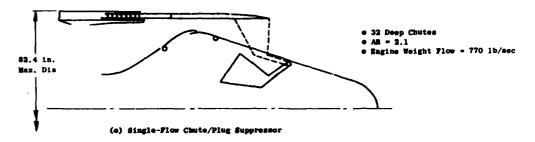
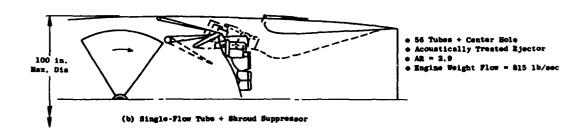


Figure 3-29. Flight Peak PNL \rightarrow EPNL Sensitivity to Suppressors Re: Conical Baseline Nozzle.

Mechanical Design/Implementation Perspective





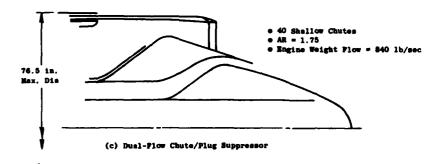


Figure 3-30. Typical Single-Flow and Dual-Flow Exhaust System Schematics.



to provide storage space for suppressor devices during unsuppressed (stowed) operation. Plug nozzle performance is excellent over a wide range of exhaust pressure ratios.

- A translating, external, cylindrical shroud positioned axially to obtain the optimum internal expansion area ratio for performance throughout the wide range of pressure ratios experienced in the mission.
- Integration of thrust-reverser cascades into the translating shroud to minimize actuation requirements.
- A low-temperature augmentor for thrust augmentation during climb.

Since the maximum-diameter sizing requirement of the exhaust system has the largest effect on weight and exhaust nozzle drag, it should be determined as a result of one of the following sizing checks:

- A stackup should be made through the turbine allowing for structure outside of the turbine tip, height of the bypass airflow duct, space for the translating shroud support structure, thickness of the translating shroud, and thickness of the outer cowl.
- A stackup should also be made, through the exhaust duct, that provides for the plug support beam, which in turn sizes the duct for the augmented reference Mach number.
- The translating shroud exit should be sized to closely maintain the full expansion area at supersonic cruise.
- The primary suppressor sizing requirements for jet noise-suppressor implementation must be considered, such as suppressor exit radius ratio and area ratio.

In general, the stackups through the turbine frame and the exhaust duct do not determine the nozzle maximum diameter for high speed aircraft/engine cycles. Unsuppressed exhaust system maximum diameter is usually dictated by the full expansion at supersonic cruise; however, suppressor area ratio and radius ratio requirements tend to make the nozzle larger than required for full expansion. The relationship, which is further discussed in Section 6.0, between the nozzle exit radius (Rg), throat area (Ag), area ratio (AR), exit angle (β) , and radius ratio (R_1/R_0) is illustrated on Figure 3-31. Previous studies have shown that cant angle (β) has little effect on nozzle radius R9. Figure 3-31 can be utilized to obtain an estimate for the nozzle exit radius (R9) for a given cycle flow area (A8) and suppressor geometry (AR and R_1/R_0). Also shown on Figure 3-31 are typical supersonic-cruise, single- and dual-flow, full-expansion, nondimensional, radius ranges obtained from previous studies of unsuppressed plug nozzle type systems. Figure 3-31 also shows a recommended maximum design limit (envelope) of R9 $\sqrt{\pi/\text{Ag} \cdot \cos\beta}$ equal to 2.1, above which an excessively large and heavy exhaust system generally results.

Figures 3-32 and 3-33 are included to further assist the user in assessing the impact of installing a suppressor (suppressor Δ weight and Δ increase in nozzle maximum diameter) on advanced engine cycles indicative of turbojet (single

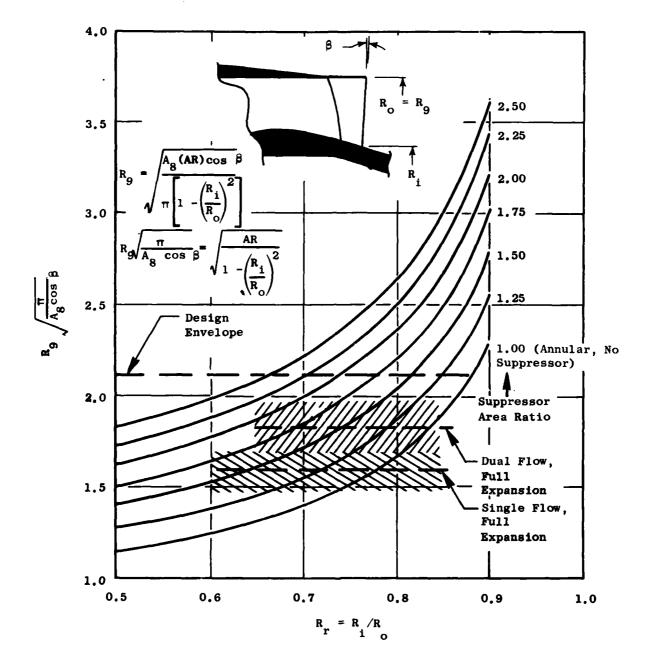
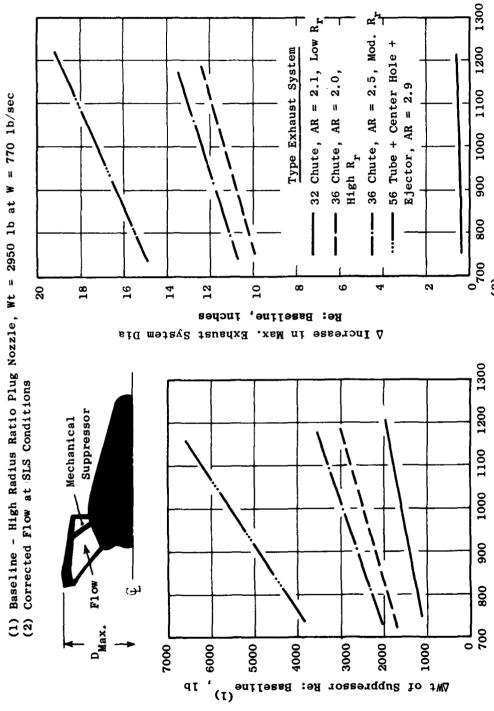


Figure 3-31. Relationship Between Nozzle Exit Radius, Throat Area, and Suppressor Area Ratio.

flow) and variable-cycle (dual flow) applications. These results are from the in-depth aircraft-integration study conducted and reported in the Task 3 Final Report (Reference 1). These curves illustrate the difference in weight and diameter increment between simple suppressors like the 40-shallow-chute, coannular, plug nozzle (Figure 3-33) and a complex suppressor such as the 56-tube + center-hole nozzle with a treated ejector (Figure 3.32). Although the results are for specific suppressor installation, they nevertheless can provide the user with a first-order estimate in assessing the impact of aerodynamic performance and suppression characteristics on engine/exhaust-system weight.





Typical Single-Flow Suppressor Weight and Geometry Effects. Figure 3-32.

W, Engine Weight Flow (2), 1b/sec

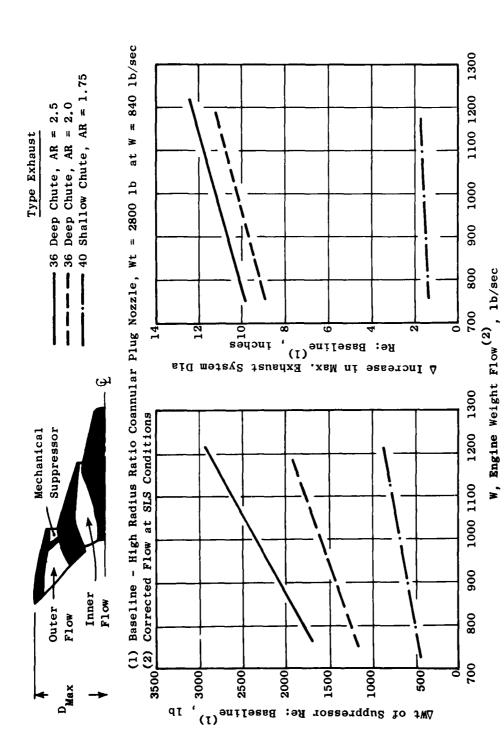


Figure 3-33. Typical Dual-Flow Suppressor Weight and Geometry Effects.

4.0 ACOUSTIC DESIGN OF JET NOISE SUPPRESSORS

In this Guide, the acoustic design method for general use consists of the M*S Engineering Correlation Prediction Method, in Section 4.1, augmented by the General Guides for Good Design Practice presented in Section 4.2. The unified aeroacoustic jet noise prediction method (M*G*B), which was based on a model of the principal jet-noise generation and emission mechanisms from engineering principles, see References 14 and 15) is not included as one of the prime paths in the basic design guide. However, its demonstrated success as a diagnostic tool for assessing the relative importance of the various jet-noise mechanisms for a given nozzle type makes it an ideal supplement to the more engineeringcorrelation-oriented M*S technique. Appendix A reviews the primary generation and emission mechanisms, summarizes the formulation of the M*G*B model, and concludes with an example of how the M*G*B model can be used as a diagnostic tool. The development of the M*S method, the nozzles for which it applies, the ranges of the variables for which the accuracy of the method has been established, and the accuracy of prediction are described in detail in Reference 12 for the case of statically generated noise; extension of the method to include flight effects is described in Appendix D of this Volume. The computer program is described in Reference 13 (which also includes the M*G*B aeroacoustic prediction method), and two sample cases are discussed in Appendix G of this document. The method has been exercised to establish the (noise) trends with pertinent variables (e.g. area ratio, element number, cycle conditions), and these illustrative results are presented in Section 4.1.2.

4.1 ENGINEERING CORRELATION NOISE PREDICTION METHOD

4.1.1 Ranges of Applicability for the Basic Method and Accuracy

The following paragraphs (abstracted from Reference 12) summarize the ranges of variables for **each** nozzle type for which the basic prediction method has been checked against experimental data. It should be noted that the ranges for nozzle pressure ratio and total temperature are interdependent in that they generally increase or decrease together as on the operating line of a turbojet engine (see Figure 4-1); that is, the data base for the correlation is generally consistent with operating conditions to be expected for typical engines. The nozzle types illustrated in Figure 4-2 are correlated in the M*S method over the ranges listed below:

Conical Nozzle - The correlation includes predictions of pure jet-mixing noise for both converging and converging/diverging (design point-only) nozzles. A separate prediction of shock noise is included for convergent nozzles.

The range of applicability of both the jet-mixing and the shock-cell noise correlations is:

Jet Velocity, V_j (ft/sec) 400 < V_j < 2860 Jet Total Temperature, T_i (° R) 519 < T_i < 2100





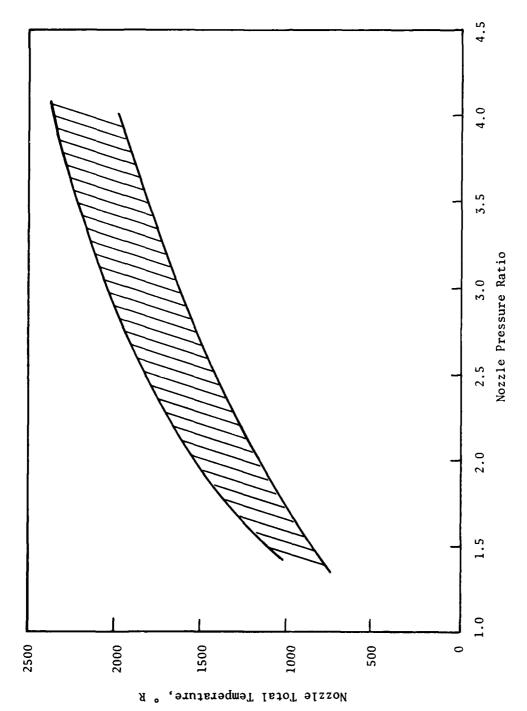


Figure 4-1. Typical Turbojet Operating Line Conditions.

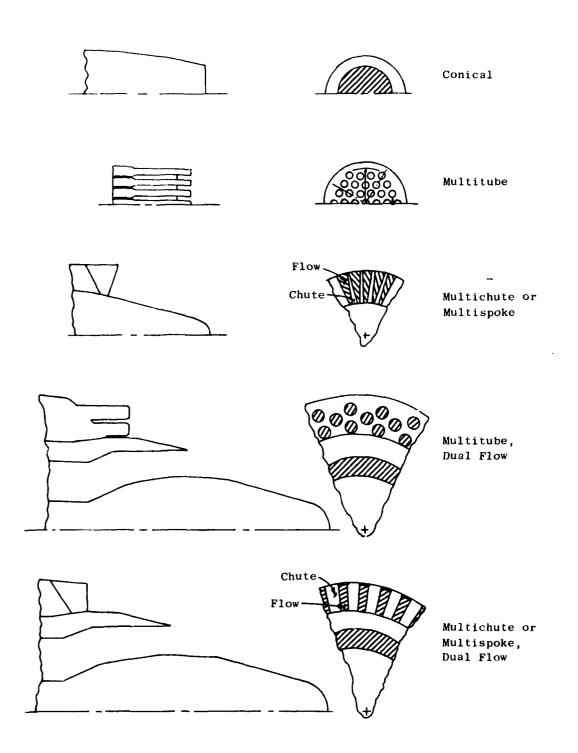


Figure 4-2. Nozzle Types Included in the Correlation.

Nozzle Pressure Ratio $1.0 < P_T/P_0 < 4.0$ Nozzle Diameter, D (ft) 0.8 < D

Multitube, Single-Flow Nozzle - The multitube, single-flow nozzle correlation includes nozzles with an arbitrary number of tubes having simple converging ends, coplanar termination, all tubes parallel (except that the outer row can be canted relative to the axis), uniform center-to-center spacing of tubes in a hexagonal array, and the option of a centerbody plug.

The ranges of the variables specifically associated with the multitube nozzles which were correlated (in addition to the variables listed under the conical nozzle) are:

Suppressor Area Ratio, AR	$2.0 \leq AR \leq 8.0$
Number of Elements, N	7 ≤ N ≤ 253
Suppressor Radius Ratio, R _r	$0 \le R_r \le 0.75$
Cant Angle of Outer-Row Tubes,β (degrees)	0 <u><</u> β <u><</u> 5

Multichute or Spoke, Single-Flow Nozzle - This correlation includes both chutes and spokes without discrimination. This concept evolved from the more complex planform variations of chute configurations and was found to apply equally well to spokes. The planform of nozzle elements may be trapezoidal (not limited to radial lines), the termination can be canted, and a centerbody plug is included.

The ranges of variables specifically correlated with the data (in addition to the variables listed under the conical nozzle) are:

Suppressor Area Ratio	$1.5 \leq AR \leq 2.5$
Number of Elements	24 <u><</u> N <u><</u> 64
Suppressor Radius Ratio	$0 \leq R_r \leq 0.783$
Exit Cant Angle (degrees)	-10 ≤ β ≤ 15

Coannular-Flow, Multielement Suppressor on Outer Stream - In this case, the multielement nozzle is applied to the outer stream of a coannular exhaust. The velocity of the outer stream may be selected to be higher or lower than the inner stream (although the case of primary practical interest is for the highest velocity stream to have the suppressor). The same conditions apply in this case that applied for the single-flow, multielement nozzles (tubes with converging ends, coplanar termination, etc.).

The ranges of variables specifically correlated with the data for dualflow nozzles with multichute/spoke suppressors on the outer stream (in addition to the variables listed under the conical nozzle) are:

Suppressor Area Ratio	$1.5 \leq AR \leq 3.0$
Number of Elements	20 <u>≤</u> N <u><</u> 40
Suppressor Radius Ratio	$0.653 \le R_r \le 0.783$
Exit Cant Angle (degrees)	β = 0

Multielement Nozzle with Ejector - Hard-wall or treated ejectors with single- or dual-flow, multielement suppressors are also included. The hard-wall ejector correlation is derived on a purely empirical basis, but the effect of adding treatment is predicted by means of the engineering correlation of the basic data. Thus the treatment for which the check against measured data was made (the single-layer liner with honeycomb separating the solid backplate and perforated faceplate, single degree of freedom) may be extrapolated to other types of point-reacting treatment provided the resistance and reactance are specified for the desired frequencies.

The range of variables for which the correlation was established (in addition to those for the conical nozzle and multielement suppressors) is:

Area Ratio of Ejector Relative to Area Ratio of Nozzle
$$1.0 < \frac{AR_{ej}}{AR_n} < 1.97$$
Ratio of Hard-wall Ejector Length to Equivalent Conical Nozzle Diameter
$$0 < L_H/D_{eq} < 4.0$$
Ratio of Treated Ejector Length to Equivalent Conical Nozzle Diameter
$$0 < L_T/D_{eq} < 2.0$$
Ratio of Ejector Inside Diameter to Nozzle Element Envelope Diameter
$$1.0 < D_{ej}/D_n < 1.28$$

The accuracy of the prediction was established by means of linear regression analysis of the measured versus the predicted noise. This was done both for the maximum value of the far-field PNL and for a so-called EPNL; in the latter case the static far-field data were used in an EPNL calculation based on a level flyover at 300 ft/sec. In order to eliminate size effects and differences in suppression levels so that the range in noise levels was a result of thermodynamic conditions alone, the noise levels were normalized relative to a "reference" level.

Thus, when sets of data were from two nozzles of different flow areas, the noise for each was predicted at a reference set of thermodynamic conditions (a pressure ratio of about 2.5 and a temperature resulting in a jet velocity of about 2000 ft/sec); noise at other conditions was then normalized relative to the reference conditions. The data were thus put in the form given by:



Measured Relative to Reference:

M = (PNL measured at test point) (PNL predicted at reference)
 + 100

versus

Predicted Relative to Reference:

P = (PNL predicted at test point) (PNL predicted at reference).
+ 100

The same was done for the case of EPNL. Then, the regression analysis was performed according to the linear relationship:

$$(M - 100) = m (P - 100) + b$$

and the values of the regression constants, m and b, were determined for each nozzle type with the results given in Table 4-1; also included are the limits of error for 80 and 95% confidence. Similar information for the prediction method as extended to flight (from Appendix D) is included in Table 4-2 for the nozzles as defined in Table 4-3.

In order to obtain a noise estimate or "expected value" within these confidence limits, it is necessary to adhere to the following procedure:

- Predict the noise for the nozzle at reference conditions (pressure ratio of about 2.5, temperature yielding a fully expanded jet velocity of about 2000 ft/sec, and the actual size and area ratio of the nozzle).
- 2. Predict the noise for the nozzle at the conditions of concern (pressure ratio, temperature, and actual size and area ratio of the nozzle).
- 3. Determine the value of P as defined in the preceeding paragraph.
- 4. Determine the expected value of the measured noise relative to the reference conditions from:

$$(M - 100) = m (P - 100) + b$$

5. Estimate the expected value of the noise from the nozzle:

Expected Value = (M - 100) + PNL Predicted at Reference Conditions or EPNL Predicted at Reference Conditions

It is of greater importance to use this form of estimating the expected value of the noise as the value of m deviates more from unity and as the value of b departs more from zero. The M*S computer program as documented in Reference 13 has been used to generate the data in the following Section.

Table 4-1. Linear Regression Analysis Results for Suppressor Nozzles.

	Nozzle Type		Regression stants b		dence s (dB) 95%	Number of Nozzles
PNL	All Suppressors	0.973	0.07	2.4	3.7	43
	Conical	1.003	0.63	1.3	2.0	1
	Single-Flow, Multitube	0.951	0.19	2.6	4.1	21
	Special Nozzles	0.883	0.59	1.9	3.1	2
	Single-Flow, Multichute/Spoke	0.995	0.05	2.4	3.6	10
	Dual-Flow, Multitube	0.887	-1.81	2.3	3.8	1
	Dual-Flow, Multichute/Spoke	1.041	0.22	1.8	2.8	9
EPNL	All Suppressors	0.968	0.29	2.1	3.3	43
	Conical	0.975	-0.34	1.2	1.9	1
	Single-Flow, Multitube	0.952	0.20	2.5	3.8	21
	Special Nozzles	0.937	0.06	1.9	3.1	2
	Single-Flow, Multichute/Spoke	1.003	0.11	2.0	3.0	10
	Dual-Flow, Multitube	0.911	-0.25	1.7	2.8	1
	Dual-Flow, Multichute/Spoke	1.000	0.89	1.6	2.5	9

Table 4-2. Predicted Versus Measured Simulated Flight by Free Jet.

	Nozzle Type		Regression stants b	Confid Limits 80%		Number of Points
PNL	All Suppressors	1.029	-0.18	2.3	3,5	59
	Conical (2)	0.966	+1.80	1.2	1.9	35
	Model 51	1.000	+0.02	2.2	3.5	22
	Model 52	1.183	-1.36	2.0	3.2	14
	Model 53	0.979	+0.82	2.0	3.3	11
	104 Tube	0.808	-0.68	2.1	3.4	12
	A11	1.004	+0.56	2.3	3.5	94
EPNL	All Suppressors	1.090	-0.12	2.3	3.5	59
į	Conical (2)	1.068	-0.98	1.5	2.4	35
	Model 51	1.057	-0.78	1.6	2.6	22
	Model 52	1.190	+0.78	2.3	3.7	14
	Model 53	1.051	+0.73	1.9	3.1	11
	104 Tube	0.825	-1.51	1.9	3.1	12
	A11	1.083	+0.29	2.1	3.2	94

Table 4-3. Data Base Used in Flight-Effects Correlation.

Nozzle Type	Model Number	Test Facility	Model Description
Conical	5 }	Cell 41	5-in. Diameter Throat
	(47	JENOTS	4-in. Diameter Throat (Aerotrain Model)
Single Flow	777	JENOTS	104 Tube, AR = 2.8, Elliptical Tubes
	(51	Cell 41	32 Deep Chute, AR = 2.1
Dual Flow Suppressor	{52	Cell 41	40 Shallow Chute, AR = 1.75, $AR_N = 1.92$
	(53	Cell 41	36 Chute, $AR_{R} = 2.0$, $AR_{N} = 3.607$
Conical		Aerotrain	J85 Size Version of Model 47 (A ₈ = 110 in. ²)
Single Flow Suppressor	-	Aerotrain	J85 Size Version of Model 44 $(A_8 = 110 \text{ in.}^2)$

4.1.2 M*S Generated Trend Data

This section contains trend data curves of noise as predicted by the M*S correlation. Predictions are presented as peak PNL or EPNL suppression relative to an equivalent-ideal-gross-thrust conical nozzle, and absolute PNL and EPNL values are given for the conical and typical suppressor nozzles. The basic size and distance for the nozzles for the various trend curves is 338 square inches and 2400-foot sideline, respectively, but changes in levels or suppression with size and distance are given for the conical and typical suppressor nozzles. This section is not meant to contain an all-encompassing set of trend curves. It does, however, contain a sufficient number of them to enable a nozzle designer to make preliminary judgements about various possible nozzle designs. The curves also give an indication of the type of more detailed studies which can be made using the supplied computer program. It should be noted that suppressor trend curves, in general, are dependent upon the source composition (postmerged, premerged, and shock) of the noise spectrum. Therefore, any change (geometric, cycle size, or distance) which changes this composition may change the trends.

The geometric parameters influencing the suppression of a multielement nozzle, which are correlated in the M*S model are given in Table 4-4. Trend curves may be run for any and all of these parameters, but only the trends with area ratio and degree of segmentation (number of elements) are presented in this section. Use of the computer program to generate other trend curves is discussed in Section 4.1.2.2. Area ratio and degree of segmentation do not necessarily result in the largest change in suppression; however, these parameters do establish the basic noise characteristics of the nozzle. Depending on these characteristics (premerged or postmerged domination), changes in the other parameters will produce varying degrees of change in suppression.

To produce the suppression trend curves presented, the program was exercised over a range of area ratios and element numbers as given in Figures 4-3 through 4-5. Radial planform, zero exit cant, and 0.75 radius ratio were assumed for chute suppressors. The representative suppressors in Figures 4-3 through 4-5 are similar to the "state of the art" suppressors proposed by various companies. The ranges of area ratio and element number covered represent feasible limits to these variables based on published studies (see Section 3.0).

The cycle conditions used are presented in Table 4-5. These conditions are representative of typical operating lines for dual-flow (VCE) and single-flow (turbojet) engines and contain takeoff, cutback, and approach power settings. The dual-flow cycle is actually from a large nozzle-area-ratio (A/A₁ \simeq 4) engine; however, it is used in this study for all nozzle area ratios to more easily assess the impact of geometry changes. Dual-flow suppression is based on the equivalent-ideal-gross-thrust-conical-nozzle noise for the dual-flow nozzle being examined. The single- and dual-flow cycles have differing thrusts at a given power setting and are therefore not directly comparable.

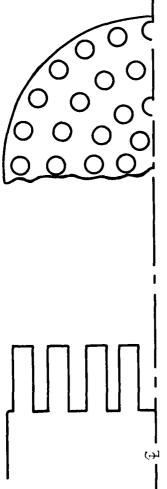
The trend curves are separated into two sections: a cycle section and a geometry section. The cycle section contains trends for conical and repre-



Table 4-4. Definition of Multielement Suppressor Geometric Parameters Included in the M*S Model.

Parameter	Definition
Degree of Segmentation, N	Number of flow or segmenting elements; i.e., tubes, holes, chutes, spokes
Area Ratio, AR	For full baseplate-tube/hole array ratio of area of a circumscribing circle skirting the outermost flow points at the exit plane to the total physical flow area
	For annulus of tubes, holes, chutes, or spokes = ratio of total annulus area to total physical flow area of annulus.
Radius Ratio, R _r	Ratio of plug radius to shroud radius at throat plane
Exit Plane Stagger (or Cant) Angle, β	Degree of exit plane angularity rela- tive to coplanar
Tube Cant Angle, β	Degree of tilt relative to centerline of tube array, outer row only.
Chute/Spoke Exit Planform	Ratio of chute/spoke width at shroud to width at plug (see Appendix F).





000	Number of Rows	က			-					• 4'	_		→
	Outer Row Spacing to Diameter Ratio	1.121	1.324	1.504	1.666	1.134	1.333	1.509	1.668	1.111	1,303	1.472	1.625
	Elements In Outer Row	16	16	16	16	20	20	20	20	24	24	24	24
	Tube Diameter (Inches)	3.788	3.788	3.788	3.788	3.092	3,092	3,092	3.092	2.678	2.678	2.678	2.678
	Area Ratio	1.50	2.00	2.50	3.00	1.50	2.00	2.50	3.00	1.50	2.00	2.50	3.00
(4)	No Of Elements	30	30	30	30	45	45	45	45	09	09	Representative 60	Suppressor—•60

Figure 4-3. Typical Multitube-Suppressor Configuration.

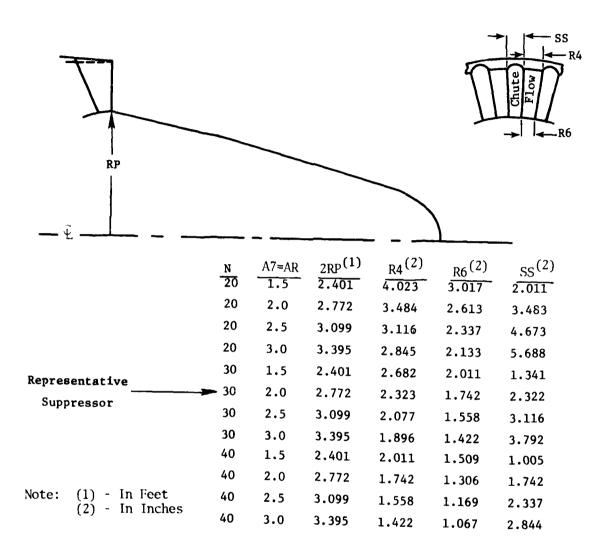
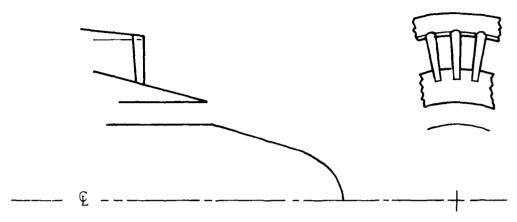


Figure 4-4. Typical Multichute-Suppressor Configuration.



Number of Elements - 20, 30, 40* Suppressor Area Ratio - 1.5, 2.0*, 2.5, 3.0 Nozzle Area Ratio - 1.0, 2.0, 3.0 (Run Only for 30 Chutes/AR = 2.0)

* Representative Suppressor

Figure 4-5. Typical Dual-Flow, Multichute Suppressor Configuration.

Table 4-5. Cycle Conditions Used In Determining Trend Curves.

Dual Flow

	Inner	3r			Outer	1 4			Mass Avg	80
$\frac{P_T}{P_0}$	TT (°R)	TT V (ft/sec)	A (in. ²)	$^{P}_{1}$	TT (°R)	T _T V (°R) (ft/sec)	(fn. ²)	$\frac{1}{1}$	T _T (°R)	V (ft/sec)
3.599	830	1748	113	3.75	2150	2881	225	3,448	1567	2380
3.127	828	1663	113	3.167	1925	2569	225	3,005	1448	2175
2.799	790	1555	113	2.651	1700	2242	225	2.609	1299	1939
2.528	757	1455	113	2.246	1531	1957	225	2,283	1184	1732
2.070	720	1274	113	1.710	1380	1539	225	1.803	1076	1417
1.568	069	1000	113	1.444	1300	1250	225	1.473	1033	1140

Single Flow

P	${\tt T}_{\!$	Δ	A
P ₀	(° R)	R) (ft/sec)	(in. ²)
3.521	1918	2661	338
3.060	1720	2393	338
2.601	1516	2096	338
2.191	1350	1810	338
1.662	1215	1407	338
1.275	1200	1125	338

sentative suppressor nozzles with varying cycle conditions including jet velocity, pressure ratio, temperature, and flight velocity. Also shown are trends with nozzle flow area and measurement distance. The plots with jet velocity are given on an absolute basis; others are normalized to some reference condition. Selected directivity and spectral plots for the trends appear in Appendix E.

The geometry section contains trends of suppression relative to conical nozzle noise for various suppressor nozzle types. The trends are presented on a static and in-flight PNL and an in-flight EPNL basis and are a function of area ratio (suppressor, nozzle, and ejector) and element number. Selected directivity and spectral plots for these trends appear in Appendix E.

4.1.2.1 Cycle Parameters

This section contains trend curves with jet velocity, flight velocity, and size and distance. The trends with jet velocity are given in Figures 4-6 through 4-14. Figures 4-6 through 4-8 give absolute static PNL, flight PNL, and flight EPNL, respectively, versus mass-averaged jet velocity for a conical nozzle on the turbojet cycle, a conical nozzle on the mass-averaged dual-flow cycle, and representative single- and dual-flow-suppressor nozzles. The noise given is not normalized for density; however, since it is plotted on a massaveraged-velocity (or specific gross thrust) basis, the generated noise may be compared. The expected increase in noise with velocity is apparent. Also, a reduction in suppression is observed with decreasing jet velocity. The in-flight suppression actually becomes negative (increased noise relative to a conical nozzle) at jet velocities below 1300 ft/sec. These figures can be used to find the absolute level of the conical nozzles for these particular sets of cycle or operating conditions. If the operating conditions vary in terms of pressure ratio or temperature from those in Table 4-5, the absolute noise is determined from Figures 4-9 through 4-11. Here, the conical nozzle in-flight PNL at 50°, maximum PNL, and EPNL are plotted versus jet velocity with lines of constant pressure ratio and temperature indicated. Section 4.1.1 has shown the range of applicability for these plots since the empirical prediction used to determine the noise becomes less accurate as the extremes of possible operating envelope are approached. At a given jet velocity, the figures indicate lower noise for lower pressure ratio. For the 50° inlet angle at high pressure ratios, Figure 4-11 indicates levels independent of jet velocity, i.e., total shocknoise domination. Appendix E contains PNL directivity and spectral plots at 50°, 90°, and 130° to the inlet (Figures E-1 through E-3), which show that both jetmixing noise and shock noise increase as pressure ratio is increased at a given jet velocity (decrease in temperature). This is, however, accompanied by an increase in thrust which is responsible for about one-half of the increase in mixing noise for high jet velocities ($V_{i} > 1800 \text{ ft/sec}$).

Figures 4-12 through 4-14 are corresponding plots for the representative, single-flow suppressor. As with the conical nozzle, high-temperature/low-pressure-ratio cycles are favored, but here the benefit is smaller. This is partly because the shock noise is less important on suppressor nozzles. These plots, as stated earlier, are for a representative suppressor nozzle at a specific size and distance. Changes in the spectral character of the suppressor

GENERAL ÉLECTRIC CO. CINCINHATI OH AIRCHAFT ENGINE BU--ETC. F/G. 20/1 HIGH VELOCITY JET NOISE SOURCE LOCATION AND REDUCTION. TASK 6. --ETCH. APR 79 J BRAUSCH, A.S. CLAPPER, C.R. GLIERE DOT-05-30034 AD-A103 671 TICLASSIFIED R79AL 6302 FAA-RD-76-79-6 NL

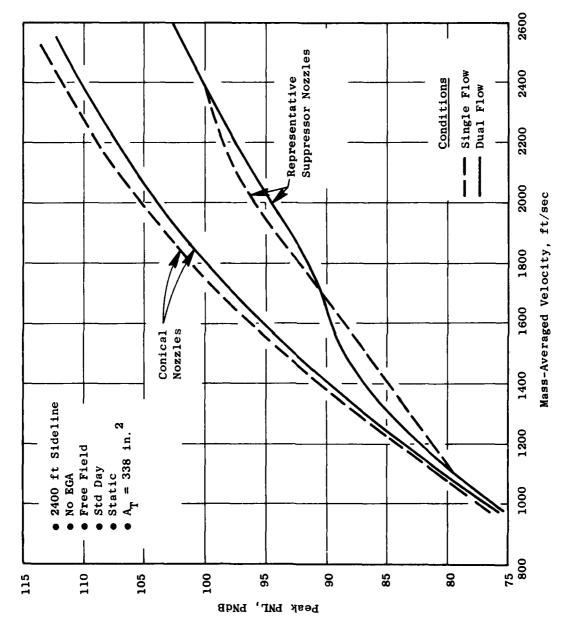


Figure 4-6. Static Predicted PNL Trends with Jet Velocity.

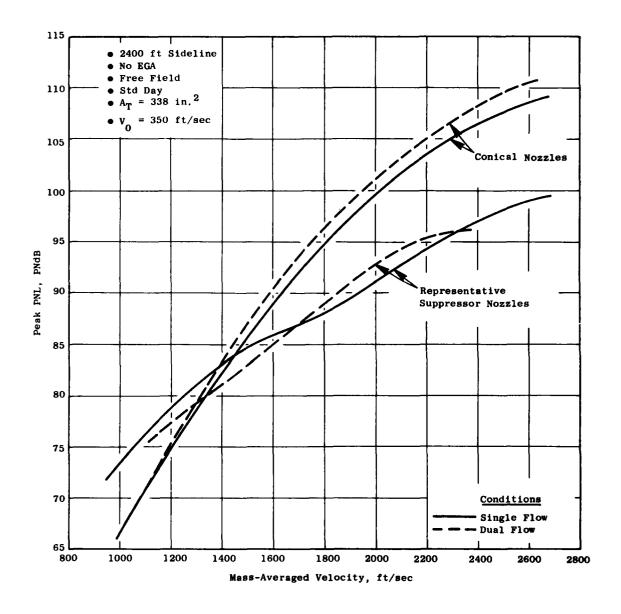


Figure 4-7. In-Flight Predicted PNL Trends with Jet Velocity.



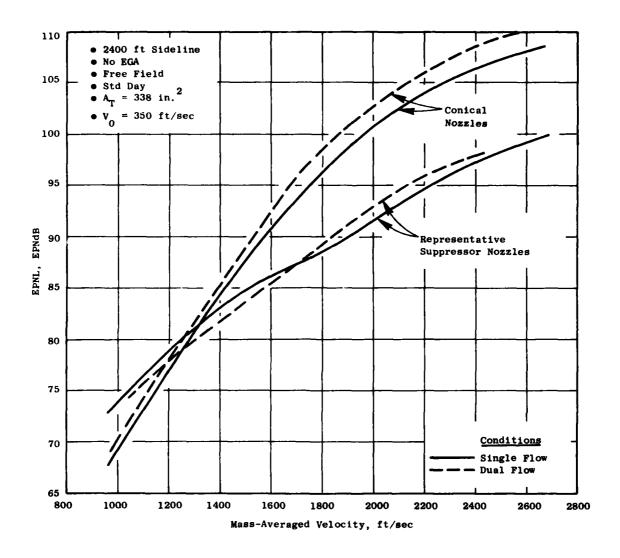


Figure 4-8. In-Flight Predicted EPNL Trends with Jet Velocity.

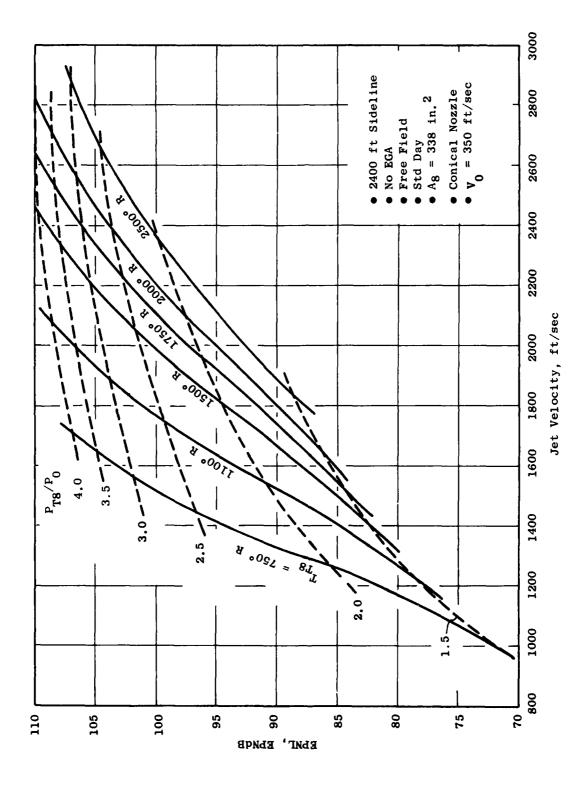


Figure 4-9. Effect of Cycle Conditions on Conical Nozzle EPNL.

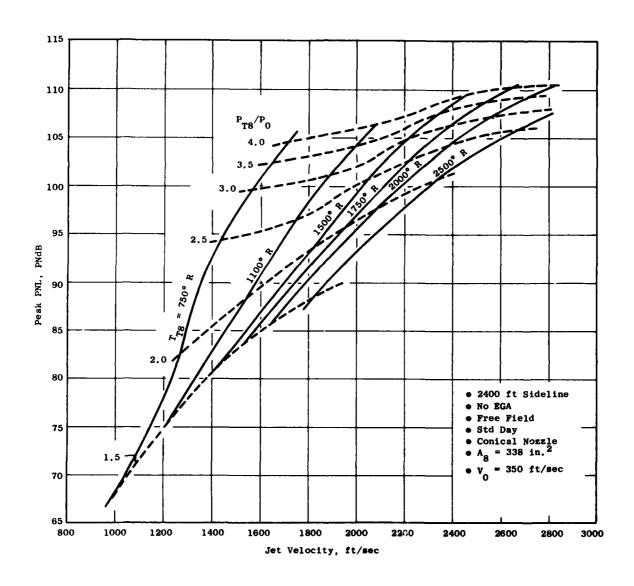


Figure 4-10. Effect of Cycle Conditions on Conical Nozzle Peak PNL.

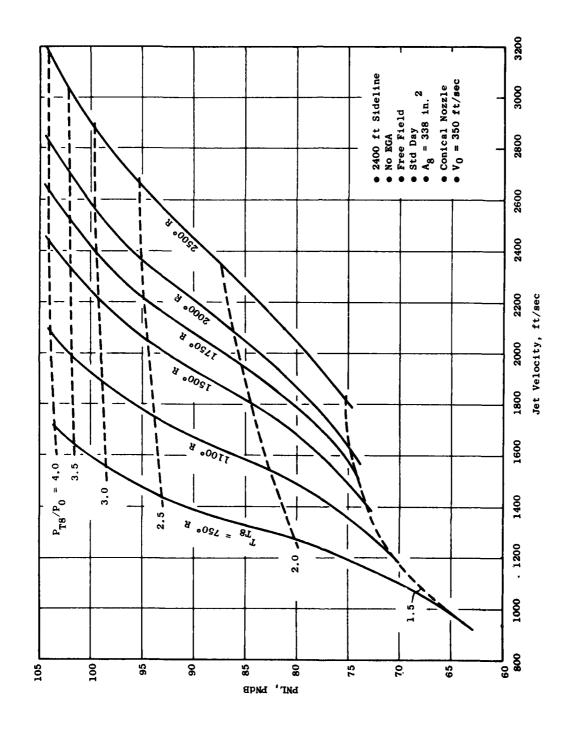


Figure 4-11. Effect of Cycle Conditions on Conical Nozzle PNL at θ_1 = 50°.



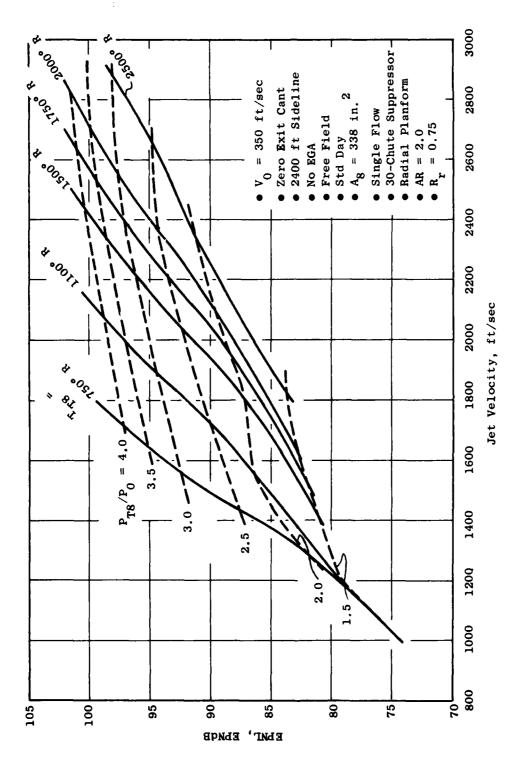


Figure 4-12. Effect of Cycle Conditions on Suppressor EPNL.

(10)

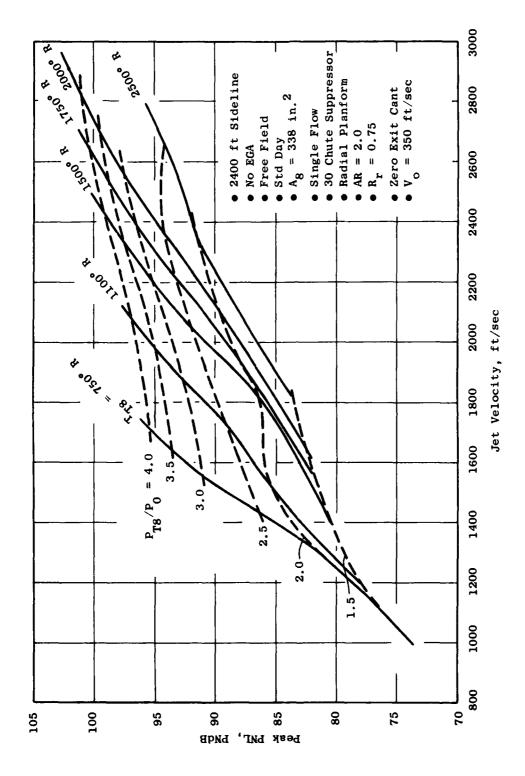


Figure 4-13. Effects of Cycle Conditions on Suppressor Peak PNL.

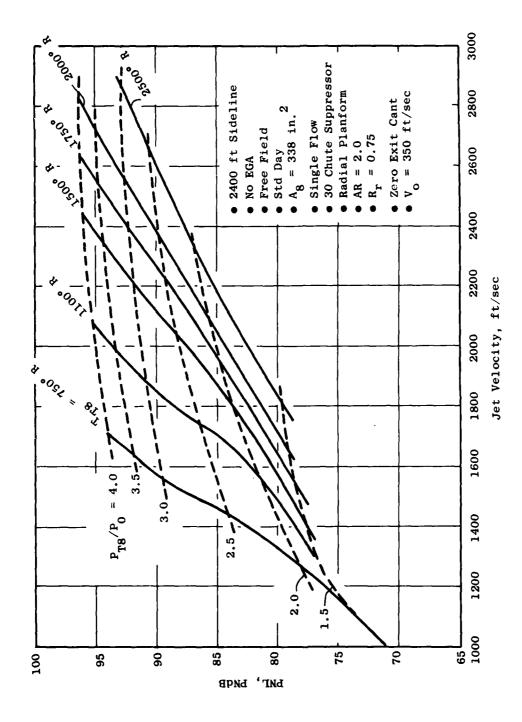


Figure 4-14. Effects of Cycle Conditions on Suppressor PNL at θ_1 = 50°.

due to changes in geometry, size, or distance can have a large effect on the relationship between noise and cycle conditions.

Figures 4-15 through 4-20 show the relationship between in-flight EPNL and size and distance. For these plots, an increase in size is accompanied by a corresponding increase in thrust. It should be noted, however, that the noise increase is at a slower rate with size than would be expected due to the increase in thrust. The reason lies in the fact that, as size increases (from 0.5 square feet up), high noise levels are shifted from high nonweight bands into less heavily weighted bands. Although the actual SPL is increasing in the expected manner with thrust, the subjective PNL and, hence, EPNL go up less rapidly.

Figures 4-15 and 4-16 give the effect of size and distance on in-flight EPNL for a conical nozzle at supersonic (with shock noise) and subsonic (without shock noise) conditions respectively. Both figures show approximately the same trends (within 2 dB). Appendix E (Figures E-4 and E-5) contain PNL directivity and spectra showing these trends.

Figures 4-17 through 4-20 give trends with size and distance at the same two conditions for two suppressors. The suppressor with an area ratio of 1.5 (postmerged or low-frequency dominated) behaves similar to a conical nozzle at the high jet velocity. The high-area-ratio (AR = 3.0) suppressor (premerged or high-frequency dominated) falls off much more quickly with distance. Also, the subsonic condition on the low-area-ratio suppressor behaves more like the high-area-ratio suppressor than the conical because of the high-frequency-noise component. As mentioned before, changes in cycle or other physical dimensions of the suppressor may have an effect on the trends shown.

The effect of flight velocity on conical nozzle noise is given in Figures 4-21 and 4-22 for maximum PNL and EPNL respectively. The noise decreases with increasing flight velocity. Figures E-6 and E-7 in Appendix E indicate the relationship between static and flight.

Figure 4-23 indicates the effect of flight velocity on the suppression (relative to conical) for the representative suppressor. At high jet velocities, the differences in flight effects between the suppressor and conical nozzles cancel each other; the result is approximately constant suppression with jet velocity. At this jet velocity, the suppressor is postmerged controlled. At a low jet velocity where the suppressor is premerged controlled, the suppression decreases rapidly with flight velocity, actually going negative at 300 to 400 ft/sec. This is due to the more favorable flight effects present with the conical nozzle. A spectral examination given in Appendix E (Figures E-8 and E-9) indicates this effect. Here, ideal gross thrust is constant. Again, changes in the spectral composition of the suppressor noise due to size, distance, or geometry can cause differences in the PNL or EPNL suppression.

4.1.2.2 Geometric Parameters

This section contains trends of suppression relative to conical-nozzle noise for various suppressor types including single-flow multichute and multitube, dual-flow multichute, and single-flow multichute and multitube nozzles with hard-wall ejectors.

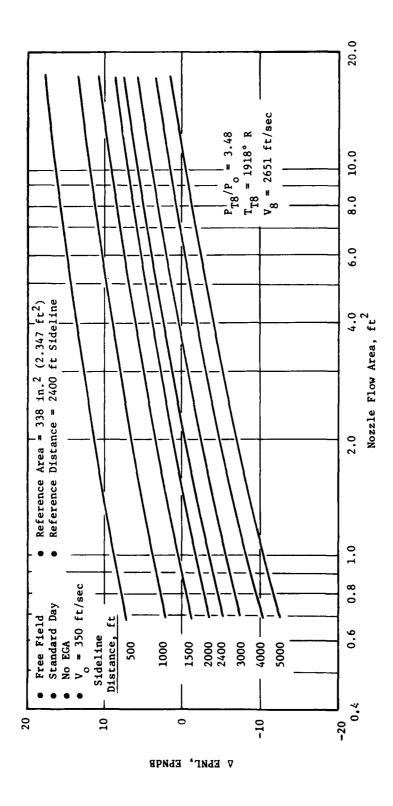


Figure 4-15. Conical Nozzle Size and Distance Study, Supersonic.

15 Car 18 Caller 1869 24

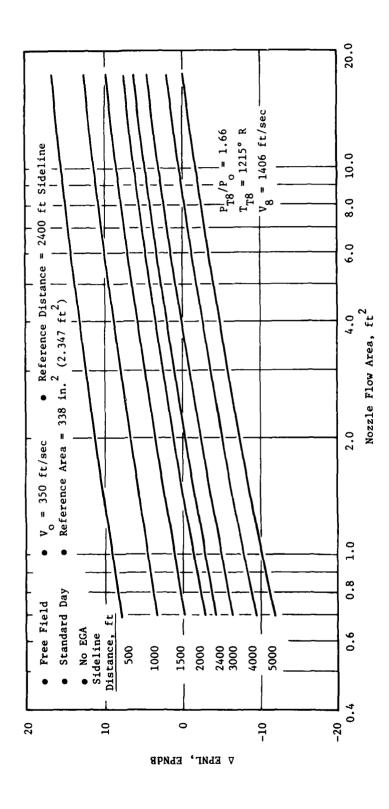


Figure 4-16. Conical Nozzle Size and Distance Study, Subsonic.

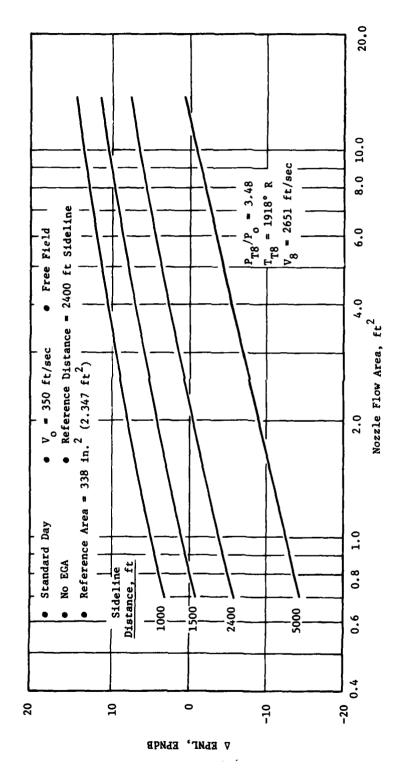


Figure 4-17. Thirty-Chute Suppressor Nozzle Size and Distance Study, Supersonic, AR = 1.5.

-

The state of the state of the second

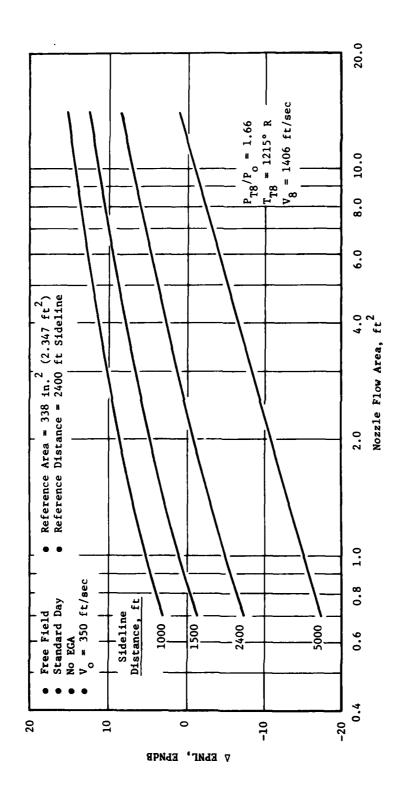


Figure 4-18. Thirty-Chute Suppressor Nozzle Size and Distance Study, Subsonic, AR = 1.5.

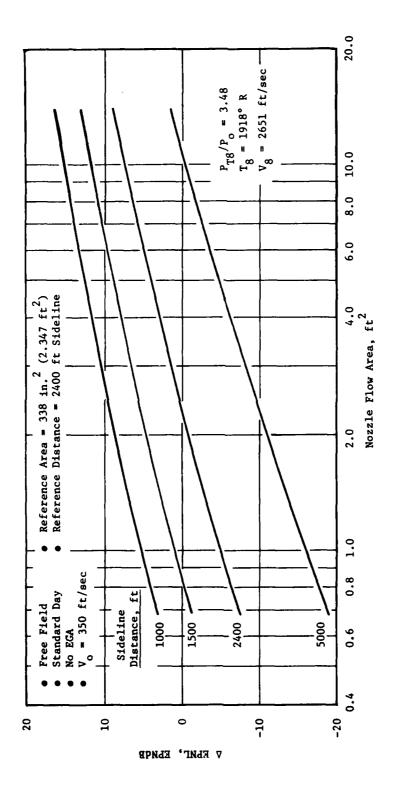
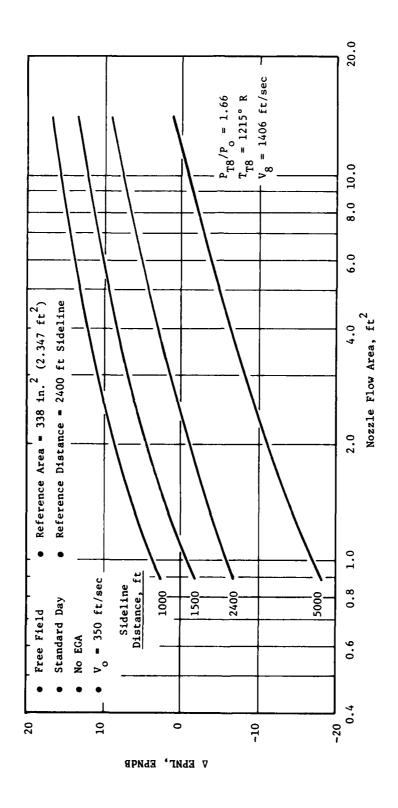


Figure 4-19. Thirty-Chute Suppressor Nozzle Size and Distance Study, Supersonic, AR = 3.0.

Secretary and the second



Thirty-Chute Suppressor Nozzle Size and Distance Study, Subsonic, AR = 3.0. Figure 4-20.

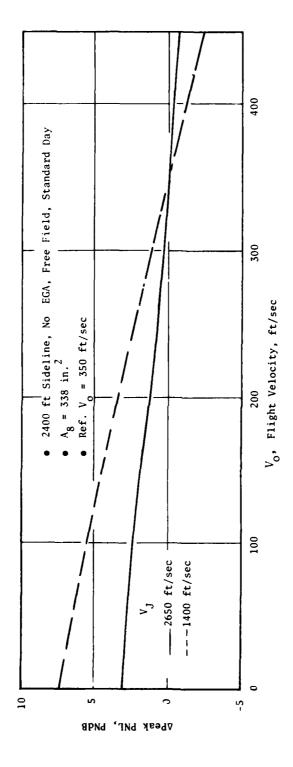


Figure 4-21. Effect of Flight on Conical Nozzle Peak PNL,

11

with the property

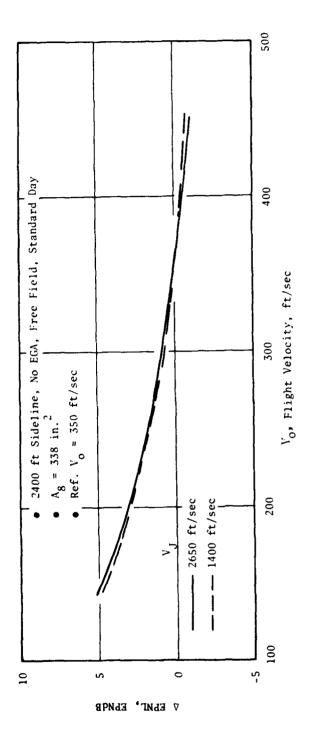


Figure 4-22. Effect of Flight on Conical Nozzle EPNL,

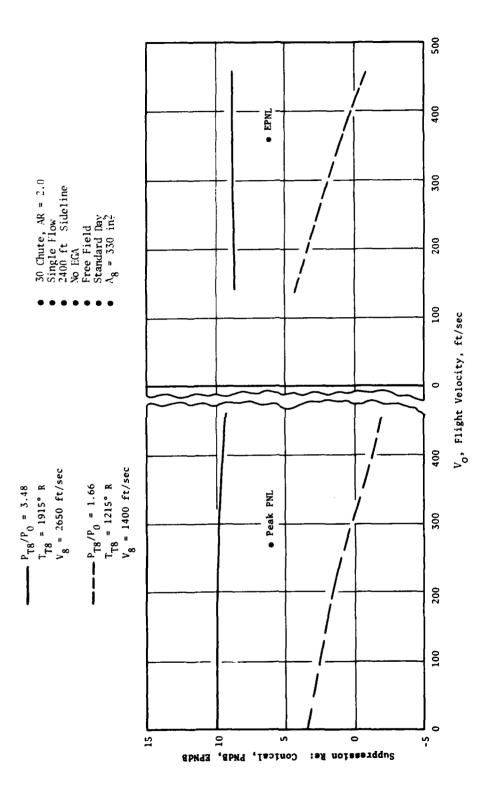


Figure 4-23. Effect of Flight Velocity on Suppression.

The second of th

Figures 4-24 through 4-26 give suppression trends with suppressor area ratio and element number for single-flow multichute and multitube nozzles on a static maximum PNL, in-flight maximum PNL, and in-flight EPNL basis respectively. Trends are given at three power settings corresponding to representative take-off, cutback, and approach conditions. Nozzle geometry descriptions are given on each plot.

The high power settings indicate that increasing area ratio is favorable, but chutes tend to increase suppression at a slower rate than tubes. Suppression is a weak function of element number with higher numbers of elements usually better. Negative suppression, seen in Figures 4-7 and 4-8, is also shown in-flight on Figures 4-25 and 4-26 at approach power. These trends and suppression levels are a function of size, distance, and geometry and cycle parameters; therefore, they may change for a given application. PNL directivity and spectral plots are given in Appendix E (Figures E-10 through E-17).

Figures 4-27 through 4-29 show trends with suppressor area ratio and element number for a dual-flow nozzle at a nozzle area ratio of 2.0. Trends with nozzle area ratio are given in Figure 4-30. Again, trends on a static PNL, in-flight PNL, and EPNL basis are given at three cycle conditions. As with the single-flow multichute nozzles, increasing area ratio improves suppression (but very slowly). Suppression is, again, a weak function of element number. Negative suppression is indicated for the low-jet-velocity, in-flight conditions.

These trends (in addition to being a function of size, distance, and geometric and cycle conditions) are a strong function of nozzle area ratio. The trends with nozzle area ratio for a representative suppressor on a dualflow nozzle are given in Figure 4-30. Except for the low-velocity condition, the best suppression is achieved at an area ratio of about 2.3. In cases where inner to outer cycle conditions and nozzle area ratio are changing, the trends can change substantially. Because of this and size, distance, and geometry considerations, it is recommended that the M*S model be exercised to generate trend curves for dual-flow nozzles for the specific case under consideration.

Figures 4-31 through 4-33 show trends with hard-wall-ejector geometry parameters. Cycle conditions also play an important role in determining ejector suppression (see Reference 12). These trends are illustrations only and should not be used to approximate ejector suppression. Ejectors work only on the premerged (high frequency) portion of the spectrum (see Figure E-18 in Appendix E); therefore, PNL and EPNL suppression are highly dependent on the bare suppressor spectral distribution. The reason for the relatively low increase in suppression due to the ejector is twofold. First, hard-wall ejectors have little effect on the side angles (70° to 120°) but a large effect on shallow angles and, therefore, show only a small increase in suppression peak to peak. EPNL shows more suppression. Second, since ejectors work on highfrequency noise, the more this part dominates the more PNL suppression can be achieved - up to the maximum for the ejector. For the nozzles shown, the small size and large distance make the spectral distribution less desirable for an ejector. A larger size and/or smaller distance would increase the premerged noise relative to the postmerged and result in a more effective ejector when the system is considered. As with dual-flow nozzles, it is recommended that the M*S model be exercised to generate trend curves for the specific nozzles with ejectors and cycle conditions under consideration.

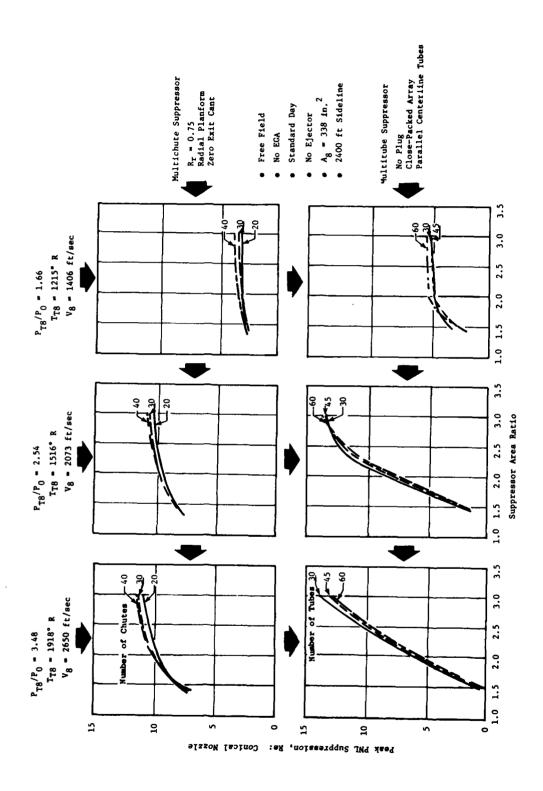


Figure 4-24. Typical Predicted Static Suppression Trends, Single Flow.

(11)

THE STATE OF THE S

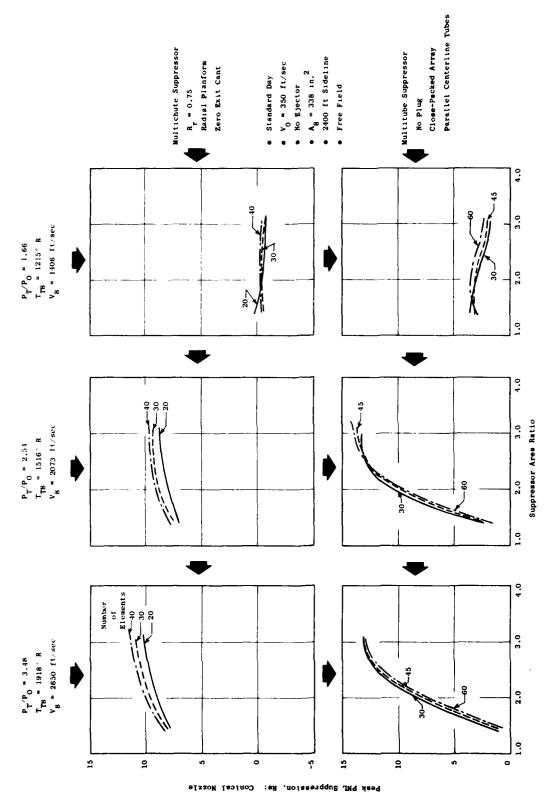


Figure 4-25. Typical Predicted Flight Peak PNL Suppression Trends, Single Flow.

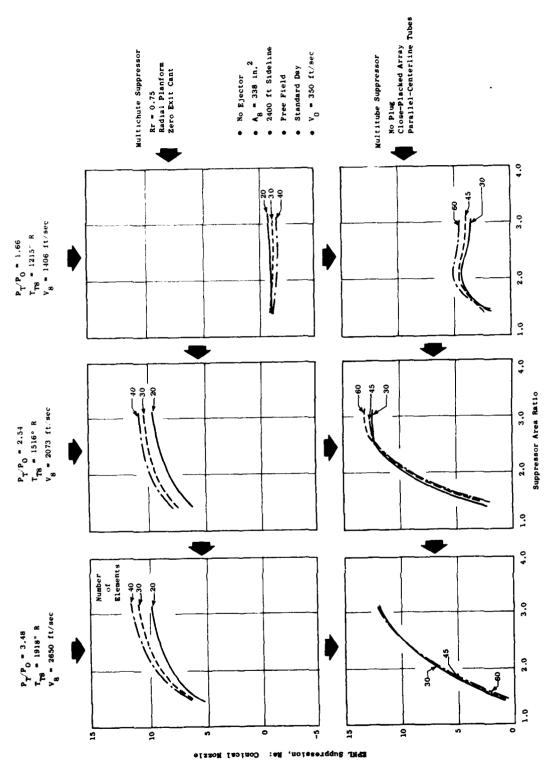


Figure 4-26. Typical Predicted Flight EPNL Suppression Trends, Single Flow.

1

्रका राज्युह

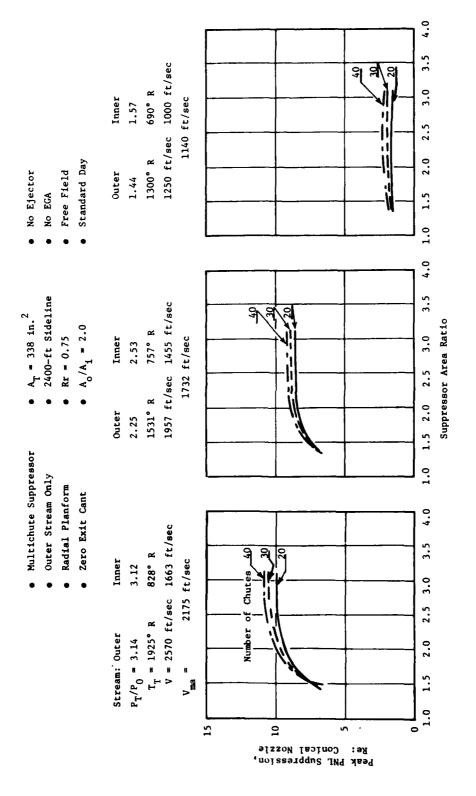


Figure 4-27. Typical Predicted Static Suppression Trends, Dual Flow.

10 To 10 (May 10 A)

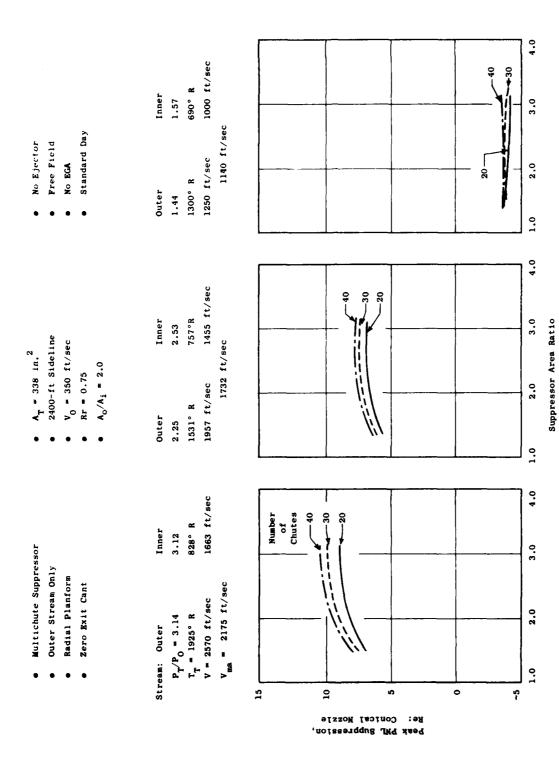


Figure 4-28. Typical Predicted Flight Peak PML Suppression Trends, Dual Flow.

一 大きな

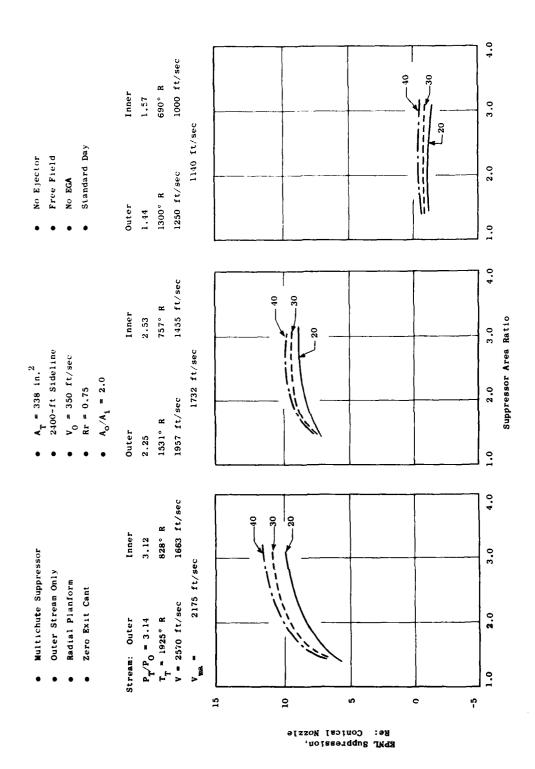


Figure 4-29. Typical Predicted Flight EPNL Suppression Trends, Dual Flow.

ない。





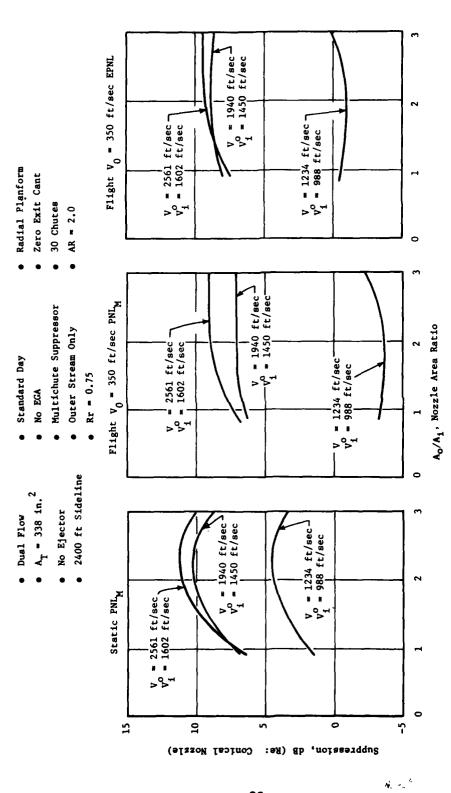


Figure 4-30. Suppression Trends.

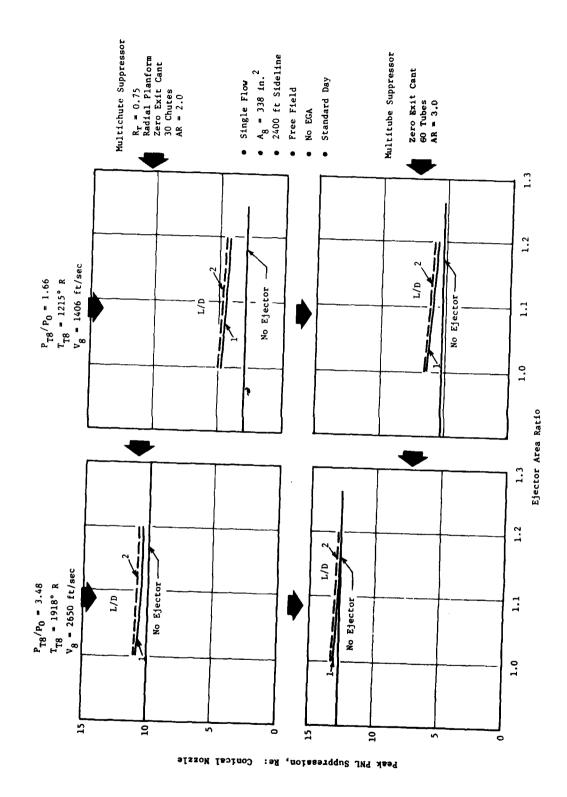


Figure 4-31. Typical Predicted Static Hard-Wall-Ejector Suppressor Trends.

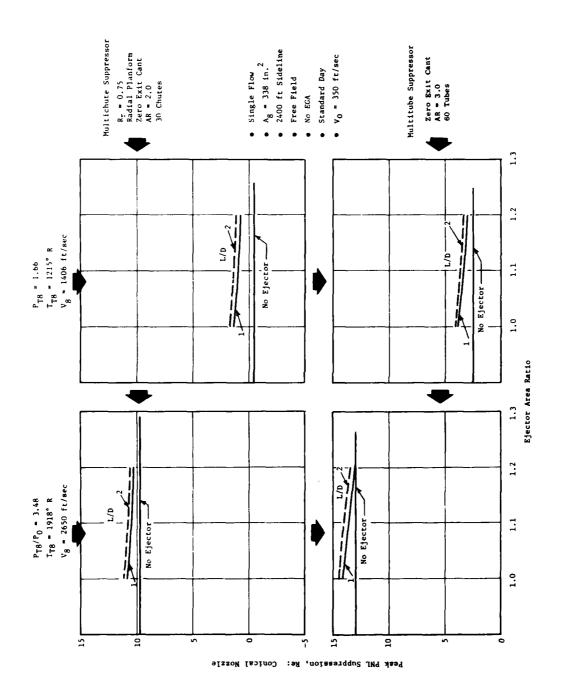


Figure 4-32. Typical Predicted Flight Hard-Wall-Ejector Peak PML Suppression Trends.

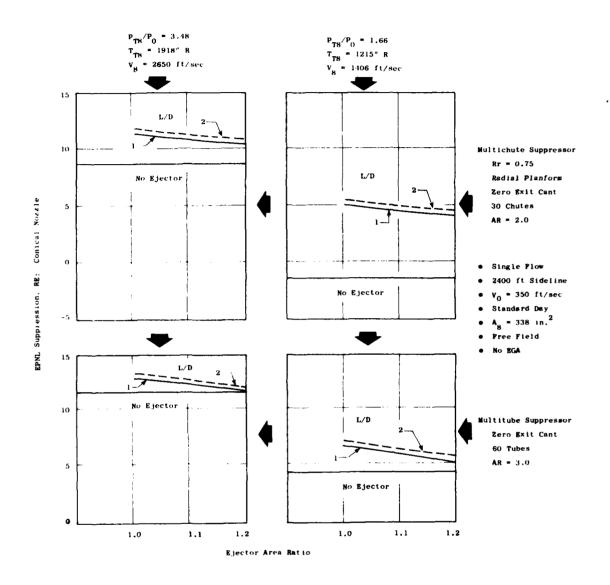


Figure 4-33. Typical Predicted Flight Hard-Wall-Ejector EPNL Suppression Trends.



The effect on noise of variables other than area ratio and element number can be predicted by the M*S model (see Table 4-4). By exercising the program over a range of these variables (or combination of these variables), trends can be discerned. Some examples are provided in Figures 4-34 through 4-36.

To generate Figure 4-34, the program was exercised over nozzle radius ratios of 0.5 to 0.9, and static maximum PNL suppression was plotted versus radius ratio. The trend indicates lower noise for radius ratios less than 0.6. The noise also decreases as radius ratio is increased above 0.7. The ramp between 0.6 and 0.7 is based on one set of data at about 0.62 radius ratio. Above 0.75 and below 0.55 in radius ratio, the curve is well-defined by data.

Figure 4-35 gives the suppression trend with outer row tube cant. The suppression decreases until a cant angle of about 6° is reached. The noise is constant above 6°. This trend occurs because, as the cant angle is increased, the outer row flows merge farther downstream, causing a loss in cutoff effect (see Reference 12) until it completely disappears at about 6°.

The effect of treating an ejector is shown in Figure 4-36. A very slight increase in suppression for the conditions chosen is observed as L/D increases; in this case the size of the nozzle and the sideline distance used for the prediction were such that the basic nozzle spectrum was not dominated by premerged noise, and the treatment in the ejector was, consequently, relatively ineffective. Other, more attractive, designs can be evolved and identified by the M*S model.

4.1.2.3 Comments

This section contains trend curves for specific nozzle types at specific cycle and geometric conditions. The curves provide a nozzle designer with the trends required to have a "feel" for what impact the various parameters have on suppressor noise. Because of the specific nature of these trends, they should only be used as a guide to generating trend curves for the specific application under consideration or to generate very preliminary noise levels for designs under consideration.

In general, large element numbers with large area ratios produce the most suppression up to a certain point. At the design condition (where the maximum suppression is needed) a balance between postmerged noise and premerged plus shock noise, including flight effects, usually yields the optimum suppression. Suppression is also higher for low-pressure-ratio, high-temperature cycle conditions. Dual-flow nozzles give highest suppression when the nozzle area ratio and jet velocity ratio are between 2 and 3. Ejectors are most effective on nozzles dominated by premerged and shock noise and have a peak effect at a pressure ratio of 2.0 and high temperature.

4.2 GUIDES FOR GOOD DESIGN PRACTICES

4.2.1 Introduction

Development work on multielement jet noise suppressors dates to the early

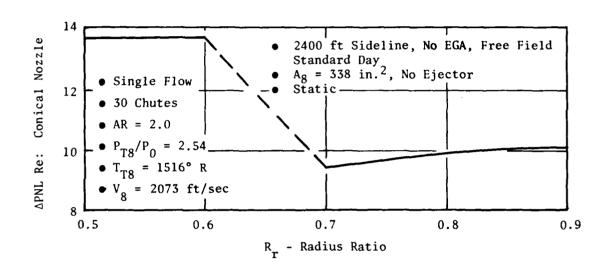


Figure 4-34. Effect of Suppressor Radius Ratio on Suppression.

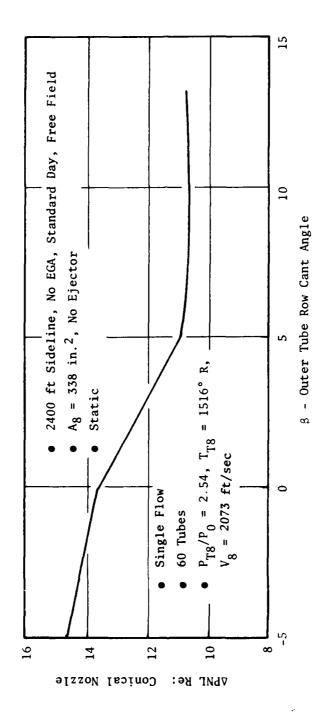


Figure 4-35. Effect of Outer Tube-Row Cant on Suppression.

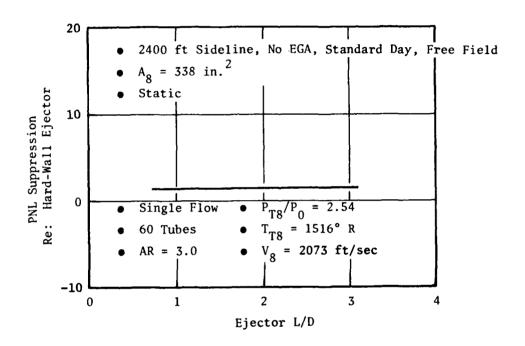


Figure 4-36. Treated Ejector Suppression Trends.

1950's (Reference 16) with the first commercial application of a 21-tube suppressor design to a U.S. built jet transport in 1958: the Boeing 707 powered by P&W's JT3C turbojet engine. A 9-tube suppressor was later installed on P&W's JT4A powering the Boeing 707. The designs were typical of suppressors later used on DC-8 and Convair 880 jet-powered transports. Suppressor development work was continued primarily by Boeing, P&W, and GE during the precontract period for the U.S. SST, and more concentrated efforts were made from 1968 through 1971 by Boeing, GE, NASA, etc. during the GE4/SST development program. During this phase of development it was found that the performance of most multielement suppressor nozzles is uniquely dependent on an array of geometric variables and on the nozzle thermodynamic-cycle composition, in terms of P_m and T_m , with the noise dependency varying for each nozzle configuration. The lack of understanding of such changes with power setting and nozzle geometry, in terms of the physics of flow and correlation with noise processes, made it necessary to conduct extensive nozzle tests to generate an empirical data base. Thus, literally hundreds of test configurations were developed and subjected to various test methods for acoustic evaluation. Following termination of the GE4/SST program, Boeing and GE continued multielement suppressor technology development through DOT/FAA sponsored contracts; Boeing primarily concentrated on developing multitube technology refinements, and GE concentrated primarily on multichute/spoke, annular-plug nozzles with multitubes of secondary interest. Static suppression levels were advanced from the 6 APNL of the early 707/JT3C and JT4A applications to more than 20 APNL for Boeing's multitube-with-treatedejector configuration. Reference 17, and in excess of 14 APNL for the GE multichute annular plug with treated ejector (when applied to a full-scale turbojet engine), Reference 18.

To further the understanding of basic suppression principles for jet noise, the "High Velocity Jet Noise Source Location and Reduction" program continued multielement-suppressor technology investigation primarily in the form of high-radius-ratio, full and half-span chute/spoke suppressors. These efforts are fully reported in the Task 3 (Volume II) and Task 5 final reports (References 19 and 3). This program also developed the M*S prediction technique which has been established as the basic, first-level, design tool for use in this design guide.

Significant design experience has, therefore, been assembled either on a first-hand basis or through available open-literature sources. This experience has helped develop the multielement suppressor nozzle design insights categorized within this section as "Guides For Good Design Practices." These suggestions for good design supplement the basic M*S model which accommodates all the primary geometric and thermodynamic design parameters. They are intended to be used as guidelines, in concert with the M*S model, to assure that the basic suppression levels are met. The data in this section have been developed from historical as well as current sources. No confidence limits have been placed on the data because they are intended to be used as guidelines rather than absolute levels. The basic suppression levels are evolved from parametrically exercising the M*S model in the static mode and selecting optional designs. General acoustic-suppression trends anticipated from exercising the M*S model over select ranges of the primary geometric and thermodynamic variables were discussed in Section 4.1.2.



In most cases within the range of practical design, the variables which fall within the "guidelines" category, and which are summarized in Section 4.2.2 and discussed in Appendix F, do not alter the acoustic and aerodynamic performance to a large degree. However, the attention these variables receive during design may mean the difference between an average and an above-average design.

4.2.2 Summary - Design Guidelines

Multielement-suppressor design involves a complex interaction among acoustic suppression potential, aerodynamic installed thrust performance, mechanical feasibility (i.e., implementation, stowability, and reliability), and ultimate impact of the above on mission. The M*S model correlation has been evolved as a working tool to readily allow parametric evaluation of suppressor geometric and thermodynamic properties - unincumbered by the limitations of implementation practicability. It can accommodate the primary multielement geometric design variables: area ratio, radius ratio, degree of segmentation, use of treated ejector, tube cant angle, chute planform shape, and chute exit plane cant. Suppression variations anticipated as a result of exercising the M*S model over selected primary variable ranges were discussed in Section 4.1. Tuning the optimal M*S selections during the design-implementation phase is accomplished by sound engineering judgement with the aid of "Guides For Good Design Practices" as discussed in Appendix F. This is to assure that suppression is not degraded by random geometry alterations when integrating the suppressor into a viable propulsion system. For tubes/holes these guidelines consider length, size and spacing uniformity, exit and base plane stagger, canting, internal geometry, and exit planform. For chutes/spokes they include element selection, exit planform, exit plane cant, and general design considerations.

Suggested Guidelines for Tube Suppressors

- Finite external tube length is necessary to allow significant ambient-air entrainment, enhanced mixing, more rapid velocity decay, slightly improved acoustic suppression, and significantly better aerodynamic performance.
- Slight variance from tube size and spacing uniformity will not significantly alter suppression potential. Moderate variation will slightly degrade suppression, and large variation will seriously degrade suppression. Using center holes or annular flows over plugs also seriously degrades acoustic performance.
- Variation from coplanar tube-array termination may be detrimental to suppression optimization; the greater the deviation from coplanar, the greater the loss.
- Base plane stagger with coplanar exit may enhance air entrainment, suppression, and aerodynamic performance.
- Tube canting inward lowers suppression, and canting outward may not significantly impact suppression.



- Internal tube geometry design is very critical primarily in terms of minimizing aerodynamic losses and impacting nozzle pumping characteristics.
- Changing tube exit planform from round to trapezoidal has minimal impact on suppression potential. Greatrix tube ends, however, enhance suppression significantly but are quite poor aerodynamically.

Suggested Guidelines for Chute/Spoke Suppressors

- Spoke or chute selection is more uniquely determined by aerodynamic performance and mechanical-implementation considerations than suppression capability.
- Planform shape within the range of $1.25 \le \text{W}/\text{W}_{.0} \le 1.5$ is considered most practical; variation most heavily impacts aerodynamic performance while moderately changing suppression.
- Chute/spoke exit plane cant aft or forward may change suppression by \pm 3 PNL for β + 15° to -15°.
- Design details of chute axial cross section are very important to good aerodynamic performance. Thirty percent convergence of flow area is a suggested guideline.

4.3 M*S COMPUTER PROGRAM EXAMPLE CASES

Two examples of M*S computer program application for various nozzles are shown in Appendix G. The cases presented in Appendix G are illustrative and are not intended to represent actual or proposed nozzle designs.

5.0 <u>AERODYNAMIC PERFORMANCE OF JET NOISE SUPPRESSORS</u>

5.1 BACKGROUND

The selection of a jet noise suppressor for a particular application requires consideration of the suppressor aerodynamic performance. This was discussed in Section 3.0, Preliminary Noise Abatement Nozzle Selection. Performance is important at takeoff where the suppressor is deployed and even more important at the supersonic-cruise design point for supersonic transport. It is crucial, then, that the selected suppressor system not adversely affect design point performance. This could occur, for instance, when the suppressor significantly increases potential leakage paths. Suppressors which significantly increase diameter, and hence pressure and friction drag, should be avoided.

During deployed operation the suppressor must perform well from static conditions up to about Mach 0.4. Although typical AST lift-off occurs at about Mach 0.3, the suppressor should work well beyond the measuring point in order to minimize community annoyance. Normally, this low Mach number range would not greatly affect nozzle performance. However, scale-model-suppressor wind tunnel tests have shown that multielement suppressors of all types are very sensitive to external flow velocity. Under static conditions, the jet, or jets, "pump down" the relatively large suppressor base areas, creating a drag force. External flow augments this pumping action to further increase drag. Noise-abatement nozzles which utilize ejectors to entrain large amounts of air are particularly sensitive to external flow. Although static thrust augmentation can be obtained (i.e., actual thrust > ideal thrust) the augmentation rapidly decreases with external flow velocity.

A performance prediction methodology which, in conjunction with Section 4.0, allows the exhaust system preliminary designer to conduct performance/suppression trades on a wide range of suppressors is presented herein. The methodology provides estimates of the static and in-flight isolated installed gross thrust coefficient, Cfg, for mechanical-type suppressors in the deployed mode as envisioned for installation on future supersonic-cruise aircraft. The mechanical suppressor includes two basic families, the multichute/spoke plug nozzle and multitube full round nozzle. The multichute/spoke plug suppressor category encompasses single- and dual-flow nozzles, with and without ejectors. The multitube category is limited to single-flow nozzles, with and without ejectors. The basis for the methodology is cold-flow, scale-model, thrust and pressure data. Appendix H reviews results from tests, conducted by GE and other contractors, on the effect of exhaust gas temperature on suppressor performance. These data suggest that, for preliminary design purposes (e.g. comparison and screening studies), cold-flow-performance results should be acceptable. The performanceprediction methodology for each category is supplemented by a discussion of major geometric variables and performance trends in Appendix I. The methodology estimates performance through a series of discrete steps. Example problems illustrating this design methodology are included in Appendix J.

5.2 AERODYNAMIC PERFORMANCE OF MULTITUBE NOZZLES

12

5.2.1 Introduction

Multitube nozzle aerodynamic performance losses can be separated into two general categories: internal losses associated with the flow within the tubes, and external losses associated with baseplate drag. Both types of losses are discussed below, and methods are presented for calculating their magnitude.

Internal losses are independent of external flow. The baseplate pressure, however, is strongly influenced as free-stream velocity increases. Although a major portion of multitube experimental work has been conducted at static conditions, some in-flight data, primarily gathered by Boeing, Reference 11, are included in Appendix I.

Ejectors are an integral part of most multitube suppressor systems designed for supersonic-cruise aircraft. Proper design of the ejector can result in thrust augmentation at static and low-velocity-external-flow conditions. A majority of the multitube/ejector nozzle performance data, especially with external flow, were generated by Boeing (Reference 11) and are summarized in Appendix I. Appendix I also includes some flight data taken by NASA with the F-106B aircraft (Reference 20).

A methodology useful in predicting nozzle aerodynamic performance is also discussed. Example problems utilizing the design methodology are presented in Appendix J.

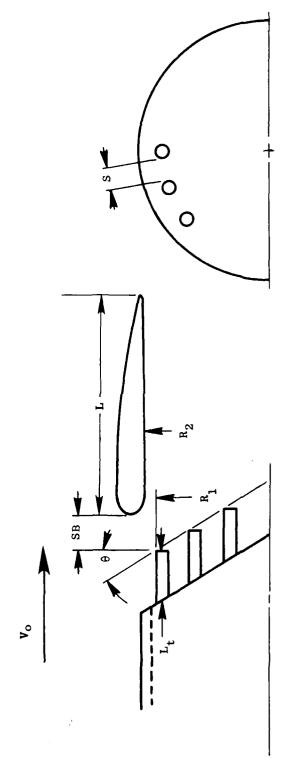
5.2.2 Performance Estimation Methodology

The discussions on individual performance-loss mechanisms are included in Appendix I to familiarize the reader with general performance trends. In the following sections, methods are presented that allow the estimation, on a preliminary design basis, of the performance of multitube nozzles.

The methodology presented "builds up" the performance estimate through a specific series of steps. The starting point, using the schematic shown in Figure 5-1, is the internal performance of the bare tube suppressor, Cfg_{int}. The baseplate drag (with no external flow) is then calculated. The next step is to apply bare-suppressor drag increments to account for external flow effects. When ejectors are employed, ejector increments are added as a function of free-stream velocity. An example case is presented in Appendix J utilizing the methods outlined.

5.2.2.1 Tube Internal Losses

The internal performance of a bare, multitube suppressor can be estimated from Figure 5-2, where Cfg_{int} is presented as a function of tube length, tube number, total flow area, and nozzle pressure ratio. This figure is the same as Figure I-6 in Appendix I, with the exception that the parameter $L_{t\,i}\sqrt{N}$ has been nondimensionalized by the square root of the total flow area. As noted in Figure 5-2, the major constraint is that the tube entrance is rounded $(R/D \ge 0.1)$, and the tube internal Mach number is ≈ 0.5 . If for some reason these contraints cannot be met, it is suggested that Reference 22 be consulted directly. Variations in Figure 5-2 would also occur as Reynolds number is varied; however, for a preliminary design estimate, Figure 5-2 should be adequate.



$$NAR = AR = \pi R_1^2 / A_8$$
$$EAR = \pi R_2^2 / A_8$$

Figure 5-1. Multitube Suppressor Nozzle Schematic.

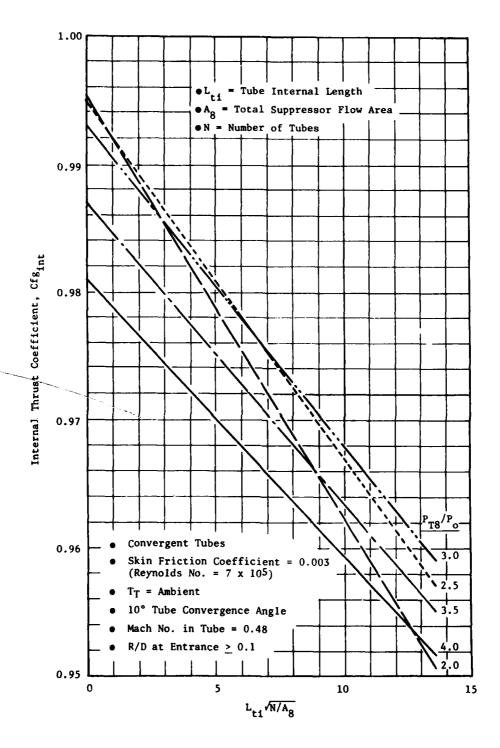


Figure 5-2. Multitube Suppressor Internal Performance.

5.2.2.2 Base Pressure Correlation (Static)

As discussed in Appendix I, a large number of geometric parameters affect the suppressor baseplate static pressure. In view of the number of variables involved, various attempts have been made to correlate the available base pressure data to a simple geometric parameter. A "ventilation" parameter (VP) has been defined which appears to collapse the base pressure data quite well. This parameter is defined as:

 $VP = [S^2 + (L_T/\cos \theta)^2]/A8 n$

where S = distance between tubes on outer row,

LT = external tube length,

 θ = baseplate/tube stagger angle,

As = total flow area,

n = total number of tubes in outer row.

The correlation of this ventilation parameter with a variety of test data is shown in Figure 5-3 for a nozzle pressure ratio of 3.0 and no external flow. Also shown on Figure 5-3 is the spread in data, $\pm 0.7\%$, and the corresponding spread in thrust coefficient assuming an area ratio of 3.0 for the suppressor. Considering the problems inherent in obtaining an accurate, average (integrated), base pressure, the above correlation is considered excellent.

Figure 5-4 presents design curves of baseplate pressure versus ventilation parameter for nozzle pressure ratios from 2.0 to 4.0. The average base pressure obtained from 5-4 can be converted to a loss in thrust coefficient as follows:

$$\Delta Cfg_{base} = K [(\bar{P}_b/P_0)_{-1}]$$
 (AR-1)

where K is obtained from Figure 5-5. The static thrust coefficient for the base nozzle is then:

$$Cfg = Cfg_{int} + \Delta Cfg_{base}$$
.

As a note of caution, the majority of the data used for the correlation were from models with evenly spaced tube patterns. The Boeing 31-tube and 37-tube radial arrays, however, seemed to fit within the data scatter band. Also, for a given model, all tubes were the same diameter.

5.2.2.3 External Flow (Bare Suppressor)

The effect of external flow is to increase nozzle drag, as shown in Figure I-20, Appendix I. The drag that contributes to the loss in Cfg with velocity shown in Figure I-20 includes the suppressor baseplate drag and the approach ramp drag. Data for the 19-, 31-, 37-, and 61-tube nozzles shown in Figure I-20, Appendix I, were correlated with the distance between tubes in the outer row. The resulting correlation is shown in Figure 5-6. This figure presents lapse rate (Δ Cfg/V_O) as a function of tube spacing and nozzle pressure ratio



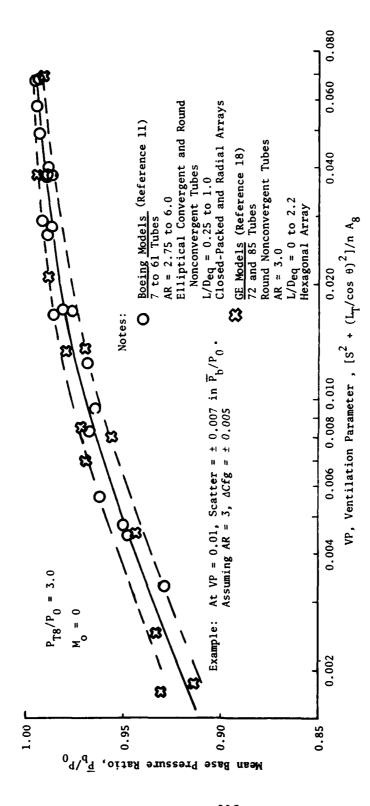


Figure 5-3. Correlation of Multitube Nozzle Baseplate Pressures.

i garaga a**t a Me**rca bah ya i

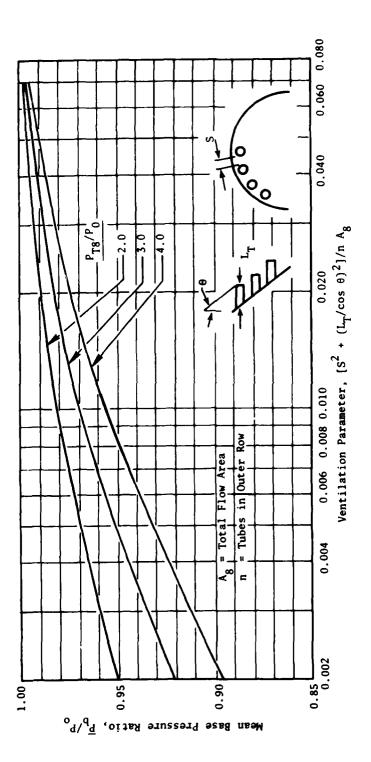


Figure 5-4. Mean Baseplate Pressure (Static).

(131)

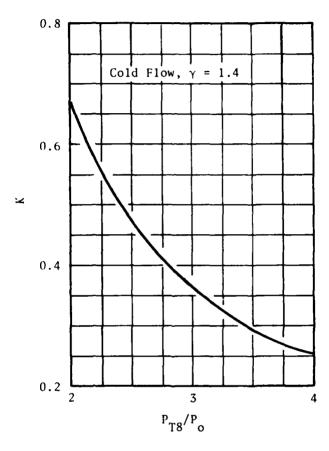


Figure 5-5. Conversion Factor (K) for Base Pressure.

- \bullet S = Distance Between Tubes in Outer Row
- $D_{eq} = 2\sqrt{A_8/\pi}$
- Λ_8 = Total Flow Area
- V_o = Flight Velocity in Knots

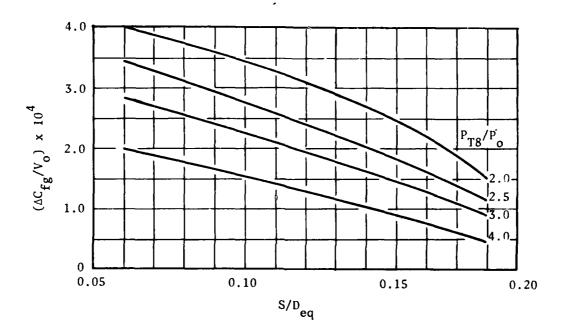


Figure 5-6. Bare Multitube Nozzle Lapse Rate.

where $\Delta Cfg = Cfg static - Cfg_{Vo}$ and $V_o = flight velocity$.

5.2.2.4 Ejector Performance

A generalized method for estimating the performance of multitube suppressor nozzles with ejectors is not available. However, the extensive work completed by Boeing as part of the SST Technology Follow-On Program, Phase II (Reference 1)), provides the trends discussed in Appendix I. Figure 5-7, from Reference 21, illustrates static suppressor/ejector performance trends as a function of major variables. Within the constraints of EAR/NAR \simeq 1.15, the static performance with ejectors at a nozzle pressure ratio of 3.0 appears to improve from 5% to 8% in Cfg as shown in Figure 5-8. Also indicated in Figure 5-8 is the rate at which the performance improvement decreases with flight velocity. Although Figure 5-8 can be used to arrive at a general level of suppressor/ejector performance, it is highly recommended that any design of a multitube/ejector exhaust system be preceded by a thorough review of References 21 through 23.

5.2.2.5 Example Performance Prediction

Performance of a typical multitube nozzle, with and without ejector, is presented in Appendix J. The empirically derived design curves discussed in the preceding sections were used to generate the data.

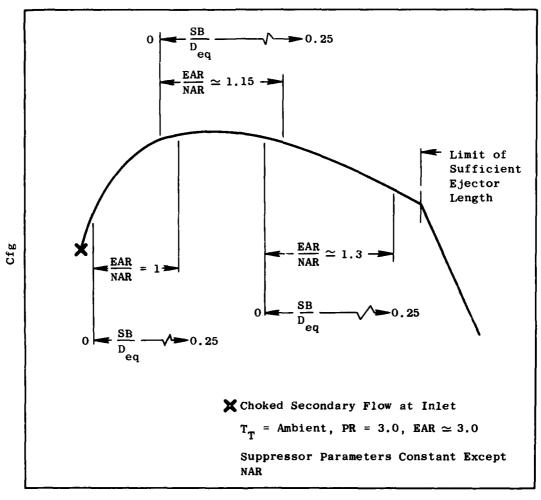
5.3 AERODYNAMIC PERFORMANCE OF MULTICHUTE/SPOKE PLUG NOZZLES

5.3.1 Introduction

One of the more promising noise-abatement-nozzle concepts investigated for suppressing the jet noise of a high-velocity flow is the multichute/spoke plug configuration. This type of noise suppressor, Figure 5-9,, breaks the large flow area into smaller flow elements through the insertion of rectangular or trapezoidally shaped, dividers into the flow. Deployment of the suppressor from brake release through the community noise measuring point results in a reduction in jet noise at the expense of nozzle performance relative to an unsuppressed exhaust system. This performance loss is a strong function of chute/spoke geometry. A good portion of the data base described in Appendix I was derived from scale-model tests conducted primarily by GE (Reference 2, 18 and 19). Flight data taken by NASA on the F-106B (Reference 24) are also included in Appendix I.

This section details the methodology used in calculating the wind-on, uninstalled performance of an exhaust system with a chute or spoke suppressor. In addition, Appendix I presents the sensitivity of the thrust coefficient to changes in certain geometric parameters for a specific suppressor nozzle in the form of plots. A detailed example of the calculation procedure used for overall nozzle performance is included in Appendix J.





Increasing Effective Ejector Inlet Area

Figure 5-7. Gross Thrust Coefficient as a Function of Effective Inlet Area, Setback, and EAR/NAR Ratio.

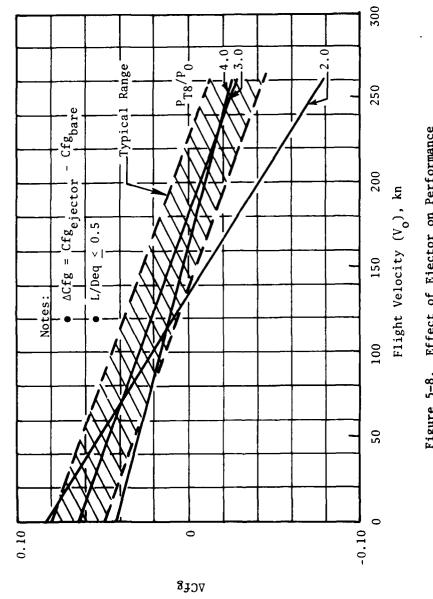


Figure 5-8. Effect of Ejector on Performance



Figure 5-9. Multichute/Spoke Nozzle.

119

X

and the second

September 1 Septem

5.3.2 Performance Estimation Methodology

5.3.2.1 Bare Suppressor

In the context of an overall airframe/engine design, many refinement iterations occur. The nozzle design is a typical engine-subsystem optimization procedure. Inputs from the cycle, technical, and acoustic groups are used to set the nozzle design constraints. Using these inputs, an optimum-performance exhaust system, as schematically shown in Figure 5-10, can be designed for the mission. Nozzle performance coefficients are then supplied to the aforementioned groups, and the next iteration commences.

The inputs from the cycle, mechanical, and acoustic groups used in calculating nozzle performance coefficients are:

$\mathbf{M}_{\mathbf{p}}$	External Mach number
$\mathbf{P}_{\mathbf{O}}$	Free-stream ambient pressure
PR_0 , PR_1	Outer and inner nozzle pressure ratios
Yo, Yi	Outer and inner ratio of specific heats
T_{To} , T_{Ti}	Outer and inner total temperature
A_O , A_i	Outer and inner nozzle throat areas
D _{max}	Maximum nacelle diameter
N	Number of spokes or chutes
W_{ci}/W_{co}	Chute width ratio
AR	Area ratio of suppressor
ß	Angle between suppressor exit plane and a line normal to the nozzle centerline (cant)
μ	Viscosity

The nozzle designer has control over the following parameters:

DR_S	Thickness of shroud at exit plane of suppressor
Rio	Inner nozzle outer radius
DR	Depth of suppressor element on outer shroud
φ	Plug angle at chute exit plane
$ar{\phi}$	Average plug angle under spoke or chute

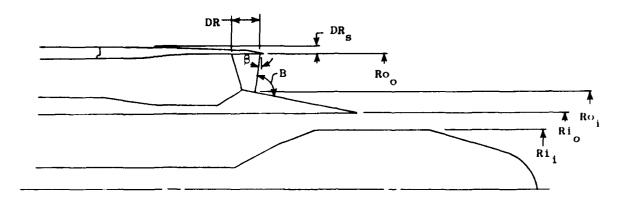
The general equation for calculating the overall nozzle thrust coefficient is:

$$Cfg_{Nozzle} = \frac{Cfg_{o} (FID_{o}) + Cfg_{i} (FID_{i})}{FID_{o} + FID_{i}}$$
(1)

More details on the above input are included in Appendix I.

The method used in calculating the terms in the preceding expression is presented below:

(144



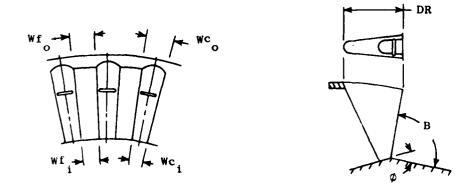


Figure 5-10. Definition of Geometric Parameters.



$$Ro_{O} = \frac{D}{2} - DR_{S}$$
 (2)

Solve implicitly using equations 3a-3h for Ro $_{i}$, Wc $_{i}$, Wc $_{o}$:

$$Wc_i/Wc_o \equiv Given$$
 (3a)

Total Chute Area =
$$A_0$$
 (AR - 1) (3b)

$$A_{\text{Chute}} = Ro_{0}^{2} \sin^{-1} (Wc_{0}/2 Ro_{0}) - (Wc_{0}/2) \sqrt{Ro_{0}^{2} - Wc_{0}^{2}/4}$$

$$+ \left[\sqrt{Ro_{0}^{2} - Wc_{0}^{2}/4} - \sqrt{Ro_{1}^{2} - Wc_{1}^{2}/4} \right] \cdot \left[(Wc_{0} + Wc_{1})/2 \right]$$

$$+ Ro_{1}^{2} \sin^{-1} (Wc_{1}/2 Ro_{1}) - (Wc_{1}/2) \sqrt{Ro_{1}^{2} - Wc_{1}^{2}/4}$$
(3d)

$$Wf_o = 2 Ro_o \sin [180/N - \sin^{-1} (Wc_o/2 Ro_o)]$$
 (3e)



$$Wf_i = 2 Ro_i \sin [180/N - \sin^{-1} (Wc_i/2 Ro_i)]$$
 (3f)

$$A_{Flow} = Total Flow Area/N$$
 (3g)

$$A_{\text{Flow}} = (1\sqrt[6]{\cos \beta}) \left\{ \text{Ro}_{0}^{2} \sin^{-1} \left(\text{Wf}_{0}/2 \text{ Ro}_{0} \right) - \left(\text{Wf}_{0}/2 \right) \sqrt{\text{Ro}_{0}^{2} - \text{Wf}_{0}^{2}/4} \right. \\ + \left[\sqrt{\text{Ro}_{0}^{2} - \text{Wf}_{0}^{2}/4} - \sqrt{\text{Ro}_{1}^{2} - \text{Wf}_{1}^{2}/4} \right] \left[\left(\text{Wf}_{0} + \text{Wf}_{1} \right)/2 \right] \\ + \left. \text{Ro}_{1}^{2} \sin^{-1} \left(\text{Wf}_{1}/2 \text{ Ro}_{1} \right) - \left(\text{Wf}_{1}/2 \right) \sqrt{\text{Ro}_{1}^{2} - \text{Wf}_{1}^{2}/4} \right\}$$
(3h)

Suppressor projected base area:

$$A_{B} = \pi \left(Ro_{O}^{2} - Ro_{I}^{2} \right) + N \sin^{-1} \left(Wc_{O}/2 Ro_{O} \right) \left[(Ro_{O} + DR_{S})^{2} - Ro_{O}^{2} \right]$$

$$- A_{O} \cos \beta$$
(4)

Suppressor discharge coefficient:

$$CD_{o} = CDV (CD\delta)$$
 (5a)

For T_{T_0} < 1000° R

CDV =
$$1.0 + [P_0]/146960][5.4913999 - 0.060446929 T_{To(cen)}]$$

 $-1.5267814(10^{-3})T_{To(cen)}^2 + 1.110391(10^{-4})T_{To(cen)}^3$ (5b)
 $-2.6897358(10^{-6})T_{To(cen)}^4 + 2.9889184(10^{-8})T_{To(cen)}^5$
 $-1.2608694(10^{-10})T_{To(cen)}^6]$

For $T_{T_0} \ge 1000^{\circ} R$, CDV = 1

$$T_{\text{To (cen)}} = (5/9)(T_{\text{To}} - 491.688)$$
 converting T_{To} to ° C (5c)

$$CD\delta = 1 - (0.130768/Re_{HR_0}^{1/6})$$
 (5d)

$$Re_{HR_o} = [12 \ HR_o(PR_o)P_0/\mu(T_{To})]\sqrt{\frac{2}{\gamma_o^2/25040} \ CP_o(\gamma_o - 1)T_{To}}$$
 (5e)

$$\mu(T_{To}) = 2.278(10^{-8})T_{To}^{1.5}/(T_{To} + 198.6)$$
 (5f)

$$HR_o = Hydraulic radius of flow area between chutes$$
 (5g)

Geometric ratios used in statistically generated equations:

$$Rr = Ro_1/Ro_0 (6a)$$

$$Wf_{i/o} = Wf_{i}/Wf_{o}$$
 (6b)

$$Wc_{i/o} = Wc_{i}/Wc_{o}$$
 (6c)

$$D\Delta R = DR/(Ro_0 - Ro_1)$$
 (6d)

$$DQ = DR/Wc_{o}$$
 (6e)

$$\phi_r = \phi(\pi/180)$$
, converting degrees to radians (6f)

$$\bar{\phi}_{\mathbf{r}} = \bar{\phi}(\pi/180) \tag{6g}$$

$$\beta_r = \beta(\pi/180) \tag{6h}$$

$$B_{r} = 1.5708 + \phi_{r} - \beta_{r}$$
 (61)

Average base pressure ratio suppression

$$P_B = 1.39237 - 0.397401 \phi_r + 0.075001 \overline{\phi}_r$$

(7)

- 0.207877
$$PR_0$$
 + 0.509907 Rr - 0.0513198 $Wf_{i/o}$

$$-0.324831 \text{ Wc}_{1/o} - 0.969623 \text{ DAR} - 0.128395 \text{ DAR}^2$$

- 0.0946673
$$Wc_{i/o}^2$$
 - 0.0300258 (DAR) $Wc_{i/o}$ + 0.0360116 PR_o^2

-
$$0.0620996(D\Delta R) Mp + 0.073894(D\Delta R)PR_0 + 0.0151679(N)D\Delta R$$

$$-0.00335317(N)PR_{o} - 0.0661407 B_{r}^{2} + 0.338926(B_{r})D\Delta R$$

- 0.0652494 (B_r) Mp + 0.0257783 (B_r)
$$PR_{o}$$

Base pressure drag of suppressor:

Base Drag =
$$P_0(1 - P_B)A_{Base}$$

(8)

(147

Outer shroud and plug pressure and friction thrust loss:

For
$$PR_O > 1.75$$
, $DR/Wc_O < 1.0$

(9a)

$$\Delta Cfg_o = 0.126999 + 0.00150249 N + 0.0046364 \beta_r - 0.0861853 B_r$$

$$-0.00362889 \text{ PR}_{0} -0.0233458 \text{ Rr} +0.0535316 \text{ Wf}_{1/0}$$

+ 2.4722
$$D\Delta R^2$$
 + 0.144784 $Wc_{1/0}^2$ + 0.0105388 PR_0^2

$$-0.0367926$$
 (Mp) PR_o + 0.0248003 (Wc_{1/o}) Mp

$$-0.0430253$$
 (Wc_{i/o}) PR_o + 0.868742 (D Δ R) Mp

- 0.306672 (D
$$\Delta$$
R) PR $_{o}$ + 0.0013177 (N) Mp - 0.000776167 (N) PR $_{o}$

+ 0.0101801 (
$$B_r$$
) Mp + 0.00935727 (B_r) PR_o

For
$$PR_0 > 1.75$$
, $DR/Wc_0 \ge 1.0$

(9b)

$$\Delta Cfg_0 = -0.209783 + 0.0800173 \beta_r -0.170768 \overline{\phi}_r + 0.193405 Mp$$

+ 0.00055485
$$PR_o$$
 + 0.202381 R_r - 0.0151082 $Wc_{i/o}$ + 0.0129846 DQ

- 0.161545
$$Wc_{i/o}^2$$
 - 0.117331 (DAR) $Wc_{i/o}$ + 0.00986606 PR_o^2

- 0.0171178 (Mp)
$$PR_0$$
 - 0.0301847 (Wc_{1/0}) Mp + 0.0290685 (Wc_{1/0}) PR_0

- 0.00365368 (N)
$$M_P$$
 + 0.000344757 (N) PR_O + 0.0950154 B_T^2

-
$$0.000342231$$
 (B_r) N - 0.0459412 (B_r) PR_o



Ideal thrust of outer flow:

$$FID_{o} = \frac{2}{CD_{o}(A_{o})PR_{o}(P_{0})\gamma_{o}} \sqrt{\frac{2}{\gamma_{o}-1} \left[\frac{2}{\gamma_{o}+1}\right]^{(\gamma_{o}+1)/(\gamma_{o}-1)} \left[1 - PR_{o}^{(1-\gamma_{o})/\gamma_{o}}\right]}$$
(10)

Suppressor base thrust loss:

$$\Delta Cfg_{B} = (Base Drag)/FID_{o}$$
 (11)

Outer-nozzle thrust coefficient:

$$Cfg_{o} = 1 - \Delta Cfg_{B} - \Delta Cfg_{o}$$
 (12)

Inner-nozzle thrust coefficient:

$$Cfg_{i} = \sqrt{\frac{1 - NPR_{i}^{(1 - \gamma_{i})/\gamma_{i}}}{1 - PR_{i}^{(1 - \gamma_{i})/\gamma_{i}}}} \quad (Peak \ Cfg_{i} - 1) + CX_{i}$$
 (13a)

Where peak Cfg is the peak internal thrust coefficient as a function of external area ratio (see Figure 5-11).

$$cx_{i} = \sqrt{\frac{1 - NPR_{i}^{(1 - \gamma_{i})/\gamma_{i}}}{1 - PR_{i}^{(1 - \gamma_{i})/\gamma_{i}}}}$$
(13b)

$$+ \frac{(NPR_{i}^{-1} - PR_{i}^{-1}) (A_{9}/A_{8})_{i}}{\sqrt{\frac{2}{\gamma_{i} - 1} \left[\frac{2}{\gamma_{i} + 1}\right]^{(\gamma_{i} + 1)/(\gamma_{i} - 1)} \left[1 - PR_{i}^{(1 - \gamma_{i})/\gamma_{i}}\right]}}$$

Where:

$$CD_{1} = 0.981$$

 $(A_9/A_8)_i$ = Internal area ratio of inner nozzle

NPR_i = Design pressure ratio corresponding to $(A_9/A_8)_i$

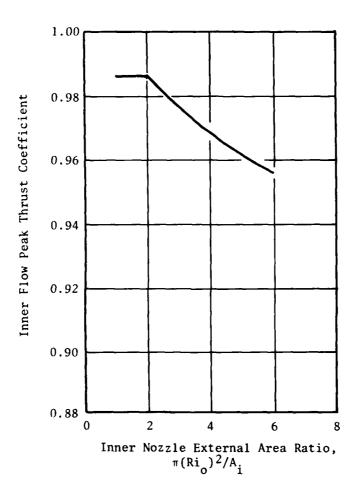


Figure 5-11. Inner-Flow Peak Thrust Coefficient as a Function of External Area Ratio.

Ideal thrust of inner flow:

FID_i = (14)

CD_i (A_i)PR_i (P₀)
$$\gamma_i$$
 $\sqrt{\frac{2}{\gamma_i - 1} \left[\frac{2}{\gamma_i + 1}\right]^{(\gamma_i + 1)/(\gamma_i - 1)} \left[\frac{(1 - \gamma_i)/\gamma_i}{1 - PR_i}\right]}$

Where $CD_{\xi} = 0.981$

Having calculated all of the terms in Equation 1, the overall thrust coefficient may be restated:

$$Cfg_{Nozzle} = \frac{Cfg_o (FID_o) + Cfg_i (FID_i)}{FID_o + FID_i}$$

It should be noted that the performance of a single-flow suppressor nozzle may be calculated from the above procedure by assuming a zero flow area and weight flow for the inner nozzle.

Equations in this analysis can be grouped according to specific geometric or aerodynamic components:

Equations 2, 3, 4,	Geometric definition of the suppressor
Equation 5	Suppressor discharge coefficient
Equations 6, 7, 8, 10, 11	Thrust loss of outer flow due to suppressor
Equation 9	Thrust loss of outer flow due to outer shroud and plug, pressure and friction drag
Equation 12	Outer nozzle thrust coefficient
Equations 13, 14	Inner nozzle thrust coefficient
Equation 1	Overall nozzle thrust coefficient

With the exception of equations 7 and 9, the performance-loss analysis is independent of the suppressor design and consists of equations which are the general tools of nozzle design. The general equations can be found in many reports and texts. Equations 7 and 9 are different; these two equations were developed under this program, using a linear regression analysis, as discussed

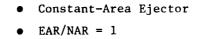
in Appendix I. Since Equations 7 and 9 are statistically generated from a given data base, the validity of these equations would be highly suspect if they were used outside the range of the data base. It is suggested that the analysis (Equations 7 and 9) for overall nozzle performance be used only between the lower and upper ranges specified in Table 5-1. In addition, the chute contour should be designed with the projected base area position as far upstream as possible from the trailing edge. If the above constraints are met, the predicted overall thrust coefficient for a given design should be within $\pm 1.0\%$ of the actual thrust coefficient.

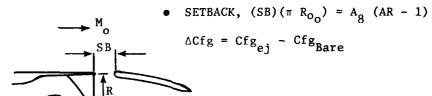
5.3.2.2 Ejectors

Ejector performance increments have been generalized based on setback ejector test results from Reference 13. These increments are shown in Figure 5-12 as a function of nozzle pressure ratio. Linear interpolation can be used for Mach numbers between 0 and 0.36.

5.3.2.3 Example of Performance Prediction

In Appendix J, a dual-flow exhaust system with a suppressor on the outer nozzle is treated as an example for the calculation procedure described above.





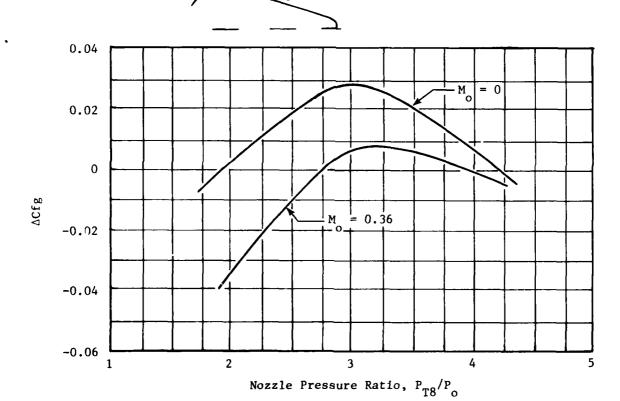


Figure 5-12. Multichute/Ejector Performance.

Table 5-1. Applicability Range of Parameters in GE Chute/Spoke Data Base.

Range of Application		Chute/Spoke Parameters		
1.5		Area Ratio, AR	≤	2.5
0.457	≤	Radius Ratio, R_i/R_o	≤	0.78
0.39	≤	Width Ratio, Wf _o /Wc _o	≤	2.2
0.5	≤	Depth Ratio, DR/Wco	≤	3.1
20	≤	Element No., N	≤	48
90°	≤	Angle Between Plug and Suppressor Exit, B	≤	110°
10°	≤	Plug Angle at Suppressor Exit Plane, ϕ	≤	15°
0°	≤	Plug Angle Under Spoke or Chute, $\overline{\phi}$	≤	15°
0	≤	Flight Mach No., Mp	≤	0.45
1.5	≤	Nozzle Pressure Ratio, PR	≤	3.5

6.0 MECHANICAL DESIGN CONSIDERATIONS

The exhaust system configuration and size are affected considerably by the jet-noise-suppression arrangement. Exhaust system configuration and size then affect the weight, complexity, and performance of the exhaust system. Single-stream exhaust nozzles employ mechanical suppression devices such as spokes, chutes, and tubes in the exhaust stream as shown in Figure 6-1. Two-stream exhaust systems are arranged with the hot, high-velocity stream on the outside and the cooler, low-velocity stream on the inside to take advantage of the so-called "coannular" suppression effect. This configuration is shown in Figure 6-2. Mechanical suppressors may be added to the hot, high-velocity stream of a dual-stream exhaust system as shown in Figure 6-3; this increases suppression beyond that obtained by the coannular effect. Additional suppression on both the single- and the dual-stream exhaust nozzles may be obtained by surrounding the exhaust discharge with an ejector shroud as shown in Figure 6-4. Single-stream nozzles can be used on turbojets or bypass engines. Dual-stream nozzles are applied to bypass engines. Either single-stream or dual-stream nozzles can be applied to Variable Cycle Engines (VCE).

6.1 MECHANICAL SUPPRESSOR EFFECTS

6.1.1 Exhaust Temperature Limit

Mechanical suppressors employing spokes, chutes, or tubes, which are immersed in the hot exhaust stream, limit the exhaust stream temperature to about 1700°F with the use of high-temperature metals. Development of ceramic suppressor elements may allow the temperature limit to increase to about 2300°F. Providing cooling for suppressor elements is generally regarded as prohibitive because of the additional cooling-system weight, cooling-air performance losses, and increased suppressor-element storage space.

6.1.2 Suppressed Performance

Mechanical suppressors decrease the exhaust system aerodynamic performance. The primary cause of lower performance is the low base pressure behind the suppressor elements (see Section 5.0 for details). Larger base areas result in larger performance losses; therefore, from a performance standpoint it is desirable to have a small base area ratio.

$$AR = \frac{Base Area}{Exhaust Throat Area} = \frac{Chute Base Area + Exhaust Throat Area}{Exhaust Throat Area}$$

The base area pressure can be increased somewhat, improving performance by ventilating the base of the suppressor elements to the ambient air. Ventilation of radial suppressor elements is improved by making the cross

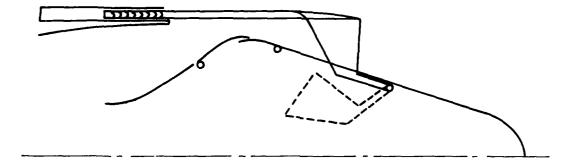


Figure 6-1. Mechanically Suppressed, Single-Stream Exhaust Nozzle Schematic.

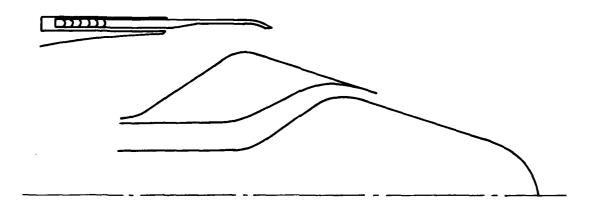


Figure 6-2. Coannular, Unsuppressed, Dual-Stream Exhaust Nozzle Schematic.

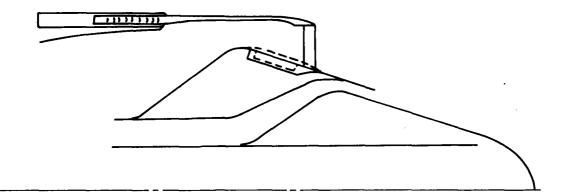


Figure 6-3. Mechanically Suppressed+Outer-Stream Exhaust System Schematic.

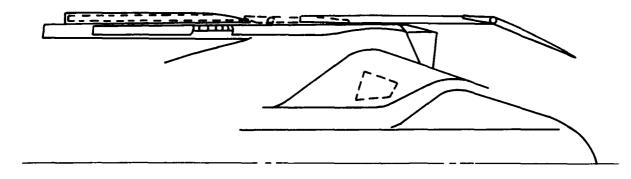


Figure 6-4. Ejector-Shrouded Exhaust System Schematic.

section "V" or "U" shaped and opening the outer radius to the ambient freestream flow. Lengthening the outer cross section also increases the ventilation. Ranking of suppressor-element geometries in terms of improved aerodynamic performance is, therefore: (1) spokes (unventilated), (2) shallow chutes, and (3) deep chutes (see Figure 6-5). Base pressure of tube suppressors is improved by ventilation and lengthening the tubes to reduce aspiration of the base. Ventilation of the suppressor base in a two-stage ejector nozzle (TSEN), typical of that evaluated during the U.S. SST program, is difficult because it requires optimum ventilation positioning of the suppressor relative to the tertiary inlet which is designed primarily for good unsuppressed performance.

6.1.3 Suppressor-Stowed Performance

During engine operation where suppression is not required, suppression devices are stowed to improve aerodynamic performance which facilitates configuration flexibility to meet operational requirements. The stowage arrangement should be such that interference (with unsuppressed flow streams) and high leakage losses do not occur. Single-flow plug nozzles provide space in the plug for stowage of a high-suppression, good-performance, deep-chute suppressor. Chute cover doors provide good aerodynamic surfaces with minimal leakage loss effects. Tube suppressors can also be stowed in plug nozzles, as shown in Figure 6-6, but the stowage constraints result in a suppressor design with a large number (\approx 200) of short tubes which do not terminate at a common plane. The desirable tube suppressor configuration for good performance (see Sections 3.0 and 5.0) and high suppression (see Sections 3.0 and 4.0) has about 60 relatively long tubes ending in a single plane.

The stowage space for suppressors in dual-stream plug nozzles is more limited. For this application, shallow-chute suppressors stowed in an inverted position, parallel to the plug surface, without cover doors is recommended. This arrangement provides the additional suppression required above the coannular suppression with negligible stowed-position performance losses.

Tube suppressors in two-stage ejector nozzles, as shown in Figure 6-7 in the stowed position, tend to interfere with the tertiary or ambient stream flow and thus reduce unsuppressed performance. Storage arrangements of the tube suppressors which have the tube inlets on main-stream expansion surfaces may cause unsuppressed-performance losses.

Mechanical, jet-noise suppressors designed for good suppression tend to make the exhaust system larger in diameter than desired for good unsuppressed performance. This increases drag and/or internal losses. Therefore a careful trade of exhaust system diameter and jet noise suppression must be made to assure good performance in the unsuppressed modes.

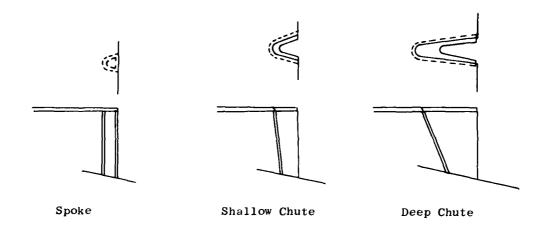


Figure 6-5. Typical Mechanical Suppressor/Plug Nozzle Elements.

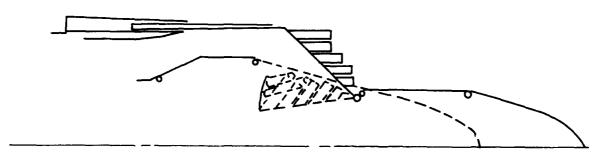


Figure 6-6. Multitube/Plug Nozzle Concept Schematic.

6.2 WEIGHT, COMPLEXITY, AND COST IMPLICATIONS OF JET NOISE SUPPRESSORS

The exhaust system weight is primarily a function of the nozzle maximum diameter. Other weight effects include the addition of hardware to implement modes of operation other than the primary function of expanding the exhaust gas efficiently (such as thrust reversers and sound suppressors). Secondary weight effects include the number of components required and the configuration, loading, and support of these components. Larger quantities of components generally result in higher weights. Components subjected to bending generally weigh more than those subjected to tensile stress; complexity also follows these trends. Increased size, number of control systems, and number of components increase complexity. Cost increases with size and complexity.

Therefore, it is important in the design of an exhaust system to minimize the size, consistent with exhaust gas flow rate and expansion requirements, and to combine other functional operations with the gas-discharge area and expansion-control hardware. This should be done primarily with components in hoop (tension) stress. An example of this is the integration of the thrust reverser in the single-stream plug nozzle shown in Figure 6-8. The thrust reverser cascades are attached to the translating shroud that controls the internal expansion area relative to the throat area for efficient expansion at varying exhaust pressure ratios throughout the flight profile. Extension of the shroud to a position that exposes the cascades to the exhaust gas and ambient air, for thrust reversing, is accomplished with the same control system, which positions the shroud for efficient expansion. Movable reverser internal or external covers are not required. The reverser blocker function is effected with the flaps and with the control system which controls the nozzle throat area. The shroud and reverser cascades are a cylinder; this results in differential pressure loads being taken in hoop tension.

Integration of a jet noise suppressor in the exhaust system requires the same approach to function integration. The moderate suppression provided inherently by the coannular nozzle is readily adaptable to the plug nozzle as shown in Figure 6-2. The primary suppression criterion affecting the coannular nozzle sizing is the outer stream radius ratio, R_{0}/R_{0} (the outerstream, inner radius divided by the outer-stream, outer radius). The sizing relationship is:

$$R_9 = \sqrt{\frac{A_0 \cos \beta}{\left[1 - \left(\frac{R_{0j}}{R_{00}}\right)^2\right]}}$$

where:

 A_0 = Outer stream throat area

 β = Discharge angle (cant)

 R_9 = Outer stream outer discharge radius equa's R_0 , i.e., R_9 = R_0



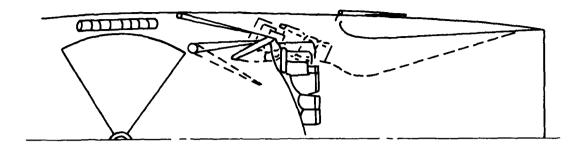


Figure 6-7. Multitube/Two-Stage Ejector Nozzle Schematic.

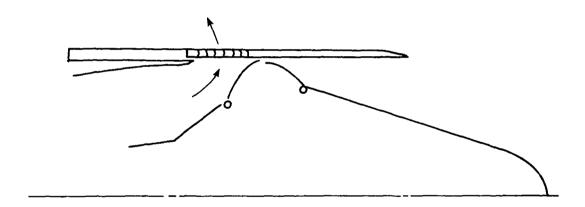


Figure 6-8. Reverser Integration in Single-Stream Plug Nozzle.

This can be rewritten as:

$$R_{9}\sqrt{\frac{\pi}{A_{o} \cos \beta}} = \sqrt{\frac{1}{1 - \left(\frac{R_{o_{1}}}{R_{oo}}\right)^{2}}}$$

This is shown in graph form in Figure 6-9 at AR = 1. For most engine cycles, R_{0i}/R_{0o} = 0.85 will yield an R_{0i} matching closely with the required supersonic-cruise, full-expansion R_{0i} .

For additional suppression, above that provided by the coannular effect, shallow-chute suppressors may be added to the outer stream as shown in Figure 6-3. The suppression criteria affecting nozzle sizing is the radius ratio, $R_{\rm O_1}/R_{\rm O_0}$, and the suppressor base area ratio, AR.

$$AR = \frac{\pi (R_{00}^2 - R_{01}^2)}{A_0 \cos \beta} = \frac{Chute Base Area + A_0}{A_0}$$

Then, the sizing relationship is:

$$R_{9} = \sqrt{\frac{A_{O} (AR) \cos \beta}{\pi \left[1 - \left(\frac{R_{O1}}{R_{OO}}\right)^{2}\right]}}$$

This is shown in graph form in Figure 6-9 for AR's 1.25 through 2.50. Single-stream nozzle suppression sizing criteria are also defined by the equation above. Figure 6-9 includes nondimensional radius values obtained from previous studies of unsuppressed single- and dual-flow plug nozzles corresponding to supersonic-cruise, full-expansion, cycle requirements. Also shown on Figure 6-9 are typical suppressed configurations evaluated in the course of the aircraft integration studies conducted in Task 3 of the program (see Reference 1). The design envelope line shown on Figure 6-9 corresponds to the most reasonable (and maximum) possible radius from the standpoint of excessive weight and drag. The mechanically suppressed nozzles tend to have a larger diameter than that required for full expansion at supersonic cruise. Therefore a trade between $R_{\rm Oi}/R_{\rm Oo}$, AR, and $R_{\rm O}$ for full expansion must be made.

The weight variation with R_9 of an exhaust system of the same configuration is given by:

Therefore the percent weight increase for a specific nozzle configuration can be defined by

(164)

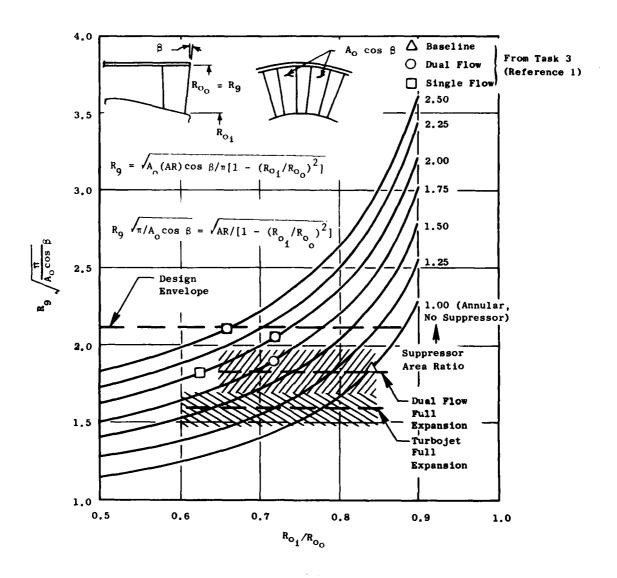


Figure 6-9. Relationship Between Nozzle Exit Radius, Throat Area, and Area Ratio.

% Increase =
$$\left[\left(\frac{R_{9}}{R_{9} \text{ Reference}} \right)^{2.4} - 1 \right] / 100$$

$$= \left[\left(\frac{\left[1 - \left(\frac{R_{01}}{R_{00}} \right)^{2} - 1 \right]}{\left[1 - \left(\frac{R_{01}}{R_{00}} \right)^{2} \right]} \right)^{1.2} - 1 \right] / 100$$

This is shown in Figure 6-10 for various area ratios for a single-stream nozzle and in Figure 6-11 for a dual-stream nozzle. The reader is referred to Section 3.0, Figures 3-32 and 3-33, where specific single- and dual-flow suppressor Δ weight and Δ maximum nozzle diameter increase trends are shown as functions of engine airflow. More details can be found in Reference 1.

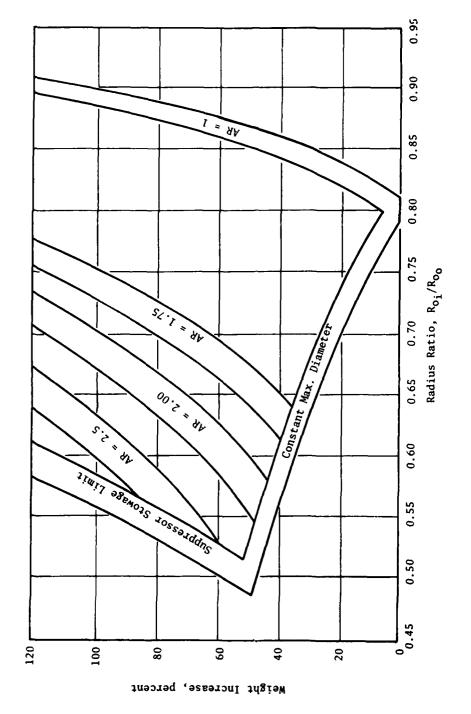
As shown in the sizing equation, the absolute Rg is affected by $\mathbf{A}_{_{\mathbf{O}}}$ which is a function of the engine airflow, the split between the inner and outer stream airflows, and the discharge temperature and pressure. These are defined by a specific engine cycle to yield a specific thrust. To change the thrust for a specific cycle, the airflow may be changed to yield a linear change in $A_{\rm O}$. This allows the exhaust system weight to be scaled as:

Weight = Weight reference
$$\left(\frac{Airflow}{Airflow reference}\right)^{1.2}$$

This is shown in Figure 6-12 for typical unsuppressed dual-stream and single-stream nozzles with a radius ratio of 0.84.

A fair indication of an exhaust system's complexity, which in turn is reflected in its reliability, is the number of actuation systems required. Added to this is the complexity involved with subsystems (which require a large number of components) such as flaps and seals, hinged doors, rotating clamshells, and an augmentor system. Accordingly, the following index was devised to compare the complexities of exhaust systems.

Subsystem	Complexity Rating
Moving structural actuation system	1
Augmentor control system	1
Flaps and seals	1/2
Hinged or sliding doors	1/2
Augmentor	1
	(16b)
142	



Single-Stream Exhaust Nozzle Weight Increase Versus Radius Ratio and Suppressor Area Ratio. Figure 6-10.



The second of the second

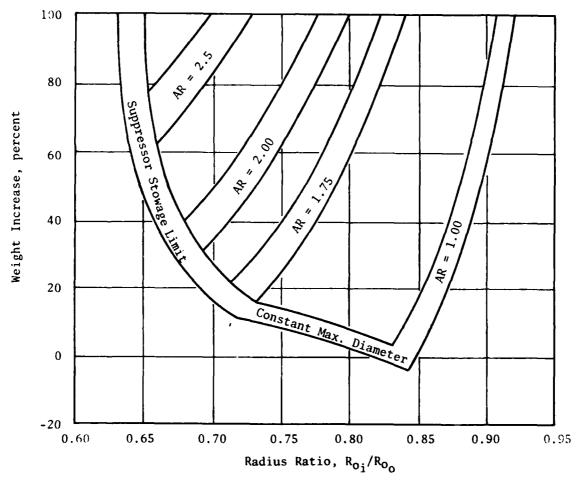


Figure 6-11. Dual-Stream Exhaust Nozzle Weight Increase Versus Radius Ratio and Suppressor Area Ratio.

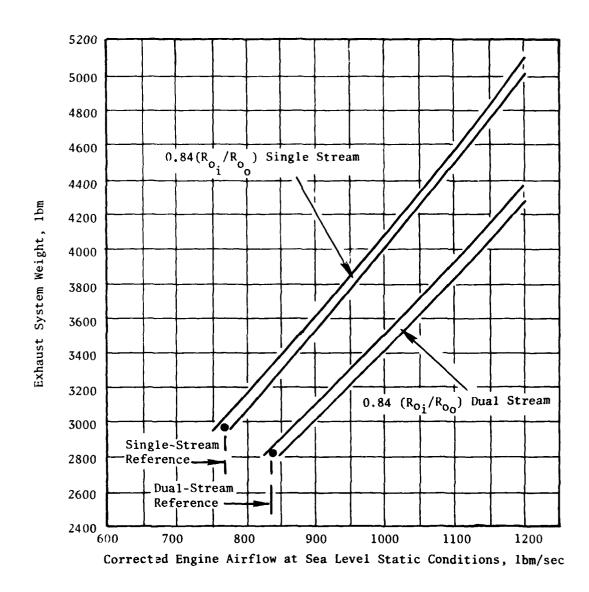


Figure 6-12. Exhaust System Weight Versus Engine Airflow.

Reverser cascades	1/4
Rotating clamshells	1/2
VCE Variable Area Bypass Injector (VABI), where applicable	1/2
Suppressor tubes chutes or spokes	1/2

Ratings of various exhaust systems based on this index are shown in Table 6-1 and also shown graphically in Figure 6-13.

6.3 TYPICAL SUPPRESSOR INSTALLATIONS

Figure 6-14 shows a typical preliminary design-layout sketch of the coannular exhaust system with $R_{01}/R_{00}=0.84$, and Figure 6-15 shows this nozzle with the addition of a 40-shallow-chute suppressor with an area ratio of 1.75 and $R_{01}/R_{00}=0.72$. The addition of the suppressor resulted in an increase of maximum radius of 0.75 inch and an estimated weight increase of 550 lbm. Referring to the complexity rating chart, the addition of one actuation system and the suppressor resulted in an increase in rating from 6.25 to 7.75, which in turn, implies an adverse impact on both system reliability and maintainability.

Figure 6-16 shows the single-flow exhaust system with a 32-deep-chute suppressor with an area ratio of 2.0 and radius ratio = 0.62. Compared to an unsuppressed, single-flow exhaust system at radius ratio = 0.80, the addition of the suppressor resulted in an increase of maximum radius of 3.9 inches and a weight increase of 1850 lbm. The addition of two actuation systems, the suppressor, and the suppressor cover doors resulted in an increase of the complexity index from 6.75 to 9.75.

The above illustrations suggest that strong consideration be given to simple shallow-chute-suppressor installations, assuming noise reduction potential and performance degradation are acceptable, since they do not appear to significantly increase the complexity rating over the unsuppressed counterparts as much as deep-chute, full-span suppressor systems.



Table 6-1. Suppressed/Unsuppressed Exhaust System Complexity Rating.

	Control Systems	ystems	Set of						Set of		
Exhaust System	Moving Structures	Augmentor	Flaps and Seals	Set of Doors	Augmentor	Reverser Cascade	Rotating Clamshells	VCE	Mechanical Suppressors	Total	Graph Symbol
Military Turbojet (No Reverser or Suppressor)	1	1	3 x 1/2		ı					4-1/2	0
Coannular Plug* (Coannular Suppression)	3			1 × 1/2	1	1 x 1/4		1 × 1/2		6-1/4	•
Single Stream Plug* (Unsuppressed)	3	-	2 x 1/2			1 × 1/4		1 × 1/2		6-3/4	
Coplanar Plug* (Dual Stream)	e -	7		1 x 1/2		1 × 1/4		1 x 1/2	1 × 1/2	6-3/4	٥
Suppressed Coamular*	4	-		1 x 1/2	r	1 x 1/4		1 x 1/2	1 x 1/2	7-3/4	•
GEAJSP TSEN (Unsuppressed)	6	-	4 x 1/2	2 x 1/2						œ	•
Suppressed Single Stream* (Shallow Chute)	4		2 x 1/2		-	1 × 1/4		1 × 1/2	1 × 1/2	8-1/4	•
Suppressed Single Stream* (Deep Chute)	8		2 × 1/2	1 × 1/2		1 × 1/4		1 × 1/2	1 × 1/2	9-3/4	•
TSEN Type* (Tube Suppressed Separate Reverser)	6 0	~	3 × 1/2	3 × 1/2	~	1 × 1/4	1 × 1/2		1 × 1/2	14-1/4	×

From Reference 1

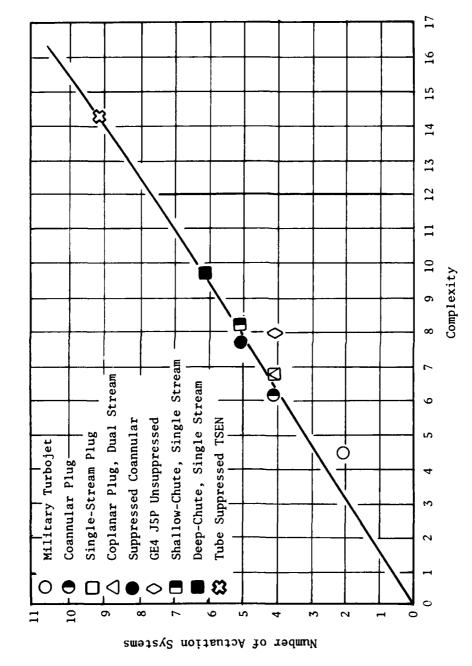


Figure 6-13. Exhaust System Complexity Rating.

11)

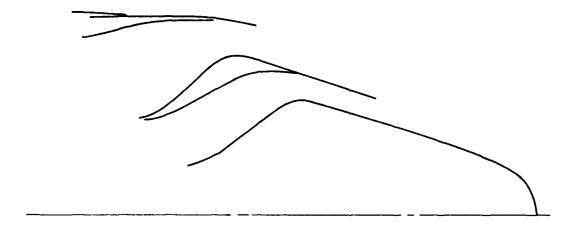


Figure 6-14. Unsuppressed Coannular Exhaust System.

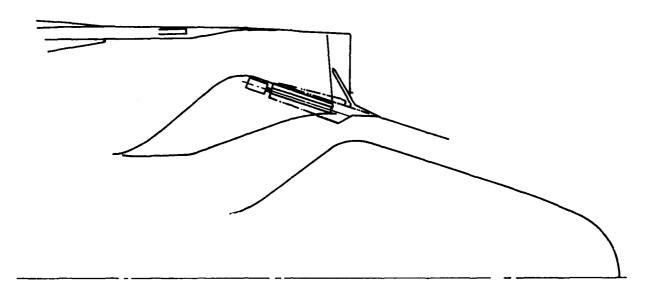


Figure 6-15. Dual-Flow Exhaust System with Mechanically Suppressed Outer Flow.

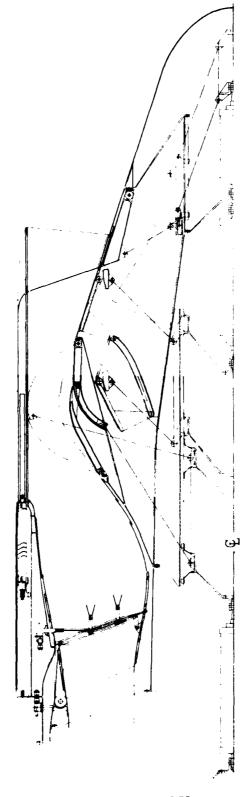


Figure 6-16. Mechanically Suppressed Single-Flow Exhaust System.

7.0 CONCLUDING REMARKS

The design guide information included herein permits the preliminary design engineer to assess how aircraft-mission goals are influenced by various engine-type/engine-cycle parameters, aircraft flight trajectory characteristics, nozzle aerodynamic performance, suppressor nozzle acoustic effectiveness, and associated mechanical design features. When possible, the design guide includes an assessment of the accuracy and range of applicability for the various computational procedures, graphs, etc.

The design guide also provides the engineer with a powerful diagnostic tool, in the form of the unified aeroacoustic prediction model developed in the course of Task 2 of this program, to study how the various and competing noise mechanisms impact the resultant noise signature. This, in turn, may provide some insight into how the nozzle geometry might be altered to bring about a more favorable balance among the various noise mechanisms. Since this prediction model is based primarily on engineering principles rather than on empirical correlations, it offers the engineer an opportunity to explore the acoustic potential of new nozzle concepts.

The techniques presented in this design guide are based on the results from Task 2, Task 3, Task 4, and Task 5 of this program, and on other contractor studies. Although most of the techniques presented herein have been verified by experiment, some lack sufficient experimental-data-bank depth to be accurately assessed. Nevertheless, the information contained in this design guide should provide a reasonably accurate and rational approach to predicting the flight noise and aerodynamic performance of a wide variety of noise-abatement nozzles over a range of flow conditions and flight velocities of interest.

8.0 RECOMMENDATIONS

Based on the information contained in this design guide, several recommendations are in order relative to further verifying the engineering correlation (M*S) and unified aeroacoustic prediction (M*G*B) models as well as understanding noise-abatement-nozzle, jet-noise characteristics during the critical flight mode.

- More flight-type data from simulated flight or actual flight tests should be obtained so that the three noise components (premerged, postmerged, and shock cell) of the M*S model can be better defined with frequency.
- This flight-data bank can also be utilized to further improve and expand the in-flight capability of the M*G*B technique.
- Shock-cell noise for baseline (single and dual flow) and multielement (single and dual flow) nozzles should be examined more closely to improve shock-cell noise prediction in both the M*S model and in the M*G*B model during "flight." This will permit discriminating shock-cell noise (which is present statically) and attendant flight effects (i.e., dynamic effect) with the so-called initial or premerged jet-noise component (especially in the aft quadrant).

Additionally, several important problems, relating to flight and full-scale aircraft, need to be addressed to minimize the current uncertainty in predicted flight-noise levels. These include:

- Procedures to reduce noise such as engine operational techniques (power management); important low-speed aircraft characteristics also need to be better defined to exploit EGA (Extra Ground Attenuation) and take full benefit of the shielding of engine noise by the air raft.
- Impact of suppressor installations on mission performance and economics must be addressed in more depth.

APPENDIX A - FUNDAMENTALS OF JET NOISE MECHANISMS

Several basic theoretical studies and critical experiments were conducted in Task 2 of this program (Reference 14) aimed at identifying and quantifying the important jet noise generation and emission mechanisms. From these studies and experiments, a unified aeroacoustic jet noise prediction method was developed based on a modeling of the principal noise generation and emission mechanisms from engineering principles rather than utilizing empirical correlations of experimental results. The unified aeroacoustic prediction computer model, designated as M*G*B, is described in detail in References 14 and 15. Extensive data/theory comparisons were carried out in Task 2, using scale-model jet noise data for a wide variety of nozzle types and operating conditions; these results are also given in Reference 14. These data/theory comparisons were carried out in model size (as measured) in order to minimize the influence of distance extrapolation and atmospheric absorption on the evaluation of the M*G*B model prediction accuracy.

Data/theory comparisons were also carried out in Task 3 of this program in order to verify the jet noise principles upon which the M*G*B prediction model is based. Task 3 data/theory comparisons and demonstration of the diagnostic capability of the M*G*B prediction model are documented in Reference 12. Emphasis was placed on the ability to predict full-size engine nozzle jet noise at typical engine takeoff and community conditions. The many data/theory comparisons carried out in Task 2 and Task 3 show that the M*G*B prediction model is capable of predicting and explaining the acoustic characteristics of many types of jet nozzles. The M*G*B model was demonstrated to be a useful diagnostic tool for assessing the relative importance of the various jet noise mechanisms for a given nozzle type; the program can serve as a design evaluation and optimization tool.

The utility of the M*G*B model lies in providing a more detailed analysis of the aerodynamic flow field and acoustic characteristics of a given nozzle configuration than would be available from trend charts or the empirically based M*S prediction model (see Section 4.0). For example, M*G*B allows the designer to investigate the impact of nozzle-element placement and shape on the jet plume decay characteristics and on the corresponding far-field noise signature. It can be used as a diagnostic tool to reveal how well the suppression of a selected configuration is being achieved and perhaps illuminate potential trouble areas at off-design conditions (cut-back or approach power).

The first discussion of this appendix reviews the primary jet noise generation and emission mechanisms relevant to high velocity jets. The next section summarizes the formulation of the unified aeroacoustic jet noise prediction model (M*G*B) based on the mechanisms discussed. Finally, a demonstration is presented of how the M*G*B prediction model can be used as a design evaluation and diagnostic tool.

JET NOISE MECHANISMS

The jet noise theories of Lighthill (Reference 25), Ribner (Reference 26), and Ffowcs-Williams (Reference 27) have identified and quantified a number of important physical characteristics of jet noise. These include: (1) the generation of sound by small-scale, random, turbulent-eddy fluctuations; (2) the "quadrupole" nature of the acoustic field, and (3) convective amplification of the sound due to motion of the turbulent-eddy sources relative to the observer. From these theoretical developments, a scaling principle for jet noise has been extracted (Ahuja and Bushell, Reference 28) as follows:

$$P(Q) = SPL - 10 \log_{10} (Vj/V_{ref})^8 - 10 \log_{10} (D/R)^2 - 10 \log_{10} (1+M_c \cos \theta_i)^{-5}$$

$$- 10 \log_{10} (\rho j/\rho_{ref})^2 \qquad (A-1)$$

$$P = 0 \quad - Doppler-shifted frequency = (fD/Vj) (1+M_c \cos \theta_i)$$

$$P = 0 \quad - normalized sound pressure level (dB)$$

$$SPL = 0 \quad - far-field sound pressure level (dB)$$

$$Vj = 0 \quad - nozzle \quad - reference \quad - velocity$$

$$V_{ref} = 0 \quad - reference \quad - velocity$$

$$P = 0 \quad - nozzle \quad - velocity$$

$$P = 0 \quad - reference \quad - velocity$$

$$P_c = 0 \quad - reference \quad - velocity$$

$$P_c = 0 \quad - reference \quad - velocity$$

$$P_c = 0 \quad - reference \quad - velocity$$

$$P_c = 0 \quad - reference \quad - velocity$$

$$P_c = 0 \quad - reference \quad - velocity$$

$$P_c = 0 \quad - reference \quad - velocity$$

$$P_c = 0 \quad - reference \quad - velocity$$

$$P_c = 0 \quad - reference \quad - velocity$$

$$P_c = 0 \quad - reference \quad - velocity$$

$$P_c = 0 \quad - reference \quad - velocity$$

$$P_c = 0 \quad - reference \quad - velocity$$

$$P_c = 0 \quad - reference \quad - velocity$$

$$P_c = 0 \quad - reference \quad - velocity$$

$$P_c = 0 \quad - reference \quad - velocity$$

$$P_c = 0 \quad - reference \quad - velocity$$

$$P_c = 0 \quad - reference \quad - velocity$$

$$P_c = 0 \quad - reference \quad - velocity$$

$$P_c = 0 \quad - reference \quad - velocity$$

$$P_c = 0 \quad - reference \quad - velocity$$

$$P_c = 0 \quad - reference \quad - velocity$$

$$P_c = 0 \quad - reference \quad - velocity$$

$$P_c = 0 \quad - reference \quad - velocity$$

$$P_c = 0 \quad - reference \quad - velocity$$

$$P_c = 0 \quad - reference \quad - velocity$$

$$P_c = 0 \quad - reference \quad - velocity$$

$$P_c = 0 \quad - reference \quad - velocity$$

$$P_c = 0 \quad - reference \quad - velocity$$

$$P_c = 0 \quad - reference \quad - velocity$$

$$P_c = 0 \quad - reference \quad - velocity$$

$$P_c = 0 \quad - reference \quad - velocity$$

$$P_c = 0 \quad - reference \quad - velocity$$

$$P_c = 0 \quad - reference \quad - velocity$$

$$P_c = 0 \quad - reference \quad - velocity$$

$$P_c = 0 \quad - reference \quad - velocity$$

$$P_c = 0 \quad - reference \quad - velocity$$

$$P_c = 0 \quad - reference \quad - velocity$$

$$P_c = 0 \quad - reference \quad - velocity$$

$$P_c = 0 \quad - reference \quad - velocity$$

$$P_c = 0 \quad - reference \quad - velocity$$

$$P_c = 0 \quad - reference \quad - velocity$$

$$P_c = 0 \quad - reference \quad - velocity$$

$$P_c = 0 \quad - reference \quad - velocity$$

$$P_c = 0 \quad - reference \quad - velocity$$

$$P_c = 0$$

According to this scaling principle, one should obtain a universal curve of P versus Q when far-field noise measurements of SPL versus f are normalized according to Equation A-1 regardless of jet velocity, diameter, density (or temperature), frequency, or angle and radius of measurement.

Recent careful experimental studies by Lush (Reference 29), Ahuja and Bushell (Reference 28), and Hoch, et al. (Reference 30) show that this scaling principle is not able to collapse parametric data onto a single curve. For example, for cold jets at small values of Q (source Strouhal number), the

factor (1 + M cos θ_1)⁻⁵ in Equation A-1 underestimates the variation of noise with angle. Conversely, at high values of Q, this factor overestimates the variation of noise with angle. For hot jets, the data are best correlated if the factor $(\rho_j/\rho_{ref})^2$ in Equation A-1 is replaced by $(\rho_j/\rho_{ref})^\omega$, where the density exponent ω is itself a function of jet velocity ratio V_j/C_0 (C_0 is the ambient speed of sound). Only for values of V_j/C_0 in excess of about 1.3 does ω approach the theoretical value of 2. Also, the observed effect of heating is to bias the SPL spectrum to lower frequencies.

Most of the above discrepancies can be resolved, while retaining the Lighthill notion of ascribing jet noise to convected quadrupoles, if the fact that the turbulent eddies do not communicate directly with ambient atmosphere (because of the shrouding effect of the mean jet flow) is accounted for. The classical theories (References 25 through 27) were based on a stationary-waveequation acoustic analogy which implicitly contains mean-flow propogation effects in the right-hand side or forcing function. To extract the mean-flow effects explicitly requires further manipulations to arrive at a governing equation for acoustic pressure which is clearly in the form of an inhomogenous, convected-wave equation driven by convected, solenoidal, turbulent velocity fluctuations. Such an equation was first derived by Phillips (Reference 31), and has been developed more fully by Lilley (Reference 32) and Goldstein and Howes (Reference 33). General solutions to these convected-wave equations have been formulated by Pao (Reference 34), Tester and Burrin (Reference 35), and Berman (Reference 36). Earlier works by Ribner (Reference 26), Schubert (Reference 37), Powell (Reference 38), and Csanady (Reference 39) have drawn attention to the importance of mean-flow shrouding effects.

Motivated by the desire to avoid obscuring the physics by complicated numerical approaches, Mani (References 40 through 44) has developed closed-form analytical solutions to the Lilley-Goldstein type equation by modeling the jet flow as simple. round, plug-flow jet. From these solutions several novel aspects of the jet noise problem, not discernible at all from the Lighthill approach, have emerged. These include the following:

- 1. The Lighthill factor $(1 + M_C \cos \theta_1)^{-5}$ for directivity emerges only as the limit for zero-flow Mach number and nonzero eddy-convection Mach number and is not even a good, low-frequency approximation. The directivity is frequency dependent.
- Due to mean-flow shrouding effects, i.e., inhomogeneity of the flow in the transverse direction, transverse quadrupoles exhibit reduced convective amplification compared to longitudinal quadrupoles.
- The combination of refraction and wave-trapping produce the observed fall-off in noise at angles close to the jet axis.
- 4. Mean-flow density gradients act to generate dipole and simple-source terms which scale with jet velocity as Vj and Vj , respectively, for a constant value of jet density. These additional noise sources counteract the reduced emission of the quadrupole sources due to

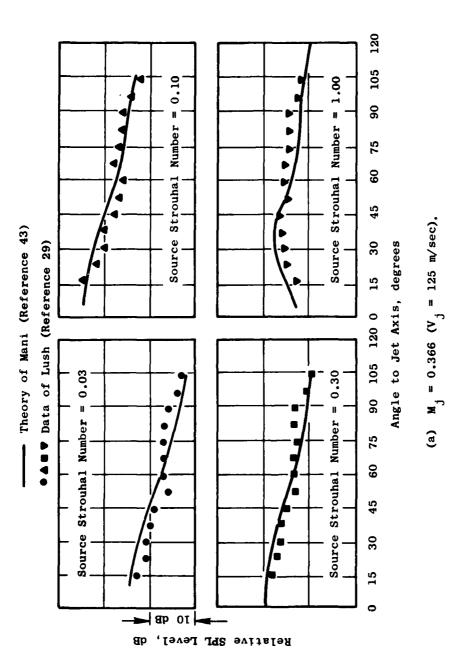
heating, becoming less important as jet velocity increases, since the quadrupole noise source scales with jet velocity as Vj^8 .

These aspects were all confirmed by Mani (References 40 through 44) through extensive data/theory comparisons with several sources of acoustic data. In particular, the variation in noise with observer angle, θ_{\star} , was verified as to frequency dependence. Additionally, the necessity for having a variable density exponent was found to be adequately expalined by the mean-flow shrouding effects and attendant additional noise-source contributions due to heating. Figure A-1 shows the agreement obtained between theory and experiment for a subsonic, round jet in terms of directivity characteristics. Figure A-2 shows a comparison of the empirically derived density exponent (ω) with the values inferred from the theoretical model as a function of jet velocity ratio Vj/C_o . These results, and many other comparisons reported in References 43 and 44, have conclusively demonstrated that mean-flow shrouding is an important jet noise mechanism. These studies have also verified that Lighthill's original concept of compact turbulent eddies convecting and decaying with the flow is a reasonable physical picture of jet noise, provided that the influence of the mean flow is properly accounted for.

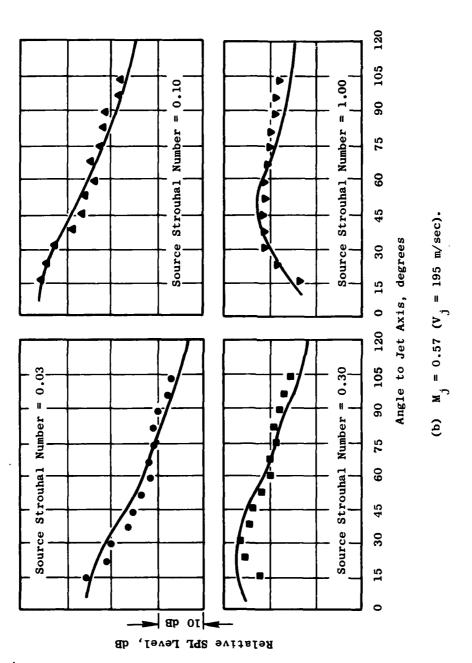
Another important noise mechanism for supersonic, choked jets is the interaction of convecting turbulent eddies with the shock-cell formations in the jet. The shock/turbulence interaction process can produce a discrete tone or "screech" component which is related to acoustic feedback with the nozzle. For actual engine nozzles and scale nozzles operating at heated engine cycle conditions, this feedback mechanism is rarely observed and can be "tuned out" if it does appear. The component of major concern is the broadband noise usually termed shock-cell noise. Although shock-cell noise is "broadband," in that it has a wide spectrum, it can exhibit a sharp peak.

A physical picture of the shock-cell noise mechanism has been proposed and modeled semiempirically by Harper-Bourne and Fisher (Reference 45). This picture is basically one of turbulent eddies passing by (or through) the shock fronts, disturbing the shocks, and causing them to emit acoustic waves. The acoustic waves interfere constructively or destructively, depending on the shock spacing, eddy convection velocity, and the lifetime of a given eddy. From the theoretical and experimental studies in Reference 45, several important features of shock-cell noise were revealed, as follows:

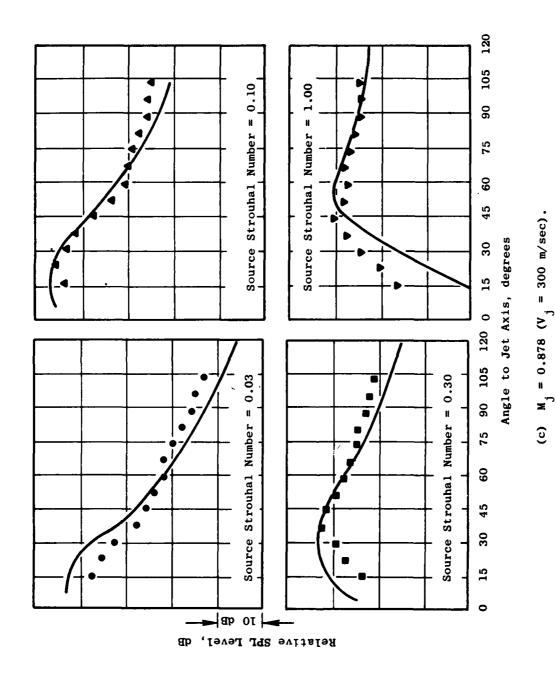
- The overall sound pressure level (OASPL) is independent of jet temperature.
- 2. The OASPL is nearly omnidirectional, i.e., independent of observer angle $\boldsymbol{\theta}_4$.
- 3. The OASPL varies as the fourth power of the shock-cell parameter β , where $\beta = \sqrt{M_j^2 1}$ and M_j is the jet exit plane Mach number based on isentropic expansion.



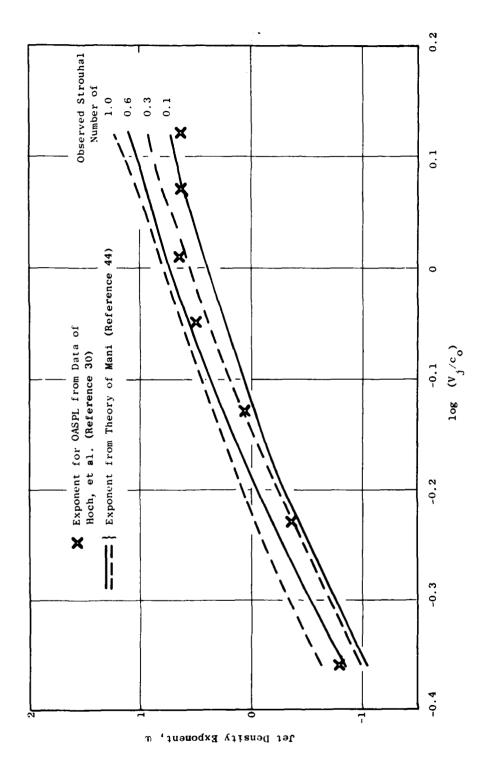
Comparison of Experimental and Predicted Jet Noise Directivity Patterns for Cold Jets, Figure A-1.



Comparison of Experimental and Predicted Jet Noise Directivity Patterns for Cold Jets (Continued). Figure A-1.



Comparison of Experimental and Predicted Jet Noise Directivity Patterns for Cold Jets (Concluded). Figure A-1.



Comparison of Experimental and Predicted Density Exponent for Heated Jets at 90° to the Inlet. Figure A-2.

4. The spectrum peak noise frequency is proportional to jet velocity and inversely proportional to shock spacing.

Shock-cell noise tends to dominate the total jet noise spectrum in the forward quadrant (θ_1 < 90°) at middle to high frequencies. This is illustrated qualitatively in Figure A-3. Experimental evidence, e.g., that of Drevit, et al. (Reference 46), indicates that basic shock-cell-noise strength is unaltered in flight and is in fact amplified (by the Doppler effect) in the forward quadrant, due to aircraft motion, by a factor (1 - Mp cos θ_1)-4 where Mp is the flight Mach number. Since the turbulent mixing noise may possibly be reduced in flight in the aft quadrant (θ_1 > 90°), it becomes increasingly important to be able to account for shock-cell noise because it may weigh heavily on the effective perceived noise level (EPNL). This calls for a thorough understanding of shock-cell-noise mechanisms and effects, especially for suppressed nozzles contemplated for Advanced Supersonic Transport (AST) aircraft.

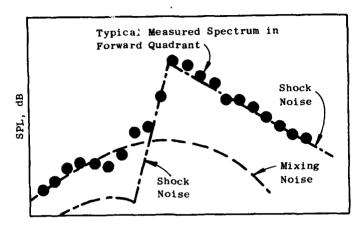
There are other mechanisms, such as lip noise and large-scale structure, which may contribute to the total observed jet noise spectrum. These mechanisms have been studied in some detail as part of Task 2. Results of studies conducted by Siddon (References 14 and 47) for General Electric show lip noise to be relatively insignificant except at very low jet velocities (Vj/C $_{\rm O}$ < 0.7). Even at these low velocities a well-designed, aerodynamically clean nozzle does not exhibit appreciable lip noise. These conclusions are based on extensive measurements of cross-correlations between far-field microphones and nozzle flush-mounted transducers (both internal and external) made over a wide range of nozzle velocities, nozzle types, and with and without external-flow flight simulation.

The question of orderly, large-scale structure as a possible noise mechanism is more difficult to address. Studies conducted by Laufer (References 14 and 48) for General Electric have not produced any concrete evidence that large-scale structure is a direct cause of noise although it may exist under certain flow conditions (e.g., low Reynolds number). Extensive data/theory comparisons using a prediction model which ignores large-scale structure as a noise mechanism have shown no consistent discrepancies which could be attributable to large-scale structure.

M*G*B AEROACOUSTIC PREDICTION

The unified aeroacoustic prediction model developed to predict the noise or arbitrary jets is based upon four primary sound-generation/emission mechanisms:

- Sound generation by small-scale turbulence produced in the mixing zones of the jet plume, convecting with the flow.
- 2. Convective amplification due to turbulent eddy motion relative to the observer.



Frequency, kHz

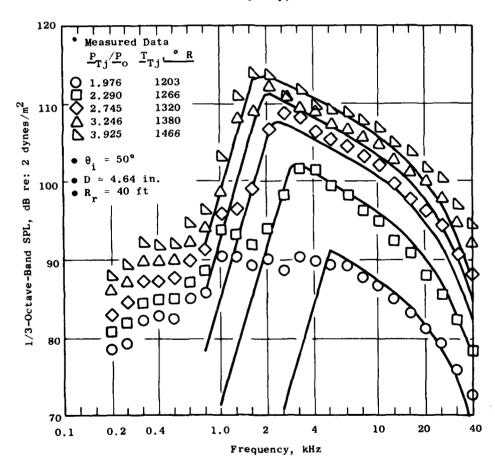


Figure A-3. Comparison of Predicted Shock Noise with Measured Conical Nozzle Spectra.

- 3. Mean-flow shrouding (fluid shielding) of the generated sound.
- 4. Shock/turbulence interaction (shock-cell, broadband noise).

The model utilizes a representation of the jet plume as a "collection" of uncorrelated (nearly compact), turbulent-eddy, multipole sources. These sources radiate sound with an intensity spectrum directly related to the local flow properties, i.e., mean velocity, density, turbulence intensity, and length scale. The net radiation of the generated sound from each eddy is a function of the flow environment of that eddy treated as an acoustic-wave propogation through a parallel, shear-flow model of the jet plume. The shock-cell noise mechanism is modeled using extensions of the Harper-Bourne/Fisher (Reference 45) method. The turbulent mixing noise and shock-cell noise are assumed to be independent of each other. Flight effects are accounted for in both the mixing noise and the shock-cell noise calculations.

The prediction model contains four major elements: (1) an aerodynamic flow-field prediction procedure, (2) a sound/flow interaction acoustic model, (3) a mixing-noise source-strength spectrum model, and (4) a shock-cell noise prediction. These four elements are described briefly in the following paragraphs.

Aerodynamic Flow-Field Model

The aerodynamic flow field is modeled using an extension of Reichardt's theory (Reference 49). This extension consists of superposition of elemental solutions of Reichardt's theory to construct complex flows from nozzles of arbitrary cross section. This approach was first suggested by Alexander, et al. (Reference 50) and applied to suppressor nozzle configurations by Lee, and Grose and Kendall (Reference 51 and 52). Reichardt's theory is based on the experimental observation that the axial momentum profiles in the similarity region of a jet (or wake) are bell shaped or Gaussian. Utilizing this observation and hypothesizing a proportional relationship between transverse momentum and radial gradient of axial momentum, a linear parabolic governing equation for axial momentum of the diffusion type was deduced. This equation has the following form for axisymmetric flow:

$$\frac{\partial F}{\partial x} = \frac{\lambda}{r} \frac{\partial}{\partial r} \left[r \frac{\partial F}{\partial r} \right]$$
 (A-2)

where F is the local axial momentum flux $F = (\rho u^2 - \rho_a u^2_a)$, (x, r) are the axial and radial coordinates respectively, ρ is the local density, and u is the local axial velocity. The subscript "a" denotes the ambient free-stream values. The proportionality factor $\lambda = \lambda(x)$ is an empirically determined mixing constant which varies linearly with axial distance along the jet. Alexander, et al. (Reference 50) have derived similar relations for stagnation enthalpy flux; i.e., $F = \rho u H$ where H is the local stagnation enthalpy relative to the free-stream value.

Because the governing equations for pu² and puH are linear, the summation of elemental solutions to Equation A-2 is also a solution. This unique feature of Reichardt's theory permits the construction of quite complex jet flow fields with relatively simple mathematics. Although more rigorous theories are available for simple jet flows, there is no other technique presently available which offers the capability of modeling jet flows typical of aircraft engine suppressor nozzles such as multiple-tube, lobe, and spoke/chute nozzles, etc.

In addition to the mean-flow quantities u and ρ , the turbulent shear stresses can be deduced from the Reichardt hypothesis: transverse momentum flux ρuv (v is the transverse velocity component) is proportional to the transverse gradient of axial momentum flux,

$$\rho uv \simeq \lambda(\partial/\partial r) \rho u^2,$$
 (A-3)

together with an assumption that the turbulent shear stress is approximated by τ = ($\rho u'v'$) $\simeq \rho uv$. The primes denote fluctuation component quantities. This flow-modeling approach has been applied to coannular jet flows by Gliebe and Balsa (Reference 53). Details of the flow-field-calculation method are given in References 14 and 15.

Sound/Flow Interaction (Shielding) Model

Based on the successful work of Mani (References 40-44) in accounting for mean-flow shrouding effects on jet noise, Balsa (References 54 and 55) has applied the plug-flow modeling approach to explaining the characteristics of noncircular jets. For example, utilizing low-frequency approximations, a solution for elliptic jets was developed (Reference 54). Also, using a plug-flow, annular-jet model, some aspects of the flow shrouding or shielding which takes place in multitube suppressor nozzles were explained. Finally, the solutions for mean-flow shrouding effects in coannular nozzles were developed in Reference 53.

It was found, however, that for high jet velocities $(V_j/C_0 > 1)$ and high frequencies $(fD/V_j > 1)$, the simple plug-flow models with centerline convecting sources overestimated the mean-flow shielding effects. This resulted in an underestimation of noise near the jet axis. It was found necessary to account for mean-flow profile shape and radial source location. Closed-form solutions for the pressure fields of various high-frequency, convected singularities immersed in a parallel shear flow were developed by Balsa (Reference 56) using Lilley's equation. A parallel shear flow is assumed with continuous velocity and temperature profiles. Lilley's equation is given by:

$$\frac{1}{C^2} D^3 p - D (\nabla \beta) - \frac{\partial}{\partial r} (\log C^2) D \left(\frac{\partial P}{\partial r} \right) + 2 \frac{\partial u}{\partial r} \frac{\partial^2 p}{\partial x \partial r} = S$$
 (A-4)

where

$$D = \frac{\partial}{\partial t} + U \frac{\partial}{\partial x} \text{ and } S = \rho D \left[\nabla \nabla u' u'' \right]$$
 (A-5)

In the above, U=U(r), C=C(r), and $\rho=\rho(r)$ are the mean jet velocity, speed of sound, and density, respectively. The symbol ∇ is the gradient operator, t is time and u' is essentially the turbulent velocity fluctuation. The coordinate system and geometry are shown in Figure A-4. Roughly speaking the aerodynamic calculation provides the distributions of U, C, ρ , and S. Equation (A-4) is solved in closed form for the acoustic pressure by the WKBJ Technique. In particular, the Green's function is constructed for this equation which, when convolved with the actual source function S, yields the solution to Lilley's equation. It turns out that the high-frequency assumption in the analysis is not very restrictive and is generally fulfilled for high-velocity jets. A similar approach was used by Pao (Reference 34) for solving Phillips' equation (Reference 31).

In the solution for the Green's function, several possibilities arise depending on the zeros of

$$g^{2} = \frac{(1 - M \cos \theta_{j})^{2}}{(C/C_{0})^{2}} - \cos^{2} \theta_{j}$$
 (A-6)

where M = M(r) = $U(r)/C_0$. Depending on the observer angle θ_j , the radial velocity U(r) profiles, and the density $\rho(r)$ profiles, the parameter g^2 can have one or more zeros or turning points. The precise form of the Green's function depends on the location of the source with respect of these turning points. Altogether there are six possibilities, and closed-form solutions have been obtained for all of these. Some correspond to (but are not identical to) Pao's (Reference 34) SO, S1, and S2 modes. When acoustic shielding is encountered (e.g., when $r_0 < r_0$, where r_0 is the location of the source and r_0 is the unique turning point), the amplitude of the Green's function is exponentially small in the far field; the argument of this exponential is $(-\omega\delta/C_0)$, where ω is the source frequency and δ is the thickness of an effective fluid layer surrounding the source. Details of the fluid shielding calculation method are given in References 14 and 15.

Source Spectrum Model

From the aerodynamic flow-field model described previously, mean velocity, density, and turbulent shear-stress profiles can be computed throughout the jet. This calculation also provides the characteristic strength, frequency, and size of the acoustic convecting quadrupole sources that drive the far-field pressure fluctuations. The characteristic frequency and the length scale are determined from the aerodynamic predictions of $\bar{\mathbf{u}}$ and \mathbf{u}' utilizing the empirically derived similarity relations of Davies et al. (Reference 50,

	WHEENSSIFIED			GENERAL ELECTRIC CO CINCINNATI OH AIRCHAFT ENGINE BUETC F/6 20/1 HIGH VELOCITY JET NOISE SOURCE LICATION AND REDUCTION. TASK 6ETCH APR 79 J BRAUSCH. A S CLAPPER F R GLIERE DOT-05-30034 R/9AEG302										
		3 1F 6									7			
													0.0	
												*	1	
i		ý.	7	/	3	1								
						1		1		ß			7	

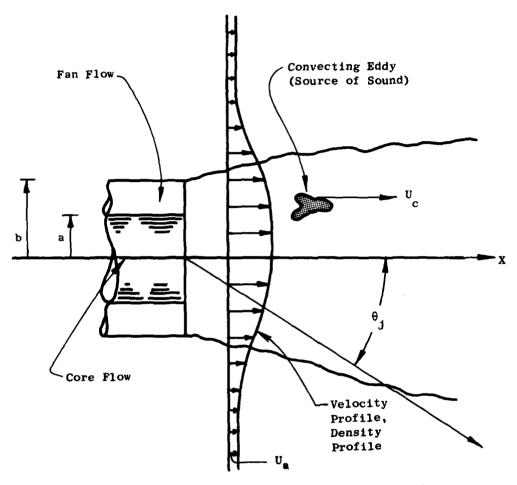


Figure A-4. Parallel Shear-Flow Model of the Jet.

$$\omega_{0} \simeq \frac{\partial \overline{u}}{\partial r}, \quad \ell \simeq \frac{\overline{u'}}{\omega_{0}},$$
 (A-7)

where \overline{u} is the local mean velocity, u' is the local turbulence intensity, and ω_0 and ℓ are the characteristic frequency and length-scale, respectively.

Ribner (Reference 58) has explained how the fundamental solutions associated with the various quadrupole types can be employed to derive the axially symmetric sound field of a round jet. By employing a model of homogeneous isotropic turbulence in the moving eddy reference frame, and by examining the directional average with respect to the azimuthal coordinate of the sound field, Ribner was able to ascribe "weighting factors" to the various quadrupole contributions. This approach is employed in the present model formulation by utilizing the various quadrupole solutions developed from the high-frequency analysis of Lilley's equation. The amplitude ascribed to each of these quadrupole types is the form:

$$dI(\omega) \simeq \rho_0^2 R^3 (u')^4 \omega^4 H(v) dv dV/R^2 c_0^5$$
 (A-8)

where dI (ω) is the acoustic intensity per elemental jet volume dV, ρ_0 is the ambient density, u' is the local turbulence intensity; $H(\nu)$ is the Fourier transform of the moving-frame, space-time cross-correlation of u'; and ν is the ratio of emission frequency ω to characteristic frequency ω_0 . Equation A-8 is used to calculate the mixing-noise amplitude and frequency content for each volume element in the jet. Details of the source spectrum calculation procedure are given in References 14 and 15.

Shock-Cell Noise Model

A shock-cell noise model was initiated to extend the work of Fisher and Harper-Bourne (FHB) to annular, dual-flow, and multielement nozzles. Considerable scale-model data were taken to extract the shock-cell noise characteristics of several nozzle types both statically and in forward flight. From detailed analysis of the data, it was concluded that the FHB concept of shock cells radiating acoustic waves as they are disturbed by turbulent eddies is a reasonable physical picture of the cause of shock-cell broadband noise. The mathematical model of this phenomenon developed by FHB for static conical nozzles has been generalized to more complex nozzle configurations. The most pertinent of these ideas are discussed in the following paragraphs.

As mentioned above, the primary physical mechanism for the production of broadband noise by the presence of shock cells in the jet plume is the emission of acoustic waves by the shock fronts as they are "disturbed" by the passage of turbulent eddies through and/or by them. The eddies, produced in the mixing of the plume, are themselves fluctuating "blobs" of vorticity; thus, the emitted acoustic waves from the shocks have characteristics which are related to the unsteadiness of the turbulent disturbances, i.e., the



characteristic frequency and amplitude. The strength of the emitted wave must also be a function of the shock strength. The process is similar to the linear "transfer function" model of Ribner (Reference 59) where a vorticity wave of given amplitude and frequency is input to a shock, and the output is a transmitted vorticity wave, an internally generated entropy wave, and a pressure (acoustic) wave.

Each shock in the jet plume emits acoustic waves in a random or broadband fashion, related to the randomness of the disturbing turbulence. The far-field mean-square sound pressure of this emission, after the summation of the contributions from all the shocks, produces a spectrum composed of two basic components. First, the sum of the mean-square pressure signals from each shock produces a "group spectrum" which is rather broadband in character, similar to a jet mixing-noise spectrum. The second component, referred to as the "interference spectrum," results from the selective reinforcement and cancellation which occurs between emitted waves from neighboring shocks. The superposition of these two components results in the rather "peaky" spectrum shape observed for shock-cell noise. This is illustrated in Figure A-5.

Through examination of data from several nozzle types and an evaluation of the FHB formulation, a plausible extension of the present FHB model to noncircular nozzles was developed. It was found that the group spectrum component (Figure A-5) was dependent on flow area for level-scaling and on equivalent diameter for frequency-scaling. The interference spectrum, however, scales with hydraulic diameter or, more correctly, shock-cell spacing. When the nozzle hydraulic diameter is significantly less than the equivalent-area diameter, the interference spectrum is displaced to higher frequencies - resulting in a total spectrum shape which is quite different from that of a conical nozzle (as shown in Figure A-6).

To demonstrate the validity of the above hypothesized model extension, data from a conical nozzle and a rectangular, 6:1 aspect-ratio nozzle were examined. Predictions of the shock-cell noise spectra were made for these nozzles using the modified FHB theory described qualitatively above. Results of the calculations and comparisons with measured data, for a supercritical pressure ratio condition, are shown in Figures A-7 and A-8. Figure A-7 shows the measured SPL spectrum at θ_1 = 60° forward-arc location, for a 1.5-inch diameter conical nozzle operating at a pressure ratio of 2.65. Data for three temperatures are shown, giving essentially the same shock-cell noise. This verifies an important feature of the FHB theory: shock-cell noise is a function of nozzle pressure ratio and is independent of jet temperature. Also shown is the FHB theory predicted spectrum which is substantially in agreement with the measurements.

The corresponding results for a 6:1-aspect-ratio, rectangular nozzle are shown in Figure A-8. SPL measurements are shown in this figure; results at two azimuthal angles (ψ) are included. These results show that, even though the nozzle is nonaxisymmetric, the sound field produced by the shock cells is axisymmetric, or nearly so. Also shown is a prediction of the spectrum based on the modifications to the FHB theory previously discussed. Again substantial agreement with the measurements is observed - indicating that the



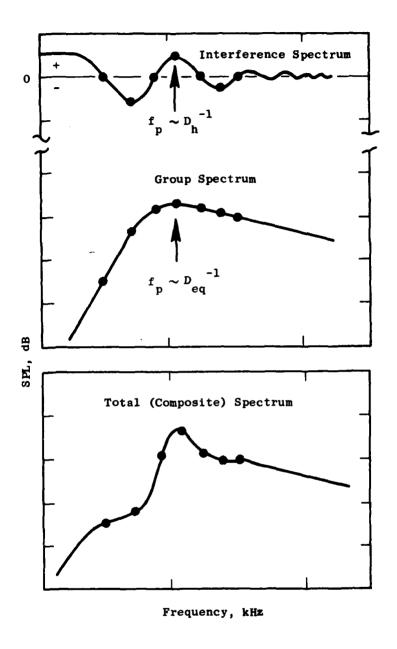
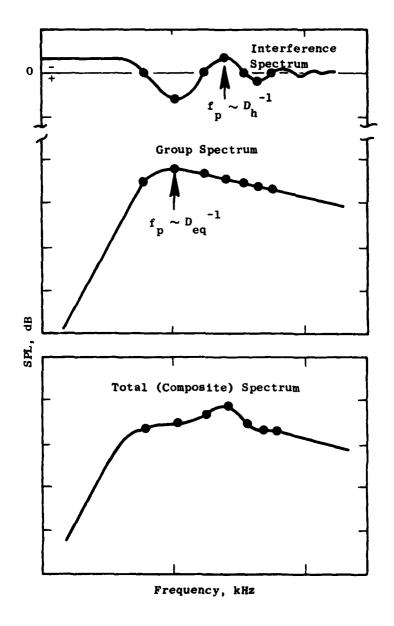


Figure A-5. Primary Components of a Conical-Nozzle Shock-Cell Noise Spectrum, $D_h = D_{eq}$.



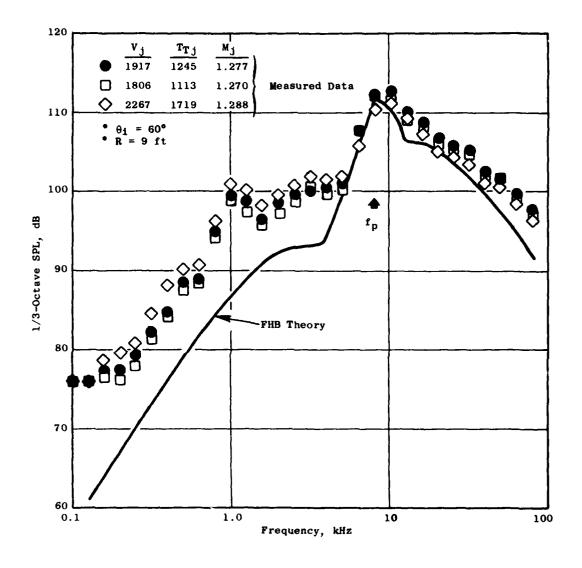


Figure A-7. Shock-Associated Noise Spectrum, 1.5-in. Diameter Conical Nozzle.

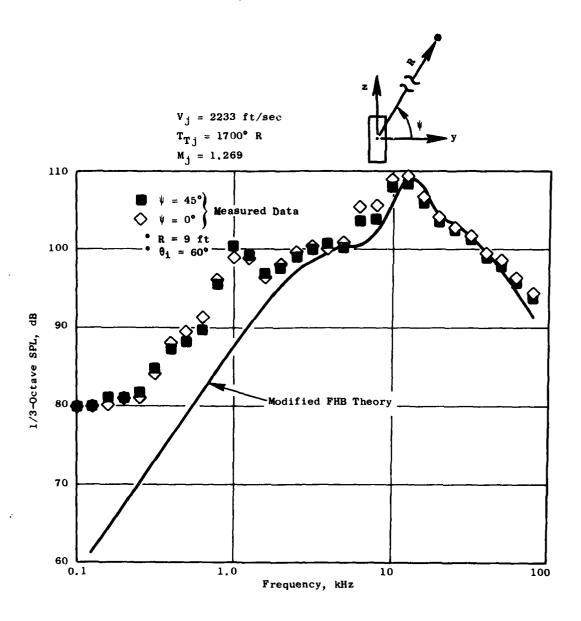


Figure A-8. Shock-Associated Noise Spectrum, 6:1 Aspect Ratio Rectangular Jet.

proposed extensions to the shock-cell noise model for round jets to predict nonaxisymmetric jet behavior is a promising approach.

As discussed in Section 3.4 of Reference 15, the M*G*B computer program utilizes a simplified version of the FHB method described above. Distinction between equivalent diameter (for round nozzles) and hydraulic diameter (for suppressors) is employed as discussed above.

Aeroacoustic Model Integration

The basic analytical-model elements have been integrated into a unified, aeroacoustic jet-noise-prediction computational procedure. The jet plume is divided into elemental jet volumes, each having its own source strength, spectrum, and flow shrouding as illustrated in Figure A-9. The mean-square sound pressure emitted from each volume element is given by

$$\overline{dp}^{2} (\omega) \simeq \frac{\Delta f}{C_{o}^{4} R^{2}} \left[\rho_{o}^{2} (u')^{7} dV \right] \left[\frac{\omega^{4}}{\omega_{o}^{4}} H(v) \right] \left[\frac{\cos^{2} \theta j + g_{o}^{2}}{(C/C_{o}) C} \right]^{2} \exp\left[-2\omega\delta/C_{o}\right]$$
(A-9)

where ${\bf g}_{\rm O}$ is given by equation A-6 evaluated at the source radius (r_O), Δf is the one-third-octave frequency bandwidth, and

$$C = \sqrt{(1 - M_c \cos \theta_j)^2 + (\alpha u'/C_o)^2}$$

is the modified Doppler factor (Reference 27). Convection Mach number $M_c = 1/2(M_O + 0.65 M_i)$. The exponential "shielding" factor argument is given by

$$\delta = \int_{r_0}^{r_0} |g^2|^{1/2} dr \qquad (A-10)$$

This simple, closed-form solution, combined with the simple aerodynamic calculation method described earlier, permits a rapid, economical computation of the entire-jet-plume aerodynamic and acoustic characteristics, including far-field spectra at all observer angles. The contributions from each elemental jet volume are simply added on a mean-square pressure basis in each frequency band. The shock-cell noise contribution is then computed separately and added to the mixing-noise contribution to yield the total far-field spectrum.

For prediction of jet mixing noise in flight, the mean-square sound pressure level is multiplied by the dynamic amplification factor $(1+M_a\cos\theta_1)^{-1}$, where M_a is the flight Mach number. In addition, the flow Mach number is replaced by $(M-M_a)$ in evaluating the shielding and convection effects given by Equations A-6 and A-9. For the shock-cell broadband noise, the mean-square pressure levels are multiplied by $(1+M_a\cos\theta_1)^{-4}$, as suggested by Drevit et al., Reference 65.



Figure A-9. Generalized Volume Element Model.

(1) はないのできる。これできる。

VIII. SERVICE PLANE.

Finally, in all predictions of one-third-octave spectra, atmospheric-attenuation corrections are applied using standard-day corrections (70% relative humidity and 59° F dry-bulb temperature) evaluated at the center frequency.

An extensive data/theory-comparison study was carried out to verify the static jet-noise-suppression mechanisms identified in Task 2. The Task 2 M*G*B jet-noise-prediction model summarized above was used to predict the acoustic characteristics of seven nozzle configurations at several operating points for each configuration. These predictions were compared to the experimental data obtained from the scale-model tests conducted in Task 3 and from the Aerotrain tests conducted in Task 4 of the present program. Comparisons were made of perceived noise level (PNL) versus jet exhaust velocity, PNL directivity, and one-third-octave sound-pressure-level spectra at selected observer angles for each configuration. The results of these comparisons are given in Reference 12. In summary, these results demonstrated that the Task 2 aeroacoustic prediction model is capable of predicting the acoustic characteristics of a wide variety of nozzle types over a wide range of operating conditions. It can serve as an accurate preliminary tool for subjective noise assessments and nozzle-geometry optimization during preliminary design and analysis.

USE OF M*G*B PREDICTION FOR DESIGN EVALUATION AND DIAGNOSTIC ASSESSMENT

To illustrate the use of the M*G*B model computer program as a detailed design and diagnostic evaluation tool, an example is presented in the following paragraphs (also see Reference 12). The use of the M*G*B computer program is described in Reference 15.

The Task 2 M*G*B aeroacoustic model is based on four noise-generation/emission mechanisms:

- 1. Turbulent-mixing noise generation
- 2. Convective amplification
- 3. Fluid shielding
- 4. Shock-cell broadband radiation

The objective of the present subsection is to identify the relative roles these mechanisms play in the suppression of jet noise. The data/theory comparisons given in References 14 and 15 have shown that the present mathematical-model representation of these mechanisms (collectively) yields a fairly accurate prediction of the far-field acoustic characteristics of turbulent jets for a wide variety of shapes and flow conditions. It is therefore of interest to evaluate how the individual mechanisms combine to yield the far-field result; more importantly, the changes which occur in these mechanisms due to the addition of a suppressor to a baseline nozzle arc of interest.

The computer study was performed to evaluate the relative contributions of the above four mechanisms to the far-field noise both for a baseline conical nozzle and for a typical, high-suppression, multielement nozzle. A 36-chute, AR = 2.0, turbojet suppressor was chosen for this study as representative of a high-element number, high-suppression (10 to 12 PNdB), exhaust system. A typical static takeoff condition of $V_j = 2400$ ft/sec and $T_{T_j} = 1630^\circ$ R was selected for evaluation. Both the baseline conical nozzle and the 36-chute suppressor nozzle exit areas were 338 in. Noise characteristics were evaluated on a 2400-ft sideline.

The computations were performed in four modes, as follows:

- a. Complete acoustic calculation
- b. As in (a), but shock-cell noise omitted
- c. As in (b), but fluid shielding omitted
- d. As in (c), but convective amplification omitted.

For the chute suppressor, mode (a) was omitted because the ability to model multichute-nozzle shock-cell noise is not yet fully established. The difference in noise levels between modes (a) and (b) is a measure of the shock-cell contribution to the total jet noise signature. The difference in noise levels between modes (b) and (c) is a measure of the influence of fluid shielding on the jet noise. Finally, the difference in levels between modes (c) and (d) indicates the amount of convective amplification present in the jet.

The results of the above series of computations are summarized in Figures A-10 through A-13. Figure A-10 shows the PNL directivity patterns for the different prediction modes. Also shown are the measured data, for reference, which should be compared with mode (a) predictions [mode (b) for the chute nozzle]. Figures A-11 through A-13 display the corresponding spectra shapes (one-third-octave SPL) at $\theta_i = 50^\circ$, 90° , and 130° respectively. The measured spectra are also shown in Figures A-11 through A-13 for reference.

Considering the conical-nozzle PNL directivity patterns, Figure A-10a, it is observed that shock-cell noise contributes substantially to the total noise in the forward quadrant, $\theta_i < 90^\circ$. This can be seen by noting the difference between mode (a) and mode (b) predictions. There is no contribution of shock noise close to thejet axis ($\theta_i > 120^\circ$) because mode (a) and (b) predictions are identical in this region. There is no fluid shielding for observer angles less than about 110° based on comparing mode (b) and (c) predictions. For $\theta_i > 110^\circ$, however, shielding effects become quite substantial, on the order of 30 PNdB. Eddy-convection effects are also large; they increase the noise in the aft quadrant ($\theta_i > 90^\circ$) and reduce the noise in the forward quadrant ($\theta_i < 90^\circ$). This effect is apparent from comparing mode (c) and (d) predictions.

The mode (d) prediction shown in Figure A-10a represents the basic turbulent-mixing noise in the absence of eddy convection and fluid-shielding effects. It possesses a basic, nonconstant, directivity pattern dictated by the weighted summation of various quadrupole types composing the turbulent eddies. This basic pattern is only symmetric about $\theta_1=90^\circ$ when the local flow Mach number is zero because the quadrupole weighting factors are a function of local Mach number and bias the radiation toward the forward quadrant. For example, if the flow Mach number M is set equal to zero and $\mathrm{C/C_0}==1.0$, Equation A-6 shows that the shielding function g^2 reduces to $\sin^2\theta_j$. Hence the mean-square sound pressure, from Equation A-9, will become independent of θ_j . The results shown in Figures A-10 through A-13 for mode (d) therefore do contain fluid/sound interaction effects. Only the eddyconvection effects () and the exponential shielding effects () have been suppressed.

The corresponding PNL directivity patterns for the 36-chute suppressor are shown in Figure A-10b. The trends discussed above for the conical nozzle are qualitatively similar for the 36-chute nozzle with the exception of the shock-cell noise contribution. The predictions were made neglecting shock-cell noise (mode b), and yet the predictions agree with the date, as Figure A-10b shows. This implies that shock-cell noise is not a significant feature of multichute nozzles. It also appears, from the results shown in Figure A-10b, that neither convection effects nor fluid-shielding effects are as strong as for the conical nozzle.

The breakdown of mechanisms for a typical, forward-quadrant angle of $\theta_1=50^\circ$ is shown in Figure A-11. No shielding occurs at this angle; therefore, the mode (c) results are omitted, as they are identical to the mode (b) results. The conical-nozzle results, Figure A-11a, show an interesting counteraction among the mechanisms. The basic mixing-noise spectrum mode (d), yields a noise level much higher than the measured level. The convection effect is to Doppler-shift and drop this spectrum to a level significantly lower than the data (except at very low frequencies) indicated by the mode (b) prediction. Finally, the addition of the shock-cell noise spectrum raises the spectrum back up to the measured level at middle-to-high frequencies.

The corresponding 36-chute, 50° spectrum results are shown in Figure A-llb. Thegood agreement between the mode (b) spectrum prediction and the measured spectrum substantiates the implication drawn from Figure A-l0b: shock-cell noise is not a significant source for multichute suppressors. Again, the effect of convection is to reduce the level and Doppler-shift the spectrum to lower frequencies.

The breakdown of mechanisms for the one-third-octave SPL spectrum at $\theta_1 = 90^{\circ}$ is shown in Figure A-12. Fluid-shielding effects are absent at 90° , and convection effects are less than 0.5 dB throughout the frequency range.



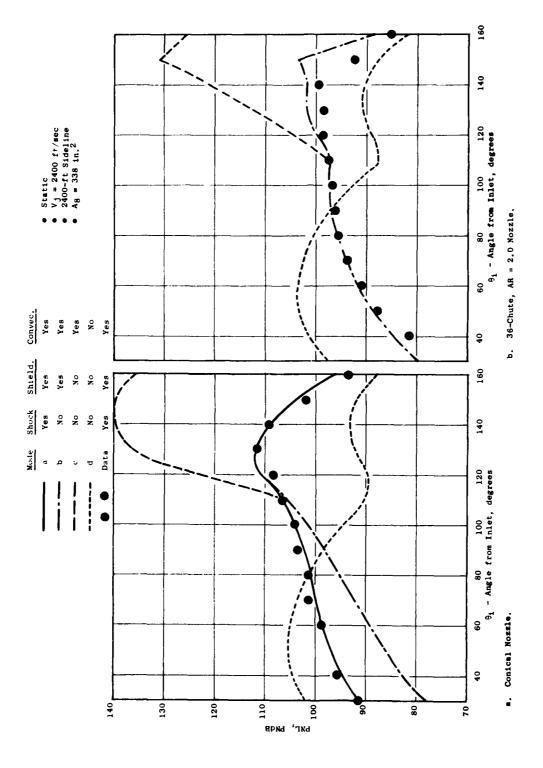


Figure A-10. Relative Contributions of Noise Mechanisms to PNL Directivity.

	Mode	Shock	Shield,	Convec.
		Yes	Yes	Yes
	b	No.	Yes	Yes
	c	No	No	Yes
	d	No	No	No
• •	Data	Yes	Yes	Yes

• Static • 2400-ft Sideline • V_j = 2400 ft/sec • A₈ = 338 in.²

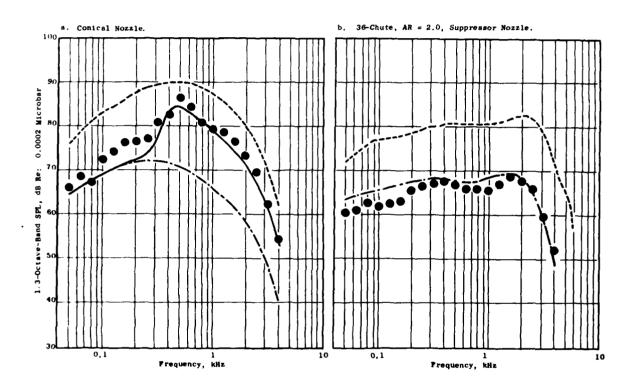


Figure A-11. Relative Contributions of Noise Mechanisms to SPL Spectra at θ_{1} = 50°.

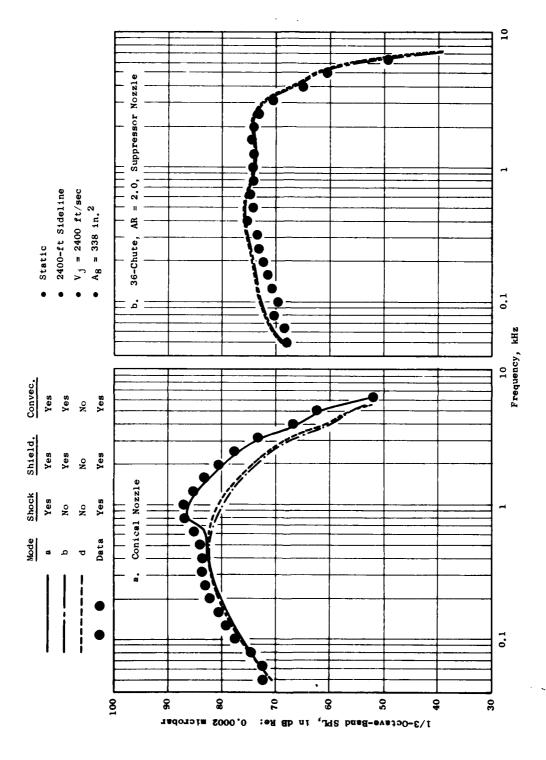


Figure A-12. Relative Contributions of Noise Mechanisms to SPL Spectra at $\theta_1 = 90^{\circ}$.

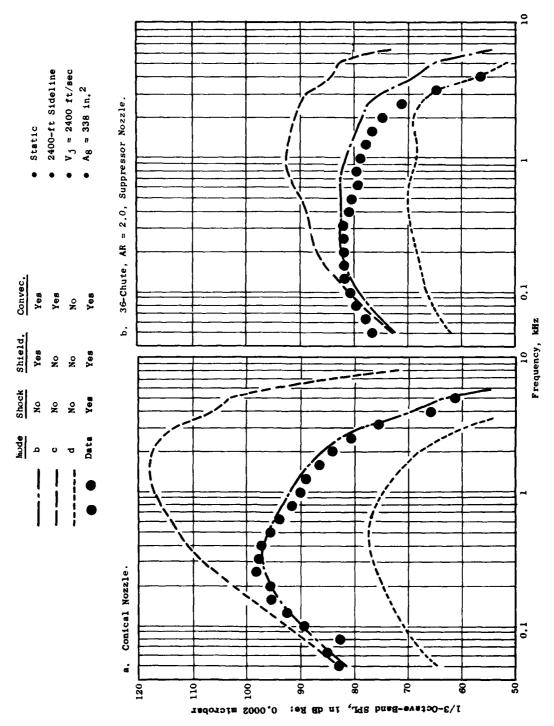


Figure A-13. Relative Contributions of Noise Mechanisms to SPL Spectra at θ_1 = 130°.

The shock-cell noise was not computed for the chute nozzle; thus, the only significant contribution at 90° for the chute nozzle is the basic, mixing-noise spectrum. The results in Figure A-12 illustrate the diminishing effect of shock-cell noise with increasing θ_{i} (compare to Figure A-11a) and the almost negligible effect of convection.

Near the peak-noise angle, $\theta_1=130^\circ$, convection effects again become significant. They produce a dramatic amplification of the mixing noise as the results in Figure A-13 show. Another counteraction of mechanisms occurs at this angle, involving the competing effects of convection and fluid shielding. The basic mixing-noise spectrum is much lower than the measured level, as shown in Figure A-13a, mode (d). The effect of convection is to increase the levels by as much as 40 to 50 dB at high frequencies. The effect of shielding, however, is to reduce the noise levels by 20 to 30 dB at high frequencies; thus, the net noise levels agree with the measured levels.

It is interesting to note that the convection effect Doppler-shifts the basic mixing-noise spectrum to higher frequencies as would be expected from classical notions of moving-source acoustics. However, the fluid-shielding effects, which increase with increasing frequency, attenuate the high-frequency portion of the convected spectrum to such a large extent that the resulting spectrum peaks at a much lower frequency, lower than even the basic unconvected spectrum peak. This is the explanation for the observed "reverse Doppler shift" at angles close to the jet axis.

The competing influences of convection and fluid shielding are also evident in the 36-chute nozzle predictions shown in Figure A-13b. The magnitudes of these effects are considerably smaller than those exhibited by the conical nozzle. For example, at 2000 Hz, the convective amplification is 22 dB for the chute nozzle, compared to 48 dB for the conical nozzle at the same frequency. Similarly, the fluid-shielding attenuation is only 12 dB at 2000 Hz for the chute nozzle, compared to 31 dB attenuation for the conical nozzle.

The various mechanisms can be isolated explicitly by examining the differences between the various prediction curves shown in Figures A-10 through A-13. First, the total PNL suppression as a function of $\boldsymbol{\theta}_1$ is the difference between the conical- and chute-nozzle total-noise PNL directivity patterns. This can be compared with measured PNL suppression and is shown in Figure A-14. The predicted total PNL suppression is seen to compare well with the measured suppression.

From the results given in Figures A-10 through A-13, it can be concluded that the multichute nozzle almost completely suppresses the static shock-cell noise so as to permit the mixing noise to dominate the forward-quadrant spectra. The static shock-noise suppression is then approximated by the difference between mode (a) and (b) conical-nozzle predictions. This estimated shock-cell noise suppression is also shown in Figure A-14. The shock-cell noise suppression is seen to be higher than the total predicted suppression in the forward quadrant; hence, some other mechanism is providing negative suppression, i.e., increasing the PNL.

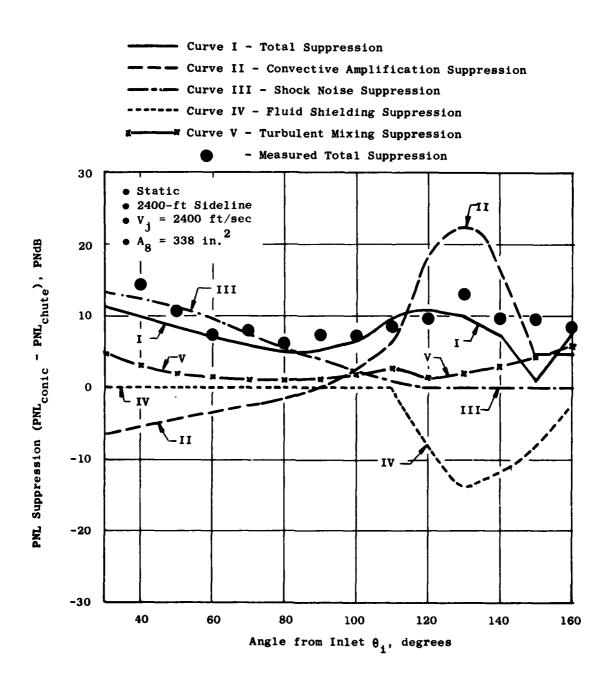


Figure A-14. PNL Suppression Composition for a 36-Chute, AR = 2.0, Suppressor Nozzle.

The suppression of convective amplification can be computed by first calculating the convective amplification for each nozzle PNL(c) - PNL(d), and then subtracting the chute-nozzle result from the conical-nozzle result. The convective-amplification suppression is shown in Figure A-14. Note that it is negative in the forward quadrant; this explains why the shock-noise suppression is greater than the total net suppression.

In a similar fashion, the difference between conical-nozzle <u>fluid-shielding attenuation</u> and 36-chute-suppressor fluid-shielding attenuation has been computed and is shown in Figure A-14. From this result, it is apparent that a multielement suppressor exhibits reduced fluid-shielding effects relative to a conical nozzle; i.e., part of the beneficial effect of fluid shielding is lost by the addition of a suppressor.

Finally, the suppression of basic turbulent-mixing noise generation has been evaluated by subtracting the mode (d) prediction for the chute nozzle from the conical-nozzle mode (d) prediction. This result is also shown in Figure A-14. The basic mixing-noise suppression is seen to be quite small, from 1 to 5 dB over the range of angles shown, which is contrary to historical conceptions of how multielement suppressors reduce jet noise. The multichute suppressor in fact generates approximately the same total mixing noise as the equivalent conical nozzle but redistributes the noise to higher frequencies. This conclusion is dramatically illustrated in Figure A-15 where the basic mixing-noise spectra [mode (d) computations] for the two nozzles are compared. Also shown are the same spectra with the atmospheric (air) attenuation removed, i.e., the lossless spectra. The multichute lossless spectrum is seen to have about the same peak level as the conical-nozzle peak-noise (lossless) frequency to conical-nozzle peak-noise (lossless) frequency is about 6:1. This is precisely the ratio of conical-nozzle diameter to chute/element equivalent-area diameter.

The major conclusions to be drawn from the above example are that: (1) the primary mechanism responsible for static noise suppression in the forward quadrant is shock-cell noise reduction; (2) the basic mixing-noise generation is not suppressed, only redistributed to higher frequencies where atmospheric attenuation can have a more pronounced effect on the spectrum shape, and (3) the observed static suppression in the aft quadrant is primarily a result of reduced convective amplification - offset somewhat by a loss in fluid shielding. This delicate balance between convection and shielding effects in the aft quadrant is very difficult to predict accurately because these two effects are of large magnitude but opposite in sign. This is dramatically illustrated in Figure A-16 where the convection and shielding effects for each of the two nozzles are compared.

The reduction in shock-cell noise produced by a multichute suppressor can be explained by the fact that breaking up a large, round jet into very small, discrete, rectangular jets will cause the shock-cell formation to be dissipated much more rapidly. The shock-cell spacings and cross-sectional dimensions will be much smaller, and the cells are likely to be fewer in number. The resulting broadband radiation is therefore likely to be much lower in level and higher in frequency than that for a conical nozzle.

The conclusion that the total generated mixing noise is not significantly different for a multichute suppressor is explained by the fact that the

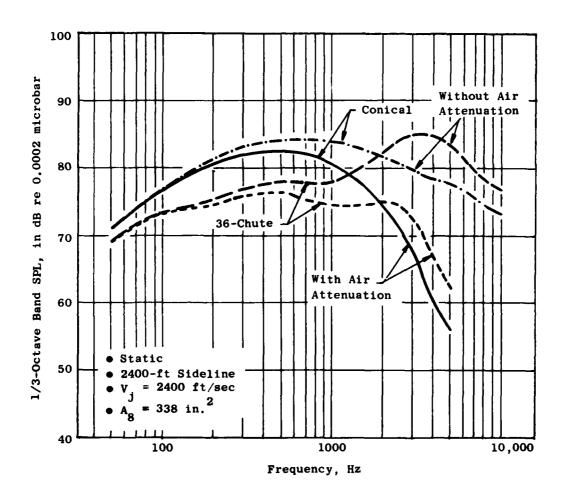


Figure A-15. Comparison of Predicted, Basic, Turbulent-Mixing Noise Spectra at θ_1 = 90° for a Concial and a 36-Chute Nozzle.

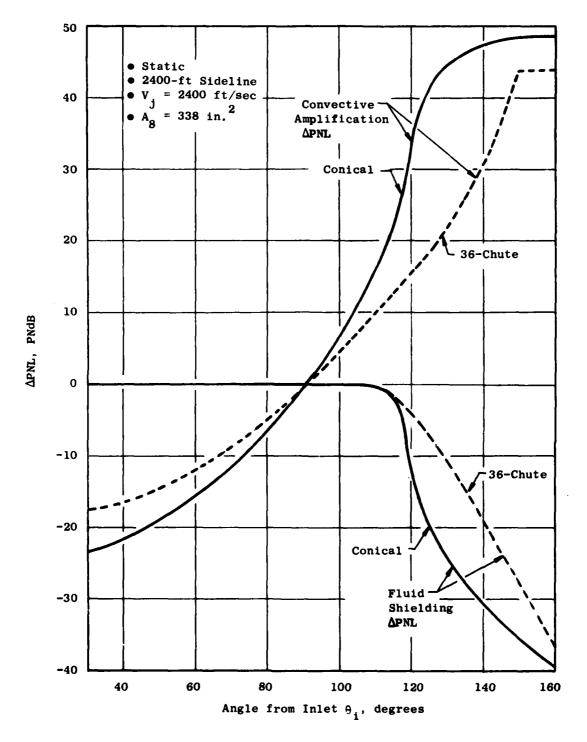


Figure A-16. Modification of Basic Mixing-Noise PNL by Convective Amplification and Fluid Shielding.

chute-nozzle mixing-layer perimeter close to the nozzle exit plane is considerably larger than an equivalent-area conical-nozzle perimeter. The high-frequency noise generated in the initial shear layers should therefore be higher by the ratio of perimeters, provided the premerged portion of the chute mixing layers have approximately the same turbulence characteristics. Once the chutes have merged, a large axisymmetric jet forms which has a substantially lower velocity than the exit value; therefore, the low-frequency noise levels should be lower than the corresponding conical-nozzle levels.

The reduction in convection effects exhibited by a multichute nozzle is the result of lower eddy-convection velocities. The rapid, plume-mean-velocity decay exhibited by a multichute nozzle suggests that the majority of the noise-producing, turbulent eddies in the plume are convecting downstream at a substantially lower velocity than in a conical nozzle.

The reduced fluid-shielding effects characteristic of a multichute nozzle can also be related to the rapid plume-velocity (and temperature) decay. Fluid shielding, as discussed in Section 3.1, increases with increasing plume velocity and temperature; therefore, the lower velocity and temperature levels resulting from the rapid chute-element mixing provides less fluid shielding than an equivalent-area, conical nozzle.

In summary, from the above example study, the suppression characteristics of a given nozzle can be explained and quantified by utilization of the M*G*B computer model as a diagnostic evaluation tool. For this particular example, it was shown that high-element-number (multielement) suppressors do not substantially reduce the turbulent-mixing-noise generation but, instead, redistribute this noise to higher frequencies where atmospheric (air) attenuation can mitigate the effects more easily. In the forward quadrant, the major effect of a multielement nozzle is to substantially reduce shock-cell broadband-noise radiation. In the aft quadrant, substantial suppression is achieved by a reduction in convective-amplification effects. This reduction is offset somewhat by an accompanying loss in fluid-shielding suppression, but (for a "good" suppressor) the net effect is still a substantial noise reduction.

All of the above mechanisms for suppression of jet noise by multielement nozzles are related to the rate at which the plume decays. High area-ratio suppressors decay the jet to a lower merged velocity level than low area-ratio nozzles, and high-element-number nozzles yield more rapid decay to the merged velocity level than do low-element-number nozzles. Therefore, acoustic considerations dictate high element number and high area ratio for best suppression.

In utilizing the M*G*B model as a design evaluation tool, the subtle tradeoffs between convective amplification and fluid shielding in the aft quadrant, between shock-noise reduction and convective amplification in the forward quadrant, and between reduced convective effects versus higher high-frequency noise, can be exploited to "fine-tune" a design for a given application.



APPENDIX B - MULTIELEMENT AND TWO-STAGE-EJECTOR NOZZLE BACKGROUND INFORMATION

The first part of this appendix reviews some of the noise/performance characteristics of afterburning-turbojet suppressor installations indicative of the U.S. supersonic transport (SST) program effort. This is followed by a discussion of the multitube and multichute that have been under continuous development subsequently. Sections 4.0 and 5.0 of the text include detailed procedures for estimating the noise and performance of the latter two suppressor types.

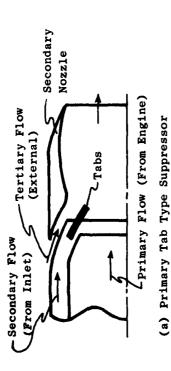
TWO-STAGE-EJECTOR NOZZLE (TSEN) WITH SUPPRESSORS

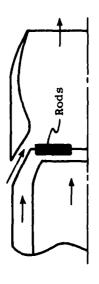
The U.S. SST suppressor efforts were primarily devoted to adapting various suppression techniques within the two-stage ejector nozzle (TSEN) system of an afterburning turbojet (References 2 and 60). Originally, considerable effort was expended on the basic TSEN (see Figure B-1) without a suppressor; the objective was promotion of primary (or engine), secondary, and tertiary flow mixing within the ejector shroud (where the high-frequency noise generated could be shielded and possibly attenuated by acoustic treatment) and of decreasing the jet exhaust velocity at the ejector nozzle exit plane (hopefully affecting the low-frequency noise with no appreciable performance degradation). Within practical ejector-diameter and length-to-primary-nozzle-diameter ratio ranges, static suppression levels relative to a simple conical nozzle of 1-2 PNdB were achieved. This was insufficient; therefore, suppressors such as illustrated in Figures B-l and B-2 were investigated.

One of these suppressor systems was the tabbed primary (Figure B-la). The tabs were an integral part of the primary-nozzle thrust-reverser system. They formed the center of the target when the primary-nozzle flap translated aft and were deployed as the thrust reverser. As the tabs represented hardware required for the reverser system, they were explored for suppression capability by partially deploying them into the jet stream in an effort to enhance the mixing of the primary, secondary, and tertiary flows within the ejector. Some nominal static suppression (≈ 3.5 PNdB, see Figure B-3a) was recorded; however, thrust decrements were such that static thrust-loss/noise-reductions ($\Delta Cfg/\Delta PNL$) remained at about 2.5 (see Figure B-4).

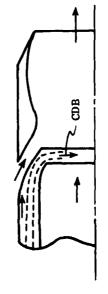
In the quest for simplicity, considerable effort was devoted to the so-called primary radial-rod-type or "spoke" suppressor (see Figure B-lb) with the spokes located just aft of the primary nozzle. In general, suppression was observed to increase almost linearly with increasing penetration up to about 40% and then decrease gradually to the 60% penetration point. Proximity of the spokes relative to the primary exit plane was noted to adversely affect suppression; however, the upstream position permitted operation at higher pressure ratios and total temperature without backflow. Static suppressions on the order of 3 PNdB (see Figure B-3b) were recorded at partial augmented conditions resulting in static-thrust-loss to noise-reduction ratios ($\Delta Cfg/\Delta PNL$) of about 2.5 (see Figure B-4).



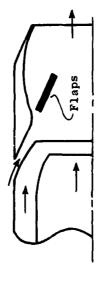




(b) Primary Rod Type Suppressor



(c) Compressor Discharge Bleed Type Suppressor



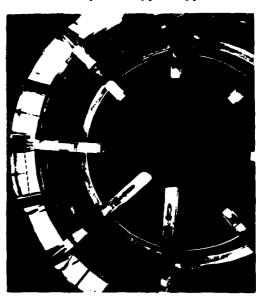
(d) Secondary (Flap) Type Suppressor

Figure B-1. Schematics of Typical Single-Flow Suppressor Nozzles for Afterburning Systems.

a. Primary Tab Type Suppressor



b. Primary Rod Type Suppressor



c. Compressor Discharge Bleed
Type Suppressor



d. Secondary (Flap) Type Suppressor

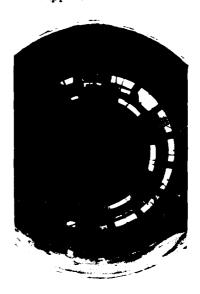


Figure B-2. Photographs of Typical Single-Flow Suppressor Nozzles for Afterburning Systems.

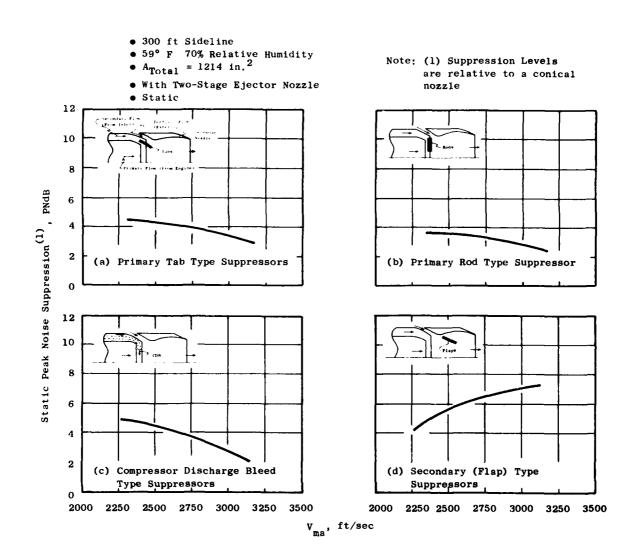


Figure B-3. Summary of Noise Reduction Characteristics for Typical, Single-Flow, Afterburning-Turbojet Suppressors.

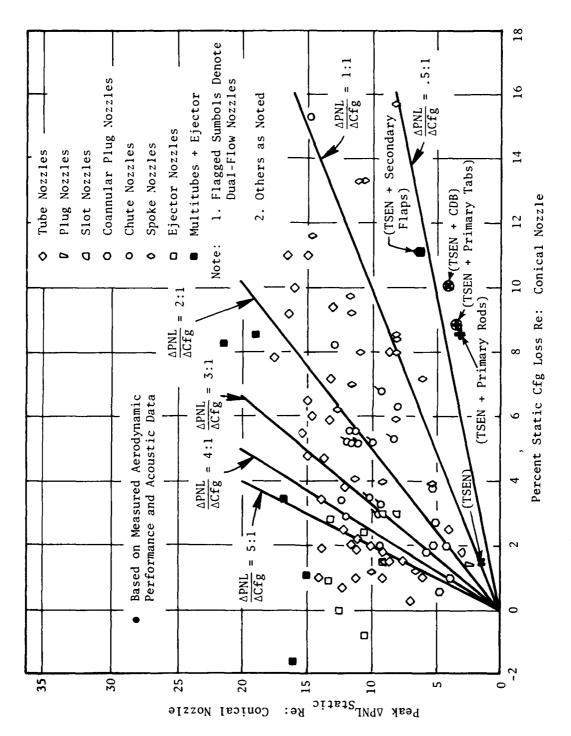


Figure B-4. Comparison of Static Performance and Suppression Levels.

(316)

As far back as 1960, industry expended considerable effort to substantiate that jet noise was indeed uniquely related to the flow-velocity (steady/ unsteady) distribution in the high velocity wake. Many feasibility studies were conducted on fluid injection as a means of influencing jet noise generation and suppressor performance. Subsequent investigations concluded that desired alteration of jet mixing could not be attained by selective water injection. Although the mean-flow velocity profiles could be altered through use of selective sprays, the jet mixing was not greatly influenced, and the suppression accomplished was less than would be possible through uniform mixing of water and air. In an effort to reduce performance penalties associated with drag losses of primary suppressors, studies were made to evaluate the effectiveness of distorting the primary stream with high pressure air from compressor discharge bleed (CDB) as illustrated in Figure B-lc. Again, this type of suppressor had characteristics similar to the primary type suppressor (see Figure B-3c), but the penalties paid for any enhancement of suppression were excessive, and suppression obtained from CDB systems alone was very poor in terms of the thrust-lossto-suppression ratio as shown in Figure B-4 (for the TSEN + CDB). Although suppression at dry operation was near 5 PNdB, at partial afterburning the effectiveness dropped off severely and resulted in thrust-loss-to-suppression levels of near 4.0 which were just above power cutback levels (~5.5).

In the postulated exhaust system for the United States SST engine (Reference 2) and the existing one for the Anglo-French Concorde (Reference 61), the variable conical primary nozzle exhausts into a variable secondary nozzle. The secondary nozzle provides support to mount a suppressor system that can be retracted in the cruise mode. This represents the fourth-type suppressor for the TSEN nozzle, Figure B-ld. This time, however, the suppressor elements are protruding into a supersonic environment. Thus, in addition to increasing the flow mixing rate, the suppressor fingers are also shock-wave generators. Many suppressor designs of this type were tested - ranging from systems where the suppressor flaps were designed aerodynamically, to minimize performance losses, to crude systems where flat plates or "spades" were introduced into the stream to "scoop" out the hot flow in alternate segments of the jet. In addition, these flaps could serve as part of an overall multiflap system which, when fully deployed, could form a target reverser with primary efflux gases exiting through the ejector blow-in doors. The basic suppression characteristics of these secondary suppressors were such that high suppression values were obtained at high velocities. In fact, some of the configurations tested in the SST Program (Figure B-1d) were most effective at jet velocities in excess of 2700 ft/sec. In addition to having different general suppression characteristics versus jet velocity compared to the primary systems, the magnitude of peak static suppression for fairly simple designs was larger, and deltas of up to 6 to 7 PNdB were achieved (unfortunately not without significant performance penalties). Typical secondary-flap acoustic performance characteristics are summarized in Figure B-3b. This type of suppressor generally falls in the regime of about 1.7% static thrust loss per ΔPNL as shown on Figure B-4 (TSEN + secondary flaps).

As already implied by reference to Figure $^{B-4}$, the thrust loss per unit reduction in noise was excessive for these TSEN suppressor nozzles. The $\Delta \text{Cfg}/\Delta \text{PNL}$ fell in the vicinity of 2:1 or, in terms of $\Delta \text{PNL}/\Delta \text{Cfg}$, 0.5:1. The other nozzle data shown on Figure B-4, which are for static measurements of both the noise reduction and the thrust coefficient reduction, are much superior; for this

reason, no further mention is made of a TSEN type in this Guide.

ANNULAR, COANNULAR, AND MULTIELEMENT SUPPRESSORS

Information is included in this section to enable the reader to establish the approximate maximum suppression obtainable from annular nozzles, coannular nozzles, and multielement suppressors (single- and dual-flow cycles) and to estimate the associated performance level. The two principal types of multielement suppressors are the multitube and multichute (or spoke); both are discussed in detail in Section 4.0, Section 5.0, and Section 6.0 of the text. The short-form information included in this appendix is representative of the information used in the preliminary selection process given in Section 3.3 of the text.

Typical suppression data for single- and dual-flow (higher velocity in the outer stream) nozzles, relative to a conical nozzle, are given in Figure B-5. This figure shows the static, peak PNL suppression for an annular-plug nozzle, for a coannular-coplanar nozzle, and for several chute nozzles on both the single-flow and dual-flow engines. A multitube nozzle with ejector is also shown for a single-flow engine. These data are representative of the achievable suppression levels as a function of nozzle isentropically expanded exhaust velocity (where a constant-area, constant-pressure, ideally mixed, mass-averaged velocity is used in the case of the dual-flow engines). Note that the data in Figure B-5 are based on experimental results; similar information is included in Section 4.1.2 of the text based on analytical results from the M*S prediction method. Included on this figure are the recommended multitube-plus-ejector and multichute/plug nozzles evolved in the course of scale model and engine testing by Boeing and General Electric in the SST Phase II program (References 11 and 18).

The DOT/FAA SST Phase II (Reference 18), the NASA Duct Burning Turbofan (DBTF) Program (Reference 5) and the current program results documented in the Task 3 and 4 reports (References 1 and 6) have provided this data base. Far-field acoustic data, as well as aerodynamic performance data, are included in all the referenced documents. The impact of varying area ratio and element number was parametrically studied both for single-flow and for dual-flow suppressors; core plug geometry, velocity ratio, and weight flow ratio were evaluated for dual-flow suppressors. This parametric testing has shown the following primary trends for single-flow and dual-flow suppressors during static operation:

Single Flow

- Suppression increases with increasing area ratio at high jet velocity.
- Suppression decreases with increasing area ratio at low jet velocity.
- Suppression level is affected by element type (spoke systems suppress slightly better than chutes).

Dual Flow

Suppression increases with increasing area ratio.

31)

- Suppression increases with increasing element number at high jet velocity.
- Suppression level is affected by core plug geometry by 2 to 3 dB.
- Suppression increases 3 to 4 dB when a treated ejector is added to a suppressor configuration.

Work performed on multitube systems (References 2, 11, 18, and 60) can be considered as an outgrowth of the early studies conducted by Boeing for the 707 jet suppressor design. One advantage of a multitube system is that the design can be tailored somewhat to meet the engine-cycle exhaust conditions. If peak suppression is required at a relatively low jet velocity, a small area ratio design is generally needed; however, for higher jet velocities larger ratios are more effective.

The selection of tube number, tube bundle area ratio, tube length, tube spacing (equal/unequal), tube geometry, and shroud geometry (lined/unlined) leading to a viable suppressed exhaust system has been done on an empirical basis. Extensive parametric scale-model testing has been conducted to assure a maximum of variable resolutions, as discussed in detail in Section 4.0 of the text. Scale-model and static-engine tests simulating typical takeoff, cutback, and approach flight velocities were pursued by Boeing in the DOT/FAA SST Phase I and II Follow-On Program (References 11 and 60). Results to date (Reference 11) indicate static suppression levels, with an ejector, of about 15 to 18 PNdB (sideline) accompanied by little or no thrust loss; in some cases the thrust increases (e.g., static thrust augmentation). A summary of some Boeing static suppression and performance loss data is shown on Figure B-4. The impact of forward flight on noise reduction and performance loss is discussed later in this section.

Many aerodynamic-performance tests have been conducted on single- and dual-flow configurations at both static and wind-on conditions. The nominal gross thrust coefficient levels determined for baseline nozzles (References 1, 7, and 18) at an aircraft Mach number of 0.36 are given in Table B-1. Base pressure measurements were taken on several of the suppressor models in order to determine base drag (which is generally responsible for the poor aerodynamic performance of most mechanical suppressors in flight). These wind tunnel tests identified the following primary trends in aerodynamic performance:

- Performance decreases with increasing element number.
- Performance increases with increasing chute depth.
- Performance increases with increasing ratio of inner flow area to outer flow area.
- Performance is affected by element type (chutes perform better than spokes because spokes have higher base drag).

The aforementioned static suppression and static aerodynamic trends are summarized on Figure B-4 for some of the single- and dual-flow multichute (spoke)/plug suppressor systems. In terms of $\Delta PNL/\Delta Cfg$, multitubes and multichutes are



- e 2400-ft Sideline
- 59° F, 70% Relative Humidity
- A_{total} = 338 in, 2
- Static

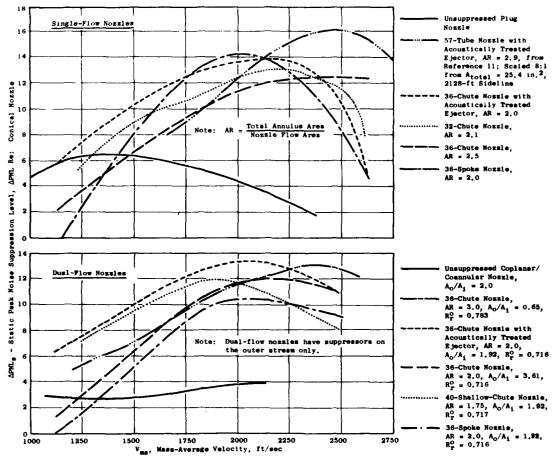


Figure B-5. Typical, Static, Peak PNL Suppression Characteristics.

comparable; however, multitube systems seem to be more effective in absolute noise reduction potential. The Aircraft/Engine Suppressor Integration Case Studies of Appendix K show that aerodynamic performance and noise reduction alone cannot establish the impact of a given engine jet noise suppressor on the aircraft without aeromechanical integration consideration (i.e., size, weight, complexity, reliability, etc.).

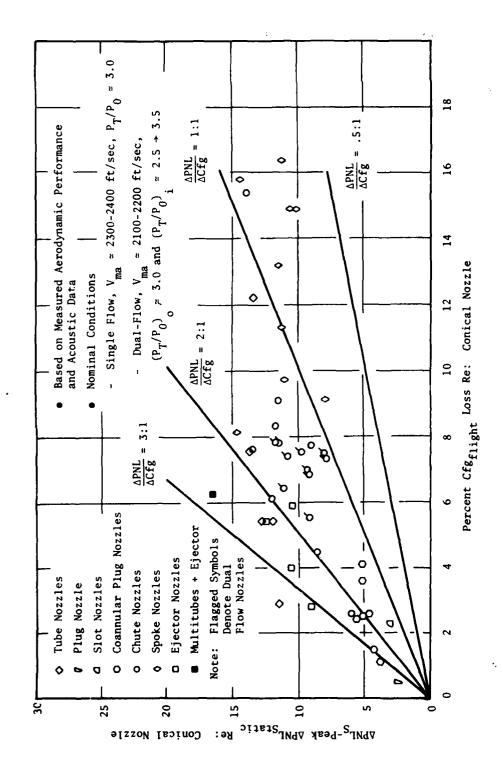
Table B-1. Nominal Gross Thrust Coefficients for Baseline Type Exhausts.

• $M_o \simeq 0.36$ • Applicable for Takeoff/Community Noise				
Type Exhaust Nozzle	Nominal Gross Thrust Coefficient (Cfg)			
• Conical	≃ 0.985			
Annular Plug	≃ 0.981			
• Inverted Flow, Coannular Plug	≃ 0.965			

The static suppression levels are summarized on Figure B-6 as a function of flight thrust coefficient loss. There is a significantly smaller data base compared to the static/static information discussed above.

The results presented on Figure B-6 again show ejectors to be very effective suppressors; however, the suppressor effectiveness ratio has changed significantly from Figure B-4. In flight, ejectors do not exhibit an increase in performance relative to a conical nozzle. The maximum ($\Delta PNL_{static}/\Delta Cfg_{flight}$) ratio achieved was approximately 3. The coannular plug nozzles do not have a significant performance loss in flight relative to a conical nozzle and have a suppressor effectiveness ratio of approximately 2 to 3 with a maximum suppression level of 6 PNdB (References 5 and 7). The chute nozzles have a $\Delta PNL_{static}/\Delta Cfg$ flight ratio between 1 and 2 with a maximum suppression level of 13.5 PNdB. The dualflow suppressor nozzles do not appear to offer any significant advantage over the single-flow configurations. The spoke nozzles, in general, yield peak suppression levels equivalent to chute nozzles; however, an additional 2 to 9% performance loss is incurred due to increases in base drag.

In order to get a better perspective on noise suppression and thrust degradation during static and flight operation, it is necessary to review in some detail the data in Figures B-4 and B-6. The measured, static, suppression levels presented on Figures B-4 and B-6 are nominally at a jet velocity of 2300 to 2400 ft/sec for the single-flow configurations and a mass-averaged velocity of about 2100 to 2200 ft/sec for the dual-flow configurations. The static comparisons in B-4 show that the ejector configurations yield the highest static suppression level and the minimum performance loss. In fact, several



Generalized Flight Performance and Static Suppression Levels. Figure B-6.

of the ejector configurations exhibit a performance increase (i.e., thrust augmentation) due to flow entrainment. Static peak PNL suppression levels better than 20 PNdB have been demonstrated with ejector configurations. Tubetype suppressors without ejectors are second best with $\Delta PNL's$ in excess of 14 dB for select configurations. However, the average static $\Delta PNL/\Delta Cfg$ ratio for this family of suppressors ranges from 3 to 4. The coannular nozzles have a similar suppressor-effectiveness ratio, but the maximum suppression level which may be achieved with this type of configuration is 4 to 6 PNdB. The chutenozzle family is ranked fourth with absolute suppression levels reaching a maximum of 12 to 13 PNdB. The static $\Delta PNL/\Delta Cfg$ ratio ranges from 1 to 5 depending on the configuration being evaluated. The spoke nozzles yield the poorest ratio of suppression to performance, 1 to 2, with a maximum suppression level of 14 dB.

Ejector configurations would seem, based on the data presented thus far, to be the most effective type of suppression device if static performance and suppression are considered the appropriate yardsticks for ranking suppressors. However, the suppressor must function in a flight environment; therefore, the flight suppression level and flight performance level must be established. In-flight information required to establish this relationship is not as abundant as static data. An intermediate step was therefore taken in the preliminary design procedure of Section 3.3 of the text. The suppressor families are compared, where data are available, for static suppression levels and flight performance levels. This comparison is valid only if the static suppression level and flight suppression level are assumed to be equivalent (i.e., flight effects and duration of noise, P -E, are identical for the baseline and suppressor nozzles).

No comparisons of flight suppression levels and flight performance are included since the data base to establish such a relationship is very limited. The Task 3 Report (Reference 1) includes some flight/flight information obtained from free-jet, wind tunnel, high-speed-train, and aircraft test series. The simulated in-flight suppressor test results, reported in Task 5 of this program (Reference 3) and utilized in the case studies shown in Appendix K. provide further insight. Single-flow, plug nozzles are generally the most effective in terms of flight ΔPNL/ΔCfg ratio; however, absolute levels of suppression are quite low (2 to 3 PNdB). The Boeing 56-tube-plus-center-hole-withtreated-ejector suppressor and the General Electric 32-chute/plug suppressor each exhibit suppression levels of approximately 10 PNdB and flight ΔPNL/ΔCfg ratios of about 1.5 to 2.0. The 104-tube-with-treated-shroud suppressor was evaluated on an aircraft and yielded the highest suppression (14 PNdB); however, the aerodynamic performance was poor, and the suppressor effectiveness in terms of flight ΔPNL/ΔCfg was slightly below 1.0. Most of the remaining suppressor flight data which has been compiled suggests that suppressor effectiveness is 0.5 to 1.0 for the flight/flight parameter.

APPENDIX C - EXAMPLES OF PRELIMINARY DESIGN SELECTION METHODS

The following pages present three sample calculations utilizing the procedure outlined in Section 3.3.1 of the text at conditions representative of take-off (sideline) and community flight modes. The examples include:

- Unsuppressed Engine/Baseline Nozzle Conical (Single Flow) Nozzle.
- Suppressed Engine/Single-Flow Nozzle Multichute/Plug Nozzle With Acoustically Treated Ejector
- 3. Suppressed Engine/Dual-Flow Nozzle Multichute/Plug Type in Outer Stream only, Inner Stream Unsuppressed.

EXAMPLE NO. 1: UNSUPPRESSED ENGINE/BASELINE NOZZLE

• Given Conditions

- Estimate/Calculation of Baseline (Unsuppressed) Flight Noise
 - Follows methodology and steps in Section 3.3.1 of the text for a conical nozzle:
 - (1) All parameters available, Figure 3-10 not necessary
 - (2) Calculate single-flow, ideal gross thrust, (Fg) at appropriate V and W_T, i.e. $Fg = \frac{W_T}{g} \times V = \frac{644}{32.2} \times 2195 = \frac{43,900 \text{ lb}}{2}$
 - (3) Estimate of V_{ma} and T_{Tma} not required since it is single flow, i.e., $V_{ma} = V$ and $T_{T} = T_{Tma}$
 - (4) Estimate 10 log $(\rho_{ma}/\rho_{o})^{\omega-1}$
 - Use $V_{ma} = V$ and $T_{T_{ma}} = T_{T}$ from Step (3) and obtain from Figure 3-13: 10 log $(\rho_{ma}/\rho_{o})^{\omega}$; i.e., 10 log $(\rho_{ma}/\rho_{o})^{\omega} = -7.2$ dB

- Use Figure 3-12 to obtain ω at V_{ma} = 2195 ft/sec; i.e., ω = 2 at log (V_{ma}/A_o) = 0.286
- 10 log $(\rho_{\rm ma}/\rho_{\rm o})^{\omega-1}$ is obtained from

[10 log
$$(\rho_{\text{ma}}/\rho_{0})^{\omega}$$
] x $\frac{\omega-1}{\omega}$ = (-7.2) x $\frac{2-1}{2}$ = -3.6 db

- (5) Estimate Normalized Static Peak PNL, NPNL_s, at $R_{ref} = 2128$ ft
 - Utilize Figure 3-14 at V from Step (3) and read NPNL for conical nozzle; i.e.,

 $NPNL_s = 70.6 PNdB$ at $R_{ref} = at 2128 ft$ and $V_{ma} = 2195 ft/sec$

- (6) Estimate Static Peak PNL, PNL_s at R = 1250 ft
 - Calculate PNL_s using Fg from Step (2), NPNL_s from Step (5), actual overhead distance correction using Figure 3-15, and 10 log $(\rho_{\rm ma}/\rho_{\rm o})^{\omega-1}$ from Step (4); i.e.,

$$PNL_s = NPNL_s + 10 \log Fg + \log (\rho_{ma}/\rho_o)^{\omega-1}$$

+ 25 log R/2128 (Figure 3-15 at R = 1250 ft)

=
$$70.6 + 46.4 + (-3.6) + 5.8 = 119.2 \text{ PNdB}$$

- (7) Determination of Flight Peak PNL, PNL_f
 - Correct PNL_S from Step (6) for flight effects using Figure 3-16, i.e.,

Flight Effects (at $V_{ma} = 2195$ ft/sec and $V_{a} = 397$ ft/sec) = 5.4 dB

$$PNL_f = PNL_s - Flight Effects = 119.2 - 5.4 = 113.8 PNdB$$

- (8) Calculate Baseline (Unsuppressed) Flight Noise, EPNL
 - Adjust PNL_f from Step (7) for net [P → E] effects using Figure 3-17; i.e.,

Basic $[P \rightarrow E]$ = 0.7 dB at V_{ma} = 2195 ft/sec, R = 2400 ft and V_a = 400 ft/sec (From Figure 3-17a). Correct basic $[P \rightarrow E]$ for actual overhead distance, R = 1250 ft, and actual V_a = 397 ft/sec using Figures 3-17b and 3-17c or:

$$\Delta(P \rightarrow E)_R = -2.8 \text{ dB}$$

$$\Delta(P \rightarrow E)_{V_a} \simeq 0$$

Net
$$[P \rightarrow E]$$
 = Basic $[P \rightarrow E]$ + $\Delta[P \rightarrow E]_R$ + $\Delta[P \rightarrow E]_{Va}$
= (-0.7) + (-2.8) + 0 = -3.5 db
EPNL = PNL_f = Net $[P \rightarrow E]$ = $\underline{110.3}$ EPNdB

The system baseline flight noise EPNL can be corrected for any or all of the aircraft engine factors discussed after Step (8) in Section 4.3.1 of the text.

EXAMPLE NO. 2: SUPPRESSED ENGINE/SINGLE-FLOW NOZZLE

- Given Conditions: Same as Example No. 1
- Follows Methodology and Steps in Section 3.3.1 of the text for a Suppressed, Single-Flow Nozzle
- Suppressor type: Multichute/Plug Nozzle with Treated Ejector
 - (1) Determination of Required Static Noise Reduction, PNL $_{\rm S}$ and Suppressor Flight Performance, Cfg $_{\rm f}$

Assuming that the noise goal established prior to calculation would require from 12 to 15 PNdB of suppression, Figure 3-19 can be used to obtain suppressor type and accompanying flight performance loss; i.e.,

- From Figure 3-19, a bare chute plug suppressor can provide $\simeq 13$ PNdB static noise reduction, ΔPNL_s , for a flight Cfg loss $\simeq 6.2\%$. Since actual flow conditions (i.e., $V_{\text{ma}} = 2195$ ft/sec, $P_{\text{T}}/P_0 = 2.71$) are different from nominal conditions stated on Figure 3-19, Cfg loss must be corrected using the single-flow, multichute-derived curve on Figure 3-20 at $P_{\text{T}}/P_0 = 2.71$ or $\Delta \text{Cfg}_p = -0.009$. Moreover, since static suppression is still somewhat low, a treated ejector will be included (because it can provide, based on entering at V = V = 2195 ft/sec for single-flow multichute/plug systems curve in Figure 3-25, an additional 2.3 PNdB of noise reduction with accompanying Cfg loss decrement at $P_{\text{T}}/P_0 = 2.71$ from Figure 3-21 or $\Delta \text{Cfg}_E = -0.010$).
- Suppressor (multichute/plug + ejector nozzle) Cfg loss is obtained from:

 $(Cfg_f)_{Suppressor} = (Cfg_f)_{Baseline} [1 - Cfg loss] + \Delta Cfg_A$

where

(Cfgf)_Baseline = 0.985, from Table 3-2 for conical nozzle, Cfg loss = 0.062, from Figure 3-19 as described above, and Δ CfgA = Sum of additional suppressor Cfg adjustments for P_T/P_0 and ejector effects:



 $\Delta Cfg_p + \Delta Cfg_E = -0.009$ (From Figure 3-20) - 0.010 (From Figure 3-21) = -0.019

or

 $(Cfg_f)_{Suppressor} = 0.985 (1 - 0.062) - 0.019 = 0.924 - 0.019 = 0.905$

- (2) Find Scale Factor (S.F.) to Compensate Baseline Engine For Suppression System Loss
 - Following methodology of Figure 3-9 and Figure 3-23 at appropriate V_{ma} , flight Cfg, and V_{a} estimate S.F.; i.e.,

S.F. =
$$\Psi_{\text{Baseline}}/\Psi_{\text{Suppressor}} = \frac{\text{(Weight Flow) Suppressor}}{\text{(Weight Flow) Baseline}}$$

where $\Psi_{Baseline}$ = 1750 ft/sec (From Figure 3-23 at Baseline Cfg_f = 0.985) and $\Psi_{Suppressor}$ = 1600 ft/sec (From Figure 3-23 at Suppressor System Cfg_f = 0.905), or :

$$S.F. = \frac{1750}{1600} = 1.094$$

- As a matter of interest, the unsuppressed/suppressed engine (or upsized baseline) would be increased to 1.094 x 644 = 704.5 lb/sec.
- (3) The Unsuppressed/Suppressed Flight Noise, ${\tt EPNL_{U/S}}$
 - Upsized baseline flight noise, EPNL_{U/S}, is estimated from Example No. 1 flight noise (Step 8) and above scale factor (Step 2); i.e.,

$$EPNL_{U/S} = EPNL + log S.F.$$

where EPNL = 110.3 EPNdB (Example No. 1, Step 8) and S.F. = 1.094 (Step 2)

or

$$EPNL_{U/S} = 110.3 + 0.4 = 110.7 EPNdB$$

- (4) Calculate Interim Suppressed Flight Noise, $EPNL_{I/S}$
 - Interim suppressed EPNL, EPNL_{I/S}, is calculated using the upsized baseline EPNL, EPNL_{U/S} (from Step 3); the baresuppressor ΔPNL, ΔPNL (from Step 1); the ejector suppression benefit, Δ(Ejector) from Step 1; and then correcting ΔPNL_S [which is at the nominal (2300-2400 ft/sec) rather than actual velocity (2195 ft/sec)] by the dropoff characteristics of a suppressor shown on Figure 3-24 at appropriate velocity ratio and ΔPNL_{Peak} (equal to ΔPNL_S = 13 PNdB); i.e., 203

$$EPNL_{I/S} = EPNL_{U/S} - \Delta PNL_{s} + \Delta \left(\frac{V_{ma}}{V_{ma} \text{ at } \Delta PNL_{Peak}} \right) - \Delta (Ejector)$$

where EPNL U/S = 110.7 EPNdB (Step 3),
$$\Delta$$
PNL = 13.0 PNdB (Step 1), and $\Delta \left(\frac{V_{ma}}{V_{ma} \text{ at } \Delta PNL_{Peak}} \right) = + 0.6 \text{ PNdB}$ at $\left(\frac{V_{ma}}{V_{ma} \text{ at } \Delta PNL_{Peak}} \right) = \frac{2195}{2350} = 0.93$

From
$$\Delta PNL_{Peak} = 13.0 \text{ PNdB on Figure 3-24:}$$

$$\Delta$$
(Ejector) = 2.3 PNdB at V_{ma} = 2195 ft/sec

or (Figure 3-25 and Step 1):

$$EPNL_{I/S} = 110.7 - (13.0) + (0.6) - (2.3) = 110.7 - 14.7$$

= 96.0 EPNdB

- (5) Determine Δ [Flight Effects] and Δ [Basic (P \rightarrow E)] Corrections for Suppressor System
 - Estimate Δ [F.E.] of suppressor system relative to the conical baseline from Figure 3-28, and Δ [Basic (P \rightarrow E)] via Figure 3-29; i.e.,

$$\Delta$$
[F.E.] = 2.7 dB at V_{ma} = 2195 ft/sec and V_{a} = 397 ft/sec (Figure 3-28)

$$\Delta[Basic (P \rightarrow E)] = + 0.2 dB at V_{ma} = 2195 ft/sec$$
 (Figure 3-29)

 $\Delta[Basic\ (P \rightarrow E)]$ need not be corrected for actual V and overhead distance, R, since this has been already included in the baseline (unsuppressed) flight noise, EPNL, in Step 8 of Example No. 1.

- (6) Determine Suppressed (Multichute/Plug Plus Treated Ejector) Flight Noise, EPNL
 - Adjust EPNL $_{1/S}$ from Step 4 using Δ [F.E.] and a Δ [Basic (P + E)] from Step 5; i.e.,

EPNL_S = EPNL_{I/S} +
$$\Delta$$
[F.E.] + Δ [Basic (P + E)]
= 96.0 (Step 4) + 2.7 (Step 5)

=
$$98.9 \text{ EPNdB}$$
 at 1250 and V_a = 397 ft/sec

As was the case in Example No. 1, the system suppressed flight noise can now be obtained by appropriate aircraft/engine corrections (Figure 3-9).

EXAMPLE NO. 3: SUPPRESSED ENGINE/DUAL-FLOW NOZZLE

• Given:
$$V_o$$
 = 2569 ft/sec V_i = 1663 ft/sec T_{T_O} = 1926° R T_{T_i} = 828° R Pr_o = 3.14 Pr_i 3.12 Pr_i 3.12 Pr_i 3.12 Pr_i 222.2; Pr_i = 900.2 lb/sec Pr_i = 2400 ft Overhead Distance, Pr_i = 341 ft/sec

- Estimate/Calculate of Suppressed Flight Noise
 - Follows methodology and steps in Section 3.3.1 of the text for a dual-flow, suppressor-in-outer-stream nozzle.
 - Since all acoustic and performance figures and charts are relative to a conical nozzle at the mass-averaged conditions of the dual-flow nozzle, the procedure will include both baseline (mass-averaged conical) and suppressed dual-flow noise determinations.
 - (1) Estimate V_{ma} from Figure 3-11; i.e., calculate
 - $W_o/W_i = \frac{678.0}{222.2} = 3.05$ and read at appropriate V_o and V_i ... $V_{ma} = 2350$ ft/sec
 - (2) Estimate ${\rm T_{T_{ma}}}$ also from Figure 3-11 at appropriate ${\rm W_{o}/W_{i}}$, ${\rm T_{T_{o}}}$ and ${\rm T_{T_{i}}}$
 - $T_{T_{ma}} = 1650^{\circ} R$
 - (3) Estimate 10 log $(\rho_{ma}/\rho_{o})^{\omega}$ from Figure 3-13
 - 10 log $(\rho_{ma}/\rho_o)^{\omega}$ = -7.4 dB, using V_{ma} = 2350 ft/sec (Step 1) and T_{Tma} = 1650° R (Step 2)
 - (4) Estimate ω From Figure 3-12
 - At log V_{ma}/A_0 for $V_{ma} = 2350$ ft/sec, $\omega = 2$
 - (5) Calculate 10 log $(\rho_{\text{ma}}/\rho_{\text{o}})^{\omega-1}$ from (3) and (4)

10 log
$$(\rho_{ma}/\rho_{o})^{\omega-1}$$
 = [10 log $(\rho_{ma}/\rho_{o})^{\omega}] \frac{\omega-1}{\omega}$
= (-7.4) x $\frac{2-1}{2}$ = -3.7 dB

- (6) Dual-Flow Gross Thrust (Fg)
 - Read $V_i + V_0$ (W_i) from Figure 3-11 at appropriate V_0 , V_i , W_0/W_i conditions; i.e.,
 - = 9500 ft/sec
 - Then Fg is simply

=
$$W_i/g [V_i + V_o (W_o/W_i)] = 65,556 lb$$

- (7) Estimate Normalized Static PNL, NPNL_s at R_{ref} = 2128 ft
 - Utilize Figure 3-14 at V from Step (1) and read NPNL for conical nozzle; i.e.,

$$NPNL_s = 72.0 PNdB$$
 at $R_{ref} = 2128 ft$ and $V_{ma} = 2350 ft/sec$

- (8) Estimate Static Peak PNL, PNL_s at R = 2400 ft
 - Calculate PNL using Fg from Step (6), NPNL from Step (7), actual overhead distance correction using Figure 3-15, and 10 log $(\rho_{ma}/\rho_{o})^{\omega-1}$ from Step (5); i.e.,

$$PNL_s = NPNL_s + log Fg + 10 log (\rho_{ma}/\rho_o)^{\omega-1} + 25 log R/2128$$

= 72.0 + 48.2 - 3.7 - 1.3 = 115.2 PNdB

- (9) Determination of Flight PNL, PNL
 - Correct PNL_s from Step (8) for flight effects using Figure 3-16; i.e.,

F.E. [at
$$V_{ma} = 2350 \text{ ft/sec}$$
 and $V_{a} = 341 \text{ ft/sec}$] = 4.4 dB

...
$$PNL_f = PNL_s - F.E. = 110.8 PNdB$$

- (10) Calculate Baseline (Unsuppressed) Flight Noise, EPNL
 - Adjust PNL_f from Step (9) for Net $[P \rightarrow E]$ effects using Figure 3-17; i.e.,

Basic [P \rightarrow E] = -0.8 at V = 2350 ft/sec, R = 2400 ft and V = 400 ft/sec (from Figure 3-17a)

Correct basic $[P \rightarrow E]$ for actual overhead distance, R = 2400 ft, and actual $V_a = 341$ ft/sec using Figures 3-17b and 3-17c.

$$\Delta(P \to E)_{R} = 0$$

$$\Delta(P \to E)V_{a} = +0.7 \text{ dB}$$

$$Net [P \to E] = Basic [P \to E] + \Delta[P \to E]_{R} + \Delta[P \to E]_{V_{a}}$$

$$= -0.8 + 0 + 0.7 = -0.1 \text{ dB}$$

$$\therefore EPNL = PNL_{c} + Net [P \to E] = 110.7 EPNdB$$

- (11) Static Noise Reduction, ΔPNL_s , and Suppressor Flight Performance, Cig_f Definition
 - Assuming that a static suppression, ΔPNL_s , of about 8.0 PNdB is adequate, Figure 3-19 can be utilized to obtain the Cfg loss in flight for a partial-span/chute type suppressor. From Figure 3-19 at $\Delta PNL_s \approx 8.0$, a conservatively high flight Cfg loss of 8.2% is estimated. Since flow conditions (i.e., $V_s = 2350 \text{ ft/sec}$, $(P_T/P_0)_o \approx (P_T/P_0)_i \approx 3.14 \approx 3.12$) are different from nominal conditions stated on Figure 3-19, Cfg loss must be corrected using the dual-flow curve of Figure 3-20 for

 $(P_T/P_0)_0 \simeq 3.14$ or $\Delta Cfg_p = +0.001$ (Increase in Performance)

Dual-flow suppressor (chute type) Cfg loss is obtained from:

 (Cfg_f) Suppressor = (Cfg_f) Baseline [1-Cfg Loss] + ΔCf_g

where (Cfg_f) = 0.985, from Table 3-2 for conical baseline nozzle Cf_g Loss = 0.082, from Figure 3-19 as described above, and Δ Cf_{gA} = Sum of additional suppressor Cf_g adjustments for pressure ratio and ejector (if applicable) effects:

 $\Delta Cf_g + \Delta Cfg_E = +0.001 + 0$ (No Ejector) = +0.001

or

$$(Cf_g)_{Suppressor} = 0.985 [1 - 0.082] + 0.001$$

= 0.904 + 0.001 = 0.905

- (12) Estimate Scale Factor (S.F.) to Compensate Baseline Engine for Suppressor System Loss
 - Following methodology of Figure 3-9 and Figure 3-23 at appropriate V_{ma} , flight Cf_g , and V_a , estimate S.F.; i.e.,

S.F. =
$$\Psi_{\text{Baseline}}/\omega_{\text{Suppressor}} = \frac{\text{(Weight Flow) Suppressor}}{\text{(Weight Flow) Baseline}}$$

where
$$\Psi_{\text{Baseline}} = 1980 \text{ ft/sec}$$
 $\frac{\text{From Figure } 3-23}{\text{at } \text{Cfg}_{\text{f}} = 0.985}$ at Baseline and $\Psi_{\text{Suppressor}} = 1800 \text{ ft/sec}$ $\frac{\text{From Figure } 3-23}{\text{at } \text{Cg}_{\text{f}} = 0.905}$ at Suppressor

or S.F. =
$$\frac{1980}{1800}$$
 = 1.100

- As a matter of interest, the unsuppressed/suppressed engine (or upsized baseline) would be increased to 1.100 x 900.2 = 990.2 lb/sec.
- (13) Determination of Unsuppressed/Suppressed Flight Noise, $EPNL_{U/S}$
 - Upsized baseline flight noise, $EPNL_{U/S}$, is estimated from Step (10) and the above scale factor, Step (12); i.e.,

$$EPNL_{U/S} = EPNL + 10 \log S.F.$$

or

$$EPNL_{U/S} = 110.7 + 0.4 = 111.1 EPNdB$$

- (14) Calculate Interim Suppressed Flight Noise, EPNLI/S
 - Interim suppressed EPNL, EPNL_{I/S}, is calculated using EPNL_{U/S} from Step (13), the basic suppressor Δ PNL, Δ PNL_S from Step (11), and then correcting Δ PNL_S (which is at the nominal, 2100-2200 ft/sec, rather than actual velocity, 2350 ft/sec), by the dropoff characteristics of a suppressor shown on Figure 3-24 at the appropriate velocity ratio at appropriate Δ PNL_{Peak} (equal to Δ PNL_S = 8 PNdB); i.e.,

$$EPNL_{I/S} = EPNL_{U/S} - \Delta PNL_{s} + \Delta \left(\frac{V_{ma}}{V_{ma} \text{ at } \Delta PNL_{Peak}} \right)$$

where

$$EPNL_{U/S} = 111.1 EPNdB (Step 13)$$

$$\Delta PNL_{s} = 8.0 \text{ PNdB (Step 11)}$$

$$\Delta \left(\frac{V_{ma}}{V_{ma} \text{ at } \Delta PNL_{Peak}} \right) = +0.1 \text{ PNdB at}$$

$$\frac{V_{\text{ma}}}{V_{\text{ma}} \text{ at } \Delta PNL_{\text{Peak}}} = \frac{2350}{2150} = 1.093 \text{ and}$$

From $\Delta PNL_{g} \simeq 8.0$ PNdB on Figure 3-24

or

$$EPNL_{I/S} = 111.1 - 8.0 + 0.1$$

= 111.1 - 7.9 = 103.2 EPNdB

- (15) Determine Δ [Flight Effects] and Δ [Basic (P \rightarrow E)] Corrections for Suppressor System
 - Estimate Δ [Flight Effects] of suppressor Re: conical nozzle from the table in Step (13) of Section 3.1.2 and Δ [Basic (P-E)] via Figure 3-29.
 - Δ [F.E.] = 2.0 dB at V_{ma} = 2350 ft/sec and V_a = 341 ft/sec from Tabulation in Step (13) of Section 3.1.2.
 - $\Delta [Basic~(P \rightarrow E)]$ = 2.35 \simeq 2.4 dB at V = 2350 ft/sec and V = 400 ft/sec, R = 2400 ft, Figure 3-29

 $\Delta[Basic\ (P \to E)]$ need not be corrected for actual V and overhead distance, R, since this is already included in the baseline (unsuppressed) flight noise, EPNL, in Step (10).

- (16) Determine Suppressed (Partial-Span, Multichute/Plug) Flight Noise, EPNLs
 - Adjust EPNL_{I/S} from Step (14) using Δ [F.E.) and Δ [Basic (P \rightarrow E)] from Step (15); i.e.,

EPNL_s = EPNL_{I/S} +
$$\Delta$$
[F.E.) + Δ [Basic (P + E)]
= 103.2 + 2.0 + 2.4 = 107.6 EPNdB

As was done in Example No. 1, the suppressed flight noise can now be obtained by appropriate aircraft/engine corrections (Figure 3-9).

APPENDIX D - EFFECT OF SIMULATED FLIGHT UPON NOISE FROM HIGH VELOCITY JET NOZZLES

A prediction method for estimating the noise from conical and suppressor nozzles under conditions of simulated flight is derived within this Appendix and shown to be valid within ± 3.5 PNdB at the angle of maximum perceived noise level and with ± 3.2 EPNdB for 95% confidence limits.

The prediction method is an extension of the M*S (Motsinger*Sieckman) engineering correlation procedure described in Reference 12 for predicting jet noise from conical and suppressor nozzles when operated statically and without ancillary flow to induce relative velocity effects. The extension is based upon data from free-jet testing conducted in the JENOTS and Cell 41 facilities (Reference 62 and 63) on two conical nozzles; two multielement suppressors, one a multitube and the other a multichute, both for a single-flow turbojet cycle; and two multichute suppressors on the higher velocity stream of an inverted-flow turbofan cycle. The free-jet data used in the correlation were transformed by Mani's method (Reference 6) including a modification that reduces the turbulence-absorption correction from the previously used maximum of 6 dB down to 3 dB (Reference 3).

Data for a conical nozzle and a 104-tube, multielement nozzle from the moving-reference-frame Aerotrain tests (Reference 6) are shown to fall within the 95% confidence limits of the transformed free-jet prediction method documented in this Appendix.

CORRELATION METHOD AND DATA BASE

The M*S engineering correlation model is based upon the fact that noise from suppressor nozzles originates from three primary sources: (1) the premerged flow regime, that region of the jet in which the flow from individual elements of a multielement nozzle is clearly identifiable as discrete elements; (2) the postmerged flow regime, that region of the jet where the flow from individual elements from multielement nozzles has merged into one overall stream; and (3) the supersonic flow regime containing shock cells caused by improper expansion of flow from nozzles having supercritical pressure ratios. For each of these sources, the free-jet data indicate that the effects of relative velocity are independent of frequency, when no Doppler shift is present, to a good approximation, and this was assumed to be the case in this correlation.

The noise from the premerged regime is high frequency, generated relatively close to the nozzle (because of the relatively small scale of the individual elements from the multielement nozzle), and the data show it to be essentially unaffected by relative velocity effects upon generation levels; therefore, the high-frequency, premerged noise is treated as one entity in the correlation. The noise from the postmerged regime is low frequency, generated

relatively far from the nozzle after the individual flows have had sufficient length to merge and to mix with ambient air so as to assume a flow profile quite like that from a large conical nozzle, and the data show it to be significantly reduced in level by relative velocity affects. This low-frequency noise is therefore treated as a second, separate entity in the correlation. The noise from the shock cells is also considered to be affected only in level, retaining the same spectral distribution.

The data base used for developing the correlation is summarized in Table D-1 showing the nozzle type, the reference describing the test, the facility used in the test, and a summary description of the nozzle. The thermodynamic conditions of the test points (identified on the Figures in the following Section) are defined in Table D-2.

DEVELOPMENT OF THE CORRELATION

Conical Jets and Merged Flow Region of Multielement Suppressor Nozzles

The postmerged mixing noise of a suppressor nozzle is like that from a conical nozzle and will be affected by flight in the same way. The velocity of the postmerged jet used in this correlation was calculated by the M*S model (Section 3.2.2.5 of Reference 12), assuming no change due to flight. The data were plotted (overall directivity and spectra) with Doppler shift removed. Data were only used in the frequency range where it was fairly certain that only the source of concern was significant (Figure D-1). Due to dominant contamination of overall levels by other sources (Figure D-1), it was felt that an average, constant delta over the uncontaminated frequency range would be more accurate than an attempt to determine an OASPL delta from data using a prediction to remove contamination. The SPL deltas (within ±0.5 dB) from static to flight were determined for each nozzle.

The deltas are plotted against $\log_{10}(V_j/VR)$ for each angle after being normalized by $10~\log_{10}(1$ - Mp $\cos\,\theta_1)$. The results are given in Figures D-2 through D-13. The data collapse is, in general, within ± 2.5 dB for the six nozzles over a jet velocity range of 1200 to 2600 ft/sec and a flight velocity range of 140 to 400 ft/sec. Mean lines through the data, fitted through the origin, are shown on the figures. The slope of the line is the exponent (m) in the equation:

$$OASPL_{Static} - OASPL_{Flight} = 10 \log_{10}(v_j/v_R)^{m/10} (1 - Mp \cos \theta_i)$$

These exponents in terms of relative velocity indices $[m/10 = m(\theta_1)]$ are tabulated in Table D-3. The indices are applicable both to suppressor postmerged mixing noise and to conical nozzle mixing noise.

Since this delta represents the "un-Doppler shifted" case, a Doppler shift must be applied to the flight spectrum as required.

Table D-1. Data Base Used in Flight-Effects Correlation.

Nozzle Type	Model Number	Reference	Test Facility	Model Description
Conical	5 }	Unpublished Data	Cell 41	5-in. Dia. Throat
	47	12	JENOTS	4-in. Dia. Throat (Aerotrain Model)
Single-Flow	77 (12	JENOTS	104-Tube, AR = 2.8, Elliptical Tubes
Suppressor	21	m	Cell 41	32-Deep-Chute, AR = 2.1
Dual-Flow	52	m	Cell 41	40 -Shallow-Chute, $AR_s = 1.75$,
ouppressor	6 53	က	Cell 41	36-Chute, AR ₈ = 2.0, AR _N = 3.607
Conical		ø	Aerotrain	J85 Size Version of Model 47 $(A_8 = 110 \text{ in.}^2)$
Single-Flow Suppressor		9	Aerotrain	J85 Size Version of Model 44 $(A_8 = 110 \text{ in.}^2)$

Table D-2. Cycle Conditions.

		1	nner Fl	ow	0	uter Fl	ow
Configuration	Test Point	P _T /P ₀	T _T	V (ft/sec)	P _T /P _O	T _T	V (ft/sec)
	6				3.83	1738	2597
40-Shallow-Chute Dual-Flow Suppressor Nozzle, Model 52	16	1.50	1454	1381	4.04	1690	2605
	20	1.53	1141	1247	3.79	1702	2558
	21	1.57	1002	1202	1.76	825	1215
	22	1.55	1005	1198	2.09	994	1504
	31	2.51	859	1546	3.22	1668	2400
	32	2.93	830	1631	3.56	1708	2510
	34	2.68	840	1573	2.67	1796	2248
	35	2.53	764	1462	2.18	1498	1914
	36	2.49	783	1469	1.94	1374	1692
	6				3.74	1751	2609
	11	2.24	619	1240	3.32	1629	2397
36-Chute, Dual-Flow Suppressor Nozzle, Model 53	16	1.49	1478	1390	4.01	1730	2620
	18	1.53	1226	1303	2.25	1071	1633
	21	1.54	992	1182	1.75	825	1208
	30	2.52	851	1540	2.40	1735	2158
	32	3.11	832	1662	3.62	1753	2564
	35	2.54	766	1467	2.23	1510	1930
	42	1.99	841	1344	3.02	706	1514
	43	1.50	882	1069	3.02	1702	2369

Configuration	PT8/P0	T _{T8}	V ₈ (ft/sec)	V ₀ (ft/sec)
Aerotrain Conital Nozzle	1.99	1578	1852	0
	2.47	1837	2253	0
	1.98	1574	1839	132
	2.40	1813	2222	138
	1.96	1559	1851	278
	2.35	1744	2148	271
Aerotrain 104-Tube Suppressor Nozzle	1.95	1538	1800	0
	2.32	1786	2160	0
	1.93	1570	1810	136
	2.32	1771	2148	136
	1.95	1528	1795	264
	2.36	1777	2173	265

Configuration	Test Point	P _{T8} /P ₀	^T T8 (* R)	V ₈ (ft/sec)
4-in. Conical Nozzle, Model 47	12	2.55	1693	2197
	30	2.28	1693	2079
	31	2.47	1003	1658
	32	3.00	999	1800
	33	3.51	1001	1904
	34	3.50	1407	1981
	35	2.99	1411	2145
	36	3.49	1387	2245
	37	2.39	1799	2198
	38	3.14	1692	2396
	39	3.43	1708	2486
5-in. Conical Nozzle,	1	2.74	1690	2270
	4	2.51	1676	2171
	7	2.17	1075	1606
	10	2.95	1730	2368
Model 5	13	3.16	1702	2411
	16	. 81	1676	2546
	19	1.52	1093	1219
	9	3.26	1608	2367
	11	1.94	1506	1772
	12	2.55	1681	2190
	13	4.05	694	1658
104-Tube Suppressor Nozzle, Hodel 44	14	3.44	753	1642
	15	2.42	1041	1673
	16	2.00	1257	1649
	17	1.75	1479	1629
	18	1.67	1650	1647
	20	1.75	1642	1718
32-Deep-Chute Suppressor Nozzle, Model 51	2	3.04	1480	2210
	7	4.02	1740	2632
	9	2.62	695	1415
	10	3,22	735	1585
	11	3,18	1745	2443
	12	2.77	1750	2322
	13	2.41	1714	2153
	16	1.76	824	1214
	17	2.26	1524	1959
	20	2.03	1374	1745

Table D-3. Tabulation of Jet-Mixing Noise Relative Velocity Indices.

$DASPL_{Static} - OASPL_{Flight} = 10 \log_{10} \left[\left(\frac{V_{j}}{VR} \right)^{m(\theta_{j})} (1^{i} - M_{p} \cos \theta_{j}) \right], \text{ where } m(\theta_{j}) = m/1$			
Acoustic Angle From Inlet (θ _i)	Index "m(\theta_{1})"		
20°	0.7*		
30°	1.0*		
40°	1.25		
50°	1.8		
60°	2.35		
70°	2.7		
80°	3.4		
90°	4.2		
100°	5.0		
110°	5.5		
120°	5.2		
130°	4.9		
140°	4.5		
150°	3.8		
160°	2.8*		

*Extrapolated

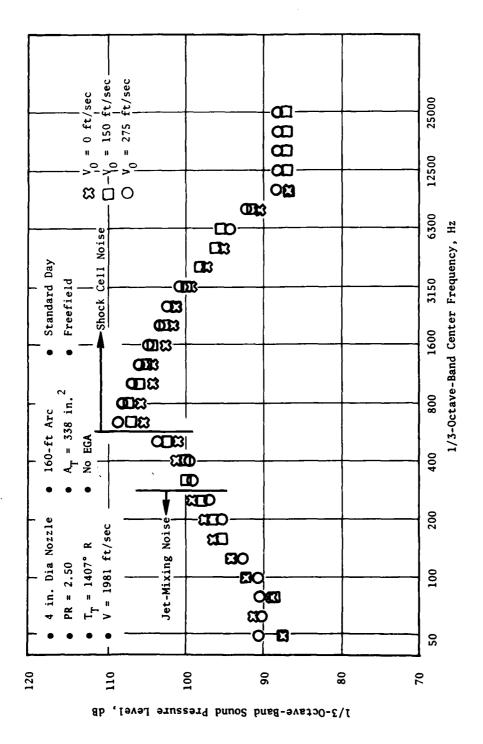


Figure D-1. Conical Nozzle Spectra at $\theta_1 = 60^{\circ}$.

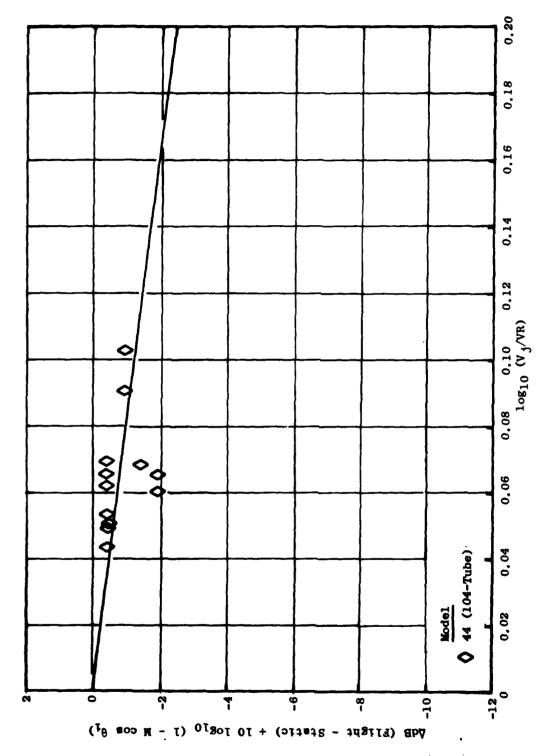
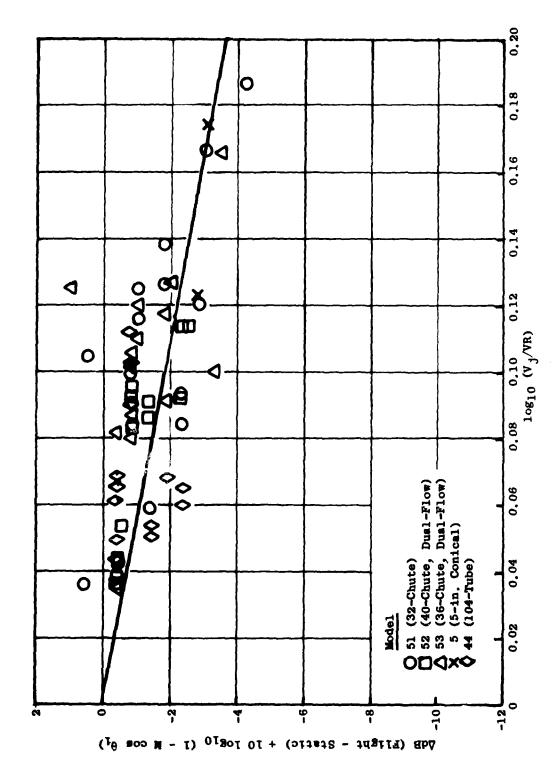


Figure D-2. Free-Jet Flight Effects on Low-Frequency Jet-Mixing Noise, θ_1 = 40°.

では、大学の大学の大学では、



 $= 50^{\circ}$. Figure D-3. Free-Jet Flight Effects on Low-Frequency Jet-Mixing Noise, $heta_1$

11/1

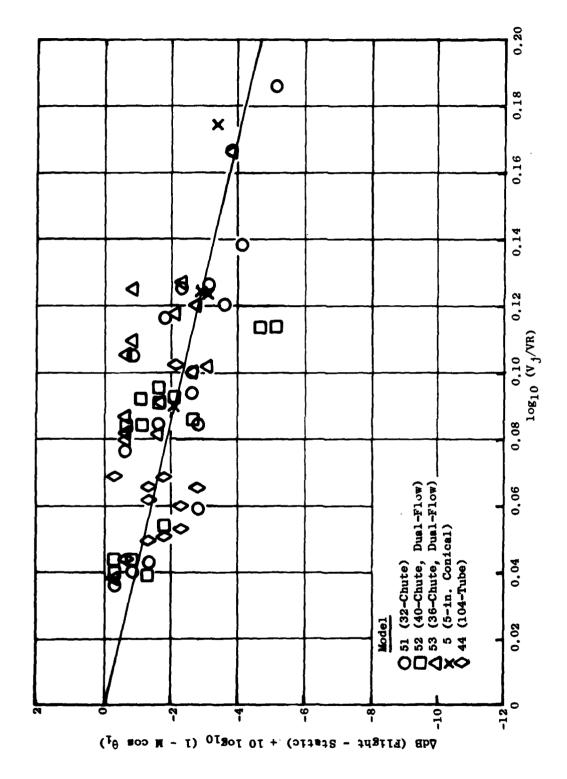
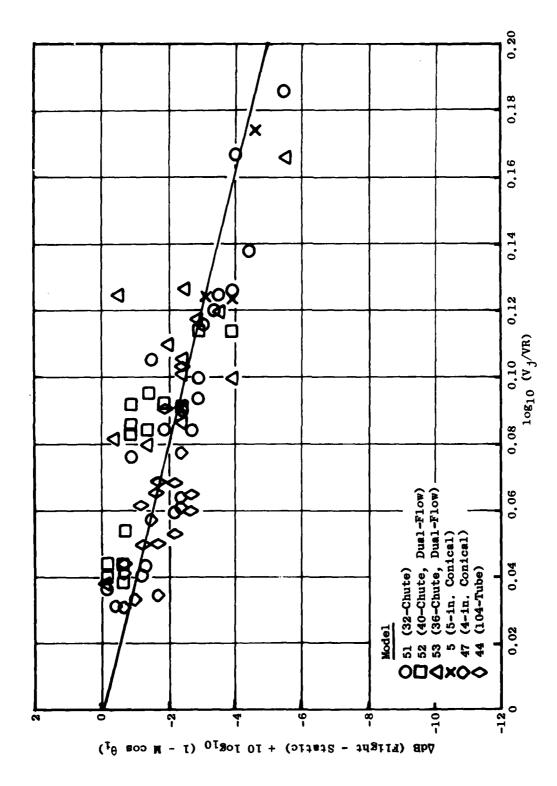


Figure D-4. Free-Jet Flight Effects on Low-Frequency . - -Mixing Noise, θ_1 = 60°.



Free-Jet Flight Effects on Low-Frequency Jet-Mixing Noise, θ_1 = 70°. Figure D-5.

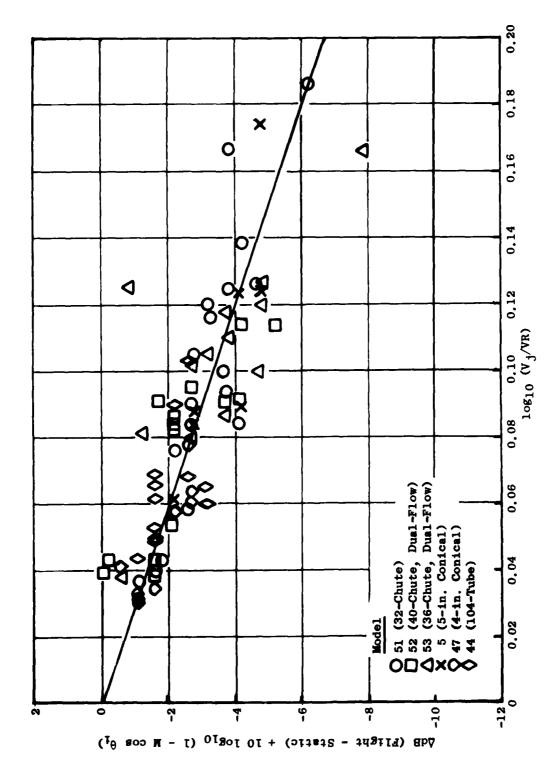
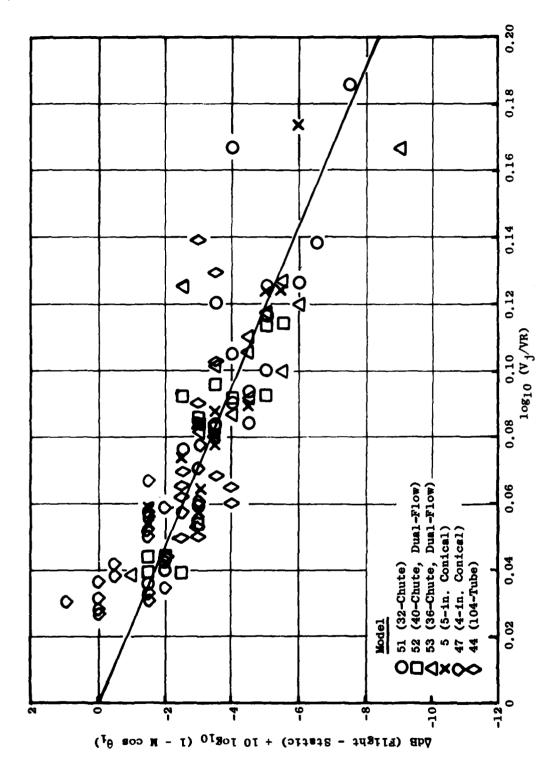


Figure D-6. Free-Jet Flight Effects on Low-Frequency Jet-Mixing Noise, θ_1 = 80°.



°06 = Figure D-7. Free-Jet Flight Effects on Low-Frequency Jet-Mixing Noise, $heta_{f i}$

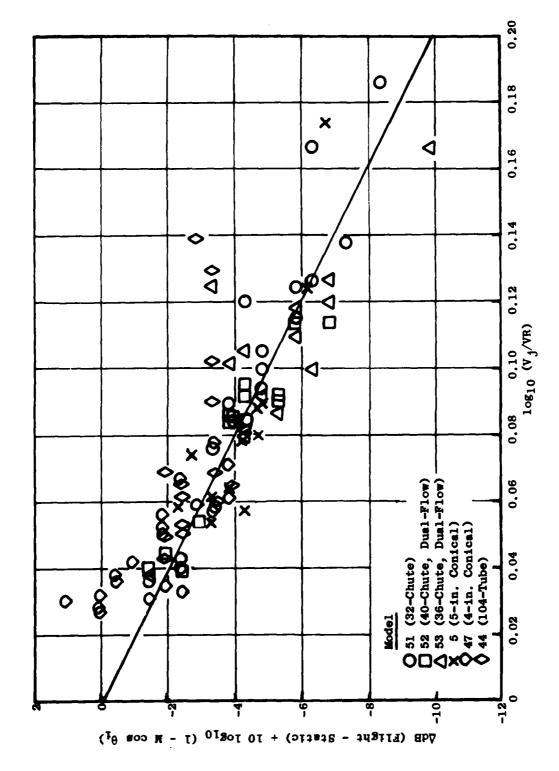


Figure D-8. Free-Jet Flight Effects on Low-Frequency Jet-Mixing Noise, θ_{1} = 100°.

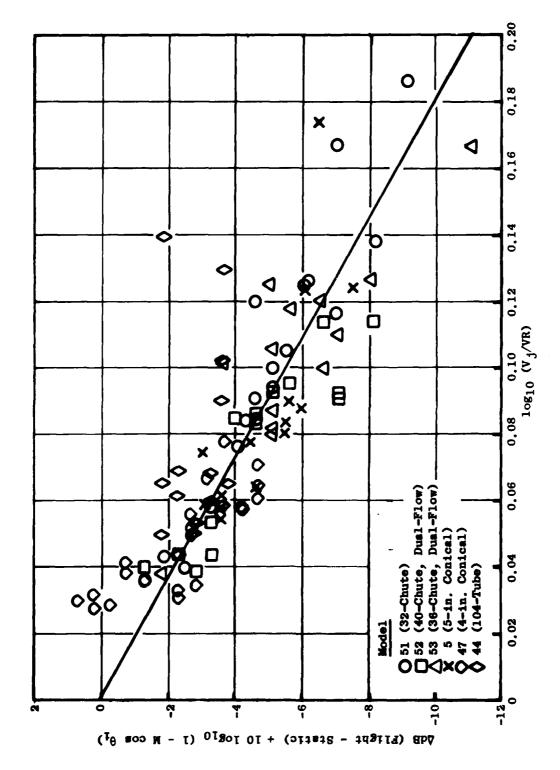


Figure D-9. Free-Jet Flight Effects on Low-Frequency Jet-Mixing Noise, θ_1 = 110°.

(247)

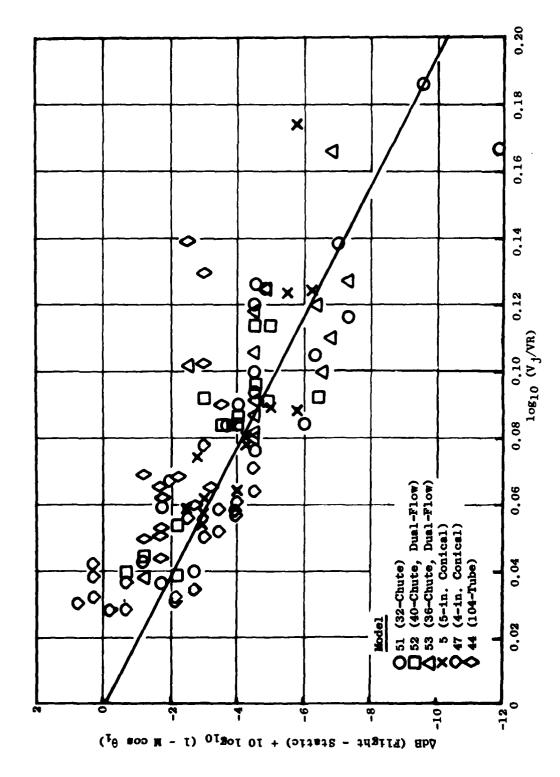


Figure D-10. Free-Jet Flight Effects on Low-Frequency Jet-Mixing Noise, θ_1 = 120°.



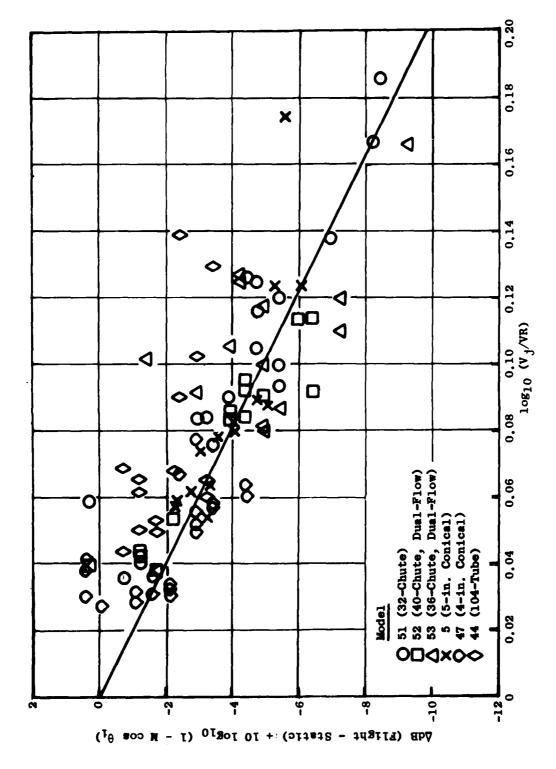


Figure D-11. Free-Jet Flight Effects on Low-Frequency Jet-Mixing Noise, θ_1 = 130°.

(119)

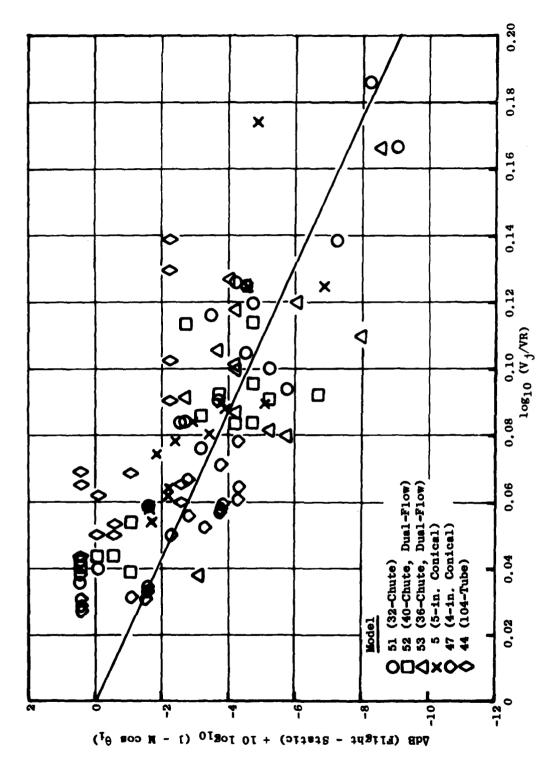


Figure D-12. Free-Jet Flight Effects on Low-Frequency Jet-Mixing Noise, $^{\theta}{}_{i}$



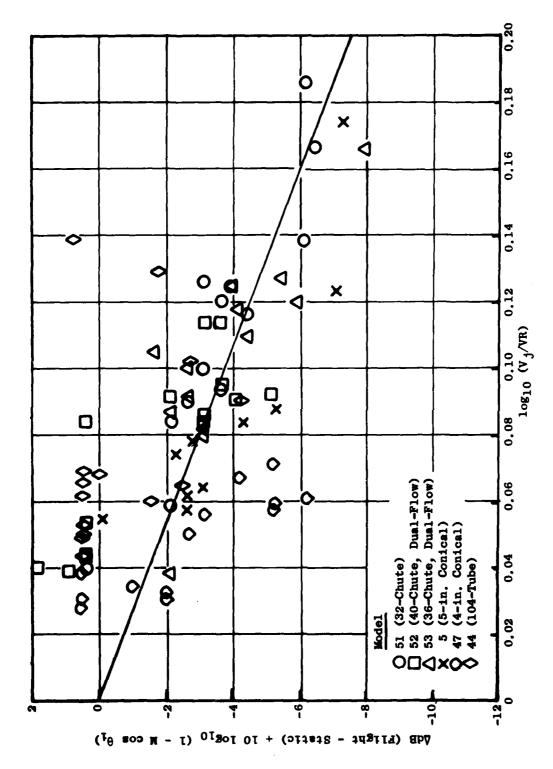


Figure D-13. Free-Jet Flight Effects on Low-Frequency Jet-Mixing Noise, θ_1 = 150°.



Premerged Flow Region

The same suppressor data used in the postmerged flight effects correlation are used to determine the premerged effects. The postmerged noise component in the premerged frequency range was determined based on the M*S prediction, and only uncontaminated data (at least 10 dB higher than the postmerged prediction) were used in determining deltas. Here, however, it is very difficult to separate the premerged mixing noise from possible shocknoise contamination. Nevertheless, deltas between static and flight were determined and tabulated.

Because no known correlation was available for the flight effects on this specific noise source, the deltas were plotted various ways so trends might be identified. It is evident that no trends with jet velocity, pressure ratio, or temperature exist, as shown in Figures D-14 through D-16, respectively. Plotting all data together against angle shows that the data generally fall into two groups: high supersonic (above 2.8 pressure ratio), and low supersonic and subsonic as shown in Figure D-17 for Model 51. An increase at 90° is evident, however, indicating some source effect. Further analysis of the high supersonic data indicates the possible presence of shock noise in the aft quadrant as shown in Figures D-18 and D-19. The flight effects on shock noise are covered in detail in the following paragraphs. Plotting only low supersonic and subsonic data versus angle indicates a simple dynamic effect on this mixing noise source as follows:

$$OASPL_{Static}^{-} OASPL_{Flight} = 60 log_{10} (1 - Mp cos \theta_i)^{-1}$$

This is shown in Figures D-20 through D-22. No significant source effect is evident in this set of data when the high supersonic data is removed.

Shock Cell Noise

Conical Nozzles - For the conical nozzle data, the shock noise at angles aft of 90° was ignored because, even though shock noise was noticeable, it was heavily contaminated by jet-mixing noise. In the 70° to 90° angles some consideration of the mixing noise effect in the shock-noise-frequency range was made. This was possible because of the relatively high confidence in jet-mixing and shock-cell noise predictions available for conical nozzles.

Pressure ratio, aircraft velocity, and acoustic angle were considered as the primary correlating variables for this noise component. When the deltas are plotted against angle for constant free-stream velocity, $V_{\rm O}$, the dynamic effect is found to be a 40 log [1 - Mp cos θ_1] function, and there is a slight increase in level at 90°; this is shown in Figures D-23 through D-26. The increase at 90° is possibly due to either an increase in effective pressure ratio due to flight, an increase in shock-cell length due to flight, or both, but no trends were noticed except for that with $V_{\rm O}$. Accordingly, for this correlation, a simple empirically derived equation for the increase with flight velocity was used as shown in Figure D-27; the choice of the curve was influenced by similar data for suppressors, shown in Figure D-28, and by the fact that the changes were relatively small.



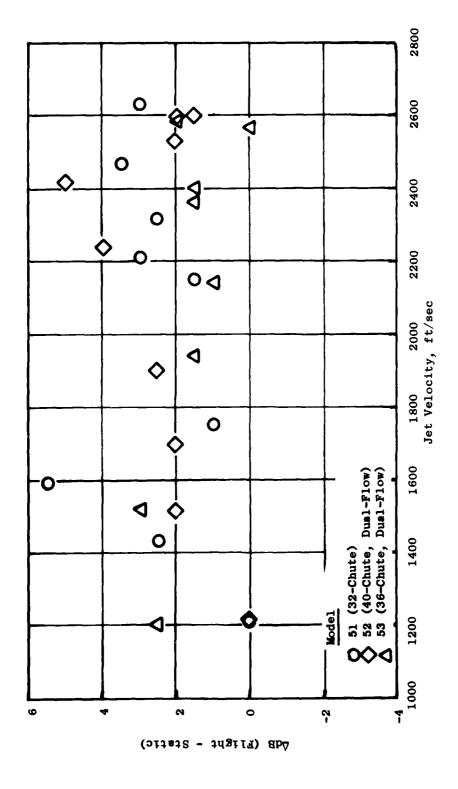
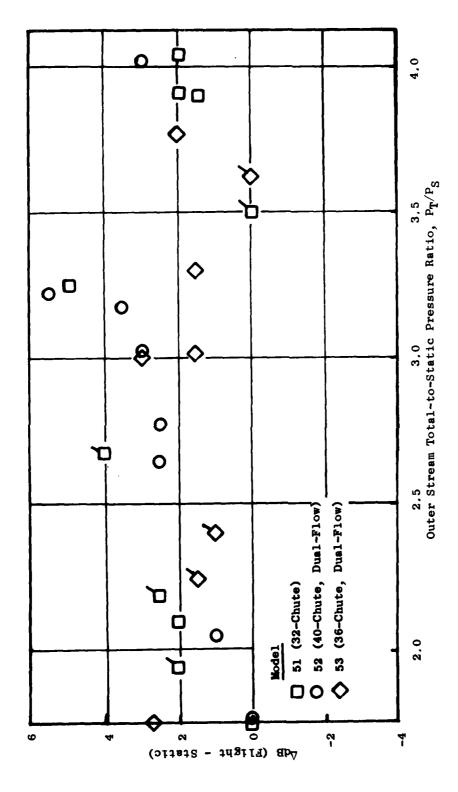
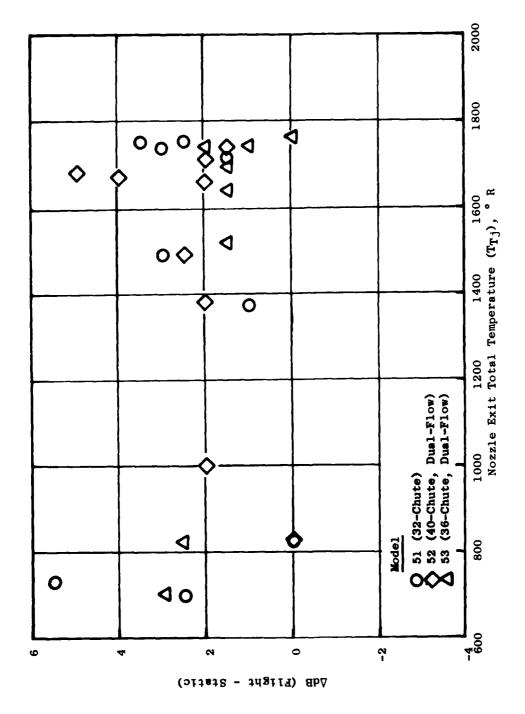


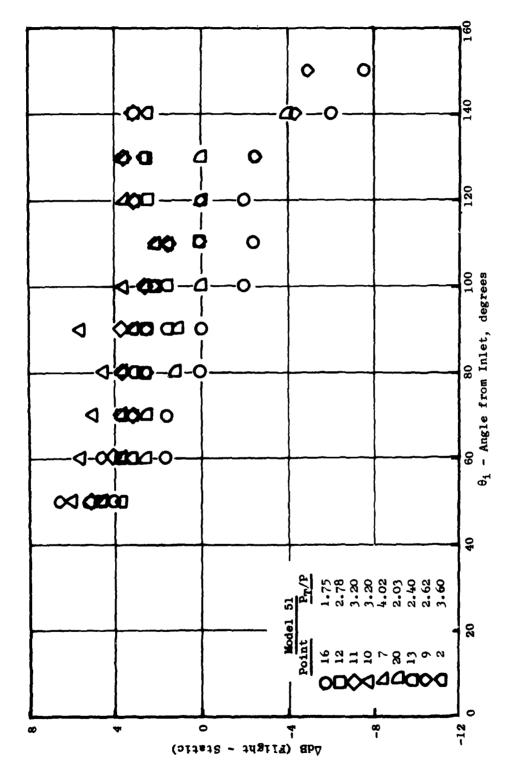
Figure D-14. Effect of Jet Velocity on High-Frequency Noise at θ_1 = 90° (V_0 = 300 ft/sec).



Effect of Outer Stream Pressure Ratio on High-Frequency Noise at θ_1 = 90° (V_0 = 300 ft/sec). Figure D-15.



Effect of Exhaust Total Temperature on High-Frequency Noise at $\theta_1 = 90^\circ$ (for $V_0 = 300~{\rm ft/sec}).$ Figure D-16.



Free-Jet Flight Effects on High-Frequency Noise Versus Angle (V $_{
m O}$ = 300 ft/sec, Doppler Shift Removed). Figure D-17.



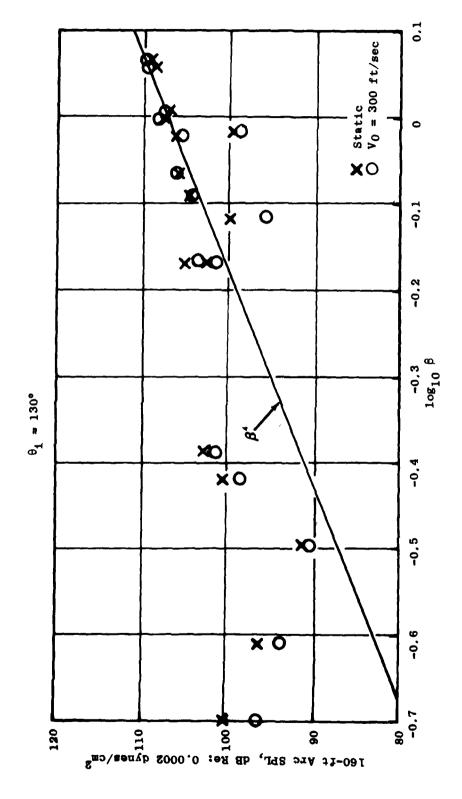


Figure D-18. High-Frequency SPL as a Function of Shock-Noise Parameter (8), Model 51, 2500 Hz.

35)

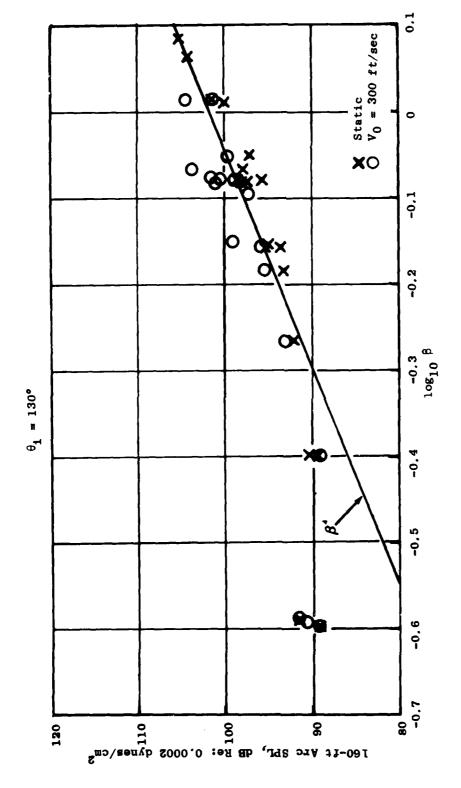
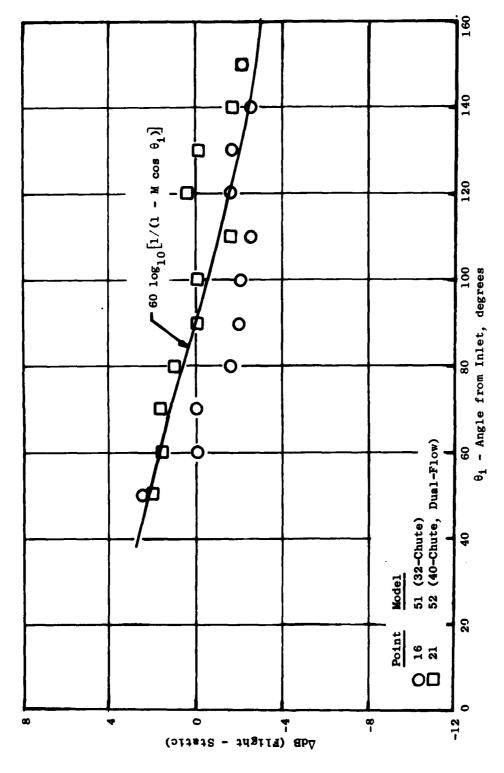
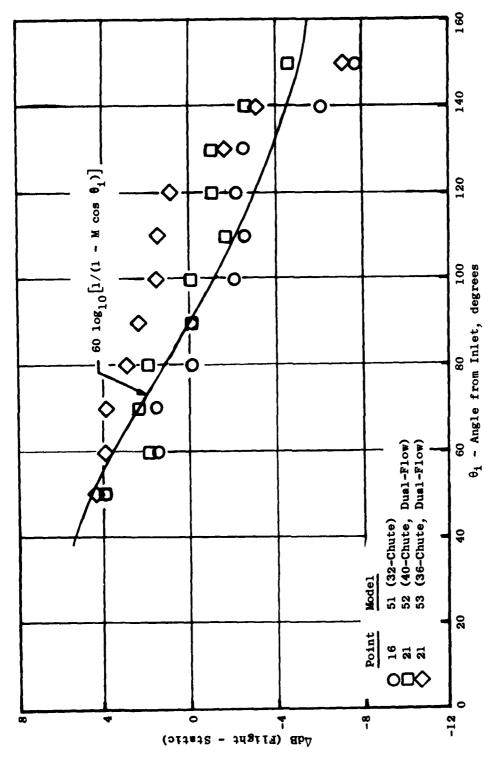


Figure D-19. High-Frequency SPL as a Function of Shock-Noise Parameter (B), Model 52, 5000 Hz.



Free-Jet Flight Effects on High-Frequency Noise Versus Angle for Subsonic Exhaust Velocity (v_0 = 150 ft/sec, Doppler Shift Removed). Figure D-20.



Free-Jet Flight Effects on High-Frequency Noise Versus Angle for Subsonic Exhaust Velocity (V $_0$ = 300 ft/sec, Doppler Shift Removed). Figure D-21.

(269)

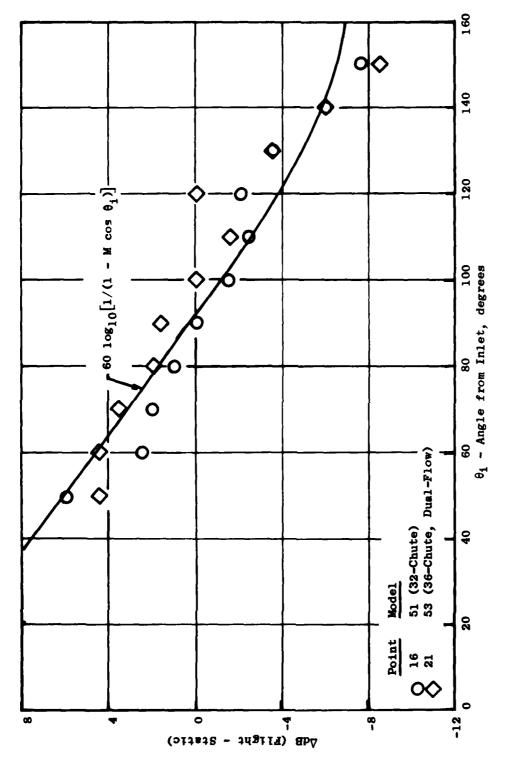


Figure D-22. Free-Jet Flight Effects on High-Frequency Noise Versus Angle for Subsonic Exhaust Velocity (V_0 = 400 ft/sec, Doppler Shift Removed).

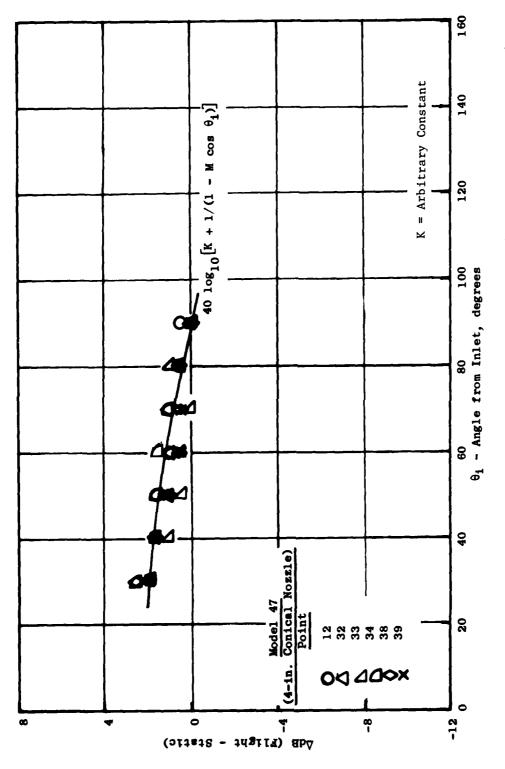


Figure D-23. Free-Jet Flight Effects on Shock Noise (V_0 = 150 ft/sec, Doppler Shift Removed).

(20)

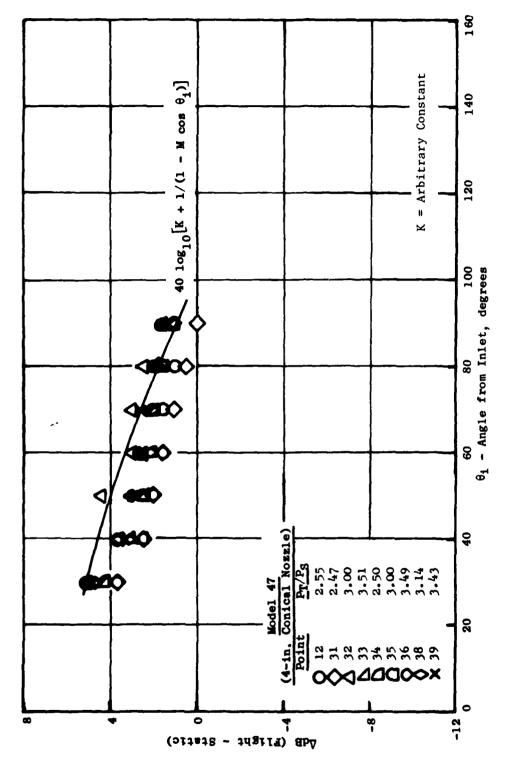


Figure D-24. Free-Jet Flight Effects on Shock Noise (V_0 = 275 ft/sec, Doppler Shift Removed).

J63)

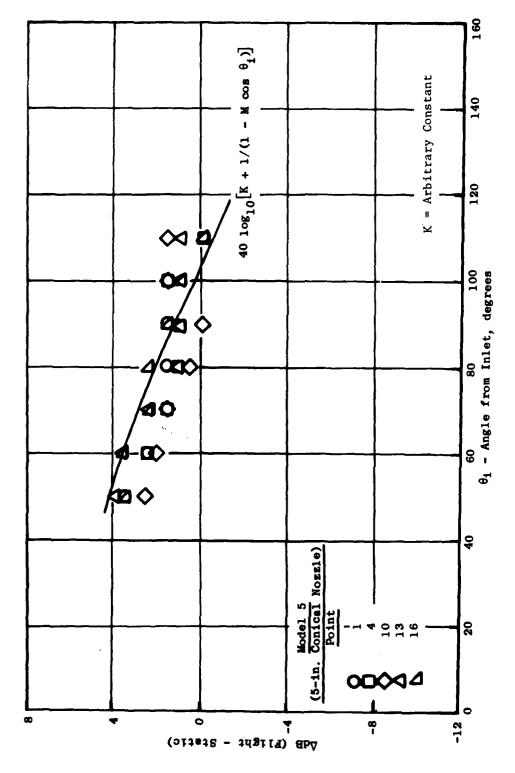


Figure D-25. Free-Jet Flight Effects on Shock Noise (V_0 = 300 ft/sec, Doppler Shift Removed).

الناو

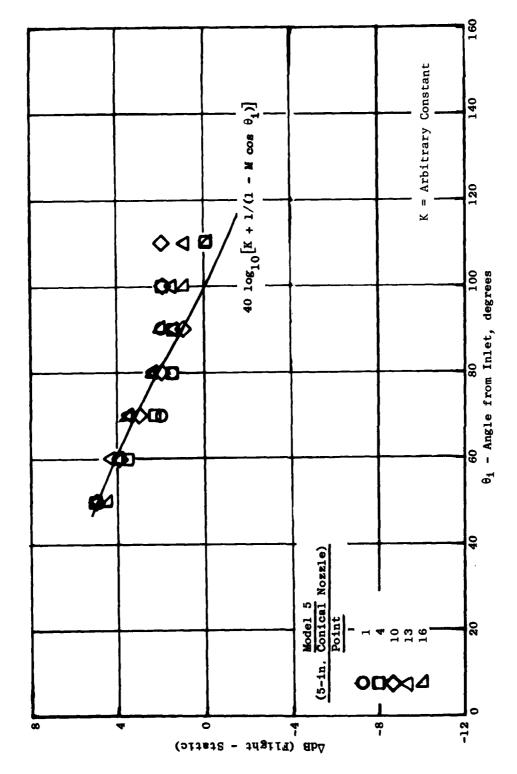


Figure D-26. Free-Jet Flight Effects on Shock Noise (V_0 = 400 ft/sec, Doppler Shift Removed).



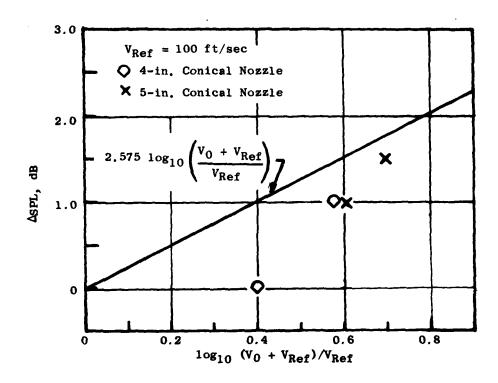


Figure D-27. Increase in Shock Noise Due to Flight - Conical Nozzles.

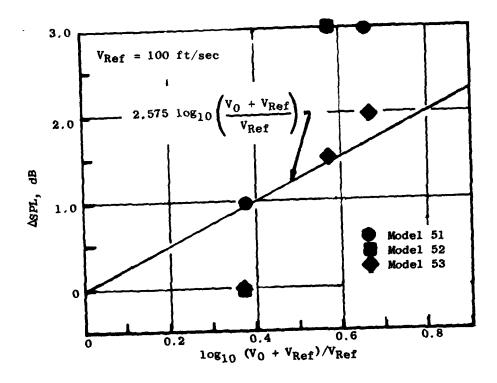


Figure D-28. Increase in Shock Noise Due to Flight - Suppressor Nozzles.

Aft-quadrant flight effects appeared to be similar to those of the suppressor shock noise which is discussed in the next section.

Shock Cell Noise From Suppressor Nozzles - As mentioned previously, it is very difficult to separate the premerged mixing noise from the shock-cell noise. However, this source is similar to that found in conical nozzles and may, therefore, have similar flight effects. If the data set is limited to the high supersonic data (above 2.8 pressure ratio) and plotted versus angle, Figure D-29 results. This shows a similar trend to the conical shock in the forward quadrant; an increase at 90° is indicated in addition to a "40 log" dynamic effect. The aft quadrant has flight effects approximately constant with angle. Review of data in the 1.6 to 2.5 pressure ratio range, Figure D-30, shows flight effects intermediate between those of subsonic and supersonic cases. It is hypothesized that in these cases the high frequencies become dominated by shock noise, but complete domination is not achieved until characteristic pressure ratios of over 2.8 are reached. This is illustrated by the predictions given in Figure D-31.

As with the conical nozzle, an empirical curve of source increase versus aircraft velocity is used for this prediction technique. This curve is shown in Figure D-28.

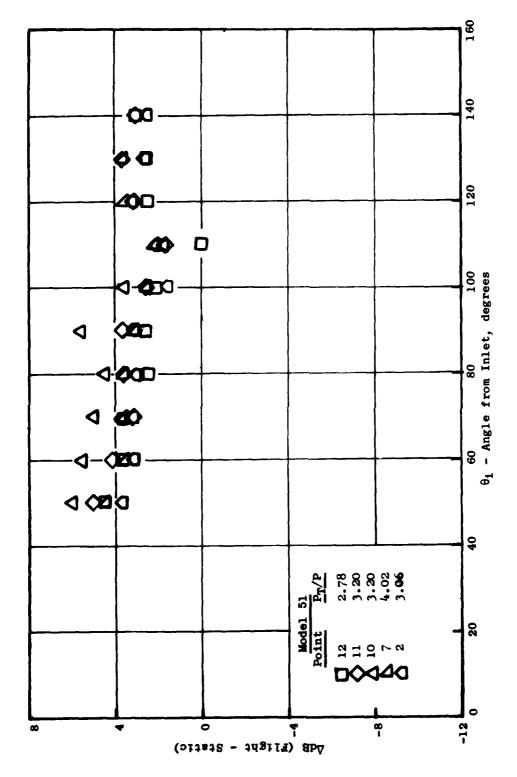
COMPARISON OF PREDICTED VERSUS MEASURED FLIGHT EFFECTS

Maximum PNL and EPNL from Free Jet

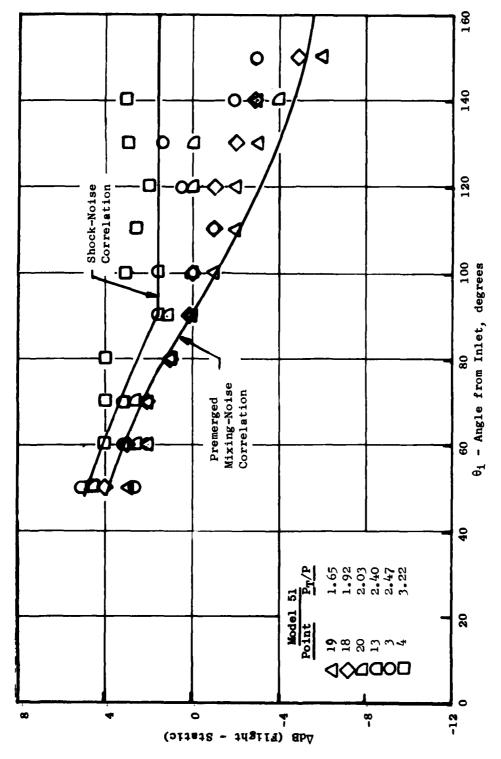
The correlation between predicted and measured data is summarized in Tables D-4 and D-5. Table D-4, for static conditions, is simply another check of the basic M*S method as presented in Reference 12. In general, the results of the static cases are about the same as in Table 3-1 of Reference 12; i.e., for all suppressors:

All Suppressors		Linear Regression Constants		Confidence Limits (dB)		
		m	<u>b</u>	80%	95%	
PNI.	eference 12	0.973	0.07	± 2.4	± 3.7	
	urrent	1.098	-1.82	± 1.9	± 2.9	
EPNI.	eference 12	0.968	0.29	± 2.1	± 3.3	
	current	1.094	-0.46	± 2.0	± 3.1	

Table D-5 shows the correlation for the simulated-flight case which, on the same basis as above, is as good as for the static case:



Free-Jet Flight Effects on High-Frequency Noise Versus Angle for Supersonic Exhaust Velocity (V $_0$ = 300 ft/sec, Doppler Shift Removed). Figure D-29.



Free-Jet Flight Effects for Various Pressure Ratios from Subsonic to Supersonic Case (V $_0$ = 300 ft/sec, Doppler Shift Removed). Figure D-30.

O.

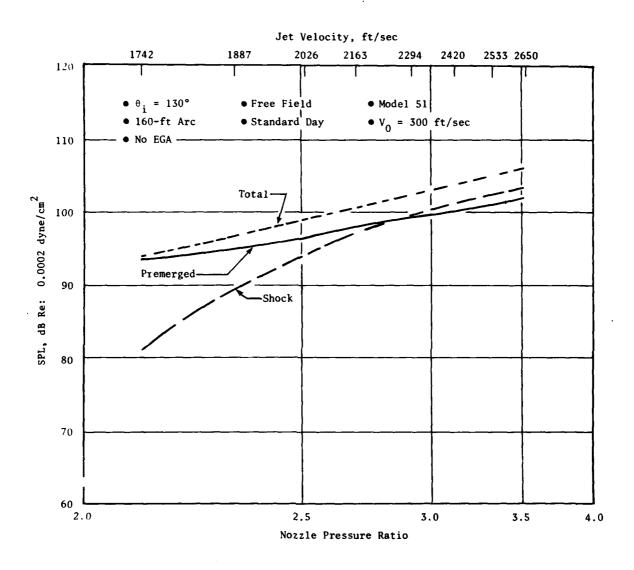


Figure D-31. Comparison of Predicted Premerged and Shock Noise in the Aft Quadrant.

Table D-4. Predictions Versus Measurements, Static.

Nozzle	1	Regression stants b	Confide Limits 80%	ence s (dB) 95%	Number of Points
PNL Suppressors	1.098	-1.82	± 1.9	± 2.9	28
Conical (2)	1.018	+1.35	± 1.1	± 1.7	17
Model 51	0.983	-1.96	<u>+</u> 1.9	± 3.2	9
Model 52	1.235	-2.12	± 2.12	± 3.3	10
Model 53	1.039	-1.49	± 1.8	<u>+</u> 2.9	9
104 Tube	-	-	-	-	-
ALL	1.065	-0.61	± 2.5	<u>+</u> 3.9	45
EPNL Suppressors	1.094	-0.46	<u>+</u> 2.0	± 3.1	28
Conical (2)	1.004	+0.94	± 0.9	<u>+</u> 1.5	17
Model 51	1.006	-1.57	± 1.7	± 2.8	9
Model 52	1.155	+0.21	± 2.0	± 3.4	10
Model 53	1.029	-0.10	± 1.4	± 2.4	9
104 Tube	-	••	_	-	-
ALL	1.063	+0.09	<u>+</u> 1.8	<u>+</u> 2.8	45

Table D-5. Predictions Versus Measurements, Simulated Flight by Free Jet.

Nozzle		Regression stants b	Confid Limits 80%	dence s (dB) 95%	Number of Points
PNL Suppressors	1.029	-0.18	± 2.3	± 3.5	59
Conical (2)	0.966	+1.80	<u>+</u> 1.2	<u>+</u> 1.9	35
Model 51	1.000	+0.02	<u>+</u> 2.2	± 3.5	22
Model 52	1.183	-1.36	± 2.0	± 3.2	14
Model 53	0.979	+0.82	± 2.0	± 3.3	11
104 Tube	0.808	-0.68	+ 2.1	± 3.4	12
ALL	1.004	+0.56	± 2.3	± 3.5	94
EPNL Suppressors	1.090	-0.12	± 2.3	<u>+</u> 3.5	59
Conical (2)	1.068	-0.98	<u>+</u> 1.5	± 2.4	35
Model 51	1.057	-0.78	± 1.6	± 2.6	22
Model 52	1.190	+0.78	± 2.3	± 3.7	14
Model 53	1.051	+0.73	± 1.9	± 3.1	11
104 Tube	0.825	-1.51	<u>+</u> 1.9	± 3.1	12
ALL	1.083	+0.29	<u>+</u> 2.1	± 3.2	94

The state of the s

All Suppressors		Linear Regression Constants		Confidence Limits (dB)	
		m	<u>b</u>	80%	<u>95%</u>
PNL	Static	1.098	-1.82	± 1.9	± 2.9
	"Flight"	1.029	-0.18	± 2.3	± 3.5
EPNL	Static	1.094	-0.46	± 2.0	± 3.1
	"Flight"	1.090	-0.12	± 2.3	± 3.5

This overall comparison for all suppressors shows that the "flight" EPNL prediction is within 1/4 to 1/2 EPNdB of the static correlation, indicating that the prediction method is doing the intended job very well.

By the way of illustrating the correlation of the data for all the points checked (per Table D-2), Figures D-32 through D-35 are presented (in the same format as presented and discussed in Section 3.3 of Reference 12). Figures D-32 and D-34 show the correlation of the static data, and Figures D-33 and D-35 show it for the simulated-flight data. In addition to the linear regression line (solid), a dashed line representing the "measured equals predicted" case is shown for reference.

Application of the Method to Aerotrain Data

The flight effects correlation has been applied to predict the noise from the conical and from the 104-tube nozzles on the Bertin Aerotrain (as documented in Reference 6). The cycle points used in this check, from those actually run during the tests reported in Reference 6, are also listed in Table D-2 including the speed of the moving-frame source during the measurement. Note that the conical nozzle on the J85 engine used on the Aerotrain was a scaled-up version of the 4-in. conical nozzle (model 47) tested in the JENOTS free-jet facility.

The predicted and measured PNL and EPNL values are also shown on Figures D-32 and D-34 for the static case and on Figures D-33 and D-35 for the actual moving-frame case. These plots show that the correlation works as well on the Aerotrain data as it does on the free-jet data.

Typical checks of the far-field PNL versus angle and of the spectral distribution at three far-field angles are shown in Figures D-36 and D-37 for the conical nozzle, static and moving-frame respectively, and in Figures D-38 and D-39 for the 104-tube nozzle.

Comment on the $m(\theta_i)$ Relative Velocity Index

The value of the index, $m(\theta_1)$, as defined in Table D-3 and as determined quantitatively by the free-jet data in this program, is shown in Figure D-40 together with the one currently under consideration by the ICAO Working Group E (Reference 64); both are allowed as options in the M*S correlation.

• The "Reference" level is the predicted value of noise for each nozzle, at a specified set of thermodynamic conditions, plus an arbitrary value of 100 dB.

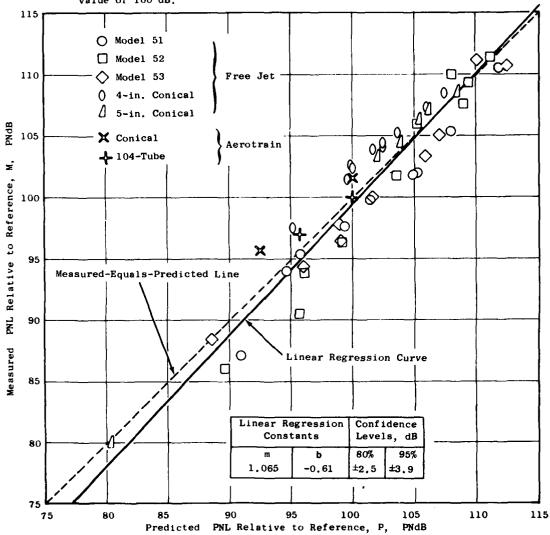


Figure D-32. Correlation Between Measured and Predicted Maximum Perceived Noise Level (PNL), All Nozzles - Static.

• The "Reference" level is the predicted value of noise for each nozzle, at a specified set of thermodynamic conditions, plus an arbitrary value of 100 dB.

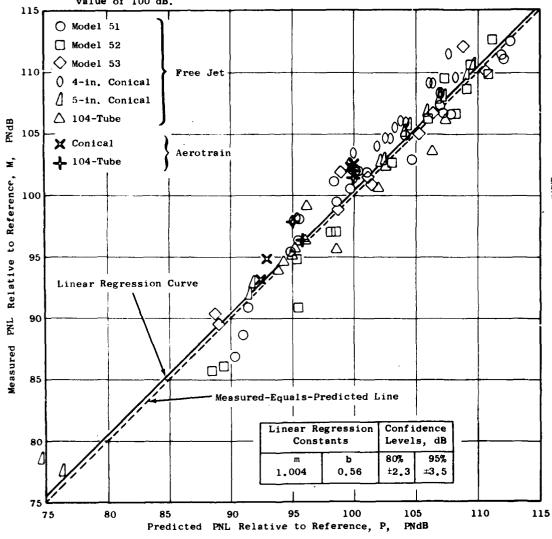


Figure D-33. Correlation Between Measured and Predicted Maximum Perceived Noise Level (PNL), All Nozzles - Flight.

- Flyover calculation using static data corrected to free-field conditions.
- The "Reference" level is the predicted value of noise for each nozzle, at a specified set of thermodynamic conditions, plus an arbitrary value of 100 dB.

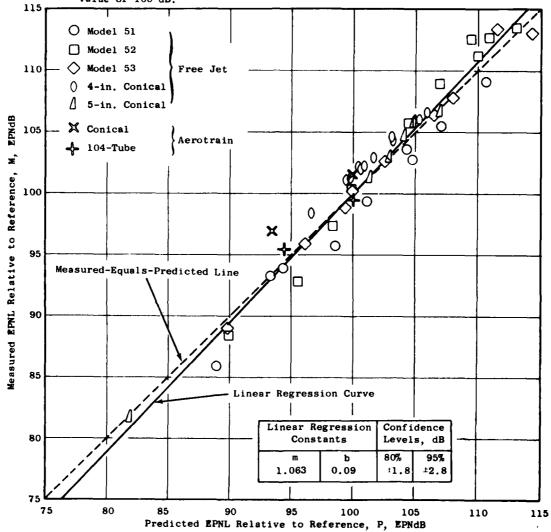


Figure D-34. Correlation Between Measured and Predicted Effective Perceived Noise Level (EPNL), All Nozzles - Static.

• The "Reference" level is the predicted value of noise for each nozzle, at a specified set of thermodynamic conditions, plus an arbitrary value of 100 dB.

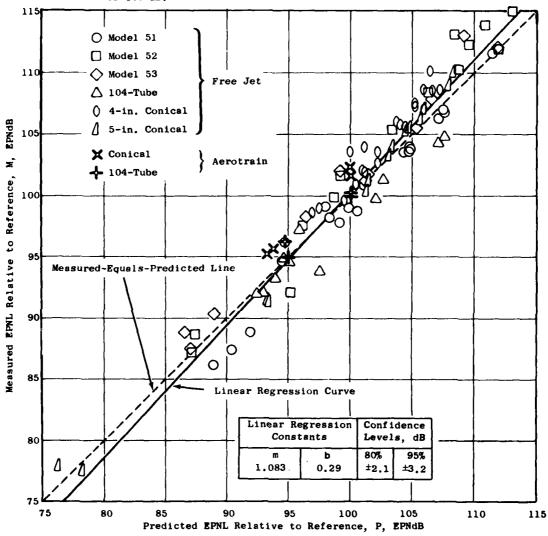


Figure D-35. Correlation Between Measured and Predicted Effective Perceived Noise Level (EPNL), All Nozzles - Flight.

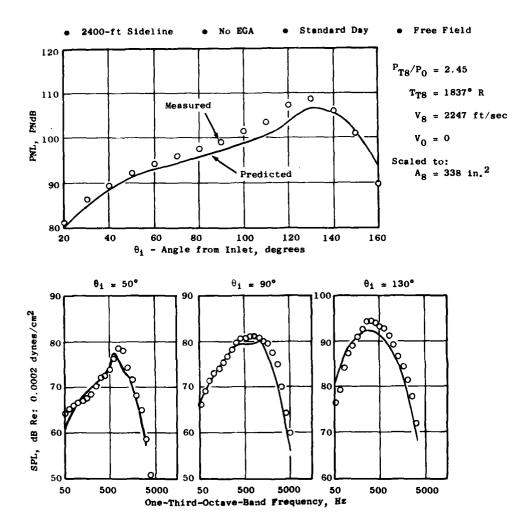


Figure D-36. Predicted and Measured Static Noise from the Conical Nozzle on the Bertin Aerotrain.

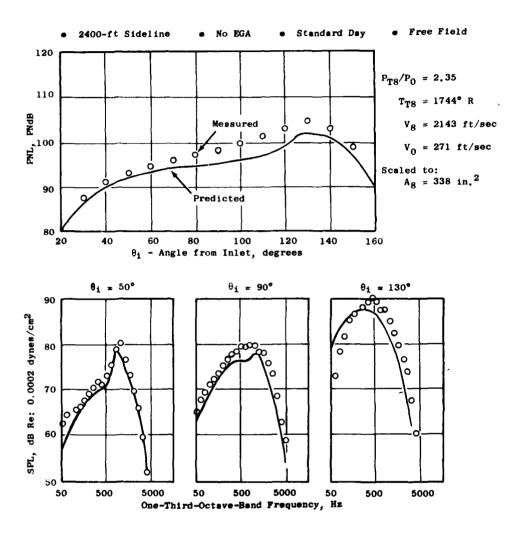


Figure D-37. Predicted and Measured Moving-Frame Noise from the Conical Nozzle on the Bertin Aerotrain.

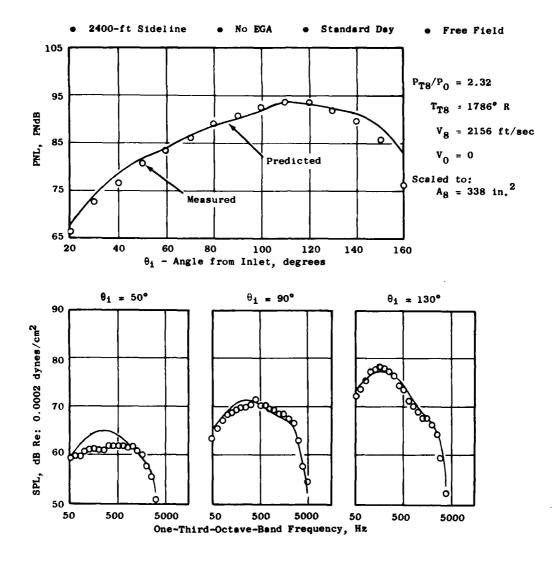


Figure D-38. Predicted and Measured Static Noise from the 104-Tube Nozzle on the Bertin Aerotrain.

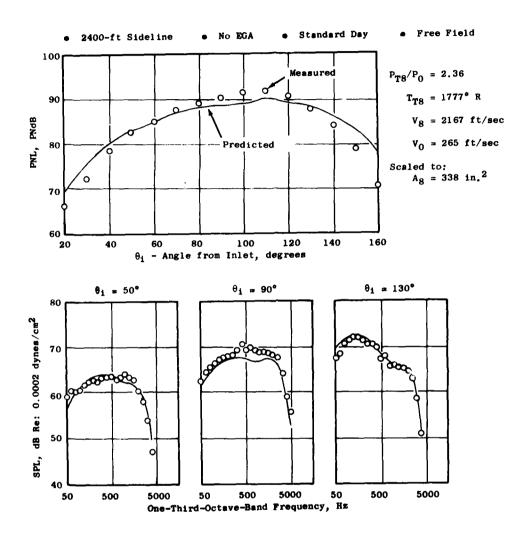


Figure D-39. Predicted and Measured Moving-Frame Noise from the 104-Tube Nozzle on the Bertin Aerotrain.

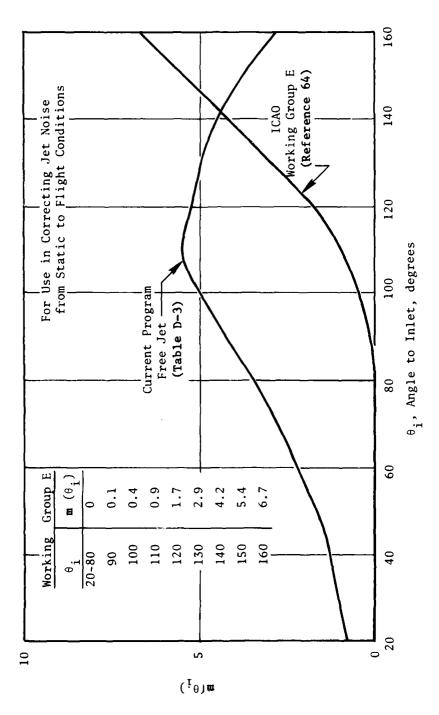


Figure D-40. Relative Velocity Index $\mathfrak{m}(\theta_{\underline{1}})$.

M*S COMPUTER PROGRAM REVISION

Because the flight-effect-prediction method is on a "delta SPL" basis, the changes to the M*S computer program were minor. The program containing the flight effects is fully documented in Reference 13. In general, the flight effects are applied to the basic source noise (jet mixing or shock cell) in the appropriate subroutines.

In the "SUB1" subroutine, the source is determined (postmerged or premerged noise), and the appropriate flight effects are determined (exponent method for postmerged, dynamic effect for premerged). These corrections are then applied to each predicted, static SPL. In the premerged-noise, multi-element-shielding routine, an adjustment is made to allow for the correct flight effects even though the source levels are changing. In the "SHKSUB" subroutine, the predicted increase at 90° is determined. This correction is applied to all predicted, static SPL's in the aft quadrant while the correction plus the dynamic effect are applied to all SPL's in the forward quadrant.

APPENDIX E

PREDICTED ACOUSTIC DESIGN TRENDS FROM M*S METHOD

This appendix presents selected directivity and spectra plots to supplement the discussion of trend curves in Section 4.1.2 of this document.

GENERAL ELECTRIC CO. CINCINNATI OH AIRCRAFT ENGINE BU--ETC. F/G. 20/1 HIGH VELOCITY JET NOISE SOURCE LOCATION AND REDUCTION. TASK 6. --ETC(1/1) APR 79. J BRAUSCH, A.S. CLAPPER, F. R. GLIERE. DOT-05-38034 AD-A103 671 WICE ASSIFIED R79AL6302 FAA-RD-76-79-6 NL 4 º 6

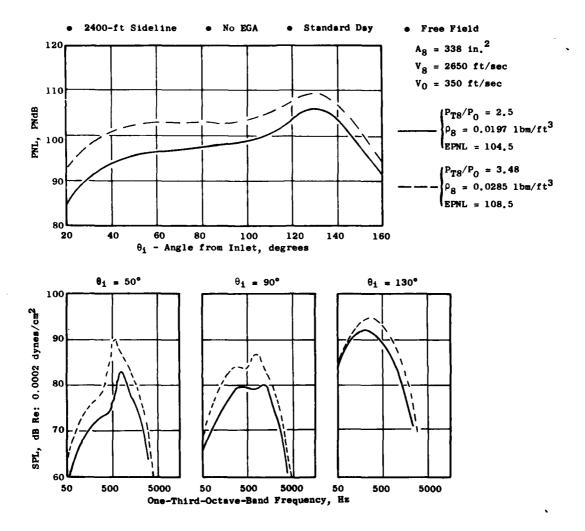


Figure E-1. Effect of Cycle Conditions on Conical Nozzle Noise at High Jet Velocity.

ogdini i alteritione.

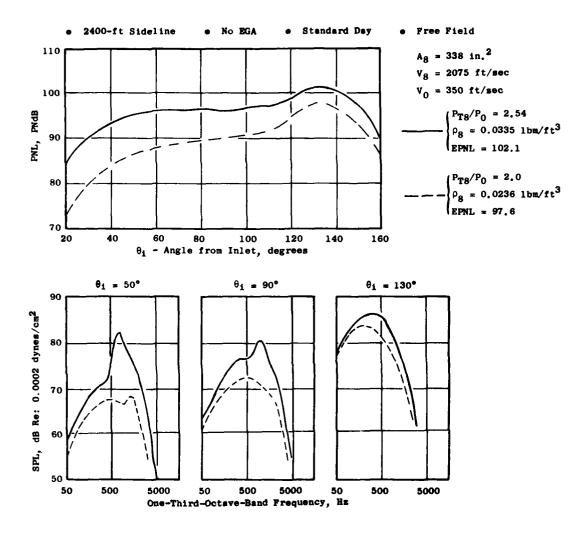


Figure E-2. Effect of Cycle Conditions on Conical Nozzle Noise at Medium Jet Velocity.

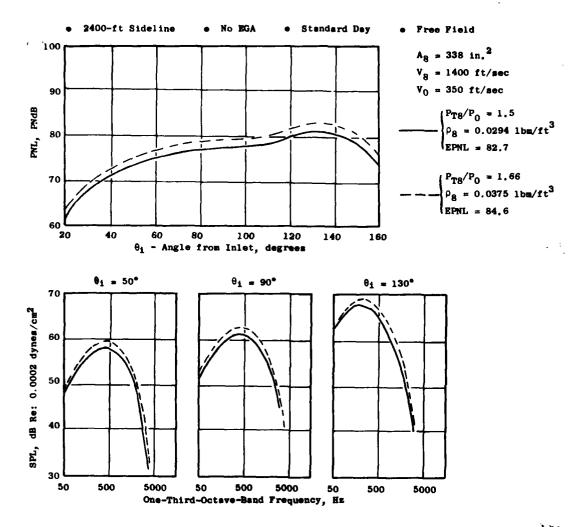


Figure E-3. Effect of Cycle Conditions on Conical Nozzle Noise at Low Jet Velocity.

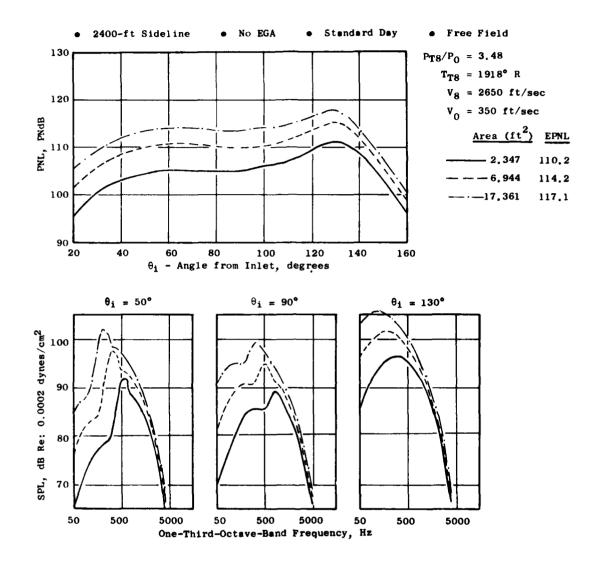


Figure E-4. Effect of Area on Conical Nozzle Noise at High Jet Velocity.

Contract Contract of the Contr

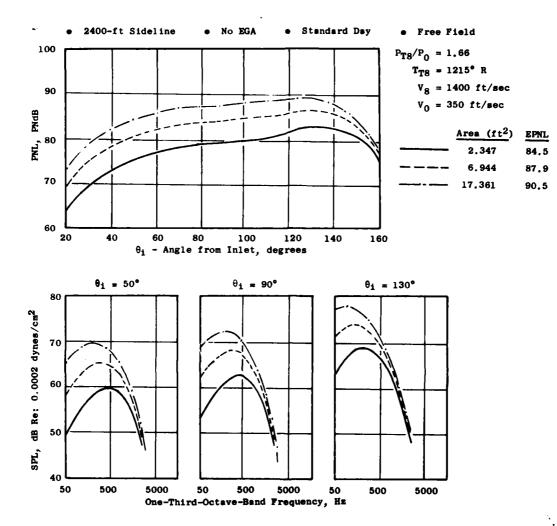


Figure E-5. Effect of Area on Conical Nozzle Noise at Low Jet Velocity.

1-12

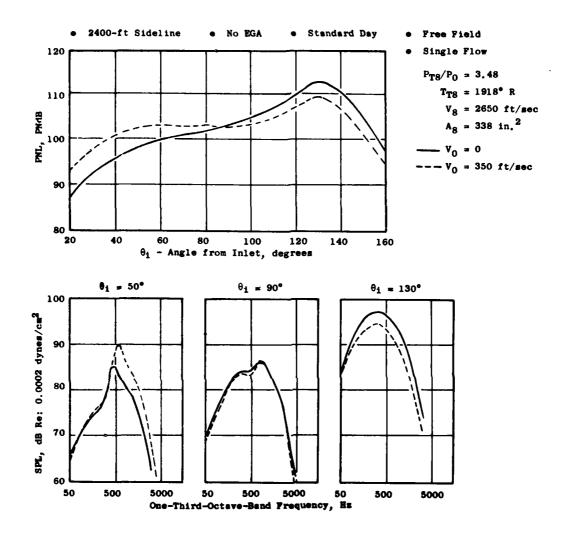


Figure E-6. Effect of Flight on Conical Nozzle Noise at High Jet Velocity.

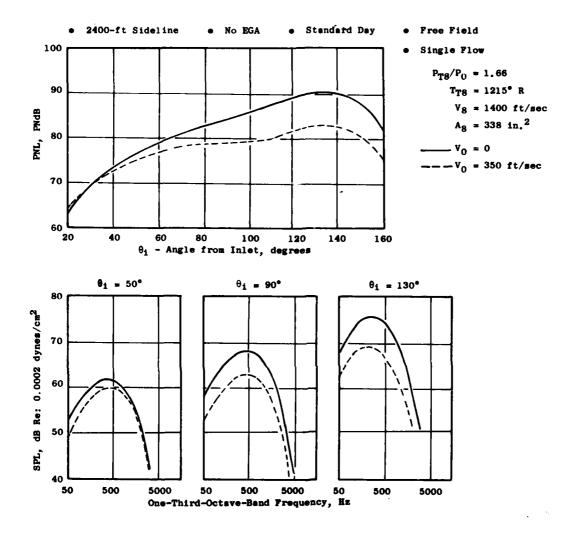


Figure E-7. Effect of Flight on Conical Nozzle Noise at Low Jet Velocity.

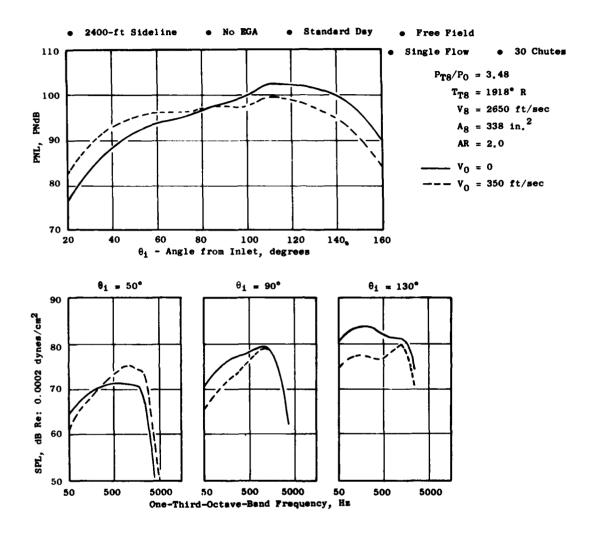


Figure E-8. Effect of Flight on Suppressor Nozzle Noise at High Jet Velocity.

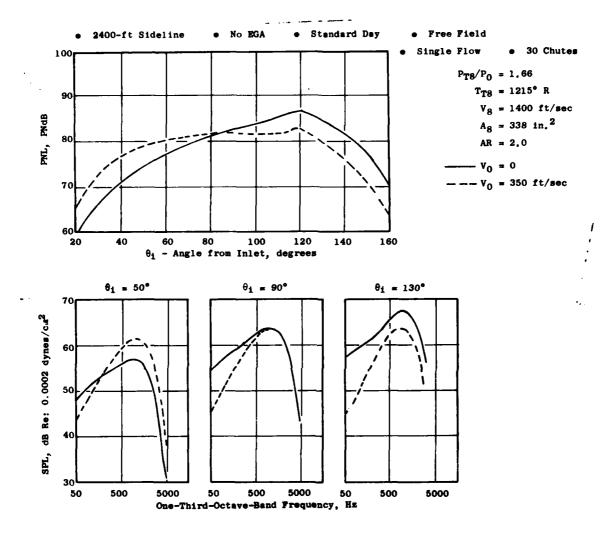


Figure E-9. Effect of Flight on Suppressor Nozzle Noise at Low Jet Velocity.

(11)

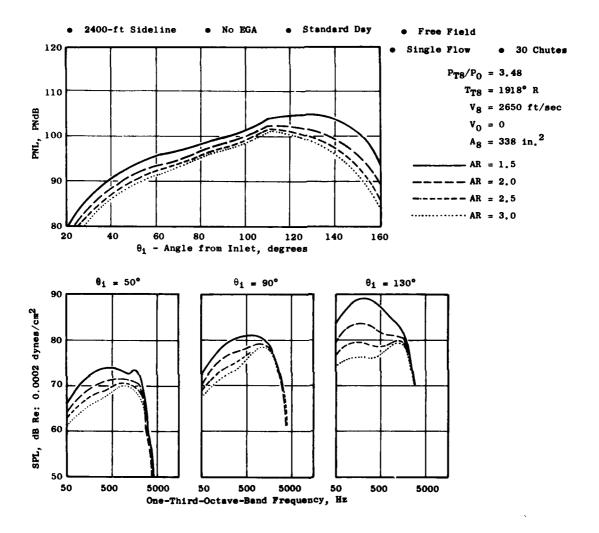


Figure E-10. Effect of Area Ratio on Multichute Nozzle Noise at High Jet Velocity.

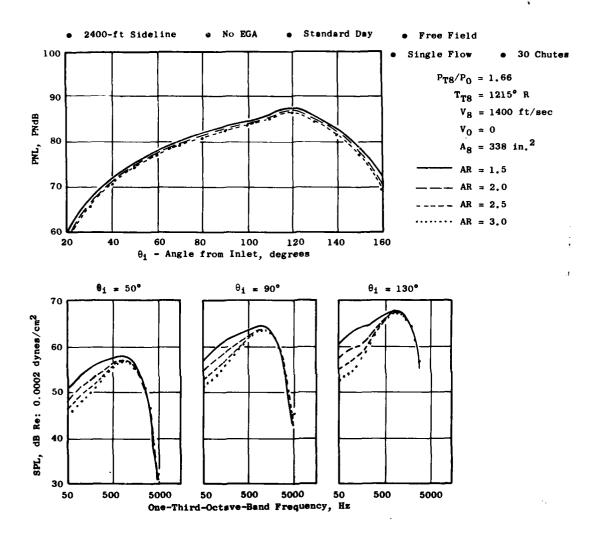


Figure E-11. Effect of Area Ratio on Multichute Nozzle Noise at Low Jet Velocity.

: 10

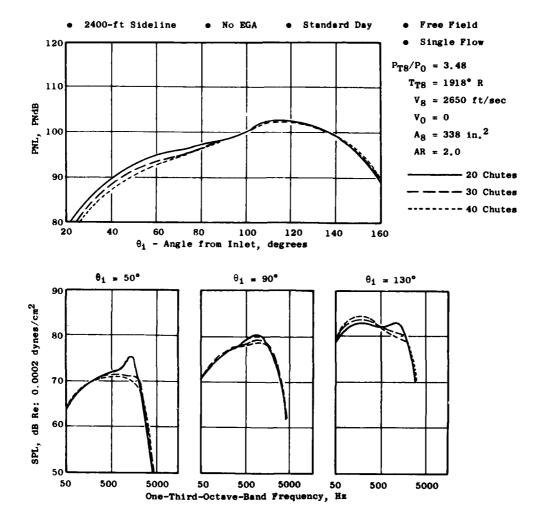


Figure E-12. Effect of Element Number on Multichute Nozzle Noise at High Jet Velocity.

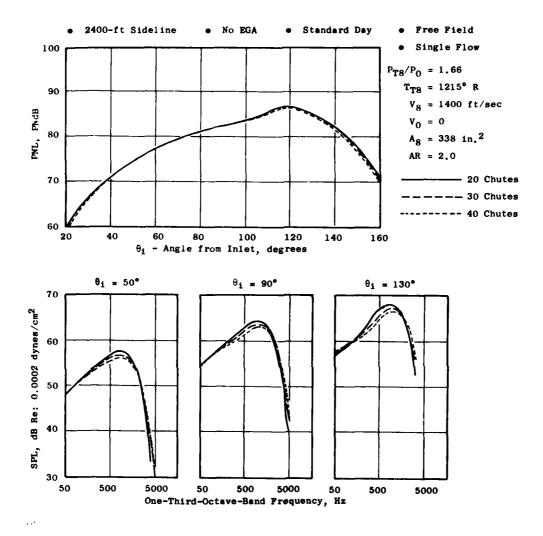


Figure E-13. Effect of Element Number on Multichute Nozzle Noise at Low Jet Velocity.

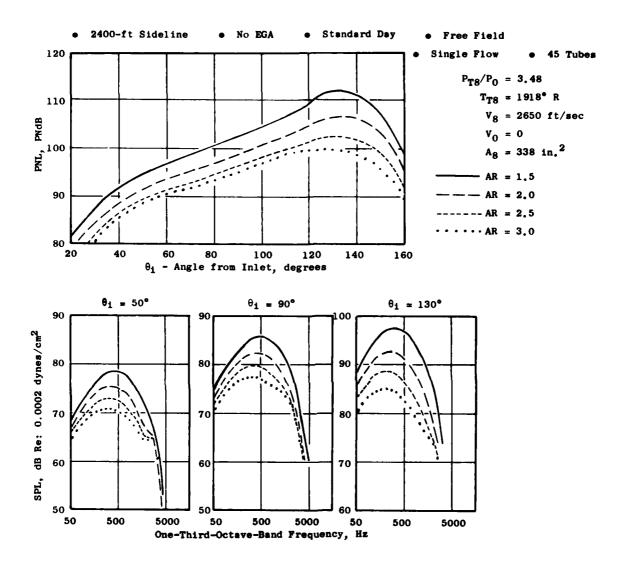


Figure E-14. Effect of Area Ratio on Multitube Nozzle Noise at High Jet Velocity.

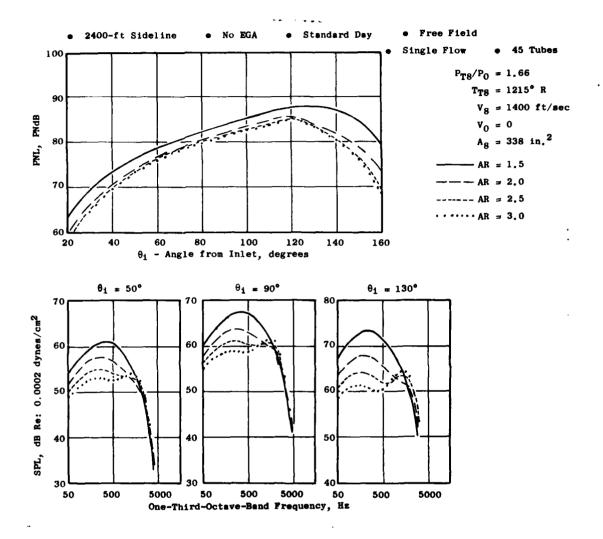


Figure E-15. Effect of Area Ratio on Multitube Nozzle Noise at Low Jet Velocity.

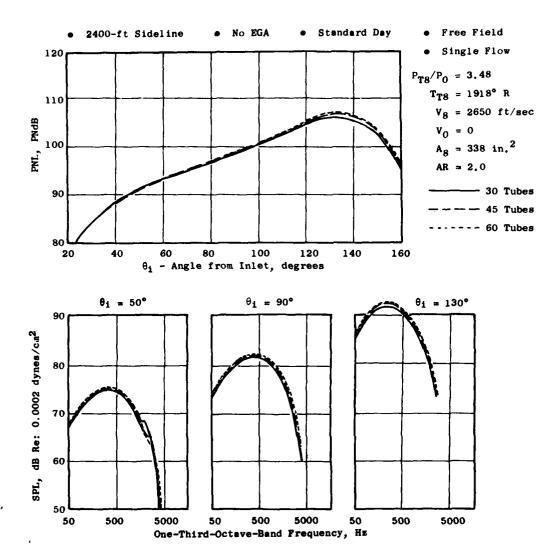


Figure E-16. Effect of Element Number on Multitube Nozzle Noise at High Jet Velocity.

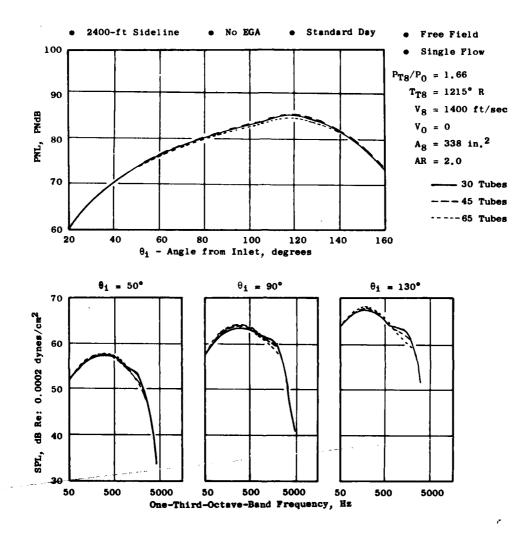


Figure E-17. Effect of Element Number on Multitube Nozzle Noise at Low Jet Velocity.

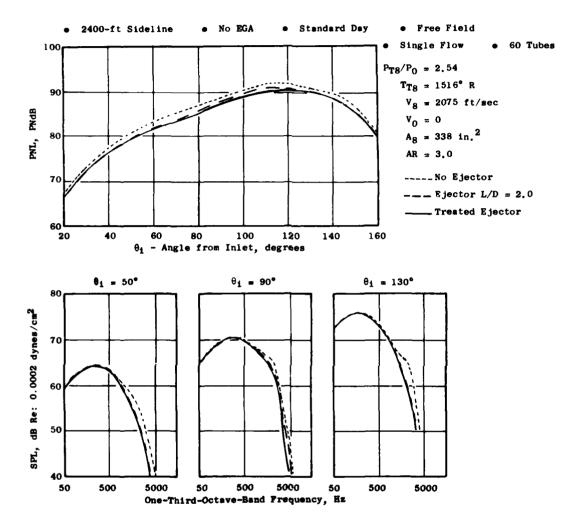


Figure E-18. Effect of Ejectors on Multitube Nozzle Noise.

APPENDIX F - GUIDE TO GOOD-ACOUSTIC DESIGN PRACTICES

This appendix presents information supplementing Section 4.2.1 of the text. It is intended to be used, in concert with the primary geometric and thermodynamic design parameters incorporated in the basic M*S model, as "guidelines" to assure that basic suppression levels are attained.

DEFINITION OF MULTIELEMENT SUPPRESSOR GEOMETRIC PARAMETERS

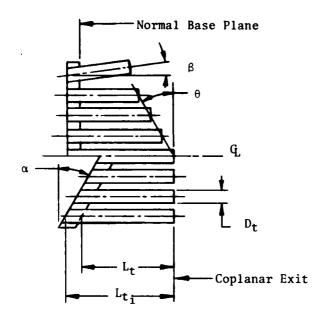
For the two primary families of multielement suppressors, i.e., tubes/holes and chutes/spokes, the geometric design variables are defined, with the aid of Figure F-1, as follows:

- \bullet <u>Tube</u> Circular or pseudocircular flow element of some finite external length, $L_{\scriptscriptstyle +}$
- \bullet Hole Circular or pseudocircular flow element having no external length, $L_{\scriptscriptstyle +}$
- <u>Deep Chute</u> Radial flow-segmenting element designed for good ventilation capability and normally stowed within the plug centerbody
- Shallow Chute Radial flow-segmenting element designed for moderate ventilation capability and normally stowed on the plug or centerbody surface
- Spoke Radial flow-segmenting element having no ventilation capability and normally stowed on the plug or centerbody surface
- Area Ratio, AR For full baseplate tube/hole array: ratio of area
 of a circumscribing circle skirting the outermost flow points at the
 exit plane to the total physical flow area

For annulus of tubes, holes, chutes or spokes - ratio of total annulus area to total physical flow area

Radius Ratio, Rr - Ratio of plug radius, Rp, to shroud radius, Rs, at throat plane





 θ = Exit Plane Stagger Angle α = Base Plane Stagger Angle

 β = Cant Angle

 L_{t} = External Tube Length

 L_{t} = Internal Tube Length

D_t = Internal Tube Diameter

R_p = Plug Radius

 R_s = Shroud Internal Radius

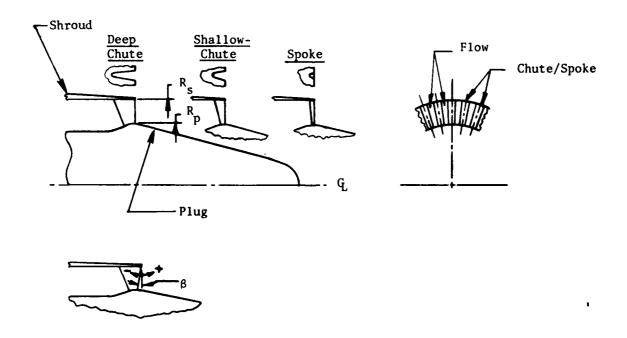


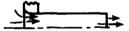
Figure F-1. Definition of Multielement Suppressor Geometric Parameters.

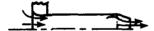
- Degree of Segmentation, N Number of flow or segmenting elements;
 i.e., tubes, holes, chutes, spokes
- Tube Diameter, Dt Internal diameter of tube at throat plane
- Tube Length, Lt External exposed tube length, not including baseplate thickness
- Internal Tube Lengths, Lti Internal total tube length, including baseplate thickness
- <u>Tube Size Equity</u> Measure of departure from uniformity of tube size within an array
- <u>Tube Spacing Uniformity</u> Measure of departure from equal tube spacing within an array
- Exit Plane Stagger Angle, θ Degree of exit plane angularity relative to coplanar
- Base Plane Stagger Angle, α Degree of nonnormal-to-centerline design
- Cant Angle, β Degree of tilt relative to centerline of tube or chute array; normally outer tube row only but may apply to complete tube array in either (+) outward or (-) inward direction
- Tube Axial-Flow Geometry

Straight

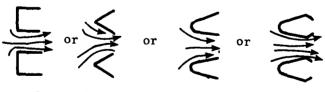
or

Convergent





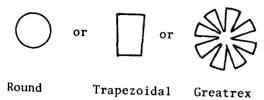
• Chute Axial Flow Geometry



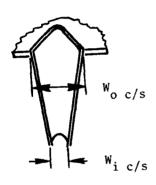
Rectangular

Sharp Triangular Contoured Convergent Contoured Convergent-Divergent

Tube/Hole Exit Planform



• <u>Chute/Spoke Exit Planform</u> - Wo_{C/S}/Wi_{C/S} = Ratio of chute/spoke width at shroud to width at plug



DESIGN PRACTICES FOR MULTIELEMENT JET NOISE SUPPRESSORS

The M*S model has been evolved to accommodate the primary geometric and thermodynamic design variables of multielement tube and chute suppressors as well as unsuppressed round jets and annular plug nozzles. Either single- or dual-flow systems can be simulated; the multielement suppressor is applied to the outer stream of the coannular exhaust system where current practical interest is for the high-velocity stream to be mechanically suppressed. Ranges of applicability and accuracy for the basic M*S method are presented in Section 4.1.1 of this document.

For the multitube/hole suppressor family, the M*S model correlation includes nozzles with an arbitrary number of tubes of identical size with simple convergent ends, coplanar termination, all tubes parallel to the nozzle centerline (except the outer tube row can be canted relative to the axis), uniform center-to-center spacing of tubes in a hexagonal array, and the option of incorporating a centerbody plug.

Data are presented and discussed for variations in tube:

- Length
- Size Equity and Spacing Uniformity
- Exit Plane Stagger
- Base Plane Stagger
- Canting
- Internal Geometry
- End Planform

For the multichute/spoke suppressor family, the M*S model correlation includes both chutes and spokes without distinction, radial as well as trapezoidal planforms, canted as well as normal-to-centerline exit planes, plus incorporation of a centerbody plug, and includes single- and dual-stream suppressor systems (with suppressor applied to the outer stream).

Further data are presented and discussed here for chute/spoke:

- Element Selection
- Exit Planform
- Exit Plane Cant
- General Design Considerations

These guidelines are intended for transposing the generic, optimal, M*S designs to practical suppressor systems. In support of the design guidelines, available quantitative static acoustic data comparisons are included as a general calibration of the importance of considering alternate design options. The guidelines are to be used, however, primarily on a qualitative basis: as a means of assuring that the M*S model-predicted static suppression levels are maintained rather than degraded through random alteration of the basic physical design to accommodate real-engine nozzle implementation considerations.



Tube Length

The M*S model applies for a tube length (or the nondimensional parameter of the tube length-to-diameter ratio, $L_{\rm t}/D_{\rm t}$) which was found by experience to provide essentially the highest suppression. Data show that there is an optimum value for this ratio. For values on either side of this optimum, for example a tube of no external length (baseplate-hole configuration) or an extremely long tube ($L_{\rm t}/D_{\rm t}>8$), the suppression is lower than the optimum by a significant amount. Results from six data sources indicate the range of $L_{\rm t}/D_{\rm t}$ for optimum acoustic design is nominally between 2.5 and 5.0. In all instances, nozzle designs with some external tube length exhibited somewhat greater suppression than baseplate models of no external tube length and/or configurations for which the external air-entrainment passage was blocked. This is observed at most jet velocities tested, and differences in suppression range from approximately 0 to 4 $\Delta \rm PNL$.

Of the six empirical data comparisons, the first three include variation of tube length-to-diameter ratio accomplished by shortening the external tube length while maintaining the baseplate design fixed. The fourth data comparison alters both internal and external tube length, but not consistently for the entire tube array; greater change in ventilation potential is made for the peripheral tubes. The last two comparisons maintain internal tube length or $L_{\rm ti}/D_{\rm t}$ but eliminate external tube length by methods which substantially reduce ventilation potential between the individual tubes. Review of the data sources follows.

Set 1 - A very controlled study of tube-length-to-diameter ratio was performed by GE, Reference 2, using an 85-tube configuration of AR = 3.19; see Figure F-2. All tubes were of equal length and terminated within a coplanar exit. Shortening of the tubes in seven incremental steps over the range of 3.75 in. $\geq L_t$ 0 effected an L_tD_t range of 8.7 to 0. Peak PNL suppression trends, presented at 250 ft/sec increments of jet velocity, indicate: (a) An optimum range of improved design exists, normally within 2.5 $\leq L_t/D_t \leq$ 5, for the V, range of 1750 to 3000 ft/sec; (b) trends are fairly consistent at all Vj values, showing from 1 to 2 Δ PNL improvement in comparison to the longest tube length; (c) up to 3 Δ PNL suppression gain is seen in comparison to the baseplate at the lowest Vj of 1250 ft/sec; and (d) for most velocities, little distinction in acoustic performance is seen between very short and very long tubes.

Set 2 - Boeing data sources on tube studies, using 37- and 61-tube clusters of AR = 2.75 and 3.3, respectively, with incremental tube lengths of 3, 2, and 1 in., have reported (Reference 66) that tube length has minimal influence on acoustic performance, particularly in comparison to the more influential parameters of area ratio and tube number. However, closer review of the data, Figure F-3, indicates a variance of up to 1.5 Δ PNL within the range of tube length tested. The trend is not as consistent with velocity or tube length as in data Set 1, but it still suggests that an intermediate tube length is an improved design.

Set 3 - A second GE data set, Reference 2 and Figure F-4, compares a 72-hole, AR = 2.65, flat-baseplate model of $L_{\rm t}/D_{\rm t}$ = 0 to a moderately short-tube



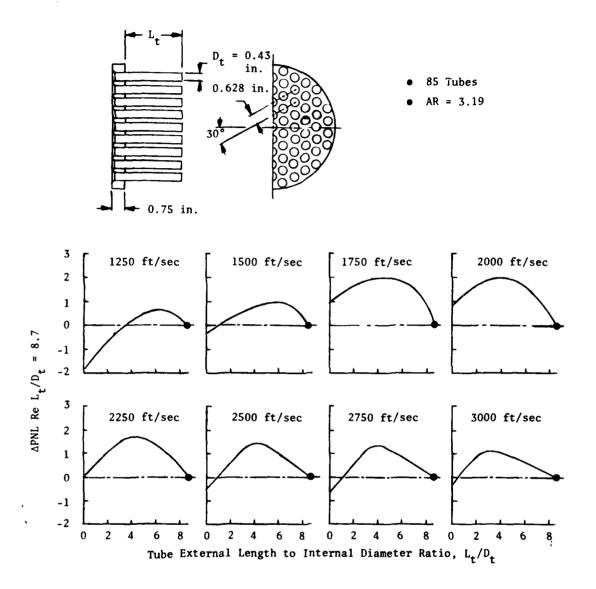


Figure F-2. L_t/D_t Variation Effects on 85-Tube Configuration at Various Jet Velocities.

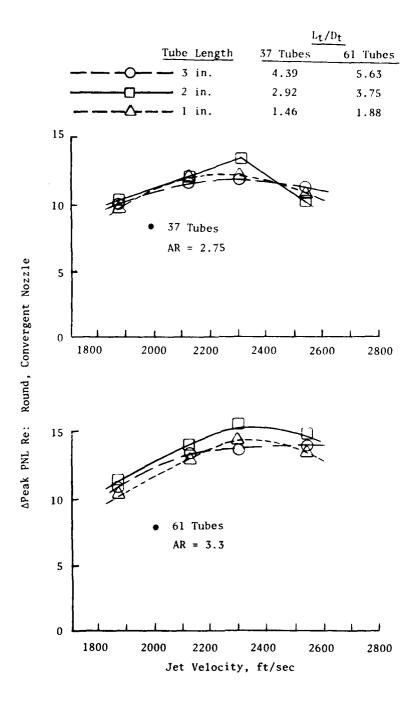
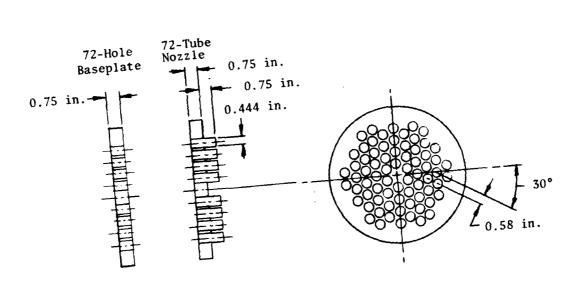


Figure F-3. Effect of Tube Length Variation on 37- and 61-Tube Configurations.



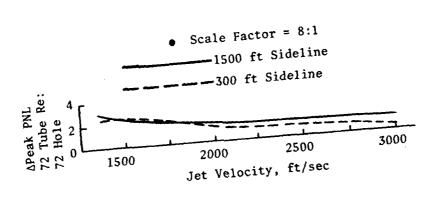


Figure F-4. Effect of Tube Length Variation on 72-Tube Nozzle vs. 72-Hole Baseplate.

configuration of the same tube size and spacing pattern but of L_t/D_t = 1.7. Sideline (300 and 1500 ft) peak PNL suppression change, with reference to the baseplate configuration, indicates from \approx 1 to 2.5 Δ PNL suppression improvement for the moderate tube length over the entire V_i test range.

Set 4 - The fourth model set is a similar type of comparison to that of the previous 72-hole/tube models in that a 97-hole baseplate of AR = 2.0 with unequal-size holes and nonuniform spacing is duplicated in a tube geometry, Figure F-5 and Reference 2. The tube configuration has a contoured base region in lieu of a flat baseplate and establishes varying $L_{\rm t}/D_{\rm t}$ for the four outer-to-inner tube rows, the central hole having no external tube length. Sideline maximum PNL suppression, referenced to the baseplate model, indicates up to 1.5 ΔPNL greater suppression at moderately high $V_{\rm j}$ for the improvement in ventilation capability. Lower $V_{\rm j}$ data indicate no preferential distinction for external tube length.

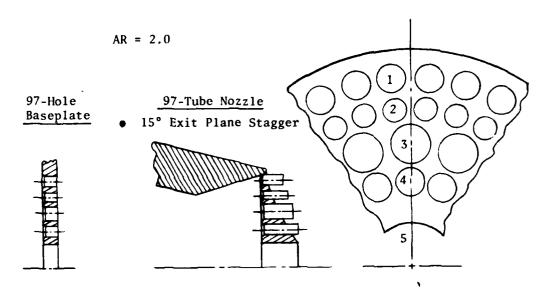
Set 5 - The tube nozzle for this comparison, Figure F-6 and Reference 2, is the same as in data Set 4 (above) but is now compared to a 97-hole nozzle which has a baseplate thickness equal to that of the tube length - such that no external ventilation between individual tubes is possible. Results are very similar to the previous comparison; sideline peak PNL suppression increases up to \simeq 3 ΔPNL at high V_j and \simeq 1.5 ΔPNL at low V_j , again indicating external tube length of some degree is very necessary to allow ventilation of ambient air to enhance mixing and improve velocity-decay rates.

Set 6 - The final configuration, a 104-elliptical-tube array of unequal tube size and nonuniform spacing, again maintains internal tube length but effectively eliminates external tube length through application of a baseplate cover. Figure F-7 (from Reference 19) shows that arc and sideline suppression potential is enhanced by the finite external tube length relative to the pseudobaseplate model. Approximately 1 Δ PNL improvement is seen at most velocity conditions tested. The tube effective external-length-to-diameter ratio varies from 3.1 to 0.7 for the five rows of tubes; the outer row is in the more optimal range of design as seen from the 85-tube study of data Set 1.

In general it can be concluded that finite external tube length is necessary to allow significant ambient air entrainment, enhanced mixing, and more rapid velocity decay. The first of the six empirical data sets was a systematic tube-length-variation study within a fixed AR = 3.19 system. It showed definite trends for optimal sideline peak PNL suppression within an $L_{\rm t}/D_{\rm t}$ range of 2.5 to 5.0. Normal improvements of from 1 to 2 Δ peak PNL were suggested relative to a very long or very short tube. All other data sources supported the trends of the more systematic study, each indicating a direct link between external-tube-length/ambient-air-entrainment-capability and suppression performance.

Two data comparison sets (5 and 6) modified only external tube length while maintaining internal tube length. These comparisons exhibited characteristics similar to the sets which simultaneously altered both external and internal tube length.

End View - Enlarged Size



Row No.

(32) 0.422 in. Dia.	1	(32) 0.453 in. Dia.
(32) 0.332 in. Dia.	2	(32) 0.348 in. Dia.
(16) 0.562 in. Dia.	3	(16) 0.594 in. Dia.
(16) 0.362 in. Dia.	4	(16) 0.391 in. Dia.
(1) 1.332 in. Dia.	5	(1) 1.415 in. Dia.

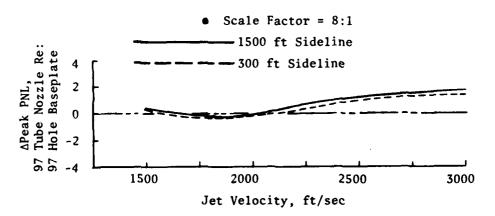
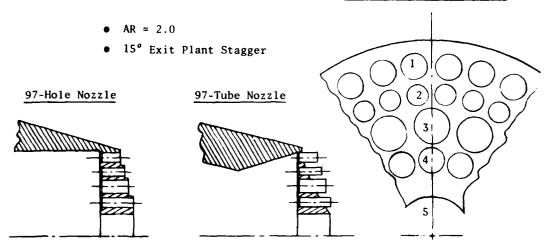


Figure F-5. Effect of Tube Length Variation on 97-Tube Nozzle Vs. 97-Hole Baseplate.

End View - Enlarged Scale



Row No.

1	(32) 0.453 in. Dia. Holes/Tubes on 6.07 in. Dia.
2	(32) 0.348 in. Dia. Holes/Tubes on 5.03 in. Dia.
3	(16) 0.594 in. Dia. Holes/Tubes on 3.93 in. Dia.
4	(16) 0.391 in. Dia. Holes/Tubes on 2.71 in. Dia.
5	(1) 1.415 in. Dia. Center Hole

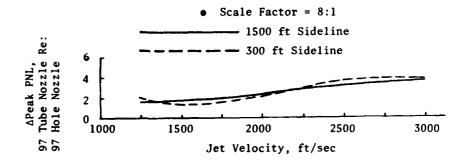
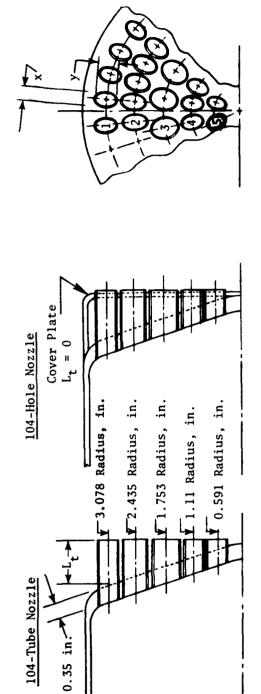


Figure F-6. Effect of Tube Length Variation on 97-Tube Vs. 97-Hole Nozzles.



						•
$L_{t}/(x+y)/2$	3.06	2.09	1.23	1.18	99.0	2500
ľ,	1.11	68.0	0.65	0.43	0.24	y, ft/
y (in.)	0.465	0.535	0.589	0.465	0.465	2000 Jet Velocity, ft/sec
x (in.)	0.260	0.317	0.466	0.260	0.260	Jet
No. Tubes	32	32	16	16	8	1500
Row No.	1	2	3	4	3:	104 Tube Re
	-					VPeak PUL,

- 2400 ft Sideline

-160 ft Arc

 $AT = 338 \text{ in.}^2$

Figure F-7. Effect of Tube Length Variation on 104-Tube vs. 104-Hole Nozzles.

From an aerodynamic-performance viewpoint, tube length (and resultant ventilation capability) is a prime consideration (see Section 5.0 of the text). Short tube length inhibits flow entrainment, decreases base pressure, and increases the base drag component of system thrust loss - normally the most significant system performance loss mechanism. Increasing tube length removes the lowpressure region from the base area and systematically decreases base drag; however, internal tube pressure loss (due to friction, internal shock, etc.) becomes greater if the tube is not designed optimally. This loss is generally of much less significance than base drag. Mechanical implementation of a deployable/stowable suppressor, however, generally dictates allowable tube length. In most system considerations, an array in which all tubes are of similar length is not readily stowable within a central plug or secondary ejector envelope. The empirical data presented herein suggest that the tube length of the outer row is of primary importance, and reducing effective tube lengths for internal tube rows is a viable alternate to the full array of equal-length tubes. Penetration of the entrained air to the center of the tube array, to enhance mixing for improved suppression and to alleviate low base pressure for improved aerodynamic performance, then becomes a consideration of tube size, area ratio, and tube spacing.

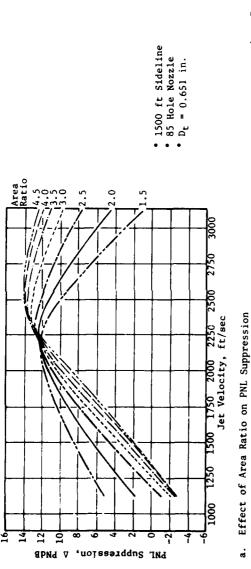
Tube Size Equity and Spacing Uniformity

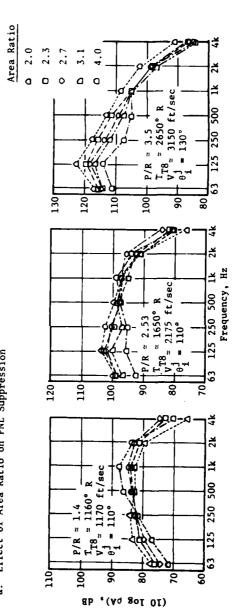
The M*S correlation for multitube nozzles assumes all tubes are of equal diameter, D_t , and are spaced uniformly in an equilateral, triangular array within a hexagonal pattern. This section considers variations from this norm. Additionally, changes in the center tube cluster using a center hole (either round or segmented) or center plug are considered; each is normally considered to accommodate a particular nozzle system or means of realistically implementing a multitube suppressor.

Categorically, data show that uniform tube size and spacing are prerequisites for better suppressor designs; however, these optimal designs are generally not readily implementable in a realistic deployable/stowable suppressor. Additionally, they are generally not optimized for aerodynamic performance because the ventilation flow to the central base region is inhibited by the uniformly spaced outer tube rows.

Optimal acoustic suppression results from establishing a uniform coalescing plane for the individual jets to merge into a single jet. Dominance of either premerged individual jet noise source, postmerged jet noise sources, or a mixed equality of both, is primarily dependent on jet thermodynamic conditions, the number of tubes for a given flow area, and suppressor area ratio. Controlled parametric tests, Figure F-8 (from Reference 2), for area ratio variation at fixed tube number, flow area, and jet thermodynamic conditions have shown that:

• At low jet velocities, high area ratio suppressors are less effective than low area ratio suppressors. When the nozzle is operated at subcritical pressure ratios, the highest frequency noise sources are in the immediate vicinity of the nozzle exit plane, radiating from the individual premerged jets. The larger the area ratio, the more





(Octave-Band SPL) -

b. Effect of Area Ratio on Spectra

Figure F-8. Effect of Area Ratio on Sideline PNL and Spectra.

20

distinct is the identity of the individual jets due to greater center-to-center spacing. The individual jets have a greater ambient-air entrainment capability so that mixing and velocity decay rates are enhanced, effecting lower merged velocity and reduced postmerged low-frequency noise. Additionally, the larger spacing in the outer tube rows diminishes premerged jet shielding effectiveness and enhances the high-frequency noise dominance. Decreasing area ratio improves outer tube row shielding, reduces ambient air entrainment and resultant velocity decay rates, and causes the individual jets to merge sooner while they are at a higher velocity. Therefore, the high-frequency, premerged jet noise is decreased at the expense of an increase in the low-frequency, postmerged jet noise.

- At high jet velocities, where nozzles are operated at supercritical pressure ratios, the noise sources are further downstream than for subsonic jets. Also, the peaks at the highest frequencies are radiated only after a characteristic distance downstream, in contrast to the subsonic operation for which highest frequency noise sources were in the vicinity of the nozzle exit. At these high-velocity conditions, opposing trends to low jet velocity exist; i.e., higher area ratio suppressors are acoustically more efficient. Peak noise spectra are solely low-frequency, postmerged-jet-noise controlled. Decreasing the area ratio to compact the tube array forces quicker merging at a higher jet velocity and smaller effective merged jet diameter. The higher merged velocity results from a combination of (a) reduced entrained mass flow due to the smaller center-to-center tube spacing and (b) the shorter distance prior to merging in which the jet mixes and decays.
- Intermediate jet velocity conditions exhibit a crossover of data trends with suppressor area ratio. The location of the trend change is influenced by the overriding impact of either pre- or postmerged jet noise.

Because of these phenomena, changes in tube size and spacing have less impact at lower jet velocity (particularly if outer row tube size and spacing are maintained) because the high-frequency-dominated peak-noise is from the vicinity of the tube exit where the outer tube row still shields noise from the internal plume. Conversely, at higher velocity the low-frequency noise stems primarily from the postmerged jet, and alterations in tube size and spacing (which change the uniformity of merging) extend the low- to mid-frequency source locations, resulting in less suppression. Also, alteration of the central tube bundle to include a center hole or plug with annular flow produces a similar effect; i.e., uniform merging and velocity decay are destroyed, turbulent mixing zones are extended, low-frequency noise increasingly dominates the spectra, and suppression decreases.

Empirical data illustrating these facts are presented and discussed in the following paragraphs.

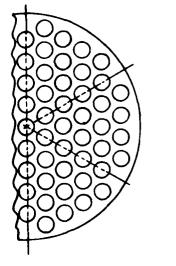
Set 1 - This set, Reference 2 and Figure F-9, compares one model of the series used within the parametric area-ratio study, i.e. the uniformly spaced 85-hole nozzle of AR = 3.1 with uniform hole diameter (D_t = 0.651 in.),

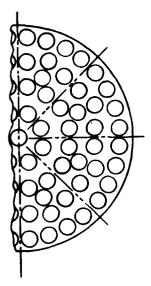
85 Hole Nozzle

- Equal Hole Size, $D_t = 0.651$ in.
- Uniform Spacing
- AR = 3.1

89 Hole Nozzle

- Equal Hole Size, D_t = 0.453 in.
- Nonuniform Spacing
- $\bullet \quad AR = 3.0$





- Scale Factor = 8:1
- 1500 ft Sideline

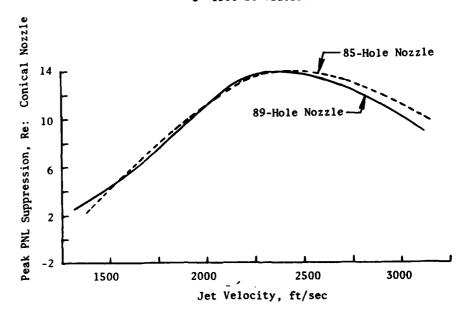


Figure F-9. Effect of Tube Spacing Uniformity on 85- and 89-Hole Nozzles.

to an 89-hole nozzle of AR = 3.0 with uniform diameter (D_t = 0.453 in.) but nonuniformly spaced. As illustrated in the figure, the spacing is varied inside the outer row (which is still uniform). The change in peak noise suppression relative to a conical nozzle is almost nonexistent, particularly at low jet velocity. At higher velocity, a maximum suppression decrease of \simeq 1 APNL occurred for the nonuniform 89-hole nozzle relative to the uniformly spaced 85-hole nozzle.

Set 2 - Boeing data, Reference 67 and Figure F-10, for tube arrays of higher area ratio and lower tube number than Set 1 (i.e., AR = 3.3 and 4.5, each with 37 tubes), illustrate the difference between close-packed, uniform arrays and radially aligned arrays. The radially aligned pattern allows better access to ambient air for entrainment throughout the tube bundle; however, the sideline peak PNL data show a loss of suppression relative to the close-packed array. The AR = 3.3 model set shows approximately 1 Δ PNL, and the AR = 4.5 shows about 2 Δ PNL change. Deviation in the uniformity of tube spacing is greater than for model Set 1 (above), and loss in noise suppression is slightly greater; however, the higher area ratio with large center-to-center spacing is felt to somewhat negate the influence of nonuniform spacing. Additionally, the radial tube arrangement provides one-on-one tube shielding, and only 12 tubes are in the outer row compared to 18 for the close-packed array. Shielding impact should thus be maintained.

Set 3 - This model set, Reference 2 and Figure F-11, compares two arrays of unequal hole size and nonuniform spacing to an equally sized/uniformly spaced array. Each model has 97 holes and AR = 2.0. Model 1 is of uniform hole diameter and spacing. Model 2 has equal outer-row hole size, $D_{\text{t}}=0.422$ in., on a uniform spacing but varies the spacing and size of each internal row. Model 3 has a somewhat larger hole size, $D_{\text{t}}=0.562$ in., for the primary flow area, has a large center hole of $D_{\text{t}}=1.332$ in., and randomly uses smaller holes throughout the array. Models 2 and 3 are designed to represent suppressors which would be deployed on pivoting-flap systems within a secondary ejector, thus approaching a more realistic, implementable design than Model 1.

Peak noise suppression characteristics for Models 2 and 3, relative to Model 1, are the same, as shown at 300 and 1500-ft sidelines in Figure F-11. At low jet velocity the three arrays have nearly equal suppression potential, near 5 to 6 ΔPNL at 1500-ft sideline, but suppression becomes poorer as Vj increases; nonequal size and nonuniform spacing degrade up to 5 ΔPNL at 2750 to 3000 ft/sec.

<u>Set 4</u> - Within a given tube nozzle array, designed to be deployed/ retracted on a hinged-flap system, design of a center void area where flaps meet is also critical to suppressor performance. Two GE 96-tube models, one as shown in Figure F-12 and the other per Reference 2, have identical design for the 96 tubes of the array, but the center hole, remaining when the 16 hinged flaps are deployed in the suppressed mode, was altered in size from 1.764 to 1.415 in. by slightly lengthening the flaps. The 36% reduction in central jet flow area alters the extended jet structure sufficiently to increase noise suppression by up to 2 ΔPNL at 300 and 1500-ft sidelines.

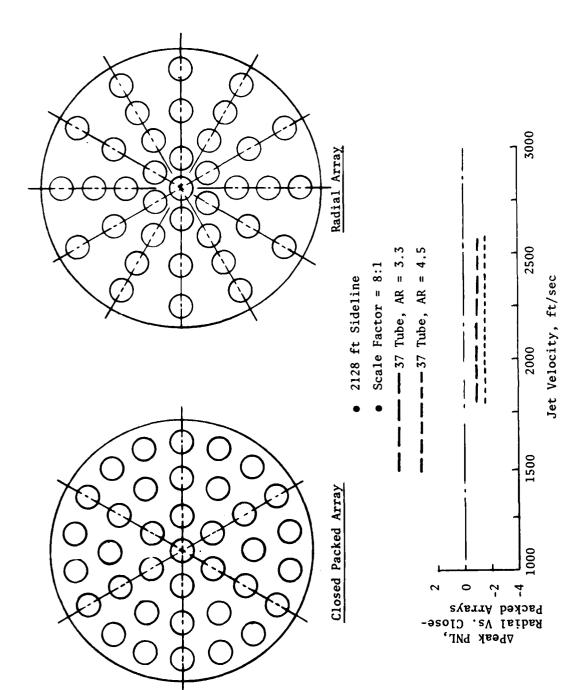
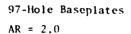


Figure F-10. Effect of Tube Spacing Uniformity on Boeing 37-Tube Radial and Close-Packed Arrays.



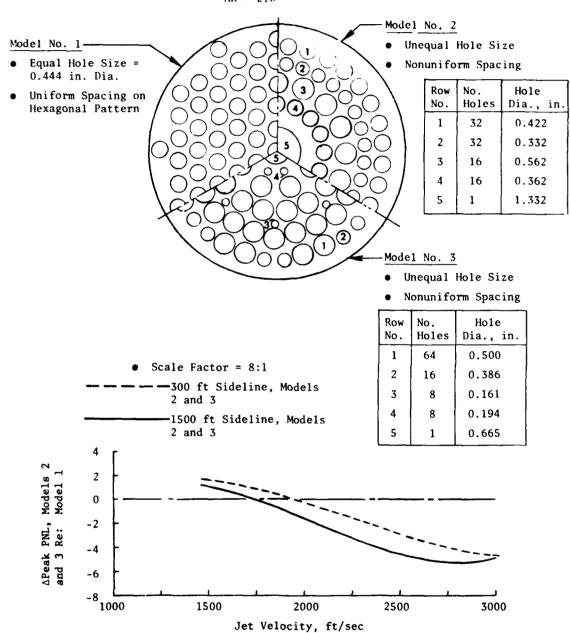
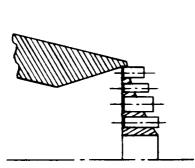
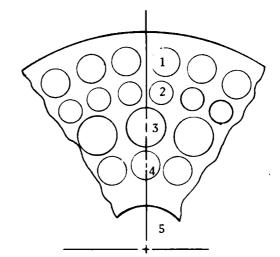


Figure F-11. Effect of Tube-Size Equity and Spacing Uniformity on 97-Hole Baseplate.

End View - Enlarged Scale

- \bullet AR = 2.0
- 15° Exit Plane Stagger





Row No.	No. Tubes	Tube Dia., in.
1	32	0.453 on 6.07 in. Dia.
2	32	0.348 on 5.03 in. Dia.
3	16	0.594 on 3.93 in. Dia.
4	16	0.391 on 2.71 in. Dia.
5	1	1.415 or 1.764 in. Center Hole

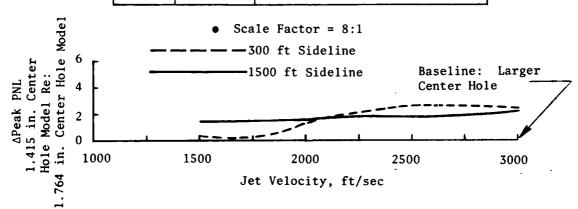


Figure F-12. Effect of Tube-Size Equity on 97-Tube Nozzle with 1.415 and 1.764-in. Diameter Center Holes.

Set 5 - Further alteration of the center hole of a GE 97-hole, AR = 2.0 nozzle (similar in design to the 96-tube-plus-center-hole configuration of data Set 4) to accommodate an 8-lobe Greatrex center hole of equivalent flow area is seen in Figure F-13 and Reference 2. For implementation purposes this would be accomplished by extending every other flap of the 16-flap base region to nearly 100% penetration to the nozzle centerline. Essentially the core jet, which forced extended low-to-midfrequency noise source regions, is now segmented to allow decay rates and merging more compatible with the basic tube array. Sideline noise reductions relative to the circular hole are enhanced by a nominal 2 Δ peak PNL.

Set 6 - Within the same framework of design as data Sets 4 and 5, Boeing, Figure F-14 and Reference 67, replaced the central 19 tubes of a 61-tube close-packed array of AR = 3.3 with a center hole of 3.9-in. diameter. The outer two tube rows, 41 tubes total, maintain the same tube size and pattern as the 61-tube array. Sideline peak PNL suppression for the system is reduced from 11 to 5 at \approx 1900 ft/sec and from 14 to 4 at \approx 2550 ft/sec, or, as seen in Figure F-14, a loss of from 6 to approximately 10 dB as jet velocity increases, due to the dominance of the core jet extended noise sources. Changes in spectra occur primarily toward low-to-midfrequency domination.

Set 7 - The 42-tube, two-row-cluster design of data Set 6 was also used by Boeing, Reference 67 and Figure F-15, to incorporate a center plug of 12° half angle. The center plug geometry was altered to effect annulus heights of 0.383, 0.533, 0.800, and 1.067 in. The 0.383 in. annulus/42-tube model has the same equivalent flow area as the basic 61-tube array. The 0.533 in. annulus height has the same characteristic flow dimension as the individual tubes, i.e., $D_{\rm t}=0.533$ in. The 1.067 in. annulus has annular flow area equivalent to that of the peripheral 42-tube array.

As seen from sideline data in Figure F-15, peak PNL suppression, relative to the full 61-tube array, is progressively eroded as core annulus height increases. Increasing the core annulus size negates the effectiveness of a common, uniform, merging plane of the base tube bundle, increasingly extending the central jet plume and generating low-to-midfrequency dominance in the noise spectra.

In summary, the empirical data comparisons have elicited the following guidelines:

- Slight variance from equal tube size or from uniform center-tocenter spacing in an equilateral triangular pattern associated with a hexagonal array will not significantly alter suppression potential. This is particularly true at low velocity if tube size and spacing in the outer row are maintained uniform.
- Moderate variance from equal tube spacing, particularly for fairly high-area-ratio systems as seen in data Set 2, will only moderately decrease suppression, if the change is from a close-packed to a radial array which still maintains good peripheral-tube noise shielding.

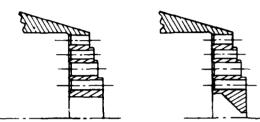


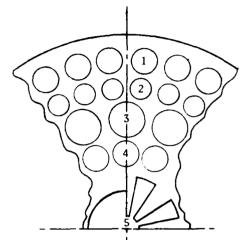
 $\bullet \quad AR = 2.0$

• 15° Exit Plane Stagger

End View - Enlarged Scale

1.415 in. Dia. 1.415 in.
Round Center Hole Greatrex Center Hole





Row No.	No. Holes	Hole Dia., in.
1	32	0.453 on 6.070 in. Lia.
2	32	0.348 on 5.030 in. Dia.
3	16	0.594 on 3.932 in. Dia.
4	16	0.391 on 2.708 in. Dia.
5	1	1.415 Center Hole or 8-Lobe Greatrex

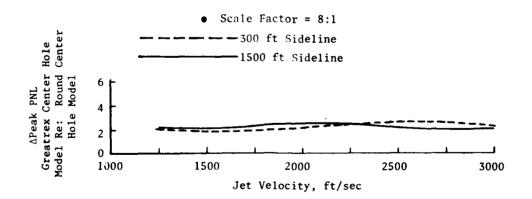
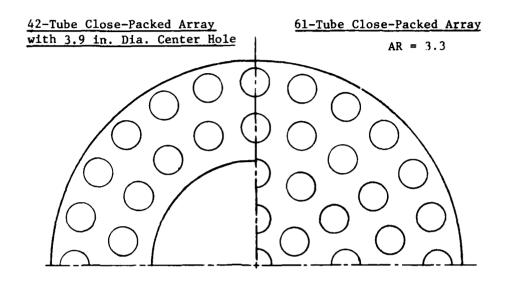


Figure F-13. Effect of Tube-Size Equity on 97-Hole Nozzle with 1.415-in. Round and Greatrex Center Holes.



- Scale Factor 8:1
- 2128 ft Sideline

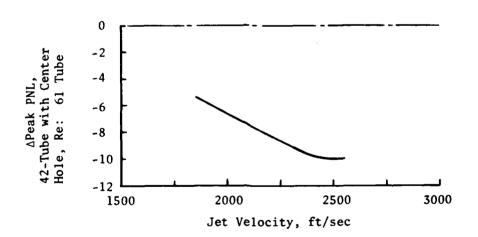
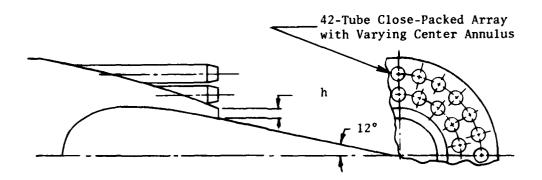


Figure F-14. Effect of Tube-Size Equity on Full Tube Array vs. Tubes with Center Hole.



- Scale Factor = 8:1
- 2128 ft Sideline

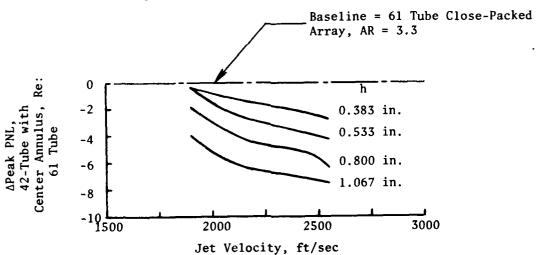


Figure F-15. Effect of Tube-Size on Full Tube Array vs. Tubes with Varying Center Annulus.

- Large variance from equal tube size and uniform center-to-center spacing will seriously degrade suppression potential as seen for data Set 3, particularly at mid-to-high V_i .
- Incorporation of a center hole or plug resulting in an annular flow normally degrades suppression potential. Comparison of the design under consideration to the data sets and configurations discussed herein is suggested as a guideline to minimize impact on acoustic performance.

Tube Exit Plane Stagger

The M*S model assumes coplanar termination of tube ends for the tube array. Variance from coplanar may introduce a criterion detrimental to suppression optimization, due to extension of the merging region of the individual jets and the corresponding enhancement of low-to-midfrequency noise generation. Stagger of the tube exit plane may, however, be necessary to facilitate a stowable design. Several empirical data sets are presented, as follows, to qualitatively assess the impact of such a change.

Set 1 - Figure F-16 and Reference 2 compare results of 30° and 60° tube exit plane stagger to a coplanar 72-tube array of similar AR = 3.0 and tube L_t/D_t \simeq 1.7. Sideline PNL changes, relative to the Model 1 coplanar system, indicate suppression losses of 1 to 2 Δ PNL in the mid-to-higher velocity design region for the 30° staggered Model 2 and an additional \simeq 1 dB loss for the 60° staggered Model 3.

Spectra changes at peak noise angle, per Figure F-17, are seen to be primarily low-to-midfrequency range influenced due to the extended merging/mixing regions.

Set 2 - This model set, Figure F-18 and Reference 2, is for an 85-tube array of AR = 3.0. The first of the two models has a coplanar exit and the second has an exit plane stagger angle of 30°, maintaining internal tube and inlet geometries within the uniformly spaced hexagonal pattern. Sideline noise comparisons indicate up to slightly in excess of 2 Δ PNL suppression loss for the 30° stagger relative to the coplanar exit model; trend and magnitude are consistent with data Set 1. Changes in spectra impacting the PNL decrease were again within the low-to-midfrequency range.

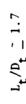
Tube Base Plane Stagger

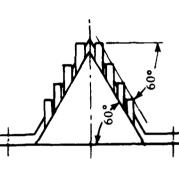
As with exit plane stagger, the tube array base plane may be staggered to facilitate mechanical implementation. Again, the M*S model assumes good design practice has been followed in selecting tube length, and the model implicitly assumes the base plane normal to the nozzle centerline (it was developed using such a data base). The data set of Figure F-19, from Reference 2, includes three (72-tube, AR = 3.0) nozzles of different base plane stagger: 0°, 30°, and 60°; the tube exits are coplanar. The minimum tube length-to-

(3)



AR = 3.0





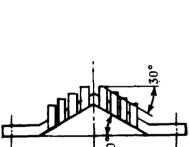
End View Models 1, 2 and 3:

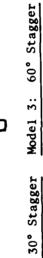
Baseline = Model 1, Coplanar

Model 2, 30° Stagger

Model 3, 60° Stagger

3000



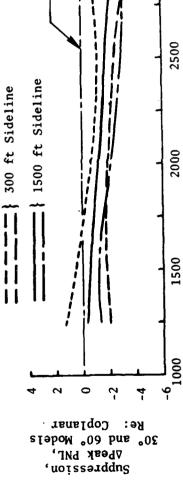


Model 2:

Coplanar

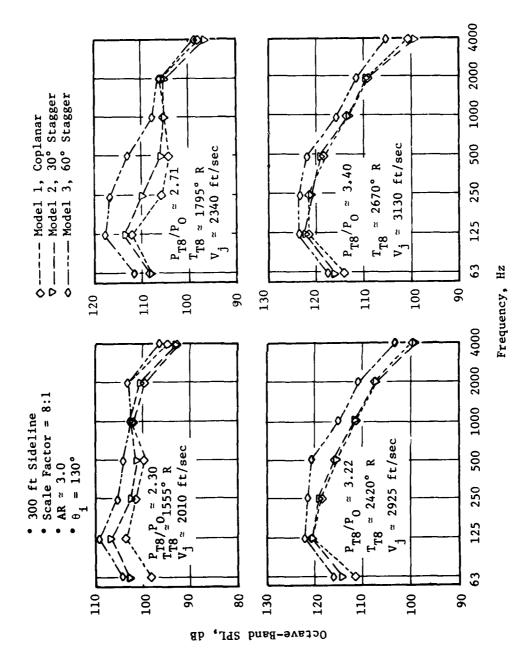
Model 1:





Jet Velocity, ft/sec





Effect of Tube Exit Plane Stagger on Peak Noise Angle Spectra Comparisons at Four Jet Velocities. Figure F-17.

1

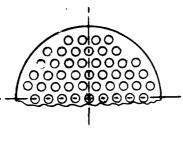
85-Tube Nozzles

AR = 3.0

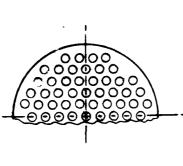
30° Exit Plane Stagger Angle

Coplanar Exit

End View - Coplanar and 30°

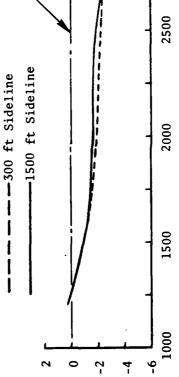


30°



Scale Factor = 8:1

-Coplanar Baseline



3000

∆Peak PNL, 30° Model, Re: Coplanar

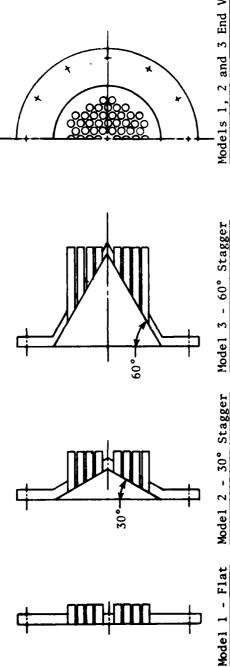
Effect of 30° Tube Exit Plane Stagger Relative to Coplanar. Figure F-18.

The same was the same of the s

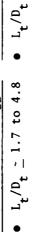
Jet Velocity, ft/sec



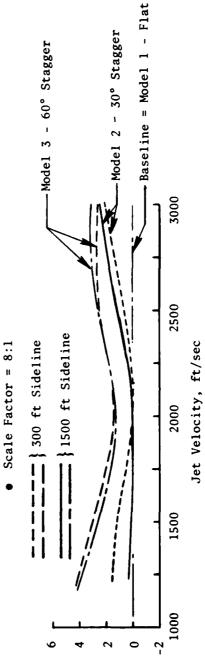




Models 1, 2 and 3 End View







30° and 60° Models, YPeak PNL,

Effect of 30° and 60° Tube Base Plane Stagger Relative to Flat. Figure F-19.

diameter ratio, L_t/D_t , is 1.7 in each case; the maximum L_t/D_t depends upon the stagger angle; it is 4.8 for the 30° case and 10.8 for the 60° case.

Sideline peak PNL data comparisons relative to the flat baseplate of Model 1 indicate: (a) suppression for the staggered baseplate is equivalent to or greater than the flat baseplate; (b) suppression gain for the Model 2, 30° base stagger system ranges from 0 to 2 ΔPNL with greater impact at high V_j ; and (c) suppression gain for the Model 3, 60° base stagger system ranges from 1.5 at midrange V_j to 4 at low V_j and 3 at high V_j . Peak noise angle spectra changes, Figure F-20, are primarily in the low-to-midfrequency range, particularly at mid-to-high V_j due to the enhanced air entrainment, more complex mixing, and lower merged V_j . At lower V_j the high-frequency, premerged jet noise is also somewhat reduced.

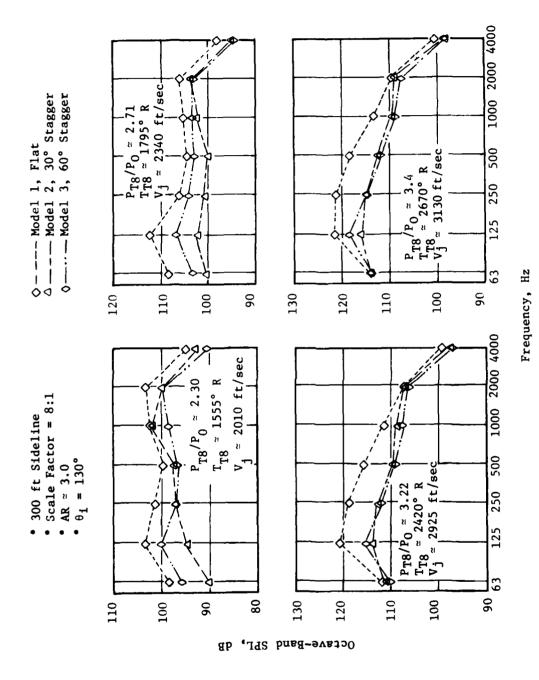
Trends of acoustic results from this study are consistent with those of the tube-length study. Variation of base plane stagger angle, while maintaining a coplanar exit, in essence maintains moderate to long tubes in the outer row while shortening tubes in the central part of the array. This allows for easier base ventilation (as turning angle for the flow is reduced) and possibly greater flexibility for mechanical implementation (shorter tubes are normally easier to stow). Placement of tubes on a staggered or evencontoured baseplate may thus allow a viable method for mechanical design with improved aerodynamic performance while deriving acoustic benefits commensurate with good design practice with regard to the length of tubes.

Tube Canting

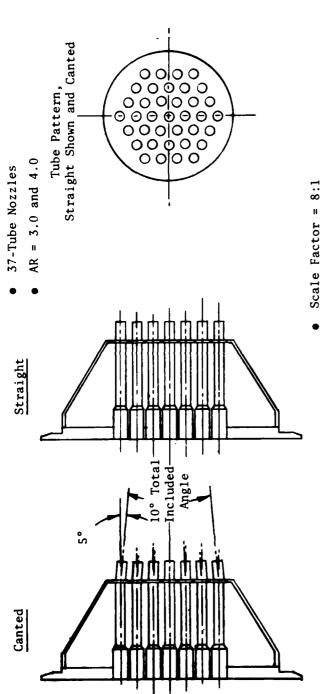
Canting the outer tube row with respect to the nozzle centerline can be accommodated within the M*S correlation model. Canting of the tubes outward aerodynamically simulates a larger area ratio and may enhance suppression; however, when considering an ejector application, care must be exercised to avoid direct flow impingement on the ejector lining or flow spillage back through the ejector inlet. The following paragraphs discuss data from several nozzles tested to assess tube canting which was more complicated than that accounted for in the M*S model.

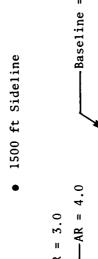
Set 1 - Reference 2 documents the results summarized in Figure F-21 for two 37-tube configurations (of AR = 3.0 and 4.0) having tubes canted within the vicinity of the exit. The degree of canting varied radially, from 9° at center to 5° in the outer row, to intersect the projected centerlines through the apex of a 10° included-angle cone. Straight end-tube arrays of the same flow area and area ratio were tested as baselines. Scaled sidine data indicate losses of 0 to \simeq 3 ΔPNL for the canted-tube nozzle, the greater loss associated with higher area ratio. Inward tube canting forces merging of the individual jets closer to the nozzle exit plane at a higher merged V_{j} and extends the merged-jet, turbulent-mixing-noise generation region. Therefore, spectra changes (particularly at higher V_{j} conditions) are primarily in the low-to-midfrequency region.

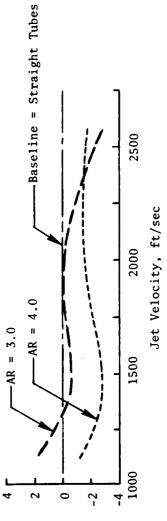




Effect of Tube Base Plane Stagger on Peak Noise Angle Spectra Comparisons at Four Jet Velocities. Figure F-20.







∆Peak PNL, Canted, Re: Straight Tubes

Effect of Tube Canting on 37-Tube Configuration. Figure F-21.

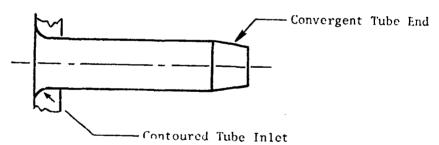
Set 2 - Boeing (Reference 67 and Figure F-22) considered canting the outer tube row of a 61-tube array, AR = 3.07, such that the tubes were alternately canted outward 12° and 3.8°. Relative to a straight-tube configuration, this nozzle produced a minor change in sideline PNL suppression. Indication at higher V_j , above 2500 ft/sec, was for slight suppression loss relative to the straight tubes.

Tube Internal Geometry

Variations from the conventional, circular cross section for the full tube length have been observed to change performance, particularly from an aerodynamic-thrust viewpoint. A tube of continuous circular cross section

may induce (a) high entrance losses, (b) P_T loss due to shock structure within the tube, and (c) increased skin-friction loss due to higher internal flow Mach number. These internal flow conditions establish the aerodynamic effective flow area and normally result in low discharge coefficients. Thus, physical flow area must be increased to accommodate a design of fixed mass flow.

Contoured tube inlets and convergent tube ends may be considered to

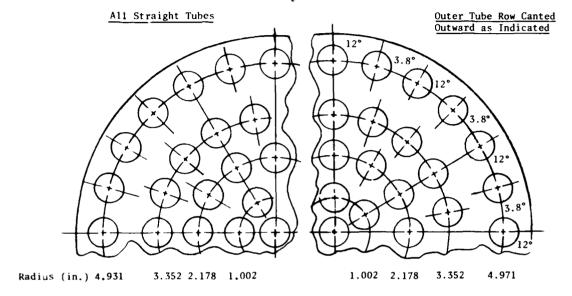


alleviate the problems associated with straight tubes. A good-design-practice rule-of-thumb has been to use 30% flow area convergence in order to assure that (a) entrance Mach number is subsonic and entrance losses are minimized; (b) internal flow Mach No. is lowered and, correspondingly, skin friction P_T loss is reduced; (c) internal shock P_T loss is not present; (d) the throat plane is positioned at the physical exit plane, thereby providing a reasonable discharge coefficient. Static thrust degradation normally associated with the above considerations may be on the order of 2 to 3% ΔCf_g .

Introduction of a convergent tube end, however, involves other considerations, namely:

EL!

- 61 Tubes
- $\bullet \quad AR = 3.07$
- $D_t = 0.777 \text{ in.}$



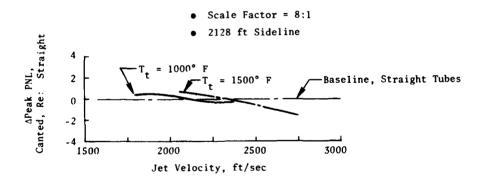
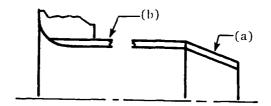


Figure F-22. Effect of Tube Canting: Boeing 61-Tube, Canted-Outer-Row Configuration.



(a) introduction of an additional base area in the vicinity of low pressure created by the high velocity flow, and (b) tube diameter/area leading to the convergent tube end is increased, thereby reducing flow-area between tubes available for ambient-air entrainment. Several Boeing designs, Reference 61, have considered maintaining nonconvergent tubes within the outer row as a trade for increasing entrainment area. Partial alleviation of base drag associated with condition (a) above may be realized by a gradual tube taper from entrance to exit planes. A further aid to improve ventilation is the use of elliptical tube cross section with the major axis directed radially toward the nozzle center to maximize flow entrainment area. This can be done for (a) the full tube length as seen in Figure F-7 for the 104-tube nozzle or (b) the tube base and with smooth transition to circular, convergent, tube ends, Reference 67.

Tube End Planform

The M*S model correlation is based on circular tube cross section at the exit plane. Other planform shapes may be considered, either to enhance acoustic suppression or to accommodate improved ventilation for lower base drag and better aerodynamic performance. For the first category, use of Greatrex ends within several tube arrays indicated substantial suppression improvement but with accompanying high thrust decrement. For the second category, elliptical and trapezoidal planform shapes have been considered. Several of the data comparison sets are discussed as follows.

Set 1 - Within two 37-tube, equal-spaced, hexagonal arrays of AR = 3.0 and 4.0, 12-lobe Greatrex tube terminations were evaluated relative to circular/convergent and circular/straight tubes, Reference 2 and Figure F-23. The Greatrex terminations penetrated deeply into the center of each flow element. Sideline peak PNL suppression for the AR = 3 Greatrex relative to plain-round tubes and for the AR = 4 Greatrex relative to plain-round and convergent tube arrays indicates suppression improvements of 4 to 7 PNdB, fairly uniform with jet velocity variance. Suppression for the AR = 3 Greatrex relative to plain-round tubes is somewhat greater than for AR = 4.0 across the entire V_j range.

Changes in spectra at peak PNdB noise angle for jet velocities from 1325 to 2525 ft/sec are shown in Figure F-24 and exemplify that the impact is generally very broad but greatest in the midfrequency range. Change in impact between AR = 3 and 4 generally shows AR = 3 to have greater suppression at high frequency than AR = 4.0 as well as in the low-frequency range at the high velocity end.

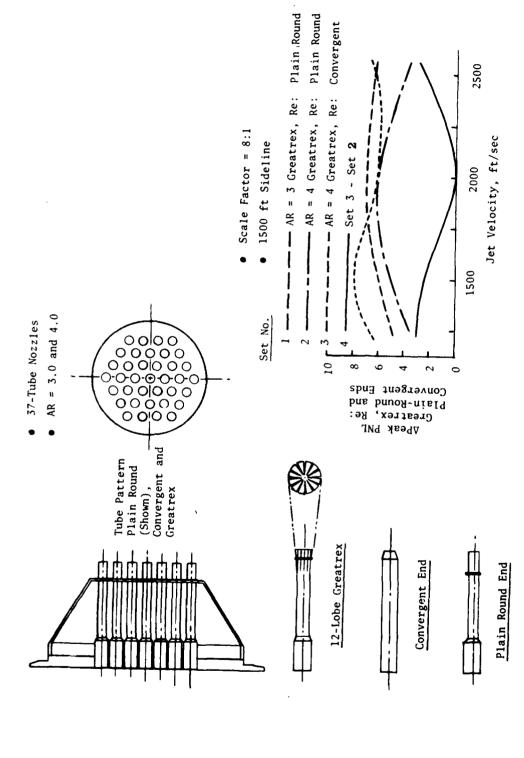
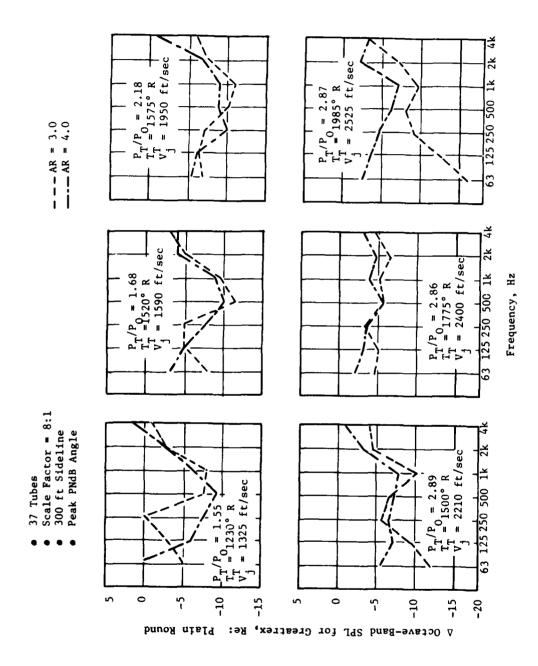


Figure F-23. Effect of Tube End Planform: 37-Tube Greatrex Relative to Plain-Round and Convergent Ends.

The state of the s



Effect of Tube End Planform on Peak Noise Angle Spectra Changes for Greatrex Relative to Plain Round. Figure F-24.

(311)

AND THE PARTY OF T

Set 2 - Greatrex tube ends of 8-lobe design were used on a more realistic 85-tube system, Figure F-25 and Reference 2, and are compared to a plain, round tube array of the same physical flow area and tube pattern. Each is of $AR \simeq 3.0$ and 30° exit plane stagger. Suppression change for the Greatrex, relative to plain round, at 300 and 1500-ft sidelines shows up to 4 APNL greater suppression for the Greatrex, primarily at low and midrange jet velocity. At higher jet velocities the Greatrex lost the acoustic performance edge and became somewhat noiser than the plain, round-tube array. Spectra changes relative to the plain-round-tube array, Figure F-26, for various jet velocities from 1700 to 3055 ft/sec, show suppression only in the mid-to-high frequency range. At the lower jet velocities shown, low-frequency noise for Greatrex and plain, round tubes is nearly equivalent; high frequency is suppressed well by the Greatrex. As jet velocity increases, the low frequency of the Greatrex rises above the plain-round-tube bundle, and the mid-to-highfrequency spectra loses suppression until the systems are nearly equal at the highest V_i .

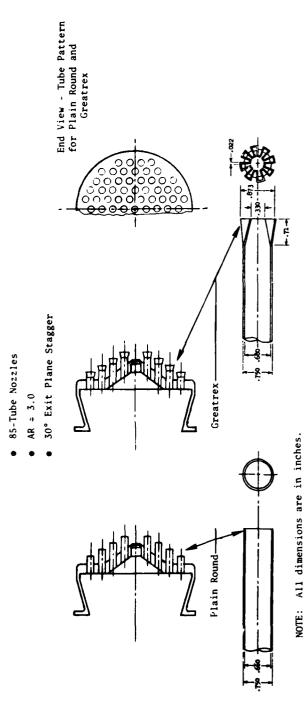
Set 3 - In an effort to improve ventilation and to enhance mixing rates, a 97-trapezoidal-shaped-hole baseplate model was tested in comparison to a 97-circular-hole baseplate; see Figure F-27. Center-to-center hole spacing was held constant as was flow area per hole. By making trapezoidal hole shapes in a radial pattern, flow area available for ambient-air entrainment between hole clusters on simulated flaps is increased. Peripheral area of trapezoidal holes is greater than circular holes, so potential for improved aerodynamic flow mixing is present. Sideline peak PNL suppression relative to a conical nozzle, however, shows only minor variance in levels achieved by both systems.

Chute/Spoke Element Selection

Initial multielement annular suppressor studies were focused primarily on the spoke concept because it was fairly easy to mechanically implement, light-weight, and stowable on the plug surface in the nonsuppressed flight mode. The chute concept evolved with time as a means to improve aerodynamic performance. Low base pressure with resultant base drag is the greatest contributor to chute or spoke thrust degradation; therefore, improving performance through use of well-ventilated chutes precluded the use of spokes instead of chutes in many applications. However, with the accompanying depth for ventilation, chutes are considerably more complex to implement in design, weigh more, and are more cumbersome to retract and stow within the plug centerbody. Thus, the choice of chutes or spokes is normally made after the particular application is reviewed for (a) suppression required, (b) thrust degradation limits during the suppressed mode, (c) mechanical implementation, actuation, and storage, (d) weight, and (e) overall impact to system and mission.

Previous test work with induced flows indicates suppression gain by means of induced/mixed ambient-air entrainment is a function of the induced flow proportionality to the core jet mass flow. Induced pumping through





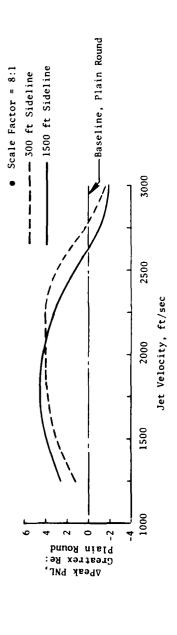


Figure F-25. Effect of Tube End Planform on 85-Tube Greatrex Relative to Plain Round.

(312)

4k

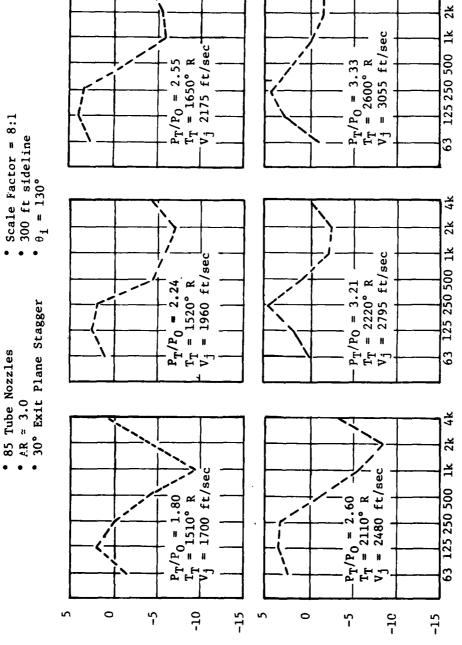


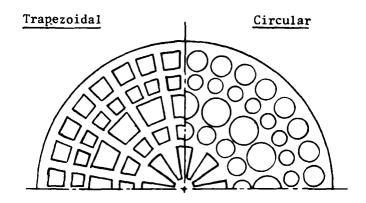
Figure F-26. Effect of Tube End Planform on 85-Tube Greatrex Spectra Changes Relative to Plain Round.

Frequency, Hz

△ Octave-Band SPL, Greatrex Re:

Plain Round

- 97-Hole Baseplate
- $\bullet \quad AR = 2.0$
- Greatrex Center



- Scale Factor = 8:1
- 1500 ft Sideline

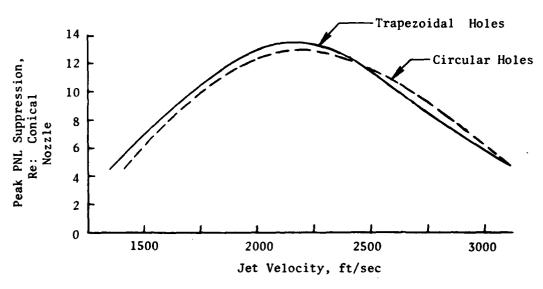
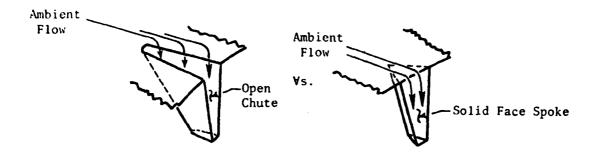


Figure F-27. Effect of Trapezoidal and Circular Tube End Planform on 97-Hole Baseplates.



vented-to-ambient chutes (in comparison to spokes with minimal depth only instead of area exposed to ambient surroundings) causes initial mixing, temperature and velocity decay, lower mixed-jet velocity at merging and, therefore, shorter turbulent-mixing and subsonic-decay regions. This should result in lower low-frequency noise levels. The magnitude of suppression gain of chute over spoke is partially a function of the ambient-air-entrainment capability; however, as previous work has indicated (Reference 2), a substantial portion of the primary mass flow must be induced and mixed to anticipate even a moderate suppression gain.

Allowing for flow induction through the chutes also permits the local static pressure, P_s (to which the individual core jet flows expand), to be higher (closer to external ambient pressure) than that of the local P_s of the spoke base, which is severely sucked down below external ambient pressure. Expanding the flow to a higher local P_s can lower the jet expansion angle and continue the flow identity (as individual jets prior to merging) to a greater length/volume than that of the spoke nozzle and, at the same time, more thoroughly mix with the jet entrained flow. The longer length/greater volume of flow identifiable as discrete small jets, however, allows for increased high-frequency-noise generation. This is particularly true at low V_j for subcritical-pressure-ratio operation where high-frequency-noise sources are in proximity to the nozzle exit plane. At high V_j for supercritical-pressure-ratio operation, where high-frequency-noise sources are removed from the vicinity of the jet exit, masking of high-frequency changes between spoke and chute may or may not occur, depending on relative axial source location.

The various physical flow changes introduced by chutes (i.e., greater entrained flow, better mixing, lower merged temperature and velocity, shorter turbulent mixing zone, higher local $P_{\rm S}$, and more pronounced identity of individual jets) should produce higher high-frequency/lower low-frequency noise at low $V_{\rm j}$, and lower high-frequency/lower low-frequency noise at high $V_{\rm j}$, than the spoke configurations if the rate of induced mass flow is sufficient to substantially impact mixing and decay rates. The dominance of either the high- or low-frequency portions of the spectra, and the degree of change between spoke and chute, establish the relevance in terms of change in subjective PNL.

Several empirical data sets are available to show the differences between vented chute designs and similar, nonvented spokes. Figure F-28a (from Reference 2) is for a 32-chute/spoke, AR = 2.0, comparison on a turbojet system. The spokes were a shallow 'V' design and on a low-radius-ratio, R_r =

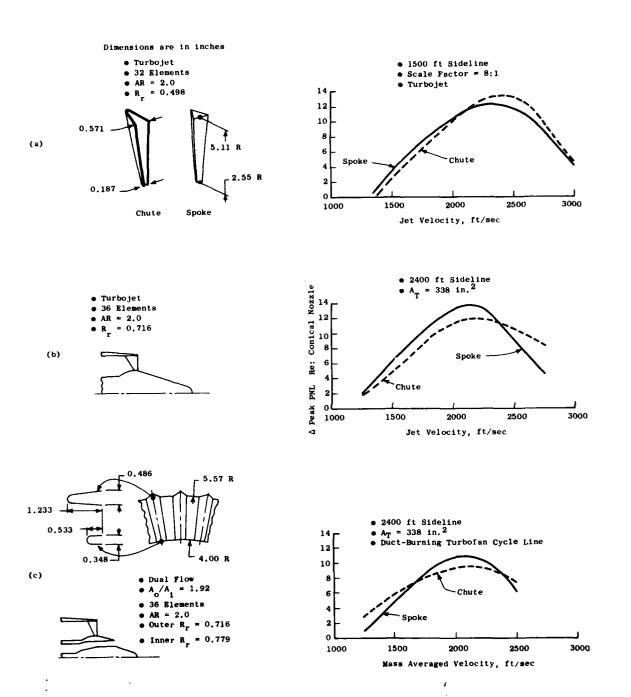


Figure F-28. Effect of Element-Type Variation.

0.498, annular suppressor. Sideline PNL suppression indicates fairly minor changes between element designs; however, the direction of the small changes is within the framework of the above discussion. Spectra comparisons at $V_j \simeq 1670$, 2010, and 2660 ft/sec, Figure F-29, indicate:

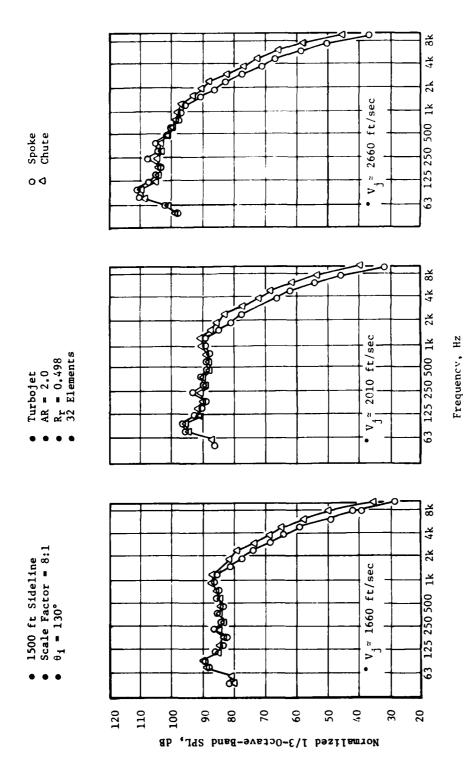
- At low V_j chutes have somewhat higher high-frequency noise and equivalent-to-spoke low-frequency noise. PNL suppression of chutes is lower because the high-frequency of the double-humped spectra dominates subjective PNL.
- At high V_j chutes have somewhat lower low-frequency noise and slightly higher high-frequency noise. The low frequency is dominant; therefore, chutes have somewhat better PNL suppression. The low-frequency changes indicate enhanced mixing. The high-frequency level increase indicates the chutes do retain individual-jet identity longer. The high-frequency levels are well below the dominating low frequency; thus, changes do not impact PNL.

Figure F-28 (b and c), from Reference 19, are for 36-element, AR = 2.0, $R_{\rm r}$ = 0.716, annular suppressors; (b) is for a turbojet system, and (c) is for a dual-flow system of $A_{\rm O}/A_{\rm i}$ = 1.92 and inner $R_{\rm r}$ = 0.779. Chutes were converted to spokes through the use of filler inserts; therefore, the physical depth of the element is maintained but with no open-to-ambient surface area. Changes in PNL suppression trends are again minimal; spokes maintain somewhat better suppression in midrange $V_{\rm j}$, and all three data sets indicate chutes are somewhat better at highest jet velocities. Review of spectra comparisons would again show minor changes in low-to-high-frequency regions; the degree of change and relevance to lower high-frequency dominance establish the impact on PNL.

As an overview, spoke or chute selection is more specifically dictated by aerodynamic-performance and mechanical-implementation considerations than by acoustic suppression capability. Once selection has been made, however, design of spoke or chute particulars should be performed with cognizance of the previously discussed considerations of noise sources, how they are altered by physical geometry changes, and the anticipated impact of the changes on final suppression level.

Chute/Spoke Exit Planform

Planform shape of a chute or spoke at the nozzle exit plane is important both to the acoustic and to the aerodynamic design. Planform is defined by the ratio of chute width at the shroud to width at the plug: $W_{O_C/S}/W_{I_C/S}$. Variation of planform can be exercised within the M*S model. Correlation of the model includes the spoke data base shown in Figure F-30 from Reference 2. For this particular comparison the planform shape is at $W_{O_S}/W_{I_S} = 1.0$ and 3.05 for parallel-sided and highly tapered spokes, respectively. The parallel-sided design exhibits a peak PNL suppression that is upwards of 2 PNdB better than the tapered-spoke counterpart. Suppression superiority of the parallel-



Spectral Comparison of 32-Element Spoke/Chute Configurations. Figure F-29.

MENNE ANTEN

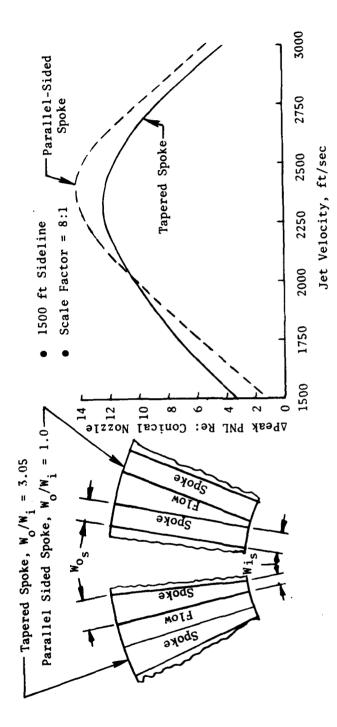


Figure F-30. Effect of Chute/Spoke Exit Planform Variation.

sided spoke design is maintained at the high jet velocity end ($\simeq 1$ PNdB better); however, at low jet velocity it is 1 to 1.5 PNdB poorer than the tapered configuration. The two systems performed equivalently in the 2000 ft/sec v_j vicinity.

Parallel-sided spokes allow for a much larger portion of the flow to be directed through the outer part of the annulus to aerodynamically simulate a higher area ratio. This is seen to be more effective in multielement nozzles at high jet velocities. At low jet velocity, where subcritical nozzle operation generates high-frequency noise in the vicinity of the exit plane, the highly flow-weighted outer annulus for parallel-sided spokes generates greater high-frequency content in the peak-noise-angle spectra. This results in decreased PNL suppression.

Of secondary importance, parallel-sided spokes allow for uniform separation between individual jets and a more consistent merging plane downstream of the exit plane. This is important for high V_j , supercritical nozzle operation where peak and high-frequency noise are generated further downstream from the exit-plane vicinity (see Section 3.2 of text). The more uniform merging plane shortens the turbulent mixing region and subsequently lowers low-frequency-noise generation, as observed in the peak noise spectra.

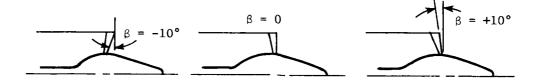
Aerodynamic performance loss is considerably greater for the parallel-sided spokes because they have greater base area at deeper penetration into the flow and are at much lower base pressure. The large loss, on the order of $\simeq 5\%$ Cfg, is not anticipated to be as large for deep-chuted designs where ambient-air pumping alleviates the low base pressure of the center region.

The above data comparison set would generally represent the limiting cases of W_O/W_1 variance; 3.05 is generally considered much too high for good design practice. More current multielement designs used the range of 1.25 $\leq W_O/W_1 \leq$ 1.50. Designs near or below $W_O/W_1 =$ 1.0 should not be considered because of the associated high aerodynamic performance loss.

Chute/Spoke Exit Plane Cant

The M*S model can accommodate exit plane cant angle variation for the chute/spoke family of suppressors. The model correlation considers the data and resultant acoustic performance variations as shown in Figure F-31 (from Reference 2). The exit plane is canted plus (+) and minus (-) 10° from the base configuration which has the throat plane normal to the nozzle centerline. This produces a shift in the velocity at which peak suppression occurs (shifting $\simeq 200$ ft/sec as β changed from $+10^{\circ}$ to 0° to -10°); this suggests a relationship similar to noise dependency on area ratio.

Canting the exit plane in the negative β direction (flow directed inward) may be considered in order to assure flow attachment to the plug surface, plug pressurization, and improved aerodynamic performance. The flow would thus simulate a lower area ratio, and individual jets would tend to coalesce sooner (closer) to the nozzle exit plane, at a higher mixed temperature and



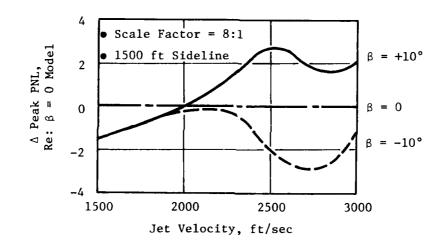


Figure F-31. Effect of Chute/Spoke Exit Plane Cant Variation.

velocity, thereby resulting in a longer length/greater volume of transonic-mixing/turbulent-decay region and higher component of low-frequency noise. Loss of several dB peak PNL suppression is seen at higher jet velocities.

Canting the exit plane in the positive β direction (flow directed outward) aerodynamically simulates larger area ratio and may thus normally enhance high-velocity suppression. Positive β canting maintains individual jet identity longer prior to merging and, therefore, allows for more complete mixing with entrained ambient air, lower mixed temperature and velocity, shorter/less volume of the transonic-mixing/turbulent-decay region, and lower low-frequency noise. A gain of several dB in peak PNL suppression is seen in the higher jet velocity region.

As the flow angularity relative to the plug angle is increased, the static pressure on the plug surface decreases in the vicinity immediately aft of the suppressor throat plane. The decreased plug pressure is reflected in base pressure on the suppressor elements, thus, resulting in higher base drag and lower aerodynamic performance. Thrust decrement may also result from the angularity component of outward flow vectoring.

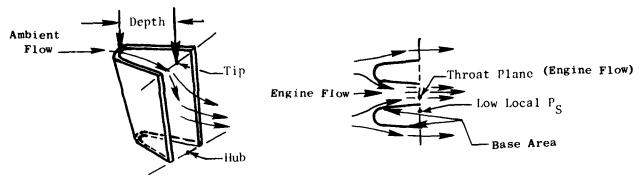
Again, when considering application of an acoustically treated secondary ejector, care must be exercised to avoid direct flow impingement on the ejector lining or flow spillage through the ejector inlet.

Chute/Spoke General Design Consideration

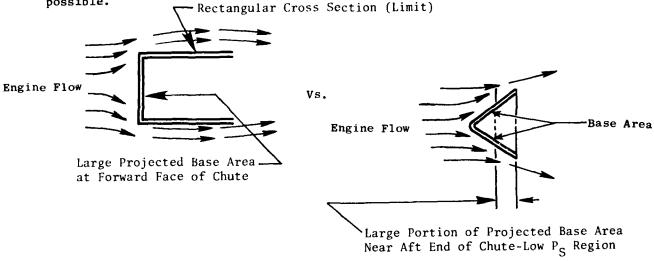
Assuming that:

- (a) for aerodynamic performance considerations, the choice of chutes has been made instead of more simplistic spokes for a particular application, and
- (b) suppressor system area ratio, radius ratio, element number, exit plane planform, and cant angle have all been selected from (1) parametrically exercising the M*S correlation, (2) selecting optimal designs, and (3) implementing the optimal design in the physical nozzle while maintaining cognizance of the general design guidelines;

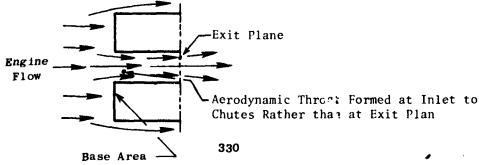
the remaining major geometric parameter is chute cross section in the axial flow direction. Aerodynamic performance should be the primary design consideration. Aerodynamically, base drag is the major contributor to thrust loss both in spoke and in chute designs (other losses being entrance $P_{\rm T}$ loss and skin friction; see Section 5.0 of the text). Chute cross section should be designed to (a) maintain high (close to ambient) base pressure and, hence, low base drag for aerodynamic performance, (b) improve ventilation and mixing for acoustic performance, and (c) be of reasonable size for mechanical implementation. The following guidelines are offered:



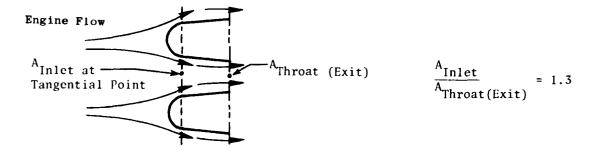
Make chute cross section as deep as possible, within the restraints of mechanical implementation, in order to remove the projected base area as far as possible from the low local P_s region near the expanding core jets at the throat plane. Retain chute depth at the hub as near to that of the tip as feasible. The chute cross section, in limit, should approach that of a rectangular shape to position the projected area, upon which low pressure acts, as remotely from the low local P_s region of the expanding core jets as possible.



In the limit the rectangular cross section has all base area, except for metal thickness, removed from the exit plane, whereas a shallow 'V' design has a large percentage of projected base area near the throat plane. A true rectangular chute cross section, however, is impractical because flow between chutes would seek a throat plane forward of the exit plane, thus, precipitating venacontracta, internal shock, and $P_{\rm T}$ loss (i.e. poor flow discharge coefficients).

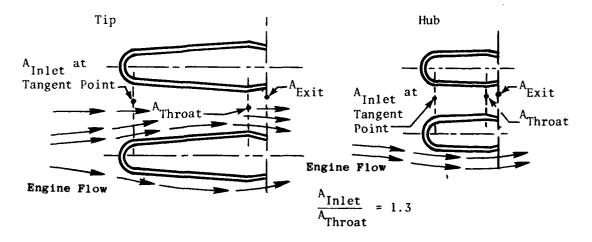


Therefore, a compromise in chute cross section is necessary to eliminate the losses associated with premature choking and still minimize base pressure loss. A suggested rule of 30% convergence of flow area, from inlet to exit plane, is suggested.



Chute planform design at the exit plane (see 5.2.3.9 Chute/Spoke Exit Planform) can be based primarily on acoustic considerations; it is fairly independent of aerodynamic performance, as long as depth and cross section designs are tailored for good aerodynamic performance. As planform changes with radial location, a proportionality in cross-sectional dimensions to those at the largest cross section should be maintained. Common design places the largest cross section ($W_{\rm OC/S}$ and depth) at the tip or shroud with proportionally decreasing cross section toward the hub or plug. The suggested 30% convergence of flow area should be maintained across the full radial span of the chute to assure uniform flow distribution and exit plane Mach number.

For a particular multichute suppressor application, where shock-cell-generated noise is critical, a convergent/divergent flowpath design through the chutes may be considered at the design point to minimize shock structure. The above design considerations should be maintained through the throat plane with the remaining, divergent, flow path designed for the specific flow case under consideration. A nominal 10° flow-path convergence angle is suggested.



APPENDIX G - ENGINEERING CORRELATION (M*S) COMPUTER PROGRAM EXAMPLE CASES

Two examples of the use of the M*S computer program in generating predictions for various nozzles are shown in this appendix. These cases are simply examples for illustrative purposes and are not intended to represent actual or proposed nozzle designs. The first example consists of the prediction of noise from a prescribed nozzle at takeoff and at cutback conditions. Conical and suppressor predictions are both made, first through the use of the trend curves (which were developed utilizing the M*S model), and then by the M*S computer program. The second example shows a sample input case for the prediction of trend curves versus area ratio and element number by the M*S computer program. (It should be noted that the M*S computer inputs presented in these examples are for the GE Honeywell 6080 computer; therefore, some minor differences in the input exist as compared with the CDC computer program input format described in Reference 13.)

CASE 1

Determine the EPNL for the following nozzle at the given conditions and compare to an equal-ideal-gross-thrust, conical nozzle:

Given/Assumed

- $A_8 = 1310 \text{ in.}^2 = 9.1 \text{ ft}^2$
- Single-Flow Chute with Plug

AR = 2.1

Number of Elements = 32

Rr = 0.62

Exit Cant = 5° (Down Plug)

Plug Radius = 1.925 ft

- Four Engines
- + 1.5 EPNdB Ground Reflections

• <u>Conditions</u>	Takeoff	Cutback
P_{T8}/P_0	3.23	2.16
T _{T8} (° R)	1650	1320
V ₈ (ft/sec)	2375	1762
V ₀ (ft/sec)	397	397
EGA and Shielding (EPNdB)	4	0
Altitude (ft)	900	1040
Sideline (ft)	2128	0

Tables G-1 through G-4 delineate the sequence of steps required to make the computations. The figures referenced on these tables are in Section 4.12 of this document.

Table G-1. Determination of Conical Nozzle Noise at Takeoff.

Step	Description	Figure	Noise
1	Find conical absolute level at given suppressor trend curve point (V_8 = 2375 ft/sec, P_{T8}/P_0 = 3.23)	4-9	106.9E
2	Adjust to new size and distance $(A_8 = 9.1 \cdot ft^2, Distance = 2310 ft)$	4-15	+5.3*
3	Adjust to new flight velocity	4-21	-0.6
4	Correct for number of engines, shielding and EGA, and ground reflections	Given	+3.5 ————————————————————————————————————

 $[\]star$ Interpolated

Table G-2. Determination of Conical Nozzle Noise at Cutback.

Step	Description	Figure	Noise
1	Find conical absolute level at given suppressor trend curve point ($V_8 = 1762$ ft/sec, $P_{T8}/P_0 = 2.16$)	4-9	95.1E
2	Adjust to new size and distance $(A_8 = 9.1, ft^2, Distance = 1040 ft)$	4-15	+11.1*
3	Adjust to new flight velocity	4-21	-0.6
4	Adjust for number of engines, shielding and EGA, and ground reflections	Given	+7.5
			113.1 EPNdB

^{*}Interpolated

Table G-3. Determination of Suppressor Noise at Takeoff.

Step	Description	Figure	Noise
1	Find suppression at $V_8 = 2650$ ft/sec, $P_{T8}/P_0 = 3.48$	4-26	-9.3
2	Adjust suppression to new flight velocity	4-23	0.0
3	Adjust suppression for R_{r}	4-34	-3.2
4	Adjust suppression for cant		+0.9*
5	Adjust suppression for planform		0.0*
6	Total suppression		-11.6
7	Find reference conical level at $V_8 = 2650 \text{ ft/sec}$, $P_{T8}/P_0 = 3.48$	4-9	108.5
8	Determine suppressor level		96.9
9	Adjust to new cycle ($V_8 = 2375$ ft/sec, $P_{T8}/P_0 = 3.23$)	4-12	-2.0
10	Adjust to new size and distance	4-17 and 4-19	+6.3**
11	Correct for number of engines, shield- ing and EGA, and ground reflections	Given	+3.5
			104.7 EPNdB
		or 10.4 EPNdl	Suppression

^{*}No Figure Supplied

^{**}Interpolated

Table G-4. Determination of Suppressor Noise at Cutback.

Step	Description	Figure	Noise
1	Find suppression at $V_8 = 2073$ ft/sec, $P_{T_8}/P_0 = 2.54$	4-26	-9.5
2	Adjust suppression to new flight velocity	4-23	+0.3**
3	Adjust suppression for R	4-34	-3.2
4	Adjust suppression for cant		+0.9*
5	Adjust suppression for planform		0.0*
6	Total suppression		-11.5
7	Find reference conical level at $V_8 = 2073 \text{ ft/sec}, P_{T_8}/P_0 = 2.54$	4–9	102.1
8	Determine suppressor level		90.6
9	Adjust to new cycle ($V_8 = 1762$ ft/sec, $P_{T_8}/P_0 = 2.16$	4-12	-5.0
10	Adjust to new size and distance	4-17 and 4-19	+14.1**
11	Correct for number of engines, shield- ing and EGA, and ground reflections	Given	+7.5
			107.2 EPNdB
	 	or 5.9 EPNdB	Suppression

^{*}No Figure Supplied

^{**}Interpolated

The following twenty pages contain the input and output for the nozzle noise determined by the M*S computer. The noise components are split out for comparison, and the corrections for the number of engines, shielding and EGA, and ground reflections are applied to the total noise EPNL. The seventh page is comparable to Table G-3; the twelfth is comparable to Table G-4, and the sixteenth and Twentieth compare to Tables G-1 and G-2.

			· · · · · · · · · · · · · · · · · · ·	we amount of		т .		,
			1 1					
								1
	! !							İ
	1					1		1
		Ì						
								-
	† l						ĺ	
	i i							1
							İ	
	1 1							1
							ĺ	ĺ
	1		!					
	1				ŀ			
						1 1		
	}							
	}				.			
							l	İ
			1				į	1
			1					
	! !							:
	!							!
	!			j	į			
	1			1 1				
		Ì						
	8							
	2							
~	₹	1 1		1				1
<u>-</u> -	F 2	بر						ļ
_ 4 ⊼ _	₹ -	2		1 1			1	1
25 S	2 2	CONICAL		1				
A S E				1 1				
5 2 A	. 8	9 '	.T=1040, SL=Q.					1
U + 0	8	3	ल्	ļ				
ĔΩM	88	5ES	4					
80 É	4 6 0	CASES CASES P=0,	-		Ì			:
\$ 8 0	щ о о	H 8	į i					ĺ
82	F 1 / 9,	. <u>1</u> 5	· ·	1	ĺ			
ACCUSTIC ENGINEERING BLDG 300 EXT 6713/5354 H-77 TREND CURVE GENERATION	4 6 9 5	2.16,AL SAMPLE 3,U=2,E	<u>ت</u> مٰ					1
	20.0	, L 22 ' L						;
20	ii - 0		4					
8 6 8 8 8 8 8 8 8 8 8 8 8 8 8 8 8 8 8 8	92		^			1 1		
ELMEIR Bin 79 Ask 6	3.00 3.00 10.00	300 4 4 5 5 5 5 5 5 5 5 5 5 5 5 5 5 5 5 5 5	0					
30H SELMEIR 3=60H BIN 79 60H TASK 6	7983, 380H 181 925, 895. 0, R4.2. 866, R6.2. 868, SS.4. 564, A7.2. 08, 150, P9.3. 23, VO:387, 17.900, 22, Z2, Z6, U.2, E9.0, 9.0, A.4.0,	TT3=1300, P9=2.16, ALT=1040, SL=0, TY9=1, A9=9.1, 3AMPLE CASES - 13, TT3=1650, LT=900, SL=2128, U=2, E9=0, B=0, A=4=0,	TT3=1300, P9=2.16, AL					

(36

PAGE 2			XXXXXX	XX XX XX XX XX XX XX XX XX XX XX XX XX	X X XXXXX XXXXXX X XXXXX X X X X X X X	HIGH VELOCITY JET NOISE PROGRAM (CONTRACT DOT-05-30034) HIGH VELOCITY JET NOISE PROGRAM (CONTRACT DOT-05-30034) TASK 3 ENGINEERING CORRELATION SELMEIER ACOUSTIC ENGINEERING BIN 79 BLDG 300 X-6713-5354 TASK 6 TREND CHR'E GENERATION		
--------	--	--	--------	--	--	---	--	--

2.060 3.454 A5= 9.369 A5= 24.947				
	0.611 AF 5.000 VG 5.000 VG EQUIV AREA DIA	SAMPLE CASES - 32 CHUTE ** INPUT *** OF CHUTES/SPOKES* 32 ** 519. PO ** 14.700 ** 519. PO ** 14.700 ** 519. PO ** 3.230 ** 519. PO ** 3.230 ** 610 PARAMETER* 0.000 ** 5.000 ** 5.000 ** 5.000 ** 5.000	3.454 A8= A8= 2	

														***	<u></u>		-	~-					
₹				PWL 163.9	164.0	163.6	162.8	162.2	161.0	159.3	58.3	157.2	9.79	153.4	150.7	47.0	146.4	140.0	142.7	9.5			
PAGE				160	6 6 6 6 6 6 6 6 6 6 6 6 6 6 6 6 6 6 6	- 6	9 9	7.7	68.7	62.3	58.7	00 10 44 00 60 10	45.5	9 6	24.0	9 -	-14.7	-86.7	147.3	96.0	2		
				150	88.2 87.3	86.3	. S. S. S. S. S. S. S. S. S. S. S. S. S.	4 9 4	-12	75.	69.2	62.9 62.8	58.8	6 4 6 6 6 -	7.0	22.2	4.4	9 G	-78.3	888			
				140	87.8	87.2	9 60	9 6 9 3 0	81.5	7.77	75.4	5 0 2 0 2 0 3 0	6 99	0 0 0 0 0 0 0 0 0 0	53.6	37.0	30.6	4 0	-42.8	90.0			}
LATION				130	95.7	96.7	900	0 -	93.0	00	78.2	73.8	71.0	67.7	9.0	45.2	39.6	N -	-22.6	9 09 0 0 7 0 1 10 H			
HIGH VELGCITY JET NOISE PROGRAM - ENGINEERING CORRELATION				120	62.7	83.3	900	82.9	69.7	90.0	78.4	76.7	72.2	60 K	6.	49.4	4.	. 4 . 6	-11.4	96.7			
3 NEER IT		101 64	DAY	110	77.6	79.7	200	9 6	80.9	79.6	78.5	7.5	73.3	70.6	63.8	51.7	0.74	0.00	-3.2	- 65 d	2		
AR - EK	CHUTE	MERGED NOISE 900 0 FOOT ALTITUDE 2128 0 FOOT SIDELINE	STANDARD DAY	100	76.6	78.6	90.00	80.18	00 t	9 2	77.8	76.0	73.1	57.5	4.0	25.0	89 F	22.0	- 6	9 09 0 5 10 10 8 04 0	2		
E PROGR	- 35	ED NOIS 0 FOOT 0	POREE	75.8	76.9	78.6	- 4C (79.0	7 97	77.0	76.7	73.7	71.8	69	625	51.6	47.3	20.0	10 g	9 00 9 44 6 60 6 60	3		
ET NOTS	CASES	# MERG # 900	* 519.Di	78.0	76.6	78.3	76.0	2.67	78.3	77.4	76.4	2.4. 0.6.	71.4	60 KG	6.01	51.0	46.6	20.0	6 6 6	900			
00 17	SAMPLE			7.87	75	7;	4.67	20,00	7.8	2 ~	2	73	7	8 9	91	9				9 60 6 6 60 6	4		
тэх ноп				71.6	74.6	76.6	7.77	780	77 8	9.92	75.6	72.6	70.6	58	61.1	40.0	43.7	13.0	-10.0	9 69 6 9 69 6			
1				50 70.8	73.8	75.7	76.7	0.77	76.7		74 3	72.8	6 60	66.2	9	44.9	39.4	6. 1	-20.8	9 G			
				69.7	72.7	74.5	0.0	30.00	2. Z	73.6	72.4	70.8	66.5	0 E	20.0	38.9	32.7	-6.6	-38.3	9 60 0			
				30									1					١.	'				
				ı				1			ı					-		• •	_	900	eg		
				FREG 50.	8	9	160.	250	9.00	200	630.	000	1250.	1600	2500.	4000	3000	6000	10000		EPNL=		

20 30 40 90 80 70 1018E 2120 FOOT SIDELINE 2 1220 FOOT SIDELINE	## PREPHINGED HOUSE ## 1900, 0 FOON ALTHURE	# 1900.0 FOOT ALTITUDE # 1900	## PREPRINCIPLE INCLUSION FOR TAILUNE ## 2126.0 FOOT SIDELING ## 2126.0 FOOT S				S	SAMPLE C	CASES -	32	CHUTE								
20 30 40 50 60 70 60 90 100 110 120 130 140 180 160 160 40. 40. 50 60 40 60 100 110 120 130 140 180 160 160 40. 40. 40. 40. 60. 40. 100 110 120 130 140 180 160 160 40. 40. 40. 40. 40. 40. 40. 40. 40. 40	ACOUSTIC ANOLE STANDARD DAY ACOUSTIC ANOLE FROM INLET ACOUSTIC ANOLE FROM INLET ACOUSTIC ANOLE FROM INLET ACOUSTIC ANOLE FROM INLET BE 1	ACOUSTIC ANOLE FROM INLET ACOUSTIC ANOLE FROM INLET ACOUSTIC ANOLE FROM INLET ACOUSTIC ANOLE FROM INLET ACOUSTIC ANOLE FROM INLET 32.4 49.6 48.6 49.4 49.6 49.6 49.0 470 80.9 51.0 100 120 120 120 130 140 140 140 140 140 140 140 140 140 14	## ACOUSTIC ANOLE FROM INLET ## ACOUSTIC ANOLE FROM INLET ## ACOUSTIC ANOLE FROM INLET ## ACOUSTIC ANOLE FROM INLET ## ACOUSTIC ANOLE FROM INLET ## ACOUSTIC ANOLE FROM INLET ## ACOUSTIC ANOLE FROM INLET ## ACOUSTIC ANOLE FROM INLET ## ACOUSTIC ANOLE FROM INLET ## ACOUSTIC ANOLE FROM INLET ## ACOUSTIC ANOLE FROM INLET ## ACOUSTIC ANOLE FROM INLET ## ACOUSTIC ANOLE FROM INC. ## ACOUSTIC ANOLE FROM INLET ## ACOU		1			14 M M M	PREMER 900.0 2128.0	GED NO! FOOT AL	SE TITUDE DELINE								
20 30 40 50 100 110 120 130 140 150 150 150 150 150 150 150 150 150 15	20 30 40 50 60 70 60 90 100 110 120 130 140 180 160 160 40. 52.3 52.5 52.5 52.5 50.7 50.5 48.0 140 180 160 160 40. 52.3 52.5 52.5 52.5 52.5 50.7 50.5 48.0 140 150 150 140 150 150 140 150 150 140 150 150 140 140 140 140 140 140 140 140 140 14	20 30 40 50 60 70 60 90 100 110 120 130 140 150 160 160 40.6 52.9 52.9 52.9 54.0 150 140 150 160 160 60.5 52.9 52.9 52.9 52.9 52.9 52.9 52.9 52	20 30 40 50 60 70 80 90 110 120 130 140 180 160 160 160 160 160 160 160 160 160 16						519.DE	OREE ST	ANDARD	DAY							
20 30 40 90 100 110 120 130 140 180 160 40 90 100 110 120 130 140 180 160 40	20 30 40 80 60 70 80 100 110 120 130 140 180 180 160 80.6 82.3 82.8 82.8 82.8 82.8 82.8 82.8 82.8	20 30 40 60 60 70 60 90 100 110 120 130 140 150 160 160 60 6 52.3 52.9 52.7 50.5 48.0 40.0 41.0 150.6 52.3 52.9 52.7 50.5 48.0 40.0 41.0 150.6 52.3 52.9 52.7 50.5 48.0 40.0 41.0 150.6 52.3 52.9 52.7 50.5 48.0 40.0 41.0 150.6 52.3 52.9 52.7 50.5 48.0 40.0 41.0 150.6 52.3 52.9 52.7 50.5 48.0 40.0 41.0 150.6 52.9 50.7 50.5 50.7 50.5 50.7 50.5 50.7 50.7	20 30 40 40 60 70 60 90 100 110 120 130 140 180 140 40 60 40 60 60 60 60 60 60 60 60 60 60 60 60 60					4				ET							
47.7 48.4 48.6 <th< td=""><td>47.7 49.4 49.6 49.6 49.6 40.6 50.1 50.1 50.2 50.7 40.6 40.6 40.6 40.6 40.6 40.7 40.6 40.6 40.6 40.6 40.6 40.6 40.6 40.6</td><td>47.7 49.4 49.6 49.6 49.6 49.6 49.6 51.7 10.12 52.2 52.7 50.5 48.0 47.7 43.7 13.3 49.4 49.6 49.6 49.6 49.6 49.6 49.6 49.6</td><td>47.7 49.4 49.6 49.6 49.4 410 6 91.6 51.7 51.2 52.2 59.7 49.4 6 91.0 61.0 61.0 61.0 61.0 61.0 61.0 61.0 6</td><td>20</td><td>1</td><td>1</td><td>09</td><td>70</td><td></td><td>ļ</td><td></td><td></td><td>-</td><td></td><td></td><td>1</td><td>160</td><td>1</td><td></td></th<>	47.7 49.4 49.6 49.6 49.6 40.6 50.1 50.1 50.2 50.7 40.6 40.6 40.6 40.6 40.6 40.7 40.6 40.6 40.6 40.6 40.6 40.6 40.6 40.6	47.7 49.4 49.6 49.6 49.6 49.6 49.6 51.7 10.12 52.2 52.7 50.5 48.0 47.7 43.7 13.3 49.4 49.6 49.6 49.6 49.6 49.6 49.6 49.6	47.7 49.4 49.6 49.6 49.4 410 6 91.6 51.7 51.2 52.2 59.7 49.4 6 91.0 61.0 61.0 61.0 61.0 61.0 61.0 61.0 6	20	1	1	09	70		ļ			-			1	160	1	
53.4 55.2 <th< td=""><td>53.4 53.5 53.4 53.6 53.6 53.0 46.2 56.2 66.1 66.7 66</td><td> Section Sect</td><td>19.2 <th< td=""><td>47.7</td><td></td><td>4 6</td><td>40.4</td><td>9 0</td><td></td><td></td><td></td><td></td><td>۸.</td><td>ın c</td><td></td><td></td><td>- 1 4</td><td>131.5</td><td></td></th<></td></th<>	53.4 53.5 53.4 53.6 53.6 53.0 46.2 56.2 66.1 66.7 66	Section Sect	19.2 19.2 <th< td=""><td>47.7</td><td></td><td>4 6</td><td>40.4</td><td>9 0</td><td></td><td></td><td></td><td></td><td>۸.</td><td>ın c</td><td></td><td></td><td>- 1 4</td><td>131.5</td><td></td></th<>	47.7		4 6	40.4	9 0					۸.	ın c			- 1 4	131.5	
56 56<	96 2 96 1 96 7 96 0 60 0 <th< td=""><td>98.6 59.1 59.6 69.6 59.0 60.0 <th< td=""><td>98 2 39 1 39 7 36 6 69 6 5 5 7 6 0 7 60 7 60 0 60 0 60 0 60 6 9 6 1 6 1 6 1 6 1 6 1 6 1 6 1 6 1 6 1</td><td>. E</td><td></td><td>9 10</td><td>0 10 0 10 1 4</td><td>. 40 . 00</td><td></td><td></td><td></td><td></td><td>•</td><td>u on</td><td></td><td></td><td>46.2</td><td>137.4</td><td></td></th<></td></th<>	98.6 59.1 59.6 69.6 59.0 60.0 <th< td=""><td>98 2 39 1 39 7 36 6 69 6 5 5 7 6 0 7 60 7 60 0 60 0 60 0 60 6 9 6 1 6 1 6 1 6 1 6 1 6 1 6 1 6 1 6 1</td><td>. E</td><td></td><td>9 10</td><td>0 10 0 10 1 4</td><td>. 40 . 00</td><td></td><td></td><td></td><td></td><td>•</td><td>u on</td><td></td><td></td><td>46.2</td><td>137.4</td><td></td></th<>	98 2 39 1 39 7 36 6 69 6 5 5 7 6 0 7 60 7 60 0 60 0 60 0 60 6 9 6 1 6 1 6 1 6 1 6 1 6 1 6 1 6 1 6 1	. E		9 10	0 10 0 10 1 4	. 40 . 00					•	u on			46.2	137.4	
50.0 61.2 62.9 63.4 63.5 61.7 62.8 63.9 64.1 64.2 66.2 66.2 66.2 66.2 66.3 66.2 66.3 <th< td=""><td>61. 66.0 6 61. 5 61.4 64.1 64.1 64.1 65.2 66.3 66.1 65.2 66.3 61.7 62.8 65.3 61.3 61.1 56.0 51.8 61.8 65.8 65.8 66.5 64.3 61.1 56.0 51.8 61.8 65.8 65.8 65.8 65.8 65.8 65.8 65.8 65</td><td>86. 8 6 6 6 6 6 6 6 6 6 7 6 7 6 7 6 7 6 7 6</td><td>56. 6 6 6 6 6 6 6 6 6 6 6 6 6 6 6 6 6 6</td><td>56.2</td><td></td><td>20</td><td>58.5</td><td>57.7</td><td>ļ</td><td>(</td><td></td><td></td><td>60</td><td>9</td><td></td><td></td><td>40.9</td><td>140.2</td><td></td></th<>	61. 66.0 6 61. 5 61.4 64.1 64.1 64.1 65.2 66.3 66.1 65.2 66.3 61.7 62.8 65.3 61.3 61.1 56.0 51.8 61.8 65.8 65.8 66.5 64.3 61.1 56.0 51.8 61.8 65.8 65.8 65.8 65.8 65.8 65.8 65.8 65	86. 8 6 6 6 6 6 6 6 6 6 7 6 7 6 7 6 7 6 7 6	56. 6 6 6 6 6 6 6 6 6 6 6 6 6 6 6 6 6 6	56.2		20	58.5	57.7	ļ	(60	9			40.9	140.2	
63.4 68.0 68.1 66.2 66.2 68.2 68.2 68.2 68.2 68.2 68.2	63. 4 6 6 6 6 6 6 6 6 6 6 7 6 7 7 7 7 7 7 7	63. 63. 66. 66. 66. 66. 66. 66. 66. 67. 67. 67	65.3 66.9 66.1 66.2 66.2 66.2 66.3 66.3 66.3 66.3 66.3			9		60.5					.	.				143.0	
65.4 66.0 691 692 692 693 69.6 71.2 71.3 69.7 71.0 71.7 69.4 66.7 63.5 56.9 66.7 69.0 69.1 69.0 691 69.2 71.6 71.6 71.7 71.7 69.0 66.7 69.0 66.7 69.0 69.9 71.6 71.6 71.6 71.7 71.7 71.7 71.7 71.4 71.5 72.9 72.1 72.5 72.1 72.5 72.9 72.1 72.5 72.9 72.1 72.5 72.9 72.1 72.5 72.9 72.1 72.5 72.9 72.9 72.1 72.5 72.9 72.1 72.2 72.9 72.1 72.2 72.9 72.1 72.2 72.2 72.9 72.1 76.3 72.2 72.1 76.3 72.2 72.2 72.2 72.2 72.2 72.2 72.2 72	65.4 € 69.0 69 1 € 92 € 69.3 69.6 71.2 71.3 69.7 71.0 71.7 69.4 66.7 69.8 58.9 69.0 65.9 69.9 69.9 71.1 71.4 71.5 70.9 73.4 73.5 72.1 73.5 71.0 71.7 69.4 66.7 60.9 65.7 60.9 65.3 71.6 72.9 73.3 73.5 73.5 73.6 73.6 73.6 73.6 73.6 73.6 73.6 73.6	65.4 68.0 6891 692 693 699 691 712 713 6897 710 71.7 69.4 669.7 693 689 687 689 687 689 710 71.8 71.9 71.9 71.9 71.9 71.9 71.9 71.9 71.9	65.4 69.0 69.1 69.2 69.3 69.5 71.2 71.3 69.7 71.0 71.7 69.4 66.7 68.5 56.7 66.8 65.7 66.8 65.7 66.9 65.7 66.9 65.7 66.9 69.7 71.0 71.1 71.3 71.5 71.0 71.2 71.3 71.0 71.3 71.0 71.3 71.0 71.3 71.5 71.0 71.3 71.0 71.3 71.0 71.3 71.0 71.3 71.0 71.3 71.0 71.3 71.0 71.3 71.0 71.3 71.0 71.5 71.0 71.5 71.0 71.5 71.0 71.5 71.0 71.5 71.0 71.5 71.0 71.5 71.0 71.5 71.0 71.5 71.0 71.5 71.0 71.5 71.0 71.5 71.0 71.5 71.0 71.5 71.0 71.5 71.0 71.5 71.0 71.5 71.5 71.5 71.5 71.5 71.5 71.5 71.5	- K		9 6	9 9	66.2					۰.	, 0			9.6	46.0	
69. 71.1 71.4 71.5 70.9 73.4 73.5 72.1 73.5 74.1 71.7 69.0 65.7 60.9 68.3 76.8 72.8 72.8 72.8 72.8 72.8 72.8 72.8 72	69. 67. 1 69. 69. 71. 1 71. 4 71. 5 70. 9 73. 4 73. 5 72. 1 73. 5 74. 1 71. 7 69. 0 65. 7 60. 9 69. 3 71. 6 72. 9 72. 1 75. 5 74. 9 71. 7 71. 7 71. 7 71. 9 72. 9 72. 1 75. 5 74. 9 72. 1 75. 5 74. 9 72. 9	67. 0 69- 9 71, 1 71.4 71.5 73.0 73.4 73 5 72.1 73.5 74, 1 71.7 69.0 65.7 60.9 95.4 66.3 17.2 67.2 17.2 72.2 72.4 72.5 72.5 72.0 72.5 72.5 72.5 72.5 72.5 72.5 72.5 72.5	67. 0 69.9 71.1 71.4 71.5 70.9 73.4 73.5 72.1 73.5 74.1 71.7 69.0 68.7 66.0 3 71.6 69.0 68.7 74.3 71.5 72.9 72.9 72.9 72.9 72.9 72.9 72.9 72.9	65.4		69	69 3	69.6	ļ	ļ		1		4		l	56.9	151.0	
69.3 71.6 72.9 73.5 73.5 73.0 75.4 75.5 74.3 75.8 76.0 73.6 70.9 67.4 62.4 62.4 63.4 73.6 73.5 73.5 73.5 73.5 73.5 73.5 73.5 73.5	69. 3 71.6 72.9 74.5 73.5 73.5 74.3 75.8 76.0 73.6 70.9 67.4 662.4 68.8 63.5 73.6 73.5 73.5 73.5 73.5 73.5 74.3 75.8 76.0 73.5 70.9 67.4 662.4 68.8 63.5 73.6 73.7 663.9 64.1 76.3 77.5 77.5 77.5 77.5 77.5 77.5 77.5 77	68.3 71.6 72.9 73.3 73.5 73.0 75.5 74.3 75.8 76.0 75.6 77.6 77.8 77.8 77.8 77.8 77.8 77.8 77	69. 7 1, 6 72, 9 73, 7 73, 7 75, 7 4, 3 75, 8 74, 9 75, 8 74, 9 75, 8 74, 9 75, 8 74, 9 75, 8 74, 9 72, 7 72, 7 75, 9 72, 9 73, 7 72, 9 72, 7 72, 7 72, 9 72, 7 72, 7 72, 9 72, 7 72, 9 72, 7 72, 7 72, 9 72, 9 73, 7 72, 7 72, 9 72, 9 73, 7 72, 9 72, 7 72, 9 72, 7 72, 9 72, 7 72, 9 72, 7 72, 9 72, 7 72, 9 72, 7 72, 9 72, 7 72, 9 72, 7 72, 9 72, 7 72, 9 72, 7 72, 9 72, 7 72, 7 72, 9 72, 7 72, 9 72, 7 72, 9 72, 7 72, 9 72, 7 72, 9 72, 7 72, 9 72, 7 72, 9 72, 7 72, 9 72, 7 72, 9 72, 7 72, 9 72, 7 72, 9 72, 7 72, 9 72, 9 72, 9 72, 9 72, 1 72, 9 72, 1 72	67.0		7.1	71.5	20.9					_	~			60.09	153.4	
69. 6 73. 8 75. 6 76. 3 76. 7 76. 3 76. 4 79. 1 76. 6 73. 7 69. 9 64.1 69. 5 74. 7 76. 7 77. 4 79. 2 79. 4 79. 1 76. 6 73. 7 69. 9 64.1 66. 5 77. 6 77. 7 77. 4 79. 2 79. 4 79. 1 70. 7 79. 5 70. 7 79. 6 79. 6 79. 7 79. 7 79. 6 79. 2 79. 2 79. 2 79. 2 79. 2 79. 5 79	69. 6 73. 8 75. 6 76. 3 76. 7 76. 3 76. 4 79. 1 76. 6 73. 7 69. 9 64.1 69. 5 73. 7 66. 9 64.1 66. 7 7 6. 3 77. 7 77. 4 79. 2 79. 4 79. 1 76. 6 73. 7 69. 9 64.1 66. 7 7 6. 5 77. 7 77. 4 79. 2 79. 2 80. 7 7 7 7 7 7 7 7 7 7 7 7 7 7 7 7 7 7 7	69.4 73.6 75.8 75.7 77.7 76.3 76.4 77.6 79.1 75.4 79.1 75.5 76.7 79.2 76.2 76.2 76.2 76.2 76.2 76.2 76.2 76	69. 6 73. 8 75. 6 76. 7 76. 3 76. 7 7 7 8 7 8 7 8 7 8 7 8 7 8 7 8 7 8 7	683			73.5	73.0					۰.	φ.			4.29	155.7	
69.4 74.1 76.3 77.2 77.7 77.4 79.2 79.4 79.1 80.7 79.2 76.7 73.6 69.5 63.3 66.5 66.7 66.7 75.2 72.0 67.6 60.7 75.2 72.0 76.7 60.7 75.2 72.0 67.6 60.7 75.2 72.0 76.7 60.7 75.2 72.0 67.6 60.7 75.2 72.0 67.6 60.7 75.2 72.0 72.0 67.6 60.7 75.2 72.0 72.0 67.6 60.7 75.2 72.0 72.0 67.6 60.7 75.2 72.0 72.0 72.2 72.0 72.0 72.0 67.6 60.7 75.2 72.0 72.0 72.2 72.0 72.0 72.0 72.0 72	69.4 74.1 76.3 77.2 77.7 77.4 79.2 79.4 79.1 80.7 79.2 76.7 73.6 69.5 60.3 66.5 74.6 77.6 77.6 77.2 77.7 77.4 79.2 79.2 80.7 77.9 75.2 72.0 67.6 60.7 75.5 72.6 67.7 86.1 1 58.1 72.5 72.6 77.6 77.2 77.3 77.2 77.3 77.2 77.3 77.2 77.3 77.3	68.4 74.1 76.3 77.2 77.7 77.4 79.2 79.4 79.1 80 7 79.2 76.7 79.6 69.8 69.9 69.9 68.9 68.9 68.9 68.9 6	69. 4 74.1 76.3 77.2 77.7 77.4 79.2 79.4 79.1 80 7 79.2 76.7 73.6 69.5 63.6 68.5 74.0 76.6 77.6 77.2 77.7 77.4 79.2 79.4 79.1 80.7 77.2 77.7 77.6 77.2 77.8 77.8 77.8 77.8 77.8 77.8 77.8	9 69		9 %	76.7	76.3	1	ļ		1	J_	ا ي لاد		ł	64 -	20.00	
68.5 74.6 77.8 78.2 79.2 79.2 79.2 77.9 75.2 72.0 67.6 60.7 68.1 72.5 77.6 77.7 77.7 77.8 79.2 79.0 75.2 75.7 77.7 77.8 79.9 73.3 70.3 66.5 64.9 57.2 57.3 70.3 66.5 61.1 52.2 73.3 70.3 66.5 61.1 52.2 73.3 70.3 66.5 61.1 52.2 73.9 70.3 66.5 61.1 52.2 73.9 70.0 66.8 65.5 56.1 52.2 73.0 70.0 66.8 65.5 56.1 52.2 73.0 70.0 66.8 65.5 56.1 57.0 56.1 56.0 56	68.5 74.6 77.8 79.2 79.2 79.2 77.9 75.2 72.0 67.6 60.7 68.1 63.6 77.6 77.7 77.7 77.8 79.2 75.7 75.7 77.8 79.2 75.9 75.7 75.7 77.8 79.2 75.9 75.7 75.7 75.7 75.7 75.9 75.7 75.7 75.8 75.9 75.7 75.7 75.8 75.9 75.7 75.7 75.7 75.7 75.8 75.9 75.7 75	68.5 77.6 77.6 77.7 77.7 77.9 75.2 75.2 72.0 67.6 60.7 77.9 75.2 75.2 75.2 75.2 75.2 75.7 77.7 77.7 77.7 77.8 75.9 <td< td=""><td>68.5 74.0 76.6 77.8 78.4 73.2 79.2 79.2 79.2 77.9 <td< td=""><td>69.4</td><td></td><td>7</td><td>7.77</td><td>77.4</td><td></td><td></td><td></td><td></td><td>. ^1</td><td>٠,</td><td></td><td></td><td>63.3</td><td>160.9</td><td></td></td<></td></td<>	68.5 74.0 76.6 77.8 78.4 73.2 79.2 79.2 79.2 77.9 <td< td=""><td>69.4</td><td></td><td>7</td><td>7.77</td><td>77.4</td><td></td><td></td><td></td><td></td><td>. ^1</td><td>٠,</td><td></td><td></td><td>63.3</td><td>160.9</td><td></td></td<>	69.4		7	7.77	77.4					. ^1	٠,			63.3	160.9	
BB (7.2) (7.4) (7.5) (7	BB 7.2 7.3 <td> 10</td> <td>61.1 63.2 72.6 74.4 75.5 75.2</td> <td>68.5</td> <td></td> <td>77</td> <td>78.4</td> <td>C) 1 C) 1</td> <td></td> <td></td> <td></td> <td></td> <td>.</td> <td>Q.</td> <td></td> <td></td> <td>60.7</td> <td>161.4</td> <td></td>	10	61.1 63.2 72.6 74.4 75.5 75.2	68.5		77	78.4	C) 1 C) 1					.	Q.			60.7	161.4	
54.6 66.1 67.7 73.7	54.6 64.1 68.7 71.0 72.3 72.2 72.3 74.0 70.0 66.8 62.5 56.5 56.5 66.5 66.5 66.5 66.5 66.5 66.5 66.5 66.5 66.5 66.5 66.5 66.5 66.5 66.5 66.5 67.0 66.5 67.0 66.5 66.5 66.5 66.5 66.5 66.5 66.5 66.5 66.5 66.5 66.5 66.5 66.5 67.0 66.5 67.0 66.5 67.0 66.5 67.0 66.5 67.0 66.5 67.0 66.5 67.0 66.5 67.0 66.5 67.0 66.5 67.0 66.5 67.0 66.5 67.0 66.5 67.0 66.5 67.0 66.5 67.0 66.5 67.0 66.5	54.6 66.1 68.7 74.3 73.7	54.6 64.1 68.7 72.6 72.7	1 22		17	8 77	777		į	-	ı		-,		1	27.6	7 091	
46 6 36 1 63 6 66 7 66 5 66 9 68 2 68 5 69 4 70 2 65 7 62 1 57 3 50 2 37 7 35 0 43 7 5 6 8 9 60 2 37 7 35 0 43 7 3 6 8 9 6 9 4 70 2 65 7 62 1 57 3 50 2 37 7 3 6 9 4 2 2 26 5 5 6 9 3 4 4 7 0 5 2 5 5 7 7 5 6 6 5 7 5 6 6 7 5 6 7 5 6 7 7 5 6 7 7 5 6 7 7 7 7	46.6 56.1 63.6 66.7 66.5 66.9 66.2 66.5 69.4 70.2 65.7 62.1 57.3 50.2 37.7 35.0 43.7 56.2 37.7 35.0 43.5 56.8 56.8 56.8 56.8 57.8 57.8 57.8 57.8 57.8 57.8 57.8 57	46.6 56.1 63.6 66.7 66.5 66.9 66.2 66.5 69.4 70.2 65.7 62.1 57.3 50.2 37.7 35.0 43.7 56.8 50.8 56.8 56.8 56.8 56.8 56.8 56.8 57.7 56.8 57.8 56.8 57.7 56.8 57.8 56.8 57.8 57.8 57.8 57.8 57.8 57.8 57.8 57	46.6 58.1 63.8 66.7 68.5 68.9 69.2 69.4 70.2 65.7 62.1 57.3 50.2 37 35.0 43.2 43.4 53.4 63.4 66.2 68.5 69.4 70.2 65.7 65.1 57.3 50.2 22.2 17.2 29.7 47.0 56.3 45.4 56.7 56.4 56.7 56.6 56.7 56.	. 6			4.6	75.6						9 00			46.0		
13. 0 15. 0	13. 9 1 2 1 2 1 2 1 2 1 2 1 2 1 2 1 2 1 2 1	13. 9 15. 47.0 55.2 55.4 55.7 56.6 57.0 56.1 56.2 54.2 59.9 42.2 20.9 11.1 11.1 12.1 5.2 5.7 47.0 55.2 55.1 53.1 53.6 54.1 56.2 54.5 49.9 44.6 56.9 24.6 11.4 11.1 11.1 11.1 11.1 11.1 11.1 1	17. 9 37. 5 47. 0 52. 2 55. 4 55. 4 55. 4 55. 4 55. 5 5. 5	46.6		99	68.5	68.9									37.7	156.8	
7.2 29.7 40.8 46.8 50.5 52.1 53.1 53.6 54.7 54.5 49.9 44.6 56.9 24.6 1.4 26.2 20.2 10.9 26.0 34.4 39.5 42.0 43.3 44.0 45.0 44.0 38.4 31.7 21.7 5.4 2.6 1.4 20.2 10.9 26.0 34.4 39.5 42.0 43.3 44.0 45.0 44.0 38.4 31.7 21.7 5.4 2.6 6.8 4 12.0 2.8 2.8 2.8 2.8 2.8 2.8 2.8 2.8 2.8 2.8	7.2 29.7 40.8 46.8 50.5 52.1 53.1 53.6 54.5 49.5 49.5 44.6 56.9 24.6 1.4 1.2 1.2 1.3 26.0 34.4 39.5 42.0 43.3 44.0 45.0 44.0 38.4 31.7 21.7 5.4 26.4 1.2 1.2 1.2 1.2 1.2 1.2 1.2 1.2 1.2 1.2	7.2 29.7 40.8 46.8 50.5 52.1 53.1 53.6 54.5 49.5 49.5 44.6 56.9 24.6 1.4 26.2 2.0 34.4 28.5 32.2 2.0 34.4 28.5 32.5 24.6 1.4 28.3 24.6 24.6 34.4 28.5 2.1 2.2 2.2 2.2 2.2 2.2 2.2 2.2 2.2 2.2	7.2 29.7 40.6 46.8 50.5 52.1 53.1 53.6 54.7 54.5 49.9 44.6 36.9 24.6 1 -20.2 10.9 26.0 34.4 39.5 42.0 43.3 44.0 45.0 44.0 38.4 31.7 21.7 54.4 26.6 -53.3 -18.8 2.9 15.0 22.3 26.1 1.2 4.4 7.2 8.4 8.9 5.7 20.7 11.8 -1.9 -24.6 -69.8 121.9 -59.0 -28.5 -11.5 -1.2 4.4 7.2 8.4 8.9 8.7 -51.1 16.9 -35.5 -67.0 -130.7 82.8 82.1 84.3 85.5 85.8 86.8 86.9 86.1 86.6 84.1 81.0 77.1 77.8 82.1 84.2 83.7 93.7 93.7 94.4 95.6 93.1 90.3 87.9 83.8 75.8 82.8 82.1 90.3 87.9 83.8 75.8 82.8 82.1 91.1 92.7 83.7 93.7 94.1 94.3 94.4 95.6 93.1 90.3 87.9 83.8 75.8 84.9 95.6 93.1 90.3 87.9 83.8 75.8 84.9 95.6 93.1 90.3 87.9 83.8 75.8 84.9 95.6 93.1 90.3 87.9 83.8 75.8 84.9 95.6 93.1 90.3 87.9 83.8 75.8 84.9 95.6 93.1 90.3 87.9 83.8 75.8 84.9 95.6 93.1 90.3 87.9 83.8 75.8 84.9 95.6 93.1 90.3 87.9 83.8 75.8 84.9 95.6 93.1 90.3 87.9 83.8 75.8 84.9 95.6 93.1 90.3 87.9 83.8 75.8 84.9 95.6 93.1 90.3 87.9 83.8 75.8 84.9 95.6 93.1 90.3 87.9 83.8 75.8 84.9 95.6 93.1 90.3 87.9 83.8 75.8 84.9 95.6 93.1 90.3 87.9 83.8 75.8 84.9 95.6 93.1 90.3 87.9 83.8 75.8 84.9 95.6 93.1 90.3 87.9 83.8 75.8 93.	17.9		3 6	55.4	26.4				1		9 6		1	0 -	53.7	
-20.2 10.9 26.0 34.4 39.5 42.0 43.3 44.0 45.0 44.0 38.4 31.7 21.7 5.4 -26.4 11.8 3.3 -18.8 8.1 11.8 3.1 12.2 2.8 1.8 1.8 1.8 2.8 1.8 1.8 2.8 1.8 2.8 1.8 2.8 1.8 2.8 1.8 2.8 2.8 1.8 2.8 1.8 2.8 1.8 2.8 2.8 1.8 2.8 2.8 2.8 2.8 2.8 2.8 2.8 2.8 2.8 2	-20.2 10.9 26.0 34.4 39.5 42.0 43.3 44.0 45.0 44.0 38.4 31.7 21.7 5.4 -26.4 11.8 3.1 3.1 3.1 3.1 3.1 3.1 3.1 3.1 3.1 3.1	-20.2 10.9 26.0 34.4 39.5 42.0 43.3 44.0 45.0 44.0 38.4 31.7 21.7 5.4 -26.4 11.8 3.1 11.8 3.1 12.2 12.0 43.3 44.0 45.0 44.0 38.4 31.7 21.7 5.4 -26.4 11.8 3.1 11.8 3.1 12.2 4.4 7.2 84.8 29.7 2.7 2.0 1.8 11.8 3.1	-20.2 10.9 26.0 34.4 39.5 42.0 43.3 44.0 45.0 44.0 38.4 31.7 21.7 5.4 -26. -20.2 10.9 26.0 34.4 39.5 42.0 43.3 44.0 45.0 44.0 38.4 31.7 21.7 5.4 -26. -21.3 -21.3 -22.3 -21.1 2.7 2.0 7.1 11.9 -1.9 -24.6 -6.9 12.1 20.3 24.6 -6.9 12.1 20.3 24.6 -6.9 12.1 2.2 24.6 -6.9 12.1 20.3 24.6 -6.9 12.1 20.3 24.1 20.3 24.1 24.3 24.4 25.6 23.1 20.3 27.0 130.2 24.1 24.3 24.4 25.6 23.1 20.3 27.0 130.2 24.1 24.3 24.4 25.6 23.1 20.3 27.0 130.3 27.0 130.3 24.4 25.6 23.1 20.3 27.0 27.0 130.3 27.0 130.3 27.0 24.1 24.3 24.4 25.6 23.1 20.3 27.0 27.0 130.2 24.1 24.3 24.4 25.6 23.1 20.3 27.0 27.0 27.0 130.2 24.1 24.3 24.4 25.6 23.1 20.3 27.0 27.0 130.2 27.0 27.0 27.0 27.0 27.0 27.0 27.0 2	7.2		46	50, 5	52.1						9		9.4.	4	63.0	
-83 4 -183 6 -183 6 -183 6 - 1	12.13 - 18.14 2.1 2.	121 3 - 181 3 - 181 6 - 183 6	121 9 - 58 1 11.5 1 - 22.3 28 1 27.3 28 1 28 1 28 1 27.7 27.7 20.7 11.6 1 28 1 28 1 28 1 28 1 28 1 28 1 28 1 2	-20.5		8	39,5	42.0					₩ (~		4	26.4	152.8	
77.6 82.1 84.3 85.3 85.9 85.6 86.8 86.9 86.6 88.1 86.6 84.1 91.0 77.1 71.3 182.5 87.9 91.1 92.7 93.7 94.1 94.3 94.4 95.6 93.1 90.3 86.9 82.4 75.8 82.5 82.1 91.1 92.7 93.7 93.7 94.1 94.3 94.4 95.6 93.1 90.3 87.9 83.8 75.8 84.9	77.6 82.1 84.3 85.3 85.9 85.6 86.8 86.9 86.6 86.1 86.6 84.1 91.0 77.1 77.3 82.5 87.9 91.1 92.7 93.7 93.7 94.3 94.4 95.6 93.1 90.3 87.9 87.9 77.8 82.5 87.9 91.1 92.7 93.7 93.7 94.3 94.4 95.6 93.1 90.3 87.9 87.9 83.8 75.8 84.9	77.6 82.1 84.3 85.3 85.9 85.6 86.8 86.9 86.6 86.1 86.6 84.1 91.0 77.1 77.3 82.5 87.9 91.1 92.7 93.7 94.1 94.3 94.4 95.6 93.1 90.3 87.9 93.8 75.8 82.5 87.9 91.1 92.7 93.7 94.1 94.3 94.4 95.6 93.1 90.3 87.9 93.8 75.8 84.9 95.6 93.1 90.3 87.9 93.8 75.8 94.9 95.6 93.1 90.3 87.9 93.8 75.8 94.9 95.6 93.1 90.3 87.9 93.8 75.8 94.9 95.6 93.1 90.3 87.9 93.8 75.8 94.9 95.6 93.1 90.3 87.9 93.8 75.8 94.9 95.6 93.1 90.3 87.9 93.8 75.8 94.9 95.6 93.1 90.3 87.9 93.8 75.8 94.9 95.6 93.1 90.3 87.9 93.8 75.8 94.9 95.6 93.1 90.3 87.9 93.8 75.8 94.9 95.6 93.1 90.3 87.9 93.8 75.8 94.9 95.6 93.1 90.3 87.9 93.8 75.8 94.9 95.6 93.1 90.3 87.9 93.8 75.8 94.9 95.6 93.1 90.3 87.9 93.8 75.8 94.9 95.6 93.1 90.3 87.9 93.8 75.8 94.9 95.6 93.1 90.3 87.9 93.8 75.8 94.9 95.6 93.1 90.3 87.9 93.8 75.8 94.9 95.6 93.1 90.3 87.9 94.9 95.6 93.1 90.3 87.9 94.9 95.6 93.1 90.3 87.9 94.9 95.6 93.1 90.3 87.9 94.9 95.6 93.1 90.3 87.9 94.9 95.6 93.1 90.3 87.9 94.9 95.6 93.1 90.3 87.9 94.9 95.6 93.1 90.3 87.9 94.9 95.6 93.1 90.3 87.9 94.9 95.6 93.1 90.3 87.9 94.9 97.9 94.9 95.6 93.1 90.3 87.9 94.9 97.9 97.9 97.9 97.9 97.9 97.9 9	77.8 82.1 84.3 85.3 85.6 86.8 86.8 86.1 86.6 84.1 81.0 77.1 77.8 82.1 81.1 82.7 83.7 93.7 94.1 94.3 94.4 95.6 93.1 90.3 87.9 83.6 75.8 73.8 82.1 84.3 94.4 95.6 93.1 90.3 87.9 83.6 75.8 73.8 73.8 73.8 73.8 73.8 73.8 73.8 73	121.0	1.		22.3	797	1	1	1	-]		Ή.	24.6	69	152.0	
62.5 67.9 91.1 92.7 93.7 93.7 94.1 94.3 94.4 95.6 93.1 90.3 96.9 82.4 75.6 82.5 82.1 91.1 92.7 93.7 93.7 94.1 94.3 94.4 95.6 93.1 90.3 67.9 63.6 75.8 44.9	62.5 67.9 91.1 92.7 93.7 93.7 94.1 94.3 94.4 95.6 93.1 90.3 96.9 82.4 75.6 82.5 82.1 91.1 92.7 93.7 93.7 94.1 94.3 94.4 95.6 93.1 90.3 67.9 63.6 75.6 4.9	82.5 87.9 91.1 92.7 93.7 94.1 94.3 94.4 95.6 93.1 90.3 86.9 82.4 75.6 82.5 82.1 91.1 92.7 83.7 93.7 94.1 94.3 94.4 95.6 93.1 90.3 87.9 83.6 75.8	82.5 87.9 91.1 92.7 83.7 93.7 94.1 94.3 94.4 95.6 93.1 90.3 86.9 82.4 75 82.5 89.1 91.1 92.7 93.7 94.1 94.3 94.4 95.6 93.1 90.3 87.9 63.8 75	77.8		- 69	. 60	921					- 40	. –		7.7	2.5	169.7	
6.41	6. 4	9 P		80 20 20 30 30 30 30 30 30 30 30 30 30 30 30 30		9 0	93.7	93.7						ص د		4.6	73.8		
[[[1 [6.						\		1			l				

0 0 10 10 10 1 1 1 1 1 1 1 1 1 1 1 1 1

							-					- 603											
				7	163.9	163.6	163.3 162.9	162.5	167.1	161.7	162.6	163.6 164.2	164.5	164.2	160.5	156.8	155.1	154.5	175.9				
PAGE		:		160	60 60 60 40 4 64 6	81.1	79.0 76.0	74.5	69.8	60 60 60 60 60 60 60 60 60 60 60 60 60 6	69.0	68.3 66.0	62.0	56.0 48.0	39.3	12.6	23.7	-67.3	9.08	88 86 51			
				1	666.7						1		- 1					- 1 '			1 1		
					87.7			- i					ĺ					1	•				
NTION				-	85.7 85.7								1					6	1.0	_	ections		
JET NOISE PROGRAM - ENGINEERING CORRELATION								- [!		- !					- 1			Į.		
EERING			DAY ET		76.2			İ			l		- :					-					1
ENGIN	CHUTE	ALTI IUDE SIDELINE	STANDARD DA		76.8			i			ŀ		- 1			ł					•		
ROGRAM	35 CH	NCISE FOLT ALT FOOT SID	GREE STA		7 6 6 6	İ		Ţ					1			1					Bnd		
WISE P	9	TOTAL NCISE 900.0 FOLT 2128.0 FOOT NO EGA	* 519 DEG ACOUSTIC A	1	75.5	Ì		Ì					- 1								Ġ.	:	
Y JET 1	LE CASES	* * * *	¥ ¥	-	72.2	ļ		Ì			ļ					į							ļ !
אופא אברפנוד	SAMPLE	İ	į	ļ		1		j			į		•			}			9 49	60 69	f en		İ
H01H			i i	!	9 71.6	1					1		- !					- [86	er		: :
					7 73.8	۵	ကစာ	ď.	റത	0.4	40	~ 0	ادما		us a	i dec	o 4	~	2 10		for	: :	 -
		1		4	926	8 4 4	200	97	2 2	7,	3 77	 	77	7 7 7 7 7 7 7 7 7 7 7 7 7	90	30	7 S	9 5	98	96 8	ection	1	
į				36	26.	72	6 6	4	4 4	4 6	75	5.4	74	733	200	4	. 4 . 4	- 1		92.		 	
:				1	67.7	1		- 1				20	99	999	80.00	8	- 9	20	6	96	01.8 05.3		
				FRED	888	100	22.00	200	3150 3150	9 6	630	000	1250								M S S S S S S S S S S S S S S S S S S S	!	!

(561

MA OF CHUTES/SPUKES. 32 DIA OF CHITE EQUIV ANEA TURE TO : 519 TINE: 1300. PT8/PO: 2.1 TINE: 1300. PT8/PO: 2.1 TINE: 1300. PT8/PO: 2.1 TINE: 1300. PT8/PO: 2.1 MOZZLE EXIT CONDITIONS US: 1761.3 RHOS: 0 MERGED FLOW CONDITIONS US: 1124.1 RHOS: 0		SAMPLE CASES	•	32 CHU						
9. VO= 292.V 5.000 VO= 392.V EQUIV AREA DIA= 3.454 376 AT= 0.293 A8= 549 D6= 5.802 A5= 26				, *						
ELECTOR AFER RAILS FLUG DIA* 1 350 FLUG DIA*	NO OF CHUI	ESZSPUKESE (TE EQUIV AREA PO =	12 106E 14 700	0.611	ARCE		0 36			
BIA OF GUTER ROW: 6.300 EQUIV AREA DIA: 3.454 NGZZLE EXII CONDITIONS US: 1761.3 RHOS: 0.0376 AT: 0.293 AB: NERRED FLOW CONDITIONS US: 1124.1 RHOS: 0.0549 DE: 5.802 AS: 28	EJECTOR AE	PT8/PO= EA RAIIC PAR/ 3.850	2.160 AMETER= CANT :	5.000		. 7927.	- - - -			
DIA OF GUTER ROW= 6.300 EQUIV AREA DIA= 3.454 NGZZLE EXIT CONDITIONS US= 1761.3 RHOS= 0.0376 AT= 0.293 AB= HERBED FLOW CONDITIONS US= 1124.1 RHOS= 0.0549 DG= 5.802 AS= 26 US= 1124.1 RHOS= 0.0549 DG= 5.802 AS= 26			*** OUTPU	**						
NGZLE EXIT CONDITIONS US: 1761.3 RHOS= 0.0376 AT= 0.293 AS= HERGED FLOW CONDITIONS US: 1124.1 RHOS= 0.0549 DGs 5.802 AS= 26	BIA OF OUT	ER ROW=	300	EQUIV ARE,	4 DIA=	3.4	3			
NERGED FLOW CONDITIONS US. 1124.1 RH05= 0.0549 DBs 5.802 AS=	NGZZLE EXI	T CONDITIONS		i		93	A8=	9.369		
	MERGED FLC US* 112	W CONDITIONS	0					26.435		
			1							
						<u>.</u>	; 			
									. :	

			150 160 PW	.6 79.3 78.0 149.5 4 78.5 76.7 149.4	9 77.4 75.1 149	2 76.1 73.2 148 3 74.7 71.3 148	3 73 1 69 2 148 1 71 3 66 9 147	6 69,3 64.3 147	1 67.3 61.9 146 4 65.1 59.2 145	5 62.7 56.3 144	4 57.9 50.5 142	4 52 1 43 4 139	7 48.9 39.4 138	4 40.5 28.3 135	3 34.4 20.0 134	8 20.6 0.9 132	7 -14 3 -48 2 130	9 86.4 84.4 159	1 85.0 80			
ELATION			1 4 4 4 4 4 4 4 4 4 4 4 4 4 4 4 4 4 4 4	76.9 78.	77	76 4	0 75	22.	69	67	63	3 58	6 55	3 40	0 43	2 6	2 20	4 86	4 4 8 8 8			
ENGINEERING CORRELATION	DAY	ĒΤ	120	71.8 75.0	5 75	4 76.	5 75	4.6	5 /3. 9 72.	77.	8	0 0 66	0 8	0 20	7 52.	2 43.	7 22	8 85.	90°			
	DISE ST ALTITUDE ST SIDELINE	L.	_ "	77.05	0.0	N 4	4 0	100 (, 4	4 :	40	4 80	ъ с	ا ا	e	40	ω, r	_				
HIGH VELOCITY JET NOISE PROGRAM SAMPLE CASES - 32 CI	MERGED NO.: 1040.0 FOOT 0. FOOT 1. NO E3A	رن	6.	73.0 72.	9	. 6	e0 (c	, cu :	o e o	6	9 (7)	0	on u	-7	- e) -	ر ا) -	10 10			
VELOCITY J		•	0,0	71.8 72.3	4	3 2 4	25 75	14.	8 74 1 73	27.2	9 20 2	6 67	-4 C	ان ام م	0 53	2.2	200	7 85	0 0 0 0			! ! !
H81H			200	7 7 7 8 9 9 9 9 9	72.9	73.5 73.8	73.0	73.7	73.2	71 6	69.1	67.6	4.0	57.7	53.3	43.6	8.6	94.2	89.7 89.7			†
			9	68.5 70.3	72.	22.22	73	12.	72.	70.	67.	64		2 10	9	3.0	28.		98			
			500		6.99	67.4 67.6	67.7	67.1	66.4 65.5	64.3	60.09 09.09	2.86.7	52.4	42.2	34.4	15.7	-31 4	27.6		89.9		

	}	PVL 128.0 132.0 132.0 137.6 140.6	24.20 24.20 20.10 20.10 20.20	0.001 0.001 0.001 0.001 0.001 0.001 0.001 0.001 0.001 0.001 0.001 0.001 0.001 0.001 0.001 0.001	
		0.1444000000000000000000000000000000000	63.2 63.2 65.2 67.2 67.9 66.7 69.8	500.7 500.7 500.2	26 15
		0.00 0.00 0.00 0.00 0.00 0.00 0.00 0.0	65 3 67.7 71.2 72.5 72.5 69.3	8 8 8 8 8 8 8 8 8 8 8 8 8 8 8 8 8 8 8	7.
2			1 1	0 0 0 0 0 0 0 0 0 0 0 0 0 0 0 0 0 0 0	
RELATIO				6. 1 6. 1 6. 1 6. 1 6. 1 6. 1 6. 1 6. 1	
SI NG COR				4 4 5 5 5 5 5 5 5 5 5 5 5 5 5 5 5 5 5 5	
- ENGINEERING CORRELATION	UDE INE ARD DAY			9 0 0 0 0 0 0 0 0 0 0 0 0 0 0 0 0 0 0 0	
	GED NOISE FOOT SIDELINE OREE STANDARD ANDLE FROM INL		(9 8 9 4 4 5 6 6 6 6 7 4 4 8 8 9 7 7 8 9 8 8 9 7 7 7 8 9 9 9 7 7 7 8 9 9 9 9	
NOISE PROGRAM	PREMERGED N 1040.0 FGGT 1070.0 FGGT 1070.0 FGGT 1070.0 FGGT 1070.0 FGGT 1070.0 FGGT 1070.0 FGGT 1070.0 FGGT			78.9 78.9 78.9 78.9 78.9 74.1 74.2 74.1 74.2 74.1 74.1 74.1 74.2 74.1 74.1 74.1 74.1 74.1 74.1 74.1 74.1	
JEI E CA	* * * * * * * * * * * * * * * * * * *	1] /	900 99 99 99 99 99 99 99 99 99 99 99 99	
HIGH VELOCI IY		O & r 4 w	100010-0	00000000000000000000000000000000000000	0
HIGH			1 1	7 1 2 2 2 2 2 2 2 2 2 2 2 2 2 2 2 2 2 2	
		4 22 K 80 00 00 00 00 00 00 00 00 00 00 00 00	71.4 73.6 77.6 77.6 80.0 80.9	7 6 6 6 6 6 6 6 6 6 6 6 6 6 6 6 6 6 6 6	1.78
		2 1 2 2 2 2 2 2 2 2 2 2 2 2 2 2 2 2 2 2	70.3 72.4 76.3 76.3 76.3 76.3 76.3	- 0.00 0.00 0.00 0.00 0.00 0.00 0.00 0.	20
		4 1 2 2 2 2 2 2 2 2 2 2 2 2 2 2 2 2 2 2	69. 7. 7. 7. 7. 7. 7. 7. 7. 7. 7. 7. 7. 7.	25	8 9
		580. 100. 180. 180.	23 25 25 25 25 25 25 25 25 25 25 25 25 25	2500 2500 2500 3150 5000 6300 6300 6300 6300 6300 78FL	ENL T

								•																	
3E 11				PE	100	108.3	0.11	110.7	122.6	126.0 20.0	32.4	135.2	139.6	140.7	141.7	146.0	45.9	4.0.0	143.2	141.7	154.1				
PAGE				160	25.5	29 -	33.0	30.4	43.4	4 g	53.5	36.8	9 09	60 3	57.7	2	48.7	36.0	22.0	26.3	67.4	76.2			
				150	10 C	35.0	36.5	2 4 0 6 0 10	47.0	80 E	22.0	60.09	. 49 . 6	65.3	6.4 6.0	61.4	27.3	. 4	30.6	200	72.6	8 62 52 53 53 53			
				140	27.3	34.8	38.7	4 4 7 10 10 6	49.4	60 E	90.0	63.5 63.5 63.5	67.3	68.1	67.9	64.7	610	32.5	6.9	20 50	78.00	85.7			
LATION				130	200.1	36.4	40.3	2. 7. 2. 0.	51.0	40 E	61.6	65.1	68.89	69.5	68	65.4	4	25.0	9. 0 0	35.7	76.8	86.8 86.8			
- ENGINEERING CORRELATION				120	30.0	37.5	4.	4 4 6 8 9 4	52.0	10 to	62.5	0.98	9 00	9 69	68.6	63.9	0	83 O	51.1	3.6	76.8	86.35 25.35			!
INEERIN		> *		110	27.5	34.6	38.1	24 4	49.0	00 E	59.5	62.00	0.69	9.89	66.0	63.9	9 0	200	55.0	37.6	75.6	80 80 80 80 80 80			
M - ENG	CHUTE	ALTITUDE SIDELINE STANDARD	FKOM IN	100	27.6	35.0	38.5	4 4 4 0	49.4	(1) (2) (3) (4) (5)	59.7	62.8	67.4	67.5	66 3	19	60 8 4. 0	61.4	57.9	38.0	74.8	89 69 1. 1.			
PROGRA	. 32	CM - E F001 F001	ANGLE	96.5	27.7	35.1	38.6	2 4 4 2 6 0 0	49.4	50 F0 60 A	59.5	62.4	66.3	62.8	63.9	0.00	ر ان ان	63.2	57.0	39.5	74.1	93.0			
T NOISE	SES	SHO 1040 0	COUST	08.2	28.7	36.1	39.6	6 4 6 6 6 6	50.3	53.7	60.0	62.7	92.0	64.8	62.6	62.5	0 0	6.00 6.00 6.00	56.5	90.00	74.7	87.4 87.4			
פו דדום	SAMPLE CA		<	70,	200	33.2	36.7	4 4 7 - 7	47.5	50.8 8.6	57.3	60.0	64.1	64.5	0 09	60.9	7 99	2 4 2 4 1 2	57.7	000	73.9	87.2			
HIGH VELOCLIY JET NOISE PROGRAM	9			9	200	33.6	37.1	0 4 0 4 0 4	47.8	2 Z	57.4	39.9	63.4	63.3	60.5	63.0	- 67.79	9.00	56.4	38.0	74.1	87.6			
Ŧ				စ္တင္မ	200	33.6	37.1	4 0 4 0 4 0	47.7	00.00 00.00	57.0	59.3	- 2	8 9	60 60 60 60	7.40	- F	67.8	6, 10	340	73.7	87.6 87.6			
				40	0 0 0 0 0 0	33.1	36.5	40.0	47.0	- 00 - 00 - 00 - 00	56.0	58.1	60.09 .00	29.0	28 e	65.0	079	57.3	51.2	25.0	72.3	86.2 87.2			
				30	5 2 6	31.7	35.1	26.5 20.5	45.5	4.00 10.00 10.40		56.0	0.70	57.0	33.9 38.4	63.1	4 6	9 60	43.8	20.00	69.4	82.7 83.8			
				02	. 57 . 60 . 60 . 60	20.00	32.3	30.7	42.4	4 4 4 -	30.6	52.2	63.2	52.2	0 -	57.3	22.2	6 6	28.3	7 2 2	63	76.1			
				FREG		00	125	160. 200.	250.	315.	200	630.		250	. 600	.200	000	000	3300.	0000	SPL	부 부 **	PN		[

				!		SAMPLE	CASES	- 32	CHUTE								
							* TOTAL * 1040.0 * 0.	F001	ALTITUDE SIDELINE	MA							
				!			* JE	FORFE	100	RD DAY							
							Acoustic		<u>. </u>	N E							
	!	4	i I	i	09	70	80	6	00.	= :			140	150	160	l '	
50. 62.6		~ 9	N 4		66.9	69 72 0	727	72.7	70 Z	22			78.6	9 69	- 0 - 0 - 0 - 0 - 0	0. 04 0. 00 0. 00	
ł		9	4	i	3 2/	73.3	73 9	73 5	72.6	73	- 1		78.4	78.5	76.7		
		rc. e	ი (7.5.7	- 0	74.6	74.2	73.4	5,73			7 10 0 0	77.5	73.2		
		, 0	o 1^		4 6	4 10 0 4	7 0	7.4	- 4	4 5			76.5	. 4	, <u>r</u>	_	
	-	80	4	-	75.6	75.9	76.4	76.1	75.4	75			75.8	73.5	69.5		
		6 0 (ω.		76.3	76.0	7.	76.9	76 2	1 2			7.25	72.3	67.9		
		.	~ N		78.2	78.1	79.5	2 - OS	78.6) P			10.0	9.5	0.99		
-			6		79.4	79.2	80.3	80.3	79.8	90	1	1	78.7	72.3	67.6	٦	
		a :	so s		90 10 10 10	80.3	4.6	4	- 6	60 6			76.6	13	69.3		
		٠.	. -		. 4	95.5	82.4	9 60	9 60	9 6			9 60	2 2 2	67.1		
- 1		60	7		82.2	92.0	81.1	91.1	81.5	82	İ	-	74.5	70.9	65 4		
		6	_		80.5	80.5	79.2	79.3	79.0	90			72.8	69.1	63	_	
		n c	8 N		75.4	76.0	74.6	74.5	73.8	7.5			67.9	63.8	5 6 5 6 6 6		
Į	Ì				73.5	73.2	72.1	71.5	72.0	72		ļ	64.1	59.5	50.7		
		e 0 (- 1		70.4	400	9 69	58.7	68.6	99			9 6	2. 2. 2. 2. 2. 2. 2. 2. 2. 2. 2. 2. 2. 2	43.0		
		O #	\ (67.0	90	 4	67.4	4.6	9 6			0 4 0 4 0 4	00 F	9 6 N C		
			۰ د	•	- 0 - 0 - 0	5.4	54	0 R.	2 10	- K			37.1	26.9	3.4	_	
ľ			01		42.3	44	44.9	44 9	45.	43			20.3	6.2	-24 0	-	
		7	9		91.0	C .	91.2	16	91.0	9			88.7	87.4	85.0	_	
	96.	966	တ ဟ	200 200 200 200	မ (၁)	100.6	100.2	001	100.2	100 6	98.7	97.0	9 9 2 4 0 0	<u> </u>	6 6 6 6 6 6		
7.78 =						1	! i !										
105.2	Corr	Correction	for	number	of en	engines	and gro	ground rei	reflections	ns.							

PAGE									**************************************	
EERING CORRELATION		VO= 397.0	DIA* 3,404	100						
ISE PRO	SAMPLE CASES - CONICAL SEE INPUT SEE	TO = 518. PO = 14.700 TTB= 1650. PTB/PO= 3.230 EJECTOR AREA RATIO PARAMETER= 0. PLUG DIA= 0. CANT= 0.	***OUTPUT *** DIA OF GUTER ROW: 5.663 EQUIV AREA DIA-	TIONS RHO8= 0.037						

				- 0	8	. ~ .	o e.	7	v 00	OH -	- (v	6 6		~ 4	· O	0 •	. N	9				
			-	172.0	7-					٦-			1-		٠			7.	99			
			160	2 5	86.5	96.3	9 2	78.2	77.00	67.9	50.00	95.3	44	37.0	16.5	4 6	40.0	-84-1	97.6	0.00 0.00 0.00		
			50.0	9	95.7	6.0	, 6. 20 30 30 30	68.7	83.7	90.0	4	1.1.	62.4	57.2 7.2	42.1	30.5	9 0	28.	2 2	102 3		
			140	100	9 69	98.1	9.08 4.08 4.4	95.0	7 W.	89.5	94.6	81.8 78.5	74.7	4.08	56.0	48.4	23.0	0 1		0.60		
ATTON			30	201	96.6	7 1	7.70	6.96		93.6	. O	98 2 2 2 2	92.4	7.8.7	58.1	9.6	. o	8 6	27.5	0.0		
HIGH VELGGITY JET NOISE PROGRAM - ENGINEERING CORRELATION SAMPLE CASES - CONTCAL							n (0	10 5	۰.	go. u	. –	m a		~ 4		o a	. N	6		0.00		
E R ING			i		İ			i		1			ĺ						-	05.5		
ENGINE	COURT TOUR	INLEY			-			ļ							Ì							
CONTCAL	MIXING NOISE FOOT ALTITUDE FOOT SIDELINE		l					!							-					103.8		
- FRE	CONICAL MIX 900.0 F001. 2128.0 F001.	C ANGLE			-					1										102.4		
CASES	2 2 2 8 8 8 8 8 8 8 8 8 8 8 8 8 8 8 8 8	8	90,77	0	81.9	83.0	8 8 6 4	88	9 69	85.0	 	4.0	78.6	76.1	68.2	61.6	46.5	30.3	9 10	101		
SAMPLE			0,2	76.4	79.0	800	92.08	93.4	93.0	83.8	95.9	. C. C.	78.0	4.07	67.4	60.8		28.3	9 6	0.0		
S AET			90,	3 10	79.5	80.2	82.2	82.6	83.0	82.8	9:0	80.3	9.92	73.8	65	- 0	4 . 	23.2	0.0	0.0		
H			3.20	74.9	76.5	79.1	0.08	81.3	6 60	61.2	79.7	78.3	74.2	71.1	61.7	53.7	35.4	2 2	- O	0.76		
			}					ļ		1			}		j			- ['	•	0 0 0 0		
			Ì,	- m			· -		• ~	<u>.</u>		~ ~		.		.	• ~	ر ا		91.3		
			1		1					1			1		- 1			1		0.00		
			İ						400. 72	-			1				•	1	7		106.4	

									_									_	1	-							
•							56.3 59.1	a «	. 0	ω . σ		0.	- 4	•	~ 6	a	۳. د	. IO (2) ID (n c	N -	-				
PAGE						1 '		7"]_		7	7		٦			7-		7	156.2	-				
•						160	7 6	78	93.	83.7	9	2.2	73.8	74.2	20.0	65	9 5	4.6	9 -	80	-63	-124.4	9 6 6				
						150	7.6.7	82.5 6.5	87.6	98.7	67.1	4 c	79.2	77.2	76.8	73.6	6.69	80	38.6	30.8	-19	6. 6. 6.	100.7				
						140	62.2 62.2	85.5	9.0	9 9 2 0 2 4	9.15	60.0	96.2 86.2	83.7	78.4	75.5	72.7	20.	48.7	4.0	9 0	90.0	103				
i	LATION					130	0 0 0 0 0 0 0 0	97.2	20.00	2 2 - 2	93.9	92.5	9.0	87.8	0 0 0 0 0 0 0 0 0 0	80.4	76.9	9.69	54.9	49	15.6	-13.1	0.90				
	HIGH VELOCITY JET NOISE PROGRAM - ENGINEERING CORRELATION SAMPLE CASES - CONICAL					120	6 4 7	0.68	80.0	9. 49 6. 6. 6.	93.2	e .	96.7	84.2	92.0	91.6	7 6 7 7 7 7 7 7 7 7 7 7 7 7 7 7 7 7 7 7 7	7.5	0 10	53.5	23.4	-2.3	7.50				
	NEERIN			DAY	INLET	110	9.7.6 9.1.3	87.9	96	9 9 - 0 6 4	91.0	4 4	80.0	96.6	87.8 86.9	83.9	80.7 77.6	74.0	62.2	57.6	29.4	2.0	200		;		
	GRAM : ENG		CONICAL SHOCK NOISE 900.0 FOOT ALTITUDE 2128.0 FOOT SIDELINE	STANDARD DAY	FROM .	100	9 9	86.4	88.4	6.00	87.5	66.1	90.0	6 06	999	84.4	7.10	74.8	63.5	20.0	32.0	0 0 0 0 0 0	100 100 100 100 100 100 100 100 100 100				
	PROGRA - CON		FOOT A	EOREE S	ANGLE	06	0.00	83.3	- 6 - 6 - 6 - 6 - 6 - 6 - 6 - 6 - 6 - 6	96 0.0 8.0 8.0 8.0	96.0	9 00	. 6	89.4	87.9	84.9	78.7	120	63.9	200	32.6	1.9 0.5	106.2				
	ET NOISE CASES		2128.0	319 EQ	ACOUSTIC	0	60.4 6.4	82.7		40 4 60 4 60 4 60 4	200	9.5	2 G	90.2	86.9	92 2	82.7 7.07	9	64.6	60.1	33.1	6.1.0	4.701				
!	SAMPLE C		* * *	* -	₹	0,	7.7.7	79.9	62.4	82.4 4.6	89.3	9.40	- C.	91.3	60 60 60 60 60 60 60 60 60	8 9	84.0 8.0	77.6	65.9	9.5	33.2	7.0.1	108.35 58.35				
ı	OH VELO					90	74.9	79.1	9 0	81.08 0.08	93.0	96.7	. 60	92.0	90 90 90 90	87.2	84.6 6.0	17.1	64.7	59.7	29.5	B. 60	0 0 0 0 0 0 0 0 0				
	Ī					20	73.5	78.0	9 6	81.4 4.4	92.	8.96	2. 6.	91.6	90 90 3	86.6	93.0	78.7	95.0	56.6	25.2	4.0	108.2				
						40	2 2 2 3 3 3 3 3 3 3 3 3 3 3 3 3 3 3 3 3	76.4	78	91.6	95.4	920	200	80.08	89.2 27.2	83.0	82.0 77.	72.0	57.0	30.0	35.2	0.10	6.90	ı			
						30	70.2 73.1	74.1	76.4		94.0	93.2	. O	0.69	96 94 5	81.8	78.2	67.4	47.8	40.	10.0	-20.9	0.70				
						50	8. 8. 8. 9. 9. 9.	70.6	73.4	79.2	9.06	69.	- 60	2 10	78.5	75.3	20.5 6.5	26.0	28.6	9	- 0	113.1	- 00 00 - 00 00	9			
						1		- 1			1			ı		- 1			1			•	PNL				
	_L	l	L	_1_		_					L			L											L	11204	l '

		,			ĺ	8 171.2	- 1			- }						1			1			1								
						96.9 92.				ļ											•	1	· •	2. 96.6						
					1		- 1			- [Ί'	_	10.4 105			}			
TION										-												1	_	9.11			reflections.			
HIGH VELOCITY JET NOISE PROGRAM - ENGINEERING CORRELATION					Ì	9.06	7	e c	n on	0	4 4	n	٥	n o	9	9	- 01	- (9	. •	4		7 7	109.90	!					
UNEERING			DAY	LET	110	60 - 40 - 60 - 60 - 60 - 60 - 60 - 60 - 60 - 6	87.3	69.7	93.2	94.0	93.6	9.16	91.0		83.8	67.5	. 7	78.0	73.0		49.9	32.9	102.9	106.1			and ground			
AM - ENG	CONICAL	CONICAL TOTAL NOISE 800.0 FOOT ALTITUDE 2128.0 FOOT SIDELINE	STANDARD	FROM INLET	100	93.7	96.1	88.3	90.06	6 06	6.00 6.00 6.00 6.00	6 6 6	92.4	92.08	98.7	278	9 6	78.4	7 5	62.5	7.15	35.4	101	107.6			and EGA,		, , ,	
SE. PROGR	8	1CAL TOT 0 FOOT 0 FOOT	DEGREE	CRUSTIC ANGLE	1		Į			1			1			1			1			1	_	107.8			shielding a			
JET NOT	CASES	* CGN	8 ×	ACOUST		80.6				1			1			1						ı		108.5						
ELOCITY	SAMPLE				1					1			-										_	1 109.2			f engines,			
и нети										1			-						-				-	7 109.1	1		number of			
							i	ì					-{									1	_	07.3 108.7]		for			
						6 P	. 01	0	1 0	-	- 0	7 01	2		. 60	٥,	4 0	^	7	- 40	~	٦,	- به	7 107]		Correction			
									- A			u A1	~	. "		ا.	۰ ۳],			-53.7	9.21	100.2		- K	2 2 2	0.61		
					1			l		- [- 1			-			- 1			- 1	•	Z	1 :	EPAL : 12	T -	-		

21													
PAGE													
Ž													
							1			;			
	•						}					:	
					9.100								
Z	5				A8=	i			,				
RRELAT!			397.0	404									
9 9 2			•0>		9 . 100								
ZO SEE				AREA DI	AT.								
	CONICAL	T	00	UT *** FOULY AREA DIA:	9								
MIGH VELOCITY JET MOISE PROGRAM - ENGINEERING CORRELATION	8	*** TUPUT ***	4.700 2.160 TER=	<u>2</u>	0.03								
	ASES	*	TG = 518 P0 = 14.700 TTG= 1300. PT6/P0= 2.160 EJECTOR AREA RATIO PARANETER= PLUG DIA= 0. CANT=	# 85 # 85 # 85	EHGB=		:						
21 TV JE	SAMPLE CASES		RAT10.	ğ	MOZZLE EXIT CONDITIONS U6= 1761.3 RMG6=		!						
5 2 3	\$		519. 1300. 38 AREA 31 A=	DIA OF CUITER ROWs	EXIT						'		
I			TTG: EJECT	0 4 10	NGZZLI U8=							ł	

FREG 20 30 40 50 60 70 80 E0A TATITUDE 1040.0 FOOT ALTITUDE 20 66.3 69.2 71 0 75 0 75 8 75 4 76 8 75 8 10 80.3 80.3 78 1 100. 71.7 74.8 75 75 75 75 75 75 8 75 75 75 75 75 75 75 75 75 75 75 75 75	M	2 2 3 3 3 3 3 3 3 3 3 3 3 3 3 3 3 3 3 3	9 9 9 9 9 9 9 9 9 9 9 9 9 9 9 9 9 9 9	0 0 0 0 0 0 0 0 0 0 0 0 0 0 0 0 0 0 0	160 PWL 91.6 161.7 91.0 162.4 90.0 162.6 88.6 162.6 84.8 162.2
## STORTER STORT S	7 7 7 6 7 7 7 7 6 7 7 7 7 6 8 8 8 8 8 8				
20 30 40 50 60 70 60 70 60 77.3 66.9 77.3 66.9 77.3 77.3 77.4 76.6 77.4 77.4 77.4 77.4 77.4 77.4	0 4 4 6 9 0 9 0 9			_ a a w a r c	
20 30 40 50 60 70 60 90 66:3 72:2 71:0 72:0 72:0 73:4 76:0 77:3 70:2 73:2 73:4 76:4 78:0 77:0 77:0 77:0 77:0 77:0 77:0 77:0 77:0 77:0 77:0 77:0 77:0 80:0 81:0 <th< th=""><th>0.77 0.00 0.00 0.00 0.00 0.00 0.00 0.00</th><th></th><th>!!!</th><th></th><th></th></th<>	0.77 0.00 0.00 0.00 0.00 0.00 0.00 0.00		!!!		
66.3 68.2 71.0 72.0 72.8 73.4 76.8 77.3 73.5 73.5 73.5 73.5 73.5 75.0 77.3 75.8 75.4 76.8 77.3 77.3 77.3 77.3 76.4 77.8 76.4 77.8 76.4 78.4 78.9 77.3 77.3 77.3 76.4 77.3 77.3 77.3 76.5 78.5 78.6 78.6 78.6 78.8 78.6 78.8 78.6 78.8 78.6 78.8 78.8	6 6 6 6 6 6 6 6 6 6 6 6 6 6 6 6 6 6 6		! !	01 02 02 02 02 02 02 02 02 02 02 02 02 02 	
69 2 72.2 73 9 75.0 75 6 76.4 70.9 70.9 70.9 70.9 70.9 80.3 70.9 80.3 70.9 80.3 80.3 80.3 80.3 80.3 80.3 80.3 80.3 80.3 80.3 80.3 80.3 80.3 80.3 80.3 80.3 80.4 81.9 80.3 82.4 70.3 70.3 82.4 80.3 82.2 80.3 82.2 80.3 82.2 80.3 80.3 82.2 80.3 80.3 80.2 80.3 80.3 80.3 80.3 80.4 80.2 80.3 80.3 80.3 80.4 80.3 <td< td=""><td>2</td><td></td><td>1</td><td>3 4 6 GO 6</td><td></td></td<>	2		1	3 4 6 GO 6	
71.7 74.6 76.6 77.8 78.7 79.3 80.9 81.4 72.5 75.7 77.7 78.6 79.8 80.4 81.9 82.4 73.2 77.7 78.6 79.8 80.7 81.9 82.4 73.6 77.4 79.5 80.9 81.0 82.2 73.6 77.4 79.6 80.9 82.0 82.2 83.0 83.8 84.4 73.8 77.4 79.6 80.9 82.0 82.2 83.0 83.8 84.4 73.5 77.3 79.7 81.2 82.2 83.0 83.8 84.4 73.5 77.3 78.9 79.4 81.2 82.2 83.0 83.5 84.0 72.0 75.3 78.9 80.5 81.8 82.7 83.0 83.5 84.0 77.7 75.3 78.9 80.5 81.2 82.1 82.2 83.0 83.5 83.5 83.1 74.0 77.0 77.5 88.8 80.3 81.2 82.8 83.0 83.5 83.5 83.1 74.0 77.0 77.5 88.8 80.3 81.2 82.8 83.8 83.8 83.8 83.8 83.8 83.8 83	8 8 8 8 8 8 8 9 9 9 9 9 9 9 9 9 9 9 9 9		!	6 V 6	
72.5 75.7 77 78.6 79.6 80.4 81.9 82.4 73.2 77.1 78.6 79.8 80.4 81.9 82.4 83.2 73.6 77.1 79.5 80.7 81.3 82.7 83.2 73.6 77.1 79.5 80.4 81.5 82.2 83.0 83.8 84.4 73.8 77.3 79.7 81.2 82.2 83.0 83.8 84.4 73.5 77.3 79.7 81.2 82.2 83.0 83.8 84.4 73.5 77.3 79.7 81.2 82.2 83.0 83.8 84.4 72.9 76.9 79.4 81.0 82.2 83.0 83.5 84.0 72.0 75.3 78.9 80.5 81.8 82.7 83.0 83.5 84.0 77.7 75.3 77.0 77.5 88.1 88.2 82.1 82.2 82.8 83.6 83.5 83.1 74.0 77.0 77.5 88.0 80.3 80.3 80.3 87.1 72.5 77.5 77.6 77.6 77.6 77.6 77.6 77.6 77	8 8 8 8 8 8 8 8 8 8 8 8 8 8 8 8 8 8 8		ļ	N 69	
73.2 76.5 76.5 79.7 80.7 81.3 82.7 83.2 73.6 77.1 79.2 80.4 81.5 82.2 83.3 83.8 87.3 87.1 77.3 79.2 80.4 81.5 82.2 83.0 83.8 84.4 73.8 77.3 79.7 81.2 82.2 83.0 83.7 84.2 73.5 77.3 79.7 81.2 82.2 83.0 83.1 83.8 84.4 73.5 77.3 79.7 81.2 82.2 83.0 83.5 84.3 72.0 76.3 79.4 81.0 82.2 83.0 83.5 84.0 70.7 75.3 78.1 79.8 81.2 82.1 82.2 82.8 83.1 83.5 83.5 83.5 83.1 74.0 77.0 78.9 80.3 81.2 82.8 83.8 83.8 83.1 74.0 77.0 78.9 80.3 80.3 81.2 80.1 80.2 82.8	တ္တန္တာ မေရာ မေရာ မေရာ မေရာ မေရာ မေရာ မေရာ မေရ		ļ	,	_
73.6 77.4 79.5 60.9 82.0 62.7 83.7 84.2 73.6 77.3 79.7 91.2 82.2 83.0 83.7 84.2 73.5 77.3 79.7 81.2 82.2 83.0 83.8 84.4 73.5 77.3 79.7 81.2 82.3 83.1 83.8 84.3 72.9 76.9 79.4 81.0 82.2 83.0 83.5 84.0 72.0 76.3 78.9 80.5 81.8 82.7 83.0 83.5 69.1 74.0 77.0 78.9 80.3 80.3 81.2 82.8 83.6 69.1 74.0 77.0 78.9 80.3 80.3 81.2 82.8 83.8 83.1 83.8 83.8 83.8 83.8 83.8 83	86 86 36 36		Į.	•	_
73.8 77.5 79.7 81.2 82.2 83.0 83.8 84.4 73.5 77.3 79.7 81.2 82.3 83.1 83.8 84.3 72.9 76.9 79.7 81.2 82.3 83.1 83.8 84.3 72.0 76.3 78.4 81.0 82.2 83.0 83.5 84.0 70.7 75.3 78.9 80.5 81.8 82.7 83.0 83.5 83.1 82.2 82.8 83.1 74.0 77.0 78.9 80.3 80.3 81.2 82.8 87.1 72.5 77.6 77.6 78.9 80.3 80.3 81.2 82.8 87.1 72.5 77.6 77.6 79.1 80.2 80.1 80.2	96.6			9	7
73.5 77.3 79.7 81.2 82.3 83.1 63.8 84.3 72.9 76.9 79.4 81.0 82.2 83.0 83.5 84.0 72.0 75.3 78.9 80.5 81.8 82.7 83.0 83.5 70.5 75.3 78.9 80.5 81.8 82.7 83.0 83.5 89.8 89.1 74.0 77.0 78.9 80.3 81.2 81.3 81.8 87.1 72.5 75.6 77.6 78.9 80.3 81.2 81.3 81.8 87.1 72.5 75.6 77.6 78.9 80.3 81.2 81.3 81.8				0	-
72.9 76.9 79.4 61.0 82.2 83.0 83.5 84.0 72.0 76.3 78.9 80.5 81.8 82.7 83.0 83.5 70.7 75.3 78.1 79.8 80.2 81.2 81.3 81.8 69.1 72.5 77.6 77.6 78.9 80.3 81.2 81.3 81.8 67.1 72.5 75.6 77.6 77.6 79.1 80.2 80.1 80.2	86.6			٠,	
72.0 76.3 76.9 60.5 61.6 62.7 65.0 65.2 70.7 75.3 76.7 76.9 60.3 61.2 61.3 61.6 69.1 72.5 75.6 77.6 78.9 60.3 61.2 61.3 61.6 67.1 72.5 75.6 77.6 79.1 60.2 60.1 60.2	4 9 9	1		4 0	7"
69.1 74.0 77.0 78.9 60.3 81.2 81.3 61.8 67.1 72.5 75.6 77.6 79.1 80.2 60.1 80.2	92.0			9 0	-
67.1 72.5 75.6 77.6 79.1 80.2 80.1 80.2	0.4.0			6	-
	9 0			0 4	7
64 4 70 4 73 6 76 0 75 7 76 9 76 7 77 3	78.6			0	9.8 152.3
56.9 64.6 68.9 71.6 73.5 74.8 74.5 75.1	76.3			o	7 150
51.3 60.3 65.4 68.4 70.6 72.0 71.7 72.3	73.3		1	6	149
43.2 54.4 60.5 64.1 66.6 68.3 68.0 68.5	69.2			4 4 4 6 4 6	4 10
24.7 30.6 40.8 50.9 53.6 53.5 59.7 59.6 60.4	- 09			33.8	6 144
3.8 26.2 37.6 44.3 48.6 51.4 51.6 52.5	51.6		- [-	143
-23.5 7.1 22.4 31.3 37.0 40.6 41.3 42.3	40.7		6	9	0.0 141.9
83.7 87.5 89.9 91.4 92.6 93.4 94.2 94.7	9.96		603	m e	ר ה
886.6 93.3 96.3 98.4 100.0 101.0 101.3 101.9 1	03.0		105.2	2.00	
				9	9.0

الناف

** CONTICAL PROPER STANDARD DAY ** STORD TOTAL TINDE ** TOOL OF FOOT ALTHURE ** TOOL OF FOOT	## 1040 0 FOOT ALTITUDE ## 104	8 8 8 8 8 8 8 8 8 8 8 8 8 8 8 8 8 8 8	2 2 2 2 2 2 2 2 2 2 2 2 2 2 2 2 2 2 2	CONICAL 1040.0 FFQ 1040.0 FFQ NO FGA S19.0 EGR E8.5 6 64 62.2 6 1 62.2 6 1 73.3 73 74.8 75 75.9 76 84.6 90 84.6 90	ACK NOT STANDING STAN	, , , ,					
## STORE FROM INLET ## SCOUSTIC ANGLE FROM INLET ## SCOUSTIC ANG	ACCUSTIC ANGLE FROM INLET ACCUSTIC ANGLE FROM INLET 5.59.9 59.0 70 80. 90. 100 110 120 130 140 150 150 5.61.8 52.5 52.5 52.6 15 51.5 51.3 64.3 64.3 65.3 61.8 55.5 52.5 52.5 52.5 52.5 52.5 52.5 52	0.00 0.00 0.00 0.00 0.00 0.00 0.00 0.0	A	200	E FROM 1000 65 0 0 0 0 0 0 0 0 0 0 0 0 0 0 0 0 0	1 3 1 1					
ACOUSTIC ANGLE FROM INLET 50 60 70 80 90 100 110 120 130 140 150 160 160 162 62 62 62 61 5 61 5 61 5 61 61 62 63 63 63 63 63 64 65 62 65 62 62 62 62 62 62 62	ACCUSTIC ANGLE FROM INLET 50	6 5 5 6 6 6 6 6 6 6 6 6 6 6 6 6 6 6 6 6	0.000 0.000	9	61.00 61.00 61.00 7.77 7.00 7.00 7.00 7.00 7.00 7.00	NLET 110 61.3 64.8 64.8 71.7 74.8 74.8 76.0					
50 60 70 80 90 100 110 120 130 140 150 160 62.6 62.9 63.0 61.5 61.5 61.6 63.6 65.7 66.7 66.0 67.1 65.7 66.0 67.1 65.7 66.0 67.1 65.7 66.0 67.1 67.1 67.1 67.1 67.1 67.1 67.1 67.1 67.1 67.1 67.1 67.1 67.1 77.2 <	50 60 70 80 90 100 110 120 130 140 150 160 160 170	6 6 6 6 6 6 6 6 6 6 6 6 6 6 6 6 6 6 6 6				011 64.00 7.17 7.17 7.00 0.00 0.00 0.00 0.00			1		
59.6 59.6 59.6 59.7 61.5 61.5 61.3 64.3 63.3 61.6 61.3 64.3 63.3 61.6 61.3 64.3 63.3 61.6 61.6 61.0 62.5 66.7 62.6 66.7 64.3 63.3 61.6 62.4 64.3 63.3 61.6 62.4 60.0 61.6 62.4 62.6 60.0 61.6 62.4 62.6 63.4 63.3 61.6 63.4 63.3 61.6 63.4 63.3 61.6 63.4 63.3 61.6 63.4 63.3 61.0 79.4 67.1 70.6 71.6 71.7 74.8 74.9 74.4 74.4 74.4 74.4 74.4 74.4 74.4 74.9 74.4 74.3 <th< td=""><td>59.6 62.9 62.7 65.5 61.5 61.3 64.3 61.9 59.6 53.6 61.8 65.2 60.0 67.1 65.6 65.4 660.0 67.1 65.6 65.4 660.0 67.1 65.6 65.4 660.0 67.1 65.6 65.4 660.0 67.1 65.6 65.4 660.0 67.1 65.6 65.4 660.0 67.1 65.6 65.4 660.0 67.1 65.6 65.4 660.0 67.1 65.6 65.4 660.0 67.1 67.0 67.1 70.6 71.0 73.3 73.5 74.4 74.6 76.7 19.7 67.6 19.2 77.8 76.6 74.3 77.8 76.4 77.8 76.6 74.3 77.8 76.4 77.8 76.4 77.8 76.4 77.8 76.4 77.8 76.6 74.3 77.8 76.4 77.8 76.4 76.0 19.2 77.8 76.4 77.8 77.8 77.8 77.8 77.8 77.8 77.8 77</td><td>62 6 62 6 67 6 67 6 67 6 67 6 67 6 67 6</td><td></td><td></td><td></td><td>61.3 64.0 7.1.7 7.4.0 7.0 7.0 7.0 7.0 7.0 7.0 7.0 8.0 8.0 8.0 8.0 8.0 8.0 8.0 8.0 8.0 8</td><td></td><td></td><td>1</td><td>}</td><td>7</td></th<>	59.6 62.9 62.7 65.5 61.5 61.3 64.3 61.9 59.6 53.6 61.8 65.2 60.0 67.1 65.6 65.4 660.0 67.1 65.6 65.4 660.0 67.1 65.6 65.4 660.0 67.1 65.6 65.4 660.0 67.1 65.6 65.4 660.0 67.1 65.6 65.4 660.0 67.1 65.6 65.4 660.0 67.1 65.6 65.4 660.0 67.1 65.6 65.4 660.0 67.1 67.0 67.1 70.6 71.0 73.3 73.5 74.4 74.6 76.7 19.7 67.6 19.2 77.8 76.6 74.3 77.8 76.4 77.8 76.6 74.3 77.8 76.4 77.8 76.4 77.8 76.4 77.8 76.4 77.8 76.6 74.3 77.8 76.4 77.8 76.4 76.0 19.2 77.8 76.4 77.8 77.8 77.8 77.8 77.8 77.8 77.8 77	62 6 62 6 67 6 67 6 67 6 67 6 67 6 67 6				61.3 64.0 7.1.7 7.4.0 7.0 7.0 7.0 7.0 7.0 7.0 7.0 8.0 8.0 8.0 8.0 8.0 8.0 8.0 8.0 8.0 8			1	}	7
64.5 63.5 63.6 63.6 63.6 63.7 71.4 71.4 71.6 71.7 74.4 70.6 74.7 74.6 74.1 74.6 74.7 74.6 74.7 74.6 74.7 74.6 74.7 74.6 74.7 74.6 74.7 74.6 74.7 74.6 74.7 74.6 74.7 74.6 74.7 76.6 74.7 76.7 77.0 <th< td=""><td>64 55 56 56 57 71 71 74 67 67 67 67 67 67 67 67 67 67 67 67 67 67 67 70 67 70<</td><td>67.9</td><td></td><td></td><td></td><td>24.0 74.0 78.0 80.4 80.4</td><td></td><td>1</td><td>1</td><td></td><td>134.2</td></th<>	64 55 56 56 57 71 71 74 67 67 67 67 67 67 67 67 67 67 67 67 67 67 67 70 67 70<	67.9				24.0 74.0 78.0 80.4 80.4		1	1		134.2
68.3 69 6 70.5 71.0 73.3 73.5 74.4 74.8 76.3 77.8 76.6 74.4 71.0 17.0 17.1 70.0 17.1 70.0 17.1 70.0 17.1 70.0 17.1 70.0 17.1 72.5 77.1 76.0 181.2 181.0 79.9 77.6 77.7 70.0 17.2 72.0 17.1 70.0 17.1 70.0 17.2 70.4 181.0 181.0 182.6 181.0 170.0 170.7 77.0 180.0 181.0	68.3 69.6 70.5 71.0 73.3 73.5 74.4 74.8 76.5 77.8 76.6 74.4 71.0 73.7 75.5 74.4 74.8 74.8 76.5 77.8 76.6 74.4 71.0 72.5 74.8 75.5 74.4 72.6 72.6 72.8 75.6 77.1 73.0 73.5 74.4 75.5 74.8 80.4 80.2 80.5 86.5 87.8 72.6 72.0 77.3 77.3 77.3 77.3 77.3 77.3 77.3 77		n a d n a a d n a a			74 8 78 0 80 4	i	İ			143.0
69. 17.6 7.18 7.26 7.36 7.7 1 78 0 61.2 61.0 73.8 77.0 72.0 73.0 73.0 73.0 73.0 73.0 73.0 73.0 73	69.1 70.6 71.8 72.6 74.8 75.6 77.1 70.0 71.2 81.0 73.8 77.0 72.7 72.0 73.5 75.6 75.8 75.8 80.4 85.1 83.4 82.8 77.0 72.7 72.0 73.5 74.4 75.6 75.9 79.4 81.6 84.4 85.3 84.5 87.9 79.3 79.3 86.9 86.1 80.5 86.5 86.5 86.5 86.5 86.5 86.5 86.5 86	9 9				90.0		İ			145.0
72.5 73.0 73.5 74.4 75.8 76.9 79.4 81.6 84.4 85.3 84.9 82.9 79.3 186.9 86.1 84.8 86.5 84.8 81.0 186.9 86.1 87.2 79.4 82.1 84.8 86.5 86.5 84.8 81.0 186.9 86.1 80.3 86.1 80.3 86.2 87.2 79.4 82.1 84.8 86.5 86.5 86.1 86.7 86.1 81.0 186.2 89.6 81.2 80.4 80.1 80.2 89.6 81.2 80.4 80.1 80.2 89.6 81.2 80.4 80.1 80.2 89.6 81.2 80.4 80.1 80.2 80.1 80.2 80.2 80.1 80.2 80.2 80.1 80.2 80.2 80.2 80.2 80.2 80.2 80.2 80.2	72.5 73.0 73.5 74.4 75.8 76.9 79.4 81.6 84.4 85.3 84.9 82.9 79.3 186.9 86.1 87.8 77.2 79.4 82.1 84.8 86.5 86.5 86.8 84.8 81.0 86.5 86.1 80.3 86.3 86.3 88.4 88.8 85.7 81.4 80.5 81.3 84.5 85.7 81.0 81.0 88.6 81.0 81.0 81.0 81.0 81.0 81.0 81.0 81.0	70.6	naadnaa			8 .				- 1	151.4
96.9 67.9 75.9 77.9 77.2 79.4 62.1 64.6 66.1 66.2 66.1 67.0 64.6 66.1 66.2 66.1 67.0 67.0 67.0 67.0 67.0 67.0 67.0 67.0	86.9 66.1 80.3 90.5 91.7 9.4 82.1 84.8 95.3 96.3 96.3 86.3 96.4 86.3 96.6 96.3 86.3 96.5 90.5 90.5 90.5 90.5 90.5 90.5 90.5 90	73.0		1							154.1
80.4 91.1 90.5 88.4 89.8 85.7 81.4 80.5 81.3 84.5 85.7 84.4 80.5 86.8 86.9 87.9 84.5 85.7 84.4 80.5 86.9 86.9 89.6 91.6 91.6 91.9 90.4 90.4 90.1 85.9 80.9 79.7 91.6 81.9 91.4 77.0 86.2 85.0 86.0 86.1 81.5 79.1 81.9 81.3 77.0 186.2 85.0 86.1 81.5 79.1 81.9 91.4 77.0 186.2 85.0 81.2 80.6 81.3 79.1 81.9 81.3 77.0 186.2 81.4 81.2 80.5 81.3 79.1 81.9 77.0 186.2 81.4 81.2 80.5 81.3 79.1 81.9 77.5 77.0 186.2 81.4 81.2 80.5 77.0 79.1 79.7 77.0 186.2 81.8 81.3 81.2 80.5 75.9 74.3 77.0 75.1 186.8 81.3 81.3 81.3 70.4 70.2 70.3 70.6 79.4 74.4 75.0 89.6 10.1 75.0 70.1 81.0 81.2 80.5 80.5 75.9 74.3 77.1 66.1 81.1 81.1 81.3 70.4 70.2 70.2 70.3 70.1 81.0 81.2 80.5 75.9 74.3 77.1 66.1 81.1 81.1 81.3 70.4 70.2 70.2 70.3 70.1 60.1 81.2 80.5 81.4 81.2 80.5 81.4 81.3 70.3 70.4 70.2 70.3 70.1 60.1 81.1 100.4 91.2 81.0 81.3 81.3 70.3 70.4 70.2 70.3 70.1 60.1 81.1 100.4 91.2 81.0 70.3 70.4 70.3 70.1 60.1 81.1 100.4 91.2 81.0 70.3 70.4 70.3 70.1 60.1 81.1 100.4 91.2 81.0 70.1 100.4 91.2 81.0 70.3 70.1 100.4 91.2 81.0 70.3 70.1 100.4 91.2 81.0 70.3 70.1 100.4 91.2 81.0 70.3 70.1 100.4 91.2 81.0 70.3 70.1 100.4 91.2 81.0 70.3 70.1 100.4 91.2 81.0 70.3 70.1 100.4 91.2 81.0 70.3 70.1 100.4 91.2 81.0 70.3 70.1 100.4 91.2 81.0 70.3 70.1 100.4 91.2 70.3 70.1 100.4 91.2 70.3 70.1 100.4 91.2 70.1 100.4 91.2 70.3 70.3 70.1 70.1 100.4 91.2 70.3 70.3 70.3 70.3 70.3 70.3 70.3 70.3	80.4 91.1 90.5 88.4 89.8 85.7 81.4 80.5 81.3 84.5 85.7 84.4 80.5 81.6 89.5 91.6 91.6 91.6 91.6 91.6 91.6 91.6 91.6	9 86.1	4000	1		67.9					161.7
86.2 88.2 88.8 89.7 87.3 88.0 88.0 84.3 81.3 79.1 81.9 81.4 77.0 86.2 88.2 88.6 85.7 87.3 88.0 84.3 81.3 79.1 81.9 81.4 77.0 86.2 85.0 85.1 86.2 85.0 85.1 85.5 77.8 79.7 79.7 79.7 79.7 79.7 79.7 79.7	86.2 87.1 86.8 89.7 87.3 88.0 88.0 84.3 81.3 79.1 81.9 81.4 77.0 86.2 87.1 86.2 85.0 86.1 83.5 77.8 79.1 81.9 81.4 77.0 86.2 87.1 86.2 85.0 86.6 86.1 83.5 77.8 79.7 79.7 79.7 79.7 79.7 79.7 79.7	1 100				80.5			1		162 0
86.9 87.9 88.0 87.1 86.2 85.0 86.6 86.1 83.5 77.8 78.7 78.7 78.7 78.7 78.7 78.7 78	86.9 87.9 88.0 87.1 86.2 85.0 86.6 86.1 83.5 77.8 78.7 79.7 75.7 75.6 75.6 83.9 83.9 83.9 83.9 84.0 87.1 86.2 87.1 86.2 87.2 84.1 86.2 87.2 87.2 87.2 87.2 87.2 87.2 87.2 87	98.2	0			84.3					160.8
83.9 85.1 85.6 85.7 84.1 82.9 82.7 81.6 80.6 79.4 74.4 75.0 69.6 179.7 72.1 81.6 82.7 81.8 81.2 80.6 75.8 75.9 74.3 71.1 81.1 81.2 80.6 75.8 75.9 74.3 71.1 86.1 81.1 81.2 80.6 75.8 75.9 74.3 71.1 86.1 81.1 81.2 80.6 75.8 75.9 74.3 71.1 86.1 81.1 81.2 80.6 75.8 75.9 74.3 71.1 86.1 81.1 81.1 81.2 80.6 75.8 75.9 74.3 71.1 86.1 81.1 81.1 81.1 81.1 81.1 81.1 8	83.9 85.1 85.6 84.1 82.9 82.7 81 8 80.6 79.4 74.4 75.0 69.6 179.7 12.1 83.5 83.8 83.8 83.8 82.2 81.4 81.2 80.6 75.8 74.3 77.1 86.1 81.1 86.1 81.2 80.6 75.8 74.3 77.1 86.1 81.1 81.2 80.6 75.8 74.3 77.1 86.1 81.1 81.2 80.6 75.8 74.3 77.1 86.1 81.1 81.1 81.2 80.6 75.8 74.3 77.1 86.1 81.1 81.1 81.2 80.6 75.8 74.3 77.1 81.1 81.2 80.6 81.6 81.6 81.1 81.1 81.1 81.1 81.1 81	87.9	0	,		92					159.4
82.1 83.5 83.8 83.9 83.5 82.2 81.4 81.2 80 5 78.3 78.0 72.7 72.7 72.7 72.7 72.7 72.7 72.7 72	82.7 83.5 83.8 83.9 82.2 81.4 81.2 80 5 75.3 74.3 71.1 68.1 61.1 104.0 105.1 105.3 104.0 105.1 105.3 104.0 105.1 105.3 104.0 105.1 105.3 104.0 105.1 105.3 104.0 105.1 105.3 104.0 105.1 105.3 104.0 105.1 105.3 104.0 105.1 105.3 104.0 105.1 105.3 104.0 105.1 105.3 104.0 105.1 105.3 104.0 105.1 105.3 104.0 103.2 102.7 101.7 101.1 100.4 98.7 98.7 98.7 98.7 98.7 98.7 98.7 98.7	95.1	80 (}	Ì	81.6	ł				158.5
76.3 78.2 79.2 77.3 76.4 76.2 75.6 72.8 70.7 68.2 63.1 54.7 7 7 7 7 7 7 7 7 7 7 7 7 7 7 7 7 7 7	76.3 78.2 79.2 77.3 76.4 76.2 75.6 72.8 70.7 68.2 63.1 54.7 7 7 7 7 7 7 7 7 7 7 7 7 7 7 7 7 7 7	9 6 7	0 00			7 00 20 03 20 03					156.7
67.6 70.4 71.8 72.3 70.6 69.8 69.5 68.6 65.8 63.4 59.4 52.9 40.9 159.4 53.9 52.8 63.4 59.8 59.4 52.9 40.9 159.4 53.9 56.5 65.6 63.6 63.6 53.8 63.4 59.8 59.8 63.4 27.5 159.8 63.9 56.9 56.9 56.3 57.1 56.5 56.0 59.6 50.7 46.5 40.1 22.0 7.1 133.2 41.0 45.3 45.7 43.9 37.5 32.1 23.3 8.2 -21.8 159.6 59.7 4 97.5 97.1 96.5 95.1 94.4 93.6 93.7 94.0 94.1 100.4 98.7 94.2 104.0 105.1 105.3 104.6 103.4 103.2 102.7 101.7 101.1 100.4 98.7 94.2	67.6 70.4 71.8 72.3 70.6 69.6 69.5 68.6 65.8 63.4 59.4 59.9 40.9 159.6 63.9 63.9 40.9 159.6 63.9 63.9 63.9 63.9 63.9 63.9 63.9 6	73.8	N			7.5.6	1			1	153.7
59.6 63.7 65.7 66.5 65.2 64.4 64.1 63.0 59.6 56.5 51.6 43.4 27.5 14.4 53.9 56.5 51.6 43.4 27.5 14.5 51.0 51.0 51.0 51.0 51.0 51.0 51.0 51	59.6 63.7 65.7 66.5 65.2 64.4 64.1 63.0 59.6 56.5 51.6 43.4 27.5 1 48.4 53.9 56.5 51.6 43.4 27.5 1 33.2 41.0 45.3 45.7 1 56.5 56.0 56.0 56.5 56.0 56.0 57.6 10.2 20.0 2.1 1 33.2 41.0 45.5 105.3 104.6 103.4 103.2 102.7 101.7 101.1 100.4 98.7 94.2 104.0 105.1 105.5 105.3 104.6 103.4 103.2 102.7 101.7 101.1 100.4 98.7 94.2	70.4	.			68.6					152.3
33.2 41.0 45.3 47.5 46.8 46.3 45.7 43.9 37.5 32.1 23.3 8.2 -21.8 196.6 97.4 97.5 97.1 98.7 98.6 97.4 97.5 97.1 96.5 95.1 94.4 93.6 93.7 94.0 94.1 92.7 88.7 104.0 105.1 105.5 105.3 104.6 103.4 103.2 102.7 101.7 101.1 100.4 98.7 94.2 104.0 105.1 105.5 105.3 104.6 103.4 103.2 102.7 101.7 101.1 100.4 98.7 94.2	33.2 41.0 45.3 47.5 46.8 46.3 45.7 43.9 37.5 32.1 23.3 8.2 -21.8 36.6 97.4 97.5 95.1 96.3 95.1 96.4 93.6 97.4 97.5 97.1 96.7 98.7 94.4 93.6 93.7 94.0 94.1 92.7 98.7 94.2 104.0 105.1 105.5 105.3 104.6 103.4 103.2 102.7 101.7 101.1 100.4 98.7 94.2 104.0 105.1 105.5 105.3 104.6 103.4 103.2 102.7 101.7 101.1 100.4 98.7 94.2	63.7	۰, ۵			63.0					151
96 6 97.4 97.5 97.1 96.5 95.1 94.4 93.6 53.7 94.0 94.1 92.7 88.7 104.0 105.1 105.5 105.3 104.6 103.4 103.2 102.7 101.7 101.1 100.4 98.7 94.2 104.0 105.1 105.5 105.3 104.6 103.4 103.2 102.7 101.7 101.1 100.4 98.7 94.2	96 6 97.4 97.5 97.1 96.5 95.1 94.4 93.6 53.7 94.0 94.1 92.7 88.7 104.0 105.1 105.5 105.5 104.6 103.4 103.2 102.7 101.7 101.1 100.4 98.7 94.2 104.0 105.1 105.3 104.6 103.4 103.2 102.7 101.7 101.1 100.4 98.7 94.2	41.0	0		1	43.9				'	148.3
104.0 105.1 103.5 103.3 104.6 103.4 103.2 102.7 101.7 101.1 100.4 98.7 94	104.0 105.1 108.5 105.3 104.6 103.4 103.2 102.7 101.7 101.1 100.4 98.7 94	97.4	en e	_	-	93.6	-	•		8 6	170.7
		105.1	r)	٦	٦	102.7	7	1	1	9	

8		PWL 162.4 162.6 162.6 162.1 162.1 163.1 163.3	163.7 165.1 161.6 161.6 161.6 163.7 163.3 163.3 163.3 174.7 174.7	
PAGE		0 0 0 0 0 0 0 0 0 0 0 0 0 0 0 0 0 0 0	0 0 0 0 0 0 0 0 0 0 0 0 0 0 0 0 0 0 0	
		2 4 4 4 6 2 1 - 0 0 0 0 0 0 0 0 0 0 0 0 0 0 0 0 0 0	2 4 2 2 2 2 2 2 2 2 2 2 2 2 2 2 2 2 2 2	
		200 0 0 0 0 0 0 0 0 0 0 0 0 0 0 0 0 0 0	89 3 887 4 78 6 78 6 79 6 70 7 73 3 73 3 73 3 73 3 73 3 73 3 73 3	
ATION		130 990 990 990 990 990 990 990 990 990 9	90 9 9 9 9 9 9 9 9 9 9 9 9 9 9 9 9 9 9	
HIGH VELOCITY JET NOISE PROGRAM - ENGINEERING CORRELATION SAMPLE CASES - CONICAL			98 6 6 4 4 4 4 4 4 4 4 4 4 4 4 4 4 4 4 4	
NEERING	DAY	V 0 4 0 4 0 0 0 0	87.4 88.7 1.7 88.7 1.7 1.7 1.7 1.7 1.7 1.7 1.7 1	
- ENG!	NO ARO		7 4 6 6 6 6 6 6 6 6 6 6 6 6 6 6 6 6 6 6	reflections
PROGRAM -	CONICAL TOTAL 1040. 0 FOOT ALT NO EGA 519 DEGREE STA 6USTIC ANGLE FR		0 0 0 0 0 0 0 0 0 0 0 0 0 0 0 0 0 0 0	d refle
MOLSE P	CONICAL TO 1040.0 FOOT 0 FOOT NO EGA 519 DEGREE		9 9 9 9 9 9 9 9 9 9 9 9 9 9 9 9 9 9 9	ground
OCLIY JET NO SAMPLE CASES	* * * * * * * * * * * * * * * * * * *		0.00 0.00 0.00 0.00 0.00 0.00 0.00 0.0	nes and
VELOCI			991 1 7 8 8 8 9 1 9 9 9 9 9 1 1 9 9 9 9 1 1 9 9 9 9	of engines
нідн			9 9 9 9 9 9 9 9 9 9 9 9 9 9 9 9 9 9 9	number o
		99797847	74 4 6 6 6 6 6 7 6 6 - 7 6 7 6 6	for
		00000000000	9 9 9 9 9 9 9 9 9 9 9 9 9 9 9 9 9 9 9	Correction
!		9 10 00 - C 10 00 - C 10		
		1 1	200 0 0 0 0 0 0 0 0 0 0 0 0 0 0 0 0 0 0	113.8
		0 0 0 0 0 0 0 0 0 0 0 0 0 0 0 0 0 0 0	2000 2000 2000 2000 2000 2000 2000 200	M POST ALEWY BOOK

CASE 2

This case gives sample input to the computer program for running a set of single-flow, multichute, trend curves with area ratio and element number as variables.

GENERAL ELECTRIC CO. CINCINNATI OH AIRCRAFT ENGINE BU--ETC. F/G 20/1 HIGH VELOCITY JET NOISE SOURCE LOCATION AND REDUCTION. TASK 6. --ETC(1). APR 79 J BRAUSCH, A S CLAPPER, F R GLIERE DOT-05-30034 AD-A103 671 UNCLASSIFIED. R79AL6302 FAA-RD-76-79-6 NL 5 1 6 els I

December December	### ### ### ### ### ### ### ### ### ##	00000900 0000980 00000980 00000980 00000980 00001020 00001030 00001080 00001100 00001120 00001190 00001190 00001190 00001120 00001190 00001120 00001120 00001120 00001120 00001120 00001120 00001120 00001120
DDRES 60H BIN 79 BLDG 300 X-673/334 BINEUT Y823 BINEUT Y823 BINEUT Y823 BINEUT Y823 BINEUT Y823 BINEUT Y823 BINEUT Y823 BINEUT Y823 BINEUT Y823 BINEUT Y823 BINEUT Y823 BINEUT Y823 BINEUT Y823 BINEUT Y823 BINEUT Y8236	ADDRESSEON BIN 79 BLDG 300 X-673/8354 H-77 DENTSEON TASK 6 TREND CURVE GENERATION BINDUT Y983 ATEL DESCH TREND CURVE GENERATION SFC CASE ID=60H TREND CURVE GENERATION SFC A7=1.5 TT3=1818, P9=2.54 V0=0, BINDUT TT3=1818, P9=2.54 V0=0,	00000940 00000960 00000960 00001010 00001010 00001010 00001020 00001020 00001020 00001100 00001100 00001100 00001100 00001100 00001100 00001100 00001100 00001100 00001100 00001100 00001100 000001100 00001100 00001100 00001100 00001100 00001100 00001100 000001100
### STATE OF TASK 6 TREND CURVE OENERATION ### STATE OF TASK 6 TREND CURVE OENERATION ### STATE OF TASK 0 TREND CURVE OENERATION SPC ### STATE OF TASK 0 TREND CURVE OENERATION SPC ### STATE OF TASK 0 TREND CURVE OENERATION SPC ### STATE OF TASK 0 TREND CURVE OENERATION SPC ### STATE OF TASK 0 TREND CURVE OENERATION SPC ### STATE OF TASK 0 TREND CURVE OENERATION SPC ### STATE OF TASK 0 TREND CURVE OENERATION SPC ### STATE OF TASK 0 TREND CURVE OENERATION SPC ### STATE OF TASK 0 TREND CURVE OENERATION SPC ### STATE OF TASK 0 TREND CURVE OENERATION SPC ### STATE OF TASK 0 TREND CURVE OENERATION SPC ### STATE OF TASK 0 TREND CURVE OENERATION SPC ### STATE OF TASK 0 TREND CURVE OENERATION SPC ### STATE OF TASK 0 TREND CURVE OENERATION SPC ### STATE OF TASK 0 TREND CURVE OENERATION SPC ### STATE OF TASK 0 TREND CURVE OENERATION SPC ### STATE OF TASK 0 TREND CURVE OENERATION SPC ### STATE OF TASK 0 TREND CURVE OENERATION SPC ### STATE OF TASK 0 TREND CURVE OENERATION SPC ### STATE OF TASK 0 TREND CURVE OENERAL OENERA	## INPUT TT3=1516, P9=2.54, VO=0, ## INPUT Y0=350, ## INPUT Y0=350, ## INPUT Y0=350, ## INPUT Y0=350, ## INPUT Y0=350, ## INPUT TT3=1516, P9=2.54, VO=0, ## INPUT Y0=350,	00000960 00000960 00001000 00001020 00001020 00001020 00001060 00001100 00001100 00001110 00001110 00001110 00001110 00001110 00001120 00001120 00001120
### STATE TO CURVE GENERATION SFC CASTIDEGH TREND CURVE GENERATION SFC (ASTIDEGH TREND CURVE GENERATION SFC (ASTIDEGH TREND CURVE GENERATION SFC (ASTICL ST TG = 18) 8, P9 = 3, 46, V0 = 0. ### ST TG = 18) 8, P9 = 3, 46, V0 = 0. ### NPUT TT3 = 1516, P9 = 1, 66, V0 = 0. ### NPUT TT3 = 1516, P9 = 1, 66, V0 = 0. ### NPUT TT3 = 1516, P9 = 2, 54, V0 = 0. ### NPUT TT3 = 1516, P9 = 3, 46, V0 = 0. ### NPUT TT3 = 1516, P9 = 3, 46, V0 = 0. ### NPUT TT3 = 1516, P9 = 3, 46, V0 = 0. ### NPUT TT3 = 1516, P9 = 3, 46, V0 = 0. ### NPUT TT3 = 1516, P9 = 2, 54, V0 = 0. ### NPUT TT3 = 1516, P9 = 2, 54, V0 = 0. ### NPUT TT3 = 1516, P9 = 2, 54, V0 = 0. ### NPUT TT3 = 1516, P9 = 2, 54, V0 = 0. ### NPUT TT3 = 1516, P9 = 2, 54, V0 = 0. ### NPUT TT3 = 1516, P9 = 3, 46, V0 = 0. ### NPUT TT3 = 1516, P9 = 3, 46, V0 = 0. ### NPUT TT3 = 1516, P9 = 3, 46, V0 = 0. ### NPUT TT3 = 1516, P9 = 3, 46, V0 = 0. ### NPUT TT3 = 1516, P9 = 3, 46, V0 = 0. ### NPUT TT3 = 1516, P9 = 3, 46, V0 = 0. ### NPUT TT3 = 1516, P9 = 3, 46, V0 = 0. ### NPUT TT3 = 1516, P9 = 3, 46, V0 = 0. ### NPUT TT3 = 1516, P9 = 3, 46, V0 = 0. ### NPUT TT3 = 1516, P9 = 3, 46, V0 = 0. ### NPUT TT3 = 1516, P8 = 3, 46, V0 = 0. ### NPUT TT3 = 1516, P8 = 3, 46, V0 = 0. ### NPUT TT3 = 1516, P8 = 3, 46, V0 = 0. ### NPUT TT3 = 1516, P8 = 3, 46, V0 = 0. ### NPUT TT3 = 1516, P8 = 3, 46, V0 = 0. ### NPUT TT3 = 1516, P8 = 3, 46, V0 = 0. ### NPUT TT3 = 1516, P8 = 3, 46, V0 = 0. ### NPUT TT3 = 1516, P8 = 3, 46, V0 = 0. ### NPUT TT3 = 1516, P8 = 3, 46, V0 = 0. ### NPUT TT3 = 1516, P8 = 3, 46, V0 = 0. ### NPUT TT3 = 1516, P8 = 3, 46, V0 = 0. ### NPUT TT3 = 1516, P8 = 3, 46, V0 = 0. ### NPUT TT3 = 1516, P8 = 3, 46, V0 = 0. ### NPUT TT3 = 1516, P8 = 3, 46, V0 = 0. ### NPUT TT3 = 1516, P8 = 3, 46, V0 = 0. ### NPUT TT3 = 1516, P8 = 3, 46, V0 = 0. ### NPUT TT3 = 1516, P8 = 3, 46, V0 = 0. ### NPUT TT3 = 1516, P8 = 3, 46, V0 = 0.	## STANDON YEAR CONTRIBUTION SEC CASEI D=60H TREND CURVE GENERATION SEC A7=1 5, 173=1919, 9=92.4 d-023, R6=3.017, SS=2.011, A7=1 5, 173=1919, 9=93.4 d-023, R6=3.017, SS=2.011, A8=0, L9=0, A=440, A8=0, L9=0, A=440, A8=0, L9=0, A=440, A8=0, L9=0, A=440, A8=0, L9=0, A=440, A8=0, L9=0, A=440, A8=0, L9=0, A=480, A8=0, L9=1 66, VO=0, A8=0, L9=1919, P9=2.54, VO=0, A7=2, R4=3, 484, R6=2.54, VO=0, A7=2, R4=3, 484, R6=2.54, VO=0, A8=0, L9=0, L9=0, R9=1 .66, VO=0, A8=0, L9=0, L9=0, L9=0, L9=0, L9=0, A8=0, L9=0, L9=0, L9=0, L9=0, A8=0, L9=0, L9=0, L9=0, L9=0, A8=0, L9=0, L9=0, L9=0, L9=0, A8=0, L9=0, L9=0, L9=0, L9=0, A8=0, L9=0, L9=0, L9=0, L9=0, A8=0, L9=0, L9=0, L9=0, L9=0, A8=0, L9=0, L9=0, L9=0, L9=0, A8=0, L9=0, L9=0, L9=0, L9=0, A8=0, L9=0, L9=0, L9=0, L9=0, A8=0, L9=0, L9=0, L9=0, A8=0, L9=0, L9=0, A8=0, L9=0, L9=0, A8=0, L9=0, L9=0, A8=0, L9=0, L9=0, A8=0, L9=0, L9=0, A8=0, L9=0, L9=0, A8=0, L9=0, L9=0, A8=0, L9=0, L9=0, A8=0, L9=0, L9=0, A8=0, L9=0, A8=0, L9=0, L9=0, A8=0, L9=0, A8=0, L9=0, A8=0, L9=0, L9=0	00000980 00001020 00001020 00001020 00001030 00001050 00001050 00001100 00001110 00001110 00001110 00001110 00001120 00001220 00001220
CASE D=60H TREND CURVE GENERATION SFC A7=1.5, T73=1918, P8-2.40, A3-40, A6=0, 18-20, A4-40, A6=0, 18-20, A4-40, A6=0, 18-20, A4-40, A6=0, 18-20, A4-40, A6=0, 18-20, A4-40, A6=0, 18-20, A4-40, A6=0, 18-20, A4-40, A6=0, 18-20, A4-40, A6=0, 18-20, A4-40, A6=0, 18-20, A4-40, A6=0, 18-20, A4-40, A6=0, 18-20, A4-40, A6=0, 18-20, A4-40, A6=0, 18-20, A4-40, A7=2, A4-4, R6=2, B4, V0=0, A7=2, R4-3, A4-4, R6=2, B4, V0=0, A7=2, B4, R4-3, A16, P8-2, B4, V0=0, A1-20, A4-3, A16, P8-2, B4, V0=0, A1-20, A4-3, A16, P8-2, B4, V0=0, A1-20,	CASE D=60H TREND CURVE GENERATION SFC A7=1 5, T13=1916, P9=3.44 - 0.23, R6=3.017, SS=2.011, A7=1 5, T13=1916, P9=3.44 - 0.20, A6=0, L9=0,A=4.0. BINPUT V0=350, BINPUT T73=1215, P9=1.66, V0=0, BINPUT T73=1215, P9=1.66, V0=0, BINPUT T73=1215, P9=1.66, V0=0, BINPUT T73=1215, P9=1.66, V0=0, BINPUT T73=1215, P9=1.66, V0=0, BINPUT T73=1215, P9=1.66, V0=0, BINPUT T73=1215, P9=1.66, V0=0, BINPUT T73=1215, P9=1.66, V0=0, BINPUT T73=1215, P9=1.66, V0=0, BINPUT T73=1215, P9=1.66, V0=0, BINPUT T73=1215, P9=1.66, V0=0, BINPUT T73=1215, P9=1.66, V0=0, BINPUT T73=1215, P9=1.66, V0=0, BINPUT V0=350, BINPUT V0=350, BINPUT V0=350, BINPUT V0=350, BINPUT V0=350, BINPUT V0=350, BINPUT V0=350, BINPUT V0=350,	00001 010 00001 020 00001 020 00001 030 00001 030 00001 030 00001 10 00001 110 00001 140 00001 140 00001 150 00001 190 00001 190 00001 120 00001 220 00001 220
##20.RP11.2.89=0.R844.023.R6=3.017,SS=2.011, A7=1.3.T73=1910,P9=3.40,V0=0, A8=0,L9=0,A=44.0, A8=0,L9=0,A=44.0, A8=0,L9=0.A=44.0, A8=0,L9=0.A=44.0, A8=0,L9=0.A=44.0, A8=0.L9=0.A=44.0, A8=0.L9=0.A=44.0, A8=0.L9=0.A=44.0, A8=0.L9=0.A=44.0, A8=0.L9=0.A=44.0, A8=0.L9=0.A=44.0, A8=0.L9=0.A=44.0, A8=0.L9=0.A=44.0, A8=0.L9=0.A=0.A=4.0, A8=0.L9=0.A=0.A=4.0, A8=0.L9=0.A=0.A=0.A=0.A=0.A=0.A=0.0, A8=0.L9=0.A=0.A=0.A=0.A=0.A=0.A=0.A=0.A=0.A=0.A	M=20, RP=1 2, 89=0, R4=4 023, R6=3.017, SS=2.011, ANT=12.400, 81=0, U=2, E92.0. AB=0, L9=0, A=4±0, BINPUT V0=350, BINPUT TT3=1215, P9=2.54, V0=0, BINPUT TT3=1215, P9=1.66, V0=0, BINPUT TT3=1215, P9=1.66, V0=0, BINPUT TT3=1215, P9=1.66, V0=0, BINPUT TT3=1215, P9=1.66, V0=0, BINPUT TT3=1215, P9=2.54, V0=0, BINPUT TT3=1215, P9=2.54, V0=0, BINPUT TT3=1215, P9=2.54, V0=0, BINPUT TT3=1215, P9=2.46, V0=0, BINPUT TT3=1215, P9=2.46, V0=0, BINPUT TT3=1215, P9=2.54, V0=0, BINPUT V0=350, BINPUT V0=350, BINPUT V0=350, BINPUT V0=350, BINPUT V0=350, BINPUT V0=350, BINPUT V0=350, BINPUT V0=350, BINPUT V0=350, BINPUT V0=350, BINPUT V0=350, BINPUT V0=350, BINPUT V0=350, BINPUT V0=350, BINPUT V0=350, BINPUT V0=350,	00001020 00001030 00001030 00001060 00001060 00001100 00001100 00001100 00001100 00001100 00001100 00001100 00001100 00001100 00001120 00001120 00001120 00001120 00001120
A7=1.5.173=1916, P9=3.46, V0=0, A8=0,L9=0,A*4±0, BINPUT V0=350, BINPUT T73=1516, P9=2.54, V0=0, BINPUT T73=1516, P9=2.54, V0=0, BINPUT T73=1516, P9=2.54, V0=0, BINPUT T73=1918, P9=3.48, V0=0, BINPUT T73=1918, P9=3.48, V0=0, BINPUT T73=1918, P9=2.54, V0=0, BINPUT T73=1918, P9=2.54, V0=0, BINPUT T73=1918, P9=2.54, V0=0, BINPUT T73=1918, P9=2.54, V0=0, BINPUT T73=1918, P9=2.54, V0=0, BINPUT T73=1918, P9=2.54, V0=0, BINPUT T73=1918, P9=2.54, V0=0, BINPUT T73=1918, P9=2.34, V0=0, BINPUT T73=1918, P9=2.34, V0=0, BINPUT V0=350, BINPUT V0=350, BINPUT V0=350, BINPUT V0=350, BINPUT V0=350, BINPUT V0=350, BINPUT V0=350, BINPUT V0=350, BINPUT V0=350, BINPUT V0=350, BINPUT V0=350, BINPUT V0=350, BINPUT V0=350, BINPUT V0=350, BINPUT V0=350, BINPUT V0=350, BINPUT V0=350, BINPUT V0=350,	AATEL S, TT3=1916, P9=3.46, VO=0, KEEL, ALT=ZAGO, 34=0, U=2, E9±0, BINPUT VO=350, BINPUT TT3=1216, P9=2.54, VO=0, BINPUT TT3=1216, P9=2.54, VO=0, BINPUT TT3=1316, P9=3.46, VO=0, BINPUT TT3=1316, P9=2.54, VO=0, BINPUT TT3=1316, P9=2.54, VO=0, BINPUT TT3=1316, P9=2.54, VO=0, BINPUT TT3=1316, P9=2.54, VO=0, BINPUT TT3=1316, P9=2.54, VO=0, BINPUT VO=350, BINPUT TT3=1316, P9=2.54, VO=0, BINPUT VO=360, BINPUT VO=360, BINPUT TT3=1215, P9=1.66, VO=0, BINPUT VO=360, BINPUT TT3=1215, P9=1.66, VO=0, BINPUT VO=360, BINPUT VO=360, BINPUT VO=360, BINPUT VO=360,	00001030 00001040 00001040 00001050 00001050 00001100 00001120 00001150 00001150 00001150 00001150 00001150 00001150 00001150 00001150 00001150 00001150 00001150 00001150
AGEOLUSIO, ARAGO, BINPUT TOS:1215, P9=2.54, VO=0, BINPUT TT3:1215, P9=1.66, VO=0, BINPUT TT3:1215, P9=1.66, VO=0, BINPUT TT3:1215, P9=1.66, VO=0, BINPUT TT3:1215, P9=1.66, VO=0, BINPUT TT3:1215, P9=1.66, VO=0, BINPUT TT3:1216, P9=2.54, VO=0, BINPUT TT3:121916, P9=2.54, VO=0, BINPUT TT3:121916, P9=2.54, VO=0, BINPUT TT3:121916, P9=2.54, VO=0, BINPUT TT3:1215, P9=1.66, VO=0, BINPUT T	AGE-0. L'3-0, A44=0, \$1 NPUT V0=350, \$1 NPUT TT3=1216, P9=2.54, V0=0, \$1 NPUT TT3=1215, P9=1.66, V0=0, \$1 NPUT TT3=1215, P9=1.66, V0=0, \$1 NPUT V0=350, \$	00001 050 00001 050 00001 050 00001 100 00001 110 00001 120 00001 150 00001 150 00001 150 00001 150 00001 150 00001 210 00001 210 00001 220 00001 220
## INPUT TT3=1516, P9=2.54, V0=0, ## INPUT TT3=1516, P9=2.54, V0=0, ## INPUT TT3=1215, P9=1.66, V0=0, ## INPUT TT3=1215, P9=1.66, V0=0, ## INPUT TT3=1316, P9=3.48, V0=0, ## INPUT TT3=1316, P9=2.54, V0=0, ## INPUT TT3=1316, P9=2.54, V0=0, ## INPUT TT3=1316, P9=2.54, V0=0, ## INPUT TT3=1316, P9=2.54, V0=0, ## INPUT TT3=1316, P9=2.54, V0=0, ## INPUT TT3=1316, P9=2.54, V0=0, ## INPUT TT3=1315, P9=1.66, V0=0, ## INPUT TT3=1315, P9=1.66, V0=0, ## INPUT TT3=1315, P9=1.66, V0=0, ## INPUT TT3=1315, P9=3.48, V0=0, ## INPUT TT3=1315, P9=3.48, V0=0, ## INPUT TT3=1319, P9=3.48, V0=0, ## INP	## INPUT VO=350, ## INPUT VO=350, ## INPUT VO=350, ## INPUT VO=350, ## INPUT VO=350, ## INPUT TT3=1918, P9=1.66, VO=0, RP=1.386, ## INPUT TT3=1918, P9=3.48, VO=0, RP=1.386, ## INPUT TT3=1918, P9=2.54, VO=0, ## INPUT TT3=1215, P9=1.66, VO=0, ## INPUT TT3=1215, P9=1.66, VO=0, ## INPUT TT3=1918, P9=3.48, VO=0, ## INPUT TT3=1918, P9=2.44, VO=0, ## INPUT TT3=1918, P9=2.54, VO=0, ## INPUT VO=350, ## INPUT VO=350, ## INPUT VO=350, ## INPUT TT3=1215, P9=1.66, VO=0, ## INPUT VO=350, ## INPUT VO=350, ## INPUT VO=350, ## INPUT TT3=1215, P9=1.66, VO=0, ## INPUT TT3=1215, P0=1.66, P0=0, ## INPUT TT3=1215, P0=1.66, P0=0, ## INPUT TT3=1215, P0=0, P0=0, ## INPUT TT3=1215, P0=0, P0=0, P0=0, P0=	00001050 00001070 00001100 00001110 00001120 00001130 00001150 00001150 00001150 00001150 00001150 00001120 00001220
### INPUT V0=350, ### INPUT V0=350, ### INPUT TT3=1215, P9=1 . 66 , VO=0, ### INPUT TT3=1215, P9=1 . 66 , VO=0, ### INPUT TT3=1215, P9=1 . 66 , VO=0, ### INPUT TT3=1319, P9=3 . 48 , VO=0, ### INPUT TT3=1319, P9=2 . 54 , VO=0, ### INPUT TT3=1319, P9=2 . 54 , VO=0, ### INPUT V0=350,	#INPUT V0=350, #INPUT V0=350,	00001970 00001980 00001100 00001110 00001120 00001150 00001150 00001180 00001180 00001180 00001220 00001220
### INPUT TT3 = 1516, P9=2 . 54 . VO=0, ### INPUT VO=350, ### INPUT VO=350, ### INPUT TT3 = 1218, P9=1 . 66 . VO=0, ### INPUT TT3 = 1218, P9=3 . 48 . VO=0, RP=1 . 386, ### INPUT TT3 = 1318, P9=2 . 54 . VO=0, ### INPUT TT3 = 1218, P9=2 . 54 . VO=0, ### INPUT TT3 = 1218, P9=3 . 48 . VO=0, ### INPUT TT3 = 1318, P9=3 . 48 . VO=0, ### INPUT TT3 = 1218, P9=2 . 54 . VO=0, ### INPUT TT3 = 1218, P9=2 . 54 . VO=0, ### INPUT TT3 = 1218, P9=1 . 66 . VO=0, ### INPUT TT3 = 1218, P9=3 . 48 . VO=0, ### INPUT TT3 = 1218, P9=3 . 48 . VO=0, ### INPUT TT3 = 1218, P9=3 . 48 . VO=0, ### INPUT TT3 = 1218, P9=3 . 48 . VO=0, ### INPUT TT3 = 1218, P9=3 . 48 . VO=0, ### INPUT TT3 = 1318, P9=3 . 48 . VO=0, ### INPUT TT3 = 1318, P9=3 . 48 . VO=0, ### INPUT TT3 = 1318, P9=3 . 48 . VO=0, ### INPUT TT3 = 1318, P9=3 . 48 . VO=0, ### INPUT TT3 = 1318, P9=3 . 48 . VO=0, ### INPUT TT3 = 1318, P9=3 . 48 . VO=0, ### INPUT VO=360, ### IN	\$INPUT TT3=1516, P9=2.54, V0=0, \$INPUT V0=350, \$INPUT TT3=1215, P9=1.66, V0=0, \$INPUT TT3=1215, P9=1.66, V0=0, \$INPUT TT3=1318, P9=3.48, V0=0, \$INPUT TT3=1318, P9=3.48, V0=0, \$INPUT TT3=1216, P9=2.54, V0=0, \$INPUT TT3=1215, P9=1.66, V0=0, \$INPUT TT3=1215, P9=1.66, V0=0, \$INPUT TT3=1215, P9=2.54, V0=0, \$INPUT TT3=1216, P9=2.54, V0=0, \$INPUT TT3=1216, P9=2.54, V0=0, \$INPUT TT3=1216, P9=2.54, V0=0, \$INPUT V0=350, \$INPUT V0=350, \$INPUT V0=350, \$INPUT V0=350, \$INPUT V0=350, \$INPUT V0=350,	00001090 00001100 00001110 00001120 00001150 00001150 00001190 00001190 00001200 00001220
#INPUT TT3=1215, P9=1 . 66, VO=0, #INPUT TT3=1215, P9=1 . 66, VO=0, #INPUT TT3=1318, P9=3 . 48, VO=0, RP=1 . 386, #INPUT TT3=1318, P9=2 . 54, VO=0, #INPUT TT3=1318, P9=2 . 54, VO=0, #INPUT TT3=1318, P9=1 . 66, VO=0, #INPUT TT3=1318, P9=3 . 48, VO=0, RP=1 . 549, #INPUT TT3=1318, P9=2 . 54, VO=0, #INPUT TT3=1318, P9=2 . 54, VO=0, #INPUT TT3=1318, P9=2 . 54, VO=0, #INPUT TT3=1318, P9=1 . 66, VO=0, #INPUT TT3=1318, P9=3 . 48, VO=0, #INPUT TT3=1318, P9=3 . 48, VO=0, #INPUT TT3=1318, P9=3 . 48, VO=0, #INPUT TT3=1318, P9=3 . 48, VO=0, #INPUT TT3=1318, P9=3 . 48, VO=0, #INPUT TT3=1318, P9=3 . 48, VO=0, #INPUT VO=350, #INP	# INPUT V0=350, # INPUT TT3=1215, P9=1 · 66, V0=0, # INPUT TT3=1216, P9=3 · 46, V0=0, RP=1 · 386, # A7=2, R4=3 · 484, R6=2 · 613, SS=3 · 483, # INPUT TT3=1316, P9=2 · 54, V0=0, # INPUT TT3=1215, P9=1 · 66, V0=0, # INPUT TT3=1215, P9=1 · 66, V0=0, # INPUT V0=350, # INPUT TT3=1316, P9=3 · 46, V0=0, # INPUT TT3=1316, P9=2 · 54, V0=0, # INPUT V0=350, # INPUT V0=360, # INPUT V0=360, # INPUT V0=360, # INPUT V0=360, # INPUT V0=360, # INPUT V0=360, # INPUT V0=360,	00001100 00001110 00001120 00001130 00001150 00001150 00001190 00001190 0000120 00001220
#INPUT TT3=1916, P9=1.66, VO=0, #INPUT TT3=1916, P9=3.48, VO=0, #INPUT TT3=1918, P9=3.48, VO=0, #INPUT TT3=1918, P9=2.48, VO=0, #INPUT TT3=1918, P9=2.54, VO=0, #INPUT TT3=1215, P9=1.66, VO=0, #INPUT TT3=1215, P9=1.66, VO=0, #INPUT TT3=1215, P9=2.54, VO=0, #INPUT VO=350,	#INPUT TT3=1215, P9=1 · 66, VO=0, #INPUT TT3=1316, P9=3 · 48, VO=0, RP=1 · 386, #A7=2, R4=3 · 484, R6=2 · 613, SS=3 · 483, #INPUT TT3=1316, P9=2 · 54, VO=0, #INPUT TT3=1215, P9=1 · 66, VO=0, #INPUT TT3=1215, P9=1 · 66, VO=0, #INPUT TT3=1215, P9=3 · 48, VO=0, #INPUT TT3=1316, P9=3 · 48, VO=0, #INPUT TT3=1316, P9=2 · 54, VO=0, #INPUT VO=350, #INPUT VO=350, #INPUT VO=360, #INPUT VO=360, #INPUT VO=360, #INPUT VO=360, #INPUT VO=360, #INPUT VO=360,	00001120 00001130 00001140 00001150 00001150 00001190 00001190 0000120 00001220
#INPUT TT3=1915, P9=1 · 66, V0=0, #INPUT V0=350, #INPUT TT3=1916, P9=3 · 48, V0=0, RP=1 · 386, #INPUT TT3=1916, P9=2 · 54, V0=0, #INPUT TT3=1916, P9=2 · 54, V0=0, #INPUT TT3=1916, P9=3 · 48, V0=0, #INPUT TT3=1916, P9=3 · 48, V0=0, #INPUT TT3=1916, P9=2 · 54, V0=0, #INPUT V0=350,	#INPUT TT3=1215, P9=1 · 66, V0=0, #INPUT V0=350, #INPUT V0=350, #INPUT TT3=1916, P9=3 · 48, V0=0, RP=1 · 386, #INPUT TT3=1916, P9=2 · 54, V0=0, #INPUT V0=350, #INPUT TT3=1916, P9=3 · 48, V0=0, #INPUT TT3=1916, P9=3 · 48, V0=0, #INPUT TT3=1916, P9=3 · 48, V0=0, #INPUT TT3=1916, P9=2 · 54, V0=0, #INPUT TT3=1916, P9=2 · 54, V0=0, #INPUT V0=350, #INPUT V0=350, #INPUT V0=350, #INPUT V0=350, #INPUT V0=350,	00001130 00001140 00001150 00001170 00001190 00001190 0000120 00001220
### ### ### ### ### ### ### ### ### ##	#INPUT TT3=1916, P9=3.48, V0=0, RP=1.386, #A7=2.R4=3.484, R6=2.613, SS=3.483, #INPUT TT3=1916, P9=2.54, V0=0, #INPUT V0=350, #INPUT TT3=1916, P9=3.48, V0=0, #INPUT TT3=1916, P9=3.48, V0=0, #INPUT TT3=1916, P9=3.48, V0=0, #INPUT TT3=1916, P9=2.54, V0=0, #INPUT TT3=1816, P9=2.54, V0=0, #INPUT TT3=1816, P9=2.54, V0=0, #INPUT TT3=1816, P9=2.54, V0=0, #INPUT TT3=1815, P9=1.86, V0=0, #INPUT V0=350, #INPUT V0=350,	00001150 00001150 00001170 00001190 0000120 00001220 00001220
### ### ### ### ### ### ### ### ### ##	### ### ### ### ### ### ### ### ### ##	00001160 00001170 00001190 00001190 00001210 00001220 00001240
## INPUT TT3=1916, P9=3.48, V0=0, RP=1.386, ## A7=2, R4=3.484, R6=2.613, SS=3.483, ## INPUT V0=350, ## INPUT TT3=1516, P9=2.54, V0=0, ## INPUT TT3=1215, P9=1.66, V0=0, ## INPUT TT3=1916, P9=3.48, V0=0, RP=1.549, ## INPUT TT3=1916, P9=2.54, V0=0, ## INPUT V0=350,	### NEUT TT3=1916, P9=3.48, V0=0, RP=1.386, ####################################	00001170 00001180 00001200 00001210 00001220 00001230
### Note 1	### Note 1	00001190 00001210 00001210 00001220 00001230
#INPUT TT3=1516, P9=2.54, VO=0, #INPUT TT3=1516, P9=2.54, VO=0, #INPUT TT3=1215, P9=1.66, VO=0, #INPUT TT3=1215, P9=1.66, VO=0, #INPUT TT3=1316, P9=3.48, VO=0, RP=1.549, #INPUT TT3=1316, P9=2.54, VO=0, #INPUT VO=350, #INPUT VO=350, #INPUT VO=350, #INPUT TT3=1316, P9=3.48, VO=0, RP=1.697, #INPUT VO=350, #INPUT VO=350, #INPUT VO=350, #INPUT VO=350, #INPUT VO=350, #INPUT VO=350, #INPUT VO=350, #INPUT VO=350,	#INPUT TT3=1516, P9=2.54, VO=0, #INPUT TT3=1516, P9=2.54, VO=0, #INPUT TT3=1215, P9=1.66, VO=0, #INPUT VO=350, #INPUT VO=350, #INPUT VO=350, #INPUT VO=350, #INPUT VO=350, #INPUT VO=350, #INPUT VO=350, #INPUT VO=350, #INPUT VO=350, #INPUT VO=350, #INPUT VO=350, #INPUT VO=350, #INPUT VO=350,	00001200 00001210 00001220 00001230
### INPUT TT3=1516, P9=2.54, V0=0, ### INPUT TT3=1215, P9=1.66, V0=0, ### INPUT TT3=1215, P9=1.66, V0=0, ### INPUT TT3=1215, P9=3.48, V0=0, ### INPUT TT3=1316, P9=2.54, V0=0, ### INPUT V0=350, ### INPUT V0=350, ### INPUT V0=350, ### INPUT V0=350, ### INPUT V0=350, ### INPUT V0=350, ### INPUT V0=350, ### INPUT V0=350, ### INPUT V0=350, ### INPUT V0=350, ### INPUT V0=350, ### INPUT V0=350, ### INPUT V0=350, ### INPUT V0=350, ### INPUT V0=350, ### INPUT V0=350, ### INPUT V0=350, ### INPUT V0=350, ### INPUT V0=350,	### INPUT TT3=1516, P9=2.54, VO=0, ### INPUT VQ=350, ### INPUT VQ=350, ### INPUT TT3=1916, P9=3.46, VO=0, ### INPUT TT3=1916, P9=3.46, VO=0, RP=1.549, ### INPUT TT3=1916, P9=2.337, SS=4.673, ### INPUT VO=350, ### INPUT VO=350, ### INPUT VO=350, ### INPUT VO=350, ### INPUT VO=350, ### INPUT VO=350, ### INPUT VO=350, ### INPUT VO=350, ### INPUT VO=350, ### INPUT VO=350,	00001210 00001220 00001230 00001240
# INPUT TT3=1516, P9=2.54, VO=0, # INPUT TT3=1215, P9=1.66, VO=0, # INPUT TT3=1215, P9=1.66, VO=0, # INPUT TT3=1215, P9=3.48, VO=0, RP=1.549, # INPUT VO=350,	# INPUT TT3=1216, P9=2.54, VO=0, # INPUT YO=350, # INPUT TT3=1215, P9=1.66, VO=0, # INPUT TT3=1219, P9=3.46, VO=0, RP=1.549, # INPUT TT3=1316, P9=2.337, SS=4.673, # INPUT TT3=1516, P9=2.54, VO=0, # INPUT TT3=1215, P9=1.66, VO=0, # INPUT TT3=1215, P9=1.66, VO=0, # INPUT TT3=1215, P9=1.66, VO=0, # INPUT VO=350, # INPUT VO=350, # INPUT VO=350,	00001 220 00001 230 00001 240
#INPUT VORSEO, #INPUT TT3=1215, P9=1.66, VO=0, #INPUT TT3=1916, P9=3.46, VO=0, RP=1.549, #A7=2.5, R4=3.116, R6=2.337, SS=4.673, #INPUT VO=350, #INPUT TT3=1215, P9=2.54, VO=0, #INPUT TT3=1215, P9=1.66, VO=0, #INPUT TT3=1215, P9=1.48, VO=0, RP=1.697, #INPUT TT3=1319, P9=3.48, VO=0, RP=1.697, #INPUT VO=350, #INPUT VO=350, #INPUT VO=350, #INPUT VO=350,	#INPUT V0=350, #INPUT TT3=1215, P9=1.66, V0=0, #INPUT TT3=1916, P9=3.46, V0=0, RP=1.549, #A7=2.5, R4=3.116, R6=2.337, SS=4.673, #INPUT V0=350, #INPUT V0=350, #INPUT V0=350, #INPUT TT3=1215, P9=1.66, V0=0, #INPUT V0=350, #INPUT V0=350,	00001240
# INPUT TT3=1215, P9=1.66, VO=0, # INPUT TT3=1215, P9=1.66, VO=0, RP=1.549, # A7=2.5, R4=3.116, R6=2.337, SS=4.673, # INPUT VO=350, # INPUT VO=350, # INPUT TT3=1215, P9=1.66, VO=0, # INPUT TT3=1215, P9=1.66, VO=0, # INPUT TT3=1219, P9=3.48, VO=0, RP=1.697, # INPUT VO=350, # INPUT VO=350, # INPUT VO=350, # INPUT VO=350, # INPUT VO=350, # INPUT VO=350, # INPUT VO=350, # INPUT VO=350, # INPUT VO=350, # INPUT VO=350,	# INPUT TT3=1215, P9=1.66, VO=0, # INPUT TQ=350, # INPUT TC3=1910, P9=3.46, VO=0, RP=1.549, # A7=2.5, R4=3.116, R6=2.337, SS=4.673, # INPUT VO=350, # INPUT VO=350, # INPUT VO=360, # INPUT TT3=1215, P9=1.66, VO=0, # INPUT TT3=1215, P9=1.66, VO=0, # INPUT VO=350, # INPUT VO=350,	
# INPUT TT3=1215, P9=1.66, VO=0, # # INPUT VO=350, # INPUT TT3=1919, P9=3.48, VO=0, RP=1.549, # A7=2.5, R4=3.116, R6=2.337, SS=4.673, # INPUT VO=350, # INPUT VO=350, # INPUT VO=350, # INPUT VO=350, # INPUT VO=350, # INPUT VO=350, # INPUT VO=350, # INPUT VO=350, # INPUT VO=350, # INPUT VO=350, # INPUT VO=350, # INPUT VO=350, # INPUT VO=350, # INPUT VO=350, # INPUT VO=350,	# INPUT TT3=1215, P9=1.66, VO=0, # INPUT VO=350, # INPUT VO=350, # INPUT VO=350, # INPUT VO=350, # INPUT VO=350, # INPUT VO=350, # INPUT VO=350, # INPUT VO=350, # INPUT VO=350, # INPUT VO=350, # INPUT VO=350, # INPUT VO=350, # INPUT VO=350, # INPUT VO=350, # INPUT VO=350, # INPUT VO=350,	06210000
BINPUT 173=1910, P9=3.48, VO=0, RP=1.549, A7=2.5, R4=3.116, R6=2.337, SS=4.673, BINPUT 173=1916, P9=2.54, VO=0, BINPUT VO=350, BINPUT VO=350, BINPUT T73=1215, P9=1.66, VO=0, BINPUT T73=1216, P9=3.48, VO=0, RP=1.697, BINPUT T73=1910, P9=3.48, VO=0, RP=1.697, BINPUT VO=350, BINPUT VO=350, BINPUT VO=350, BINPUT VO=350,	# INPUT VD=350, # INPUT TT3=1910, P9=3.46, VO=0, RP=1.549, # A=2.5, R4=3.116, R6=2.337, SS=4.673, # INPUT VO=350, # INPUT VO=350, # INPUT VO=350, # INPUT TT3=1215, P9=1.66, VO=0, # INPUT TT3=1215, P9=1.66, VO=0, # INPUT TT3=1215, P9=1.66, VO=0, # INPUT VO=350, # INPUT VO=350,	00001260
### INPUT TT3=1916, P9=3.46, V0=0, RP=1.549, ###################################	### INPUT TT3=1916, P9=3.46, V0=0, RP=1.549, A7=2.5, R4=3.116, R6=2.337, S3=4.673, #### INPUT V0=350, #### INPUT V0=350, #### INPUT V0=350, #### INPUT V0=350, #### INPUT TT3=1215, P9=1.66, V0=0, #### INPUT V0=350, #### INPUT V0=350, #### INPUT V0=350,	00001280
# SINPUT TT3=1916, P9=3.48, V0=0, RP=1.549, # A7=2.5, R4=3.116, R6=2.337, SS=4.673, # BINPUT V0=360, # SINPUT V0=360, # SINPUT V0=360, # SINPUT TT3=1916, P9=1.66, V0=0, # SINPUT TT3=1919, P9=3.48, V0=0, RP=1.697, # SINPUT V0=360, # SINPUT V0=360, # SINPUT V0=360, # SINPUT V0=360, # SINPUT V0=360, # SINPUT V0=360, # SINPUT V0=360,	## NPUT TT3=1916, P9=3.46, VO=0, RP=1.549, ## A7#2.5, R4=3.116, R6=2.337, SS=4.673, ## INPUT VO=350, ## INPUT TT3=1516, P9=2.54, VO=0, ## INPUT TT3=1515, P9=1.66, VO=0, ## INPUT TT3=1215, P9=1.66, VO=0, ## INPUT VO=350, ## INPUT VO=350, ## INPUT VO=350, ## INPUT VO=350,	00001290
# MATEL D, MATEL 15, 10, 105 E. 337, 305 4.073, 4 minut V0=360, 4 minut V0=360, 5 minut V0=360, 5 minut V0=360, 5 minut V0=360, 7 minut V0=360	# MINEUT V0=350, 89=2.54, V0=0, 9	00001300
######################################	### ### ##############################	00001310
### ### ##############################	## INPUT TT3=1516, P9=2.54, VO=0, ## INPUT VO=350, ## INPUT TT3=1215, P9=1.66, VO=0, ## INPUT VO=350, ## INPUT VO=350,	00001330
## INFUT V0=360, ## INFUT TT3=1215, P9=1.66, V0=0, ## INFUT TT3=1219, P9=3.48, V0=0, RP=1.697, ## INFUT TT3=1919, P9=3.48, V0=0, RP=1.697, ## INFUT V0=350, ## INFUT V0=350,	# BINPUT V0=360, # BINPUT TT3=1215, P9=1.66, V0=0, # BINPUT TT3=1215, P9=1.66, V0=0,	000001340
### ### ##############################	### ### ##############################	00001360
\$1NPUT TT3=1215, P9=1.66, V0=0, \$1NPUT V0=350, \$2NPUT TT3=1916, P9=3.46, V0=0, RP=1.697, \$2.73, R4#2.845, R6#2.133, SS#5. 888, \$1NPUT V0=350,	## INPUT TT3=1215, P9=1.66, V0=0, ## INPUT V0=350, ## INPUT V0=350,	00001370
# INPUT V0=350, # INPUT TT3=1919, P9=3.48, V0=0, RP=1.697, # Z=3, R4#2 845, R6#2 133, SS#5, R88, # INPUT V0=350,	# SINPUT VO=350,	00001380
\$INPUT V0=350, \$ INPUT TT3=1910, P9=3.48, V0=0, RP=1.697, \$Z=3, R4#2_845, R6#2_133, \$\$#5.888, \$ INPUT V0=350,	SINPUT VO=350,	00001400
8 BINPUT TT3=1918, P9=3.48, V0=0, RP=1.697, AZ=3, R4=2.845, R6=2.133, SS=5.888, 8 9 INPUT V0=350,		00001410
BINTOL 113-1310, FB16.46, VOIO, RF1.08/, AZE3, RA12, B45, R612, 133, 53.15, 888, B SINPUT VO=350,		00001420
8 8INPUT V0=350,	## NTC	00001430
#INPUT V0=350,		00001450
-	#INPUT V0=350,	00001460
	-	00001470

SINPUT V0=350, SINPUT TT3=1215,P9=1.66,V0=0,		
	00001500	
	00001510	
	00001530	
SIMPUT V0=350,	00001550	
SINDUT YOUR,	00001560	
]=	00001380	
A7=1.5, TT3=1918, P9=3.48, V0=0,	00001590	
K##1, ALT#2460, SL#0, U#2, E9#0,	00001600	
	00001620	
81MPUT V0=350,	00001630	
\$1MPUT TT3=1516 P9=2 54 VO=0,	00001850	
	00001660	
	06010000	
\$1MPUT IT3#1215,P9#1 56, VO#O.	00001690	
	00001700	
	00001720	
A7=2. R4=2. 323. R6=1. 742. S3=2. 322.	00001740	
	00001750	
BINPUT VO=350,	00001760	
BINPUT TT3#1516, P9=2.54, VO=0,	00001780	
BINPUT VO=350,	00000	
- 1	00001810	
BINFUT 173=1215, P9=1.66, VO=0,	00001820	
BINPUT V0=350,	000001840	
BINPUT TT3=1918, P9=3, 48, V0=0, RP=1, 549,	00001860	
to.	00001870	
OSCHOOL TIGHT	000010000	
	00001800	
SIMPUT TT3=1516, P9=2.54, V0=0,	00001910	
BINEUT VORSEO.	00001920	
	00001940	
# MEDI 113*1215, FB*1.66, VC=C,		
PLINEUT VORGEO	0000 1880	
	00001990	
SINTUT T13=1916, F9=3.48, VO=0, RP=1.697, A7=3, R4=1.696, R6=1.422, SS=3.792,	000000000000000000000000000000000000000	

(35%)

	00002020	
	00002030	
\$1MPUT TT3=1516, P9=2.54, VO=0,	00002040	
	00002050	
SIMPUT VORSEO	00002060	
	0/02000	
8[MPUT 113=1215, PS=1.56, VO=U,		
	00002110	
	00002120	
CARTIOL TOTAL TENEDATION OF C	06.190000	
	00002140	
	00002150	
#1. ALT#2400 SL #0 U#2. E9#0.	00002160	
CHERT CHERT	90002170	
	00002180	
BINDUT VOE350	00002190	
	00002200	
CONTRACT TIME THE POST NA VOED	00002210	
	00002220	
SIMPUT VOR350	00002230	
	00002240	
\$INPUT TT3=1215,P9=1.66,V0=0,	00002250	
	00002260	
81MPUT V0=350,	00002270	
	00002280	
\$1NPUT TT3=1916, P9=3.46, V0=0, RP=1.386,	00002280	•
12, R4=1, 742, R6=1, 306, SS=1, 742,	00002300	
	00002310	
SINTUL VORSEO,	DARROODO	
	00002330	
SIMPLI II. SIDIG PREZ DA VOSO	UNIVERSAL	
	0000000	
	00005370	
STATISTE PORT RE VORD	00002380	
	00002390	
OSCHOV TURNING	00002400	
	00002410	
\$fMPUT_TT3=1916_P9=3.48_V0=0.RP=1.549_	00002420	
A7=2.5, R4=1, 558, R6=1, 169, S3=2, 337,	00002430	
	00002440	
SIMPUT VO*350,	00002450	
	00002460	
\$[NPUT TT3=1516,P9=2.54,V0=0,	00002470	
	00002480	
\$INFUT V0*350,	00002490	
	00002500	
SINPUT TT3=1215, P9=1.66, VO=0,	00002510	
•	00002520	

|--|

APPENDIX H - EFFECT OF EXHAUST GAS TEMPERATURE ON SUPPRESSOR AERODYNAMIC PERFORMANCE

This appendix presents test results that indicate suppressor performance is affected by exhaust gas temperature. The impact on performance can be assessed by examining the recorded thrust and the accompanying static pressure distributions on all the force-producing projected areas. This is aptly illustrated in Figure H-1 which shows results of a one-to-one comparison test of hot- and cold-flow performance on a typical multitube suppressor nozzle with ejector shroud (Reference 5). At most nozzle pressure ratios, Figure H-1 shows a small but measurable difference in thrust coefficient between the hot-flow and cold-flow conditions. These performance effects should be reflected in the static pressure on the nozzle surfaces. Figures H-2, H-3, and H-4 show comparative pressure distributions for the multitube nozzle at the different exhaust gas temperatures. A pressure-area integration of the pressures on all nozzle external surfaces, nondimensionalized by the nozzle ideal thrust (inner plus outer streams), forms thrust coefficient increments due to the pressure force on these surfaces and illustrates the magnitude of the pressure differences due to temperature. These increments are shown in Figure H-5. The pressure force increment is 0.7 to 1.2% lower in thrust coefficient for the hot tests at the lower two pressure ratios while at the high pressure ratio point the cold and hot flow pressure forces were 0.6% and 1.0%, respectively, below the intermediate temperature point. Both the trend and the magnitude of these pressure integrations are very close to those differences recorded in the thrust measurements, as shown in Figure H-1. Thus, the small differences experienced in thrust coefficient levels between hot and cold testing are indicative of the static pressure distributions on the nozzle surfaces downstream of the nozzle throat.

Differences in suppressor base pressures due to exhaust temperatures are also evident for configurations without ejector shrouds; Figure H-6 shows chute base pressures measured in three separate tests on a plug nozzle with multichute suppressor (Reference 18). The hot-flow pressures are consistently slightly higher than those measured with cold exhaust flow. To evaluate what this pressure difference means relative to the nozzle thrust coefficient, the pressure force on the total suppressor base area may be integrated and compared to the nozzle ideal thrust. For the multichute suppressor pressures shown in Figure H-6, the chute base force for the hot-flow tests is 0.4% of gross thrust higher than for the cold flow tests. This 0.4% is not discernible, however, in comparisons of the full-scale (hot) and model-scale (cold) thrust coefficients, Figure H-7, due to data scatter.

Nozzle static pressures downstream of the nozzle throat can be expected to vary with gas temperature due to differences in exhaust velocities and expansion characteristics. For example, pressure differences occur for different gas temperatures in the divergent section of convergent/divergent nozzles; the expansion rate is dependent on the ratio of specific heats. Thus, for a given expansion ratio, A/A*, the resultant static-to-total pressure ratio varies with

γ according to the relationship

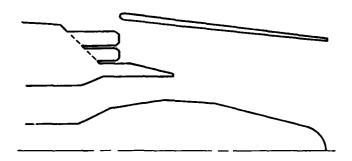
$$\frac{A^{\star}}{A} = \left[\frac{2}{\gamma-1} \left(\frac{\gamma+1}{2}\right)^{\frac{\gamma+1}{\gamma-1}}\right]^{1/2} (P/P_T)^{1/\gamma} \left[\frac{\gamma-1}{\gamma}\right]^{1/2}$$

For a given nozzle, these temperature effects will change the thrust coefficient versus nozzle pressure ratio curve by shifting the curve relative to the pressure ratio axis. An example of this is shown in Figure H-8 for a convergent nozzle operating with exhaust temperatures of 530 and 1800° R. This figure illustrates that, for a specific nozzle pressure ratio, the thrust coefficient will generally be different for different temperatures although the peak remains at the same level.

Similarly, when the jet exhaust exits the nozzle, the initial expansion angle at the exit lip is also dependent on the exhaust gas γ . Figure H-9, from Reference 68, shows the initial expansion angle as a function of lip-to-ambient static pressure ratio for different γ with an exit Mach number of 1.0.

In summary, the exhaust gas temperature influences the exhaust jet velocity and expansion characteristics which, in turn, affect the static pressures on the nozzle surfaces downstream of the nozzle throat. The static pressures generally increase at the higher temperatures. The magnitude of the resultant change in pressure force is small in relation to the nozzle gross thrust but may produce a measurable difference in thrust coefficient.

For preliminary design purposes (e.g., comparison and screening studies), cold-flow performance results should be acceptable. The performance prediction techniques on multitubes and multichutes which are included in the main text therefore based on thrust performance and base pressure data taken under ambient (cold) temperature conditions.



• From Reference 5

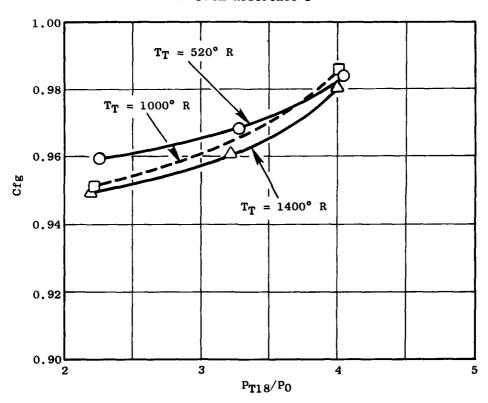
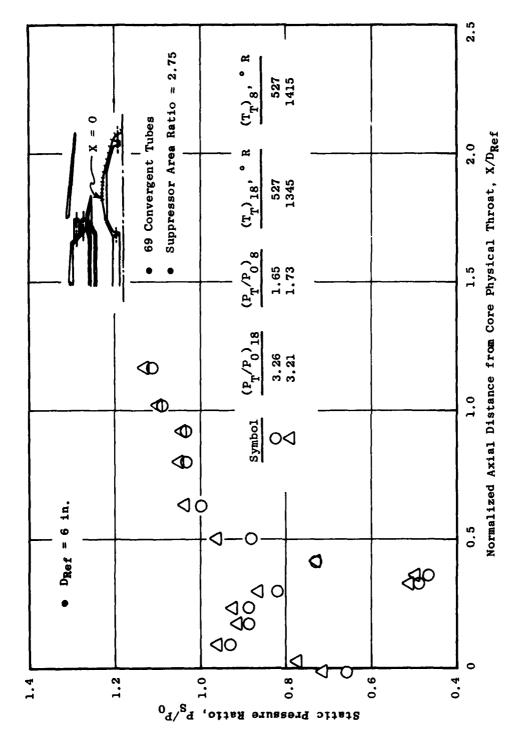


Figure H-1. Measured Thrust Coefficients for Multitube Suppressor with Ejector.



Core Plug Pressure Distributions for Tube Suppressor with Ejector, Hot vs. Cold Flow. Figure H-2.

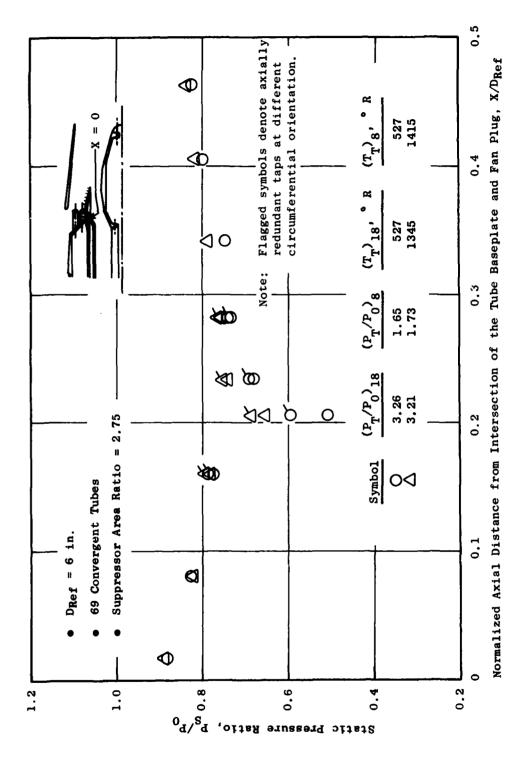
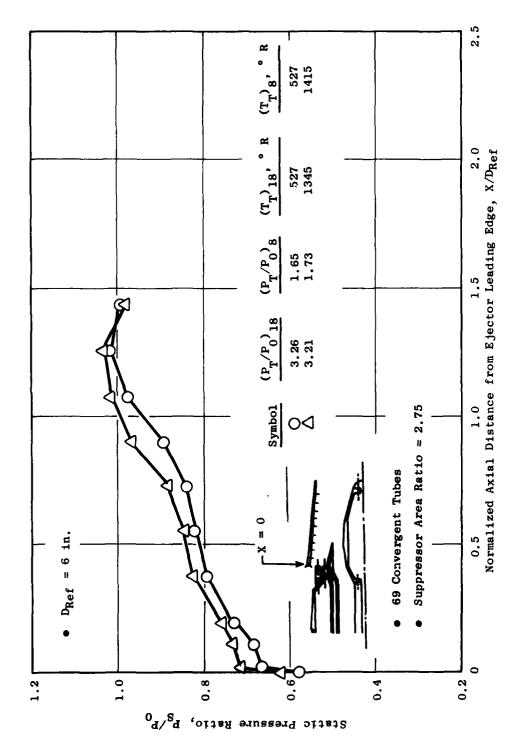


Figure H-3. Fan Plug Pressure Distributions for Tube Suppressor with Ejector, Hot vs. Cold Flow.

(390)

こうかい かっかんないこう かいこうかい あっちゅう まままの 幸なる かんかなかんない



Ejector Shroud Pressure Distributions for Tube Suppressor with Ejector, Hot vs. Cold Flow. Figure H-4.

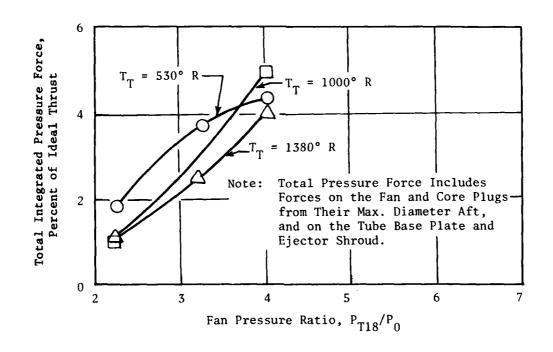


Figure H-5. Integrated Pressure Forces for Tube Suppressor with Ejector, Hot vs. Cold Flow.

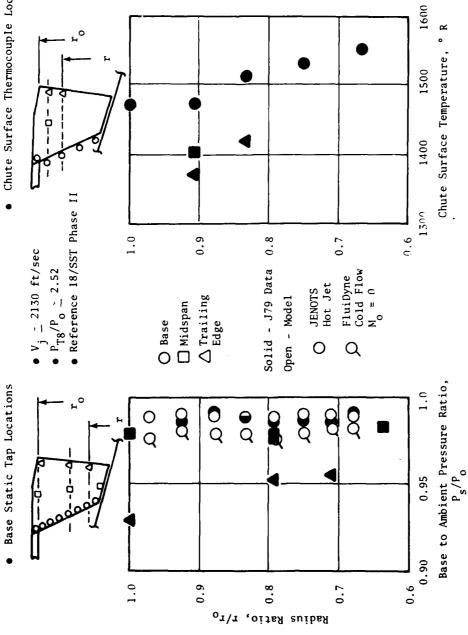


Figure H-6. Base-Pressure and Surface-Temperature Distributions for 32-Chute Suppressor.

- 32-Chute Suppressor
- ☐ J79 (Hot Flow)
- Scale Model (Cold Flow)

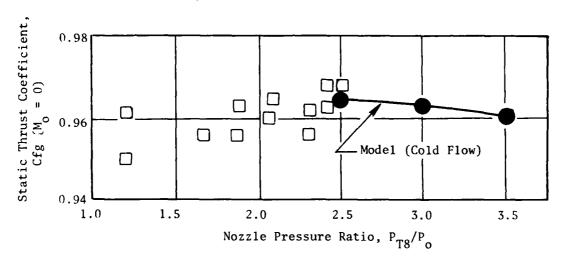


Figure H-7. Model and Engine Static Performance Comparisons.

211

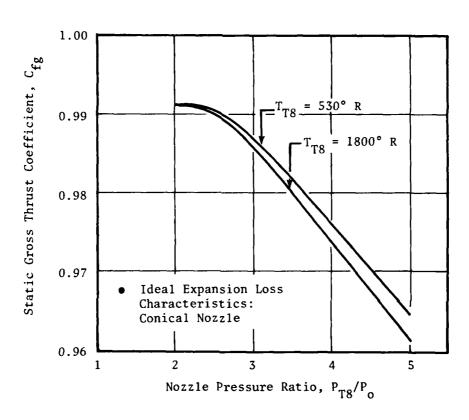


Figure H-8. Conical Nozzle Performance for Exhaust Temperatures of 530° and 1800° R.

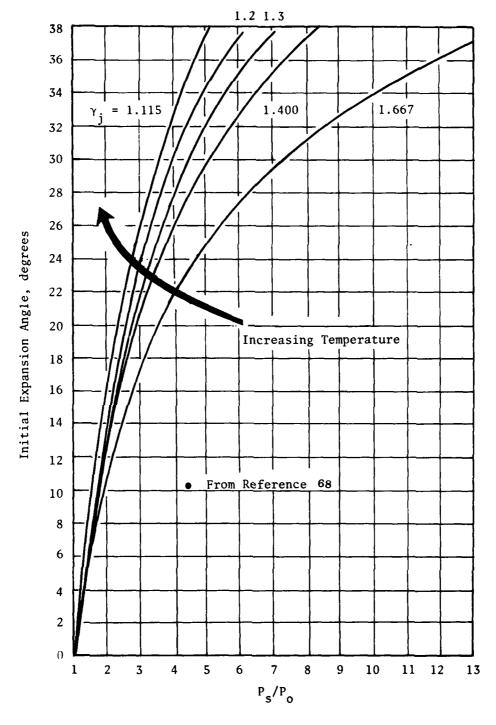


Figure H-9. Effect of the Ratio of Specific Heats of the Jet Upon the Initial Inclination of the Jet Boundary, $\rm M_{1} = 1.00$.

APPENDIX I - MULTIELEMENT NOZZLE AERODYNAMIC PERFORMANCE DATA

This appendix presents aerodynamic data and results from various multielement suppressor tests conducted by Industry and NASA. Most of the data are from scale-model tests conducted by The Boeing Company and General Electric. A limited amount of flight data, taken by NASA on an F-106B aircraft, is included.

MULTITUBE NOZZLES

Design Variables and Trends

The major geometric factors affecting multitube nozzle performance include:

- Suppressor Area Ratio
- Tube Number
- Tube Geometry
- Tube Pattern
- Tube Length
- Tube-Exit/Baseplate Stagger
- External Flow

Each of these factors affects the drag of the nozzle; internal performance is primarily a function of the tube length and shape.

The nozzle drag is caused by the entrainment action of the individual jets. This jet entrainment, or pumping, lowers the static pressure on the baseplate below ambient, producing a drag force on the nozzle.

Internal losses are primarily due to friction. Additional losses can occur as a result of flow underexpansion when the nozzle pressure ratio is above the critical value.

Geometric and Aerodynamic Terminology

This section defines the terminology that is used in the following sections, and discusses major constraints of the performance prediction methodology.

Symbols and Abbreviations

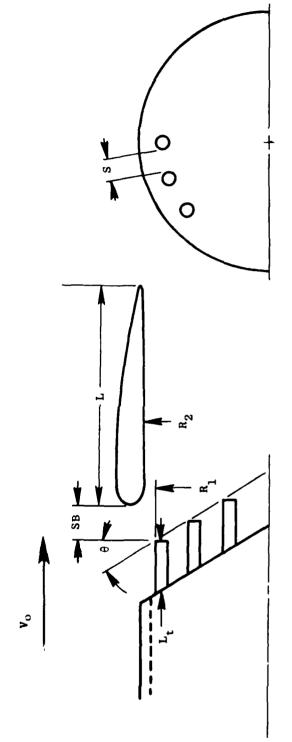
 A_b Baseplate Projected Area = A_8 (AR - 1)

Ao Total Nozzle Throat Area

A_S Area Between Tubes in Outer Row of Suppressor

37/

Minimum Area Between Ejector Lip and the Exit of the Outer Row of AA Tubes AR Suppressor Area Ratio (also NAR), where AR = Area of Circle Circumscribing the Outer Row of Tubes Divided by the Total Nozzle Throat Area c_{v} Nozzle Velocity Coefficient Cfg Nozzle Gross Thrust Coefficient, Fg/Fi Nozzle Internal Gross Thrust Coefficient (Fg + Daft)/Fi Cfgint D, d Diameter Equivalent Diameter, 2 $\sqrt{A_8/\pi}$ D_{eq} Afterbody Drag Daft Tube Internal Diameter Dŧ EAR Ejector Area Ratio (Figure I-1) Fg Gross Thrust Minus Afterbody Drag (F - Daft) Fi, FID Ideal Gross Thrust Based on Isentropic Expansion of Actual Flow to Ambient Pressure L Length External Tube Length from Baseplate $\mathbf{L_{T}}$ $\mathbf{L_{ti}}$ Internal Tube Length M Mach Number Total Number of Tubes in Suppressor Total Number of Tubes in Outer Row of Suppressor n Total Pressure $P_{\mathbf{T}}$ Nozzle Throat Total Pressure P_{T8} Ambient Static Pressure Po P_h Area-Averaged Baseplate Static Pressure Radius Minimum Distance Between Adjacent Tubes in Outer Row of Suppressor S



$$NAR = AR = \pi R_1^2 / A_8$$
$$EAR = \pi R_2^2 / A_8$$

Figure I-1, Multitube Suppressor Nozzle Schematic,

- SB Setback, Distance Between Tube Ends and Ejector Lip
- V_O Flight Velocity
- Baseplate/Tube and Stagger Angle, Degrees, Measured from Plane Normal to Nozzle Centerline
- γ Ratio of Specific Heats

<u>Constraints</u> - The performance prediction methodology as discussed in Section 5.2.2 of text should be limited to the following usage:

- Number of Tubes 19 to 121
- Nozzle Area Ratio 2.75 to 4.5
- Nozzle Pressure Ratio 2 to 4
- Tube Array
 Close-Packed, Hexagonal, Radial
- Tubes Convergent, all Uniform Size
- Flight Mach No. 0 to about 0.4
- Ejectors Cylindrical, EAR/AR ≈ 1.1 to 1.2
- SB/D_{eq} 0 to 0.25
- Ejector Length $L/D_{eq} \simeq 2.0$
- Smooth, Subsonic-type Ejector Inlets

Based on these constraints, the prediction methodology presentation Section 5.2.2 should yield predictions that are good to within \pm 1% in Cfg for bare suppressors and probably to within \pm 2% for ejectors.

Internal Performance

The losses to be discussed include those between the tube entrance and exit as indicated by Stations 0 and 3 of Figure I-2. The potential losses for this type of tube include:

- Entrance losses
- Friction losses
- Underexpansion losses.

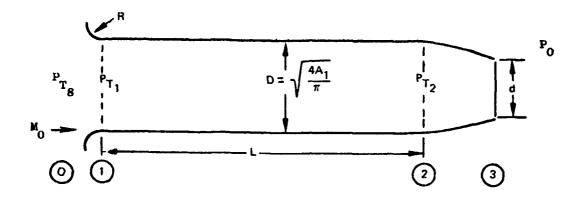


Figure I-2. Schematic of Single Tube.

Entrance Losses - Entrance losses (Stations 0 to 1, Figure I-2) are a problem only if the tubes are nonconvergent and the tube entrance has sharp corners. A combination of relatively low entrance Mach number and smoothly rounded corners can keep entrance loss at a negligible level. From Reference 69, a tube entrance radius to tube diameter ratio (R/D, Figure I-2) of at least 0.1 should be used. Figure I-3 illustrates the trend in entrance pressure losses as a function of the corner R/D and tube Mach number.

<u>Friction Losses</u> - In addition to keeping entrance losses at a minimum, converging the ends of the tubes to reduce the internal Mach number also helps to reduce viscous losses between Stations 1 and 2. The length of the tube, for a given tube diameter, also impacts viscous losses because the surface area is directly affected.

As will be discussed in the section on baseplate drag, ventilation area, which includes the distance between individual tubes, is an important parameter. Increasing the tube diameter between Stationsl and 2 has the effect of reducing the distance between tubes and, hence, restricts ventilation. Based on work by Boeing, Reference 22, a tube Mach number of about 0.5 is a good compromise considering internal losses and baseplate drag. In addition, the cross-sectional shape of the tube can be modified to increase ventilation, as will be discussed later on.

The trend in internal performance with tube length, for a given nozzle pressure ratio, is illustrated in Figure 1-4. from Reference 22. Also shown in Figure 6-13 is the reduction in losses associated with converging the tube ends to reduce internal Mach number.

<u>Underexpansion Losses</u> - Since suppressor tubes are simple convergent nozzles, underexpansion losses occur as pressure ratio increases. Ignoring viscous losses, typical convergent nozzle performance is shown in Figure I-5. Since most engine cycles for AST application operate at takeoff nozzle pressure ratios from about 2.5 to 3.5, underexpansion losses are not severe.

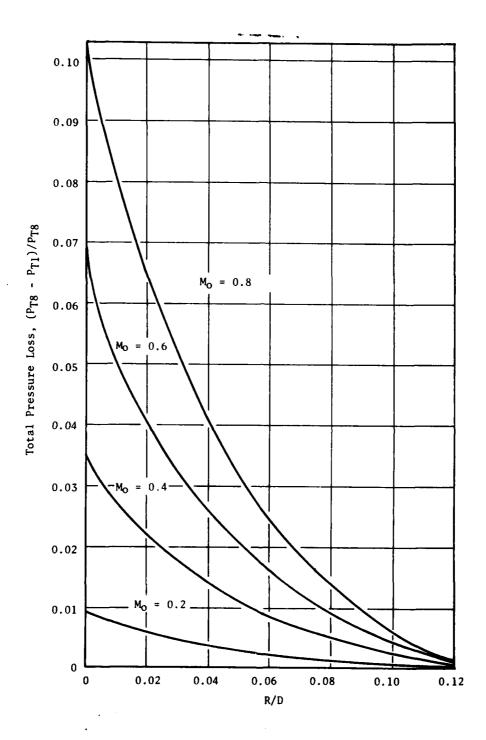


Figure I-3. Tube Entrance Losses.

こうことを持ちてきる はらている はかからはのないのではないのではないのであるとは、これのはないのでは、これのはないのでは、これのはないのでは、これのはないのでは、これのはないのでは、これのはないのでは、

- 37 Tubes, Area Ratio 3.3 Primary
- Close-Packed Array
- Pressure Ratio = 3.0
- $T_T = Ambient$

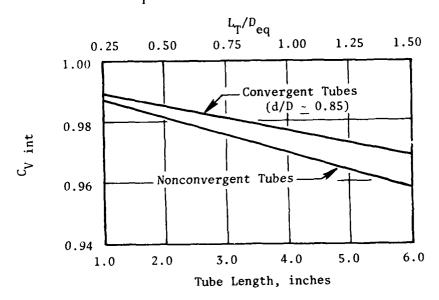


Figure I-4. Effect of Tube Length on Performance.

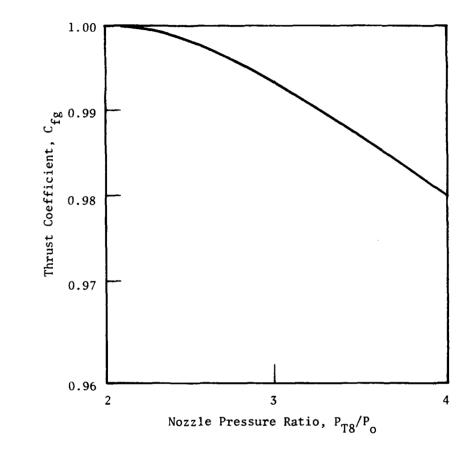


Figure I-5. Typical Convergent Nozzle Expansion Loss Characteristics.

(400)

The combination of viscous losses and underexpansion losses as a function of tube length, number of tubes, and pressure ratio is presented in Figure I-6 from Reference 22. These trends apply to a multitube suppressor with convergent tubes and a fixed total flow area.

Baseplate Drag

The pumping action of the jet from each tube lowers the static pressure on the tube baseplate, resulting in:

$$Drag = (\overline{P}_b - P_o)A_b$$

where

 \bar{P}_h = Area-weighted baseplate average static pressure

P_O = Ambient pressure

and

A_b = Baseplate projected area.

The major factors influencing the baseplate pressure are external flow conditions, the tube length, and the distance between tubes in the outer rows. The distance between tubes is determined by:

- Suppressor area ratio
- Number of tubes
- Tube geometry
- Tube pattern

Test results have shown that the stagger angle of the tube exits and baseplate can also influence the baseplate static pressure, as will be discussed.

Area Ratio - For a given total suppressor throat area and a uniform tube pattern, an increase in suppressor area ratio acts to spread the tubes apart (Figure I-7). The effect of increasing area ratio on baseplate pressure is shown in Figure I-8. Although the example is for a suppressor with no external tube length, the baseplate pressure trends are typical, showing an increase in average base pressure as area ratio is increased. However, as the area ratio increases, the baseplate area also increases. That is,

$$A_b = A_8 (AR - 1)$$

where

A = Baseplate projected area,

Ag = Physical flow area, and

AR = Suppressor area ratio.

(405)

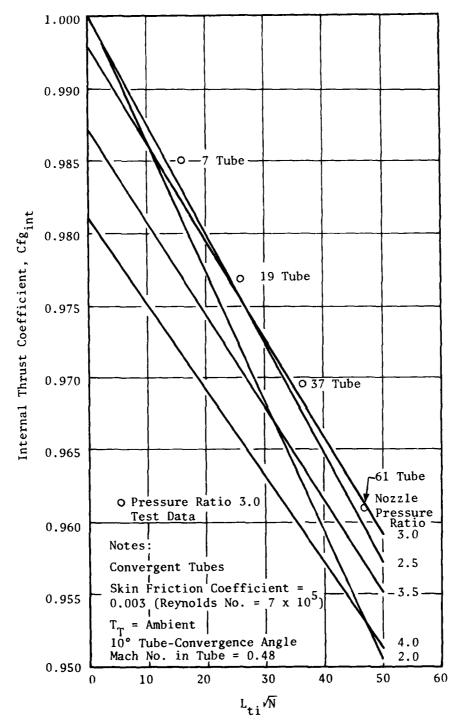
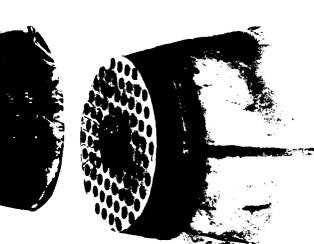
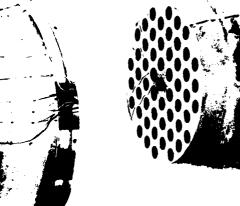


Figure I-6. Cfgint as a Function of Tube Length, Tube Number, and Pressure Ratio.











121 Holes, AR = 2.7

55 Holes, AR = 2.7

85 Holes, AR = 3.1

Multitube Nozzle Hardware used in Parametric Investigations of Area Ratio and Hole Number. Figure 1-7.

95.

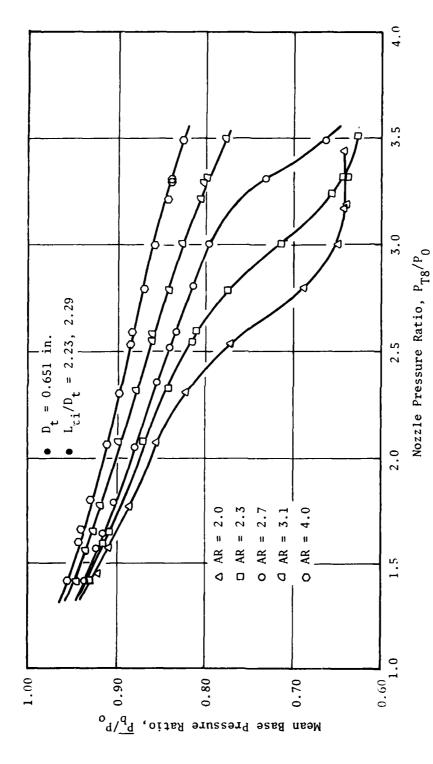


Figure 1-8. Effect of Area Ratio on Mean Baseplate Pressure Ratio for 85-Hole Nozzles.

For the example of Figure I-8, at a nominal pressure ratio of 3.0 the drag, nondimensionalized by the ideal gross thrust of the nozzle, results in a trend as shown in Figure I-9. These results illustrate that, although area ratio strongly affects baseplate pressure, the change in area over which the pressure acts tends to compensate for the higher base pressure.

Tube Number - For an evenly spaced array (Figure I-10), a given total flow area, and a given area ratio, the number of tubes also affects the distance between tubes. Figure I-11 shows the effect of the number of tubes on baseplate pressure. As the number of tubes increases, the baseplate pressure decreases. Since the baseplate area remains constant for a given area ratio, the trend in performance with increasing tube number follows the same trend as the baseplate pressure.

Tube Geometry - The cross-sectional shape of the tube can affect the distance between tubes and, hence, the base pressure. As was discussed previously, it is desirable to use convergent tubes in order to decrease tube internal losses. Unfortunately, the increase in tube diameter required to keep internal Mach numbers low also decreases the distance between tubes, as shown in Figure I-12. Boeing, in Reference 22, has shown that a tube with an elliptical shape, which transitions to round at the tube exit, can solve the problem. A tube of this type is shown in Figure I-13. Figure I-14 illustrates the advantage of the elliptical, convergent tube over the cylindrical, nonconvergent tube.

Tube Pattern - The pattern of the tube distribution on the baseplate also has a significant impact on baseplate pressure. Base ventilation and, hence, baseplate static pressure can be increased by arranging the tubes in "radial" patterns. The radial versus evenly spaced, or "close packed," pattern is illustrated by Figure I-15 from Reference 22. A comparison of base pressures for these two suppressor types is presented in Figure I-16 showing the advantage of the radial pattern.

Tube Length - Tube length has a strong impact on baseplate pressure. As the tube length increases, the entrainment action of the jet moves away from the baseplate. This trend is illustrated in Figure I-17. However, it must be remembered that the length of the tube also affects internal losses. Figure I-14 from Reference 22 shows the effect of tube length on the thrust coefficient of the suppressor. Boeing experience (with which General Electric generally concurs) with multitube designs for AST application has shown that a tube $L_{\rm t}/D_{\rm eq}$ of about 0.35 is maximum for practical, stowable configurations. In this region, the effect of tube length on internal performance is far outweighed by the effect on base drag.

Tube/Baseplate Stagger - The tube/baseplate stagger angle (θ), defined in Figure I-18, also has a significant effect on baseplate pressure. Results of static tests on the configurations shown in Figure I-18 indicate that as the stagger angle increases, baseplate pressures also increase. This trend is illustrated in Figure I-19.

External Flow - Mechanical jet-noise suppressors are sensitive to external flow conditions because of the relatively large base areas involved. As external

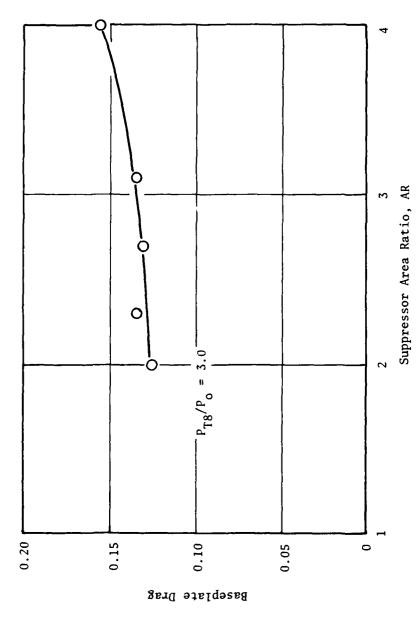
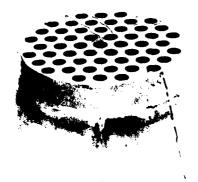


Figure I-9. Trend in Baseplate Drag with Suppressor Area Ratio.



55 Holes, AR = 2.7

85 Holes, AR = 2.7





121 Holes, AR = 2.7

Figure I-10. Multihole Nozzle Hardware Used in Parametric Investigation of Hole Number.

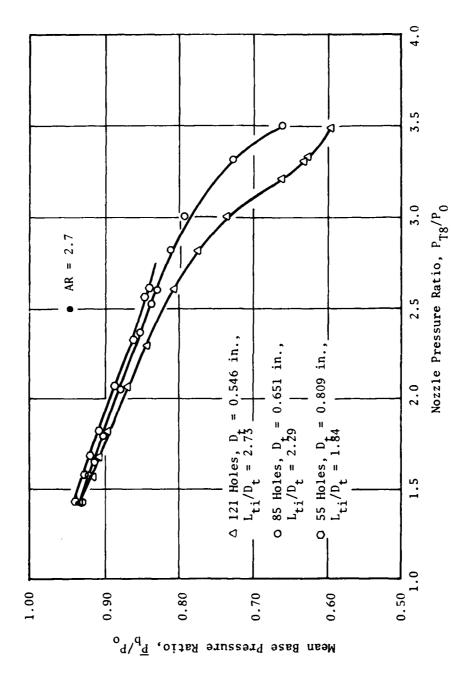


Figure I-11. Effect of Hole Number on Mean Baseplate Pressure Ratio.

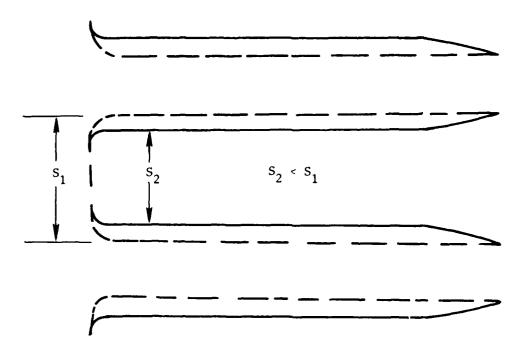


Figure I-12. Effect of Tube Convergence on Distance Between Tubes.

March Street British at British Ask Ask of the Street Stre

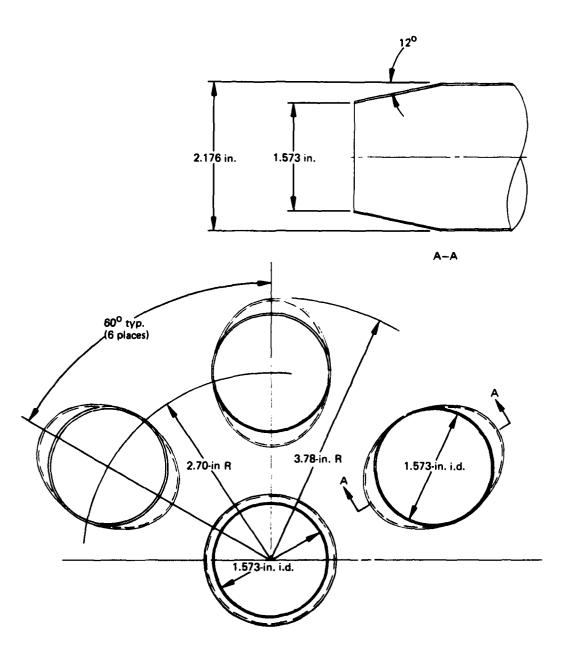


Figure I-13. Illustration of Elliptical Tubes.

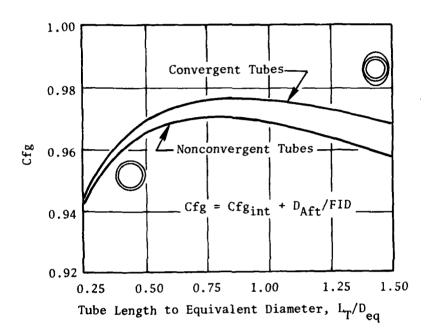


Figure I-14. Effect of Elliptical Convergent Versus Nonconvergent Tubes on Nozzle Performance.

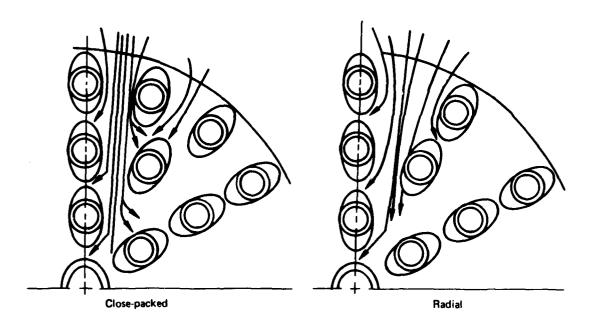
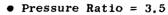


Figure I-15. Multitube Nozzle Arrays.



- 37 Tubes
- $L_{T}/D_{eq} = 0.25$
- Area Ratio = 4.5

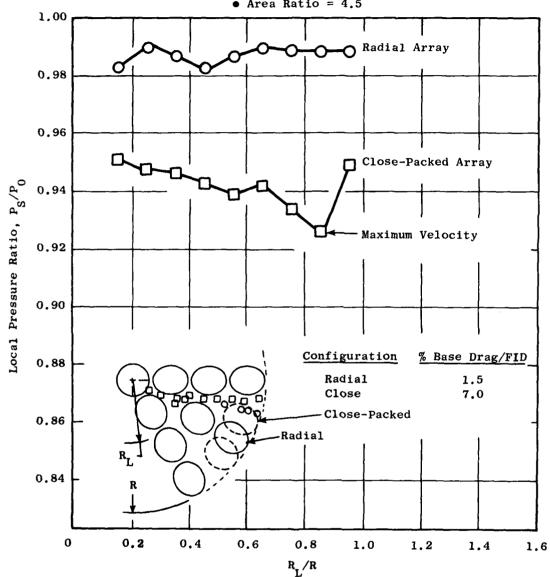


Figure I-16. Effect of Tube Array on Base Pressures and Drag.

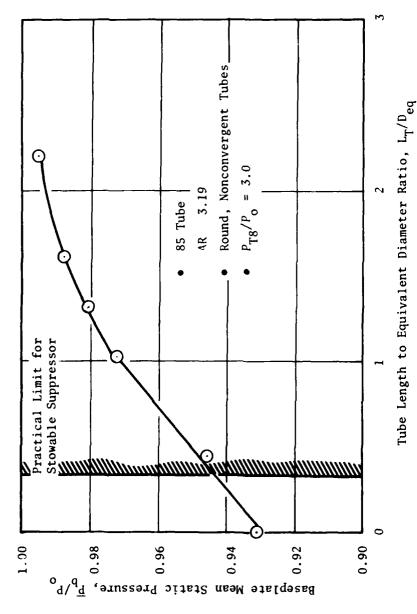


Figure I-17. Effect of Tube Length on Baseplate Pressure.

0° Base Stagger, Coplanar Exit, Dt = 0.430 in. Lt/Dt = 1.74, Lt₁/Dt = 3.49, AR = 3.06

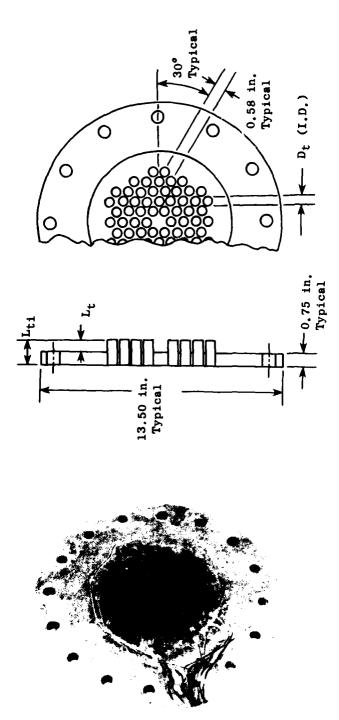
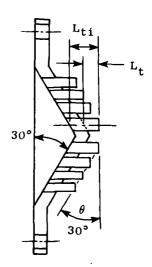


Figure I-18. Baseplate and Tube Exit Plane Stagger Variations for 72-Tube Nozzle Configurations.

30° Base Stagger, 30° Tube Exit Stagger D_t = 0.437 in., L_t/D_t = 1.72, L_{ti}/D_t = 3.43 AR = 2.96





60° Base Stagger, 60° Tube Exit Stagger D_t = 0.437, in., L_t/D_t = 1.72, L_{ti}/D_t = 3.43 AR = 2.96



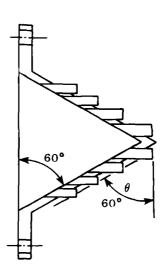
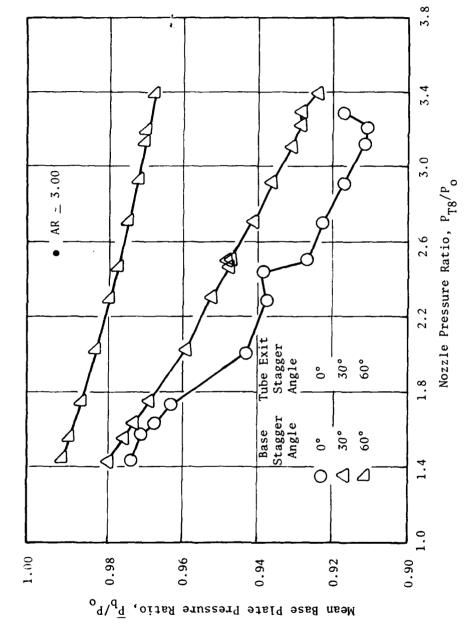


Figure I-18. Baseplate and Tube Exit Plane Stagger Variations for 72-Tube Nozzle Configurations (Concluded).



Effect of Baseplate and Tube Exit Plane Stagger on Mean Baseplate Pressure Ratio. Figure I-19.

The second secon

flow velocity increases, nozzle performance is reduced as illustrated by Figure I-20 from Reference 23. The effect of external flow on base drag alone is shown in Figure I-21 from Reference 23. The following comments from Reference 23 summarize the trends established in Figures I-20 and I-21.

- "For a constant nozzle area ratio the lapse rate is nearly constant. Comparison of the 19-, 37-, and 61-tube, NAR-3.3 suppressors with elliptical ramps (see Figure I-22) and elliptical convergent tubes shows a 2.8% variation in the static performance due to a combination of increasing internal losses and increased base drag resulting from the ventilation as the number of tubes increases. Because of the lapse rate to 167 km, a reduction in Cfg of 3.4%, 4.8%, and 4.9% occurs for the 19-, 37-, and 61-tube configurations, respectively. The 19-tube nozzle benefits from significantly better ventilation paths than the other nozzles.
- The base drag increases linearly with velocity as shown on Figure I-21. Though the static level of base drag is strongly dependent on ventilation, the rate of change of drag with velocity shows only a second-order influence of ventilation (i.e., the static base drag of the 61-tube suppressor is 2.8% greater than that of the 19-tube nozzle, yet the increase in the difference in drags at 167 km for the two configurations is only 0.75%). For all three configurations the ramp drag was less than 2% of the ideal thrust at 167 km, and the variation in ramp drag was at most 0.3% (greatest ramp drag was on the 61-tube nozzle). The ramp drag increases behaved in proportion to the square of the velocity. It is this ramp drag which produces the slight nonlinearity in the performance lapse rates shown on Figure I-20.
- Figure I-20 also shows the effects of these parameters on lapse rate. The 31-tube, NAR 2.75 radial array demonstrates the smallest lapse rate of the multitube nozzles investigated. Its shallow lapse rate is due to its lower nozzle area ratio and good base ventilation. At 167 kn the ramp drag for the configuration was 2% of the ideal thrust (which is nominally the same value as for NAR 3.3 suppressors with elliptical ramps). The base drag/FID was only 1.4% at 167 kn for the 31-tube radial array compared to 5.5% for the 37-tube, NAR 3.3, close-packed array ". "Figure I-20 also demonstrates that, for suppressors with constant nozzle area ratio and ventilation, the lapse rate is nearly independent of ramp shape and tube shape."

Ejectors

Most multitube suppressor nozzles intended for application to supersonic-cruise airplanes incorporate ejectors as part of the exhaust system. Almost all of the multitube-suppressor/ejector aerodynamic performance work has been conducted by Boeing and reported in Reference 23. The following discussion on ejector nozzle trends is excerpted from Reference 23.

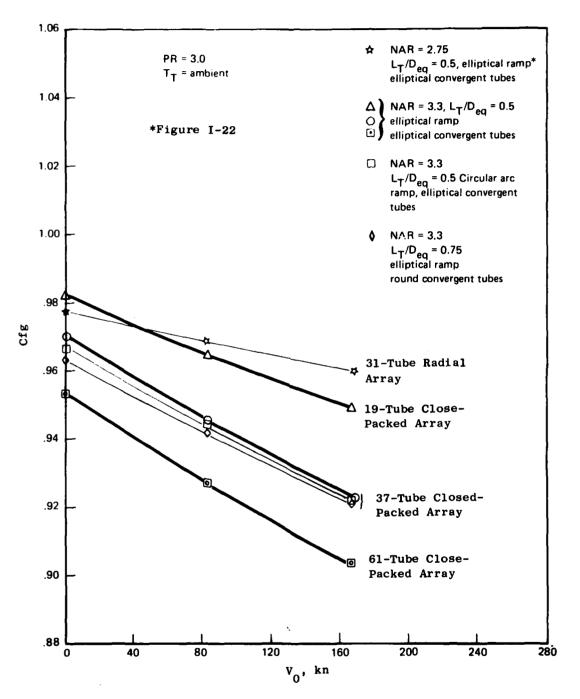


Figure I-20. Effect of Velocity on the Performance of Suppressors Without Ejector.

A STATE OF THE STA

• Close~Packed Array

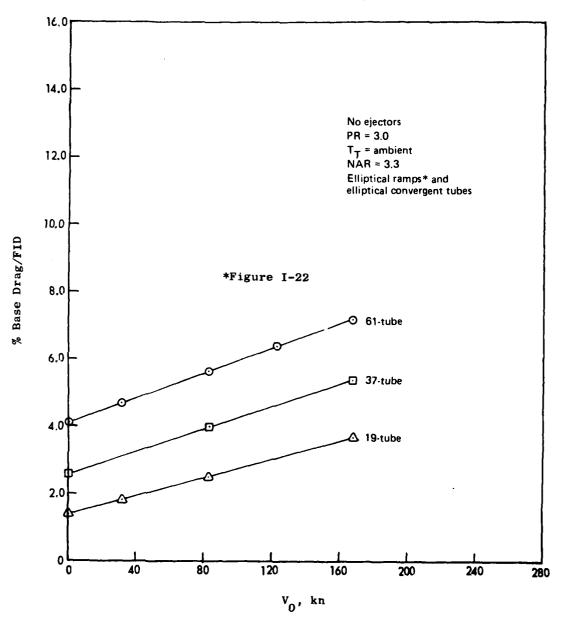
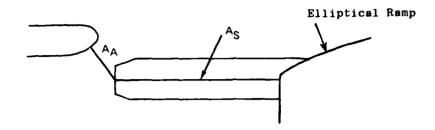


Figure I-21. Effect of Velocity on Base Drag as a Percentage of Ideal
Thrust for NAR 3.3 Suppressor with Various Numbers of Tubes.



Detail A-A

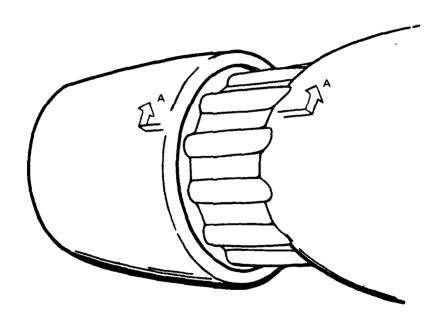


Figure I-22. Ejector Inlet Area ${\rm A}_A$ and ${\rm A}_S$.

(425)

"The addition of an ejector to an exhaust system subjected to forward velocity creates these additional concerns:

- Ejector lip suction
- Increased suppressor afterbody drag
- Ejector pressure drag (constant area)
- Skin friction losses
- Ram drag penalty

Ejector Lip Suction - As the suppressor jets mix with surrounding air, flow is entrained by the jets. Ambient air moves into the regions of pressure depression created by the entrained air. When an ejector is installed, this replacement air must flow into the ejector through the complex inlet provided between the outer tube row and the ejector lip, A_A (see Figure I-22). This inlet flow affects ejector lip suction and suppressor afterbody drag. The lip suction, a result of the pressure reduction caused by the high velocity flow entering the inlet, becomes a decreasing percentage of ideal primary thrust as pressure ratio increases (i.e., the lip force increases by a smaller amount than the ideal thrust).

Suppressor Afterbody Drag - Countering the performance benefit of the lip suction is the increased level of afterbody drag resulting from the presence of an ejector. At any fixed velocity the afterbody drag becomes a decreasing percentage of the ideal primary thrust as pressure ratio increases. The result is the same as for the suppressor without ejector, except the absolute levels are higher. At any fixed pressure ratio both the afterbody drag and lip suction become decreasing percentages of the ideal primary thrust as velocity increases.

<u>Ejector Drag</u> - The present investigation considers only constant-area mixers; thus, the only ejector pressure drag to consider is the ejector boattail drag, which is independent of pressure ratio.

Ram Drag Penalty - At a fixed velocity the amount of secondary air increases as pressure ratio increases (unless the inlet flow is choked). Therefore, by definition, the amount of ram drag increases with increasing pressure ratio. Though it is a real component in the momentum equation, the ram drag physically manifests itself as a change in lip suction. The effect of pressure ratio on ram drag is a secondary concern compared to the velocity effects on lip suction due to ram drag.

Resulting Performance - The net result of the above parameters is a pressure ratio dependence of overall performance which is similar to that of the bare suppressor case but with steeper lapse rates. The skin friction, ram drag, afterbody drag, and ejector pressure drag all increase with velocity and thus increase the lapse rate for the ejector configuration. Since increasing pressure ratio decreases both afterbody drag and lip suction with

(426)

velocity (either one of which can be dominant), the lapse rate dependence on pressure ratio for these components can go either way. At a fixed velocity both the lip suction and base drag become decreasing percentages of the ideal thrust as the pressure ratio increases. The lip suction has a stronger dependence on pressure ratio than does the base drag. Thus, over the range of pressure ratios investigated (2-4), the static gross thrust coefficient for suppressor/ejector nozzles is always at or near the maximum value of pressure ratio 2.0*. The lip suction decreases with forward velocity due to the ram drag penalty. The net result is a decrease in performance with increasing velocity and an upward shift in the pressure ratio at which maximum performance occurs."

"Crossover Velocity - A typical comparison of lapse rates for the ejector and base suppressor configurations is shown on Figure I-23. The figure shows the performance crossover velocity (i.e., the velocity above which the ejector becomes a performance handicap) at each pressure ratio. The crossover velocity decreases slightly with increasing pressure ratio and approaches a constant value. This trend held true for all configurations investigated where the inlet was not restricted.

Behavior of Restricted Inlet - If the crossover velocity is strongly dependent on pressure ratio, it is due to a restricted inlet. In these cases, as the pressure ratio increases, the ejector demands more air than can be brought through the inlet. At low pressure ratios this is manifested as increasing inlet losses, resulting in a crossover at a lower velocity as pressure ratio increases. As the pressure ratio continues to increase, the demand for secondary air increases until supersonic flow occurs at the ejector throat (monitored on static wall taps). This situation arises on 'tight' ejectors without sufficient setback"...."As the pressure ratio producing the inlet choking is approached, a steeper decrease in performance usually occurs. The experimental technique of mounting the ejector separate from the suppressor provided insight into another characteristic of the ejector behavior as inlet choking occurs. When the pressure ratio is sufficient to produce static pressures at the ejector throat indicating supersonic flow, the ejector begins to vibrate so violently that the flow must be shut down. The severe vibration and additional performance losses are attributed to shockinduced flow separations. (The vibration is low frequency, <200 Hz, and produces excursions greater than can be produced by manually pushing on the side of the ejector.) As the EAR/NAR and setback increase, the occurrence of the inlet choking moves to higher pressure ratios. The effect of inlet area on the pressure ratio at which supersonic flow occurs at the ejector throat is shown in Figure I-24. The only difference in configurations is that the upper carpet has 50% longer tubes. In both configurations, the ejector hilite is coplanar with the tube exit plane. The major effect on the additional tube lengths is the displacement of the entire carpet to a higher performance. The lapse rates are nearly the same and the onset of ejector vibration occurs at only a slightly higher pressure ratio. This behavior suggests that the amounts of secondary airflow going between the tubes is a small percentage of

^{*}The actual peak static Cfg occurs at a pressure ratio < 2.0 for most configurations.



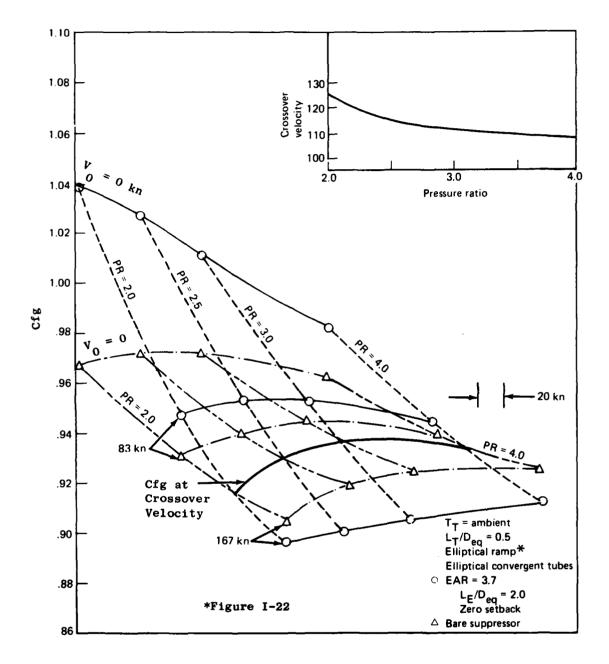


Figure I-23. Comparison of Performance and Lapse Rate and Crossover Velocity for 37-Tube, NAR 3.3, Close-Packed Array, Bare and with EAR 3.7 Ejector.

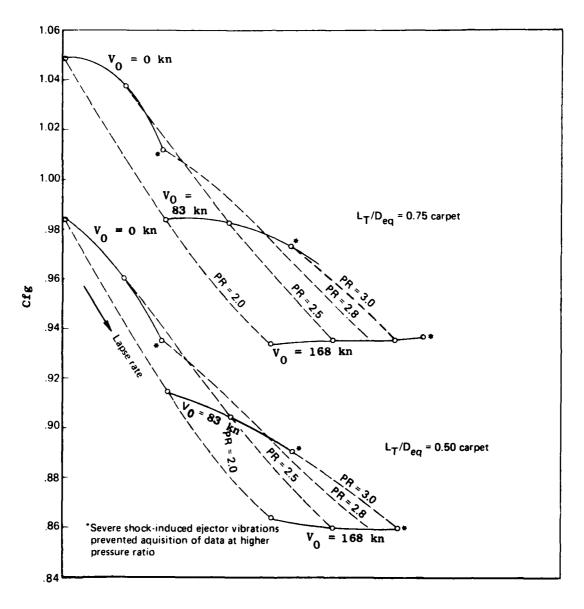


Figure I-24. Thirty-Seven-Tube, NAR = 3.3, Closed-Packed, EAR = 3.1 Ejector with Zero Setback.

(4)4

the total secondary mass flow (i.e., most of the air enters the ejector in the annulus, A_A , between the outer tubes and the ejector lip). The shift to higher performance is primarily due to a large decrease in base drag provided by the small increase in ventilating flow going between the tubes and the increased static pressure gradient between the lip and baseplate."

"[The data] show the static lip suction for these two cases to be the same at pressure ratio 2.8 for example, while the afterbody drag/FID is 9% less for the longer tubes. Now consider the same ejector and suppressor except with the short ($L_T/D_{eq}=0.5$) tubes and a setback ($SB/D_{eq}=0.25$). Thus, the total axial distance from the baseplate to the ejector hilite is the same as that for the long-tube case just considered, but the annulus area AA has been substantially increased. The carpet for this configuration is shown in Figure I-25 (along with a repeat of the carpet for the same tube length but zero setback from Figure I-24). The performance of this configuration at pressure ratio 2 is between that of the other configurations considered above. As pressure ratio increases (requiring more secondary air), the configuration with short tubes and setback not only out-performs the other two, but it continues to operate statically at a pressure ratio up to 3.5 while the others begin to vibrate at 2.8.

There are several reasons for this behavior. The afterbody drag for the short-tube configuration with setback is only 0.5% greater than for the long tubes without setback (compared to the 9% penalty of the short tubes without setback). The larger animalar opening on the setback case allows the secondary air to enter the ejector at a lower velocity than it did for zero setback. The reduced velocity decreases the lip suction, and this, combined with the afterbody drag relationship, results in the overall performance difference between the two no-setback cases at low pressure ratio. As the pressure ratio increases, the restricted inlets cannot pass any more air while the setback case benefits from: (1) a nearly constant lip suction/FID until pressure ratio = 3.0 and (2) a continued increase in secondary airflow until pressure ratio = 3.5.

Setback provides a mechanism for obtaining the appropriate inlet area necessary to optimize the performance at any given pressure ratio. The amount of setback required for peak performance increases as pressure ratio increases because of the increased demand for secondary air. At a fixed pressure ratio there is an optimum setback for each suppressor ejector or combination. If the setback is too small, supersonic flow can occur. For small increases in setback, the lip velocity (hence lip suction) decreases, but the base drag benefit increases substantially. The sketches in Figure I-26 show typical performance.....Forward velocity requires increasing setback (at a fixed pressure ratio) to produce peak performance and minimum lapse rate."

"The occurence of the ejector vibration moves to slightly higher pressure ratios as velocity increases, for a fixed geometry, because of the inlet ram effects.* If static tests do not monitor supersonic flow at the ejector

^{*}Free-steam P_{T} increases relative to P_{T8} as velocity increases and the pressure ratio is held constant.



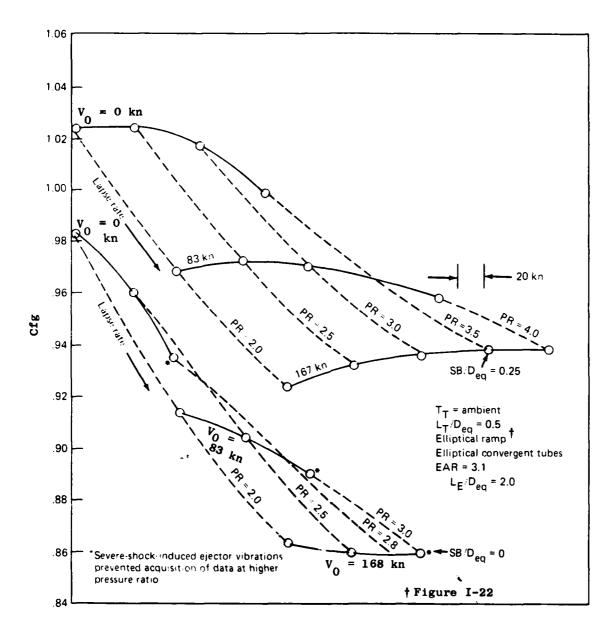


Figure I-25. Performance Carpets for Different Setbacks of the EAR 3.1 Ejector on a 37-Tube, NAR 3.3, Close-Packed Array with Tube Length Equal 0.5 $\rm D_{eq}$.



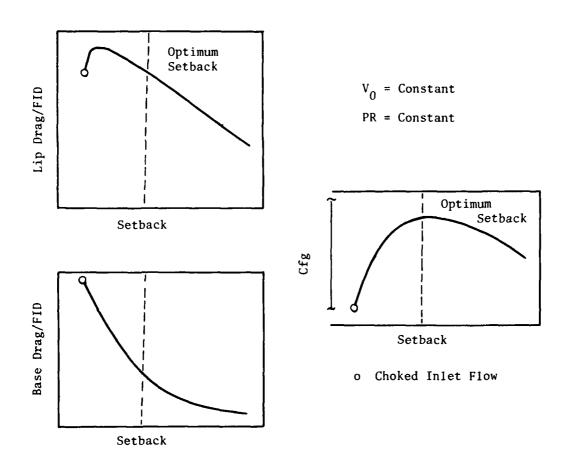


Figure I-26. Schematic of Performance Versus Setback.

throat over the desired pressure ratio range, one can be confident that the low-speed performance will not be affected by this problem. Some available information suggests that a vibrating ejector stabilizes and the rate of performance loss decreases if the system is driven to even higher pressure ratios.

"Within the present context, presumed inlet choking associated with the ejector vibration means only that supersonic flow was monitored by wall static pressure taps at the ejector throat. The ejector instrumentation included pressure taps in line with as well as between outer-row jets. The supersonic flow is noted at the tangent point between the lip and constant-area portion of the ejector and occurs around the entire circumference of the ejector (not just in line with the jets)."

MULTICHUTE/8POKE PLUG NOZZLES

Design Variables and Trends

As was the case with multitube suppressors, the base areas associated with multispoke or multichute nozzles are the largest contributors to thrust losses. A typical unsuppressed annular nozzle, designed for supersonic-cruise-design-point aircraft, will usually have a thrust coefficient, Cfg, of about 98%. This level of performance will apply to operation at Mach 0.4 as well as Mach 0 since the unsuppressed nozzle is not sensitive to external flow in this regime. The loss in performance relative to ideal thrust (about 2%) is primarily the result of viscous forces on the nozzle. With a suppressor added, the pumping action of the jet lowers the pressure on the suppressor bases below ambient, which results in a net drag force. As external velocity is increased, the flow over the top of the chute/spokes augments the jet pumping action, and element base pressure is further reduced.

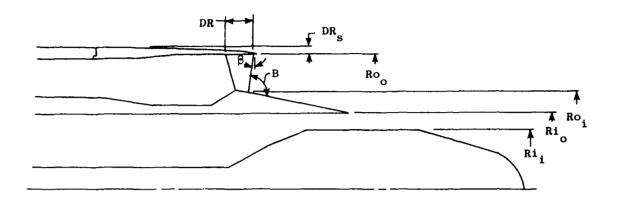
In the following section, trends in suppressed nozzle performance as a function of suppressor geometry will be discussed. Both single-flow and dual-flow nozzles are addressed. In the case of dual-flow nozzles, it is assumed that only the outer stream is suppressed.

Geometric and Aerodynamic Terminology

The analysis presented in the subsequent sections requires the definition of algebraic terms for use in describing the geometry of the suppressor nozzle and the operating environment. For the purpose of definition, the most general suppressor/nozzle design will be used. A dual-flow nozzle with a chute or spoke suppressor in the outer nozzle is the most general class of exhaust system considered in this section. In Figure I-27 those geometric parameters which are used in calculating exhaust-system, wind-on thrust performance are displayed in the form of algebraic terms. A complete list of the algebraic terms, and their definitions, for the aerodynamic and geometric parameters to be used is presented below:

- A₁ Inner-duct physical flow area, in.²
- A_O Outer-duct physical flow area, in.²
- B Angle from plug to suppressor exit

(43)



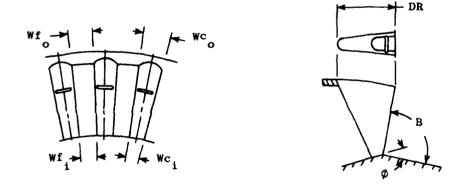


Figure 1-27. Multichute/Spoke Plug Nozzle Schematic.

(43)

- CP_{O} Outer flow specific heat at constant pressure, Btu/lbm $^{\circ}$ R
- DR Depth (length) of suppressor element on outer shroud, in.
- DRs Thickness of shroud at exit plane of suppressor, in.
- Mp External Mach number
- N Number of spokes or chutes in outer flow
- Ph Area-average of baseplate static pressure, psia
- Po Free-stream ambient pressure, psia
- PR_i Inner-flow pressure ratio, P_{T8}/P₀
- PR Outer-flow pressure ratio, P_{T18}/P₀
- Ri; Inner-duct, inner radius, in.
- Rio Inner-duct, outer radius, in.
- Ro, Outer-duct, inner radius, in.
- Roo Outer-duct, outer radius, in.
- Tro Outer-flow total temperature, ° R
- Wc: Inner-radius chute width, in.
- Wco Outer-radius chute width, in.
- Wf; Inner-radius flow width, in.
- Wfo Outer-radius flow width, in.
- eta Angle between suppressor exit plane and a line normal to the nozzle centerline (cant), degrees
- Y; Inner-flow ratio of specific heats
- γ_O Outer-flow ratio of specific heats
- φ Plug angle at chute exit plane, degrees
- $ar{\phi}$ Average plug angle under spoke or chute, degrees

Bare Suppressors

It has been found experimentally that much of the loss in an exhaust system with a spoke or chute suppressor is due to the base drag on the spoke or chute. Table I-l is a summary of the thrust losses (re: total ideal thrust) of nine configurations with spoke suppressors. For the majority of the configurations, the spoke thrust loss is over twice as large as the sum of the other nozzle losses.

411

(435)

Table I-1. Comparison of Nozzle Thrust Losses at a Pressure Ratio of 3.0.

	M _o = Thrust Lo		M _O = 0.36 Thrust Losses			
Configuration	Spoke Loss	Other	Spoke Loss	Other		
	%	%	%	%		
1	7.89	2.56	11.86	2.75		
2	2.42	2.45	6.40	4.68		
3	19.14	1.55	20.08	2.71		
4	4.04	3.01	8.07	4.63		
5	9.22	3.16	12.20	5.00		
7	15.80	4.98	16.54	6.22		
8	6.86	3.10	12.22	5.60		
9	6.12	3.04	6.68	3.80		
22	3.69	3.71	4.26	4.07		

To accurately account for the base pressure drag on a spoke or chute suppressor, the experimental results from all spoke and chute suppressor nozzles tested by General Electric were tabulated (References 18 and 19). This data base consisted of single- and dual-flow systems. The range of each important geometric and aerodynamic parameter covered by this data base is tabulated in Table I-2. This chute/spoke data base was then used in a stepwise, multiple, linear regression analysis to generate a nonlinear representation of the suppressor average base pressure divided by ambient (\vec{P}_b/P_0) as a function of the non-dimensionalized geometric and aerodynamic parameters of the suppressor nozzle. Losses associated with other factors, such as outer shroud and plug pressure and friction drag, were generated in a similar fashion. The resulting equations, which are discussed in Section 5.3.2 of the text, were used to establish trends in performance with variations in suppressor geometry.

In order to achieve a qualitative "feel" for the effect on overall nozzle thrust coefficient of changes in certain parameters, several plots are presented. Table I-3 identifies the geometric variables considered, along with the associated Figure numbers. In order to isolate the effects on thrust, only one input variable (where possible) was changed per curve. These curves are presented to illustrate trends and should not be used to quantify the change in thrust coefficient for a given change in the geometric or aerodynamic parameter of interest. Since the suppressor base pressure drag and the outer shroud and plug drags are non-linear functions of nozzle geometry and operating conditions, the change in thrust coefficient for a given change in input parameter is not constant for a family of curves. Several experimentally validated design criteria are identified in Figures I-28 through I-34. These are:

- 1. Since the two nozzles in a dual-flow system do not significantly affect each other under takeoff conditions, a more favorable overall nozzle thrust coefficient results when a greater percentage of thrust is generated by the inner flow. Increasing inner flow area, while holding every other variable constant, increases total nozzle performance (Figure I-28).
- Increasing the depth of the chutes increases suppressor base ventilation and improves performance (Figures I-29, I-30 and I-31).
 Applicable to single- and dual-flow systems.
- 3. The wind-on, uninstalled-performance coefficient for a single-flow nozzle with suppressor increases over the nozzle pressure range from 2.0 to 4.0 (Figure I-32).
- 4. For a single-flow system, increasing radius ratio (R_i/R_o) improves wind-on performance* (Figure 1-33).
- 5. Increasing Mach number for a single-flow suppressor nozzle decreases performance (Figure I-34).

*Note: Increasing the maximum nacelle diameter to achieve the above improvement must be traded against potential losses both at subsonic and at supersonic mission points.

Table I-2. Applicability Range of Parameters in GE Chute/Spoke Data Base.

Range of Application		Chute/Spoke Parameters		
1.5		Area Ratio, AR	≤	2.5
0.457	≤	Radius Ratio, R _i /R _o	≤	0.78
0,39	≤	Width Ratio, Wf _o /Wc _o	≤	2.2
0.5	≤	Depth Ratio, DR/Wco	≤	3.1
20	≤	Element No., N	≤	48
90°	≤	Angle Between Plug and Suppressor Exit, B	≤	110°
10°	≤	Plug Angle at Suppressor Exit Plane, ϕ	≤	15°
o°	≤	Plug Angle Under Spoke or Chute, ϕ	≤	15°
0	≤	Flight Mach No., Mp	≤	0.45
1.5	≤	Nozzle Pressure Ratio, PR	≤	3.5

;

A Dual-Flow A Nozzie Area A A Ratio	0.946** 0.799 0.551 0.390	0	0	0	O	0	0
Fressure Ratio	ABSC*	1	ı	ı	-	-	1
Outer Mozzle	3	ABSC	ABSC	ABSC	ABSC	ABSC	3.0
Angle Between % & Plug Suppressor Exit, degrees	101.7	100, 95	100, 95	100, 95	100	95	100
© Suppressor % Exit Cant Angle, degrees	0	ιν	20	5	ت	5	5
OR Suppressor	2.0	3.0** 2.0 1.5 1.0 0.5	3.0** 2.0 1.0	3.0** 2.0 1.0	1,2,3	1,2	3** 1
E Suppressor Chute Width Co Ratio	0.714	1.0	0.371	0.371	0.567** 0.371 0.219	0.371	0.371
S Suppressor Ratio (Suppressor)	0.716	0.614	0.680	0.742	0.614	0.783** 0.742 0.680	0.614
Number S of Chutes	36	32	32	32	28 32 36	32	32
A Effective of sea Realo	2.03	2.12	1.96	1.82	2.12	1.72 1.82 1.96	2.12
Масһ Тр) Ишврег	0.36	0.36	0.36	0.36	0.36	96.0	ABSC
Figure No.	1-28	1-29	1–30	1-31	1-32	1-33	, I-34

* Abscissa in Cfg_{noz} Plot ** Constant Value Curves on Plot

THE STATE OF THE S

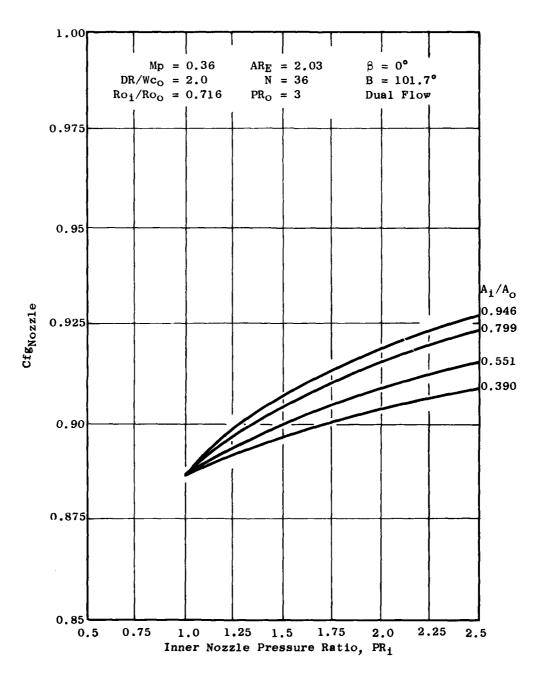


Figure I-28. Effects of Flow Area Ratio and Inner Nozzle Pressure Ratio on Wind-On, Uninstalled Performance.



 $Wc_i/Wc_0 = 1.00$ N = 32 Mp = 0.36 $Ro_i/Ro_0 = 0.614$ $\beta = 5^{\circ}$ $AR_E = 2.118$

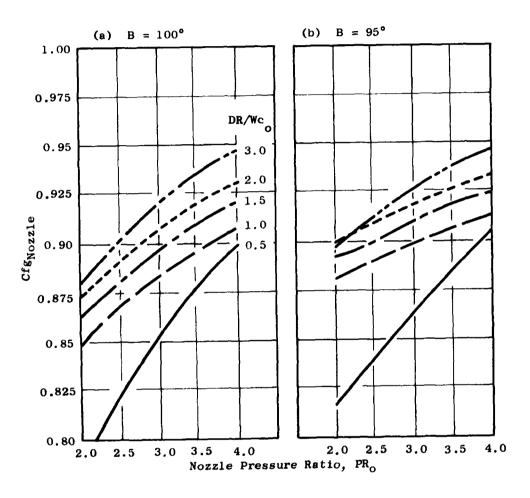


Figure I-29. Effects of Plug Suppressor Exit Angle and Chute Depth on Wind-On, Uninstalled Performance.

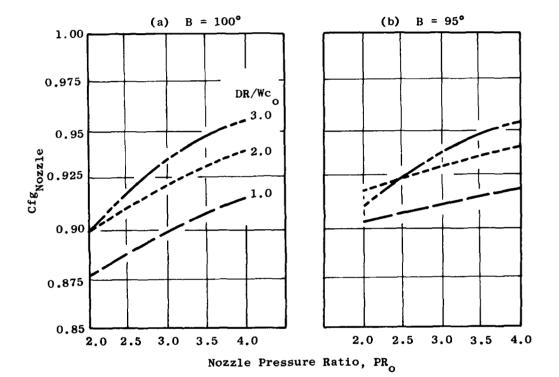


Figure I-30. Effects of Plug Suppressor Exit Angle and Chute Depth on Wind-On, Uninstalled Performance.

さんかん アナイス かんない

$$Wc_{i}/Wc_{o} = 0.371$$
 $N = 32$ $Mp = 0.36$ $Ro_{i}/Ro_{o} = 0.742$ $\beta = 5^{\circ}$ $AR_{E} = 1.82$

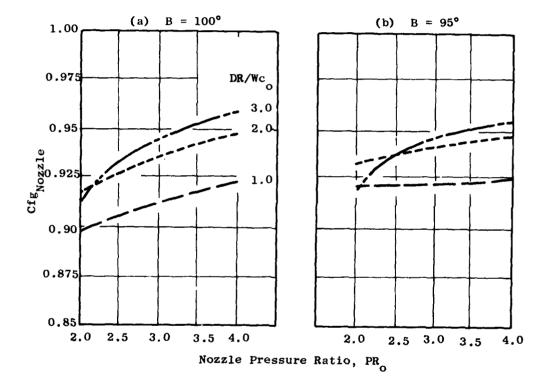


Figure 1-31. Effects of Plug Suppressor Exit Angle and Chute Depth on Wind-On, Uninstalled Performance.

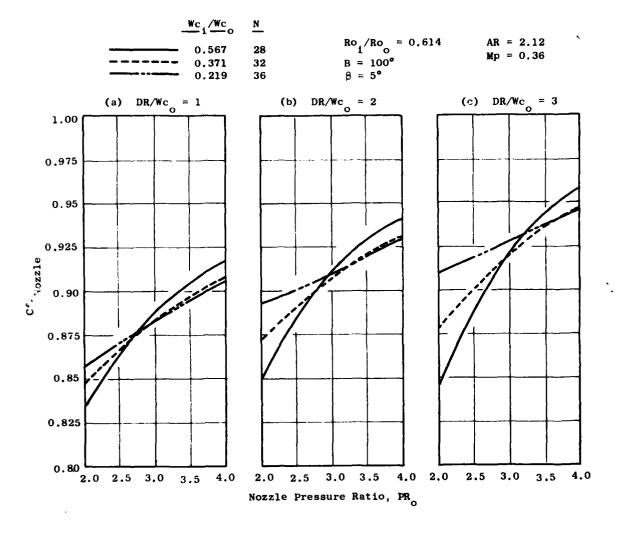


Figure I-32. Effects of Chute Depth and Chute Width Ratio (Chute Number) on Wind-On, Uninstalled Performance.

$$Wc_{i}/Wc_{o} = 0.371$$
 $\beta = 5^{\circ}$ $B = 95^{\circ}$
 $M_{p} = 0.36$ $N = 32$

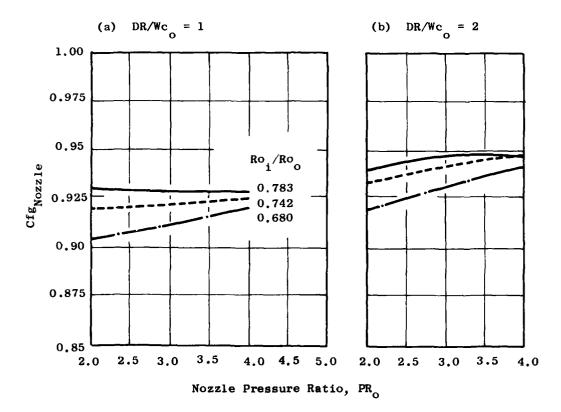


Figure I-33. Effects of Chute Depth and Outer-Duct Radius Ratio on Wind-On, Uninstalled Performance.

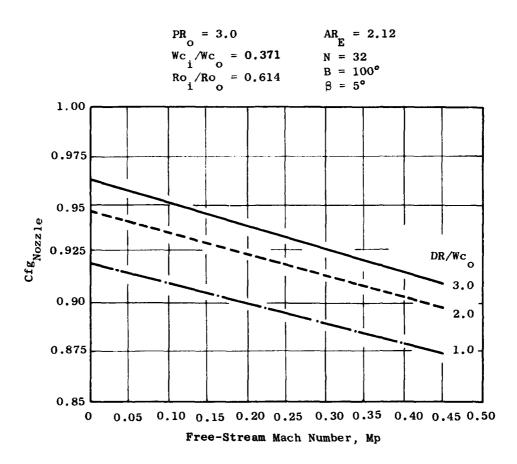


Figure I-34. Effects of Chute Depth and Mach Number on Wind-On Uninstalled Performance.



Ejectors

Ejectors for multichute/spoke, annular (plug) nozzles present a difficult design problem. Unlike the case of multitube nozzles, the ejector is used only for takeoff noise suppression and must be stowed during unsuppressed operation. This means that the ejector structure must be relatively thin and have the capability of translating forward to telescope over the nozzle shroud. Section 6.0 of the text discusses the mechanics of this translating capability.

Two types of ejectors have been tested by General Electric. The first is the setback ejector, where the ejector diameter is the same as the nozzle shroud internal diameter, and the inlet lip is set back from the suppressor to provide ventilation flow. The second type is the large-inlet ejector where the diameter is larger than the nozzle-shroud internal diameter, and the inlet lip is slightly forward of the suppressor exit plane. Both of these ejector types are illustrated in Figure I-35.

For the setback ejector, the axial spacing between the suppressor exit and the ejector lip was calculated to provide an inlet area equal to the suppressor-element base area. The diameter of the large-inlet ejector was determined in the same way. For both cases, the ejectors were designed to be constant area internally to prevent internal overexpansion.

Figure I-36 shows trends in performance for the ejectors as a function of Mach number for both shallow- and deep-chute suppressors. In both cases it can be seen that the setback ejector provided the higher level of performance. As was the case for multitube nozzles, the lapse rate is higher with ejectors than without.

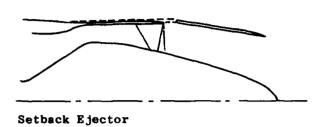
Flight Data/F-106B

In addition to the scale model data presented above, some flight data were obtained from several F-106B/J85 flyover tests sponsored by NASA Lewis (References 2,6,20, and 24. Baseline and various multielement suppressor nozzles were included in these test series.

All the flyover and static tests were conducted using an F-106B delta-wing aircraft modified to carry two underwing nacelles. The nacelles were mounted to the wing aft lower surface at approximately 32% semispan with the exhaust nozzles extending beyond the wing trailing-edge flaps. Each nacelle contained a calibrated General Electric J85 engine. A NASA-developed load cell technique was used to measure nacelle thrust minus drag to determine the impact of flight on exhaust nozzle performance.

Multispoke/Plug Nozzles

Aerodynamic performance data from two spoke-type suppressor nozzles and a baseline annular plug nozzle obtained by NASA (References 2 and 24) are summarized in the next few paragraphs. The three nozzles tested are shown schematically on Figure I-37. The baseline nozzle (Figure I-37a) consisted of a 10° half-angle plug and 17° half-angle conical primary flap. The two multispoke/





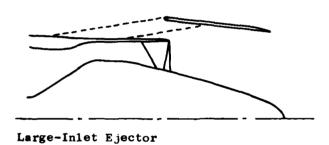




Figure I-35. Suppressor Nozzles with Two Types of Ejector.

Nozzle Pressure Ratio = 3.0

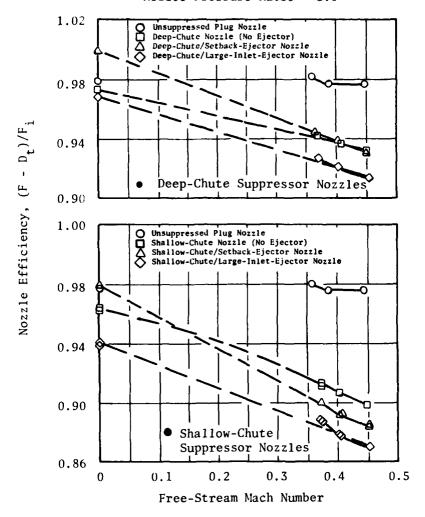


Figure I-36. External Flow Effects on Performance of Chute-Type Suppressor Nozzles.

plug suppressors (Figures I-37b and I-37c) were 2.0-area-ratio designs. The spokes of the 32-element nozzle were of the "V" gutter type which resulted in rectangular-planform flow areas; whereas, the geometry of the spokes for the 64-element was rectangular and resulted in tapered-planform flow areas. Photographs of the two multispoke/plug nozzles are shown in Figure I-38.

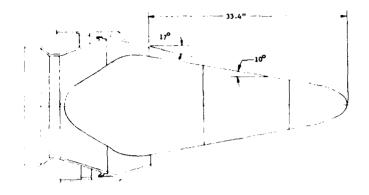
Nozzle performance (thrust minus drag) as a function of nozzle pressure ratio is shown in Figure I-39 for the three nozzles both at static and at flight (M = 0.4) conditions. Plug nozzle peak performance was good statically (about 0.98) but somewhat lower in flight (about 0.94), primarily due to primary flap drag and some centerbody losses. In general, multispoke/plug nozzles performed poorer than the baseline plug nozzle - primarily due to the drag associated with the large base area of the spokes. Thrust losses, relative to the plug nozzle, (static/flight) for the 32- and 64-element multispoke/plug nozzles ranged between 8/10 and 23/21 percent respectively. These flight results were comparable to those obtained from static and wind tunnel model tests (Reference 2 and 19) which, in turn, were used to arrive at the multichute/ spoke plug nozzle average base pressure ratio engineering correlation described in Section 5.0 of this document.

Multitube Nozzles

The effect of flight velocity on the thrust of a 104-tube suppressor nozzle with and without a treated shroud (ejector) was also investigated on this same NASA F-106B aircraft (References 6 and 20). The multitube suppressor (without shroud) shown in Figure I-40 consisted of 104 elliptical tubes divided into 5 rows, mounted on a conical baseplate with the tube major axis oriented radially, resulting in a suppressor area ratio of about 2.8. Figure I-41 depicts the 104-element multitube nozzle with the acoustically treated shroud that was also evaluated on this series of tests.

Nozzle gross thrust coefficient as a function of nozzle pressure ratio for both suppressors is shown in Figure I-42 at static and flyover conditions. External flow is seen to adversely affect the performance of both suppressor nozzles, with the shrouded configuration experiencing the more adverse effect. Flight thrust coefficient is essentially the same for both configurations and is seen to increase with nozzle pressure ratio, peaking at a C_f close to 0.84. Comparison of multitube (no shroud) flight data with those obtained with a duplicate scale model (Reference 19) in the NASA Lewis 8-by-6-foot supersonic wind tunnel was excellent.





a. Baseline Annular Plug Nozzle

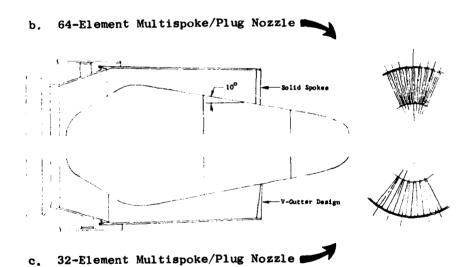


Figure I-37. Schematic of Annular Plug Nozzle and Multispoke/Plug Nozzles of 32 and 64 Elements.

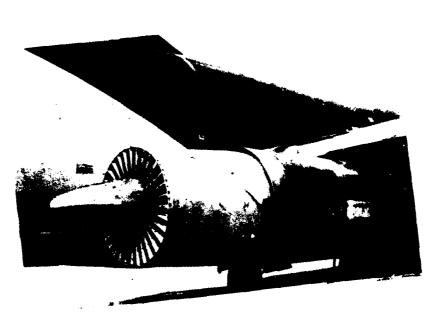
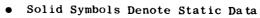




Figure I-38. Multispoke/Plug Nozzles of 32 and 64
Elements on J85 Engines Installed on F-106B.



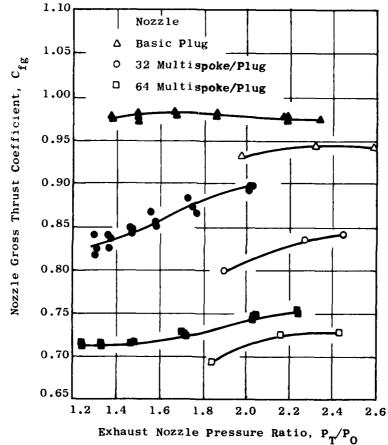
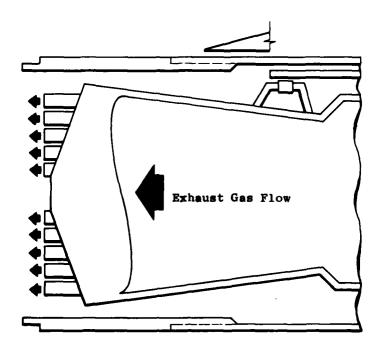


Figure I-39. Baseline and Multispoke/Plug Nozzle Static and Flyby Performance (Reference 24).

400



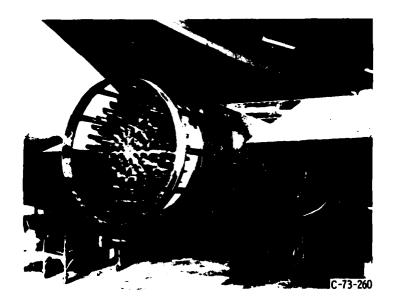
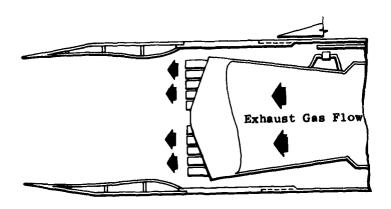


Figure I-40. Schematic and Photograph of 104-Tube
Nozzle on J85 Engine Installed on
F-106B Aircraft (Reference 20).

See Cherry



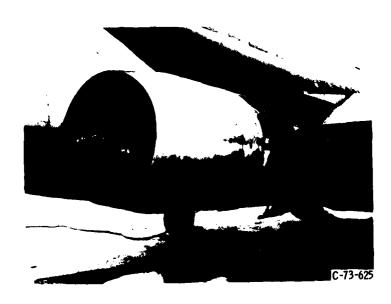


Figure I-41. Schematic and Photograph of 104-Tube Nozzle with Acoustically Treated Shroud on J85 Engine Installed on F-106B Aircraft (Reference 20).

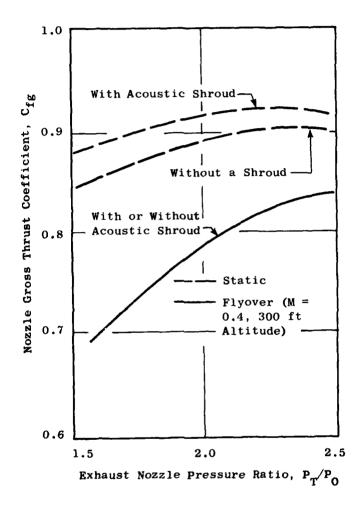


Figure I-42. Nozzle Gross Thrust Coefficient of 104-Tube Suppressor - Static and Flyby (Reference 20).

APPENDIX J - PREDICTED MULTIELEMENT NOZZLE AERODYNAMIC PERFORMANCE

This appendix presents examples illustrating the performance estimation methodology, described in Section 5.0 of this document, for multitube and multichute/spoke plug nozzles.

MULTITUBE NOZZLES

The aerodynamic performance of multitube exhaust systems is estimated through a series of stepwise calculations. The empirically derived design curves discussed in Section 5.0 of the text are used. The procedure includes:

- 1. Calculation of the nozzle internal performance
- 2. Calculation of the baseplate drag increment
- 3. Calculation of the effect of flight velocity
- If an ejector is part of the design, estimation of ejector performance increments.

The performance of a typical multitube nozzle is estimated below in order to illustrate the procedure.

Nozzle Description - The example nozzle is the 37-tube, AR 2.75, close-packed array (Reference 22) shown in Figure J-1. For stowage, a tube-length-to-equivalent-diameter ratio of 0.35 is assumed. It is also assumed that the tube entrance radius ratio, R/D, is 0.1 to eliminate entrance losses. Referring to Figure 5-2, the internal thrust coefficient is a function of $L_{ti}\sqrt{N/A_8}$.

$$D_{eq} = 2\sqrt{A_8/\pi}$$

where
$$L_{ti}\sqrt{N/A_8} = (L_T/D_{eq})(4N/\pi)^{1/2}$$

$$L_T/D_{eq} = 0.35$$
 $N = 37$

$$L_{ti} \sqrt{N/A_8} = 0.35 [(4 \times 37)/\pi]^{1/2}$$
 (For simplicity, assume $L_T = L_{ti}$)
= 2.4
433

HE J

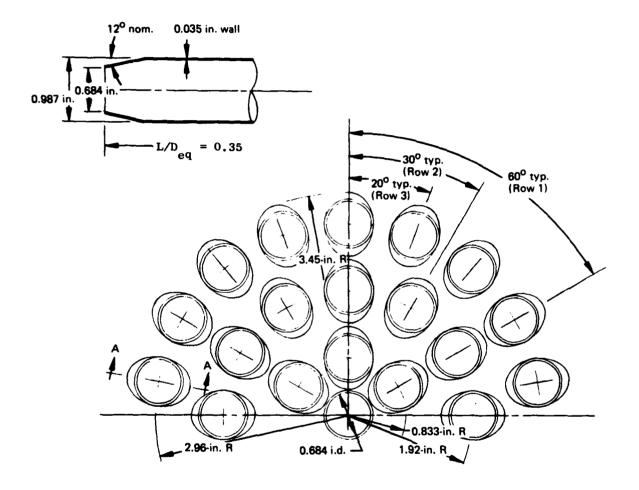


Figure J-1. Thirty-Seven Tube, 2.75 Area Ratio, Close-Packed Array with Elliptical, Convergent Tubes.

いからない いいちゅうちょう こうちゅうじょ 大変な 大変なない 日本ののの

From 5-2, $Cfg_{int} = 0.987$ at $P_{T8}/P_0 = 3.0$

Baseplate Pressure - The ventilation parameter is first calculated.

$$VP = [S^2 + (L_T/\cos\theta)^2]/n A_8$$

From Figure J-1

$$S = \frac{\pi D}{n} - d$$

where:

D = diameter of outer tube row,

n = tubes in outer row,

d = outer diameter of tube ends.

$$S = \frac{\pi(5.92)}{18} - 0.754$$

= 0.279 in.

$$A_8 = 13.6 \text{ in.}^2$$

$$L_T = 0.35(2) (13.6/\pi)^{1/2} = 1.46 in.$$

Therefore:

$$VP = [(0.279)^{2} + (1.46)^{2}]/(18)(13.6)$$
$$= 0.009$$

From Figure 5.4

$$\bar{P}_b/P_0 = 0.967 \text{ at } P_{T8}/P_0 = 3.0$$

From Figure 5.5

$$K = 0.36 \text{ at } P_{T8}/P_0 = 3.0$$

and
$$\triangle Cfg = K (\overline{P}_b/P_0 - 1) (AR - 1)$$

= (0.36) (0.967 - 1) (2.75 - 1)
= -0.021

Therefore, at $P_{T8}/P_0 = 3.0$,

External Flow Effects

$$S/D_{eq} = 0.279/(2)(13.6/\pi)^{1/2}$$

= 0.067

From Figure 5.6

$$\Delta \text{Cfg/V}_0 = 2.75 \times 10^{-4}$$
) at $P_{\text{T8}}/P_0 = 3.0$

at a typical takeoff velocity of 200 knots,

$$\Delta$$
Cfg = (2.75×10^{-4}) (200)
= 0.055

The performance of the bare suppressor at 200 knots and a pressure ratio of 3.0 is then:

$$Cfg = 0.966 - 0.055 = 0.911$$

Ejector Performance - Assuming an ejector is added where the ejector area ratio to suppressor area ratio, EAR/AR, is about 1.15 and the setback ratio, SB/D_{eq} , is about 0.25, from Figure 5-8:

$$Cfg_{static} = 0.966 + (0.065 + 0.015)$$

= 1.031 + 0.015

and at $V_0 = 200$ knots

$$Cfg_{(V_0 = 200)} = 0.911 + (-0.007 + 0.015) = 0.904 + 0.015$$

MULTICHUTE/SPOKE PLUG NOZZLES

A dual-flow exhaust system with the suppressor in the outer nozzle is assumed as an example for the calculation procedure presented in Section 5.3 of the text. Since several dual-flow systems have been tested as scale models in wind tunnels, a representative model (as shown in Figures 5-9 and 5-10 in Section 5.3 of the text), is used in the calculation. The following information is given:

Bare Suppressor - For the calculation of overall nozzle thrust coefficient, the preceding information is used, as follows, in Equations 1 through 14 from Section 5.3 of this document (Equation 1 is presented last).

$$Ro_0 = 7.772/2 \text{ in.} - 0.086 \text{ in.} = 3.800 \text{ in.}$$
 (2)

$$Wc_{i} = 0.714 Wc_{o}$$
 (3a)

Total Chute Area =
$$(11.054 \text{ in.}^2)(2.00-1) = 11.054 \text{ in.}^2$$
 (3b)

$$A_{\text{chute}} = 11.054 \text{ in.}^2/36 = 0.3071 \text{ in.}^2$$
 (3c)

0.3071 in.² =
$$\{3.80^2 \text{ sin}^{-1} [\text{W}_{\text{c}_0}/2(3.80)] - (\text{W}_{\text{c}_0}/2)\sqrt{3.80^2 - \text{W}_{\text{c}_0}^2/4}$$
 (3d)
+ $[\sqrt{3.80^2 - \text{W}_{\text{c}_0}^2/4} - \sqrt{\text{Ro}_1^2 - (0.714\text{W}_{\text{c}_0})^2/4}] [(\text{W}_{\text{c}_0} + 0.714\text{W}_{\text{c}_0})/2]$
+ $\text{Ro}_1^2 \text{ sin}^{-1} (0.714\text{W}_{\text{c}_0}/2\text{Ro}_1)$
- $(0.714\text{W}_{\text{c}_0}/2) \sqrt{\text{Ro}_1^2 - (0.714\text{W}_{\text{c}_0})^2/4}} \text{ in.}^2$

$$Wf_o = 2(3.80) \sin \{180/36 - \sin^{-1}[Wc_o/2(3.80)]\}$$
 (3e)

$$Wf_i = 2(Ro_i) \sin 180/36 - \{\sin^{-1}[Wc_0/2(3.8^\circ)]\}$$
 (3f)

$$A_{flow} = 11.054 \text{ in.}^2/36 = 0.3071 \text{ in.}^2$$
 (3g)

0.3071 in.² =
$$(1/\cos 0^{\circ}) \{3.80^{2} \sin^{-1} [Wf_{0}/2(3.80)] - (Wf_{0}/2)\sqrt{3.80^{2}} - Wf_{0}^{2}/4$$

+ $[\sqrt{3.80^{2}} - Wf_{0}^{2}/4 - \sqrt{Ro_{1}^{2}} - Wf_{1}^{2}/4][(Wf_{0} + Wf_{1})/2]$ (3h)
+ $Ro_{1}^{2} \sin^{-1} (Wf_{1}/2Ro_{1}) - (Wf_{1}/2)\sqrt{Ro_{1}^{2}} - Wf_{1}^{2}/4\}$ in.²

From the implicit solution of Equations 3d through 3h we obtain: R_{0i} = 2.720 in., W_{c_0} = 0.332 in., W_{c_i} = 0.237 in., W_{f_0} = 0.331 in., W_{f_i} = 0.238 in.

(467

$$A_{B} = \pi(3.80^{2} - 2.72^{2}) + 36 \{\sin^{-1}[0.332/2(3.80)]$$

$$[(3.80 + 0.086)^{2} - 3.80^{2}]\} - 11.054 \cos 0^{\circ} = 12.1 \text{ in.}^{2}$$
(4)

$$HR_{o} = 0.2246$$
 (5a)

$$\mu T_{T_0} = 2.278(10^{-8})(520)^{1.5}/(520 + 198.6) = 3.759(10^{-7})$$
 (5b)

$$Re_{HR_{0}} = \frac{12(0.2246)(3.0)(14.7)}{3.759(10^{-7})} \sqrt{\frac{1.4}{(1.4-1)} \frac{1.4}{25040(0.2399)520}}$$
 (5c)

$$= 3.960 (10^5)$$

$$CD\delta = 1 - 0.130768/[3.960(10^5)]^{1/6} = 0.9847$$
 (5d)

$$T_{T_{o(cen)}} = (5/9) (520 - 491.688) = 15.73^{\circ} C$$
 (5e)

$$CDV = 1.0 + [14.7(3.0)/146960] [5.4913999$$

$$- 0.060/46929(15.73) - 1.5267814(10^{-3})(15.73^{2})$$

$$+ 1.110391(10^{-4})(15.73^{3}) - 2.6897358(10^{-6})(15.73^{4})$$
(5f)

$$+2.9889184(10^{-8})(15.73^{5}) - 1.2608694(10^{-10})(15.73^{6})$$

= 1.0013

$$CD_o = (0.9847)(1.0013) = 0.986$$
 (5g)

$$Rr = 2.720/3.800 = 0.716$$
 (6a)

$$Wf_{i/o} = 0.238/0.331 = 0.719$$
 (6b)

$$Wc_{1/0} = 0.237/0.332 = 0.714$$
 (6c)

$$D\Delta R = 0.6641/(3.80 - 2.72) = 0.615$$
 (6d)

$$DQ = 0.664/0.332 = 2.0$$
 (6e)

$$\phi_r = 11.70 \ (\pi/180) = 0.2042$$
 (6f)

$$\bar{\phi}_{r} = 0 \ (\pi/180) = 0$$
 (6g)

$$\beta_{\mathbf{r}} = 0 \ (\pi/180) = 0$$
 (6h)

$$B_r = 1.5708 + 0.2042 - 0 = 1.7750$$
 (6i)

$$P_B = 1.39237 - 0.397401 (0.2042) + 0.075001 (0)$$
 (7)

$$-0.324831 (0.714) - 0.969623 (0.615) - 0.12839 (0.615)^2$$

$$-0.0946673 (0.714)^2 - 0.0300258 (0.615) (0.714)$$

$$+ 0.036 \cdot 16 (3)^2 - 0.0311525 (0.36)$$

$$+ 0.0151679 (36) (0.615) + 0.00335317 (36) (3.0) - 0.0661407 (1.7750)^{2}$$

- + 0.338926 (1.7750) (0.615) 0.0652494 (1.7750) (0.36)
- + 0.0257783 (1.7750) (3.0) = 0.8037

$$n_{ABE}$$
 Drag = (1 - 0.8037) (14.7 psia) (12.10 in.²) = 34.02 lbf (8)

$$\Delta Cfg_0 = -0.209783 + 0.0800173 (0) - 0.170768 (0)$$
 (9)

$$+ 0.193405 (0.36) + 0.00055485 (3.0) + 0.202381 (0.716)$$

$$-0.0151082 (0.714) + 0.0129846 (2.0) - 0.161545 (0.714)^{2}$$

$$-0.117331 (0.615) (0.714) + 0.00986606 (3.0)^{2}$$

$$+ 0.000344757 (36) (3.0) + 0.0950154 (1.7750)^{2}$$

= 0.0352

$$FID_0 = 0.986 (11.054) (3.0) (14.7) (1.4)$$
 (10)

$$\times \sqrt{\frac{2}{1.4-1} \left[\frac{2}{1.4+1} \right]^{(1.4+1)/(1.4-1)}} [1-3.0^{(1-1.4)/1.4}]$$

= 451.0 1bf

$$\triangle \text{Cfg}_{\mathbf{B}} = 34.92 \text{ lbf}/451.0 \text{ lbf} = 0.0774$$
 (11)

$$Cfg_0 = 1.0 - 0.0774 - 0.0352 = 0.887$$
 (12)

$$CX_{1} = \sqrt{\frac{1 - (1.89)^{(1 - 1.4)/1.4}}{(1 - 1.4)/1.4}}$$
(13a)

$$0.981(1.4) \sqrt{\frac{2}{1.4-1} \left[\frac{2}{1.4+1}\right]^{(1.4+1)/(1.4-1)} \left[1-2.5^{(1-1.4)/1.4}\right]}$$

= 1.0011

From Figure 5-11 at $\pi(Ri_0)^2/Ai = 2.46$: Peak Cfg_i = 0.980

$$Cfg_{i} = \sqrt{\frac{1 - (1.89)^{(1 - 1.4)/1.4}}{(1 - 1.4)/1.4}} \quad (0.980 - 1) + 1.0011 = 0.984 \quad (13b)$$

$$FID_{i} = 0.981(6.086)(2.5)(14.7)(1.4)$$
 (14)

$$\times \sqrt{\frac{2}{1.4-1} \left[\frac{2}{1.4+1} \right]^{(1.4+1)/(1.4-1)}} [1-2.5^{(1-1.4)/1.4}]$$

= 190.8 1bf

Having calculated all the terms in Equation 1:

$$Cfg_{Nozzle} = \frac{0.887(451.0) + 0.984(190.8)}{451.0 + 190.8} = 0.916$$
 (1)

It should be noted that the performance of a single-flow suppressor nozzle may be calculated in a manner similar to the above example. For a single-flow nozzle, Equations 13 and 14 are deleted; and FID in Equation 1 is equal to zero.

Suppressor with Ejector - A setback ejector is assumed, therefore

SB =
$$\frac{A_0 (AR-1)}{\pi (Ro_0)}$$
 = $\frac{(11.054)(2-1)}{\pi (3.8)}$ = 0.926 in.

For a pressure ratio of 3.0 and an external flow Mach number of 0.36, from Figure 5-12 Δ Cfg = 0.006

Therefore:

$$(Cfg_{Nozzle})$$
 with ejector = 0.916 + 0.006 = 0.922

APPENDIX K - AIRCRAFT-ENGINE/SUPPRESSOR INTEGRATION ASSESSMENT BY USE OF RANGE AS A MERIT FACTOR

This appendix identifies and discusses the manner in which suppressordesign variables affect aircraft range. Examples for three typical suppressor nozzles (32-chute, 40-shallow-chute, and 54-element-coplanarmixer) are presented.

The generalized procedure for performing these case studies is illustrated on Figure K-1. Aircraft range characteristics are established as a function of engine airflow. Increasing engine airflow allows the same net thrust level to be attained at a lower jet velocity, thus lowering the jet noise. The increase in engine airflow causes a significant reduction in aircraft range, however, when takeoff gross weight, payload, and balance field length are held constant; the larger engine weighs more and increases the drag (less fuel on board and higher fuel consumption). The net thrust required is established based on balance field length and aircraft characteristics. The NASA arrow-wing advanced supersonic technology design described in References 1 and 70 is the aircraft used for these case studies. A 12,500-foot balance field length was selected resulting in a net thrust requirement per engine of 53,500 lbf.

The engine size required to maintain this constant net thrust varies, for specified cycle conditions, as a function of nozzle thrust coefficient. For example, suppressor nozzles would require a larger engine to maintain constant net thrust than a conical nozzle because of a lower thrust coefficient. The addition of a suppressor to the engine generally causes an increase in exhaust system weight which results in a range penalty. A derivative is established based on the mission characteristics to account for this range loss.

Two engine cycles, representative of typical turbojet and variable-cycle engines previously described in Reference 1, were selected for the case studies. The pertinent characteristics for these engines are summarized on Table K-1.

Engine cycle performance characteristics have been generated for mission analysis at supersonic cruise, subsonic cruise, hold, and climb/acceleration flight conditions. Using this performance data, noise levels are established (mainly from scaled data) for a given design at the sideline and community monitoring points as a function of engine airflow size at constant net thrust for a given nozzle design. The minimum engine airflow size which may be used to meet a specified noise requirement is then determined. The corresponding range for a given airflow is then calculated along with the appropriate range decrement for increasing exhaust system weight.

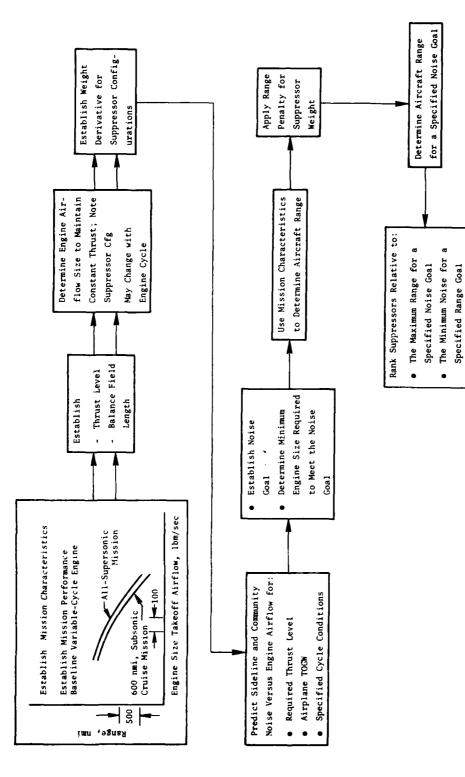


Figure K-1. Case Study Methodology.

(160.

こうかんしょうかいことはなるないのとのなっていることできませんできるないのできるないのできますのできますのできます。

Table K-1. Summary of Engine Cycle Conditions.

\	Turbojet	Variable Cycle Engine
• Engine Airflow *	770 1bm/sec	840 1bm/sec
• Fan Pressure Ratio	3.7	3.7
 Engine Overall Pressure Ratio 	16.2	16.1
Bypass Ratio	0.07	0.25
 High Pressure Turbine Rotor Inlet Temperature, Maximum High Pressure Turbine Rotor 	2500° F	2800° F
Inlet Temperature, Cruise	2400° F	2700° F
Compressor Discharge Temperature, Maximum	1120° F	1150° F

^{*}Corrected Airflow at Sea Level Static Conditions

Overall, the use of the mechanical suppressor allows the use of a higher specific thrust (relative to an unsuppressed configuration) engine to meet a specified noise requirement. Without noise constraints, a suppressor is not an effective device because it sacrifices performance and adds weight. The evaluation of a given nozzle design requires that the noise level, thrust coefficient, and weight increase (relative to a reference nozzle) be established. Most of the noise levels used in this section were based on scaling the model-test data discussed in Reference 3 to the appropriate size and distance. However, the noise characteristics for a design may be predicted using the M*G*B model described in Appendix A or the M*S model described in Section 4.0 of this document. The thrust coefficient for a specific design may be defined using windtunnel test data or the prediction procedure described in Section 5.0. The weight estimates are determined using the procedure described in Section 6.0.

The three suppressors selected for the case studies are representative of the types of designs currently being considered for application on advanced turbojet and variable-cycle engines. Photographs and schematics of the nozzles are summarized on Figure K-2. The weight estimates and aerodynamic performance characteristics are summarized on Table K-2 and Figure K-3 respectively. The noise levels for several cycle conditions are based on scaling anechoic free-jet data, Reference 3, to the appropriate size and extrapolating to the monitoring distance. The EPNL levels were calculated for the sideline and community monitoring points assuming a level flyover. Corrections were applied for the number of engines (+6.0 EPNdB), ground effects (+1.5 EPNdB), and shielding (-4.0 EPNdB). The shielding was based on the data presented in Reference 9 and applied to the sideline monitoring point only.





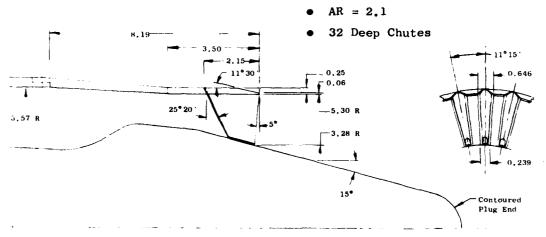
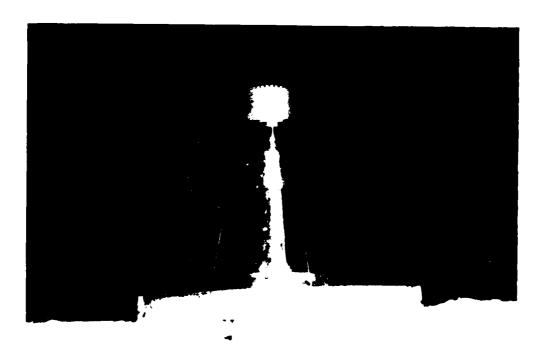


Figure K-2. Suppressor Nozzles Used for Aircraft Integration Case Studies.



- $\bullet \quad (AR)_O = 1.75$
- 40 Shallow Chutes

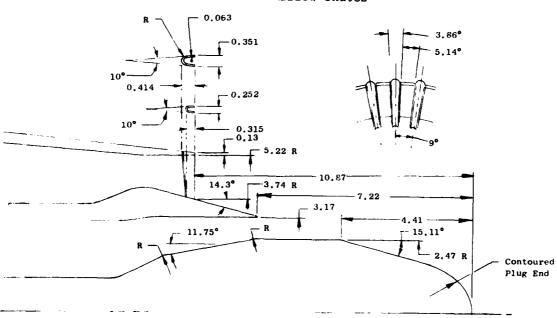
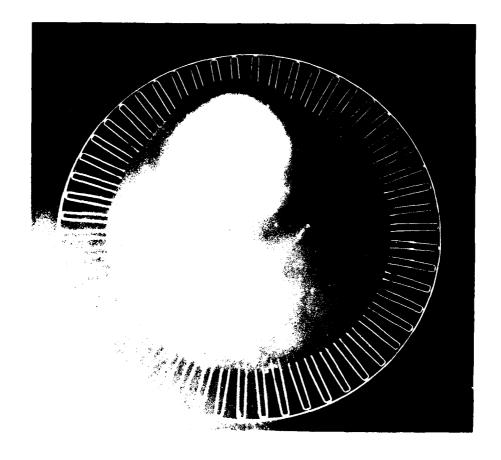


Figure K-2. Suppressor Nozzles Used for Aircraft Integration Case Studies (Continued).



• 54-Element Coplanar Mixer

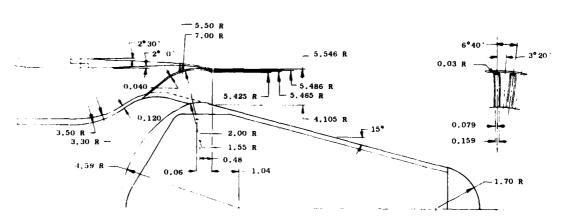
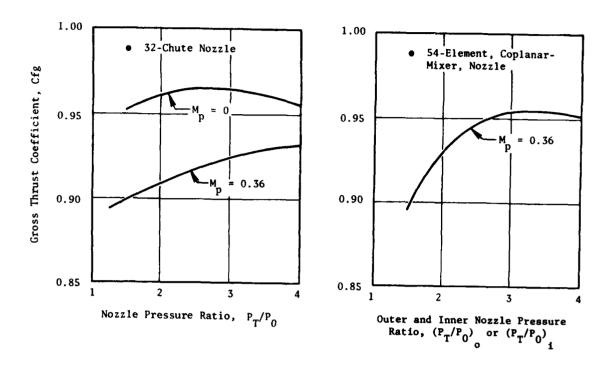


Figure K-2. Suppressor Nozzles Used for Aircraft Integration Case Studies (Concluded).



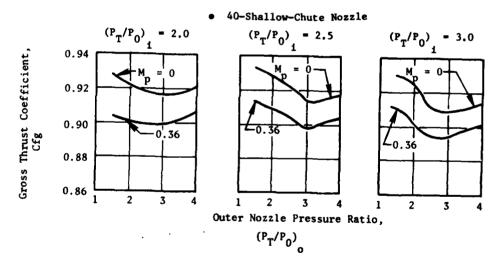


Figure K-3. Summary of Aerodynamic Performance Characteristics.

Til

The range versus noise characteristics for the three designs are summarized on Figure K-4. Fully mixed, conical-nozzle reference lines based on the procedure described in Section 4.0 are also presented. A range goal of 4000 nmi is selected in order to discuss the minimum noise which may be attained using these designs. To illustrate the maximum range attained, the maximum allowable traded noise level was set at 108 EPNdB which corresponds to FAR-36, 1969. The 32-chute nozzle (single flow) is applied to the turbojet and as a full-span suppressor on the variable-cycle engine, but the 40-shallow-chute and 54-element-coplanar-mixer nozzles (dual flow) are only applied to the variable-cycle engine.

Table K-2. Typical Exhaust System Weight Increase Due to the Addition of a Mechanical Suppressor.

Corrected Engine Airflow (1bm/sec) at SLS ⁽¹⁾	AR = 2.1, (2) 32-Chute Nozzle (1bm)	(AR) _o = 1.75, 40-Shallow(3) Chute Nozzle (1bm)	54-Element,(3) Coplanar Mixer (1bm)
800	1203	519	415
900	1386	597	477
1000	1573	678	542
1100	1764	760	608
1200	1958	844	675

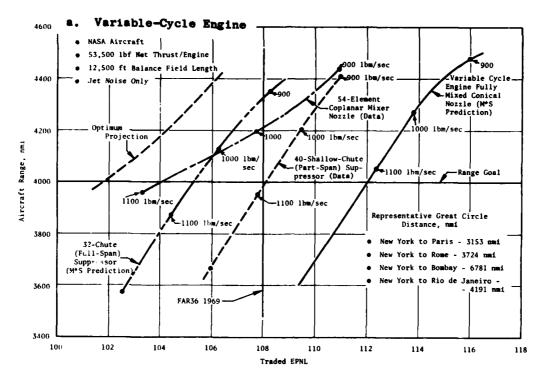
⁽¹⁾ Sea Level Static.

The maximum range of 4320 nmi, corresponding to the maximum allowable EPNL, was attained using the 32-chute, full-span suppressor installed on a variable-cycle engine. The lowest noise level achieved, while still attaining the 4000 nmi range goal, was 104 EPNL using the 54-element, coplanar mixer. The improvement using the coplanar mixer over the 40-shallow-chute nozzle was due to the superior suppression characteristics of the 54-element, coplanar-mixer nozzle at lower jet velocity and the fact that this suppressor maintains effectiveness in flight. The poorer range characteristics of the 32-chute nozzle on the advanced turbojet are due to the differences between the range characteristics of the turbojet and variable-cycle engines.

Overall, these case studies have demonstrated that traded FAR-36 levels of approximately 104 EPNL and a range of 4000 nmi may be achieved based on jet noise considerations only (assuming no margin).

⁽²⁾ This suppressor is applied to a turbojet as well as a variable-cycle engine.

⁽³⁾ These suppressors are applied to a variable-cycle engine.



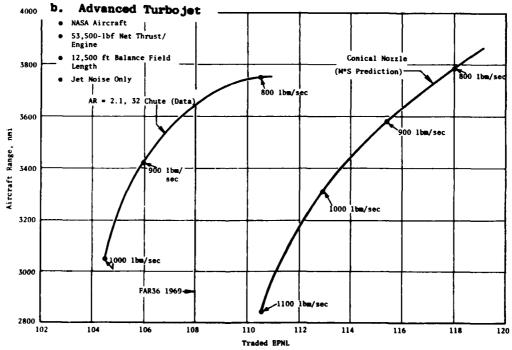


Figure K-4. Summary of Noise and Range Characteristics.

The preceding discussion has dealt with representative examples of the noise levels, performance levels, and weight increments which may be incurred when the nozzles evaluated in Reference 3 are implemented on advanced technology engines. However, the levels which may be achieved utilizing these designs are a strong function of the mission and thrust requirements for a given aircraft and do not represent a lower limit with regard to noise-suppression capability. Operational procedures, such as throttle cutback prior to the sideline and community monitoring points, climb-angle optimization, and unique engine/aircraft installations, may result in an additional 2 EPNdB reduction. Also, the levels of aerodynamic performance and acoustic suppression level may be improved. A dashed line indicating the projected noise level which may be achieved is also presented on Figure K-4.

APPENDIX L - NOMENCLATURE

A	Area (especially nozzle exhaust area)
A*	Throat area at Mach 1.0
$A_{\mathbf{A}}$	Minimum area between ejector lip and the exit of the outer row of tubes
A _a , A _o , C _o , c _o	Ambient speed of sound
$A_{\mathbf{b}}$	Baseplate projected area, A ₈ (AR - 1)
AR, NAR	Suppressor or dual-flow nozzle area ratio; for a suppressor it is determined by the total area (excluding any plug) to the flow area; for the dual-flow nozzle it is the outer-flow area to the inner-flow area (for suppressed, dual-flow nozzles see ${\rm AR}_{\rm S}$ and ${\rm AR}_{\rm N}$)
AR _{ej} , EAR	Ejector area ratio, minimum flow area of the ejector inlet to the flow area of the nozzle
AR_{N} , AR_{n}	Ratio of nozzle outer-flow area to nozzle inner-flow area for dual-flow nozzle
AR _s	Ratio of suppressor annulus area to suppressor flow area (especially for outer-flow-suppressed, dual-flow nozzles)
A_S	Area between tubes in outer row of suppressor
В	Angle from plug to suppressor exit plane, degrees
b	Linear regression analysis constant
C , c	Speed of sound
CD	Discharge coefficient
CDV	Real-gas correction to discharge coefficient
CD\delta	Geometric and Reynolds-number-dependent discharge coefficient
Cfg, C _{fg}	Gross thrust coefficient
CP _o	Outer-flow specific heat at constant pressure, Btu/lbm - ° R
cv, c _v	Nozzle velocity coefficient
D, d	Diameter; or drag

$ exttt{D}_{ exttt{t}}$	Total External Drag (viscous and pressure)
Daft	Afterbody drag
D _{eq}	Equivalent diameter, $2\sqrt{A_8/\pi}$
DR	Depth (length) of suppressor element on outer shroud
$\mathbf{D_h}$	Hydraulic Diameter
$\mathtt{DR}_{\mathbf{s}}$	Thickness of shroud at exit plane of suppressor
EAR	Ejector area ratio, Figure 5-1 (also see AR _{ej})
EGA	Extra ground attenuation
EPNL, E	Effective perceived noise level, EPNdB
F	Local axial momentum flux
f	Observer frequency
fp	Frequency at peak spectral noise level
Fg, F _g	Gross thrust minus afterbody drag, or engine ideal gross thrust
Fi, F _i , FID	Ideal gross thrust based on isentropic expansion of actual flow to ambient pressure
Н	Local stagnation enthalpy flux relative to free-stream value
HRO	Hydraulic radius
K	Constant; or conversion factor for base pressure
L	Length, especially ejector length
L _T , L _t	External tube length from baseplate
L _{ti}	Internal tube length
l	Characteristic length scale
M	Mach number
m	Slope of line, $[\Delta dB - 10 \log_{10} (1 - M_{D \cos \theta_{i}})]/\log_{10} V_{j}/VR$; or linear regression analysis constant
m (0 ₁)	Relative velocity index, m/10
M _c	Eddy convection Mach number
M _o	Local jet Mach number

Flight (or free-stream) Mach number

N Number of suppressor elements

Number of tubes in outer row of suppressor

NAR See AR

NPNL Normalized perceived noise level, PNdB

Overall sound power level, dB OAPWL

OASPL Overall sound pressure level, dB

P, p Pressure

P_h Area-averaged baseplate static pressure

PNL, P Perceived noise level, PNdB

Pressure ratio, PT/PO $PR, P_r, P/R$

Sound power level, dB Re: 10^{-13} watts PWL

Normalized, Doppler-shifted frequency

Radius; or distance from noise source to observer R

Radial coordinate; r

Reynolds number Re

Relative to or referenced to Re:

R/D Ratio of tube entrance radius to tube diameter

Ri; Inner-duct, inner radius

Inner-duct, outer radius Rio

Outer-duct, inner radius Ro i

Outer-duct, outer radius Roo

Rr, Rr Suppressor radius ratio, determined by the ratio of the inner

radius to the outer radius for the particular flow passage

Distance, especially minimum distance between tubes in outer

row of suppressor

Setback, distance between tube ends and ejector lip SB

SPL	Sound pressure level, dB
T	Temperature, ° R
t	Time
U	Mean jet velocity
u	Local axial velocity
ū	Local mean velocity
u'	Local turbulent velocity
v	Jet velocity, especially isentropic, fully expanded
v	Local transverse velocity
v_a , v_a , v_o , v_O	Flight (or free-stream) velocity
VP	Ventilation parameter
w	Weight flow rate
Wc _i , Wi _s	Inner-radius chute or spoke width
Wc _o , Wo _s	Outer-radius chute or spoke width
Wfi	Inner-radius flow width
Wfo	Outer-radius flow width
x	Axial distance
x	Axial coordinate
а	Base plane stagger angle
β	Cant angle; shock-noise parameter, $\sqrt{M^2-1}$; or ratio of outer to inner weight flow in dual-flow nozzles
γ	Ratio of specific heats
Δ	Differential quantity
ð	Effective thickness of fluid layer around a source
$oldsymbol{ heta}$	Angle, especially exit plane stagger angle
θ_{1}	Observation angle from inlet axis
$ heta_{ exttt{j}}$	Observation angle from jet axis

λ	Proportionality factor (mixing constant) or wavelength
μ	Viscosity
ν	Ratio of emission frequency to characteristic frequency
ρ	Density
τ	Turbulent shear stress
φ	Plug angle at chute or spoke exit plane
$\overline{\phi}$	Average plug angle under spoke or chute
Ψ	Cfg $(V_{ma}) - V_a$
ψ	Azimuth angle
ω	Source frequency; or density ratio exponent
ωσ	Characteristic frequency
∇	Gradient operator
Subscripts	•
a	Ambient or aircraft (free-stream)
B, b	Base
c	Convection; or chute
(cen)	Temperature expressed in Celsius (centigrade)
E, ej	Ejector
eff	Effective
eq	Equivalent dimension based on flow area, $\sqrt{4A/\pi}$
f	Flight
Н	Hard Wall
h	Hydraulic

Inlet; or inner stream of dual-flow nozzle

Internal

int

Jet (exhaust) J, j L Local Mass averaged ma Nozzle Outer row; outer stream; ambient; or local Pressure Peak; or plug Radial dimension; or angle expressed in radians Ref, ref Reference Static; shroud; or suppressor S, s Total; tube; or treated T, t Internal tube Ambient condition Condition at core (inner) stream throat Conditions at nozzle exit Conditions at outer flow throat 18

REFERENCES

- Clapper, W.S., et al., "High Velocity Jet Noise Source Location and Reduction - Task 3 - Experimental Investigation of Suppression Principles - Volume III - Suppressor Concepts Optimization, "General Electric Company, FAA-RD-76-79, III-III, December 1978.
- 2. Brausch, J.F. and Doyle, V.L., "Summary of GE4/SST Acoustic Suppression Research, Supersonic Transport Noise Reduction Technology Program, Phase I," General Electric Company, FAA-SS-72-42, December 1972.
- 3. Clapper, W.S., et al., "High Velocity Jet Noise Source Location and Reduction: Task 5 Investigation of 'Inflight' Acoustic Effects on Suppressed Exhausts," General Electric Company, FAA-RD-76-79, V, January 1979.
- 4. Hoch, R.G., Duponchel, J.J., Cocking, B.J., and Bryce, W.D., "Studies of the Influence of Density on Jet Noise," Journal of Sound and Vibration, Vol. 28, No. 4, 1973, pp. 649-668.
- 5. Knott, P.R., Brausch, J.F., Stringas, E.J., Staid, P.S., et al., "Acoustic Tests of Duct-Burning Turbofan Jet Noise Simulation," General Electric Company, NASA Contract Report 2966, July 1978.
- Clapper, W.S., et al., "High Velocity Jet Noise Source Location and Reduction: Task 4 Development/Evaluation of Techniques for Inflight Investigation," General Electric Company, FAA-RD-76-79, IV, February 22, 1977.
- 7. Knott, P.R., et al., "Acoustic and Performance Investigation of Coannular Plug Nozzles," General Electric Company, NASA Contract NAS3-19777, (to be published).
- 8. Bushell, K.W., "Measurement and Prediction of Jet Noise in Flight," AIAA Paper 75-461, presented at 2nd Aeroacoustic Conference, March 24-26, 1975.
- 9. Hay, J.A., "Lateral Noise Propagation," British Aircraft Corporation, Limited, Acoustic Report 526, April 21, 1977.
- Allan, R.D. and Joy, W., "Advanced Supersonic Propulsion Study, Phases III and IV - Final Report," General Electric Company, NASA CR-135236, November 30, 1977.
- 11. Atvars, J., Simcox, C.D., Armstrong, R.S., et al., "SST Technology Follow-On Program Phase II," Boeing Company, FAA-SS-73-11, March 1975.
- 12. Clapper, W.S., et al., "High Velocity Jet Noise Source Location and Reduction Task 3 Experimental Investigation of Suppression Principles, Volume I Verification of Suppression Principles and Development of Suppression Prediction Methods," General Electric Company Contractor Report FAA-RD-76-79, III-I, December 1978.

(462)

- 13. Sieckman, A., Motsinger, R.E., Gliebe, P.R., "High Velocity Jet Noise Source Location and Reduction: General Supplement Computer Programs; The Engineering Correlation (M*S) Jet Noise Prediction Method and Unified Aeroacoustic Prediction Model (M*G*B) for Nozzles of Arbitrary Shape," General Electric Company, FAA-RD-76-79, VIa, April 1979.
- 14. Mani, R., Stringas, E.J., et al., "High Velocity Jet Noise Source Location and Reduction - Task 2 - Theoretical Developments and Basic Experiments," General Electric Company Contractor Report FAA-RD-76-79, II, May 1978.
- 15. Gliebe, P.R., "High Velocity Jet Noise Source Location and Reduction Task 2 Supplement Computer Program for Calculating the Aeroacoustic Characteristics of Jets from Nozzles of Arbitrary Shape," General Electric Company Contractor Report FAA-RD-76-79, IIa, May, 1978.
- 16. Blumenthal, V.L., et al., "Summary Noise Reduction Research and Development," The Boeing Company, Report D6-60146, November 1971.
- 17. Armstrong, R.S., Atvars, J., Fullerton, C.R., and Wright, C.P., "SST Technology Follow-On Program Phase II Noise Suppressor/Nozzle Development, Volume X Advanced Suppressor Concepts and Full Scale Tests," Boeing Commercial Airplane Company, Report No. FAA-SS-73-11-10, March 1975.
- 18. Kazin, S.B., Stringas, E.J., Doyle, V.L., et al., "Supersonic Transport Noise Reduction Technology Program, Phase II," General Electric Company, FAA-SS-73-29-1 Volume 1, September 1975.
- 19. Clapper, W.S., et al. "High Velocity Jet Noise Source Location and Reduction, Task 3 Experimental Investigation of Suppression Principles, Volume II Parametric Testing and Source Measurements," General Electric Company, FAA-RD-76-79, III-II, December 1978.
- 20. Burley, R.R., "Suppressor Nozzle and Airframe Noise Measurements During Flyover of a Modified F-106B Aircraft with Underwing Nacelles," NASA TM X-71578, 1974.
- 21. Morden, D.B. and Armstrong, R.S., "SST Technology Follow-On Program Phase II Noise Suppressor/Nozzle Development Volume VIII Multitube Suppressor Ejector Interaction Effects on Static Performance (Ambient and 1150° F Jet Temperatures), "Boeing Company, FAA-SS-73-11-8, March 1975.
- 22. Morden, D.B., and Armstrong, R.S., "SST Technology Follow-On Program Phase II Noise Suppressor/Nozzle Development Volume VII Performance Technology Static Performance: Trends and Trades," Boeing Company, FAA-SS-73-11-7, March 1975.
- 23. Morden, D.B. and Armstrong, R.S., "SST Technology Follow-On Program Phase II Noise Suppressor/Nozzle Development Volume IX Performance Technology Analysis of the Low-Speed Performance of Multitube Suppressor/Ejector Nozzles (0-167 KN)," Boeing Company, FAA-SS-73-11-9, March 1975.

481

- 24. Chamberlin, R., "Flyover and Static Tests to Study Flight Velocity Effects on Jet Noise of Suppressed and Unsuppressed Plug Nozzle Configurations," NASA TM X-2856, 1973.
- 25. Lighthill, M.J., "On Sound Generated Aerodynamically, I. General Theory," Proceedings of the Royal Society of London, Vol. A211, 1952, pp. 564-587.
- 26. Ribner, H.S., "Aerodynamic Sound From Fluid Dilatations A Theory of the Sound from Jets and Other Flows," UTIA Report No. 86, July 1962.
- 27. Ffowcs-Williams, J.E., "The Noise From Turbulence Convected at High Speed," Phil. Trans. Roy. Soc. Lond., Vol. A255, 1963, pp. 469-503.
- 28. Ahuja, K.K. and Bushell, K.W., "An Experimental Study of Subsonic Jet Noise and Comparison with Theory," Journal of Sound and Vibration, Vol. 30. No. 3, 1973, pp. 317-341.
- 29. Lush, P.A., 'Measurements of Subsonic Jet Noise and Comparison with Theory," Journal of Fluid Mechanics, Vol. 46, Part 3, 1971, pp. 477-500.
- 30. Hoch, R.G., Duponchel, J.P., Cocking, B.J., and Bryce, W.D., "Studies of the Influence of Density on Jet Noise," Journal of Sound and Vibration, Vol. 28, No. 4, 1973, pp. 649-668.
- 31. Phillips, O.M., "On the Generation of Sound by Supersonic Turbulent Shear Layers," Journal of Fluid Mechanics, Vol. 9, 1960, pp. 1-28.
- 32. Lilley, G.M., Morris, P.J., and Tester, B.J., "On the Theory of Jet Noise and Its Applications," AIAA paper No. 73-987, October 1973.
- 33. Goldstein, M.E. and Howes, W.L., "New Aspects of Subsonic Aerodynamic Noise Theory," NASA TN D-7158, 1973.
- 34. Pao, S.P., "Analytical Properties of Noise Generating Mechanisms in a Supersonic Jet Exhaust Flow," NASA CR-1848, May 1971.
- 35. Tester, B.J. and Burrin, R.H., "On Sound Radiation from Sources in Parallel Sheared Jet Flows," AIAA Paper No. 74-57, January 1974.
- 36. Berman, C.H., 'Noise From Nonuniform Turbulent Flows," AIAA Paper No. 74-2, January 1974.
- 37. Schubert, L.K., "Numerical Solution of Sound Refraction by Jet Flow, Parts I and II," Journal of the Acoustical Society of America, Vol. 51, No. 2, 1972, pp. 439-463.
- 38. Powell, A., "Concerning the Noise of Turbulent Jets," Journal of the Acoustical Society of America, Vol. 32, No. 12, 1960, pp. 1609-1612.
- 39. Csanady, G.T., "The Effects of Mean Velocity Variations on Jet Noise," Journal of Fluid Mechanics, Vol. 26, Part 1, 1966, pp. 183-197.
- 40. Mani, R., "A Moving Source Problem Relevant to Jet Noise," Journal of Sound and Vibration, Vol. 25, No. 2, 1972, pp. 337-347.

- Mani, R., "Further Studies on Moving Source Solutions Relevant to Jet Noise," Journal of Sound and Vibration, Vol. 35, No. 1, 1974, pp. 101-117.
- 42. Mani, R., "The Jet Density Exponent Issue for the Noise of Heated Subsonic Jets," Journal of Fluid Mechanics, Vol. 64, Part 3, 1974, pp. 611-622.
- 43. Mani., R., "The Influence of Jet Flow on Jet Noise, Part 1. The Noise of Unheated Jets," Journal of Fluid Mechanics, Vol. 73, Part 4, 1976, pp. 753-778.
- 44. Mani, R., "The Influence of Jet Flow on Jet Noise, Part 2. The Noise of Heated Jets," Journal of Fluid Mechanics, Vol. 73, Part 4, 1976, pp. 779-793.
- 45. Harper-Bourne, M., and Fisher, M.J., "The Noise From Shock Waves in Supersonic Jets," NATO, AGARD Conference Paper No. CPP-131, 1973.
- 46. Drevit, P., Duponchel, J.P., and Jacques, J.R., "Effect of Flight on the Noise From a Convergent Nozzle as Observed on the Bertin Aerotrain," AIAA paper No. 76-557, July 1976.
- 47. Siddon, T.E., "Investigations of Nozzle Lip Noise," Interim Progress Report, University of British Columbia, Department of Mechanical Engineering, UBC-GE/DOT OS-30034, June 1975.
- 48. Browand, F.K., Chu, W.T., and Laufer, J., "Exploratory Experiments on the Entrance Effects in Subsonic Jet Flows," University of Southern California, Department of Aerospace Engineering Report No. USCAE 130, April 1975.
- 49. Reichardt, H., "New Theory of Free Turbulence," Royal Aeronautical Society Journal, Vol. 47, 1943, pp. 167-196.
- 50. Alexander, L.G., Baron, T., Comings, W., "Transport of Momentum, Mass and Heat in Turbulent Jets," University of Illinois Engineering Bulletin No. 413, May 1953.
- 51. Lee, R., Kendall, R., et al., "Research Investigation of the Generation and Suppression of Jet Noise," General Electric, NOas-59-6160-C, ASTIA No. AD-251887, 1961.
- 52. Grose, R.D. and Kendall, R.M., "Theoretical Predictions of the Sound Produced by Jets Having an Aribtrary Cross-Section," ASME Symposium on Fully Separated Flows, May 1964.
- 53. Gliebe, P.R. and Balsa, T.F., "The Aerodynamics and Acoustics of Coaxial Jet Noise," AIAA paper No. 76-492, July 1976.
- 54. Balsa, T.F., "Fluid Shielding of Low Frequency Convected Sources by Arbitrary Jets," Journal of Fluid Mechanics, Vol. 70, Part 1, 1975, pp. 17-36.



- 55. Balsa, T.F., "The Shielding of a Convected Source by an Annular Jet with an Application to the Performance of Multitube Suppressors," Journal of Sound and Vibration, Volume 44, No. 2, 1976, pp. 179-189.
- 56. Balsa, T.F., "The Far Field of High Frequency Convected Singularities in Sheared Flows, With Application to Jet-Noise Prediction," Journal of Fluid Mechanics, Vol. 74, Part 2, 1976, pp. 193-208.
- 57. Davies, P.O.A.L., Fisher, M.J., and Barratt, M.J., "The Characteristics of the Turbulence in the Mixing Region of a Round Jet," Journal of Fluid Mechanics, Vol. 15, 1963, pp. 337-367.
- 58. Ribner, H.S., "Quadrupole Correlations Governing the Pattern of Jet Noise," Journal of Fluid Mechanics, Vol. 38., Part 1, 1969, pp. 1-24.
- 59. Ribner, H.S., "Shock-Turbulence Interaction and the Generation of Noise," NACA report No. 1233, 1955.
- 60. Simcox, C.D., et al., "SST Technology Follow-On Program Phase 1-A Summary of the SST Jet Noise Suppression Test Program," Boeing Company, FAA-SS-72-41, February 1972.
- 61. Hawkins, R. And Hoch, R., "Studies into Concorde's Engine Noise Reduction," NATO, AGARD-CPP-131, 1973.
- 62. Savell, C.T., Stringas, E.J., et al., "High Velocity Jet Noise Source Location and Reduction Task 1 Activation of Facilities and Validation of Source Location Techniques," General Electric Company, FAA-RD-76-79, I, February 1977.
- 63. Savell, C.T., Stringas, E.J., et al., "High Velocity Jet Noise Source Location and Reduction Task 1 Supplement Certification of the General Electric Jet Noise Anechoic Test Facility," General Electric Company, FAA-RD-76-79, Ia, February 1977.
- 64. Anon, "Interim Report of Subcommittee on SST Noise Prediction Methods," ICAO Working Group E, March 21, 1978.
- 65. Drevit, P., et al, "Effect of Flight on the Noise from a Convergent Conical Nozzle as Observed on the Bertin Aerotrain," AIAA paper No. 76-557, July 1976.
- 66. The Boeing Co., "Quarterly Progress Report, April-June 1973," SST Follow-On Program Phase II, Contract DOT-FA-72-WA-2893.
- 67. Atvars, J., Wright, C.P., and Simcox, C.D., "SST Technology Follow-On Program Phase II Noise Suppressor/Nozzle Development, Volume II Noise Technology," Boeing Commercial Airplane Company Report No. FAA-SS-73-11-2, March 1975.
- 68. Love, E.S. and Grigsby, G.E., "Some Studies of Axisymmetric Freejets Exhausting From Sonic and Supersonic Nozzles into Still Air and into

Supersonic Streams," NACA RM L54L31, May 1955

- 69. Hobbs, J.L., "Pressure Loss Computations in Incompressible Fluid Flow," APEX-754, July 25, 1961.
- 70. Anon, "Advanced Supersonic Technology Concept Study Reference Characteristics," LTV, NASA CR-132374, December 12, 1973.

ALL

485

DATE FILMED OF STREET

DTIC